A High Angular Resolution Survey of Circumstellar Dust around Herbig Ae/Be stars

by

Marshall Dimsey Perrin

A.B. (Harvard University) 2000
M.A. (University of California, Berkeley) 2002

A dissertation submitted in partial satisfaction of the
requirements for the degree of
Doctor of Philosophy

in

Astrophysics

in the

GRADUATE DIVISION
of the
UNIVERSITY OF CALIFORNIA, BERKELEY

Committee in charge:
Professor James R. Graham, Chair
Professor Geoffrey W. Marcy
Professor Eugene Chiang
Professor Reinhard Genzel

Fall 2006

The dissertation of Marshall Dimsey Perrin is approved:

Chair Date

Date

Date

Date

University of California, Berkeley

Fall 2006

A High Angular Resolution Survey of
Circumstellar Dust around Herbig Ae/Be stars

Copyright 2006
by
Marshall Dimsey Perrin

Abstract

A High Angular Resolution Survey of
Circumstellar Dust around Herbig Ae/Be stars

by

Marshall Dimsey Perrin
Doctor of Philosophy in Astrophysics

University of California, Berkeley

Professor James R. Graham, Chair

This thesis presents the development of a sensitive near-infrared differential imaging polarimeter, and its subsequent use, combined with mid infrared imaging, to survey circumstellar dust around 110 Herbig Ae/Be stars.

Planets are born in dusty circumstellar disks around young stars. By imaging such disks we can learn about the environment and physical processes that assemble planets from primordial dust and gas. But these observations are challenging on account of the high angular resolution and high dynamic range necessary to detect the disk's faint reflected light against a far brighter background of stellar light.

One powerful method for obtaining the necessary contrast is the use of differential polarimetry to separate polarized dust-scattered light from unpolarized starlight. For this reason, I have developed a differential polarimetry mode for IRCAL, the adaptive optics science camera at Lick Observatory, which uses a YLF Wollaston prism beamsplitter to attenuate 98-99% of stellar light. I describe this instrument, summarize the data reduction and image analysis algorithms employed, and discuss lessons learned for future high-contrast imaging systems. A second strategy for high contrast science is to obtain observations at mid-infrared wavelengths, where dust is bright and stellar light is comparatively faint. These two techniques are complimentary, respectively probing scattered and thermal light, and their multiwavelength combination can help constrain numerical models of circumstellar disks and envelopes.

I have obtained near-IR adaptive optics imaging polarimetry and mid-IR imaging of a large sample of Herbig Ae/Be stars; 110 targets were observed with AO polarimetry and 61 with mid-IR imaging. Of these stars, 40 are found to have extended polarized nebulosity arising from scattered light. The dust geometry is highly variable, ranging from circumstellar disks to envelopes split by bipolar outflow cavities to complex arcs and lanes of dust spiraling around and between stars. I present detailed studies of a subset of these objects, including laser guide star AO observations of disks and envelopes around the stars LkHα 198 and LkHα 233; the discovery of the first resolved edge-on circumstellar disk around a Herbig Ae/Be star, PDS 144 N; and integral field spectroscopy of a narrowly collimated bipolar outflow from LkHα 233. I conclude by discussing future prospects for advances in the studies of circumstellar disks with the coming generation of high contrast instruments.

Professor James R. Graham
Dissertation Committee Chair

For my grandmother, Eileen,

whose love of family and tireless support for education
are a treasure and an inspiration.

Contents

List of Figures viii

List of Tables xiv

Acknowledgments xv

I A Survey of Circumstellar Dust around Herbig Ae/Be Stars 1

1 Introduction 2
1.1 Circumstellar Disks: the Nursery of Worlds . . . 2
1.2 Herbig Ae/Be Stars . . . 3
1.2.1 Classifications based on Spectral Energy Distributions . . . 5
1.2.2 Other Related Classifications of Herbig Ae/Be stars . . . 6
1.3 High Contrast, High Angular Resolution Imaging . . . 7
1.4 Thesis Overview . . . 8

2 Design and Calibration of the Lick Observatory Adaptive Optics Imaging Polarimeter 10
2.1 Introduction . . . 10
2.2 A Brief Review of Polarimetry Fundamentals . . . 12
2.3 Design & Implementation . . . 14
2.3.1 Choice of materials . . . 16
2.3.2 Final details and construction . . . 18
2.4 Observing Techniques and Data Reduction . . . 21
2.5 Performance . . . 22
2.5.1 Image Quality . . . 22
2.5.2 Polarizing Efficiency and Throughput . . . 23
2.5.3 Non-common Path Optical Errors . . . 24
2.6 Astronomical Calibration . . . 24
2.6.1 Darks. . . . 24
2.6.2 Flat fielding . . . 24

2.6.3 Polarization Angle Calibration . . . 25
2.6.4 Sky Subtraction . . . 27
2.6.5 Instrumental Polarization . . . 27
2.6.6 Pixel Scale . . . 29
2.6.7 Photometry. . . . 30
2.7 Astronomical demonstration data . . . 31
2.8 Conclusions . . . 31

3 The Challenges of Differential Polarimetric Data Reduction 37
3.1 Introduction . . . 37
3.2 Sources of Noise . . . 38
3.3 General Considerations . . . 41
3.4 The IRCAL Polarimetry Data Reduction Package . . . 43
3.4.1 Calibration Requirements . . . 43
3.4.2 Initial Reduction Process . . . 43
3.4.3 Saturation Masking . . . 44
3.4.4 Registration . . . 44
3.4.5 Mosaicing . . . 46
3.5 Detection of polarized light in reduced images . . . 48
3.6 Achieved Performance . . . 50
3.7 Conclusions . . . 52

4 A Near- and Mid-Infrared Survey of Dust around Herbig Ae/Be Stars 54
4.1 Introduction . . . 54
4.2 Methodology . . . 56
4.2.1 Near-Infrared Imaging Polarimetry . . . 56
4.2.2 Mid-Infrared Imaging . . . 57
4.2.3 Target Selection . . . 58
4.3 Observations and Data Reduction . . . 59
4.3.1 Near-IR AO Imaging Polarimetry . . . 59
4.3.2 Mid-Infrared Imaging . . . 60
4.4 Summary of Observation Results . . . 63
4.5 Results for Individual Herbig Ae/Be Stars . . . 67
4.5.1 HBC 1 . . . 68
4.5.2 HBC 324 . . . 70
4.5.3 MQ Cas . . . 70
4.5.4 LkHα 198 . . . 71
4.5.5 V376 Cas . . . 72
4.5.6 VX Cas . . . 77
4.5.7 CDS 50 . . . 77
4.5.8 RNO 1 . . . 77
4.5.9 RNO 1BC . . . 79

4.5.10 V594 Cas . . . 81
4.5.11 LkHα 201 . . . 84
4.5.12 HBC 334 . . . 84
4.5.13 AFGL 4029 . . . 86
4.5.14 V1185 Tau . . . 87
4.5.15 IP Per . . . 87
4.5.16 XY Per . . . 91
4.5.17 V892 Tau . . . 91
4.5.18 LkHα 101 . . . 93
4.5.19 AB Aur . . . 93
4.5.20 MWC 480 . . . 97
4.5.21 UX Ori . . . 97
4.5.22 NSV 1832 . . . 98
4.5.23 HD 35187 . . . 99
4.5.24 V346 Ori . . . 99
4.5.25 CO Ori . . . 99
4.5.26 MWC 758 . . . 104
4.5.27 HK Ori . . . 104
4.5.28 HD 36408 . . . 105
4.5.29 T Ori . . . 105
4.5.30 CQ Tau . . . 107
4.5.31 V380 Ori . . . 108
4.5.32 BF Ori . . . 108
4.5.33 HD 245906 . . . 108
4.5.34 RR Tau . . . 112
4.5.35 MWC 120 . . . 112
4.5.36 MWC 778 . . . 114
4.5.37 HD 249879 . . . 115
4.5.38 HD 250550 . . . 115
4.5.39 LkHα 208 . . . 115
4.5.40 MWC 137 . . . 118
4.5.41 NSV 2968 . . . 119
4.5.42 VY Mon . . . 119
4.5.43 LkHα 215 . . . 121
4.5.44 HD 259431 . . . 124
4.5.45 R Mon . . . 125
4.5.46 LkHα 25 . . . 125
4.5.47 HD 52721 . . . 127
4.5.48 Z CMa . . . 129
4.5.49 PDS 241 . . . 129
4.5.50 DW CMa . . . 132

4.5.51 PDS 144 . . . 133
4.5.52 HD 141569 . . . 133
4.5.53 HD 142666 . . . 136
4.5.54 HD 144432 . . . 136
4.5.55 HD 145718 . . . 136
4.5.56 PDS 415 . . . 140
4.5.57 HD 150193 . . . 140
4.5.58 KK Oph . . . 141
4.5.59 PDS 453 . . . 143
4.5.60 PDS 469 . . . 145
4.5.61 HD 163296 . . . 145
4.5.62 PDS 477 . . . 145
4.5.63 LkHα 118 . . . 149
4.5.64 HD 169142 . . . 149
4.5.65 MWC 297 . . . 150
4.5.66 VV Ser . . . 150
4.5.67 MWC 300 . . . 154
4.5.68 PDS 520 . . . 154
4.5.69 AS 310 . . . 154
4.5.70 PDS 530 . . . 157
4.5.71 PDS 543 . . . 159
4.5.72 MWC 610 . . . 159
4.5.73 PDS 551 . . . 159
4.5.74 HD 179218 . . . 163
4.5.75 WW Vul . . . 163
4.5.76 PX Vul . . . 166
4.5.77 Parsamian 21 . . . 167
4.5.78 HD 190073 . . . 167
4.5.79 HBHA 3203-03 . . . 167
4.5.80 BD +40 4124 . . . 171
4.5.81 LkHα 224 . . . 171
4.5.82 LkHα 225 . . . 173
4.5.83 V1515 Cyg . . . 176
4.5.84 BD +41 3731 . . . 176
4.5.85 Parsamian 22 . . . 176
4.5.86 MWC 349 . . . 180
4.5.87 AS 442 . . . 181
4.5.88 LkHα 134 . . . 181
4.5.89 LkHα 147 . . . 185
4.5.90 V1057 Cyg . . . 186
4.5.91 LkHα 120 . . . 186

4.5.92 HD 200775 . . . 187
4.5.93 LkHα 324 . . . 187
4.5.94 LkHα 324 SE . . . 191
4.5.95 HD 203024 . . . 191
4.5.96 LkHα 349c . . . 193
4.5.97 V645 Cyg . . . 195
4.5.98 V361 Cep . . . 197
4.5.99 LkHα 234 . . . 197
4.5.100 AS 477 . . . 200
4.5.101 LkHα 257 . . . 203
4.5.102 BH Cep . . . 203
4.5.103 BO Cep . . . 204
4.5.104 SV Cep . . . 204
4.5.105 LkHα 233 . . . 207
4.5.106 HD 216629 . . . 210
4.5.107 V374 Cep . . . 211
4.5.108 MWC 1080 . . . 211
4.5.109 BM And . . . 213
4.5.110 LkHα 259 . . . 216
4.6 Other Sources Observed . . . 216
4.6.1 PDS 465 (Hen 3-1475) . . . 216
4.6.2 MWC 922 . . . 218
4.6.3 PDS 581 (M1-92) . . . 218
4.7 Discussion . . . 220
4.7.1 Quantifying the Detection of Polarized Light . . . 220
4.7.2 Observed Source Morphologies . . . 224
4.7.3 Quantifying the Detection of Barely-resolved Mid-IR Sources . . . 228
4.7.4 Correlations with Stellar Properties . . . 229
4.7.5 The Effects of Binarity . . . 231
4.8 Conclusions . . . 234

II Studies of Individual Stars 238

5 Laser Guide Star Adaptive Optics Imaging Polarimetry of LkHα 198 and LkHα 233 239
5.1 Introduction . . . 239
5.2 LkHα 198 . . . 241
5.3 LkHα 233 . . . 243
5.4 Discussion . . . 244
5.5 Methods and Materials . . . 246

6 Discovery of an Optically Thick, Edge-on Disk around the Herbig Ae star PDS 144N 250
6.1 Introduction . . . 251
6.2 Observations . . . 253
6.2.1 Lick . . . 253
6.2.2 Keck . . . 256
6.2.3 Spitzer . . . 257
6.2.4 Spectral Energy Distribution . . . 259
6.3 The Distance to PDS 144 . . . 260
6.4 Disk morphology . . . 264
6.4.1 Basic Appearance . . . 264
6.4.2 The "wings" . . . 265
6.4.3 Disk Truncation? . . . 266
6.4.4 PAH emission . . . 267
6.4.5 The Mid Infrared . . . 268
6.4.6 PDS 144 South . . . 269
6.5 Preliminary Disk Models . . . 270
6.6 Conclusions . . . 272

7 A Tightly Collimated Bipolar Jet from the Herbig Ae star LkHα 233 275
7.1 Introduction . . . 275
7.2 Observations . . . 277
7.3 Results . . . 279
7.3.1 Mass Flux . . . 281
7.4 Discussion . . . 283

8 Conclusions 285
8.1 Principal Results . . . 285
8.2 Looking toward the future . . . 286

A An Updated Catalog of Herbig Ae/Be Stars 313

B Observations Log 322

C Point Source Photometry 328

List of Figures

2.1 Axes conventions for polarimetry . . . 13
2.2 Diagram of a Wollaston prism . . . 15
2.3 The IRCAL YLF Wollaston . . . 18
2.4 IRCAL with waveplate mechanism . . . 20
2.5 Position Angle Calibration, 2002-206 . . . 26
2.6 AO Imaging polarimetry of the unpolarized standard HD 18803 . . . 32
2.7 AO Imaging polarimetry of Uranus . . . 33
2.8 Transmission of crossed prism and Polaroid. . . . 35

3.1 Example Stokes Parameter Images . . . 49
3.2 Unpolarized Light Suppression Performance . . . 51

4.1 Survey observational completeness . . . 60
4.2 Portrait Gallery: Imaging Polarimetry of HAEBEs . . . 65
4.3 Portrait Gallery: Mid-Infrared Imaging of HAEBEs . . . 66
4.4 AO Imaging polarimetry of HBC 1 . . . 69
4.5 Mid-IR Imaging of HBC 1 . . . 69
4.6 AO Imaging polarimetry of HBC 324 . . . 70
4.7 AO Imaging polarimetry of MQ Cas . . . 71
4.8 AO Imaging polarimetry of LkHα 198 . . . 73
4.9 Mid-IR Imaging of LkHα 198 . . . 74
4.10 AO Imaging polarimetry of V376 Cas . . . 75
4.11 Mid-IR Imaging of V376 Cas . . . 76
4.12 AO Imaging polarimetry of VX Cas . . . 78
4.13 Mid-IR Imaging of VX Cas . . . 78
4.14 AO Imaging polarimetry of CDS 50 . . . 79
4.15 AO Imaging polarimetry of RNO 1 . . . 80
4.16 AO Imaging polarimetry of RNO 1B and 1C . . . 82
4.17 Mid-IR Imaging of RNO 1B and 1C . . . 82
4.18 AO Imaging polarimetry of V594 Cas . . . 83
4.19 Mid-IR Imaging of V594 Cas . . . 83

4.20 AO Imaging polarimetry of LkHα 201 . . . 84
4.21 AO Imaging polarimetry of HBC 334 . . . 85
4.22 AO Imaging polarimetry of AFGL 4029 . . . 87
4.23 Mid-IR Imaging of AFGL 4029 . . . 88
4.24 AO Imaging polarimetry of V1185 Tau . . . 89
4.25 AO Imaging polarimetry of IP Per . . . 90
4.26 Mid-IR Imaging of IP Per . . . 90
4.27 AO Imaging polarimetry of XY Per . . . 92
4.28 Mid-IR Imaging of XY Per . . . 92
4.29 AO Imaging polarimetry of V892 Tau . . . 94
4.30 Mid-IR Imaging of V892 Tau . . . 94
4.31 AO Imaging polarimetry of LkHα 101 . . . 95
4.32 AO Imaging polarimetry of AB Aur . . . 96
4.33 Mid-IR Imaging of AB Aur . . . 96
4.34 AO Imaging polarimetry of MWC 480 . . . 97
4.35 AO Imaging polarimetry of UX Ori . . . 98
4.36 AO Imaging polarimetry of NSV 1832 . . . 100
4.37 Mid-IR Imaging of NSV 1832 . . . 100
4.38 AO Imaging polarimetry of HD 35187 . . . 101
4.39 Mid-IR Imaging of HD 35187 . . . 101
4.40 AO Imaging polarimetry of V346 Ori . . . 102
4.41 AO Imaging polarimetry of CO Ori . . . 103
4.42 AO Imaging polarimetry of MWC 758 . . . 104
4.43 AO Imaging polarimetry of HK Ori . . . 105
4.44 AO Imaging polarimetry of HD 36408 . . . 106
4.45 AO Imaging polarimetry of T Ori . . . 106
4.46 AO Imaging polarimetry of CQ Tau . . . 107
4.47 AO Imaging polarimetry of V380 Ori . . . 109
4.48 AO Imaging polarimetry of BF Ori . . . 110
4.49 AO Imaging polarimetry of HD 245906 . . . 111
4.50 AO Imaging polarimetry of RR Tau . . . 112
4.51 AO Imaging polarimetry of MWC 120 . . . 113
4.52 AO Imaging polarimetry of MWC 778 . . . 116
4.53 Mid-IR Imaging of MWC 778 . . . 116
4.54 AO Imaging polarimetry of HD 249879 . . . 117
4.55 AO Imaging polarimetry of HD 250550 . . . 117
4.56 AO Imaging polarimetry of LkHα 208 . . . 118
4.57 AO Imaging polarimetry of MWC 137 . . . 119
4.58 AO Imaging polarimetry of NSV 2968 . . . 120
4.59 AO Imaging polarimetry of VY Mon . . . 122
4.60 Mid-IR Imaging of VY Mon . . . 122

4.61 AO Imaging polarimetry of LkHα 215 . . . 123
4.62 AO Imaging polarimetry of HD 259431 . . . 124
4.63 AO Imaging polarimetry of R Mon . . . 126
4.64 Mid-IR Imaging of R Mon . . . 126
4.65 AO Imaging polarimetry of LkHα 25 . . . 127
4.66 AO Imaging polarimetry of HD 52721 . . . 128
4.67 AO Imaging polarimetry of Z CMa . . . 130
4.68 AO Imaging polarimetry of PDS 241 . . . 131
4.69 Mid-IR Imaging of PDS 241 . . . 131
4.70 AO Imaging polarimetry of DW CMa . . . 132
4.71 Mid-IR Imaging of DW CMa . . . 133
4.72 AO Imaging polarimetry of PDS 144 . . . 134
4.73 Mid-IR Imaging of PDS 144 . . . 134
4.74 AO Imaging polarimetry of HD 141569 . . . 135
4.75 Mid-IR Imaging of HD 141569 . . . 135
4.76 AO Imaging polarimetry of HD 142666 . . . 137
4.77 Mid-IR Imaging of HD 142666 . . . 137
4.78 AO Imaging polarimetry of HD 144432 . . . 138
4.79 Mid-IR Imaging of HD 144432 . . . 138
4.80 AO Imaging polarimetry of HD 145718 . . . 139
4.81 Mid-IR Imaging of HD 145718 . . . 139
4.82 AO Imaging polarimetry of PDS 415 . . . 140
4.83 AO Imaging polarimetry of HD 150193 . . . 141
4.84 AO Imaging polarimetry of KK Oph . . . 142
4.85 Mid-IR Imaging of KK Oph . . . 143
4.86 AO Imaging polarimetry of PDS 453 . . . 144
4.87 AO Imaging polarimetry of PDS 469 . . . 146
4.88 AO Imaging polarimetry of HD 163296 . . . 147
4.89 Mid-IR Imaging of HD 163296 . . . 147
4.90 AO Imaging polarimetry of PDS 477 . . . 148
4.91 Mid-IR Imaging of PDS 477 . . . 148
4.92 AO Imaging polarimetry of LkHα 118 . . . 149
4.93 AO Imaging polarimetry of HD 169142 . . . 151
4.94 Mid-IR Imaging of HD 169142 . . . 151
4.95 AO Imaging polarimetry of MWC 297 . . . 152
4.96 Mid-IR Imaging of MWC 297 . . . 152
4.97 AO Imaging polarimetry of VV Ser . . . 153
4.98 Mid-IR Imaging of VV Ser . . . 153
4.99 AO Imaging polarimetry of MWC 300 . . . 155
4.100 Mid-IR Imaging of MWC 300 . . . 155
4.101 AO Imaging polarimetry of PDS 520 . . . 156

4.102 Mid-IR Imaging of PDS 520 . . . 156
4.103 AO Imaging of AS 310 . . . 158
4.104 Mid-IR Imaging of AS 310 . . . 158
4.105 AO Imaging polarimetry of PDS 530 . . . 160
4.106 Mid-IR Imaging of PDS 530 . . . 160
4.107 AO Imaging polarimetry of PDS 543 . . . 161
4.108 AO Imaging polarimetry of MWC 610 . . . 162
4.109 Mid-IR Imaging of MWC 610 . . . 162
4.110 AO Imaging polarimetry of PDS 551 . . . 163
4.111 AO Imaging polarimetry of HD 179218 . . . 164
4.112 Mid-IR Imaging of HD 179218 . . . 164
4.113 AO Imaging polarimetry of WW Vul . . . 165
4.114 AO Imaging polarimetry of PX Vul . . . 166
4.115 AO Imaging polarimetry of Parsamian 21 . . . 168
4.116 Mid-IR Imaging of Parsamian 21 . . . 168
4.117 AO Imaging polarimetry of HD 190073 . . . 169
4.118 Mid-IR Imaging of HD 190073 . . . 169
4.119 AO Imaging polarimetry of HBHA 3203-03 . . . 170
4.120 AO Imaging polarimetry of BD +40 4124 . . . 172
4.121 Mid-IR Imaging of BD +40 4124 . . . 172
4.122 AO Imaging polarimetry of LkHα 224 . . . 174
4.123 Mid-IR Imaging of LkHα 224 . . . 174
4.124 AO Imaging polarimetry of LkHα 225 . . . 177
4.125 Mid-IR Imaging of LkHα 225 . . . 177
4.126 AO Imaging polarimetry of V1515 Cyg . . . 178
4.127 AO Imaging polarimetry of BD +41 3731 . . . 178
4.128 AO Imaging polarimetry of Parsamian 22 . . . 179
4.129 Mid-IR Imaging of Parsamian 22 . . . 179
4.130 AO Imaging polarimetry of MWC 349 . . . 182
4.131 Mid-IR Imaging of MWC 349 . . . 182
4.132 AO Imaging polarimetry of AS 442 . . . 183
4.133 Mid-IR Imaging of AS 442 . . . 183
4.134 AO Imaging polarimetry of LkHα 134 . . . 184
4.135 Mid-IR Imaging of LkHα 134 . . . 184
4.136 AO Imaging polarimetry of LkHα 147 . . . 185
4.137 AO Imaging polarimetry of V1057 Cyg . . . 186
4.138 AO Imaging polarimetry of LkHα 120 . . . 188
4.139 Mid-IR Imaging of LkHα 120 . . . 188
4.140 AO Imaging polarimetry of HD 200775 . . . 189
4.141 Mid-IR Imaging of HD 200775 . . . 189
4.142 AO Imaging polarimetry of LkHα 324 . . . 190

4.143 Mid-IR Imaging of LkHα 324 . . . 190
4.144 AO Imaging polarimetry of LkHα 324 SE . . . 192
4.145 Mid-IR Imaging of LkHα 324 SE . . . 192
4.146 AO Imaging polarimetry of HD 203024 . . . 193
4.147 Mid-IR Imaging of HD 203024 . . . 194
4.148 PSF Subtractions for HD 203024 . . . 194
4.149 AO Imaging polarimetry of LkHα 349c . . . 196
4.150 AO Imaging polarimetry of V645 Cyg . . . 198
4.151 Mid-IR Imaging of V645 Cyg . . . 198
4.152 AO Imaging polarimetry of V361 Cep . . . 199
4.153 Mid-IR Imaging of V361 Cep . . . 199
4.154 AO Imaging polarimetry of LkHα 234 . . . 201
4.155 Mid-IR Imaging of LkHα 234 . . . 201
4.156 AO Imaging polarimetry of AS 477 . . . 202
4.157 Mid-IR Imaging of AS 477 . . . 202
4.158 AO Imaging polarimetry of LkHα 257 . . . 203
4.159 AO Imaging polarimetry of BH Cep . . . 205
4.160 Mid-IR Imaging of BH Cep . . . 205
4.161 AO Imaging polarimetry of BO Cep . . . 206
4.162 Mid-IR Imaging of BO Cep . . . 206
4.163 AO Imaging polarimetry of BO Cep B . . . 207
4.164 AO Imaging polarimetry of SV Cep . . . 208
4.165 AO Imaging polarimetry of LkHα 233 . . . 209
4.166 Mid-IR Imaging of LkHα 233 . . . 210
4.167 AO Imaging polarimetry of HD 216629 . . . 212
4.168 Mid-IR Imaging of HD 216629 . . . 212
4.169 AO Imaging polarimetry of V374 Cep . . . 213
4.170 AO Imaging polarimetry of MWC 1080 . . . 214
4.171 Mid-IR Imaging of MWC 1080 . . . 214
4.172 AO Imaging polarimetry of BM And . . . 215
4.173 AO Imaging polarimetry of LkHα 259 . . . 217
4.174 Mid-IR Imaging of LkHα 259 . . . 217
4.175 AO Imaging polarimetry of PDS 465 . . . 218
4.176 AO Imaging polarimetry of MWC 922 . . . 219
4.177 AO Imaging polarimetry of PDS 581 . . . 219
4.178 Centrosymmetry Histograms . . . 225
4.179 Centrosymmetry Histograms for pixels with $P > 3\sigma_P$ . . . 226
4.180 Centrosymmetric Peaks vs. θ . . . 227
4.181 Mid-IR Radial Profiles: Michelle N' . . . 229
4.182 Mid-IR Radial Profiles: Michelle Qa . . . 230
4.183 Mid-IR Radial Profiles: LWS 10.7, 11.7, 12.5, 17.65 . . . 231

4.184 Mid-IR Radial Profiles: LWS SiC . . . 232
4.185 Detected Sources versus V magnitude . . . 233
4.186 Detected Sources versus Spectral Type . . . 234
4.187 Detected Sources versus SED Classification . . . 235
4.188 2MASS Color-Color diagram . . . 236
4.189 2MASS Color-Color diagram, with source names . . . 237

5.1 The Lick Observatory LGS AO system . . . 240
5.2 LGS AO polarimetry of LkHα 198 and LkHα 233 . . . 242

6.1 Lick AO polarimetry of PDS 144N. . . . 255
6.2 Keck AO imaging of PDS 144. . . . 257
6.3 Keck AO imaging of PDS 144N . . . 258
6.4 Spectral Energy Distribution for PDS 144. . . . 259
6.5 χ^2 for possible distances to PDS 144 . . . 263
6.6 Monte Carlo model of a circumstellar disk plus envelope for PDS 144N . . . 271

7.1 OSIRIS J, H, K_s and FeII images of LkHα 233 . . . 278
7.2 Wavelength slices through the data cube . . . 279
7.3 Continuum-subtracted position velocity diagram, image of the jet, and measurements of jet FWHM . . . 281
7.4 Electron density in the LkHα 233 jet . . . 283

A.1 SEDs for Herbig Ae/Bes, part 1 . . . 318
A.2 SEDs for Herbig Ae/Bes, part 2 . . . 319
A.3 SEDs for Herbig Ae/Bes, part 3 . . . 320
A.4 SEDs for Herbig Ae/Bes, part 4 . . . 321

List of Tables

2.1 Instrumental Polarization 29
2.2 Astrometric Reference Binaries 31
2.3 Prism and waveplate transmission efficiencies 35
2.4 Polarizing Efficiency 36

4.1 Mid-IR Flux Calibration Compared with Literature Values 63
4.2 Highly Polarized Sources 224
4.3 Sources detected at $1 - 5\sigma$ 224
4.4 Sources Resolved in the mid-IR 228

5.1 Target Summary 249

6.1 Observation Log 253
6.2 Measured Fluxes 260
6.3 Additional sources detected 261

A.1 A Catalog of Herbig Ae/Be Stars. 314

B.1 Observing Log 322

C.1 IRCAL Photometry of HAEBEs 328
C.2 Mid-Infrared Photometry 330
C.3 Photometry and Astrometry of Companions 332

Acknowledgments

I want to begin by thanking all those who have guided me on the long and sometimes difficult path to "becoming a real scientist". First and foremost is my advisor, James Graham, whose knowledge, wisdom, and passion for teaching and learning continue to inspire me. I am profoundly grateful for his support, understanding, and patience these last few years. I've also benefited more than I can say from my fellow members of the Graham gang–Charles Hansen, Mike Fitzgerald, Nate McCrady, Andrea Gilbert, and especially Jamie Lloyd, who shared with me deep secrets of infrared instrumentation during the course of many trips up and down Mount Hamilton in ancient automobiles. The Center for Adaptive Optics provided an incredibly enriching scientific home, equally a place for scintillating discussion of, um, scintillation, and for overly complicated late-night poker games. Innumerable discussions at CFAO meetings, most notably with Bruce Macintosh and Anand Sivaramakrishnan, deeply shaped my thoughts about high contrast imaging. My association with the Lyot Project has brought me joy, frustration and excitement in equal measures, along with approximately 647,398 pizzas and 3×10^7 trips up and down Haleakala, and turned me into a tea drinker along the way. My thanks to Ben Oppenheimer, Anand Sivaramakrishnan, Remi Soummer, Russ Makidon, Sasha Hinkley, Doug Brenner, Andy Digby, and all the rest; I can't imagine another group of astronomers more fun to get rained on with. Dan Potter got the AO polarimetry ball rolling; I thank him for paving the way and for his willingness to share tips and tricks with a young whippersnapper like me.

Thanks to all the BADGrads who kept me happy and (semi-)sane over the last six years. You know who you are. To my officemates—Alexia, Renbin, Julia, I'll miss you all so much; good thing I'm not going anywhere just yet. Nor can I neglect the Harvard-Berkeley pipeline: Tonia D'Amelio, Susan Groppi, Matt Withers, Paul Lujan, Mike Develin, and Jeremy Condit. My life is immeasurably enriched by Candace Church, my partner in

adventure and exploration and so much more.

And lastly, but certainly not least, I owe it all to my parents and sister, who first shared with me the joy of watching the moon slowly rise above the sea on cold and clear New England nights. My mother sang "Twinkle, twinkle, little star" to me for years when I was young; read into that what you will about the influence of nursery rhymes upon career choices! (It actually turns out that making them *not* twinkle is helpful in determining what they are, but more on that in Chapter 2...)

* * *

This thesis has made extensive use of the SIMBAD, Vizier, and ADS astronomical databases, of the DSS, 2MASS, and IRAS all-sky surveys, and of data taken with many telescopes around and above this world, particularly Gemini North, Keck Observatory, and Lick Observatory. Modern astronomy would not be possible without the hard work of all those who create and maintain this vital infrastructure. Actually, truly none of this would have been possible without *money*, and for that reason I really am most grateful to the Center for Adaptive Optics, a National Science Foundation Science and Technology Center, and to the NASA Michelson Graduate Fellowship program, which has generously supported me these last three years. Many of the observations presented herein were obtained through the use of telescopes located atop Hawaii's Mauna Kea, a mountain of sacred importance to the Hawaiian people. We are fortunate to be able to conduct observations from this majestic peak.

Part I

A Survey of Circumstellar Dust around Herbig Ae/Be Stars

Chapter 1

Introduction

1.1 Circumstellar Disks: the Nursery of Worlds

Recent years have brought a revolution the study of solar systems and their origins. The idea that planetary systems form from disks of dust and gas around young stars dates all the way back to Kant (1798), but only in recent years has a substantial body of observational evidence become available. Beginning in 1995, precision Doppler radial velocity surveys have discovered scores of planets around other stars (Mayor & Queloz, 1995; Butler et al., 2006), overturning many previously-held notions in the process. Rather than resembling our own solar system, with planets in widely-spaced circular orbits, extrasolar planetary systems display a bewildering variety of properties. Many feature "hot Jupiters": massive planets orbiting extremely close to their parent stars. Others have more distant planets but with surprisingly large eccentricities. In some cases, pairs of planets are locked together in orbital resonances. Even brown dwarfs appear to possess circumstellar disks (Mohanty et al., 2006) and planets of their own (Jayawardhana & Ivanov, 2006). The diversity of planetary systems has proven far greater than we ever imagined.

A number of physical mechanisms have been proposed for these surprising results. Planet-disk interactions cause orbital migration inward, producing hot Jupiters or sweeping resonances through phase space. Close encounters and even collisions between planets have been invoked to scatter bodies into eccentric orbits. Clearly, young solar systems are exciting and violent places!

The tremendous diversity of planetary systems (Marcy et al., 2005) raises the question of whether that diversity arises from widely differing initial conditions in circumstellar

disks, or if instead all solar systems begin similarly but evolve apart via stochastic planetary dynamics. By characterizing the circumstellar environments of young stars, we can illuminate the conditions in which planet formation takes place. Since the dependency of planet formation on environmental factors is so poorly known, it is important for observations to span as broad a range of environments as possible. This thesis focuses in particular on the dusty environments of young intermediate mass stars (2-10 $M_{\odot}$). High angular resolution near- and mid-infrared observations enable the detection and characterization of the circumstellar dust present around many of these stars.

Intermediate mass stars have played a central role in our growing understanding of circumstellar disks. The first evidence for the existence of extrasolar planetary systems came from the discovery of debris disks around the A stars Vega (Aumann et al., 1984) and β Pic (Smith & Terrile, 1984). While planets have not yet been detected around these particular stars, large bodies must be present there to produce the the observed disks of micron-sized dust particles, through the collisional grinding down of larger bodies. Recent observations of perturbations to the disks of Vega and Fomalhaut strongly imply the presence of Jupiter-mass planets around those stars (Wilner et al., 2002; Kalas et al., 2005). Radial velocity surveys are just beginning to turn up evidence for planets around intermediate mass stars (Johnson et al., in prep.) Thus it seems almost certain that intermediate-mass stars can and do host planetary systems of their own.

1.2 Herbig Ae/Be Stars

The progenitors of Vega-like debris disk systems are the Herbig Ae/Be stars (frequently abbreviated as "HAEBEs"), pre-main-sequence stars of intermediate mass. They were first identified as a class by, and are named for, George Herbig, who began their study with a seminal paper in 1960 which sought to identify higher mass counterparts to the T Tauri stars. His observationally-motivated definition of the Herbig Ae/Be class was as follows:

1. Stars of spectral type B or A,
2. with emission lines of hydrogen (and possibly other elements),
3. located in an obscured region, and
4. illuminating nebulosity in its immediate region.

Subsequent years have seen this definition modified somewhat, in response to changing observational capabilities and greater physical understanding. A revised definition of the class (Davies et al., 1990; Malfait et al., 1998; van den Ancker et al., 1998; Waters & Waelkens, 1998) is:

1. Stars of spectral type B, A, or F
2. with emission lines of hydrogen, either now or in the recent past,
3. with broad spectral lines indicating luminosity class III, IV, or V, and
4. possessing an infrared excess due to circumstellar dust.

The inclusion of spectral type F is to extend the range down continuously to the upper end of the T Tauri star distribution. The "recent past" criterion allows for the variability frequently seen in Hα emission. Post-main-sequence giant branch stars are rejected by the broad line requirement. The infrared excess is truly the heart of the matter: These are young and dusty stars, still in the final throes of assembly from the interstellar medium.

The distinction of the Herbig Ae/Be stars from the T Tauri stars is not merely a matter of semantics. Rather, the nomenclature reflects a physical distinction which can be drawn between the classes. T Tauri stars' interiors are convective as they contract towards the main sequence, moving down the Hayashi tracks in the HR diagram. The more massive and thus hotter Herbig Ae/Be stars have radiative interiors; they rise in temperature as they move towards the main sequence, moving horizontally across the HR diagram. The characteristic timescale for this pre-main-sequence evolution is the Kelvin-Helmholtz time $t_{KH} = GM_*^2/R_*L_*$, or approximately $t_{KH} \sim G/R_*M_*$. This inverse dependence on mass means that Herbig Ae/Be stars ($M \sim 2 - 8\mathrm{M}_\odot$) evolve more rapidly than T Tauri stars ($M \sim 0.5 - 1\mathrm{M}_\odot$), with typical pre-main-sequence lifetimes of only a few million years. Faster yet are the lives of high mass stars ($M_* > 10\mathrm{M}_\odot$) which contract so rapidly that they reach the main sequence while still embedded in their natal material, and so lack an optically-visible pre-main-sequence phase. Thus the Herbig Ae/Be stars are a physically motivated subset of the pre-main-sequence stars, bounded below by the convective stability criterion and above by the timescales of stellar evolution.

One of the defining characteristics of stars in this class is that they possess excess infrared radiation arising from warm circumstellar dust. The existence of this dust is firmly established, but the details of its geometry and composition are less certain. A

lively debate has arisen as to whether the dust is located in a flattened circumstellar disk, or instead extends in a more nearly spherical envelope surrounding the star (e.g., Hillenbrand et al., 1992; Hartmann et al., 1993; di Francesco et al., 1994; Mannings et al., 1997; di Francesco et al., 1997; Meeus et al., 1998; Natta et al., 2001). Initially it seemed that fitting models to the observed spectral energy distributions (SEDs) could address this question, but with time it became clear that multiple models could often reproduce a given SED equally well (Chiang & Goldreich, 1997, 1999; Chiang et al., 2001a; Waters & Waelkens, 1998).

Resolved images can break these degeneracies and allow a robust discrimination between disks and envelopes. Such resolved images have been obtained in recent years either coronagraphically (Weinberger et al., 1999; Grady et al., 2000, 2001; Clampin et al., 2003; Fukagawa et al., 2004; Grady et al., 2005) or interferometrically (Mannings et al., 1997; Millan-Gabet et al., 2001; Eisner et al., 2004). It has become increasingly clear that the true answer is somewhere in between: Many HAEBEs do indeed have circumstellar disks, which span a range from very flattened to highly flared, but others possess extended envelopes. Many have both.

But the sample size is still relatively small. A larger sample size will allow better statistics, as well as an increased chance of turning up particularly interesting or unusual objects. Furthermore, many aspects of disk physics remain in question. Current active areas of research include the disk geometry and degree of flaring, grain growth and mineralogy, disk lifetimes, and the origin and role of molecular outflows.

1.2.1 Classifications based on Spectral Energy Distributions

A few schemes have been devised for systematically classifying the Herbig Ae/Be stars. The first of these was developed by Hillenbrand et al. in their widely-cited 1992 paper. They classified the Herbig Ae/Be stars based on their SEDs, as follows:

- **Hillenbrand Group I:** Stars with large infrared excesses which decline according to $\lambda F_\lambda \propto \lambda^{-4/3}$ at wavelengths $> 2\mu$m.
- **Hillenbrand Group II:** Stars with large infrared excesses and SEDs which are flat or rising beyond 2 μm.
- **Hillenbrand Group III:** Stars with only small infrared excesses.

These classifications were interpreted as being related to the circumstellar dust geometry. Hillenbrand et al. supposed Group I stars to have flat, optically thick circumstellar accretion disks, Group II objects to have dusty envelopes which occupy a large solid angle around the star, and group III objects to be similar to classical Be stars with IR excesses arising from free-free emission in a circumstellar gas disk. A different classification scheme was proposed by Meeus et al. (2001), which unfortunately uses nearly identical notation for a different set of definitions:

- **Meeus Group I:** Stars with a rising SED from 20-100 μm, which can be fit by a power law plus a blackbody
- **Meeus Group II:** Stars with a more modest infrared excess, which can be fit by a power law alone.

Acke & van den Ancker (2004) extended Meeus's classification scheme with an additional group, III, for stars which display the 10 micron silicate feature in absorption. Meeus et al. interpret these differences in terms of the vertical extent of the circumstellar disks: Group I stars have highly flared disks, the outer portions of which are directly illuminated by starlight. Group II stars have relatively flat disks, with their outer regions largely shielded from starlight by the puffed-up inner rim. See also Dullemond & Natta (2003); Dullemond & Dominik (2004).

The similarity in nomenclature between the systems proposed by Hillenbrand et al. and Meeus et al. is potentially a source of great confusion. For maximum clarity, one should always be explicit about which classification scheme is meant by a reference to "Group I" or "Group II".

1.2.2 Other Related Classifications of Herbig Ae/Be stars

Several other classes of Herbig Ae/Be stars deserve mention. The first of these is the UX Oris, a group of stars which show sudden irregular deep eclipses, with variability greater than 1 magnitude on timescales of days to weeks (Dullemond et al., 2003). During these eclipses, which can reach up to 3 mag. in depth, the stellar spectra are reddened and the polarization level is increased (Grinin et al., 1991). These eclipses have been interpreted in terms of variable extinction by orbiting circumstellar material (Wenzel 1968, Wenzel 1971, Herbst 1983, Bibo & The 1991) (Herbst et al., 1983; Bibo & The, 1991). The behavior of

these stars implies that the distribution of mass around Herbig Ae/Be stars is clumpy, not smooth. UX Oris are predominantly found among Herbig Ae stars, with a few examples also known from the T Tauri stars (Finkenzeller & Mundt, 1984; Bibo & The, 1991). van den Ancker et al. (1998) proposed that the lack of UX Ori behavior among Herbig Be stars is because those stars are optically invisible during most of their periods of accretion.

A related class of stars is the FU Orionis objects (FUOrs), another class first identified by Herbig (1977) While the majority of Herbig Ae/Be stars show little evidence for dust excess at optical wavelengths (e.g. from the veiling of spectral lines), stars in the FU Ori class derive the majority of their visible emission from accretion luminosity. The prototype FU Orionis was seen to brighten dramatically in 1937, from $V \sim 16$ to 10 mag., after which it has dimmed slowly over a period of decades. Since that first example, similar outbursts have been observed to occur around a small handful of additional stars. The outbursts are believed to arise from rapid increases in the accretion rate onto the star; for a comprehensive review see Hartmann & Kenyon (1996).

Not all FU Oris are Herbig Ae/Be stars; the class extends down into the T Tauris as well. Indeed, one of the hallmarks of the FU Oris is difficulties in establishing their spectral type due to high optical veiling. Some authors consider them a separate class of objects from Herbig Ae/Bes, but others consider them overlapping but independent classifications, and FUors are frequently included as targets in studies of Herbig Ae/Be stars and their properties.

1.3 High Contrast, High Angular Resolution Imaging

Simultaneously with the radial velocity revolution, another advance in observational technology has allowed us to probe the close circumstellar environments of young stars with increasingly greater detail. This is the development of high contrast diffraction-limited imaging, both in space with the Hubble Space Telescope and from the ground using adaptive optics on large telescopes.

The crucial observational challenges which must be overcome in order to image circumstellar dust are twofold: First, the imaging system must provide fine enough angular resolution to resolve the circumstellar environment. Typical scales for structure in circumstellar disks range from a few AU to a several hundred AU. Thus, for a target at a distance of 100 pc, angular resolution of $\sim 0.1 - 1$ arcsecond or better is required. Imaging on these

scales is possible in optical or near-infrared wavelengths using telescopes with apertures a few meters in diameter, either in space or from the ground with adaptive optics. The second challenge is one of contrast: the light scattered from circumstellar dust is faint, often no more than a few percent of the total starlight. Even a small amount of starlight can completely swamp the dust-scattered light and prevent detection.

The Hubble Space Telescope (HST) has provided spectacular images of circumstellar disks around an ever-growing list of targets—both for older debris disks such as AU Mic (Krist et al., 2005) and Fomalhaut (Kalas et al., 2005), and also for younger primordial disks like those seen around HH 30 (Burrows et al., 1996), HD 141569 (Weinberger et al., 1999), and AB Aur (Grady et al., 1999). With its extremely stable PSF and high angular resolution in optical wavelengths, HST continues to be an extremely productive observatory for disk studies: new debris disks were recently resolved around HD 53143 and HD 139644 (Kalas et al., 2006), and HD 181327 (Schneider et al., 2006, in press.).

Despite the many successes of HST, interest in high contrast imaging from the ground has been steadily increasing. Space telescope time is a precious and limited commodity, and the operational lifetime of a spacecraft is finite (and potentially very uncertain, in the case of Hubble). Furthermore, for the foreseeable future ground-based telescopes will continue to surpass space telescopes in size by a factor of several, and thus offer the potential for better angular resolution. High contrast observations with large ground-based telescopes thus represent a compelling tool for the study of circumstellar dust.

1.4 Thesis Overview

In this thesis, I present an observational survey of circumstellar dust around Herbig Ae/Be stars, on scales of tens to hundreds of AU. This survey has employed a wide range of observational tools to assess the environments of these stars, including optical and infrared imaging, polarimetry, and integral field spectroscopy.

The two approaches which have been used most extensively are near infrared adaptive optics differential polarimetry, at Lick Observatory, and mid-infrared imaging, at the Keck and Gemini Observatories. As part of this project, I enhanced the IRCAL camera at Lick Observatory with a differential imaging polarimetry mode. In combination with the Lick adaptive optics system, the IRCAL polarimeter enables high contrast, high angular resolution observations of circumstellar dust seen in near-infrared scattered light. These near-IR

observations were complimented with mid-infrared observations of thermal emission from dust grains.

Part I of this thesis describes the development of the IRCAL polarimeter, the data reduction techniques used with it, and presents my survey of Herbig Ae/Be stars. Over one hundred stars were observed, with extended dust-scattered light detected around a third of these. The revealed dust structures variously include face-on and edge-on disks, extended circumstellar envelopes, bipolar outflow cavities, and tidal streamers between binary stars.

Part II continues with more detailed studies of a few particularly interesting individual objects. One of the major results presented in this thesis is the first example of an edge-on disk around a HAEBE, PDS 144N. I also present the highest angular resolution images of a disk, envelope, and bipolar outflow around the Herbig Ae star LkHα 233. I conclude by looking ahead to future studies of circumstellar disks in the coming era of high contrast "Extreme Adaptive Optics".

Chapter 2

Design and Calibration of the Lick Observatory Adaptive Optics Imaging Polarimeter

Abstract

We have modified IRCAL, the near-infrared science camera of the Lick Observatory adaptive optics system, to add a dual-channel imaging polarimetry mode. This mode uses an optically contacted YLF ($LiYF_4$) Wollaston prism to provide dual, simultaneous images of perpendicular polarizations, providing high resolution, high dynamic range polarimetry in the near infrared. We describe the design and construction of the polarimeter and present measurements of its sensitivity to polarized scattered light.

The YLF Wollaston prism delivers excellent polarizing efficiency without compromising image quality. An instrumental polarization of about 2% in all three NIR bands arises predominantly from the dichroic in the AO system, but appears to be constant over time and will not negatively affect system performance.

2.1 Introduction

Astronomical polarimetry has greatly matured in the last century since the pioneering observations of Zeeman, Hale and others in the early 1900s. Tinbergen (1996) provides a

useful overview of astronomical polarimetry from radio to X-ray wavelengths. Modern polarimeters are capable of obtaining accuracies as good as 0.5% in the near IR, as compared with an expected polarization level due to scattering by dust grains from a few percent up to perhaps 75% for some sources (Hough, 2005).

The rapid growth of adaptive optics has opened the potential for high resolution ground-based imaging. The use of deformable mirrors to correct atmospheric distortions in real time allows even the largest ground-based telescopes to achieve diffraction limited performance in the infrared for selected targets. While space-based polarimetry with the revitalized NICMOS on HST can also provide high-resolution images, the larger diameter of ground based telescopes allows them to achieve superior resolution to HST and even the planned JWST. Thus the highest resolution near-infrared polarimetry will be obtained through the combination of polarimetric imaging with adaptive optics.

Detection limits for faint companions or circumstellar material in AO observations are dominated by speckle noise, which is substantially larger in magnitude than photon noise near bright stars (Racine et al., 1999; Soummer & Aime, 2004). Differential polarimetry suppresses this effect because the atmospheric speckles are not themselves polarized for scattering angles less than a few arcseconds. Differential AO polarimetry which reaches the photon noise limit outside of 1" has been demonstrated by Kuhn et al. (2001a) . In this regime, the signal to noise ratio for companion detection is proportional to $S/(1-S)$, where the factor of $1/(1-S)$ is due to a reduction in background stellar scattered light as that light is packed into the core of the point spread function. Due to this strong dependence on the Strehl ratio, it is important for an AO polarimeter to introduce a minimum of additional wavefront error into the optical system.

But polarimetry is not useful merely as a way to increase contrast; it provides a sensitive tool for probing the astrophysics of the scattering particles. In particular, multi-wavelength polarimetry can provide tight constraints on dust grain sizes. Mie scattering theory predicts that for spherical grains, images at a wavelength λ are most sensitive to light scattered from particles with $2\pi r_{dust}/\lambda \sim 1$. The distribution of grains which contribute to scattering at a single wavelength is roughly an order of magnitude wide, so for instance observations at 0.6 μm can provide information on grains from 0.1-1 μm in diameter. Typical ISM grains have sizes $\lesssim 1\mu$m (Kim et al., 1994; Weingartner & Draine, 2001), so by obtaining images with a range of wavelengths both less than and greater than 1 μm, one may tell whether, and where, grain growth above ISM values has occurred. For

instance, Lucas et al. (2004) used multiwavelength near-infrared polarimetry of HL Tau to derive not only a dust grain size distribution (with a maximum size slightly above 1μm, subject to assumptions about grain composition) but also information on the alignment of non-spherical grains due to magnetic fields. Imaging polarimetry of the debris disk around AU Mic (Graham et al. in preparation) indicates that dust grains in those systems are fluffy or fractal aggregates. (Tamura et al. (2006) make a similar conclusion for the disk around β Pic, but do not provide quantitative support for this assertion.) Likewise, mid-IR imaging and polarimetry can also give information on grain albedo and sizes (Whitney, 2004). Imaging polarimetry has proven to be a very effective element of the astronomer's toolkit.

The Lick/Lawrence Livermore National Laboratory adaptive optics system (henceforth, "Lick AO") was developed by UC and LLNL staff and has been in operation on the Lick 3 m Shane telescope since the mid 1990s, including in recent years a laser guide star capability (Bauman et al., 2002). The wavefront sensor is a 40-subaperture Shack-Hartmann design while the deformable mirror has 61 degrees of freedom inside the telescope pupil. In conjunction with the science camera IRCAL (Lloyd et al., 2000), it routinely achieves internal Strehl ratios $S > 0.9$, and on-the-sky Strehl ratios up to 0.7 at 2.1 μm, corresponding to an RMS wavefront error of 200 nm.

I have developed a differential polarimetry mode for IRCAL, using a YLF Wollaston prism analyzer and rotating half-wave plate modulator. This mode provides nearly two orders of magnitude reduction in the stellar PSF halo. I describe here the design of this instrument, tradeoffs inherent in its construction, and the results of calibration observations obtained during and after commissioning. The following chapter will address the data reduction process in greater depth.

2.2 A Brief Review of Polarimetry Fundamentals

The works by Tinbergen (1996) and Keller (2002) provide an excellent introduction to the science of polarimetry, while Adamson et al. (2005) provides a good summary of the current state of the art. I briefly repeat here a few basics to establish notation.

The polarization state of light may be represented using the Stokes vector $[I, Q, U, V]$ (Stokes, 1859; Chandrasekhar 1950; see Fig. 2.1). I is the total intensity of light, Q and U represents different orientations of linearly polarized light, and V denotes circular

polarization. While the Stokes vector may seem like an unintuitive or cumbersome parameterization, it has many benefits in practice: All four components of the vector have the units of intensity, erg s^{-1} cm^{-2} sr^{-1} μm^{-1} or the equivalent. Stokes vectors for superimposed incoherent beams add linearly, and normal Gaussian statistics apply; and the effects of an optical system on polarized light can be computed straightforwardly using Mueller matrix algebra. See to Tinbergen (1996) and Keller (2002) for the detailed mathematics of Mueller matrices.

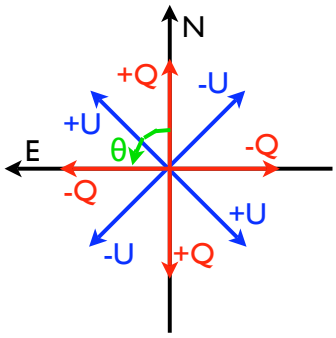

Figure 2.1: Axes conventions for polarimetry. The zero point for position angle is due north, increasing toward the East. Stokes $+Q$ is due north, $-Q$ is due east, and so on.

Polarization is also frequently expressed in terms of polarized intensity, and angle:

$$\begin{aligned} P &= \sqrt{Q^2 + U^2} \\ \theta &= \frac{1}{2} \arctan\left(\frac{U}{Q}\right) \end{aligned}$$

Conversely, given an angle and polarized intensity, one can transform back into Stokes Q and U.

$$\begin{aligned} Q &= P \cos(2\theta) \\ U &= P \sin(2\theta) \end{aligned}$$

Frequently, the Stokes parameters are expressed in a normalized form by dividing out the total intensity:

$$q = Q/I$$

$$u = U/I$$

$$p = P/I$$

P/I is often referred to as the polarization fraction or percent polarization. Inconsistent notation is a frequent pitfall, with some authors using P to refer to polarized intensity and others using it for polarization fraction. In this work, capital I, Q, U, V, P will always refer to intensities, not normalized or fractional quantities.

Stokes V denotes the amount of circular polarization. This is usually, but not always, negligible for most astrophysical sources, particularly those involving the scattering of light. In most cases, we shall neglect the presence of Stokes V.

In general, astronomical detectors are sensitive to the intensity of light, not its polarization. Hence we cannot measure polarization directly, but instead must encode it into variations in total intensity, most simply by using a linear polarizer to allow only one orientation of light to reach the detector. To fully recover the three unknowns (Stokes I, Q, U) requires at least three angles, and often more are used (see Patat & Romaniello, 2006). The Q and U Stokes parameters are cleanly separated by the use of 0, 45, 90, and 135°. If we denote the signal measured at an angle θ by p_θ, then the Stokes parameters may be recovered as

$$\begin{aligned} I &= p_0 + p_{90} = p_{45} + p_{135} = \frac{1}{2}\left(p_0 + p_{90} + p_{45} + p_{135}\right) \\ Q &= p_0 - p_{90} \\ U &= p_{45} - p_{135} \end{aligned}$$

This is the heart of astronomical polarimetry; everything else is just an elaboration upon this simple scheme to overcome real-world complications.

2.3 Design & Implementation

The most straightforward technique for polarimetry is to insert a wire-grid polarizer or Polaroid into the optical path and rotate this polarizer to measure a variety of angles. This method has the disadvantage that the Stokes parameters are obtained by subtraction of non-simultaneous images, separated by at minimum the waveplate rotation timescale. Seeing variations between these images will result in spurious apparent polarization. This is particularly a problem in AO observations, which have PSFs subject to speckle noise and changing sky conditions. Dual channel polarimetry solves this by allowing subtraction of simultaneous exposures. A Wollaston prism placed in a collimated beam will slightly deviate perpendicular polarizations, projecting two separate images of a source onto the

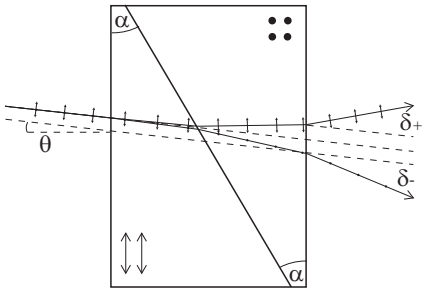

Figure 2.2: Wollaston prism and typical ray, adapted from Bennet 1995. Beam divergence is greatly exaggerated.

detector. If bias and flat-fielding effects are properly removed, the resulting difference image should be uncontaminated by seeing. A polarization modulator (such as a half-wave plate) is still required to measure both Stokes Q and U. As described in Kuhn et al. (2001a), further waveplate rotations that swap polarization states between the two sides of the detector can be used to minimize the effects of flat fielding and other instrumental errors.

A wedged double Wollaston has been proposed by Oliva (1997) for simultaneous measurement of all four polarization states, and thus simultaneous extraction of both Stokes Q and U. However, this requires dividing the pupil in half, resulting in a loss of half the resolving power of the system, so the wedged double Wollaston is not an optimal solution for high resolution imaging. This pupil division also means that the Q and U beams see different portions of the atmosphere and will have PSFs at least as divergent as in a non-simultaneous polarimeter. Furthermore, only half as many photons per unit time are delivered to each of the Q and U channels, so that to obtain the same level of signal-to-noise in both Q and U requires just as much total exposure time as in a classical polarimeter. We therefore chose to develop a classical single-Wollaston polarimeter.

Figure 2.2 is a schematic of a Wollaston prism, constructed from two pieces of birefringent material with their optical axes mutually perpendicular. Orthogonal polarizations of light experience opposite deflections due to the differing indices of refraction n_o and n_e for the ordinary and extraordinary rays, respectively. Call two perpendicular polarization states of light $+$ and $-$. The $+$ ray, which is the extraordinary ray for the first segment of the prism, becomes the ordinary ray at the internal interface, and is therefore deflected due to the change in index of refraction $\Delta n = n_e - n_o$. The $-$ ray is likewise deflected in

the opposite direction. The two deflections are roughly equal in magnitude, though with opposite sign, and only depend weakly on the angle of incidence θ. Following Oliva et al. (1997), we may therefore approximate

$$\delta = |\delta_- - \delta_+|/2 \simeq \Delta n \tan \alpha$$

where α is the prism angle. If this prism is placed in collimated space in a camera (e.g. in a filter wheel conjugate to the telescope pupil) the two polarization states will have a sky-projected separation of

$$\delta_{\rm projected} \simeq 206265'' \Delta n \tan \alpha \left(\frac{D_{\rm pupil}}{D_{\rm tel}} \right) \tag{2.1}$$

where $D_{\rm pupil}$ and $D_{\rm tel}$ are the pupil image and telescope diameters (5 mm and 3 m respectively in our case). We desire the total separation $2\delta_{\rm projected}$ to be half the field of view. For IRCAL, the field of view is 19.4 arcseconds, implying an optimal $\delta_{\rm projected} \lesssim 4.9$ arcseconds. Thus once we have chosen our material (and therefore Δn), equation 2.1 may be solved for the necessary prism angle α.

2.3.1 Choice of materials

While the most traditional material for Wollaston prisms is calcite, a number of other materials have been discussed and in some cases used. Oliva et al. (1997) provides an overview of a number of different materials. In particular, calcite is of limited utility in the infrared because it becomes opaque to the ordinary beam at 2.2 μm, and so for K-band polarimetry we are forced to turn to alternative materials. Magnesium fluoride is the most common material for IR Wollastons, but we took a more exotic route.

We chose YLF (Yttrium Lithium Fluoride, $LiYF_4$, pronounced "yilf" by its users in the laser industry) for our prism for several reasons. Its refractive index, 1.45, is comparable to that of standard optical components and cements, thus simplifying the optical design and manufacturing. The difference in index of refraction between polarizations, $\Delta n = 0.022$, allows the necessary beam divergence to be obtained with an easily achievable thickness of YLF, roughly 4 mm.

Most importantly, Δn is remarkably constant with wavelength, allowing broad-band imaging with minimal chromatic elongation. Any change of Δn with wavelength will result in different beam displacement for each wavelength within a bandpass, elongating the final image in that direction and reducing the ultimate resolution of the system. This effect,

alternately termed "lateral chromatism" or "chromatic birefringence", may be quantified over a wavelength range $\lambda_1 < \lambda < \lambda_2$ by Oliva's parameter

$$V = \frac{\Delta n_{(\lambda_1+\lambda_2)/2}}{\Delta n_{\lambda_1} - \Delta n_{\lambda_2}}$$

which gives the image elongation over the range $\lambda_1 - \lambda_2$ as $\epsilon = \delta/V$. By selecting a material to maximize V, we can minimize the effects of lateral chromatism. Typically, $V > 100$ is considered good, corresponding to chromatic elongation less than $0\farcs05$ for IRCAL, better than the diffraction limit. YLF exceeds this (spectacularly at H, with $V = 1290$), along with $AgGaS_2$ and CdSe, but YLF is most readily available at reasonable cost due to its widespread use in the laser industry. Our desire to not compromise the resolving power of the system led us to choose YLF for our Wollaston prism.

Minimizing lateral chromatism is particularly important for a high contrast polarimeter. Not only does this effect potentially decrease angular resolution, it can greatly degrade PSF subtraction quality. To the extent that the two oppositely polarized broadband PSFs are chromatically distorted in opposite directions, the speckle patterns of the two beams will no longer match and the PSF subtraction will be imperfect.

One caveat which must be noted about YLF is it is not currently available in crystals much larger than a centimeter. This posed no difficulty for IRCAL with its 5 mm pupil, but may be a stumbling block towards implementing a similar system on a 8 m or larger telescope with correspondingly larger pupils. The greater resolution of larger telescopes places an even more stringent constraint on chromatic elongation. This may force a trade-off between resolution, field of view, and imaging bandwidth if large achromatic Wollastons cannot be manufactured. MgF_2 has fairly high lateral chromatism ($V \sim 50 - 100$). Sapphire, which is moderately birefringent ($\Delta n = 0.008$) and available in sizes up to 30 cm, has less lateral chromatism ($V \sim 150 - 200$) and has been suggested as a material for large Wollastons. The effect of lateral chromatism can in part be mitigated by using a beam displacement that is only a small fraction of the total field of view. In that case, a "Venetian blind"-style field mask must be used instead of the half-field mask used in IRCAL. This approach, which is used on the VLT FORS1 polarimeter (Patat & Romaniello, 2006), allows the use of smaller beam displacements and thus reduces lateral chromatism, at the cost of introducing slightly greater complexity in the data reduction.

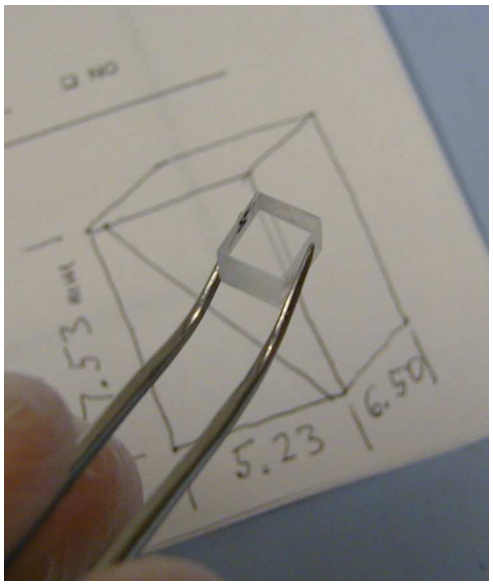

Figure 2.3: Our YLF Wollaston prism prior to installation in the IRCAL dewar. Note how the prism visibly splits the line from the diagram in the background.

2.3.2 Final details and construction

Prism. For our selected material, YLF, a Wollaston prism with a 33°prism angle produces the desired beam divergence of 1.45 °, for a sky-projected separation of 9″between the two beams. Three similar Wollaston prisms were fabricated by Onyx Optics of Dublin, CA and were received at Berkeley in March 2002. The final prism dimensions were 5 mm × 6 mm × 7 mm. The pieces were joined using optical contacting and both exterior surfaces received a 1-2.5 μm antireflection coating. All three prisms performed as expected in laboratory tests with polarized 650 nm light. Beam divergences measured at room temperature were between 1.49 and 1.55 degrees, larger than our target value but well within the acceptable range. Two of the prisms exhibited minor surface defects from the manufacturing process; the third prism was chosen for astronomical use.

One concern with any birefringent material is that the differing optical axes of the material frequently have different thermal expansion coefficients. This is the case for YLF, which has an expansion coefficient of $5 \times 10^{-6}\mathrm{K}^{-1}$ parallel to the axis and $8 \times 10^{-6}\mathrm{K}^{-1}$ perpendicular to it. Since Wollaston prisms are constructed by bonding two surfaces with perpendicular axes, temperature changes will build up stress between the two faces. For a prism cooled to 77 K, preliminary estimates indicated that the thermal stress could

be close to the yield strength of the material. While this was a concern, we chose to proceed with the prism construction nonetheless, expecting that the bond between the two YLF crystals would have sufficient elasticity to allow the necessary flexure. Practical experience has borne this out; our prism has tolerated repeated thermal cycling to nitrogen temperatures with no ill effects apparent after four years.

The Wollaston prism is installed in one of IRCAL's internal filter wheels, in collimated space just before the cold pupil. The other filter wheel allows the selection of wavelength, but note that this arrangement limits the polarimeter to use only with filters installed in wheel 1. One drawback to the geometry of IRCAL is that the location of the Wollaston results in the two beams having diverged before encountering the cold pupil, resulting in different system pupils for the two beams; more on this below.

The image displacement from our Wollaston once installed into IRCAL was found to be $3\farcs95$ for each polarization, in excellent agreement with the theoretical prediction for our 30°prism ($3\farcs88$) using the optical indices and temperature variation as measured by Barnes and Gettemy (1980). This corresponds to a beam divergence of 1.32°at the prism, which is significantly lower than the 1.49°we measured at room temperature. Indeed, one would expect a slightly lower divergence in the optical than in H band (see Fig. 2 of Oliva et al. 1997). The reason for this discrepancy remains unclear.

Aperture Mask. To prevent overlap of the two polarized images, an aperture mask corresponding to half the field of view was fabricated and installed in the IRCAL cold aperture wheel. This mask is essentially a very wide slit, with carbon lampblack painted on to darken it.

Based on our laboratory measurements of beam displacement, I initially fabricated the aperture mask with a $9\farcs9$ wide slit, which was used for our initial several observing runs. However, given the smaller than expected displacement, this mask proved too large, resulting in an overlap of the polarized beams near the middle of the detector. A replacement aperture mask with an $8''$slit was made and installed into IRCAL in October, 2002, and used for all subsequent runs. This mask is still slightly oversized, resulting in an $0\farcs4$ (6 pixels, 240 μm) beam overlap in the middle of the detector. This overlap region is simply discarded during the data reduction.

Waveplate. We chose to use a standard rotating half-wave plate as the polarization modulator. For practical reasons, we decided to mount the waveplate at the entrance window to IRCAL; ideally, the wave plate would have been better located as far upstream

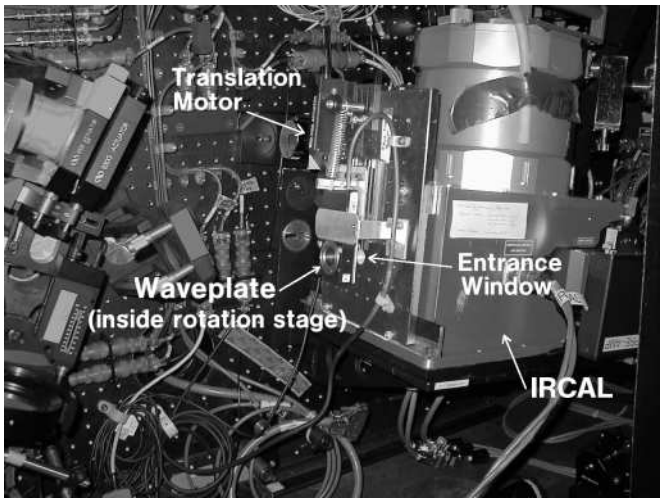

Figure 2.4: The IRCAL dewar mounted to the Lick AO optical bench, highlighting the waveplate mechanisms.

as possible, since the modulation removes instrumental polarization effects from optics after the modulator.

An achromatic waveplate optimized for 1-1.6 μm was obtained from Karl Lambrecht Corp. and mounted in a Newport PR50 rotation stage. This was itself mounted on a translation stage attached to the IRCAL dewar adjacent to the entrance window, as depicted in figure 2.4. The rotation and translation drives were connected to formerly spare channels on the Lick AO system motor controller and integrated into the Lick AO control software. The Tcl/Tk-based software interface between the IRCAL and AO user interfaces (discussed in Lloyd et al. (2000)) allows control of the waveplate from the IRCAL GUI, enabling scripts to automate polarimetry observations.

Alternative possibilities for polarization modulation include liquid crystal variable retarders (LCVRs) and ferroelectric liquid crystals. Ferroelectric liquid crystals are not feasible given the readout times necessary with present infrared detectors (though see Potter & Graham (2005) for an application of ferroelectric modulators in the optical using fast-readout EMCCDs). LCVRs have certain advantages over waveplates, and have been used to spectacular levels of precision in solar polarimetry. In addition to rotating the polarization states, a pair of LCVRs can also convert circular to linear polarization allowing measurement of Stokes V. Furthermore, the lack of any moving optical elements eliminates the image wander and flat field variations which can occur with rotating wave

plates. However, LCVRs are generally not achromatic, are difficult to obtain for wavelengths beyond 1.8 microns, and have birefringence which is temperature-dependent. In contrast, half-wave plates are available with excellent achromaticity and low sensitivity to temperature variations. Since we desired a single polarization modulator for the entire 1-2.5 micron band, we chose to use an achromatic waveplate rather than LCVRs.

2.4 Observing Techniques and Data Reduction

Observation with our polarimeter is straightforward, with most of the complications relegated to the data reduction pipeline. Once the target has been acquired by the telescope and AO system, the observer configures exposure parameters such as filter and exposure time. A polarimetry script automatically rotates the waveplate and integrates at each position. The rotation of the waveplate by an angle θ rotates the plane of polarization of incident light by 2θ[1], and thus sampling Q and U 45°apart requires 22.5°rotations. We have chosen to use eight distinct waveplate positions: 0, 22.5, 45, 67.5, 90, 112.5, 135, and 157 degrees. This provides four redundant measurements for each of Stokes Q and U, with the redundancy helping to reduce instrumental effects (Kuhn et al., 2001a; Patat & Romaniello, 2006). To obtain the necessary high dynamic range, for most targets it is necessary to combine both short and long exposures; typical exposure durations are between 1 and 90 s, depending on source magnitude. Small dithers of a few arcseconds after each set of eight exposures are used to minimize flat field effects and increase field of view. We also obtain sky frames using identical procedures on nearby regions devoid of sources (usually 30-90 arcsec away from the science target).

For calibration, we image standard stars of known polarization, as well as ordinary photometric standards. Flat fields are obtained from exposures on the twilight sky, while dark frames are obtained at the end of the night using the usual IRCAL procedures.

Data reduction techniques for the IRCAL polarimeter are presented in more detail in the following chapter. Briefly, after sky subtraction and flat fielding, images are registered and mosaiced. The mosaics for each set of waveplate angles are subtracted using an optimizing difference method, resulting in Stokes Q and U, and summed to get Stokes I.

[1]More precisely, it *mirrors* the plane of polarization through the optical axis of the rotated waveplate, but given the spin 1/2 nature of polarization, this is equivalent to a rotation by twice the waveplate angle.

2.5 Performance

The prism was installed into the IRCAL filter wheel during March 2002, and had first astronomical light on the night of 28 March 2002. Observations that night and on subsequent nights throughout 2002, as well as engineering test observations carried out on calibration sources during the day, have allowed us to quantify the performance of the system.

2.5.1 Image Quality

With the waveplate and prism retracted out of the way, the Lick AO system and IRCAL typically achieve an internal Strehl ratio of slightly better than 0.9 when observing the internal calibration source at 2.16 μm[2]

The initial insertion of the polarimetry hardware into the beam, without changing any instrument settings, reduced the Strehl ratio to 0.80. However, as the waveplate is in the converging beam, it introduces additional fixed focal path length into the system, which was experimentally found to be 1.3 mm (consistent with its thickness and index of refraction). With IRCAL moved by this amount, the Strehl ratio improved to 0.86. Further improvements were effected through iterative image sharpening. The prism appears to be somewhat astigmatic, and by applying appropriate modes to the deformable mirror to counter this astigmatism, the internal Strehl ratio was increased to $0.91 \pm .01$, essentially identical to the Strehl prior to the addition of the polarimeter optics. Using Marechal's approximation, the change from S=0.91 to S=0.86 corresponds to 85 nm of RMS wavefront error.

The magnitude of the image sharpening correction was not appreciably larger than corrections typically applied for semi-static non-common-path aberrations. Thus optical errors in the waveplate and prism do not appear to appreciably degrade image quality. The IRCAL image sharpening script is performed as part of daily maintenance, and thus the optical coefficients are always optimized after a transition between polarimetric and regular observing modes.

We briefly observed the bright star β Gemini (Pollux) to search for ghost images

[2]Strehl ratios are measured using an IDL-based PSF fitting routine developed by B. Macintosh and incorporated into the IRCAL quicklook software. There are numerous pitfalls in accurately measuring Strehl ratios, particularly for undersampled data (Roberts et al., 2004), and Strehl ratios quoted for IRCAL are uncertain by $5 - 10\%$.

caused by the additional optical surfaces. No such ghosts were observed in images highly oversaturated in the stellar core.

2.5.2 Polarizing Efficiency and Throughput

The Lick AO system contains a calibration source which may be moved into the beam at the Cassegrain focus, an Oriel Instruments 77501 Radiometric Fiber Source with photometric stability of 0.1%. We observed this source with IRCAL to determine the transmission efficiency of the Wollaston prism and waveplate; results are presented in table 2.3. In particular, the prism becomes more transparent at longer wavelengths, but the antireflection coating on the waveplate falls off rapidly at K, resulting in nearly equivalent net throughput at J and H of 92%, decreasing to about 88% at K_s.

We also observed the calibration source through a 1-2 μmIR Polaroid from Edmund Scientific. Rotating the waveplate produced the expected sine-squared modulation in illumination levels. The apparent brightness of the fiber source was measured for each polarization as a function of waveplate angle, and a model fit to these data using the Levenberg-Marquardt least-squares method. This was repeated for each of the J, H, and K_s bands. The data and models are presented in Figure 2.8 and the data summarized in Table 2.4. The measurements of the extinction ratio (that is, the minimum over maximum brightness) were limited by the polarizing efficiency of the IR Polaroid, not the Wollaston prism, particularly at K, and thus the values in Table 2.4 represent only upper limits. Wollaston prisms frequently achieve extinction ratios better than 10^{-5}; at this time we are unable to more precisely quantify the polarizing performance of our prism but believe that it is most likely performing at that level.

The most notable result beyond the above is that the throughput of the two polarized beams can differ by 5-10%. The throughput difference is variable between observing sessions. This most likely arises due to pupil clipping inside IRCAL; since the Wollaston prism changes the angle of the two polarized beams in collimated space, they encounter the IRCAL cold pupil at slightly different places and thus the effective system pupil differs for the two channels. IRCAL's moving mechanisms do not have a high degree of repeatability, and small changes in the precise positioning of the Wollaston slightly change the location of the beams with respect to the pupil, causing the amount of clipping to change. Modulation of the polarization by the rotating waveplate largely compensates for this effect.

2.5.3 Non-common Path Optical Errors

In an ideal case, the two polarization images for an unpolarized source would have precisely identical point spread functions and would subtract down to the photon noise level in the difference image. In reality, non-common path effects will lead to different wavefronts in the two channels, degrading system performance.

The two polarized PSFs of any given source are quite similar to the eye, but not perfectly identical. The variations are consistent with small levels of non-common-path optical error, or possibly with the opposite tilt of the two beams with respect to the IRCAL focal plane. Similar small PSF distortions are seen in the Lyot Project coronagraphic polarimeter (Oppenheimer et al., in prep.). The modulation scheme employed with the waveplate mitigates the effect of these aberrations to a large extent, but not perfectly.

The waveplate can only compensate for non-common-path errors which occur *after* it, not before. One of the most important non-common path effects is the different system pupils for the left and right hand channels, as described above. Not only does this mean that each polarized image is formed from a beam which sees slightly different portions of the telescope optics, the beams follow slightly displaced paths through the atmosphere. Truly static wavefront errors are removed by the modulation, but time-variable phase errors from uncorrected atmospheric speckles will not be.

2.6 Astronomical Calibration

2.6.1 Darks.

There are no special requirements for polarimetry mode darks; the usual IRCAL automated dark tool suffices. Darks are obtained at the end of each night, and are reduced into a per-night calibration file library.

2.6.2 Flat fielding

As flat-fielding errors are expected to be the limiting source of error for the detection of faint polarized circumstellar material, several methods for flat-fielding the polarimeter have been pursued.

As mentioned before, the IRCAL aperture positioning mechanism has frustratingly poor repeatability. Because of this, the aperture mask position can only be approximately

reproduced from night to night, and thus it is necessary to take flats again each night.

Because the twilight sky is itself highly polarized, it is far from ideal for flat fielding a polarimeter. Dome flat screens are typically only somewhat better. To get around this problem, polarized twilight sky exposures taken with different waveplate angles can be summed to make a "pseudo-unpolarized" flat frame. This method only works if the sky brightness and polarization are constant, a requirement notably not satisfied during twilight. IRCAL's small pixel scale allows it to take unsaturated exposures on the daylit sky up to several hours before sunset, at which point the sky polarization is more stable. Ideally it would be best to take the sky exposures while continuously rotating the waveplate, ensuring a fully unpolarized sky. In practice this is not feasible given the maximum speed of the rotation stage. The highest accuracy polarized flat fielding may require not only rotating the waveplate while exposing, but synchronizing the exposure time such that it is an integral multiple of the waveplate rotation period.

From the set of "pseudo-unpolarized" frames we compute one master median flat, which we use for all waveplate angles. Some authors have reported slight increases in performance from using a flat frames computed individually for each waveplate angle (Ageorges & Walsh, 1999). Others have reported benefits from using more complex algorithms to measure the chip's flat-field response (Kuhn et al., 1991; Kuhn, 2005). We did not investigate the use of such techniques in detail, but note that they may offer future potential for improvement to this instrument.

The flat fields are also used to measure the location of the aperture mask as it shifts from night to night. A Hough-transform-based linear edge detector locates the edges of each polarized subimage on the detector. This routine works best on frames with high sky flux, so that the edges of the field of view are easily visible; twilight sky frames work especially well (but the algorithm can also be ran on science frames in a pinch). The detected masks are undersized by 5 pixels to avoid edge effects such as scattered light from the aperture mask edge.

2.6.3 Polarization Angle Calibration

While the prism and waveplate mechanism were installed with careful attention to alignment, an angular precision of better than a few degrees is not easily possible by hand. It is necessary to calibrate the position angle of the measurements with regards to an external source of known position angle. This calibration was made using the twilight

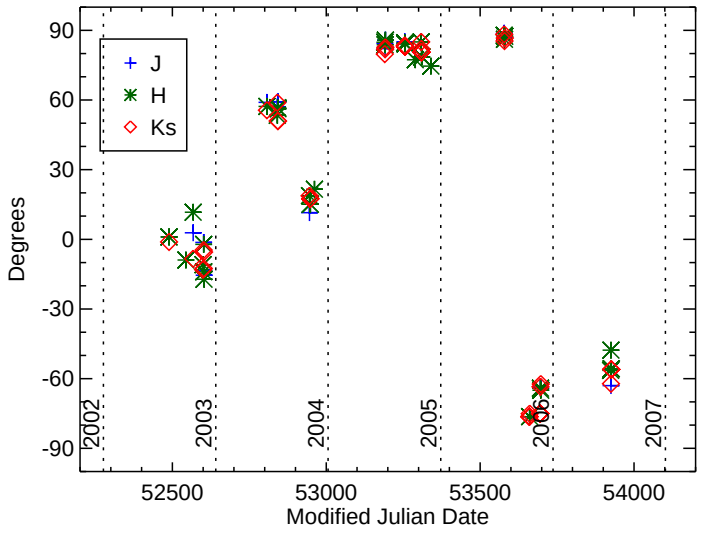

Figure 2.5: Variation in the zero point of position angle over the last four years. The position angle offset changes unpredictably once or twice a year, but stays roughly constant over shorter periods of time. There appears to be an overall positive trend of around 30 degrees per year, but with fluctuations in both directions on top of that trend. The reason for this overall pattern remains unclear.

sky, which is strongly linearly polarized normal to the direction pointing toward the sun. IRCAL's small pixel scale allows unsaturated imaging of the sky while the sun is still up and the sky polarization is strong. Using the sky as a calibrator allows us to use all pixels of the detector and thus rapidly obtain high signal to noise. Indeed, the same exact data are used for flat fielding the detector and for calibrating the positioning angle.

The position angle correction in practice has varied much more than was expected. During any given observing run it is essentially constant, but in between runs it has often changed, apparently at random and by as much as 80 degrees. It appears that the Newport PR50 rotation stage, when unpowered, is capable of rotating freely. The vibrations involved in taking IRCAL off the telescope and/or deinstalling the waveplate table from IRCAL between runs have proven to be enough to jostle the waveplate into a new position. This is not a problem in practice because it is so straightforward to calibrate the position angle using the twilight sky.

2.6.4 Sky Subtraction

The infrared sky brightness at night is primarily unpolarized emission from OH and H_2O molecules, in contrast to the twilight sky which is dominated by polarized scattered sunlight. Empirically, the infrared night sky has a very low level of polarization, except in conditions of strong moon light. In dual-channel differential polarimetry, an unpolarized background will subtract out of the Q and U images. Thus there would be no need to worry about sky subtraction, if our sole concern was the polarized images. However, we also want to produce total intensity images for each target, which requires the usual sky subtraction especially in K_s band. In many cases, the median of the science frames is an adequate sky frame, but in other cases, extended circumstellar emission or dense star fields contaminate the median and separate sky frames must be obtained offset from the science target. Each sky pointing is observed using the full waveplate rotation sequence, and multiple pointings may be averaged together to produce a master sky frame for each waveplate position. This process allows for the subtraction of any polarized sky emission, but as mentioned above, this is usually negligible.

2.6.5 Instrumental Polarization

Instrumental polarization of some degree is found in nearly all optical systems, and particularly in those where significantly non-normal reflections occur. The Lick AO opti-

cal path involves multiple such reflections, and thus nontrivial instrumental polarization is expected. Accurately modeling instrumental polarization is extremely challenging, as oxide layers on mirrors and other imperfections can play substantial roles (Keller, 2002). Furthermore, the dichroic used to separate the visible wavefront-sensing and IR science channels is expected to be partially polarizing, but this optic has been neither measured nor modeled in detail. A model was calculated for the Lick AO system (neglecting the dichroic) with the expectation that it would only provide a rough estimate of instrumental performance.

The Lick AO optical bench is oriented on the telescope such that the plane of incidence for the beam as it traverses the system is oriented parallel to the sky-projected right ascension direction (the $-Q$ direction). It is therefore symmetrical with regards to the $+U$ and $-U$ directions and so we expect little instrumental polarization in U. Neglecting any effects of the dichroic, our model predicts instrumental polarizations of 2.9%, 1.3%, and 0.5% in J, H, and K_s respectively, all in the sky-projected $+Q$ direction.

However, in light of the limited precision possible modeling instrumental effects, we undertook a program of observations of unpolarized standard stars in order to calibrate instrumental polarization. As has been noted by Ageorges & Walsh (1999), data on infrared unpolarized standards is somewhat lacking, particularly of standards dim enough to be observed on modern large telescopes without detector saturation. The derived instrumental polarizations are listed in 2.1. The instrumental polarization bias at Lick is extremely stable with time, changing $< 0.1\%$ in observations of standard stars more than a year apart. The fact that the Lick AO system is a Cassegrain instrument helps here by keeping the AO system and telescope fixed relative to one another.

The measured instrumental polarizations are all around 2.5%, in the $-Q$ direction; in other words, of comparable magnitude but perpendicular to that expected from our model. We note again that our model neglected the effects of the dichroic. However, while the detailed polarization properties of that optic are unknown, based on its orientation with respect to the beam it is expected to introduce a polarization in the $-Q$ direction, in accordance with the observed behavior. It appears that the dichroic is by far the most polarizing element of the optical train and dominates the total instrumental polarization of the entire telescope/AO/camera combination.

Instrumental polarization may be removed via the approximate method presented in in Appendix I of Goodrich (1986). But that would still leave interstellar polarization

Table 2.1. Instrumental Polarization

	J	H	K_s
Instrumental Polarization	$.0249 \pm .0005$	$.0211 \pm .0005$	$.0238 \pm .005$
Instrumental Polarization Angle	$-85° \pm 1°$	$-88° \pm 1°$	$-83° \pm 1\,\mathrm{deg}$

Note. — Instrumental polarization as measured from a collection of unpolarized standard stars.

unaccounted for, which may be nonzero for sources at distances of a few kpc (Heiles, 2000). We instead adopt an iterative optimizing subtraction process that simultaneously removes instrumental and interstellar polarization. See §3.3.

2.6.6 Pixel Scale

Lloyd et al. (2000) previously characterized IRCAL's pixel scale as $0\farcs0756 \pm 0.0002$ /pixel, but observations of HIPPARCOS calibration binaries during the course of my HAEBE survey indicated that this is an oversimplification. Slightly different plate scales were found in the x and y directions, indicating that IRCAL is anamorphic, a result not unexpected given that its internal off-axis parabolic mirrors are not of unit magnification.

To quantify the anamorphism, I obtained LGS AO observations of the core of M 53. I extracted a list of point source coordinates using the Starfinder IDL package, and compared them to the corresponding ones from HST WFPC2 imaging of the same cluster. I simultaneously fit the displacement, rotation, and x- and y-magnification between the two sets of coordinates using the MPFIT Levenberg-Marquardt nonlinear least squares routines. This analysis yielded a plate scale of $0\farcs0754$ pixel^{-1} in the RA direction, $0\farcs0780$ pixel^{-1} in Dec., and I have adopted those values for all subsequent analysis.

To compensate for this anamorphism, I developed an IDL routine `ircal_dewarp`, based on Keck's `nirc2warp` by Antonin Bouchez. This routine transforms an image from the anamorphic plate scale to a uniform $0\farcs040$ pixel sampling, using the IDL `interpolate` routine with cubic spline interpolation. It is important to note that this routine is not strictly flux conserving, nor does it account for any higher order field distortions. IRCAL

does have measurable field distortions (Michael Fitzgerald, private communication). These distortions surely differ between normal and polarimetric modes given the beam displacement by the Wollaston. Attempting to characterize these effects and compensate for them, possibly requiring sophisticated image processing techniques such as the Drizzle algorithm (Fruchter & Hook, 2002), is beyond the scope of this paper.

To assess the success of the `ircal_dewarp` correction, and to measure any shifts in the orientation of IRCAL over time, reference binary stars were routinely observed. These stars were drawn from the Suggested Calibration Targets list of the Washington Double Stars Orbits Catalog. After reduction with the standard polarimetry pipeline, the observed binary separation was measured from the image's autocorrelation, and compared to the computed separation using the orbital elements from the WDS. See table 2.2 for typical results. Because the WDS Orbit catalog itself is imperfect—indeed, most of the binaries with separations and brightnesses suitable for observation with IRCAL have orbits graded 4 or 5, the two lowest grades—some amount of discrepancy between observed and predicted values is expected. Many entries in the WDS do not contain estimated uncertainties, so we make no attempt here to separate out these two effects. A conservative estimate, based on the discrepancies between observed and predicted binary star positions, is that the plate scale in post-anamorphism-correction IRCAL images is uncertain by at most $\sim$2.5% in linear size, and by 1.0% in position angle.

2.6.7 Photometry.

Photometric standards are observed each night, except on nights with obviously non-photometric conditions. Stars from Persson et al. (1998) and the UKIRT faint and bright standards lists were used; the Persson standards gave the most consistent results and were used most often. Each standard was observed in polarimetry mode, with an identical optical setup as the science targets and identical observing procedure, except less time was spent on standards and in many cases the waveplate rotation was skipped. (Since we only measure the total intensity for the standards, there is no need to measure its full polarization.) After the standard polarimetry reduction process, aperture photometry is performed on each standard using a large aperture ($7''$ diameter). The encircled energy curve of each standard is also measured, for use as an aperture correction.

Adaptive optics photometry is a notoriously problematic area. Changes in sky conditions and in source brightness mean that wavefront correction will surely vary between a

Table 2.2. Astrometric Reference Binaries

Star	Date	ρ_m	ρ_o	$\%err$	θ_m	θ_o	$\%err$
HD 146413	04-07-03	3.33	3.33	0.1%	19.14	18.89	1.31%
HD 38	04-09-06	6.20	5.96	3.9%	182.63	184.10	-0.80%
HD 173739	05-07-26	12.42	12.15	2.2%	176.43	175.69	0.42%
HD 98231	05-11-20	1.69	1.72	-1.8%	237.80	239.90	-0.88%
Std. Dev.				2.5%			1.0%

Note. — A typical subset of astrometric reference binaries observed with IRCAL-pol.

science target and its calibration source. This will cause photometric errors as the encircled energy curve varies. A variety of techniques have been proposed to attack this problem, including PSF reconstruction from wavefront sensor data (Fitzgerald & Graham, 2006) and from the image power spectrum (Sheehy et al., 2006). We do not adopt here any of those techniques, and expect an uncertainty of 5-10% in the resulting photometry.

2.7 Astronomical demonstration data

A few brief observations serve here to demonstrate both the technical capabilities and limitations of this instrument. Fig. 2.6 presents an observation of an unpolarized standard star showing the achieved contrast. Fig. 2.7 show the first-ever H band resolved imaging polarimetry of the planet Uranus.

2.8 Conclusions

We have developed and deployed a dual-channel imaging polarimeter for use with the Lick Observatory adaptive optics system. Its unique YLF Wollaston prism and an achromatic waveplate enable polarimetry throughout the near infrared. Dual-channel po-

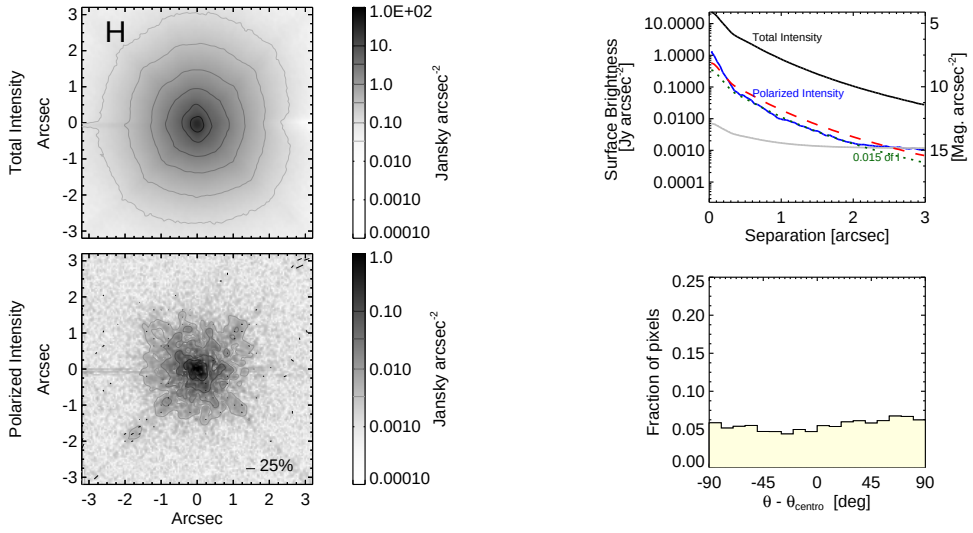

Figure 2.6: HD 18803 is a member of the UKIRT list of unpolarized standard stars (Gehrels, 1974). On the left I show both total intensity (Stokes I) and polarized intensity P. The right top image displays several radial profiles for this target. The top solid line is the mean profile for total intensity, while the second (blue) solid line is the profile of polarized intensity. As a rough estimate of the light-suppression capabilities of the polarimeter, the thin dashed line shows a copy of the I profile that has been multiplicatively scaled to roughly match the P profile. The thin solid line shows the theoretical minimum noise limit of P, based on photon statistics and read noise. Lastly, the red dashed line shows an approximate upper limit on the instrumental crosstalk between P and I, measured from the high end of the distribution for Fig. 3.2, and intended to provide a rough sense of the maximum magnitude of instrumental effects. A polarized signal above this line is definitely real, but a lower value of P than this curve does *not* necessarily imply that the polarization is instrumental in origin. Below that is a histogram showing how the polarization position vectors are oriented with respect to the expected centrosymmetric pattern that indicates circumstellar dust. The flat histogram seen here is the expected null result for an unpolarized star such as this.

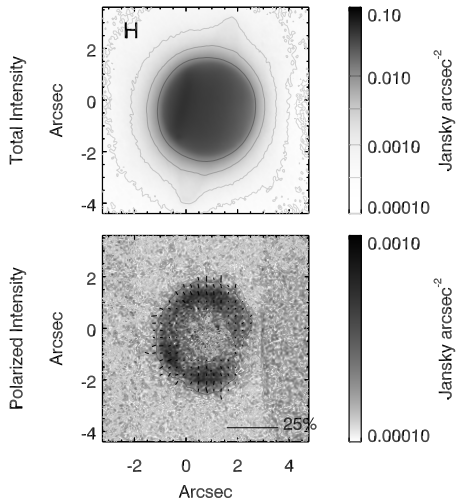

Figure 2.7: Uranus, as seen in polarized H band light on 2004 July 05. The upper frame shows total intensity, Stokes I, while the lower frame shows polarized intensity with overplotted vectors giving the percent polarization. Uranus is very limb-brightened in polarized light, with a peak polarization of about 1.5% at the edge of its disk. Unlike circumstellar disks, the polarization vectors here point radially inwards rather than perpendicular to the center, an expected effect of Rayleigh scattering in planetary atmospheres. To my knowledge, this is only the second ever resolved imaging polarimetry of this planet, after Schmid et al. (2006), and is the first such measurement in the near infrared.

larimetry provides a form of self-referenced stellar PSF subtraction, enhancing contrast for the detection of faint circumstellar dust. The IRCAL polarimeter typically provides almost two orders of magnitude reduction in stellar light, with its sensitivity ultimately limited by a complicated array of instrumental effects. It has been operating on the sky for more than four years now, and has observed a range of targets spanning from young stars to planets to planetary nebulae. In that time IRCAL polarimetry has proven to be a sensitive and powerful tool for imaging the dusty environs of young stars, as we shall explore in coming chapters.

While the IRCAL polarimeter performs well, it suffers from a number of instrumental limitations which could have been easily avoided had implementation of a polarimetric mode been considered during the initial science camera design. All too many polarimeters are born this way, as post-facto retrofits to instruments originally intended as pure imagers (Hough, 2005). This lesson is particularly relevant to the current design efforts for "Extreme AO" direct planet-imaging instruments: optimizations for polarimetric performance should be considered in trade studies early in the design process of both AO systems and science instruments. Present AO polarimeters (in every instance of this class of retrofitted instruments) have ably demonstrated their ability to detect faint scattered light in the presence of a bright stellar PSF—the potential for discovery using a truly optimized AO polarimeter is tremendous.

Acknowledgements

I would like to thank Oliver Meissner and the staff of Onyx Optics for their efforts in fabricating our Wollaston prism, and in particular for providing us with two extra prisms. Thanks also to Don Gavel and Elinor Gates for their work in integrating polarimetry mode into the Lick AO system, to Brian Bauman for useful discussions on optics, and to Chris Endicott of the Berkeley Chemistry department for the FTIR spectra measurements. This work has been supported by the National Science Foundation Science and Technology Center for Adaptive Optics, managed by the University of California at Santa Cruz under cooperative agreement No. AST - 9876783. MDP is supported by a NASA Michelson Graduate Fellowship, under contract to the Jet Propulsion Laboratory (JPL). JPL is managed for NASA by the California Institute of Technology.

Table 2.3. Prism and waveplate transmission efficiencies

	J	H	K_s
Waveplate Transmission	$.993 \pm .001$	$.983 \pm .001$	$.896 \pm .013$
Wollaston Transmission	$.935 \pm .001$	$.940 \pm .002$	$.985 \pm .018$
Net Transmission	$.923 \pm .001$	$.923 \pm .002$	$.885 \pm .020$
Polarizing Efficiency	$1.001 \pm .0015$	$.991 \pm .0015$	$.950 \pm .05$

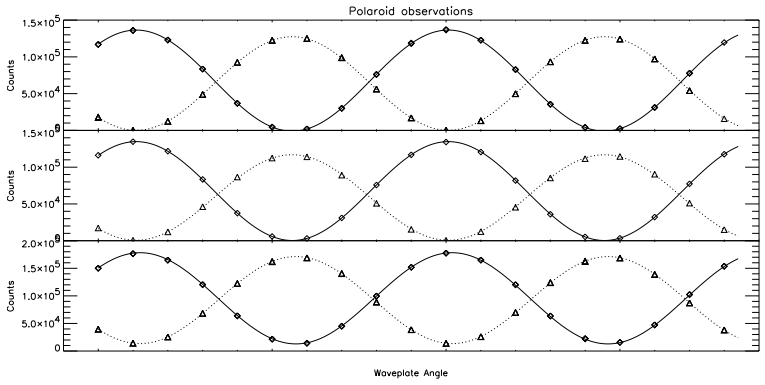

Figure 2.8: Transmitted brightness through the crossed Polaroid and prism. Solid line is the left channel, dotted is the right. From top to bottom: J, H, and K_s filters. Counts are in arbitrary units. The overall phase of the system is arbitrary and was set by the orientation of the Polaroid with respect to the waveplate zero point.

Table 2.4. Polarizing Efficiency

	J	H	K_s
LHS Extinction	0.0072	0.0087	0.0778
RHS Extinction	0.0006	0.0129	0.0850
RHS/LHS Transmission Ratio	0.94	0.87	0.095

Note. — These data were obtained from aperture photometry on roughly 200s integration per band on the AO calibration lamp. Observations were performed with and without both the waveplate and Wollaston prism. The ratios of reduced source counts with and without each optic were taken as an indication of the transmission efficiency of that component. The Wollaston prism's transmission increases slightly toward longer wavelengths, while the waveplate's transmission is excellent for J and H before falling $\sim 10\%$ at K_s. This is expected based on the design of the antireflection coating used.

Chapter 3

The Challenges of Differential Polarimetric Data Reduction

Abstract

Data reduction for differential polarimetry is a difficult and complicated subject. The goal of high-contrast polarimetry is the detection of signals many times fainter than the bright background of starlight. While differential measurement techniques help tremendously, any small factor which disturbs the relationship between the two beams will introduce noise into the differential subtraction process, compromising the contrast ultimately reached. I describe here some of the pitfalls inherent in differential polarimetry and present the data reduction algorithms deployed against those difficulties.

3.1 Introduction

Interest in differential polarimetry has surged in recent years, driven in part by the growth in circumstellar disk science and the increased availability of adaptive optics systems. There are now differential polarimeters available on the Lick 3 m, NACO at the VLT, and **others?**. Nor is differential polarimetry limited to use with adaptive optics; optical polarimetry is available at many telescopes, most notably the VLT.

But despite the growing number of differential imaging polarimeters pointed at the sky, the production of science results has been slow. This situation must in part reflect

the challenging nature of differential polarimetric data observing. It does not belittle the many technical difficulties and complexities encountered throughout all branches of observational astronomy to say that polarimetry has problems all its own. To observers and experimentalists who approach polarimetry for the first time and are not used to thinking in terms of Stokes parameters and Mueller matrices, the learning curve can be steep.

Data reduction for imaging polarimetry has been discussed before by a number of authors (Gledhill et al. 1991, Wolstencroft et al. 1995, Kuhn et al. 2001, Potter et al. 2003, Patat et al. 2006). The reduction algorithms for IRCAL build on these earlier works but also feature a number of elements specific to IRCAL. I describe here the data reduction process for polarimetry in somewhat more detail than is typical for most observational papers. This is in the spirit of sharing lessons learned from IRCAL with other aspiring differential polarimetrists. Furthermore, this is an appropriate setting to air dirty laundry: that is, to highlight what *doesn't* work about IRCAL polarimetry as well as what does, and what aspects should be changed in any future design, such as the planned polarimetry mode of the Gemini Planet Imager.

3.2 Sources of Noise

The fundamental problem at hand is the detection of linearly polarized scattered light in the presence of a much brighter halo of unpolarized starlight. Atmospheric distortions cause phase aberrations to the PSF, but these do not cause appreciable polarization, so we may consider the starlight to be unpolarized. By subtracting simultaneous images of perpendicular polarizations, we can obtain images of the Stokes parameters which are less sensitive to atmospheric aberrations.

Nearly every element of an astronomical polarimeter has the potential to introduce measurement errors. Let us consider them each in turn, in the order a photon will encounter them. Here I simply describe each effect qualitatively; each can be treated quantitatively using the technique of Mueller matrices.

- Astrophysical polarization other than the science target—in other words, interstellar polarization between the target and Earth—can contaminate the signal. For Herbig Ae/Be stars at distances of several kpc, this factor can be appreciable.

- The telescope and adaptive optics system will induce an instrumental polarization.

AO systems typically have a great many reflections, many at high angles of incidence, which cause instrumental polarization through differential transmission of the e- and o-rays. The dichroic beam-splitters used to separate science light from wave front sensing light are often even more strongly polarizing than the AO mirrors. For very high contrast applications, thin metal film effects must be considered (Breckinridge & Oppenheimer, 2004).

- The waveplate (or other polarization modulator) will be imperfect. Even a "super-achromatic" waveplate is not perfectly achromatic, and whatever residual departures from $\lambda/2$ are present will introduce a bias. To whatever extent a waveplate is not perfectly a half-wave plate, it is somewhat like a quarter-wave plate instead. Quarter-wave plates convert linear polarization into circular polarization; retarders intermediate between quarter- and half-wave plates convert linear polarization into elliptical polarization. Since the Wollaston prism analyzer is only sensitive to the linear component of polarization, the conversion to elliptical polarization is effectively a partial depolarization, reducing the efficiency of the instrument to detect polarization.

  Secondly, even leaving aside waveplate imperfections, the rotation mechanism will not be ideal. Small offsets in waveplate position will induce a crosstalk between the Stokes parameters, the result of which can be either depolarization or spurious polarization depending on the magnitude of the error and the intrinsic polarization of the source.

- There are non-common-path errors between the s- and p- polarization beams. These can occur due to birefringence in optics (such as dichroic beamsplitters, atmospheric dispersion compensators, or other transmissive optics). Reflective optics can also cause non-common-path errors, if the two polarized beams have been displaced (sheared) apart slightly due to birefringent optics. This is certainly the case for the post-Wollaston-prism optics, but can also occur pre-Wollaston if one of the earlier transmissive optics induces a beam shear. Modulation can greatly reduce the impact of such non-common-path errors, but only for those which occur *after* the modulator; anything upstream must be calibrated out by observations of standards.

- The aperture mask mechanism in IRCAL does not work very well. It has very low repeatability in its positioning, and is prone to shifting unpredictably during observations (most often as a result of mechanical crosstalk from one of the other

wheel mechanisms). Shifts in the aperture mask change the field of view and flat field for the observations.

- The Wollaston prism may not be perfect. However, Wollastons are usually very good, with a typical rejection level of $\gtrsim 10^6$, so this is likely to not be a limiting factor in the observations. On the other hand, the two beams may have different transmission efficiencies. Further, if the Wollaston's optical axis is not oriented perpendicular to the waveplate's axis at zero rotation, there will be a shift in the zero point of position angle.

- In IRCAL's case, there is a pupil shear between the two polarizations. The Wollaston is located in IRCAL before the cold pupil, so the two polarized beams have already started to diverge by the time they reach the pupil. This causes each channel to have a slightly different pupil, as projected back through the telescope and onto the sky. It would have been better to place the Wollaston immediately after the cold pupil, but the layout of the existing filter wheels didn't allow this.

- The detector's quantum efficiency may be polarization dependent, particularly if the chip is illuminated at an oblique angle of incidence. This can be an issue for single-channel polarimeters using wire grids or Polaroid analyzers (though a proper calibration of the instrumental polarization and efficiency will remove the effect). For dual-channel polarimeters, it matters far less, because the beams after the Wollaston will always have the same polarization; while the amplitude of each beam varies during the modulation process, the polarization of the actual photons that fall on the detector does not.

- Errors in flat fielding can easily be the largest source of noise in differential polarimetry. The polarization modulation reduces the impact of flat field differences between the two channels, but cannot eliminate the problem entirely; even though you measure each polarization state alternately on both sides of the detector, you then have to merge those two datasets to get the final signal, which relies on accurate flat fielding to maximize the cancellation of starlight.

- The second factor which frequently dominates real-world polarimeters is registration and shifting errors. IRCAL's coarse pixel sampling and anamorphism contribute to

this problem, but even were those issues fixed, there would still be the problem of accurately registering long exposures saturated on the central core.

- Lastly, bad pixels, read noise, and photon shot noise are issues just as in non-polarimetric observations.

In theory, it should be possible to assemble a quantitative error budget for any polarimeter incorporating the above components. In practice, it has proven very difficult to quantitatively assess the relative importance of the various factors. In part this is because of the development history of IRCAL polarimetry: it was a mode retrofitted into the camera at the telescope; no laboratory tests have ever been conducted, and no calibration source better than a piece of IR Polaroid mounted imprecisely by hand in front of a lamp has ever been observed. Furthermore, the functional form of the various terms in the hypothetical error budget are all quite similar: nearly every effect introduces a noise signal proportional to total intensity. This is in fact precisely what is observed in practice $P_{noise} \propto I$. Flat field errors, registration errors, pupil shear, and so on all introduce noise proportional to I, rendering it hard to disentangle them. But despite this situation, in practice IRCAL polarimetry has proven to be an effective observational tool, through the use of on-the-sky calibration observations and a careful approach to data reduction.

3.3 General Considerations

Before we proceed into the gory details of data processing algorithms, we must first establish what the goal of that processing is. A fundamental point is that *our goal is to measure spatially varying polarization from resolved circumstellar dust. No attempt is made to measure the total net polarization of any unresolved source.* If one seeks to measure net polarizations, an AO polarimeter is far from the optimal tool. More accurate and precise measurements are possible using dedicated polarimeters incorporating on-axis optics with low instrumental polarization, rapid modulation, and low or zero read noise detectors such as photomultiplier tubes or avalanche photodiodes (Potter & Graham, 2005). Furthermore, for distant or embedded sources like many Herbig Ae/Be stars, interstellar polarization can be substantial, at a level of a few percent. While it is possible to remove interstellar polarization based on observations of nearby stars (Heiles, 2000), this is fraught with many uncertainties. Not the least of these is the assumption that stars are embedded in a uniform

interstellar medium so that polarizations vary in a dependable way from star to star–but this is far from being the case in the clumpy, dusty environments of young stars. Is there a better approach?

We can instead allow the net polarization of the star (arising from both interstellar and instrumental polarization) to be a free parameter, and solve for it numerically. This is the approach used by Potter (2003a) in the first Ph.D. thesis devoted to this subject, and we adopt this method here as well. From the full set of images taken at each of the waveplate positions, I_ϕ, we select out those sets taken at each distinct waveplate angle: $I_{0i}, I_{22.5i}, I_{45i}, I_{67.5i}$. Rather than simply computing $Q = I_0 - I_{45}$, we allow an arbitrary multiplicative scaling factor and offset: $Q = I_0 - \alpha I_{45} + \beta$, and likewise for U. The factor α represents the difference between the two intensities resulting from the net polarization, while β simply accounts for any residual bias in the background level of the two images which was not removed by sky subtraction. An iterative numerical process solves for the α and β that minimize the total residual flux in the difference image.

This approach relies on the assumption that the total flux is dominated by inherently unpolarized light, so that any net polarization seen in the data is the result of instrumental or interstellar polarization. For our science targets, this is generally an excellent approximation, since scattered light is usually at most a few percent of the total. It is a robust approach even in the presence of some scattered light: for a symmetric distribution of dust around a star, the polarization position angle varies around the disk and the total net polarization in a large aperture is zero.

The primary drawback of this approach is that for inclined or nonaxisymmetric dust distributions, this assumption begins to break down and may introduce a systematic bias, which will take the form of a reduced degree of polarization. In an extreme case, a source which is 100% polarized would not be measurable with this technique at all. However, as mentioned above we restrict our efforts here to the detection of spatially varying polarization from resolved dust. For such systems, any uncertainty resulting from this scaling process will be negligible compared to other uncertainties in the degree of polarization.

Indeed, it is very challenging to accurately measure a percentage polarization using an AO polarimeter. While differential polarimetry results in a polarized intensity image P which is robust against atmospheric errors, the total intensity image I is identical to that from regular AO imaging, with a broad PSF halo from residual uncorrected starlight. Thus P/I will be a strongly biased quantity, giving in practice only a lower limit to the intrinsic

degree of polarization. Improving on this situation requires either accurate methods of AO PSF calibration and subtraction (Fitzgerald & Graham, 2006; Sheehy et al., 2006) or the use of a starlight-subtracted image from some other source such as HST (Hansen et al., in prep.)

3.4 The IRCAL Polarimetry Data Reduction Package

With those goals in mind—the detection of spatially resolved polarization from extended circumstellar dust, and not the precise measurement of total polarization—an IDL data reduction pipeline for IRCAL polarimetry data has been developed. This software is available online[1] and handles the reduction, calibration, and analysis of IRCAL polarimetry data. The IRCAL camera software maintains an electronic log file of observations throughout the night. A script parses this log file and produces a reduction script containing appropriate calls to IDL routines to reduce calibration and science data in turn. Minimal user intervention is required to produce first-pass science reductions, though extensive options exist for overriding or fine-tuning the behavior of the reduction pipeline.

3.4.1 Calibration Requirements

Flat field data must be taken on the twilight sky each evening. Not only are these data used to flat field the detector, they also are used to calibrate the zero point of position angle, by measuring the polarization orientation of the twilight sky, and to create region identification masks for the two polarized subimages. Differential polarimetry places particularly stringent demands upon flat fielding accuracy, since any errors in the flats will directly transfer into the final image when the two polarized PSFs are subtracted.

3.4.2 Initial Reduction Process

Once calibration files have been reduced, the science data can be processed. First, the basic instrumental signature must be removed. Images are dark-subtracted, then divided by the polarization mode flat field.

Sky subtraction can be handled in several different ways. The most straightforward is to subtract a median sky frame from all images (using sigma clipping to reject pixels containing starlight before the median process), but separate sky images produced from

[1] http://astro.berkeley.edu/ mperrin/ircal/

nearby blank fields can also be subtracted. Bad pixels are then rejected, using the combination of a dedicated bad pixel mask containing known permanently bad pixels and the `ns_fixpix` iterative bad pixel cleaning routine developed by Tom Murphy.

At this point, the images are relatively clean, and can be corrected for the field anamorphism using `ircal_dewarp`. This procedure uses two-dimensional cubic spline interpolation to correct for IRCAL's anisomorphic plate scale and transform the data onto a uniform $0\farcs040$ pixel grid. Cubic spline interpolation is a good approximation to the theoretically optimum sinc or Fourier interpolation, but not perfect, particularly given the non-Nyquist sampled nature of short-wavelength IRCAL data. "Ringing"-type numerical artifacts are sometimes seen close to the stellar PSF peak in the dewarped images.

3.4.3 Saturation Masking

Saturated pixels and/or pixels above the detector's linear regime are identified by comparison with a threshold value, set at 28,000 e-/pixel for IRCAL. The correlated-double-sample readout scheme employed with IRCAL results in an eventual turnover in the measured flux level for very highly oversaturated pixels, resulting in characteristic donut-shaped PSFs where some saturated pixels have low or even negative counts. To include these pixels, a second algorithm marks as saturated any pixels below the threshold but completely surrounded by saturated pixels. The saturated pixel lists for the two subimages are merged to make sure that if any pixel is marked as saturated, its corresponding pixel in the other subimage is also marked as saturated. Without this step, large subtraction artifacts are induced later in the image subtraction step.

3.4.4 Registration

The first step in the registration process is to determine the shift between the two polarized subimages on the detector. While the magnitude of the displacement is constant, its orientation varies slightly from night to night due to imprecision in the filter wheel mechanism. Like the aperture wheel, this mechanism does not have good repeatability, which results in slight changes to the rotation of the Wollaston with respect to the detector. causing the orientation of the two polarized images on the detector to vary. To measure this, the full stack of images is summed, and the resulting left- and right-hand subimages

are cross-correlated to find the beam displacement. [2]

The images are then registered against one another. This is accomplished by cross-correlating each image with a reference image, and fitting the correlation peak with a Gaussian to subpixel precision. Only the *left-hand* subimages are correlated, with the same shifts (plus the beam displacement) assumed correct for the right hand field. Shifts can also be read from the FITS header pointing information, but the flexure levels in the Lick AO optics render this method insufficiently accurate, so it is only used as a backup to cross-correlation[3]. If necessary, manual intervention is possible to tweak the automatic registration.

Accurate registration is of tremendous importance, particularly for extracting polarized signals very close to a star. Registration to a small fraction of a pixel is necessary. Apai et al. (2004) found that for their VLT polarimetry data, random shifts of 0.2-0.5 pixel (5-14 mas) distort the polarized signal of the inner arcsecond, and shifts of 1 pixel completely disrupt it. Long exposure images, which probe polarization on slightly larger scales, are correspondingly more robust against misalignments. Apai et al. used what they describe as a "two-level Gaussian fitting procedure" to register their data, while Potter (2003a) used an iterative shift-and-subtract process to empirically find the shift for each image which gave the lowest residuals. Which of these techniques is best will vary with details of instrument and observational conditions.

The long exposures necessary to detect faint circumstellar dust are frequently saturated on the central star, which limits the degree of accuracy possible in registration. Cross-correlation still works to some extent in this case, using the diffraction spikes and other outer PSF structure, which is why I selected that approach for the IRCAL data reduction pipeline. The highest accuracy polarimetric image registration will require the use of "satellite PSF" techniques developed for coronagraphic observations (Marois et al., 2006; Sivaramakrishnan & Oppenheimer, 2006).

An important caveat about IRCAL polarimetry is that the detector is only Nyquist sampled at K_s. At shorter wavelengths, high spatial frequency PSF structure will alias to lower frequencies, biasing the centroids and image shifts in an unpredictable and time-

[2]Note that it is an assumption here that the beam displacement is identical for all images in a set: that there is no shift of the Wollaston prism during an exposure sequence, nor do field distortions change the apparent shift on different parts of the chip. This assumption is fairly good, but not perfect.

[3]Scott Severson has been developing a flexure compensation mode for Lick AO, with good progress. If/when this upgrade becomes compensated, the FITS header astrometry will become correspondingly more accurate.

variable manner.

3.4.5 Mosaicing

The images are then mosaiced together. This step combines images with arbitrary different exposure times by performing a weighted average of the image counts in DN per unit exposure time in each image. Subpixel shifting of images is done with Fourier interpolation.

One mosaiced image is produced for each of the polarization angles $p_0, p_{45}, p_{22.5}$,and $p_{67.5}$. These mosaics include all polarized subimages from both sides of the detector, and the images from the redundant waveplate settings 90, 135, 112.5 and 167.5 are combined in with their counterparts (i.e. images taken with the waveplate at 90 are mosaiced in with the frames taken with it at 0, and so on.)

Bad and saturated pixels are of course skipped when assembling these mosaics. The resulting images are then combined according to

$$\begin{aligned} Q &= p_0 - \alpha p_{45} + \beta \\ U &= p_{22.5} - \gamma p_{67.5} + \delta \\ I &= \left(p_0 + \alpha p_{45} + p_{22.5} + \gamma p_{67.5}\right)/2 \end{aligned}$$

The scaling factors for minimizing the total power in $|Q|$ and $|U|$ are determined by IDL's Powell nonlinear optimization routine. The β and δ factors correct for residuals in the sky background levels, and are always small. Typical values for α and γ are within a few percent of unity. This order of operations—mosaicing the images, then performing the subtraction—is by no means the only way to do things. One can also perform the subtraction and then mosaic the subtracted frames, and there are also reduction algorithms which rely upon ratios rather than differences of the two channels (Tinbergen 1996). Here the mosaic-then-ratio approach was chosen because it offered somewhat greater flexibility for dealing with missing frames from AO system dropouts or moments of bad seeing, but the merits of the various algorithms should be reevaluated for future instruments.

As a part of the image combination process, exposure maps are generated for I, Q and U. More importantly, however, are the per-pixel error maps which are also generated. These are computed from the standard deviation, not of the individual input frames, but of the *double-differenced* input frames. That is, for each image i and its counterpart taken

with the waveplate rotated i', we compute the double-differenced image dd_i, where

$$dd_i = (i_L - i_R) - (i'_L - i'_R)$$

The two subtractions remove the simultaneous atmospheric speckles and the non-common-path static speckles, respectively, as in Kuhn et al. (2001). Then the per-pixel standard deviation of the mean is computed from this set of difference images. This all may seem like a cumbersome process, and it is indeed somewhat roundabout, but computing the standard deviation based on either the unsubtracted or the single-subtracted images would not provide an accurate measure of the speckle-reduced noise characteristics of the final Stokes images. To the best of my knowledge, the use of per-pixel uncertainty maps for the analysis of AO polarimetry data has not been discussed before in the literature. Experience during the course of my AO polarimetry survey of HAEBES is that such maps provide valuable additional information very useful in assessing the significance of faint signals (see §4.7.1).

The polarized intensity P is computed from Q and U in the usual manner: $P = \sqrt{Q^2 + U^2}$. Several algorithms have been developed for dealing with the biases introduced into P by its positive definite nature (Wardle and Kronberg 1974, Simmons & Stewart 1985, Stewart 1991). However, these corrections are important primarily in cases where the signal to noise ratio is low ($P/\sigma_P < 1$); we focus our analysis here only on pixels with strong detections of polarization and thus can safely neglect this correction. Besides, for AO data the bias in degree of polarization $p = P/I$ from the uncorrected PSF halo in Stokes I will be far larger than this statistical bias correction.

At this point, the reduction is finished except for a few final tasks: the FITS header World Coordinate System keywords are updated, and the image is converted from DN/s/pixel to Jy arcsec^{-2} based on the closest-in-time photometric standard. If observations were collected in multiple filters for a given object, the images in all available bands are registered together via cross-correlation. This does not necessarily give a perfect registration for cases in which there is significant morphology change across bands, as sometimes happens for deeply embedded sources, but it is an adequate first pass. The final images are stored as multi-extension FITS files containing the Stokes data cubes, exposure maps, and uncertainty images.

Data may be visualized using a number of IDL plotting routines, and interactively examined using a version of the `atv.pro` image display tool modified to accept Stokes data cubes and overplot polarization vectors. This code is available from the author's web site.

3.5 Detection of polarized light in reduced images

Merely looking by eye at reduced polarization images is not a very effective way to approach the data. The dynamic range in deep AO images is tremendous, and polarized structures are often very faint. Many of the image display techniques developed for high dynamic range images, such as log or asinh stretches, work poorly on data sets that have an equal amount of negative and positive power (as do Stokes Q and U). Furthermore, polarization is fundamentally a vector quantity, and looking at only one of Q or U at a time does not take full advantage of the richness of the data set.

Looking for a faint signal in the polarized intensity image P is also not the best approach. While P does incorporate both of the Q and U Stokes parameters, its positive definite nature biases it. Any noise whatsoever in the Q and U images results in a nonzero, positive value for P, which can easily swamp faint polarized signals. Polarization fraction is certainly the most intuitive way to think about polarized light, and for that reason it is often a useful quantity to display or plot, but we stress that its use for quantitative tasks should be minimized. Numerical fits should be done directly on the Q and U images, and transformed to P afterwards if necessary.

One way to detect a faint polarized signal is by looking for the characteristic "butterfly" pattern of axisymmetric dust. Apai et al. (2004) apply this approach in their study of TW Hya. By fitting a sinusoid to radially binned Q and U images they detect evidence for centrosymmetric scattering to within $0\farcs1$ of TW Hya.

A related technique looks instead at the polarization position angle θ. Light scattered from circumstellar dust has a distinct signature: a pattern of polarization vectors arranged perpendicular to the central source, often termed centrosymmetric. By comparing the observed position angle $\theta_{obs}(x, y)$ with the expected position angles for centrosymmetric scattering,

$$\theta_{centro}(x, y) = \arctan\left(\frac{\Delta y}{\Delta x}\right),$$

where $\Delta x = x - x_*$ and $\Delta y = y - y_*$ are the offsets from the stellar location, we can sensitively discriminate dust-scattered light from other contaminants such as residual speckle noise or registration errors. The position angle θ_{obs} also has the advantage that since it is formed from the ratio of two Stokes parameters, it is less sensitive to flat fielding errors than either of those quantities alone (Potter, 2003a).

Recently, the use of "radial Stokes parameters" has been advocated as an alternative

technique by Schmid et al. (2006). In this approach the Stokes vectors are transformed according to

$$\begin{aligned} Q_r &= +Q\cos 2\phi + U\sin 2\phi \\ U_r &= -Q\sin 2\phi + U\cos 2\phi \end{aligned}$$

where ϕ is the position angle measured from the central source. Q_r is then a measure of the polarization's centrosymmetry ($Q_r > 0$ for radial polarization as in the case of planetary atmospheres, $Q_r < 0$ for tangential polarization as in circumstellar disks). The use of these quantities for high contrast polarimetry deserves further study, but this is beyond the scope of the present paper.

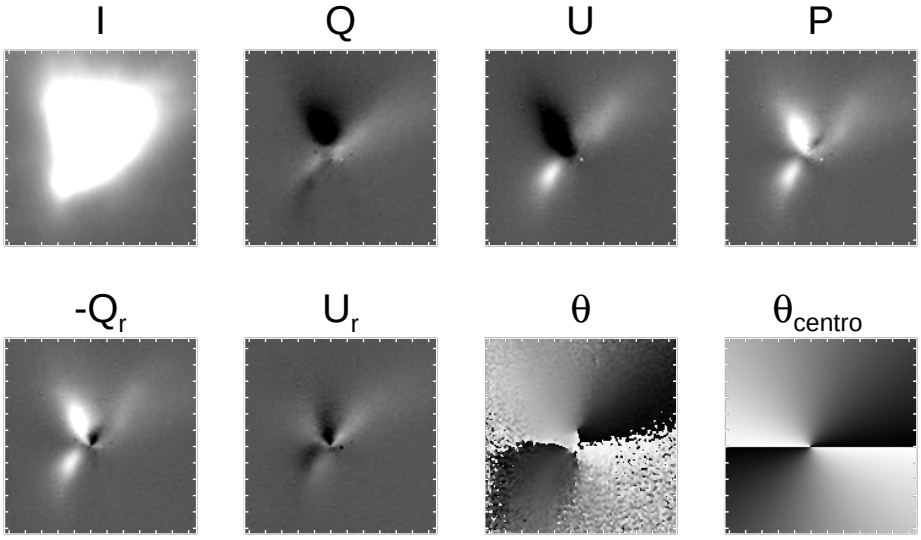

Figure 3.1: There are many ways of displaying polarimetric Stokes parameter datasets, of which I show a few here, for the highly polarized FU Ori star Parsamian 21. The first three panels plot the Stokes parameters I, Q, and U directly, and the fourth shows the polarized intensity $P = \sqrt{Q^2 + U^2}$. These are the most common representations of polarized light. The next two panels show the "radial Stokes parameters" as defined by Schmidt et al. (2006). For the strong centrosymmetric polarization of this source, most of the light goes into the negative radial Q_r term; note how similar $-Q_r$ is to the total polarized intensity P. Lastly I show the polarization position angle θ, which is in this case very similar to the expected pattern of centrosymmetric vectors θ_{centro}. The first six images are shown on the same linear stretch from -0.001 to +0.002 Jy arcsec^{-2}, while the two angle images are shown on a linear stretch from 0-180°.

3.6 Achieved Performance

In practice this instrument is capable of removing 98-99% of the unpolarized starlight, greatly attenuating the stellar background against which scattered light must be detected. The exact level of performance varies with conditions; more on that shortly.

Outside of $\sim 1''$, we reach the noise floor set by photon noise and read noise. Inwards of that, the crosstalk from I raises the polarized surface brightness above the theoretical noise floor. The precise location of the transition between photon-noise-limited and crosstalk-limited depends on several factors including source brightness and ambient seeing; for some of our targets the transition is reached inside of $1''$(though rarely inside of $0\farcs7$) and for some it is further out.

Similar to speckle noise, this crosstalk is not Gaussian and does not improve with time as $\sqrt{t}$. Additional integration increases the sensitivity only slightly if at all, similar to the behavior of semi-static speckles in non-polarimetric AO imaging (Hinkley et al. 2006). But I stress here that this crosstalk noise is not merely semi-static speckles rearing their ugly heads: a perfect polarimeter would completely reject any static speckles, no matter how aberrated the I PSF. It is imperfections in the polarimeter that allow a fraction of those speckles to bleed from I into P and ultimately limit our sensitivity.

This level of performance is roughly comparable to that achieved by Dan Potter with Hokupa'a. He reports reaching the photon noise floor outside of $1''$, and being limited inwards of that by flat fielding and non-common-path errors, quite similar to the performance achieved here.

Many factors contribute to this noise floor. Is it possible to disentangle which of these—flat fielding error, pupil shear, registration error, and so on—is the dominant effect? I have a partial answer to this question. For each target observed during the course of my Herbig Ae/Be survey, I estimated the fraction of light left as residual polarized intensity, by computing the median ratio of the radial profiles of I and P between $0\farcs2$ and $2\farcs0$. In Fig. 3.2, I plot this ratio versus the measured PSF FWHM[4]. The result is striking: As AO performance increases (the FWHM becomes smaller), a larger fraction of light "leaks through" the polarimeter on average. In other words, better seeing and higher Strehl PSFs result in (slightly) worse polarimeter performance!

[4]Really what I want to do here is plot the suppression factor versus the Strehl ratio or residual post-AO wavefront error, but measurements of Strehl ratio on undersampled data are frequently inaccurate(Roberts et al., 2004), so I opt for the less-sophisticated but more robust FWHM as a stand-in.

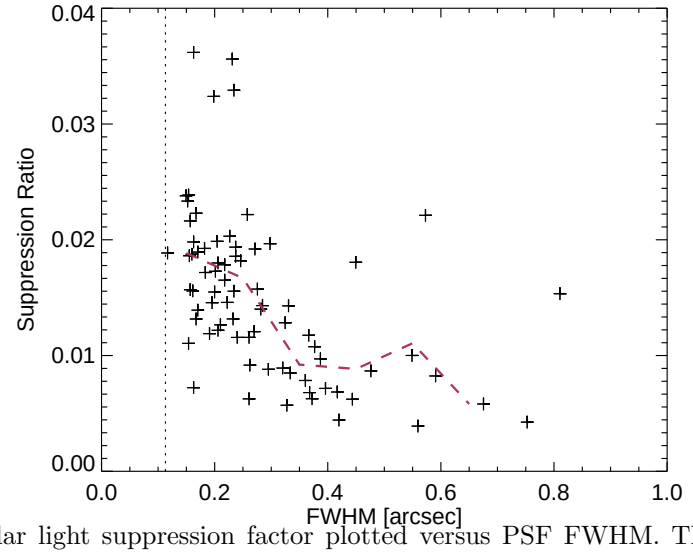

Figure 3.2: Stellar light suppression factor plotted versus PSF FWHM. The overplotted line is the average value for points in each 0.″1 wide bin of FWHMs. The trend upward for smaller FWHMs is clear.

This tells us that the crosstalk from I to P increases when the PSF has more power in high spatial frequencies. Errors in flat fielding would not cause this; such errors should be a simple multiplicative factor on the PSF, independent of PSF shape. On the other hand, PSF registration and interpolation errors *will* grow as high spatial frequency image content increases. The cubic spline interpolation used in dewarping IRCAL data is not perfect, and the present interpolation algorithm does not account for the effects of finite pixel size, so it is entirely possible that further improvement to the reduction pipeline could enhance performance.

One possible contributor to this situation is registration errors of saturated images. Read noise in IR detectors means that one must take long exposures to detect faint outer nebulae, by which point the core of the PSF will have become saturated and can no longer be used for registration. In conditions with better seeing, saturation will occur earlier, leading to the observed degradation.

Far better to avoid these effects if possible. Simply using a well-sampled detector is a positive step. "Satellite PSFs", essentially intentional ghost images, will allow the precise registration of images even with saturated (or coronagraphically occulted!) PSF cores. Beyond that, several recent designs for extrasolar planet imagers use focal plane lenslet arrays to chop the PSF into pixels *prior* to dispersion in wavelength. This can greatly

reduce the effects of non-common-path optical errors on PSF subtraction quality (Marois et al., 2004, 2005). Experiments to validate these designs are currently underway both in the laboratory (Lafrenière et al., 2006) and on the sky with OSIRIS at Keck (Larkin et al., 2006). Recent results are promising, but differential refraction (both atmospheric and in AO system dichroics) is a major challenge. However, for polarimetric applications, differential refraction poses much less of an issue, and the ability to modulate the polarization provides a powerful leverage against non-common-path errors, compared with multi-wavelength approaches. Lenslet-based differential polarimeters deserve careful study as part of the high contrast astronomer's future toolkit.

3.7 Conclusions

We have developed an imaging polarimetry mode for IRCAL, the AO science camera at Lick observatory, incorporating a YLF Wollaston prism to enable the detection of faint polarized light from circumstellar dust. In practice this system can reduce the stellar PSF halo by a factor of 50-100. The limit to this performance arises from a combination of factors, but high spatial frequency errors appear to dominate the error budget.

I end with a brief list of lessons learned from IRCAL, applicable to the design of future high contrast polarimetry instruments. Starlight suppression of about 2 orders of magnitude is attainable with IRCAL and all its flaws; a goal of 3 orders of magnitude suppression is not unrealistic for future instruments.

1. Low repeatability of the aperture and filter wheel mechanisms on IRCAL complicates data taking and reduction, but is not insurmountable. Any reasonable future design will improve on IRCAL in this regard.

2. Repeatability of mechanisms is particularly important as there are stringent requirements on flat fielding, and IRCAL's mechanism nonrepeatability prevents the development of high signal-to-noise flat libraries.

3. The Wollaston would ideally be located after the cold pupil, to prevent pupil shear between the two polarized beams.

4. To minimize instrumental polarization, the waveplate should be located as far upstream as possible. However, iterative optimizing subtraction seems to offer an effective empirical approach to removing instrumental polarization.

5. Lenslet arrays hold great promise for future high contrast polarimeters. Post lenslet array, the requirements on lateral chromatism are tremendously relaxed, potentially greatly easing manufacturing requirements on the beamsplitter.

6. Registration errors are another key component of the error budget, particularly for undersampled data and long exposures saturated on the central star; the use of artifical "satellite PSFs" as astrometric references will help solve this problem.

7. Centrosymmetry histograms provide a very useful detection metric for faint polarization, particularly when coupled with numerical uncertainty images computed as part of the data reduction process.

Chapter 4

A Near- and Mid-Infrared Survey of Dust around Herbig Ae/Be Stars

Abstract

I have conducted a large-scale survey of 110 Herbig Ae/Be stars using AO differential polarimetry to sensitively search for resolved circumstellar dust. Thirty-two stars unmistakably show polarization from dust-scattered light, while a further 20 represent probable but uncertain detections. The detected sources have a tremendously diverse range of morphologies, including circumstellar disks, bipolar envelopes, and complex arc- and fan-shaped nebulae.

The second portion of this project used high angular resolution mid-IR imaging to probe thermal emission from dust grains on the same spatial scales as the AO polarimetry probed scattered light. These two approaches are highly complimentary, with each in some cases revealing circumstellar dust undetected by the other.

4.1 Introduction

Observations of T Tauri stars have led to a general understanding of the origin of solar-type stars (Shu et al., 1987) but the formation of more massive stars is less well

understood. Herbig Ae/Be stars (HAEBEs) are young stars with masses between 1.5 and 10 $M_{\odot}$(Herbig, 1960; Hillenbrand et al., 1992, , or see Chap 1 of this work.). It has been hypothesized that the Herbig Ae/Be stars and the T Tauri stars form in similar manners (Palla & Stahler, 1993), but this remains controversial. The formation of even higher-mass stars may require additional mechanisms, such as stellar mergers, to overcome the radiation pressure that would otherwise terminate accretion (Bonnell et al., 1998), or else gravitational collapse alone may be sufficient (Krumholz et al., 2005). The Herbig Ae/Be stars are an intermediate class of objects where such effects may or may not be relevant and thus provide a useful testing ground for theories. Vink et al. (2002) suggest a transition in physical characteristics between the Herbig Ae and Herbig Be stars, based in part on different Hα line polarization effects. Spatially resolved images of these objects may help clarify whether the accretion mode does change between Ae and Be stars.

Understanding the nature of the material around these stars is also important for determining the origins of the powerful outflows often associated with young stars (see Chap. 7). Furthermore, characterizing these disks sheds light onto the conditions in which planet formation may take place. The Herbig Ae/Be stars are the progenitors of Vega-like debris disks, and there is indirect evidence for planets in disks around some of these stars (Kalas et al., 2005). Circumstellar disks have been imaged in scattered light around a handful of Herbig Ae/Be stars: for example, HD 141569 (Weinberger et al., 1999), AB Aur (Grady et al., 1999), and HD 163296 (Grady et al., 2000). However, the number of such resolved disks remains small; a larger sample is needed to understand the full parameter space of disks and how their properties may depend on spectral type, age, and/or the presence of binary companions.

To address this need, I have carried out a high angular resolution survey of circumstellar dust around Herbig Ae/Be stars. This survey consists of two parts: near IR imaging polarimetry, which is sensitive to circumstellar dust seen in scattered light, and mid-IR imaging, which probes thermal emission from dust and fluorescent emission from small particles such as polycyclic aromatic hydrocarbons (PAHs). Both surveys target dust on angular separations of a few tenths of an arcsecond to several arcseconds, corresponding to between tens and thousands of AU for typical target distances.

Multiwavelength observations provide a powerful way to constrain the nature of circumstellar dust. Numerical modeling of high resolution images allows us to constrain many properties related to disk morphology: inclination, radius, flaring, power-law density de-

pendence in both the vertical and radial direction, and the presence of any gaps or rings (e.g. Cotera et al., 2001; Wood et al., 2002) . However, there are frequently degeneracies between various model parameters which prevent the determination of a unique best-fit solution. For instance, two disks with different dust masses but also different particle size distributions may have identical total dust optical depths and hence similar appearances at a single wavelength.

In contrast to optically thin debris disks, younger primordial disks are generally optically thick. Because of this, dust properties cannot be extracted directly from images of these disks. Instead, Monte Carlo radiative transfer codes are used to produce simulated images, which are then tuned to optimize the fit between model and observation (Lefevre et al., 1982; Code & Whitney, 1995; Wolf et al., 1999). For instance, Lucas et al. (2004) used multiwavelength near-infrared polarimetry of HL Tau to derive not only a dust grain size distribution (with a maximum size slightly above 1μm, subject to assumptions about grain composition) but also information on the alignment of non-spherical grains due to magnetic fields. Duchêne et al. (2004) found that no one grain size successfully fit observations of GG Tau at all wavelengths from 0.8-3.8 μm, indicating that larger grains have settled toward the midplane of GG Tau's circumbinary disk. With each wavelength probing a different depth into the disk, and thus different a dust particle population, multiwavelength observations proved key to accurately determining the nature of dust around GG Tau.

4.2 Methodology

4.2.1 Near-Infrared Imaging Polarimetry

The first component of this project is an imaging polarimetric survey of Herbig Ae/Be stars using the Lick Observatory Adaptive Optics system, in both natural and laser guide star modes. The first results of this survey have already been presented in Perrin et al. (2004a, 2005); Perrin et al. (2006).

Laser guide star AO is needed to observe the complete population of HAEBEs; even though these massive stars are intrinsically bright, many (particularly the youngest) are very embedded and thus faint. The laser guide star system at Lick allows our survey to observe essentially all northern hemisphere HAEBEs at the high resolution ($\sim 0\farcs15$) afforded by adaptive optics.

But detecting faint circumstellar material in the midst of much brighter scattered stellar light requires high dynamic range as well as high resolution. To obtain the needed sensitivity, I developed a dual-channel polarimetry mode for the IRCAL science camera. Because dynamic range is limited by speckle noise very near stars, and speckles are unpolarized, differential polarimetry suppresses the speckle noise. Light scattered from circumstellar dust will be linearly polarized, so by rejecting unpolarized light with the polarimeter, the sensitivity to faint nebulosity near bright stars can be increased dramatically. Because the dual-beam polarimeter samples both polarization states simultaneously, it is robust against the PSF variations that trouble many AO observing programs. This technique has been previously used to obtain images of circumstellar disks around a number of young stars, including HD 169142 (Kuhn et al., 2001a), GG Tau and GM Aur (Potter, 2003b), and TW Hya (Apai et al., 2004). The IRCAL polarimeter typically rejects $\sim$ 98-99% of unpolarized light, providing two orders of magnitude improvement in contrast. This instrument is unique among current AO polarimeters in that it can observe at all three near-IR bands J, H, and K, due to its custom achromatic $LiYF_4$ Wollaston beam splitter. But imaging polarimetry is not just useful for increasing contrast—it also provides additional information compared to direct imaging which can help constrain radiative transfer models of these objects (Lucas et al., 2004) (Graham et al. in preparation).

The goals of this survey were several. In part it was technical: to demonstrate the achievement in contrast possible with differential polarimetry, and develop techniques and knowledge for future systems. We also sought to test the various disk and envelope models proposed for these systems, as well as address questions of disk geometry and flaring for systems with detected disks. A particular motivation was to assess the effects of binarity on disk properties. Simple arguments based on conservation of angular momentum suggest that disks in multiple star systems ought to be coplanar. Unresolved aperture polarimetry of a subset of Herbig Ae/Be stars tends to support this picture (Maheswar et al., 2002).

This project was very exploratory in nature: many of the systems included had never before been observed at high angular resolution, much less with a sensitive differential polarimeter. We expected (and found) surprises.

4.2.2 Mid-Infrared Imaging

The morphology of extended mid-IR emission, both in broad bands (at $\sim$ 11 and 18 μm) and in narrow PAH and silicate filters, can be used to distinguish between direct

thermal emission, scattered light, and emission from very small grains. McCabe et al. (2003) first detected mid-IR scattered light at 11.7 μmfrom the disk of HK Tau B. Unlike T Tauri stars, extended mid-IR emission is common in the more luminous HAEBEs (Siebenmorgen et al., 2000). These stars excite thermal emission from grains at relatively large distances, and their copious UV photons excite fluorescent emission from PAHs as well. Imaging in narrow-band filters is one way to trace and disentangle PAH emission from thermal and scattered mid-IR light.

Mapping extended thermal dust emission is near the resolution limit of an 8-10 m telescope, even for the nearest HAEBEs (Chen & Jura, 2003) . Operating at the diffraction limit, an 8 to 10 m telescope (Gemini or Keck) delivers approximately the same angular resolution in the mid-IR as obtained with the Lick 3 m in the near-IR. Therefore, we can match the features observed in the mid-IR to those seen in the near-IR.

4.2.3 Target Selection

In Appendix A I present an updated catalog of Herbig Ae/Be stars, drawn widely from throughout the literature. This catalog evolved during the course of the survey as I learned of new targets to add, or more rarely, removed objects found to have been misclassified.

A subset of this catalog, containing all objects observable from Lick, served as the target list for my survey. Rather than concerning ourselves with the biases inherent in selecting a subsample of stars to observe, the choice was made to be exhaustive and thorough–that is, to observe as large a fraction of the total Herbig Ae/Be star population as possible. Out of a grand total of 239 known Herbig Ae/Be systems (counting binaries and multiples as single objects for the purposes of this calculation), 150 of these are observationally accessible from Lick Observatory[1]. Of those 150, we ultimately observed a total of 110 targets (Fig. 4.1). By far the majority of non-observed stars are located in the Taurus and Orion area, notable both for its large number of young stars and its presence overhead only during the rainy California winter.

[1]defined as being located north of -30° declination for NGS targets with $R \lesssim 14$, or north of -8° for LGS targets with $14 \lesssim R \lesssim 16.5$. This difference in declination limits arises from an FAA restriction prohibiting propagation of the laser further than 45° from the zenith.

4.3 Observations and Data Reduction

The observations presented here were carried out over roughly forty nights spread over a period of four years, from April 2002 to July 2006. The wide range of conditions encountered, as well as numerous changes to instrumental hardware and software over this period, mean that any attempt to reduce this data in a truly consistent manner can be at best only partially successful. Still, I have endeavored to bring the data into a reasonably coherent whole.

4.3.1 Near-IR AO Imaging Polarimetry

Ultimately, 110 target fields were observed. Because of binarity, the total number of Herbig stars in our sample is somewhat higher.

While the IRCAL polarimeter works at all near-IR wavelengths, H band provides the optimum balance between AO performance and sky brightness: the Strehl ratios of Lick AO at J band are typically only 10-20%, 30% at the highest, while thermal sky emission reduces sensitivity to extended sources past 2 μm. Thus our primary survey wavelength was H band.

The exposure depth of the observations presented here is not uniform, as befits a target population spanning more than 8 mag. in brightness. For targets near the faint end of that range, we usually obtained $\sim$ 1 ksec integration at H. Real-time data reduction frequently allowed polarized sources to be immediately identified at the telescope, allowing rapid followup in J and K_s for sources with resolved emission at H. Multicolor photometry was also frequently obtained, particularly for targets discovered to have close companions. A detailed log of observations is available in table B.1.

Figure 4.1 shows the completeness of the survey sorted by right ascension. Essentially all known Herbig Ae/Be stars from 15 to 3 hours RA were observed. The spike in total sources (and in unobserved sources) around 5 hours is due to the Taurus and Orion star forming regions—in addition to this part of the sky having a greater concentration of Herbig Ae/Be stars, it is overhead during the late fall and winter months when the weather at Lick is most often problematic.

See Chapters 2 and 3 for information on the design of the IRCAL polarimeter and the data reduction methods employed.

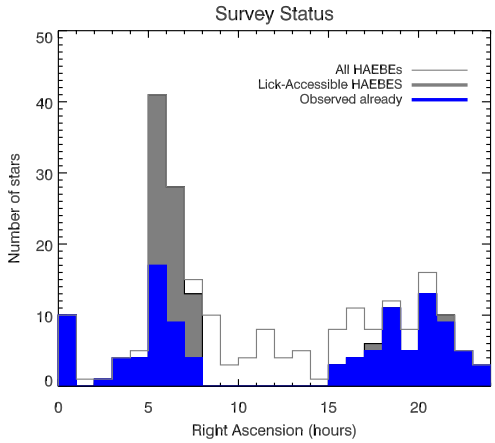

Figure 4.1: Survey completeness for Herbig Ae/Be stars. Essentially all observable Herbig Ae/Be stars outside of Taurus/Orion were observed at Lick.

4.3.2 Mid-Infrared Imaging

We obtained mid-infrared imaging using both the Long Wavelength Spectrometer (LWS; Jones & Puetter, 1993) on Keck I, and the Mid-IR Imager/Echelle Spectrometer (Michelle; Glasse et al., 1997) on Gemini North. These observations were obtained on seven nights between July 2004 and July 2006. Weather was good on all nights except the last, with clear conditions throughout and atmospheric precipitable water vapor typically in the range 1-2.5 mm. During our final night (2006-07-05 UTC) patchy clouds and fluctuating water vapor rendered the night non-photometric.

LWS was used in chop-nod imaging mode, typically with a 10″ throw and a chop frequency of 2.5 Hz. The chop position angle was usually 0° but varied for some targets in order to prevent overlap of sources. For Michelle, we use a chop throw of 15″ with a usual position angle of 30°. The chop frequency was set automatically by the Michelle control software, generally between 4.2 and 4.6 Hz depending on the filter selected. Integration times on-source varied from 60-400 s; a detailed observing log is available in table B.1.

In general, the Michelle data are of higher quality than the LWS data. The LWS data suffer from poor performance by the telescope chop-nod system, which at times resulted in variable and distorted PSFs similar to those caused by tip-tilt errors in near-infrared imaging. It is possible to improve the PSFs by registering and shifting the individual frames before the chop-nod subtraction, but this process means the sky and telescope thermal emission no longer cancels precisely, and results in substantially worse image background. In only a few cases (noted individually below) did the improved PSF quality

justify this tradeoff in background noise.

All LWS and Michelle data were reduced using a custom IDL pipeline. This software incorporates the LWSCOADD, MEF Tools and Michelle IDL routines made available by Keck and Gemini[2], but builds on them to incorporate correction for atmospheric transmission, photometric calibration and source detection.

Because mid-infrared observations are dominated by the thermal emission from the sky and telescope, accurate background subtraction is mandatory. Each chop-nod set was reduced via the standard double-differenced subtraction method to remove the background emission. No flat fielding was performed. Bad pixels were identified and replaced with the median of the neighboring pixels. LWS data were then rotated using a cubic spline interpolation to orient north up; this step is not necessary for Michelle data. On the other hand, Michelle data suffer from fluctuating DC offsets between the 16 readout channels, and for very bright sources crosstalk becomes an issue as well, but these artifacts can be cleanly removed by setting the median of each channel to zero. For both instruments, all the chop-nod-subtracted images were then registered via Fourier cross-correlation and summed into a mosaic image. The data were corrected for atmospheric transmission and flux-calibrated, as described below. The FIND source detector from the IDL Astronomy Library was used to locate sources in each reduced image. The resulting source list was in some cases edited by hand to remove obviously spurious detections, such as diffraction spikes or extended nebulosity erroneously identified as a point source.

We estimated the correction for atmospheric transmission losses as follows. A grid of atmosphere models was computed for Mauna Kea at a range of airmasses and water vapor contents, using the BFATS atmospheric transmission code (Roe, 2002). For each model, the average atmospheric transmission was computed, weighted by the relevant transmission profile for each filter, and saved into a lookup table. A record of the atmospheric water vapor content during the course of each night was obtained from the CSO Water Vapor Radiometer website[3]. The water vapor content and airmass of a given observation could then be used to obtain the atmospheric transmission from bilinear interpolation of the lookup table.

Throughout the course of each night, a number of mid-infrared photometric standards were observed, drawn from the catalog of Cohen et al. (1999). These standard observations

[2]We thank Marc Kassis and R. Scott Fisher for their invaluable help with this software.

[3]http://ulu.submm.caltech.edu/csotau/2tau.pl

were reduced in the same way as the science data. We follow the prescription provided by Cohen et al. for flux-calibrating an instrument: we first compute the Relative Spectral Response (RSR) of each instrument (consisting of the product of transmission curves for the atmosphere, instrumental optics, filter, and detector quantum efficiency). We can then calculate a RSR-weighted average over the flux-calibrated template stellar spectrum from Cohen et al., thereby deriving the isophotal wavelength and isophotal flux for each standard. The ratio of observed instrumental counts per second to the isophotal flux gives the desired flux calibration coefficient. For each standard, we also compute a radial profile of the PSF and derive from this the aperture correction factors for photometry at other aperture radii. On clear nights with stable atmospheric conditions (all of our mid-IR nights except 2006-07-05) we chose for each night to average the results from standards together to derive a master flux calibration for that night.

For LWS, the flux conversions derived for the three nights are all consistent within their uncertainties. For Michelle, the flux calibrations for 2005 December and later are all about 25% lower than those derived for 2005 July. The cause of this change is unknown, but its consistency across all filters suggests a change in instrumental configuration or output file normalization rather than atmospheric effects (which would affect various wavelengths differently). It is known that changes were made to the Michelle exposure time calculation and readout software between these two runs, which is the most likely cause for this change. Our last night on 2006 July 05 was the only non-photometric mid-IR night; some photometry during intermittent clear periods is reliable but much is not.

We can evaluate the precision of our absolute flux calibrations in comparison with the results of other authors (Table 4.1). LWS photometry has been calibrated using a near-identical procedure by McCabe et al. (2006). For the two filters we used in common with those used by McCabe et al., the agreement in absolute flux calibrations is within a few percent. For Michelle, we can compare to the zeropoints computed by Kevin Volk at Gemini Observatory[4]. The calibrations we computed are all 1-2% lower than Volk's, rising to 3% for Qa. However, Volk's calibrations were computed for zero airmass (i.e. neglecting the effects of the atmosphere), while our computation includes the atmosphere, which will slightly shift the isophotal wavelength and change the isophotal fluxes for each filter. Whether this is sufficient to account for the entire offset between the two calibrations is not yet known; so there may indeed be a systematic bias of around 1.5% in our Michelle

[4]Available online at http://www.gemini.edu/sciops/instruments/michelle/MichStdFluxes.html

flux calibrations.

McCabe et al. (2003) also characterized the pixel scale of LWS, finding 0.081 ± 0.002 arcsec pixel^{-1}. Multiwavelength observations of binary sources allow us to improve on this. The binary PDS 144 has now been observed with LWS, Michelle, NIRC2, and HST ACS and NICMOS. We assume here that the documented NIRC2 and Michelle pixel scales are correct at 0.09942 arcsec pixel^{-1} and 0.010054 arcsec pixel^{-1} respectively, and indeed, scaling our images of PDS 144 based on the ratio of these scales produces excellent alignment. However, scaling the LWS image using either the LWS documentation's $0\farcs0847$ or McCabe et al.'s $0\farcs081$ results in minor but unmistakable misregistration. An intermediate value is necessary. Empirically the agreement of LWS and NIRC2 images of PDS 144 was maximized by a ratio of 8.4 NIRC2 pixels per LWS pixel, or equivalently 0.0835 arcsec per LWS pixel. Repeating this analysis with LkHα 198 gives a very similar value of 0.0832 arcsec pixel^{-1}, so we adopt 0.0835 ± 0.0005 as our LWS platescale. This value is within 1.25σ of that measured by McCabe et al.

Table 4.1: Mid-IR Flux Calibration Compared with Literature Values

Filter	Zero Mag (my calc)	Zero Mag (literature)	Difference %	Reference.
LWS SiC	28.27	28.24	0.1	McCabe et al.
LWS 12.5	24.29	24.96	-2.7	McCabe et al.
Michelle 10.3um	35.53	35.945	-1.1	Volk
Michelle 11.6um	27.68	27.998	-1.1	Volk
Michelle 12.5um	23.92	24.553	-2.6	Volk
Michelle 7.9um	62.16	63.167	-1.6	Volk
Michelle 8.8um	47.83	48.667	-1.7	Volk
Michelle 9.7um	40.08	40.428	-0.9	Volk
Michelle N'	29.86	30.453	-1.9	Volk
Michelle Qa	11.73	12.136	-3.3	Volk

4.4 Summary of Observation Results

We present here a brief summary of the observational results of our survey. This overview serves to highlight some of the most interesting objects before we proceed into the full survey results for all 110 targets.

Figure 4.2 shows the near-IR polarimetry for a subset of our targets showing the most highly polarized, extended, and interesting objects. Figure 4.3 presents a similar "highlights gallery" for our mid-IR imaging. The two images feature different subsets of

our target sample; some stars only showed extended dust at near-IR wavelengths, while others were extended only in the mid-IR, and still others were extended in both regimes.

At first glance, every source appears unique. Assymetries and irregularities are the rule, not the exception. We have commented already that both spherical envelope and flat disk models can reproduce the SEDs of these stars—and these data make it all the more remarkable that such symmetric models can fit well to such asymmetric data. Clearly, SEDs tell a very limited part of the story for such systems!

But upon closer reflection, some natural categories become apparent in these data. Figures 4.2 and 4.3 are both organized roughly by morphology. The near-IR image progresses from resolved disks and disk-like elliptical nebulae; to bipolar envelopes, often showing limb-brightening from the edges of outflow cavities; to apparent tidal tails between elements of binary systems; to irregular wisps and arcs of circumstellar dust offset to the side of young stars. The last few images—for instance, HD 169142 and HD 163296—show stars for which the detection of polarized light is very faint. Looking only at the images presented in this figure, the cautious reader would be very skeptical about any claimed detection of polarized light, versus, say, the ever-present AO PSF variations. However, in the following sections for each object I will present statistical analyses, particularly relying on histograms of polarization position angle centrosymmetry, that will demonstrate the reality of these detections. See §3.5 for a description of what these histograms represent and how they are calculated, and §4.7.1 for a summary of the detected sources.

Likewise, the mid-IR morphologies fall into a few categories. The first is extended dusty envelopes, usually asymmetric and filamentary. MWC 778's 12″diameter spiral is a particularly unexpected example. Then there are deeply embedded companions: the two sources just west of LkHα 234, the faint companion south of RNO 1C, and so on. In a fair number of cases, substantial differences in the flux ratio of a binary are seen between the near- and mid-infrared. For instance, HD 216629 exhibits a complete flux reversal, with the optically fainter source becoming much the brighter object at 11 and 18 μm; on the other hand, HD 35187's companion is much bluer than the prinary is. The last row of images in Fig. 4.3 again displays the less visually-spectacular but nonetheless significant detections. The stars HD 169142, LkHα 324 SE, PDS 144 S, and LkHα 198 are all resolved; comparison with PSF standards and other science targets clearly shows that these sources are all more extended than pure point sources. A quantitative comparison of source radial profiles is presented in §4.7.3.

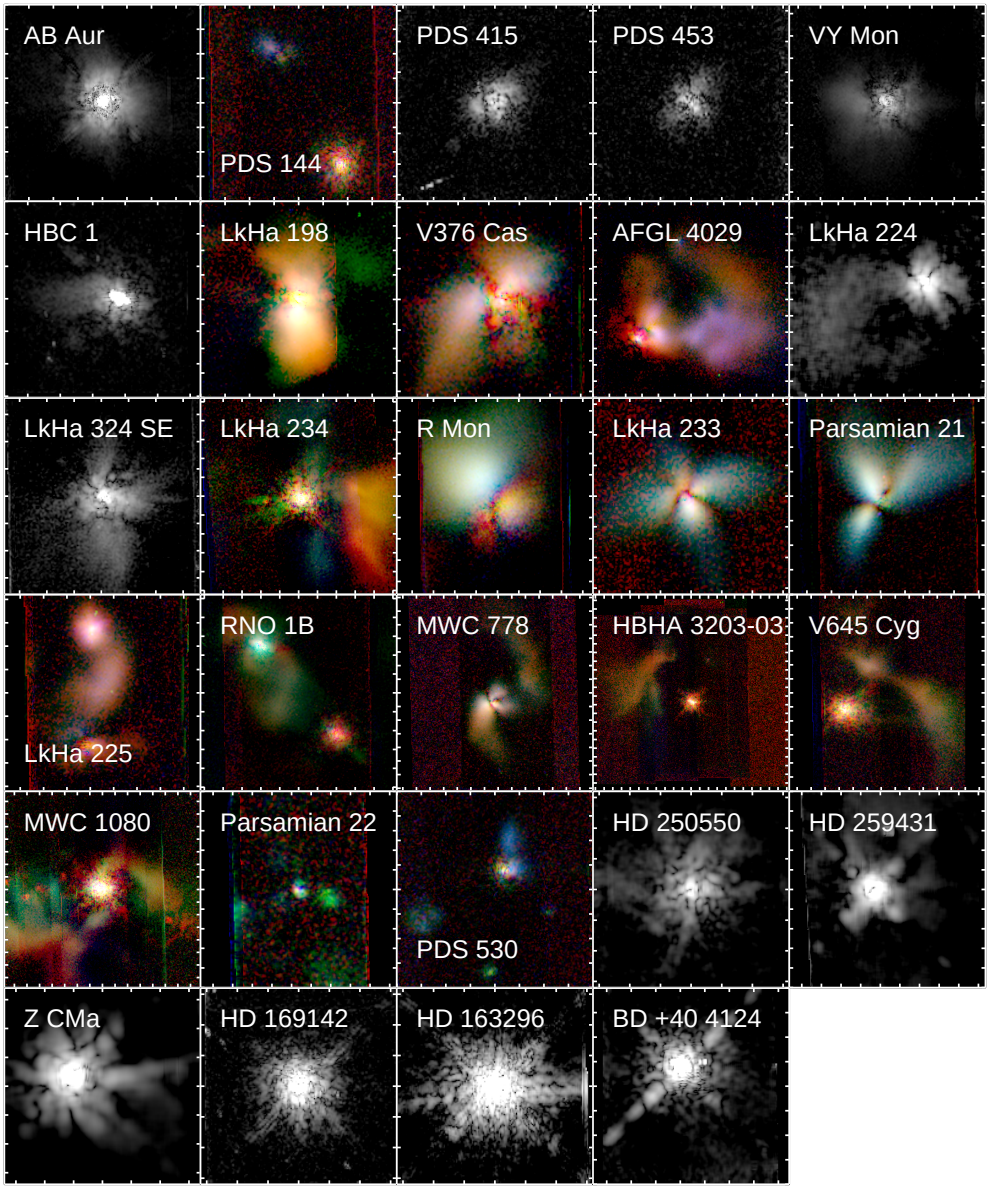

Figure 4.2: This gallery of polarimetric images showcases the diversity of morphologies found around Herbig Ae/Be stars: Disks and elliptical disk-like nebulae (for instance, AB Aur, PDS 144, and VY Mon), circumstellar envelopes, often with bipolar outflow cavities (AFGL 4029, LkHα 324 SE, LkHα 233, Parsamian 21, etc.), tails of material between and around binary stars (LkHα 225, RNO 1B and 1C, MWC 778), nebulous arcs offset from the stars (HBHA 3203-03, V645 Cyg, MWC 1080), and fainter fans of circumstellar dust (HD 250550, Z CMa). For some stars with disks, including HD 169142 and HD 163296, the polarized intensity images shown here are not very revealing, but centrosymmetry histograms do reveal the presence of polarized scattered light; see §4.7.1. Color images shown here are blue=J, green=H, red=K_s; greyscale images are H only, and all images show polarized intensity P. Angular, spatial, and intensity scales vary in this montage; see the individual object sections for quantitative figures.

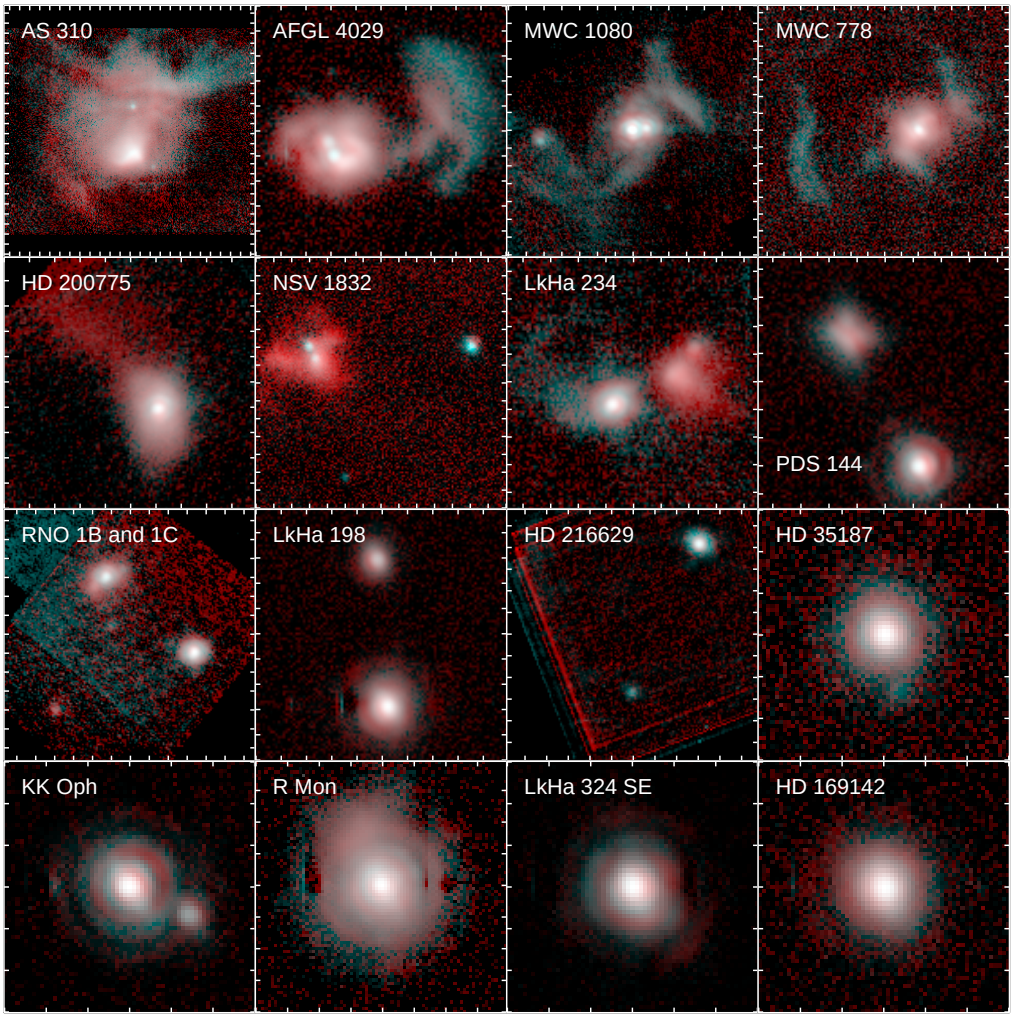

Figure 4.3: The diversity of morphologies found around Herbig Ae/Be stars continues in the mid-infrared: Complex regions of nebulosity (AS 310, AFGL 4029, MWC 1080), the stunning spiral arms of MWC 778, the edge-on disk of PDS 144N, and the less highly inclined disks of PDS 144S, LkHα 324 SE, and HD 169142. (See §4.7.3 for radial profile plots of these sources). The SEDs of companions are often uncorrelated with those of the Herbig Ae/Be stars: embedded companions near NSV 1832, LkHα 234 and RNO 1B rise in flux toward longer wavelengths, while the flux ratio in KK Oph remains roughly constant, and HD 35187's companion is bluer than the primary. Color images shown here are cyan=11 μm, red=18 μm. Angular, spatial, and intensity scales vary in this montage; see the individual object sections for quantitative figures.

4.5 Results for Individual Herbig Ae/Be Stars

I will now discuss in turn each of the observed targets. More detailed discussions, including numerical modeling, have already been presented for a few select sources (Perrin et al., 2004b; Perrin et al., 2006; see Chapters 5 and 6.). Numerical modeling of a larger set of these sources will be presented in a future work. While it is straightforward to fit models to the observed SEDs, this process is fraught with degeneracies. Fitting to the combined SED and resolved images is far more powerful, but also much more time consuming, both in terms of computer and human efforts.

For many of the Herbig Ae/Be stars targeted, we also see fainter nearby objects. Some of these are known physical companions, some are likely background objects, and many are of unknown nature. In the sections which follow, usually only brief remarks are addressed to these sources. Quantitative astrometry and photometry can be found in table C.3.

A note on image display: The following sections make extensive use of the inverse hyperbolic sin (asinh) stretch developed by Lupton et al. (1999, 2004). For readers unfamiliar with this image stretch, it is roughly similar to a logarithmic stretch with a tunable nonlinearity. By adjusting the tuning parameter appropriately, one can accomodate any amount of dynamic range and simultaneously display both image maxima and faint structures in the noise. A separate innovation in image display, also due to Lupton et al., is to create RGB images by scaling channels in a way that preserves image color locally. Thus, bright stars do not saturate to pure white, but retain the same color even as the displayed intensity changes. For more details, please see the papers by Lupton and collaborators.

For each source, I briefly summarize its known properties from the literature before discussing our new observations and their results. I present images showing total intensity and/or polarized intensity in J, H, and K_s, and in ~ 11 μm and ~ 18 μm; not all sources were observed in all wavelengths, and the wavelengths for the mid-IR observations vary slightly between LWS and Michelle. For each source, I also show a radial profile plot of the total intensity, the residual post-polarimeter polarized intensity, and an estimate of the theoretical noise floor to the polarized intensity as computed from the uncertainty maps to each image; see Chapters 2 and 3 for more information on these plots.

Targets are ordered by right ascension, starting at 0 hours.

4.5.1 HBC 1

HBC 1 is highly reddened and its spectral type is uncertain, possibly around F4 (Hernández et al., 2004). It is located at a distance of 850 pc (Porras et al., 2003), and has $V = 16.8$.

It was observed at Lick on 2004-09-07 UTC in excellent conditions, and at Keck on 2004-07-26 UTC. Our Lick observations were obtained in challenging conditions, using the $63''$ distant HBC 324 as an off-axis NGS AO guide star. The resulting images have a distorted, plus-sign-shaped PSF common in far off-axis Lick AO observations. Unfortunately, due to observer error, all the H band observations of HBC 1 are saturated in the PSF core. However, a polarized nebula can still be detected extending $3\farcs3$ east of the star. This nebula is very asymmetric, with only the faintest hints of polarized light present to the west of the star. This asymmetric nebula is possibly due to a bipolar outflow from the star, whose more distant, redshifted side is hidden from view by foreground extinction.

HBC 1 is unresolved in our MIR imaging (Fig. 4.5). Our 11 μm photometry is in excellent agreement with the IRAS 12 μm flux, indicating that the mid-IR emission region is compact.

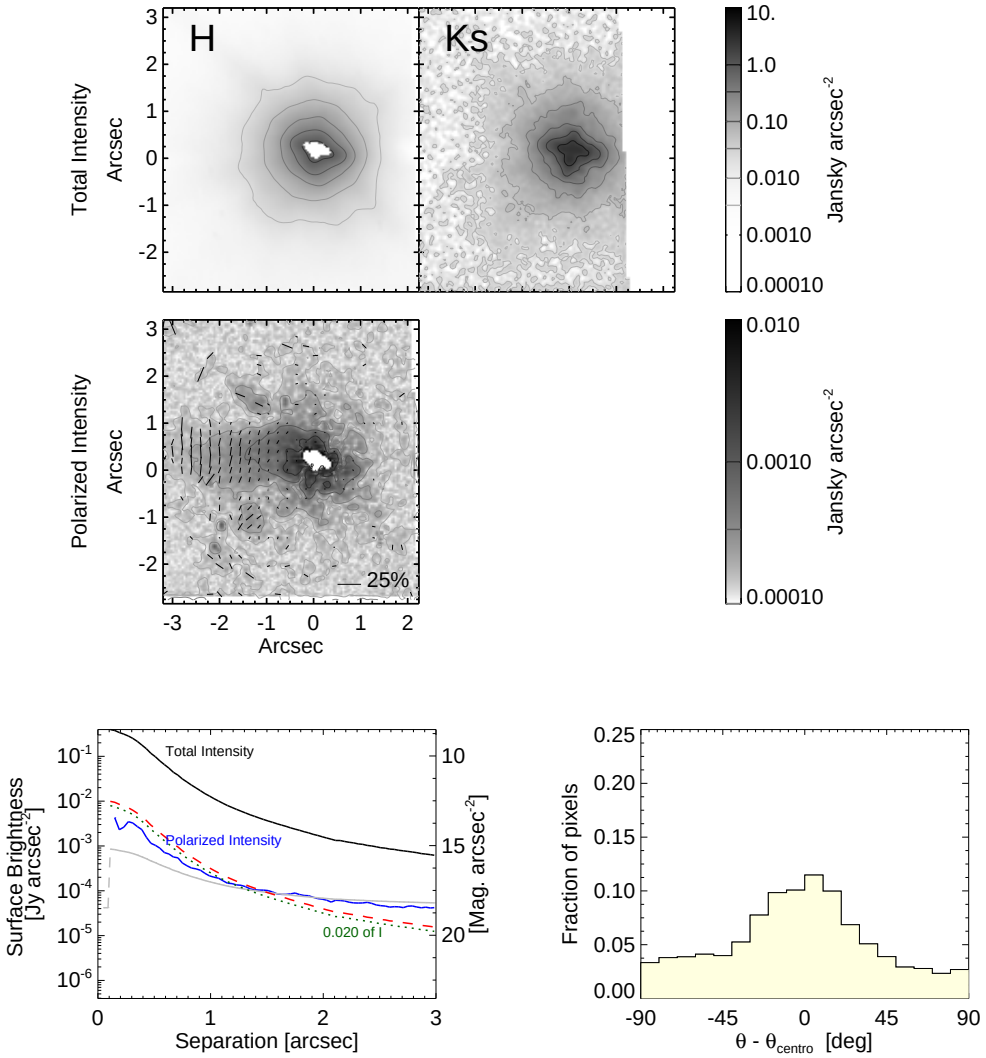

Figure 4.4: Imaging polarimetry of HBC 1.

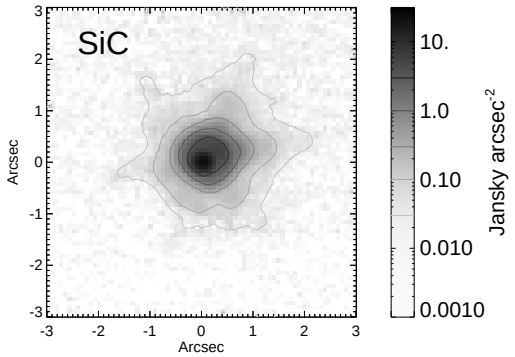

Figure 4.5: Mid-IR imaging of HBC 1.

4.5.2 HBC 324

HBC 324, also known as MC 1, is a relatively little-studied A7 star (Hernández et al., 2004) located at a distance of 850 pc (Yonekura et al., 1997), with $V = 10.7$. Its SED rises substantially from 2 to 10 μm, indicating a substantial amount of cooler dust, but as HBC 324 is not included in our LWS/Michelle target sample, we cannot directly probe the distribution of this dust.

HBC 324 was observed at Lick on 2004-09-07 UTC in excellent conditions. No polarized light was detected in the near-IR (Fig. 4.6) Three additional sources are detected in our field of view, including a $0\farcs73$ binary located approximately $8''$ north of HBC 324. It is unknown whether any of these objects are physically associated with HBC 324.

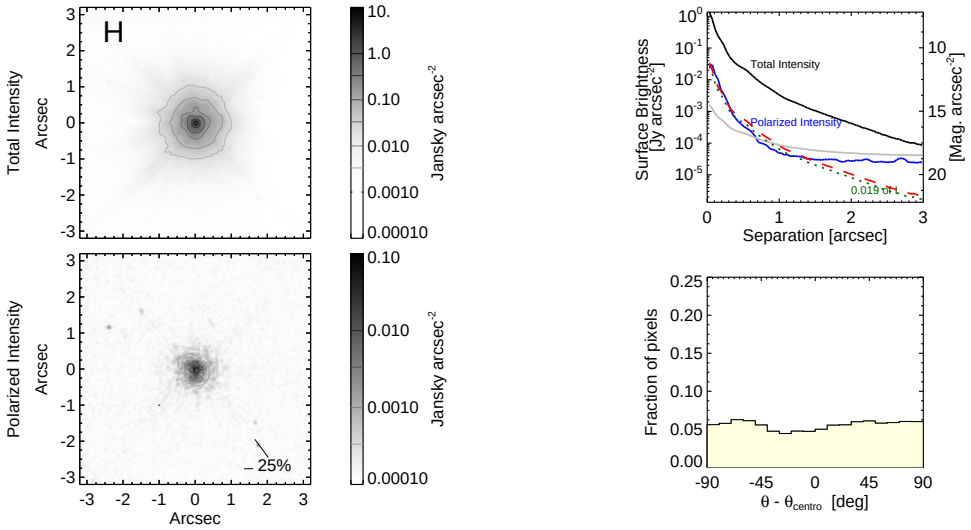

Figure 4.6: Imaging polarimetry of HBC 324.

4.5.3 MQ Cas

MQ Cas is an A0Vae star (Miroshnichenko et al., 1999) with $V = 11.7$. Its distance remains extremely uncertain. Miroshnichenko et al. (1999) identified MQ Cas as the optical counterpart to IRAS 00070+5756. They found it to be highly optically variable (amplitude 2.5 mag.) and with variability timescales and color indices similar to UX Ori. MQ Cas becomes bluer during its photometric minima, which they interpreted to mean that a significant fraction of the total light is scattered from circumstellar dust.

It was observed at Lick on 2005-11-21 UTC in good conditions. No polarized light

was detected in the near-IR (Fig. 4.7). Based on the NIR photometry, MQ Cas was in a fairly dim state at the time of our observations.

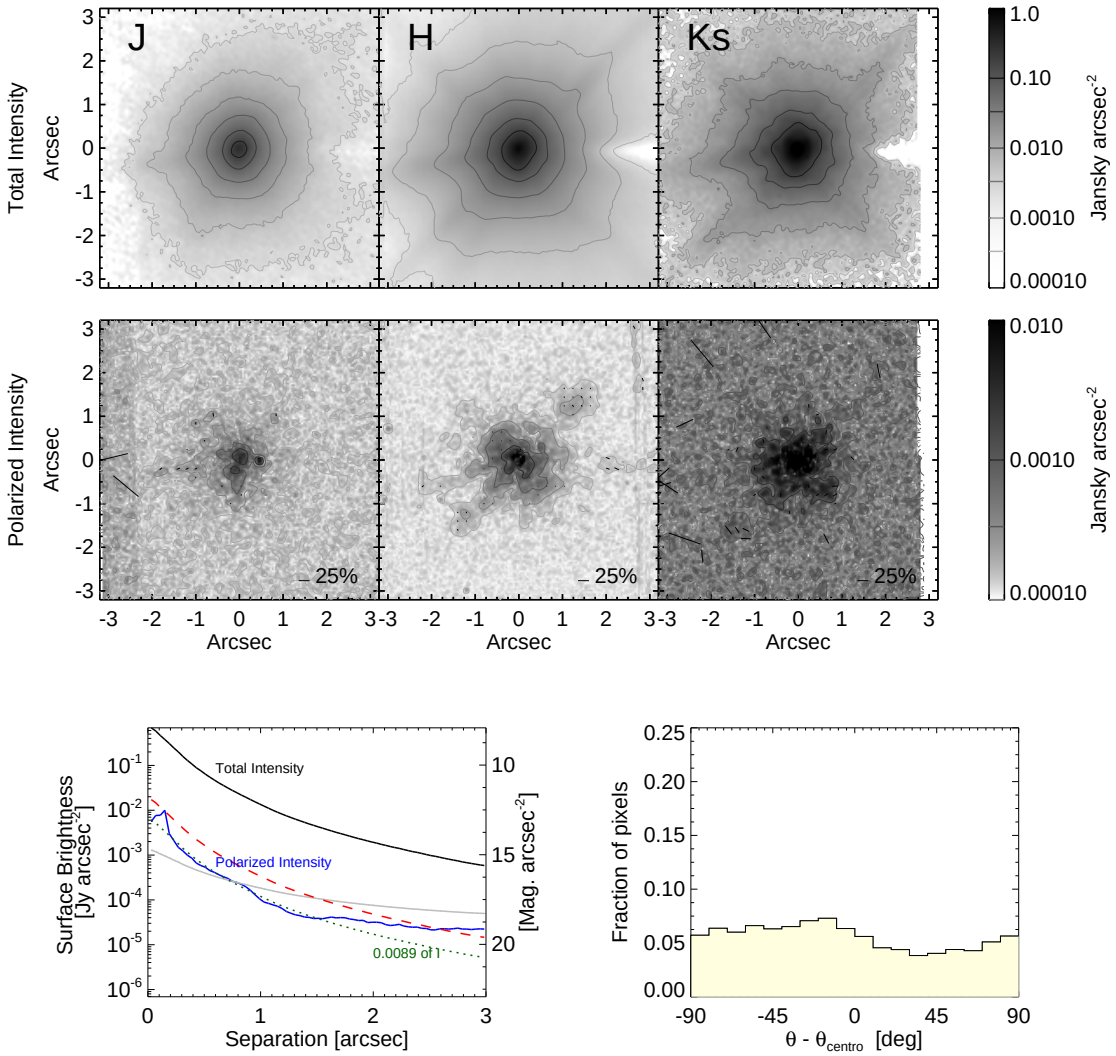

Figure 4.7: Imaging polarimetry of MQ Cas.

4.5.4 LkHα 198

LkHα 198 is a B9 star (Hernández et al., 2004) located at a distance of 600 pc (Testi et al., 1998), with $V = 14.2$. This is a well-known and heavily studied object, located in a small dark cloud along with V376 Cas. It is situated at the apex of a prominent elliptical nebula about an arcminute across. Also located in the area are two embedded sources: LkHα 198 IR, about 5″ north of LkHα 198, and LkHα 198 MM, an embedded millimeter

source to the northwest. Lagage et al. (1993) originally detected the now called LkHα 198 IR, with a separation of 5.″5 at a PA of 3°. Smith et al. (2005) report an additional companion to LkHα 198 at small separations ($\rho < 0.03''$), below the diffraction limit of our observations.

LkHα 198 has been observed at Lick on 2003-07-23, 2004-10-31, and 2005-07-27. We see a strongly polarized biconical nebula ∼10 ″ in diameter (6000 AU), oriented north-south, with polarization vectors concentric with respect to LkHα 198. Our near-IR observations of the Herbig Ae/Be stars LkHα 198 and LkHα 233 have previously been reported(Perrin et al., 2004b); see Chapter 6 for a full discussion.

It was observed in the mid-IR at Keck on 2004-07-25 and 26 and 08-28, and at Gemini North on 2005-12-16. These observations successfully resolved circumstellar dust around LkHα 198, using its neighbor LkHα 198 IR as a PSF reference; see §4.7.3.

4.5.5 V376 Cas

V376 Cas is an embedded young star located near LkHα 198 in the L1265 region at a distance of 600 pc, with $V = 15.5$ (Hillenbrand et al., 1992). Its spectral type is uncertain and could be between A3 and F2 (Hernández et al., 2004). In the optical it is resolved into a nebula extending a few arcseconds along PA=120°, and it has one of the largest linear polarizations of any pre-main-sequence star, 20-25% in R (Corcoran et al., 1995; Asselin et al., 1996; Leinert et al., 2001). This morphology was initially interpreted to be a bipolar outflow nebula, suggesting the presence of a circumstellar disk perpendicular to the nebula at around PA=30°. However, HST WFPC2 images instead reveal an irregular C-shaped nebula partially obscured by a dark cloud (Smith et al., 2004). In combination with near-IR speckle observations, Smith et al. interpret these data to show an outflow pointed west, with the disk probably nearly edge-on and oriented along PA=140°.

It was observed at Lick on 2004-10-31 UTC in mediocre conditions, and again on 2005-07-27 in much better conditions. V376 Cas shows a reflection nebula extending in an arc from the southeast to the west. In our H-band polarized intensity image, the southeast side of the arc can be seen extending as far as 7″ from the star, corresponding to 4000 AU; the extension to the northwest is much shorter, terminating after only 2.″5. As expected, the fractional polarization is very high, rising from 20-25% near the star to above 60% at the edge of the nebula 7″ southeast.

The gently curved shape of the nebula is roughly consistent with the optical WFPC2

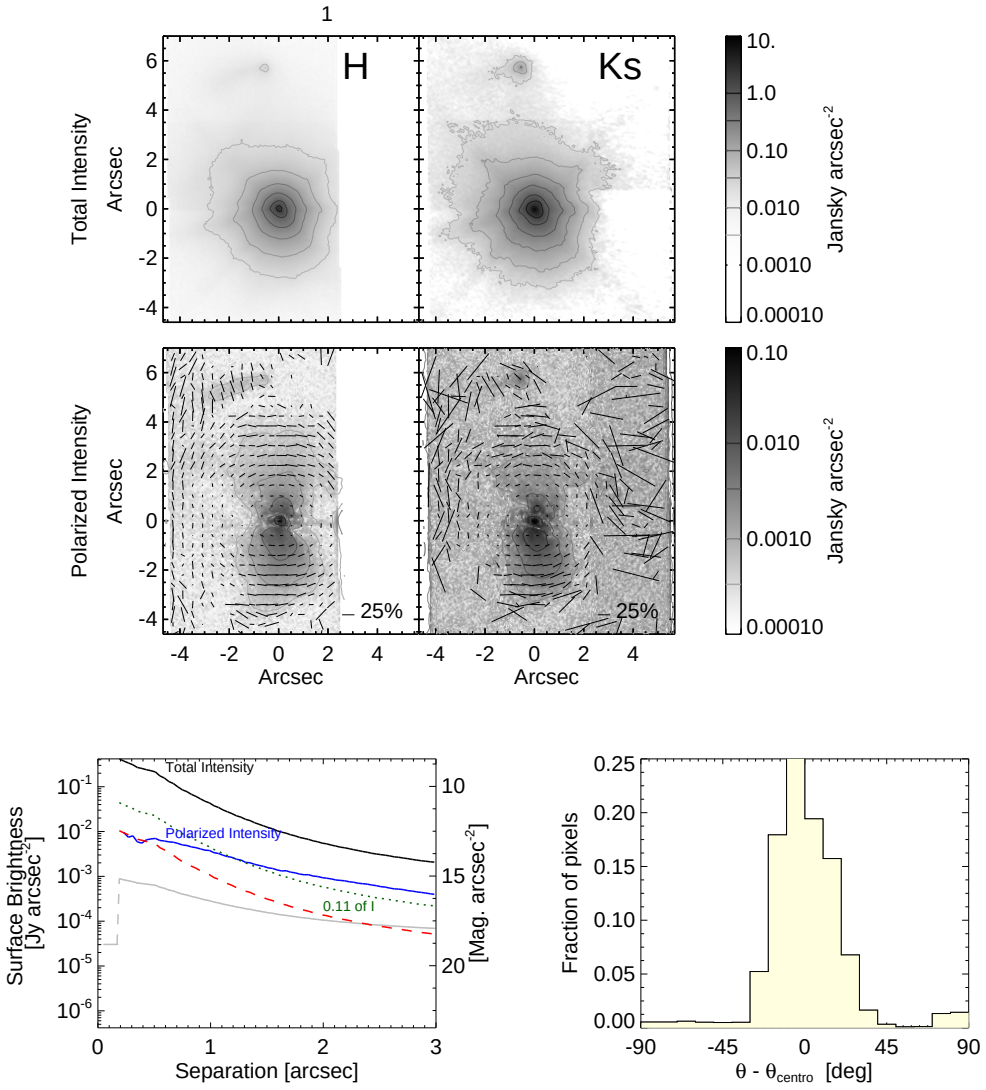

Figure 4.8: Imaging polarimetry of LkHα 198.

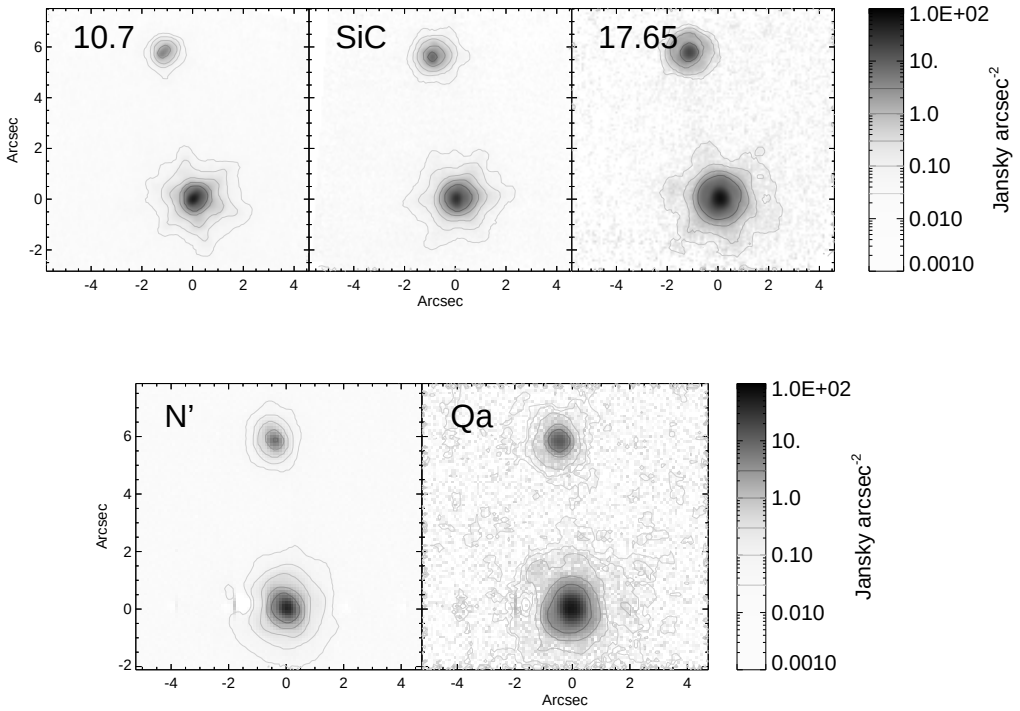

Figure 4.9: Mid-IR imaging of LkHα 198. Top is LWS, bottom is Michelle.

image, though in the IR the southeast arm is brighter and the southwest spur much fainter compared with the visible. The peak luminosity is displaced $\sim 0\farcs4$ southwest from the bright central axis of the arc. That displacement is consistent with that expected for a near-edge-on disk (see the discussion of LkHα 233 in Chap. 5), but this nebula does not particularly resemble an edge-on disk. Nor does it resemble a typical bipolar nebula, though. The HST image indicates the presence of a dark cloud just to the west of this star. I conjecture that whatever the nature of the dust immediately around V376 Cas, whether disk or envelope, we do not see that dust directly. Instead we observe the light as it scatters around and through the foreground screen of that dark cloud. This highly obscured location, even in the near-infrared, gives rise to the highly polarized and complex appearance of this source.

We obtained mid-IR images both at Keck and at Gemini North. The Michelle N' image is compromized by a highly astigmatic PSF, but the relatively good LWS PSF shows that the star is not well-resolved on the scales probed here (Fig. 4.11).

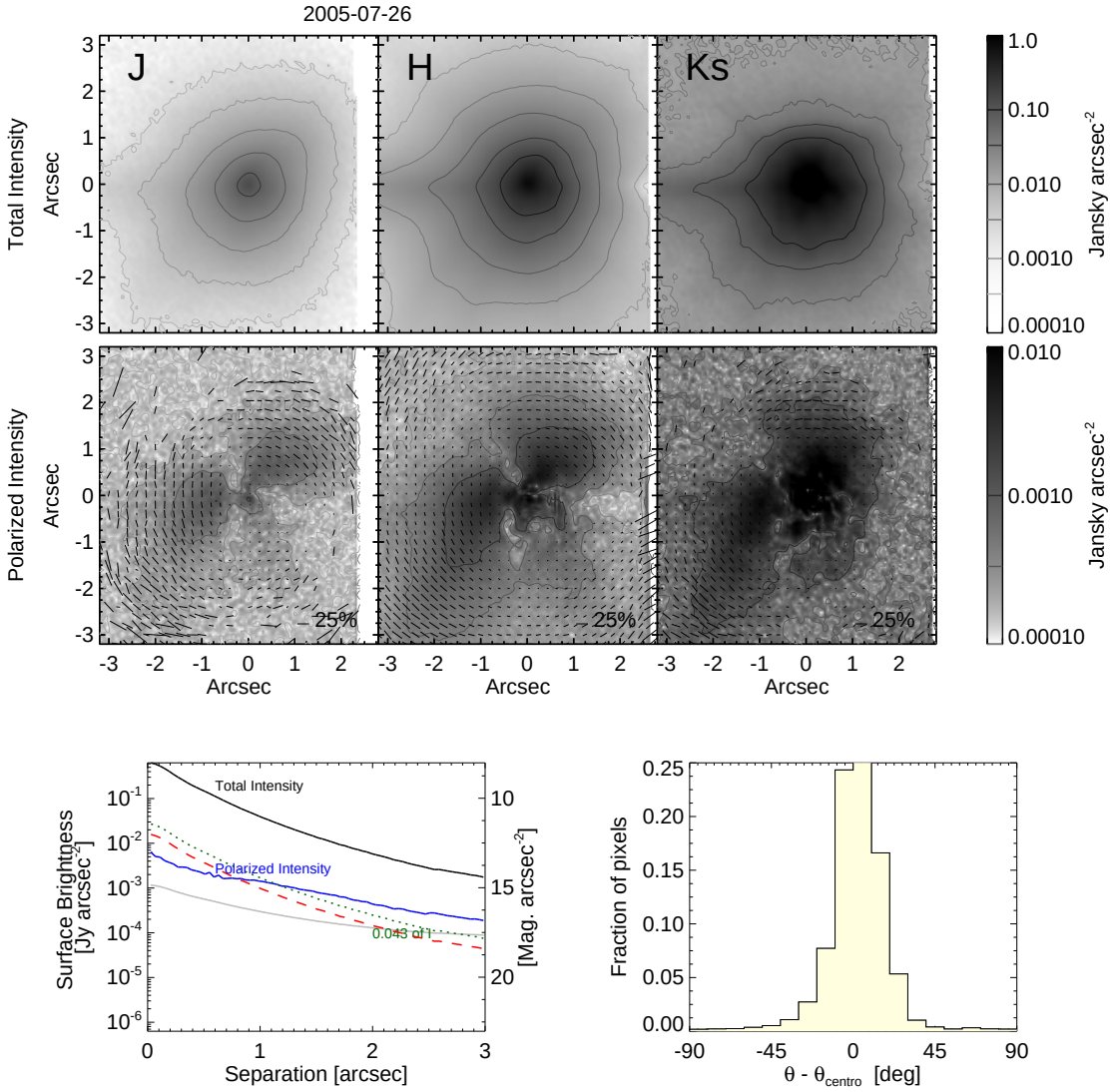

Figure 4.10: Imaging polarimetry of V376 Cas.

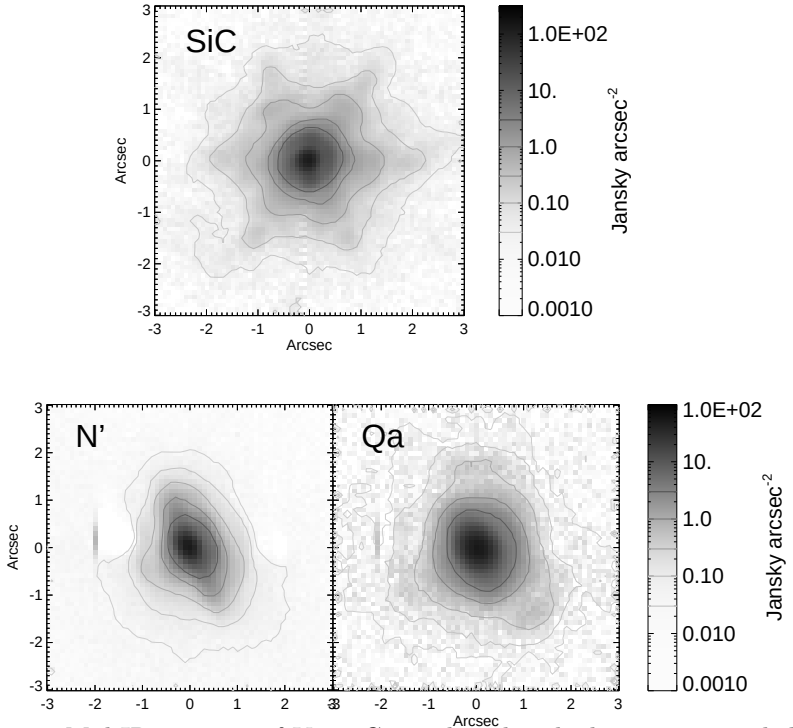

Figure 4.11: Mid-IR imaging of V376 Cas. Though it looks quite extended in the Michelle N' image, this must be a PSF artifact given its unresolved image in the LWS SiC image - one of the few cases in which our LWS data is superior to the Michelle data.

4.5.6 VX Cas

VX Cas, also called HBC 329, is an A0 UX Orionis star (Hernández et al., 2004) located at a distance of 760 pc (Natta et al., 1997), with $V = 11.3$. Testi et al. (1998) observed VX Cas and found a moderate stellar density enhancement within 0.3 pc of it. Natta et al. (1997) could not detect it at 1.3 mm.

It was observed at Lick on 2004-09-07 UTC in excellent conditions, and at Keck on 2004-07-26 UTC. No polarized light was detected in the near-IR (Fig. 4.12). A potential companion is detected 5.″25 south of VX Cas, which also shows no evidence for extended polarized scattered light. Our NIR photometry compared with 2MASS indicates moderate variability ($\sim$ 0.2 mag.), while our LWS 11 μm flux is 50% lower than the IRAS 12 μm value. The star was not resolved in the mid-IR (Fig. 4.13).

4.5.7 CDS 50

CDS 50 is a $V = 11.1$ star located in the young open cluster NGC 146, at a distance of 3500 pc (Subramaniam et al., 2005). It is star S1 from the catalog of Subramaniam et al. (2005), who found it to show Hα , He, FeII, and OI in emission, with several lines showing P Cygni profiles. They classified it as having a spectral type earlier than B3, and noted that its near-IR colors are consistent with those of Herbig Be stars.

It was observed at Lick on 2005-11-23 UTC in good conditions. No polarized light was detected in the near-IR (Fig. 4.14) A potential companion was detected 2.″8 east of CDS 50. This is consistent with the results of Subramaniam et al., who found an enhancement in stellar density around CDS 50.

4.5.8 RNO 1

RNO 1 is an F5 star (Cohen, 1980) located at a distance of 800 pc (Yang et al., 1995), with $V = 14.0$. RNO 1 is the first object from the Red and Nebulous Objects catalog of Cohen (1980). He classified it as F5 based on a low-resolution optical spectrum. It is part of the dark clouds L 1287 which also contains the FU Ori objects RNO 1B and RNO 1C, located about 1 arcminute southeast of RNO 1. RNO 1 has been studied relatively little, particularly compared with the nearby RNO 1B and 1C.

It was observed at Lick on 2004-09-08 UTC in excellent conditions. No polarized light was detected in the near-IR (Fig. 4.15)

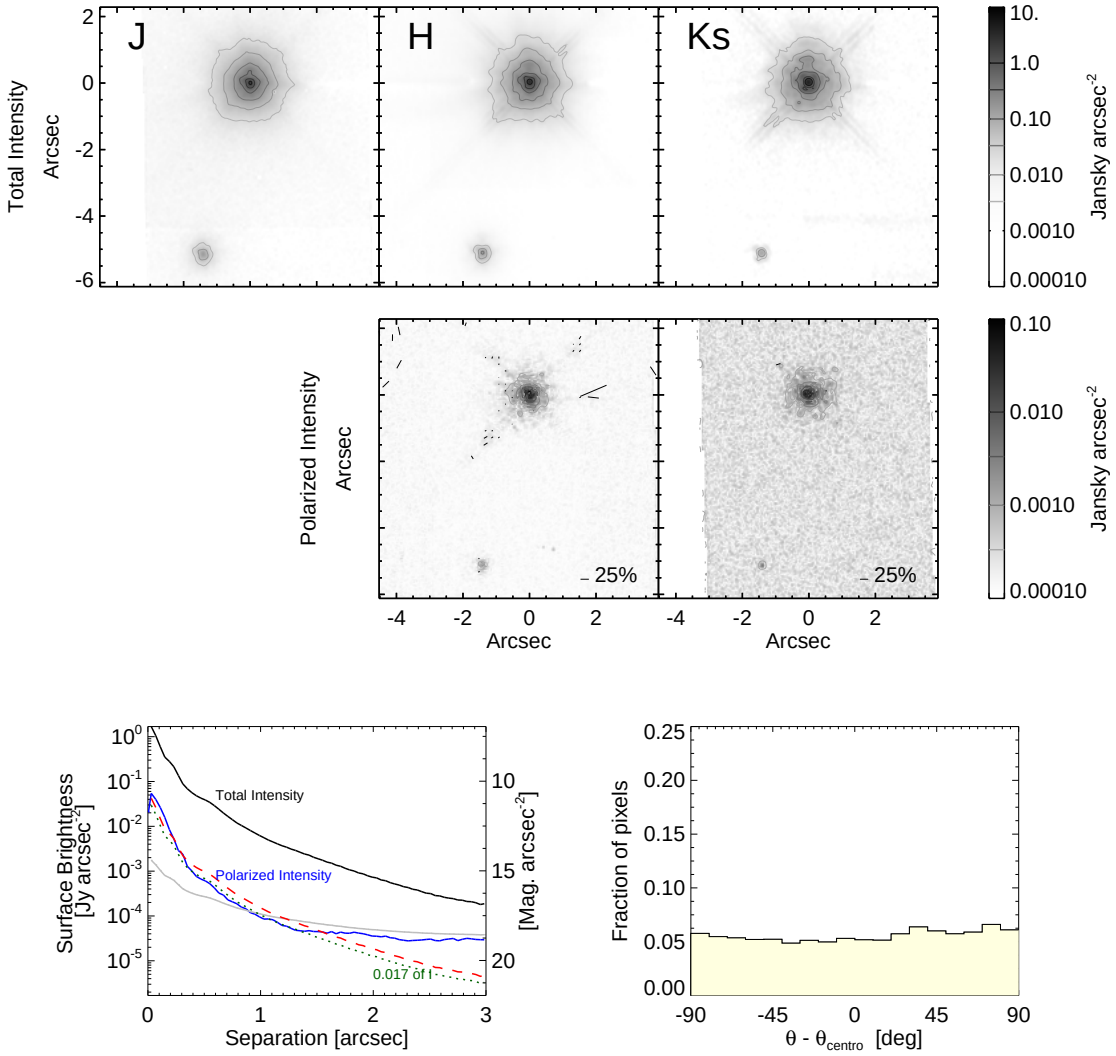

Figure 4.12: Imaging polarimetry of VX Cas.

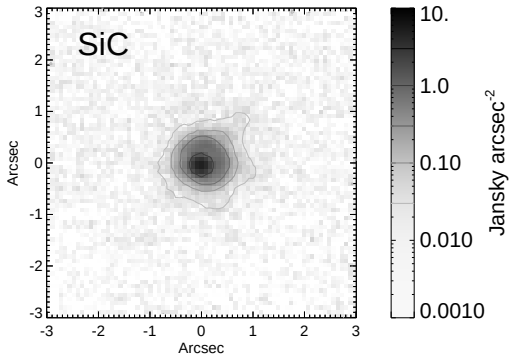

Figure 4.13: Mid-IR imaging of VX Cas.

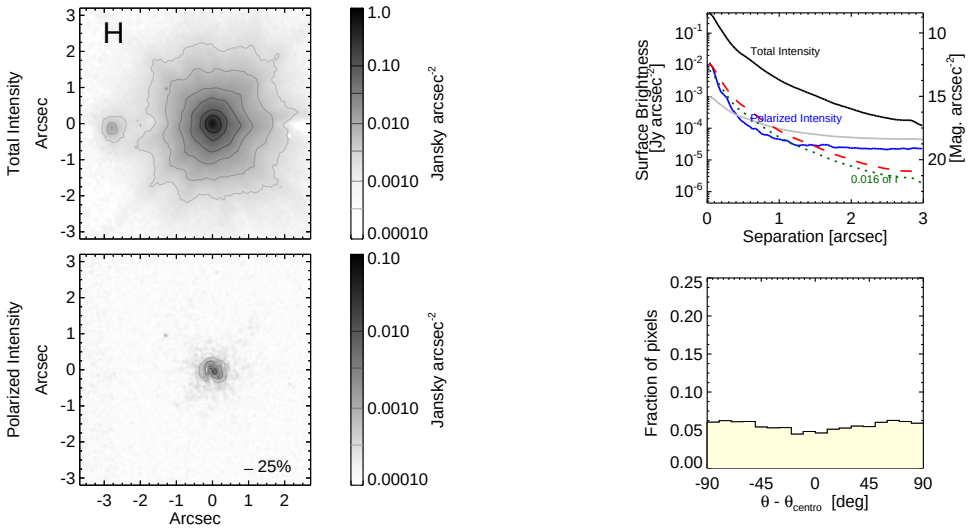

Figure 4.14: Imaging polarimetry of CDS 50.

4.5.9 RNO 1BC

RNO 1B and RNO 1C are two FU Ori stars located 50″ southwest from RNO 1 (Staude & Neckel, 1992; Kenyon et al., 1993). They are located in the L1287 dark cloud, and are surrounded by a small cluster of embedded young sources including the very deeply embedded protostar IRAS 00338+6312 (Weintraub & Kastner, 1993; Weintraub et al., 1996; Sandell & Weintraub, 2001). This complex region also includes a molecular outflow, several water masers, and multiple circumstellar disk candidates. Near and mid-IR observations by Polomski et al. (2005) detect a total of six point sources in this region. Polomski et al. find that RNO 1C is spatially resolved at 18 μm with an elongated spatial extent of 4″ along PA = -44°; RNO 1B is unresolved in their data.

RNO 1B and 1C were observed at Lick on 2004-09-08 in excellent conditions, and at Keck on 2004-08-28 and -29. For the Lick observations, we used RNO 1 as an off-axis NGS AO guide star. This worked fairly well, particularly given the good seeing, but did result in the plus-sign-shaped PSFs typical of far-off-axis Lick AO observations (see our HBC 1 data for another example). The resulting image shows an arc of dust curving from RNO 1C southwest toward RNO 1B. A counter-arm also extends from RNO 1C in the opposite direction. In our H band data, which is the deepest of our three bands, a nebulous extension is also seen pointing south from RNO 1B. This extension can also be detected in a smoothed version of our J data and does appear to be real. In the mid-IR,

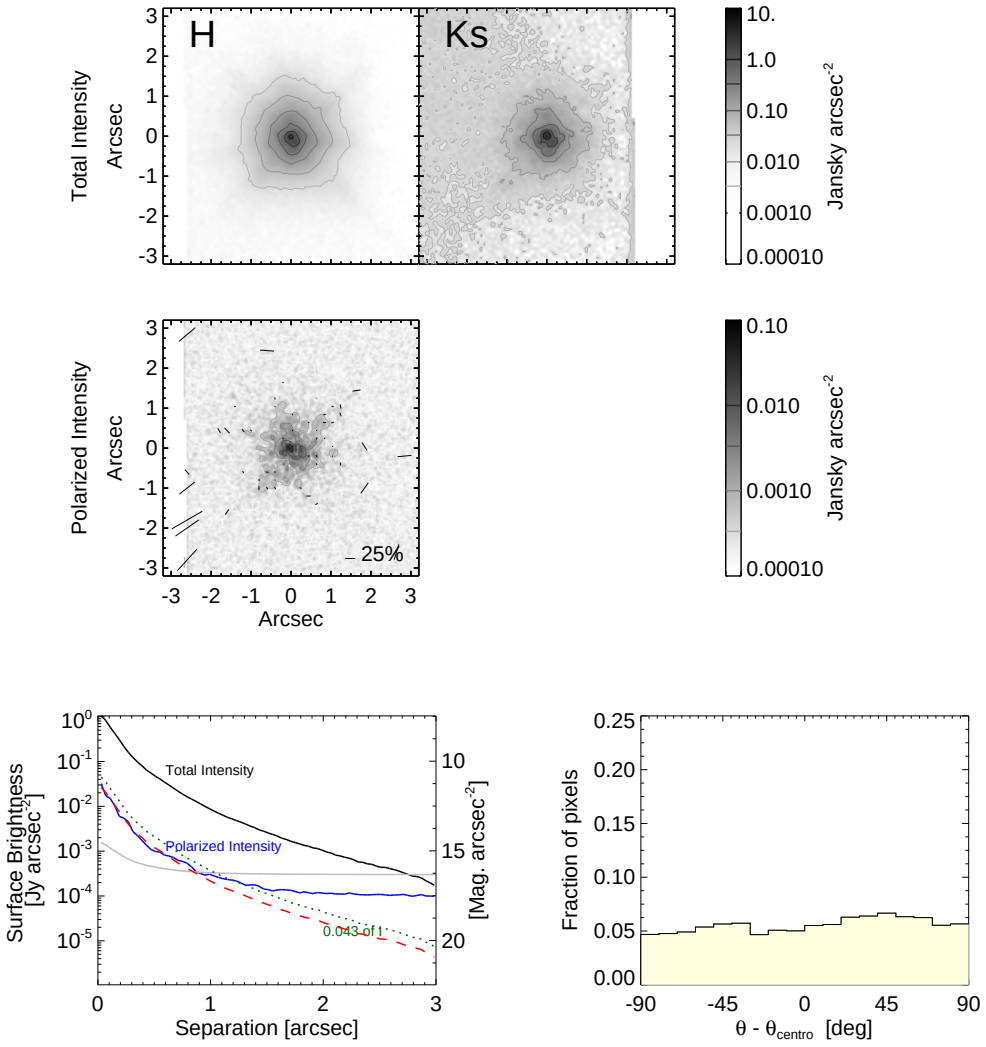

Figure 4.15: Imaging polarimetry of RNO 1.

our higher angular resolution enables us to resolve the extended dust around RNO 1C at 11.7 μm as well as at 18 μm. We find that RNO 1C is extended on a PA of $\sim -44°$, consistent with that seen by Polomski et al.

In other words, the mid-IR dust is extended roughly perpendicular to the direction of the main near-IR nebulosity. On the other hand, looking closely at the near-IR images, a kink or bend can be seen in the inner portions of the nebula: while the outer part extends southwest curving clockwise, the inner part is oriented more north-south, possibly not too far off from the orientation of the mid-IR nebula. Two possible interpretations come to mind for this nebula: First, that we see in the mid-IR a dusty ring or disk around RNO 1C, and the near-IR nebula is the light scattered from a bipolar cavity in the circumstellar envelope. Alternatively, that the near-IR nebula's curving shape is indicative of its nature as a tidal streamer, a portion of the disk around RNO 1C that has been ripped awy by the gravitational influence of RNO 1B. Indeed, theoretical investigations of binary stars indicate that dust structures larger than about 1/3 the semimajor axis cannot by stable, and here the arm of dust between these stars stretches most of the way from one to the other. Either we are seeing a transient structure in a dynamically very active system, or the true separation of these objects is at least twice the sky-projected separation. Despite the differences in apparent dust morphology, the two stars have very similar colors and SEDs from the optical to the far-IR. Further studies are needed to clarify what's going on in this system.

4.5.10 V594 Cas

V594 Cas, also called BD +61 154, is a $V = 10.6$ continuum star, possibly of spectral type $\sim$ B8 (Hernández et al., 2004), and located at a distance of 650 pc (Hillenbrand et al., 1992). It shows many emission lines with P Cygni profiles (Herbig, 1960; Strom et al., 1972). Leinert et al. (2001) found a $0\farcs7$ FWHM infrared halo around V594 Cas, extended primarily east-west.

It was observed at Lick on 2004-09-07 UTC in excellent conditions, and at Keck on 2004-08-28 UTC. We do not detect any significant resolved circumstellar dust in either our NIR or MIR observations (Figs. 4.18, 4.19).

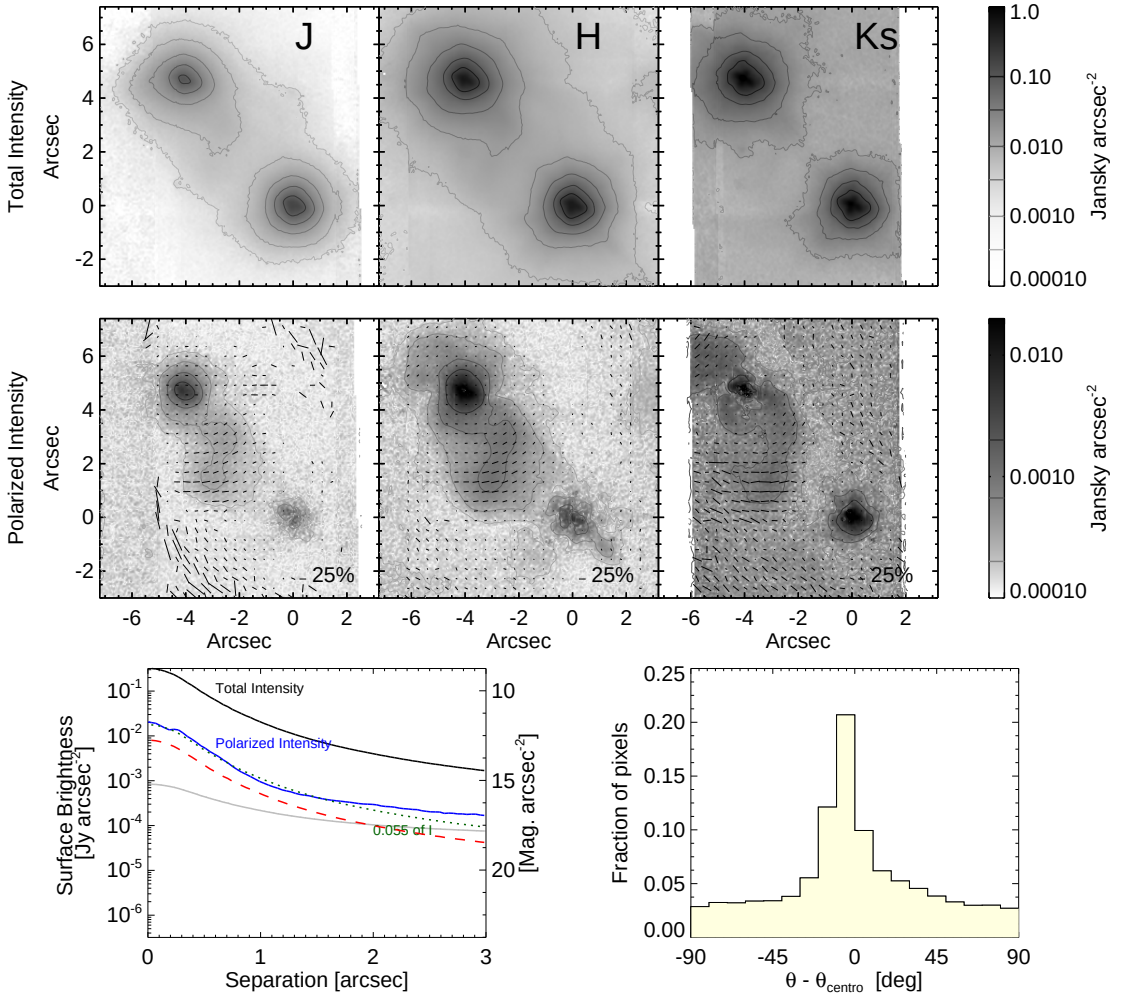

Figure 4.16: Imaging polarimetry of RNO 1B and 1C. RNO 1C is the source to the northeast and RNO 1B is to the southwest.

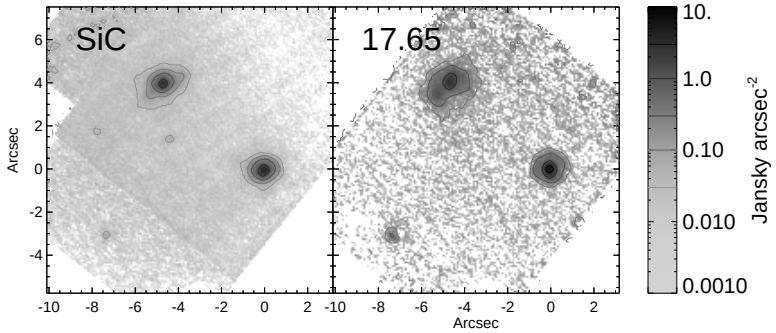

Figure 4.17: Mid-IR imaging of RNO 1B and 1C. In addition to RNO 1B and 1C, two (or possibly three?) fainter point sources are visible to the south. The southernmost and brightest is the source "DLIRIM 3" from Weintraub et al.

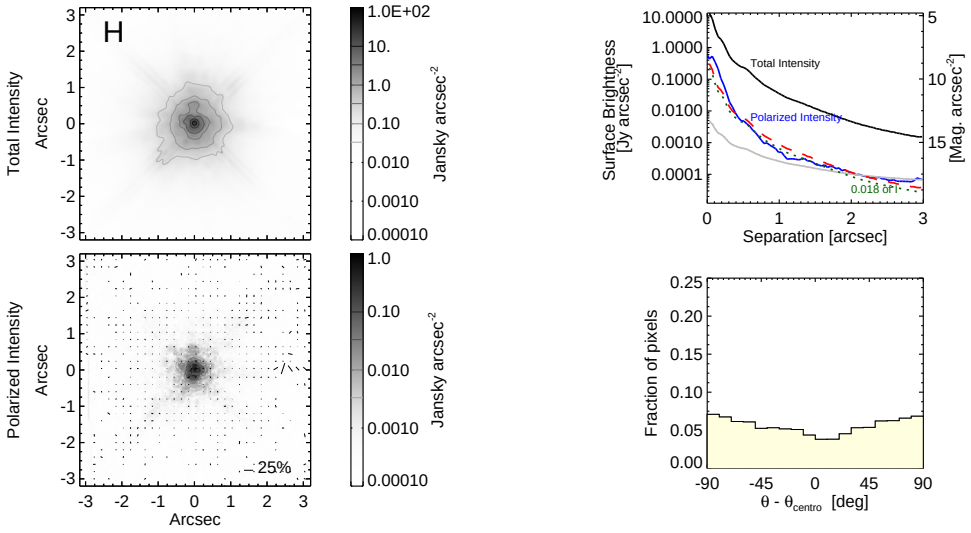

Figure 4.18: Imaging polarimetry of V594 Cas.

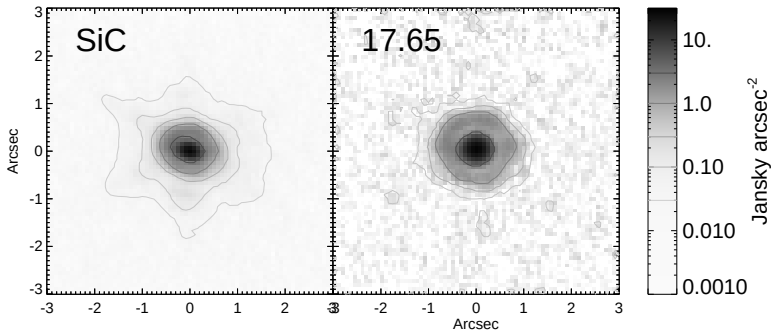

Figure 4.19: Mid-IR imaging of V594 Cas.

4.5.11 LkHα 201

LkHα 201 is a B2 star (Hernández et al., 2004) located at a distance of 850 pc (Yonekura et al., 1997), with $V = 13.6$. The evolutionary state of this star is uncertain; Hernández et al. (2004) note that it may be an evolved, post-main sequence star rather than a young one.

It was observed at Lick on 2005-07-28 UTC in good conditions. No polarized light was detected in the near-IR (Fig. 4.20), but we do see a $\Delta H = 7.5$ potential companion located 2.″3 northwest.

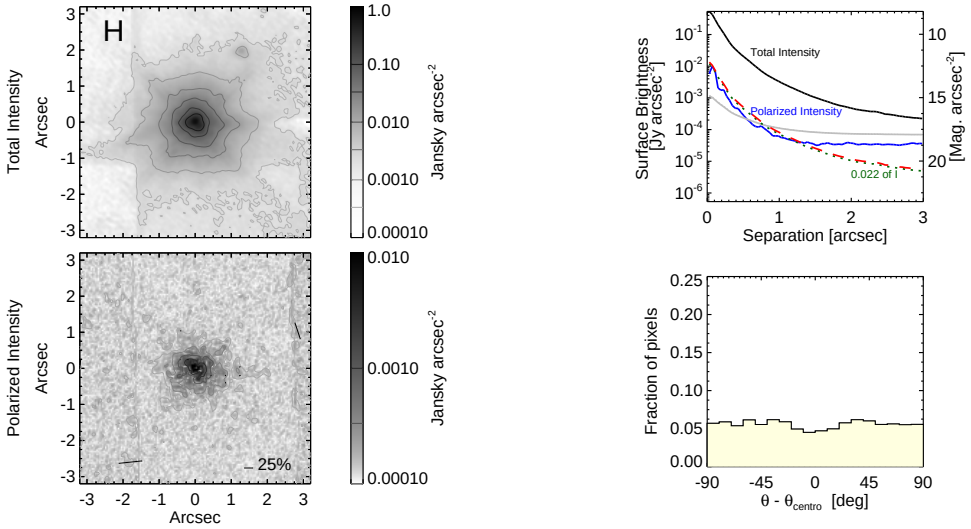

Figure 4.20: Imaging polarimetry of LkHα 201.

4.5.12 HBC 334

HBC 334, also known as RNO 6, is a B3 star (Hernández et al., 2004) located at a distance of 1600 pc (Testi et al., 1998), with $V = 14.5$. Testi et al. (1997) detect an arc-like NIR nebula whose brightness peaks approximately 20″ north of HBC 334; this nebula falls outside the field of view of our IRCAL observations.

It was observed at Lick on 2005-11-22 UTC in good conditions. A potential companion is detected several arcseconds west of HBC 334. Neither star shows evidence for resolved scattered light on the spatial scales probed here (Fig. 4.21). The companion has a SED which rises slightly from 1.2 to 2.1 μm, indicating that it too has warm circumstellar dust.

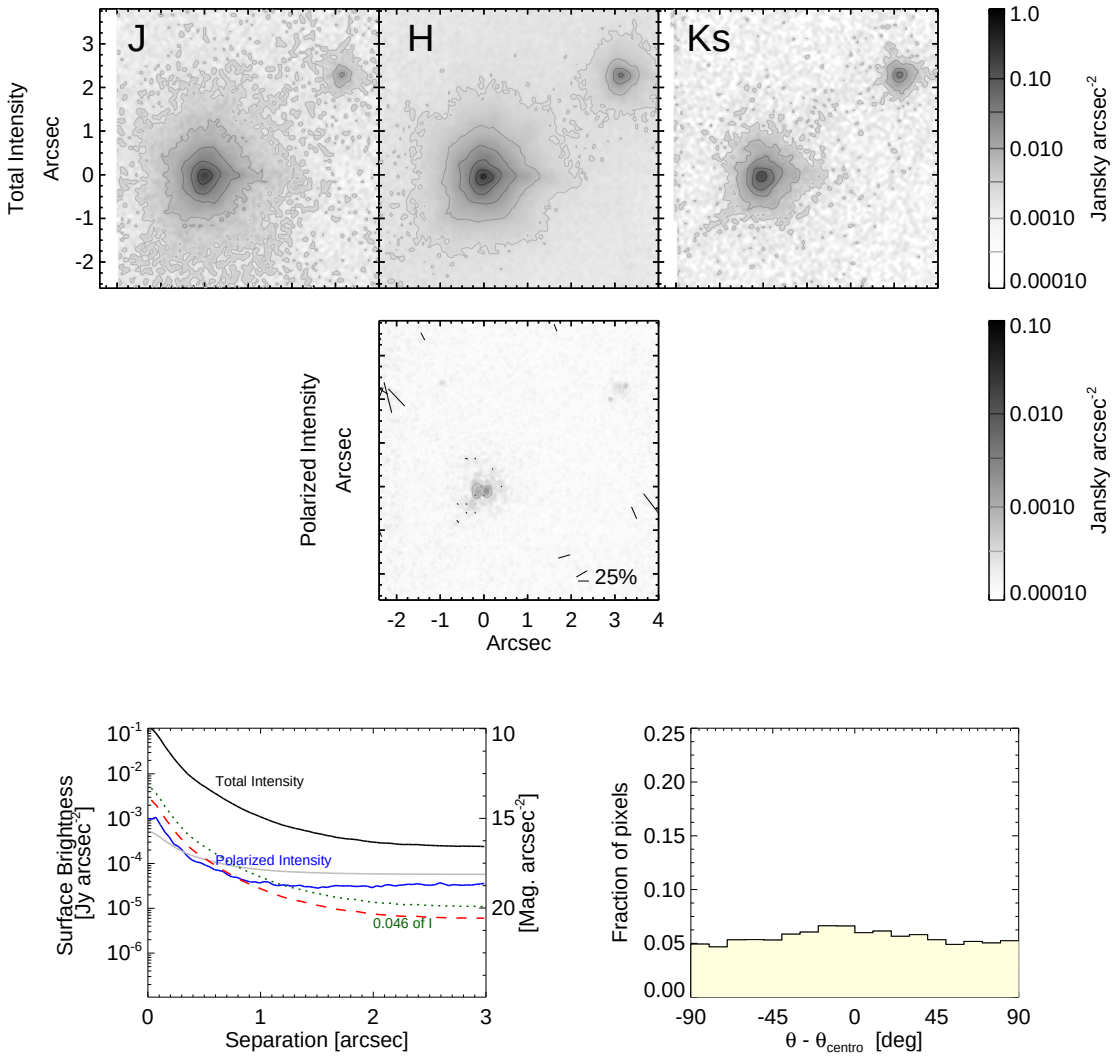

Figure 4.21: Imaging polarimetry of HBC 334.

4.5.13 AFGL 4029

AFGL 4029 is a deeply embedded cluster in the molecular cloud IC 1848 (Price & Walker, 1976). There are two main sources of mid-IR light, AFGL 4029 IRS1 and IRS2 (Beichman, 1979). The western of these, AFGL 4029 IRS1, appears to be a very young massive star with $L \sim 10^4$ and $A_V \sim 30$, while the eastern is a $\sim$ B1 ZAMS star, part of a cluster of at least 30 young B-type stars. See Deharveng et al. (1997), Zavagno et al. (1999) and Zapata et al. (2001) for detailed discussions of this region.

NIR speckle observations by Leinert et al. (2001) detected a strong halo around AFGL 4029 IRS1, offset to the northwest from the locus of peak intensity, with a brightness minimum between the extended emission and the central source. They interpreted this as resulting from an optically thick circumstellar disk occulting the more distant lobe of a bipolar halo. Zavagno et al. (1999) presented $8 - 13$ μm images of this cluster, resolving extended emission around both IRS1 and IRS2.

It was observed at Lick on 2005-11-23 UTC in good conditions, and at Gemini North on 2005-12-16. Our mid-IR observations include all 6 narrow-band Michelle filters as well as our standard N' and Qa, producing a a rich dataset on this highly complex region. The NIR and mid-IR images all show an extensive fan-shaped nebula to the northwest of AFGL 4049 IRS1. In the near-IR the inner regions have the V-shaped morphology of an outflow cavity, transitioning in the outer regions to a C-shaped arc centered on the star; in the mid-IR only the southern side of the V is visible, extending west from the star. Interestingly, even at 11 and 18 μm, no nebula is visible to the southeast, so any warm dust present there (e.g. the opposite side of a bipolar nebula) must be incredibly deeply extincted. Even more curious is the shape of the nebula near AFGL 4029 IRS2. This source has previously been interpreted as a HII region illuminated by a B1 star, source 26 of Deharveng et al. (1997). In these data a "cometary" morphology is apparent, with a curve oriented back towards AFGL 4029 IRS1 (see also Zapata et al. 2001). Our observations confirm the hypothesis of Zapata et al. that IRS2 is an extended source illuminated by a cloud of B stars, rather than a very deeply embedded point source of some kind.

The immediate vicinity of AFGL 4029 IRS1 also has some surprises. At 11 μm, three peaks are visible: a central one which I identify with the star itself, and two fainter peaks on opposite sides, consistent wit the edges of a torus of gas and dust around the star. Remarkably, by 18 μm, the central source has vanished and we see only the outer peaks. It is difficult to see how there could be enough warm dust inside the torus to account for

the 11 μm peak yet not have any compact emission there at 18 μm. This double-peaked structure is also seen at radio wavelengths by Zapata et al. (2001).

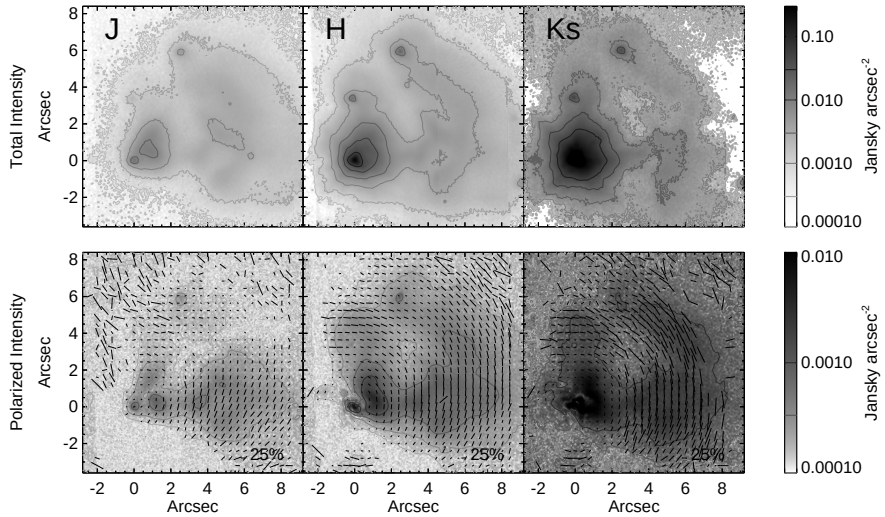

Figure 4.22: Imaging polarimetry of AFGL 4029. The bottom frame is a closeup on the region surrounding IRS1, the bright source at right in the top frame.

4.5.14 V1185 Tau

V1185 Tau, also known as PDS 4, is an A0 star located at a distance of 580 pc, with $V = 10.7$. The PDS survey found it to be an A0 star with [OI] in emission (Vieira et al. 2003); they also found it to be out of the expected location in the HR diagram.

It was observed at Lick on 2004-09-08 UTC in excellent conditions. No polarized light was detected in the near-IR (Fig. 4.24)

4.5.15 IP Per

IP Per, also known as HBC 348 or BD+32°656, is an A6 star (Hernández et al., 2004) located at a distance of 300 pc (Miroshnichenko et al., 2001), with $V = 10.3$. IP Per is likely a member the Perseus I OB association (Wood et al., 1994). Testi et al. (1998) found the area around IP Per to be "rather empty" of other stars.

It was observed at Lick on 2004-09-07 UTC in excellent conditions, and at Keck on 2004-08-28 UTC. No polarized light was detected in the near-IR (Fig. 4.25) The star was not resolved in the mid-IR (Fig. 4.26).

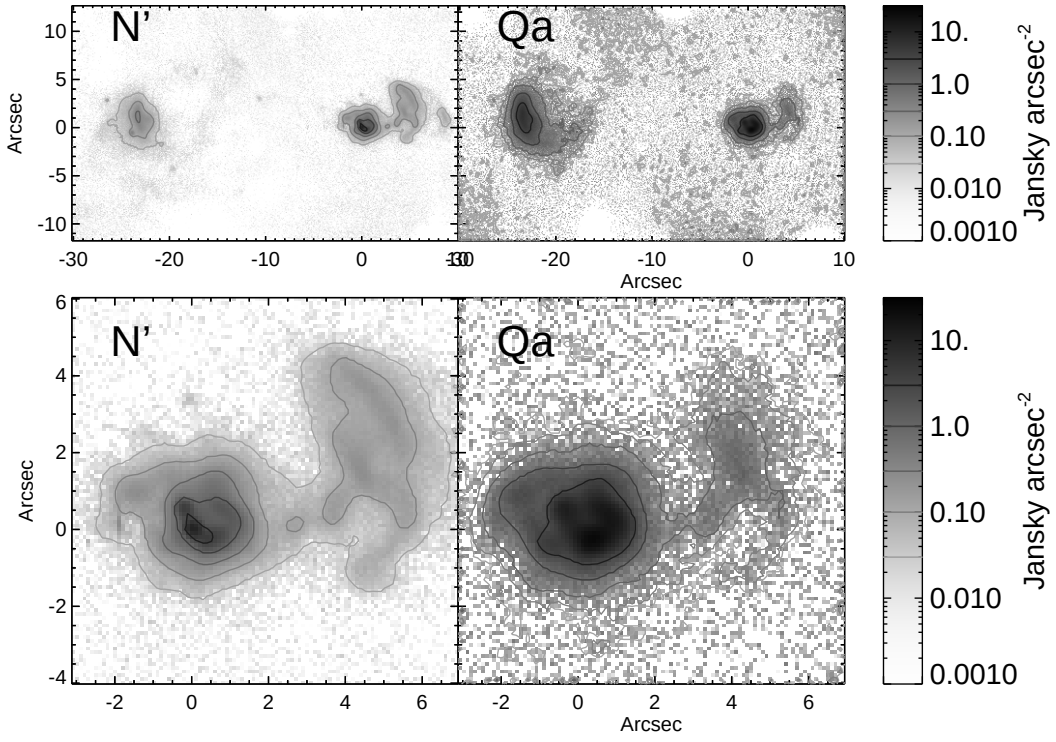

Figure 4.23: Mid-IR imaging of AFGL 4029. The top figure shows the entire region, while the bottom is a closeup of AFGL 4029 IRS1.

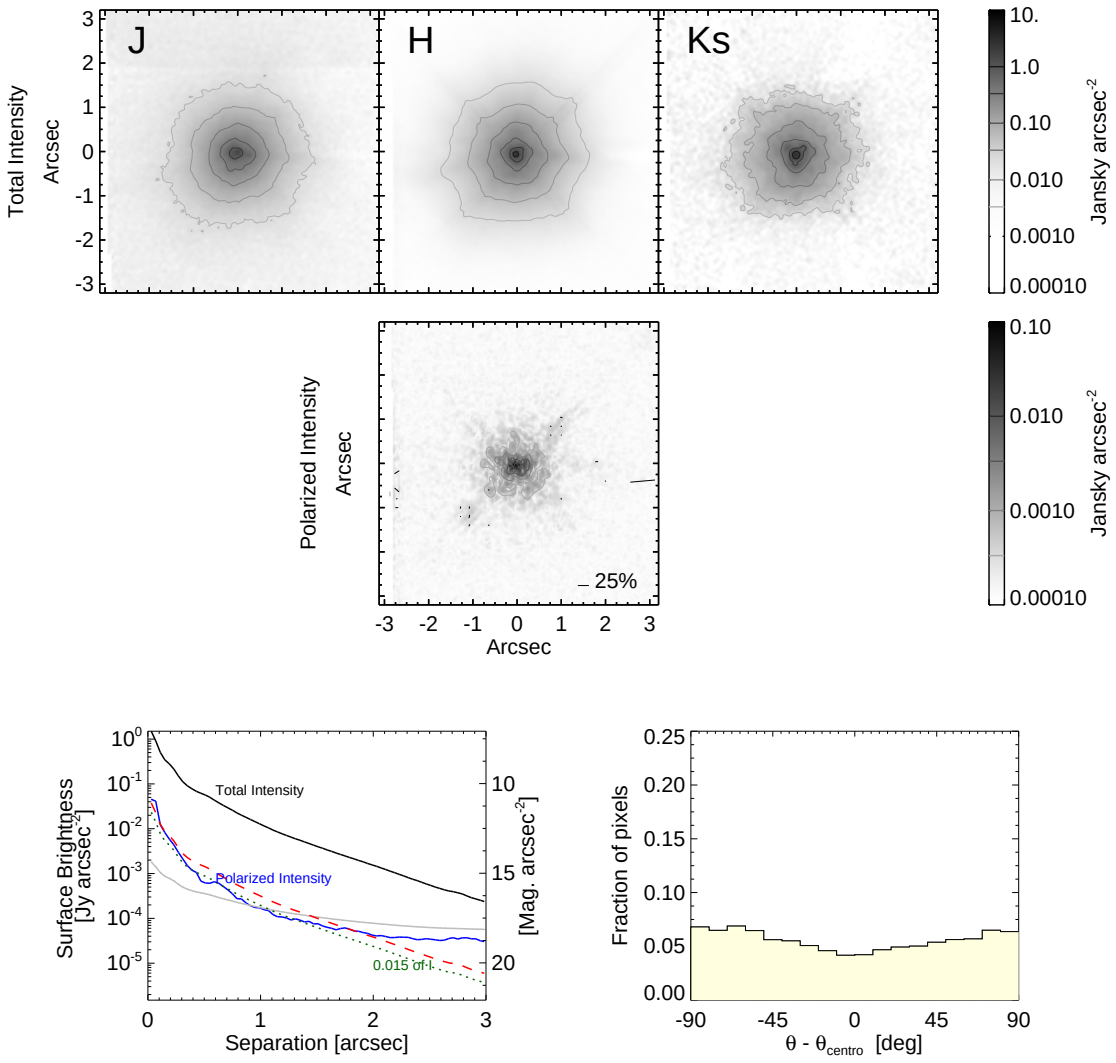

Figure 4.24: Imaging polarimetry of V1185 Tau.

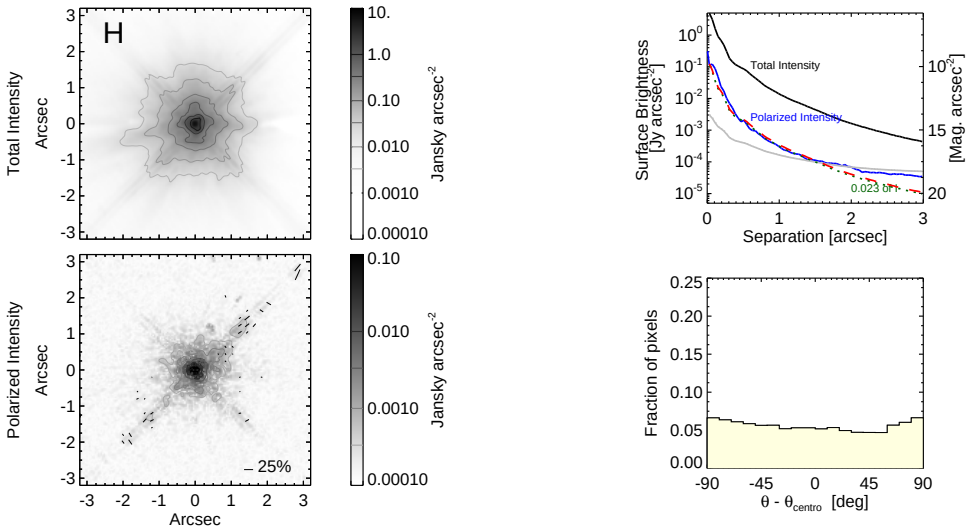

Figure 4.25: Imaging polarimetry of IP Per.

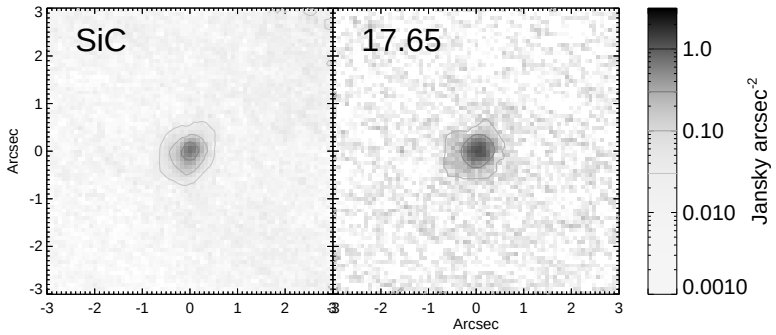

Figure 4.26: Mid-IR imaging of IP Per.

4.5.16 XY Per

XY Per E is an equal-magnitude binary with a separation of 1.″4, located at a distance of 120 pc (Herbig & Bell, 1988; Pirzkal et al., 1997; Mora et al., 2004). The stars' combined spectral type is A5 (Hernández et al., 2004).

It was observed at Lick on 2002-11-25 UTC in very poor conditions, resulting in very limited AO correction, and at Keck on 2004-08-27 and 28. While the binary is easily resolved at all wavelengths, we find no evidence for resolved circumstellar dust. Just as in the optical and near-IR, the two stars have very nearly equal brightnesses in the mid-IR. (Figs. 4.27, 4.28

4.5.17 V892 Tau

V892 Tau (also known as Elias 1) is a deeply embedded source at a distance of 160 pc in the nebula IC 359 (Elias, 1978; Haas et al., 1997), with $V = 15.2$ and an SED rising toward longer wavelengths. Its spectral type has been variously estimated as A0, A6, and B8 (Finkenzeller, 1985; Hillenbrand et al., 1992; Hernández et al., 2004). Kataza & Maihara (1991) resolved a east-west nebula around the star, which they interpreted to be reflected light from a circumstellar disk. Leinert et al. (1997) instead argued based on multiwavelength speckle data that the nebulosity is from bipolar lobes in a circumstellar envelope, not a disk. A fainter companion $\sim 4''$ northeast of V892 Tau was found in a radio survey by Skinner et al. (1993). Subsequent observations of this source, termed V892 Tau NE or Elias 1 NE, established its nature as a T Tauri star with $L \sim 0.4 L_\odot$ (Pirzkal et al., 1997; Leinert et al., 1997). Smith et al. (2005) detected a second companion at $\rho = 0.''05, \theta = 50°$, and suggest that this may be the source of the X-ray radiation seen at V892 Tau. The deep NIR images of Testi et al. (1998) reveal an almost empty field around these stars, and the system is unresolved in millimeter wavelengths (di Francesco et al., 1997; Henning et al., 1998)

It was observed at Lick on 2005-11-22 UTC in good conditions, and at Keck on 2004-08-27 UTC. There is a peak in the near-IR centrosymmetry histogram, but with its center offset roughly -25 °from zero (Fig. 4.29). This is an instrumental artifact resulting from imperfect sky subtraction, visible to the east of V892 Tau. No statistically significant evidence for actual polarized scattered light is seen. V892 Tau is unresolved in our 11 μm LWS image (Fig. 4.30), but mediocre image quality reduces our detection limits.

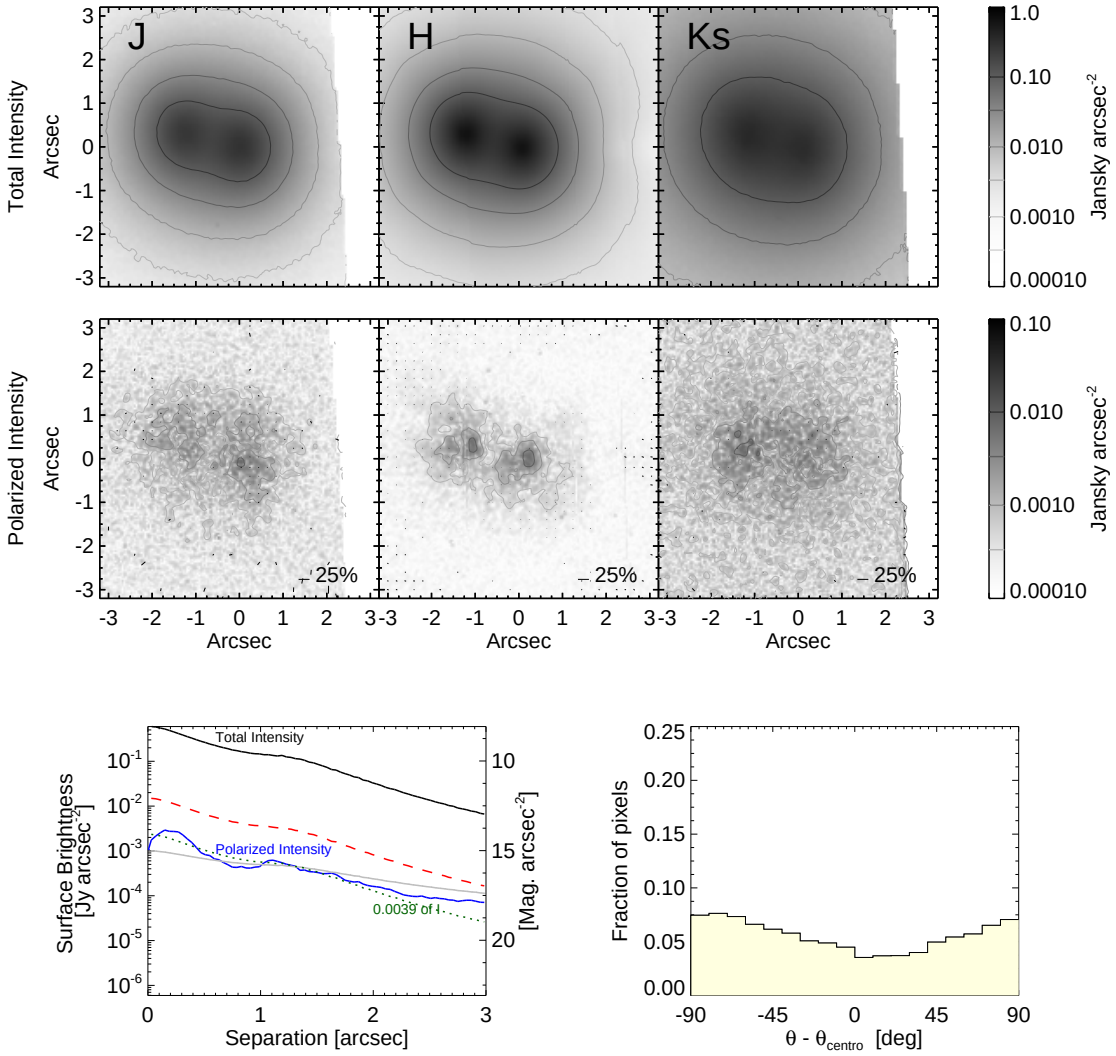

Figure 4.27: Imaging polarimetry of XY Per.

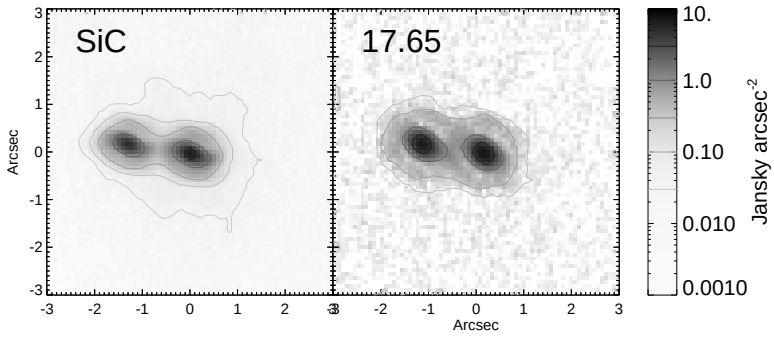

Figure 4.28: Mid-IR imaging of XY Per.

V892 Tau NE is clearly detected in the IRCAL images. In the 11.7 μm LWS image, a very faint source is marginally detected at its location, indicated by the arrow in the figure.

4.5.18 LkHα 101

LkHα 101 is a $V = 15.9$ continuum star (Hernández et al., 2004). While the distance to LkHα 101 has long been believed to be 800 pc, the star may instead lie only 140 pc distant (Stine & O'Neal, 1998). Aperture masking interferometry by Tuthill et al. (2001) resolves the inner edge of the circumstellar material, showing an arc of emission 21 mas from the star plus a companion 180 mas northeast, while speckle observations by Leinert et al. (2001) reveal the outer nebula as a $\sim 0\farcs9$ halo contributing about 15% of the total flux.

LkHα 101 was observed at Lick on 2003-11-02 UTC in mediocre conditions. No polarized light was detected in the near-IR (Fig. 4.31). Nor can we resolve the 180 mas companion found by Tuthill et al., but that is near the Lick 3 m's diffraction limit and would be challenging even in good conditions.

4.5.19 AB Aur

AB Aur is a well-known A1 star located at 144 pc with $V = 7.0$ (Hernández et al., 2004). A $\sim 3''$ disk has been detected around it using CO interferometry (Mannings & Sargent, 1997), and space- and ground-based coronagraphic observations (Nakajima & Golimowski, 1995; Grady et al., 1999; Fukagawa et al., 2004).

It was observed at Lick on 2002-11-21 UTC through intermittent clouds conditions but with decent seeing, and at Keck on 2004-08-27 UTC. The star was not resolved in the mid-IR (Fig. 4.33). In the near-IR, we do detect its well-known disk: a roughly elliptical pattern of polarization is visible, strongest to the northeast and southwest. But the morphology of the disk is not particularly clear, and we cannot see the spiral density waves or other substructure reported by Fukugawa et al.

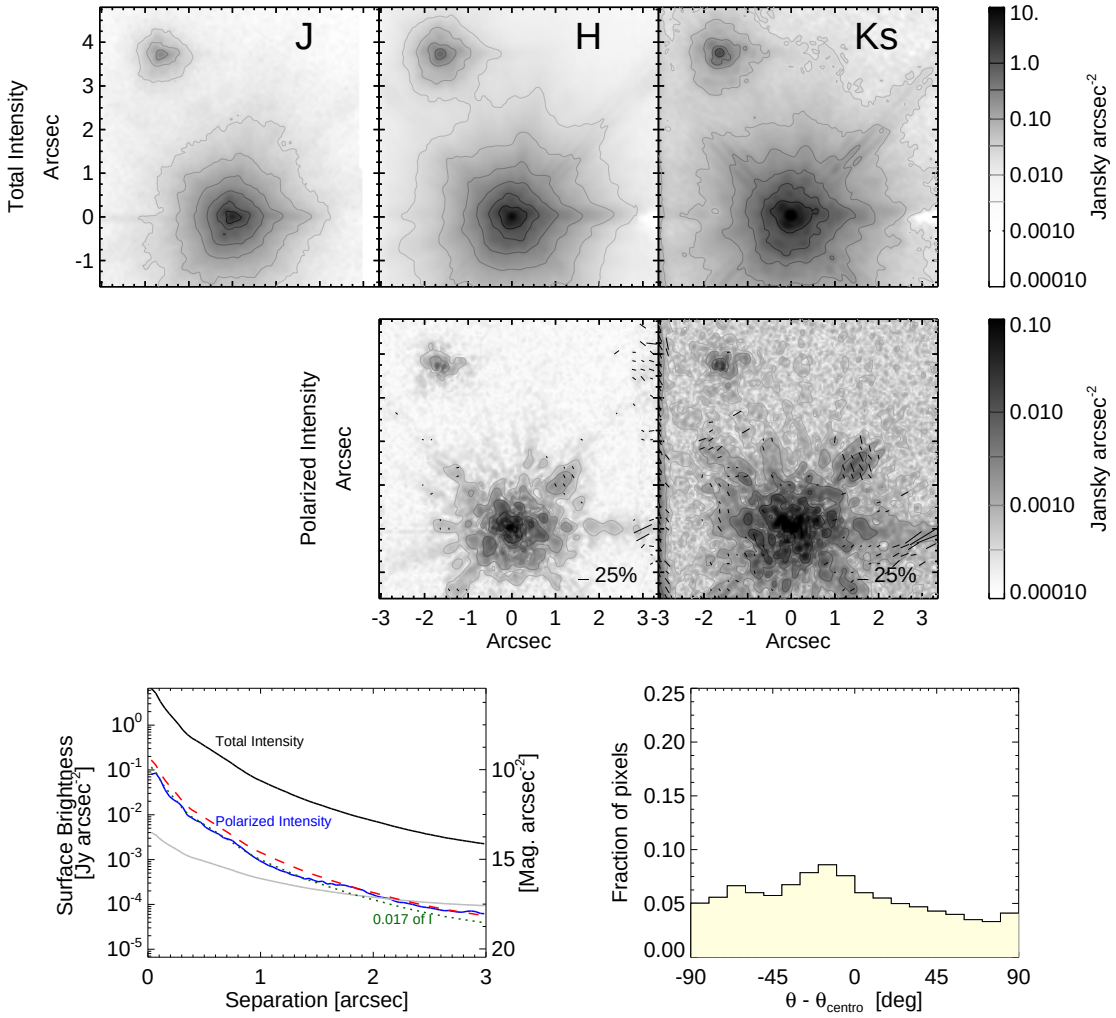

Figure 4.29: Imaging polarimetry of V892 Tau.

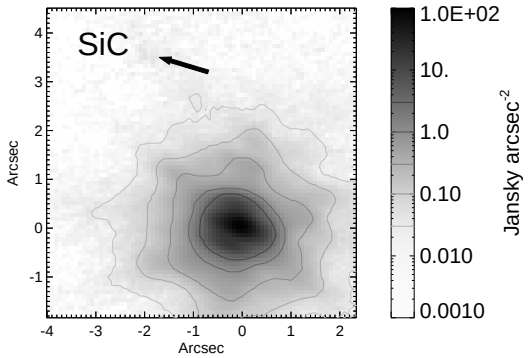

Figure 4.30: Mid-IR imaging of V892 Tau. The arrow indicates the location of the faint V892 Tau NE.

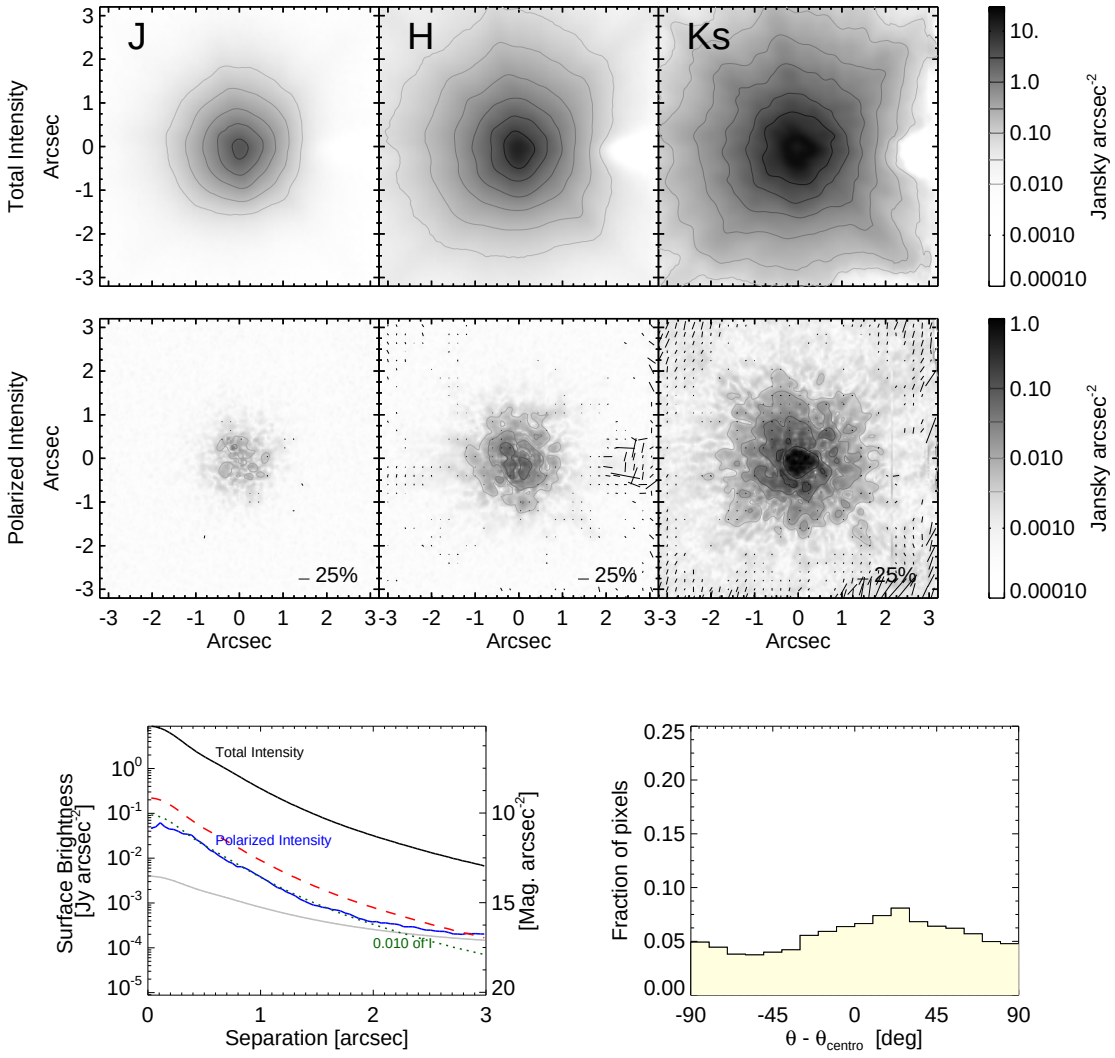

Figure 4.31: Imaging polarimetry of LkHα 101.

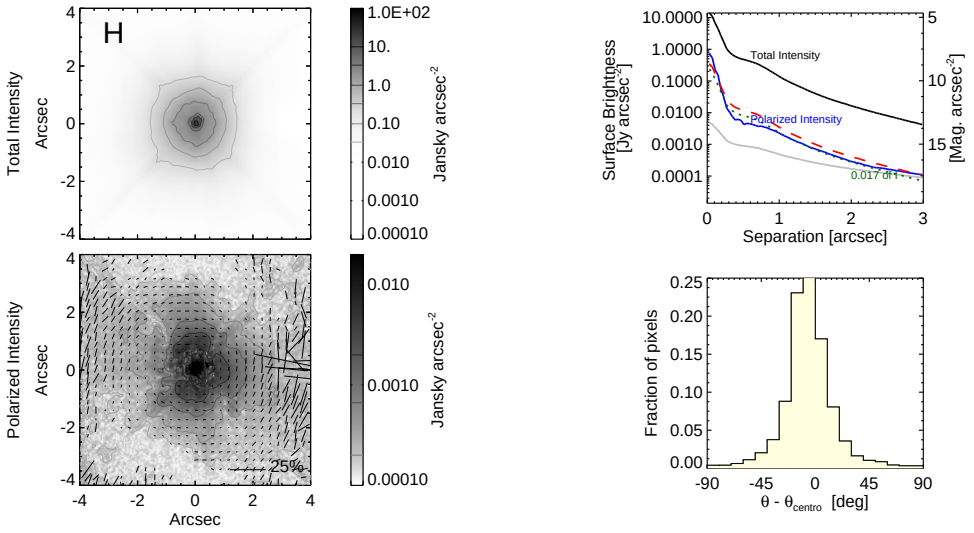

Figure 4.32: Imaging polarimetry of AB Aur.

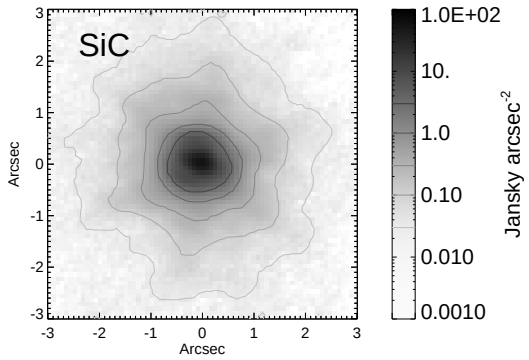

Figure 4.33: Mid-IR imaging of AB Aur.

4.5.20 MWC 480

MWC 480 is an A3 V star located at a distance of 150 pc with $V = 7.8$ (Testi et al., 1998; Vieira et al., 2003). Mannings et al. (1997) detected a rotating circumstellar gas disk in CO, with radius about 680 AU.

It was observed at Lick on 2002-11-25 UTC in very poor conditions. The polarized image is noisy, but a faint pattern of centrosymmetric polarization vectors can be detected, particularly to the west of the star. (Fig. 4.34) On the other hand, on the other side of the star is a large patch of non-centrosymmetric vectors. Statistical analysis of the overall histogram indicates the potential detection of scattered starlight at a 1.1σ significance level; see §4.7.1.

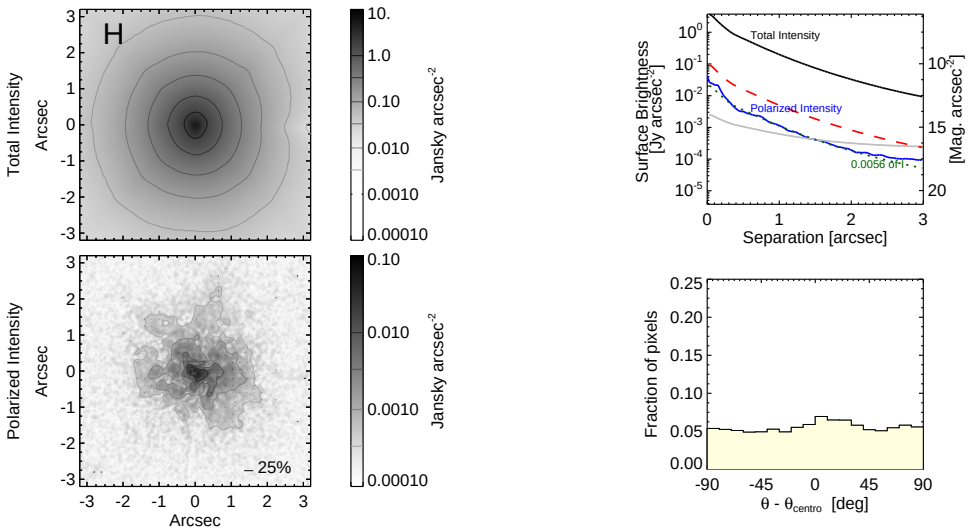

Figure 4.34: Imaging polarimetry of MWC 480.

4.5.21 UX Ori

UX Orionis is an A3 star (Hernández et al., 2004) located at a distance of 340 pc (de Zeeuw et al., 1999), with $V = 10.4$. It is the prototypical object of the UX Ori class, a group of HAEBEs which show irregular deep photometric minima caused by variable extinction from circumstellar dust Dullemond et al. (2003). Keck Interferometer observations detect a relatively large disk around it (Monnier et al., 2005).

It was observed at Lick on 2005-10-18 UTC in cloudy and humid conditions. No polarized scattered light was detected in the near-IR (Fig. 4.35). (The blob in that

direction visible in the polarized intensity image does not have the correct position angle to be scattered light and appears to be a PSF artifact.)

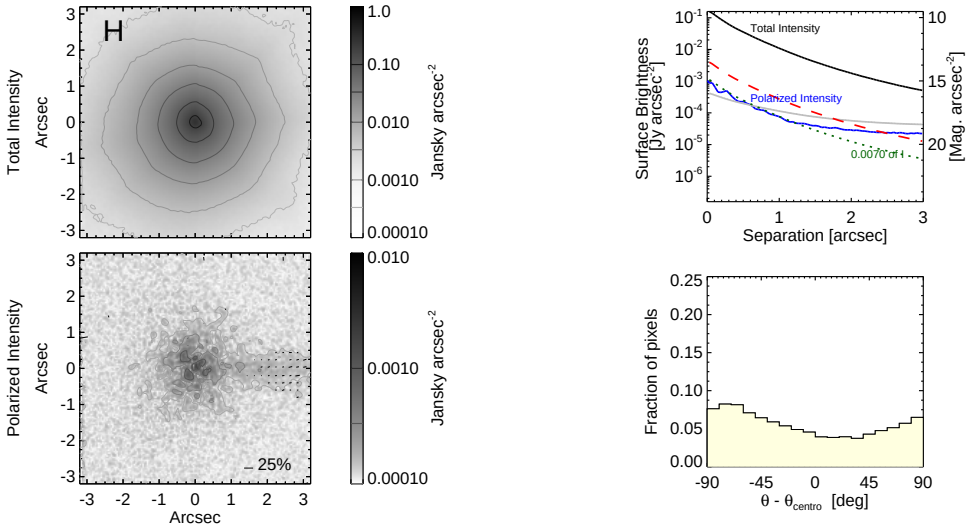

Figure 4.35: Imaging polarimetry of UX Ori.

4.5.22 NSV 1832

NSV 1832, also called PDS 174 and L1616 MIR3, is a $V = 12.8$ star located in the L1616 molecular cloud on the outskirts of Orion. Its spectral type is somewhat in doubt: Vieira et al. (2003) classify it as B3, while Alcalá et al. (2004) estimate K5 based on the SED. Previous studies of the L1616 cloud indicate that it ha been the site of ongoing star formation for the last 1-2 Myr (Stanke et al., 2002; Alcalá et al., 2004).

It was observed at Lick on 2005-11-21 UTC in good conditions, and at Gemini North on 2005-12-16 UTC. No polarized light was detected in the near-IR (Fig. 4.36). However, we resolve NSV 1832 into a 0.″75 binary, with the fainter companion becoming brighter at longer wavelengths. Also visible is a third source, 2MASS 05065540-0321199, located 6.″9 south of NSV 1832 A .

In the mid-IR there is a S-shaped nebula about 4″ across, centered on NSV 1832 and extending east and northwest (Fig. 4.37). At 11 μm, the northern star (the fainter secondary in the NIR) has become equally bright as the primary. At 18 μm, this region is entirely nebulous and neither star is detected as a point source. The brightest mid-IR point source in the region, is in fact a star 8.″8 west, called L1616 MIR4 or 2MASS 05065493-0321126. Of the four stars visible here, NSV 1832 A has an SED which peaks around 1 μm

while the rest are more deeply embedded and peak somewhere between $2 - 10$ μm. See Alcalá et al. (2004) for a discussion of these stars.

4.5.23 HD 35187

HD 35187 is a $1\farcs4$ binary with spectral types A2Ve and A7Ve, and combined magnitude $V = 7.8$ (Dunkin & Crawford, 1998). Its distance has been variously estimated as 150-220 pc (Vieira et al., 2003).

It was observed at Lick on 2004-10-11 UTC in very poor conditions, and again on 2005-10-18 in cloudy and humid conditions; and at Gemini North on 2005-12-16 UTC. No polarized light was detected in the near-IR (Fig. 4.38). Our mid-IR observations reveal that most of the circumstellar dust in the system is located around the primary. While the two stars have $\Delta K = 0.2$, by 11 μm the difference is 4.3 mag, and by 18 μm the southern source is undetected (Fig. 4.39) .

4.5.24 V346 Ori

V346 Ori, also called PDS 180, is an A8 V star located at a distance of 300 pc with $V = 10.1$ (Vieira et al., 2003). It was observed at Lick on 2005-10-18 UTC in cloudy and humid conditions, resulting in poor AO performance. No polarized light was detected in the near-IR (Fig. 4.40)

4.5.25 CO Ori

CO Ori is a F8 star located at a distance of 460 pc, with $V = 10.6$; it is a UX Orionis star (Natta et al., 1997). It was observed at Lick on 2004-11-01 UTC in poor and windy conditions, and on 2005-10-18 in cloudy and humid conditions. No polarized light was detected in the near-IR (Fig. 4.41)

It has a companion located $2''$ west, with $\Delta K = 3$ (Bouvier & Corporon, 2001). This companion also has spectral type F, so it must be very dusty to be so much fainter than the F8 primary. The companion is also the source of most of the emission lines in the system (Rodgers et al., 2005).

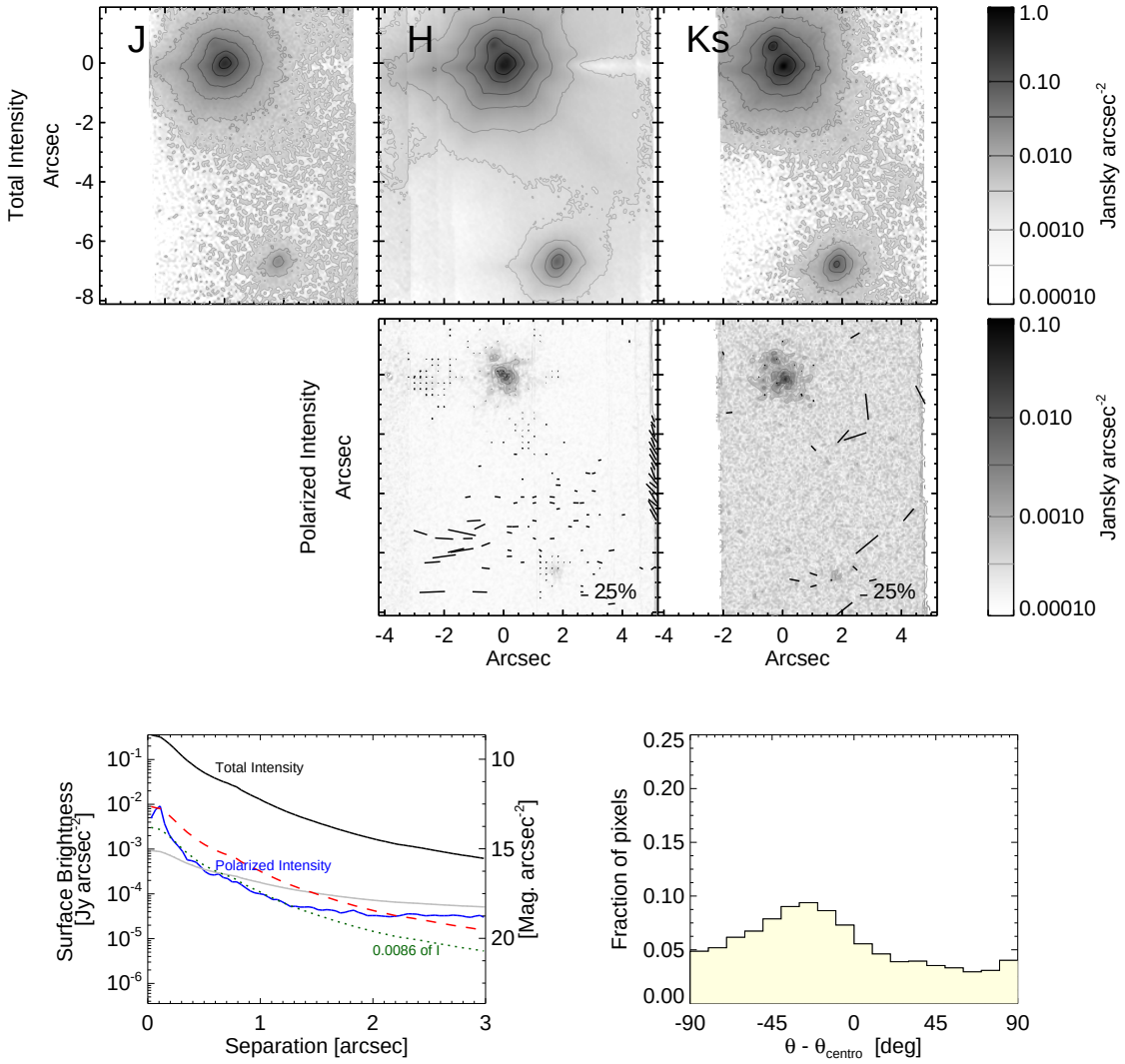

Figure 4.36: Imaging polarimetry of NSV 1832.

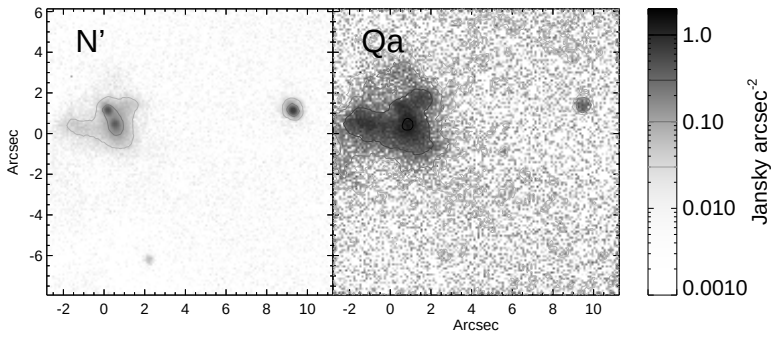

Figure 4.37: Mid-IR imaging of NSV 1832.

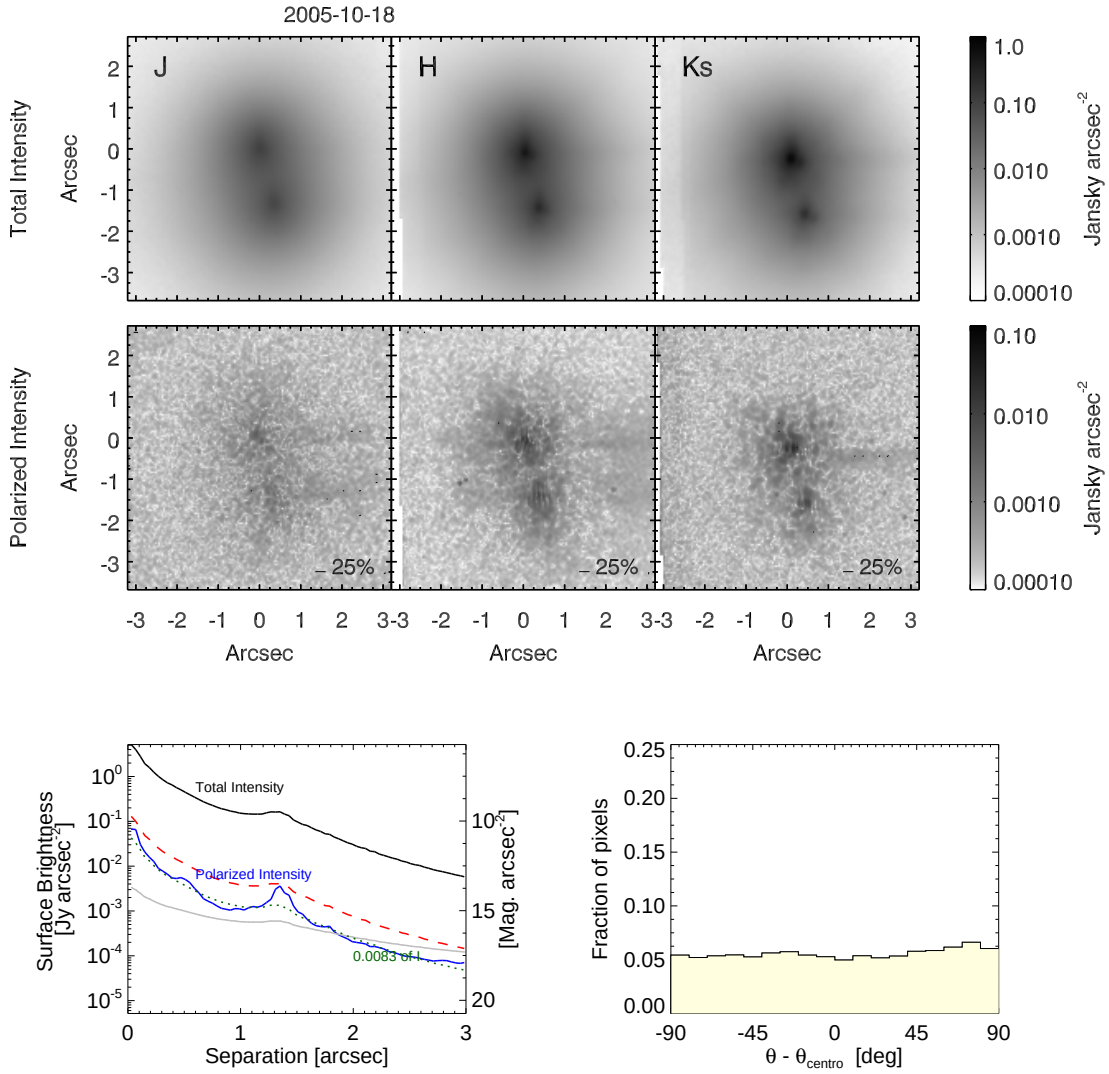

Figure 4.38: Imaging polarimetry of HD 35187.

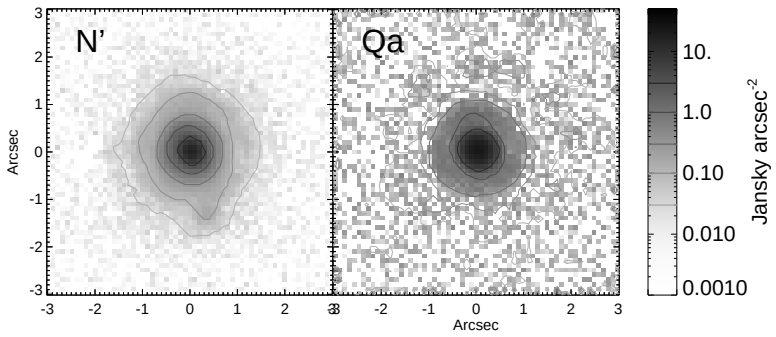

Figure 4.39: Mid-IR imaging of HD 35187.

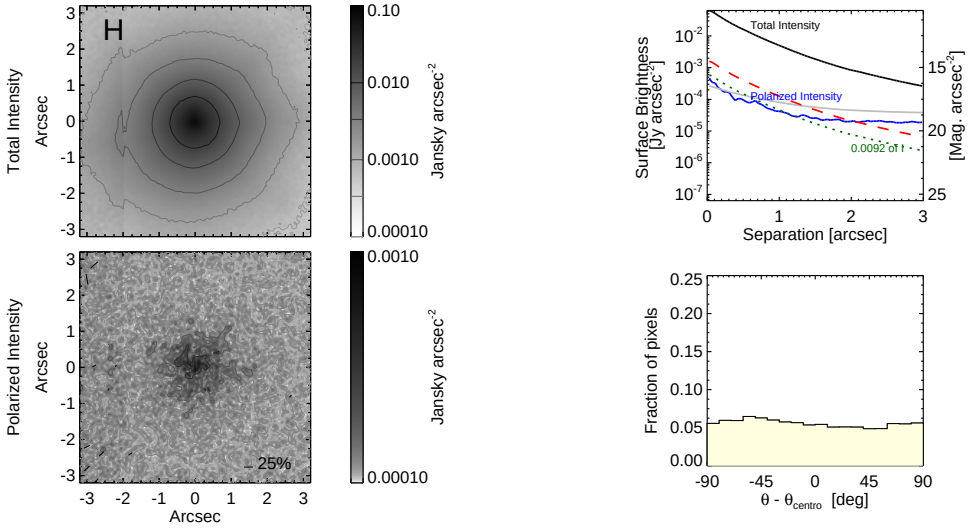

Figure 4.40: Imaging polarimetry of V346 Ori.

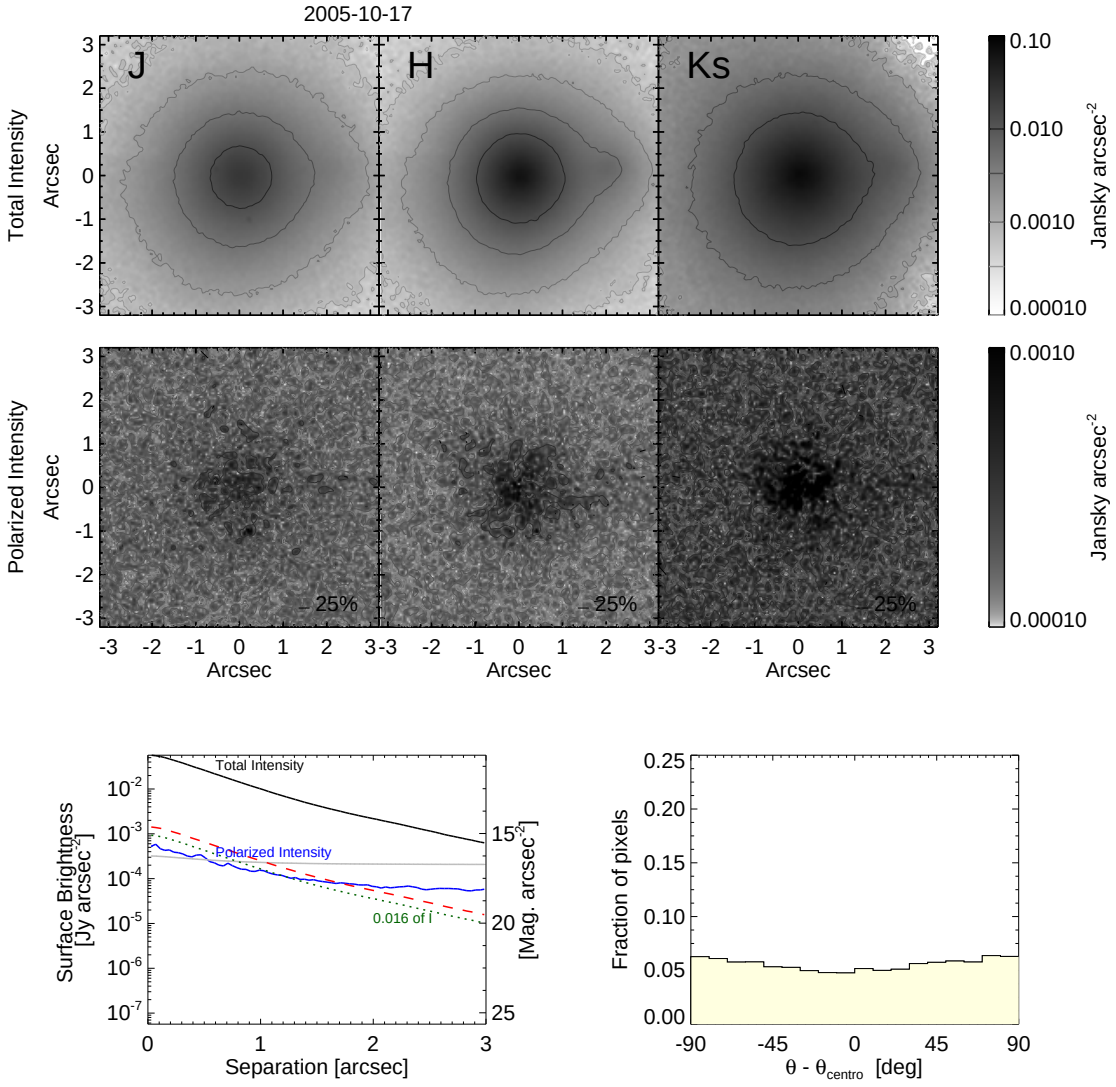

Figure 4.41: Imaging polarimetry of CO Ori.

4.5.26 MWC 758

MWC 758 is an A8 V star located at a distance of 140 pc (Vieira et al., 2003), with $V = 8.3$. Mannings & Sargent (1997) detected millimeter continuum and CO emission likely due to a circumstellar disk.

It was observed at Lick on 2004-12-01 UTC in windy conditions. No polarized light was detected in the near-IR (Fig. 4.42)

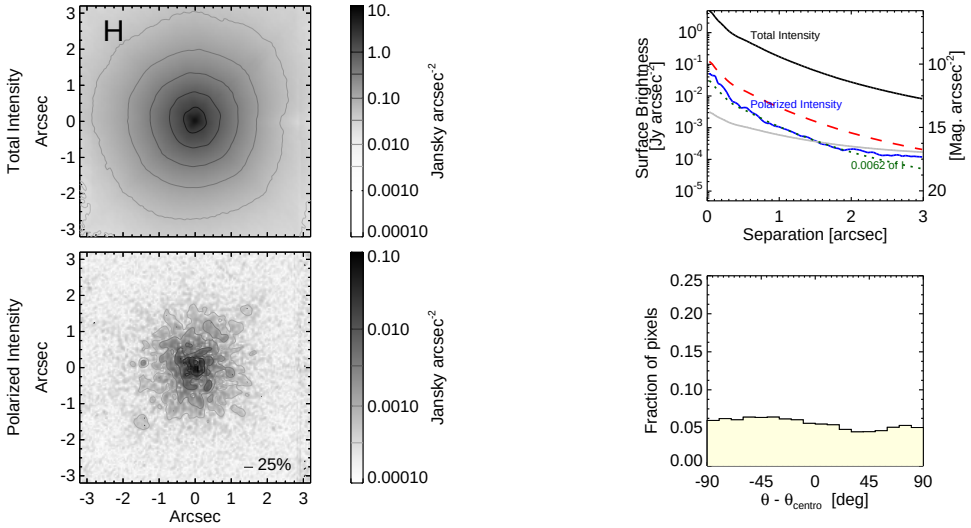

Figure 4.42: Imaging polarimetry of MWC 758.

4.5.27 HK Ori

HK Ori was found to be a 0.34″ binary by Lienert et al. (1997,2001), at a PA of 41.7 °. It is located at a distance of 460 pc and has $V = 11.7$ (Hillenbrand et al., 1992). Corporon and Lagrange (1999) observed Li absorption in the combined spectrum, indicating the T Tauri nature of the companion. Hernández et al. (2004) found numerous emission lines in the combined spectrum. They were unable to assign a reliable spectral type, with various portions of the spectrum alternately looking like F2, G0, or A2. They speculate that this might be due to contamination from the spectrum of the companion. This is supported by the fact that at optical wavelengths, the flux ratio of the two is much smaller than in the IR (Smith et al., 2005). See Smith et al. for a detailed discussion of these two stars.

It was observed at Lick on 2004-12-01 UTC in windy conditions. In spite of relatively poor seeing, we do barely resolve this system. There is also a companion 4″ nearly due

north (Bouvier & Corporon, 2001), which we easily detect. However, no polarized light was detected in the near-IR (Fig. 4.43)

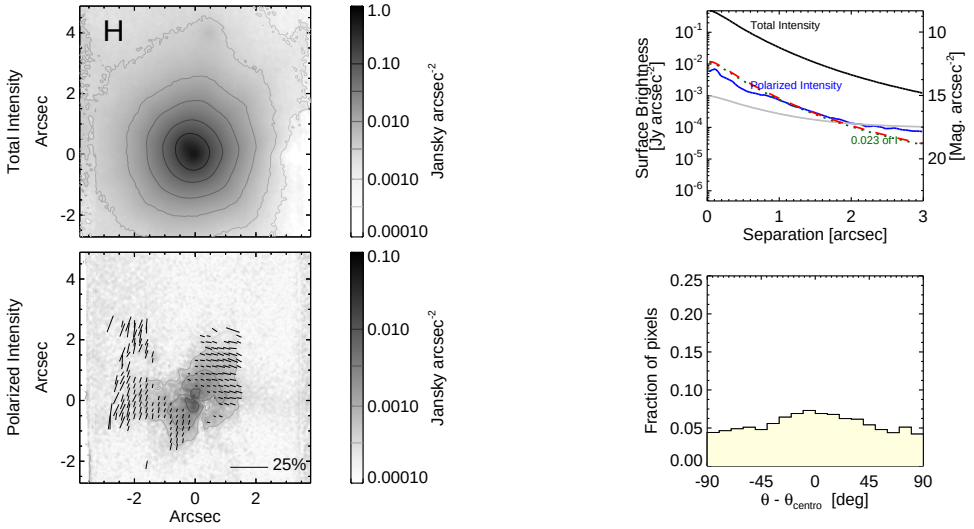

Figure 4.43: Imaging polarimetry of HK Ori.

4.5.28 HD 36408

HD 36408, also called PDS 185 and HR 1847, is a $V = 6.5$ binary Be star system located at a distance of 342 pc (van den Ancker et al., 1998; Vieira et al., 2003). As a 5th magnitude, $10''$ binary this system attracted attention early in the history of binary star astronomy; see Struve (1837). Gahm et al. (1983) found both stars to have spectral type B7. This system has been identified as the optical counterpart to IRAS 05293+1701 (Cote & Waters, 1987; Gregorio-Hetem et al., 1992). Its evolutionary status is under debate, with some authors considering these to be classical Be stars; van den Ancker et al. (1998) include HD 36408 on their list of stars lacking evidence for circumstellar dust.

It was observed at Lick on 2004-12-01 UTC in windy conditions. No polarized light was detected in the near-IR (Fig. 4.44)

4.5.29 T Ori

T Ori is an A0 star (Hernández et al., 2004) located at a distance of 460 pc, with $V = 10.6$ (Testi et al., 1998). Leinert et al. (1997) detected a companion located at $\rho = 7\farcs7, \theta = 72.6°$; this companion falls outside the field of view of my IRCAL observations.

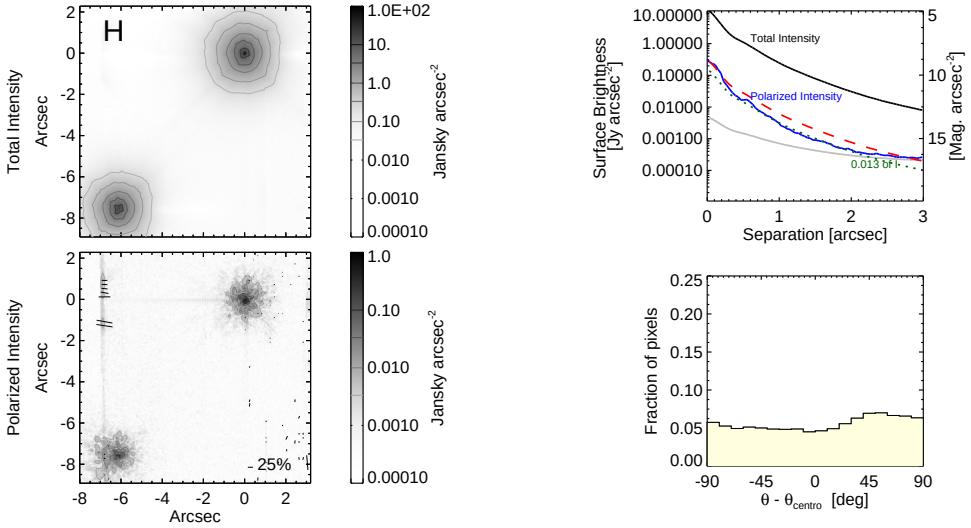

Figure 4.44: Imaging polarimetry of HD 36408.

Corporon & Lagrange (1999) found it to be a spectroscopic binary.

It was observed at Lick on 2004-10-11 UTC in poor conditions, resulting in large PSF subtraction residuals. No polarized light was detected in the near-IR (Fig. 4.45)

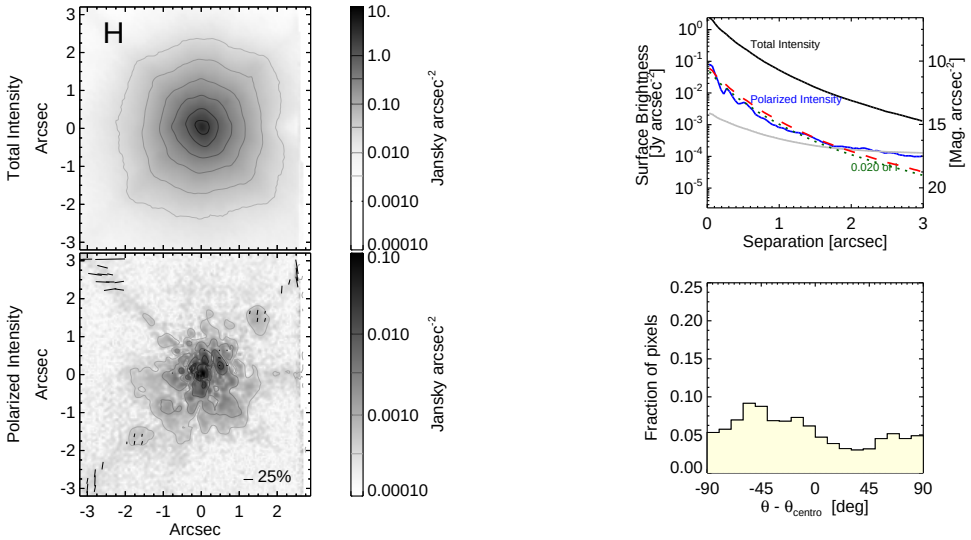

Figure 4.45: Imaging polarimetry of T Ori.

4.5.30 CQ Tau

CQ Tau is a F3 star (Hernández et al., 2004) located at a distance of 130 pc (van den Ancker et al., 1998), with $V = 10.3$. It is believed to be a UX Ori star, with a disk oriented at an inclination of 66°(Natta & Whitney, 2000). The 7 mm continuum shows resolved ~ 100 AU emission in observations by Testi et al. (2003). Dent et al. (2005) argue for the combination of a compact gas disk and more flared dust disk, based on their single-dish CO spectrum.

It was observed at Lick on 2005-10-17 UTC in poor conditions, and again on 2005-11-21 in good conditions. No polarized light was detected in the near-IR (Fig. 4.46)

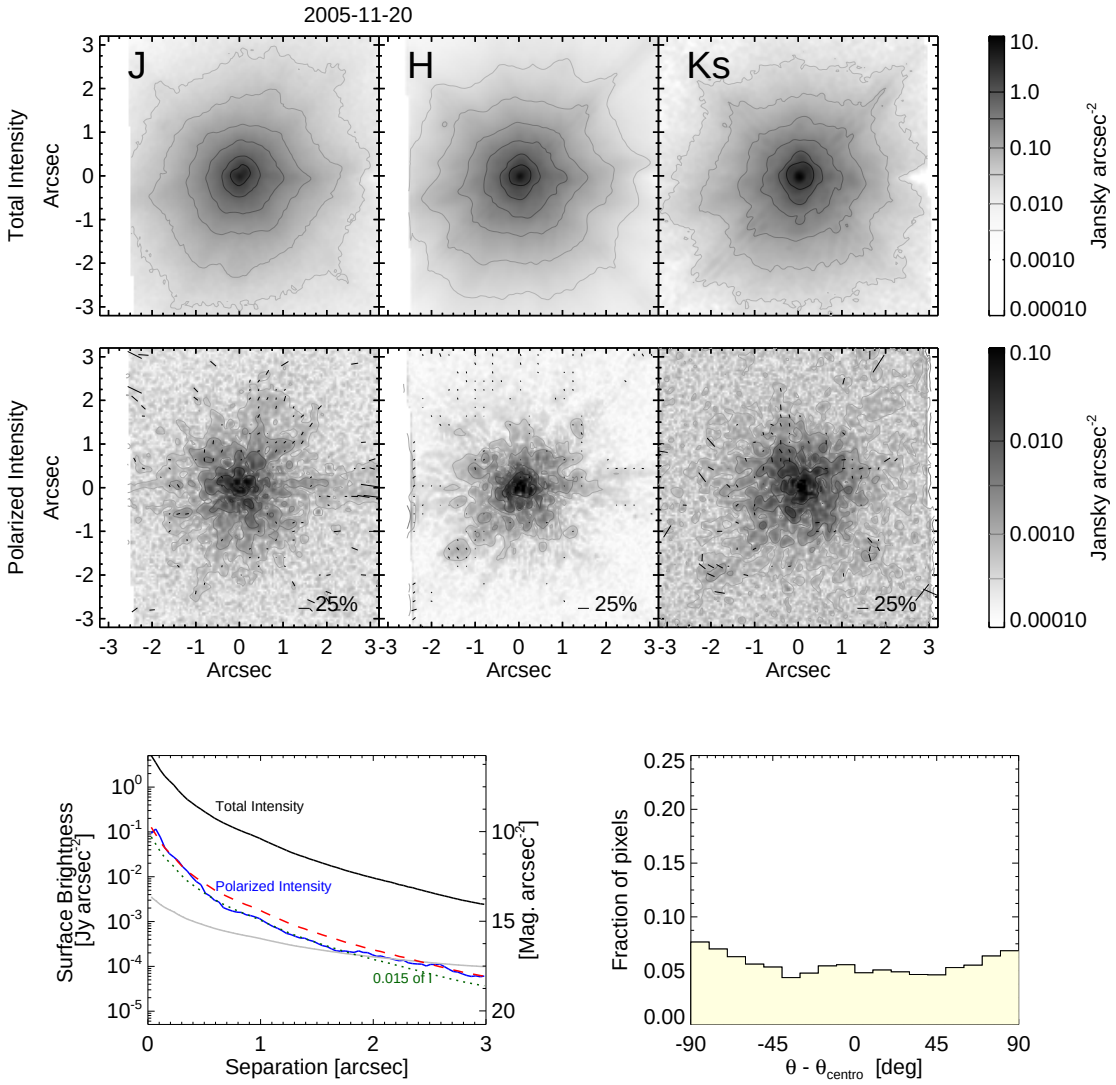

Figure 4.46: Imaging polarimetry of CQ Tau.

4.5.31 V380 Ori

V380 Ori is a continuum star located at a distance of 460 pc, with $V = 10.5$ (Hillenbrand et al., 1992; Hernández et al., 2004; Shevchenko, 1999). Leinert et al. (1997) found a companion at $0\farcs134$, PA 204.2°, and subsequent observations suggest the detection of orbital motion (Smith et al., 2005). Corporon & Lagrange (1999) observed Li absorption in the combined spectrum, indicating the companion is of T Tauri type. At I band the two sources are of equal brightness, decreasing until at K_s the fainter is 1.14 mag. dimmer than the primary. Leinert et al.'s 2001 study found no evidence for resolved light from a circumstellar halo.

It was observed at Lick on 2005-11-21 UTC in good conditions. No polarized light was detected in the near-IR (Fig. 4.47) We marginally detect the companion found by Lienert et al., but at a PA of $\sim 225°$ and a separation of $\sim 0\farcs17$ instead. Given the marginal level of the detection, it is unclear whether the change in position is due to actual stellar motion or is just due to observational uncertainty.

4.5.32 BF Ori

BF Ori is a $V = 10.4$ UX Orionis star located at a distance of 460-510 pc (Natta et al. 1997, de Zeeuw et al. 1999). Hernandez et al. 2004 encountered difficulties in spectrally classifying this star due to strong abnormal absorption in many of its spectral lines; it is most likely in the range A0-A5. No nearby nebulosity is visible (Finkenzeller & Mundt, 1984).

It was observed at Lick on 2005-11-21 UTC in good conditions. No polarized light was detected in the near-IR (Fig. 4.48). We do see an apparent companion located $2''$ northeast of BF Ori; a brief search of the literature turned up no prior references to this object.

4.5.33 HD 245906

HD 245906 is an A6 star (Hernández et al., 2004) located at a distance of 2000 pc (Kawamura et al., 1998), with $V = 10.7$. It was observed at Lick on 2005-10-18 UTC in cloudy and humid conditions, and on 2005-11-21 in good conditions. No polarized light was detected in the near-IR (Fig. 4.49)

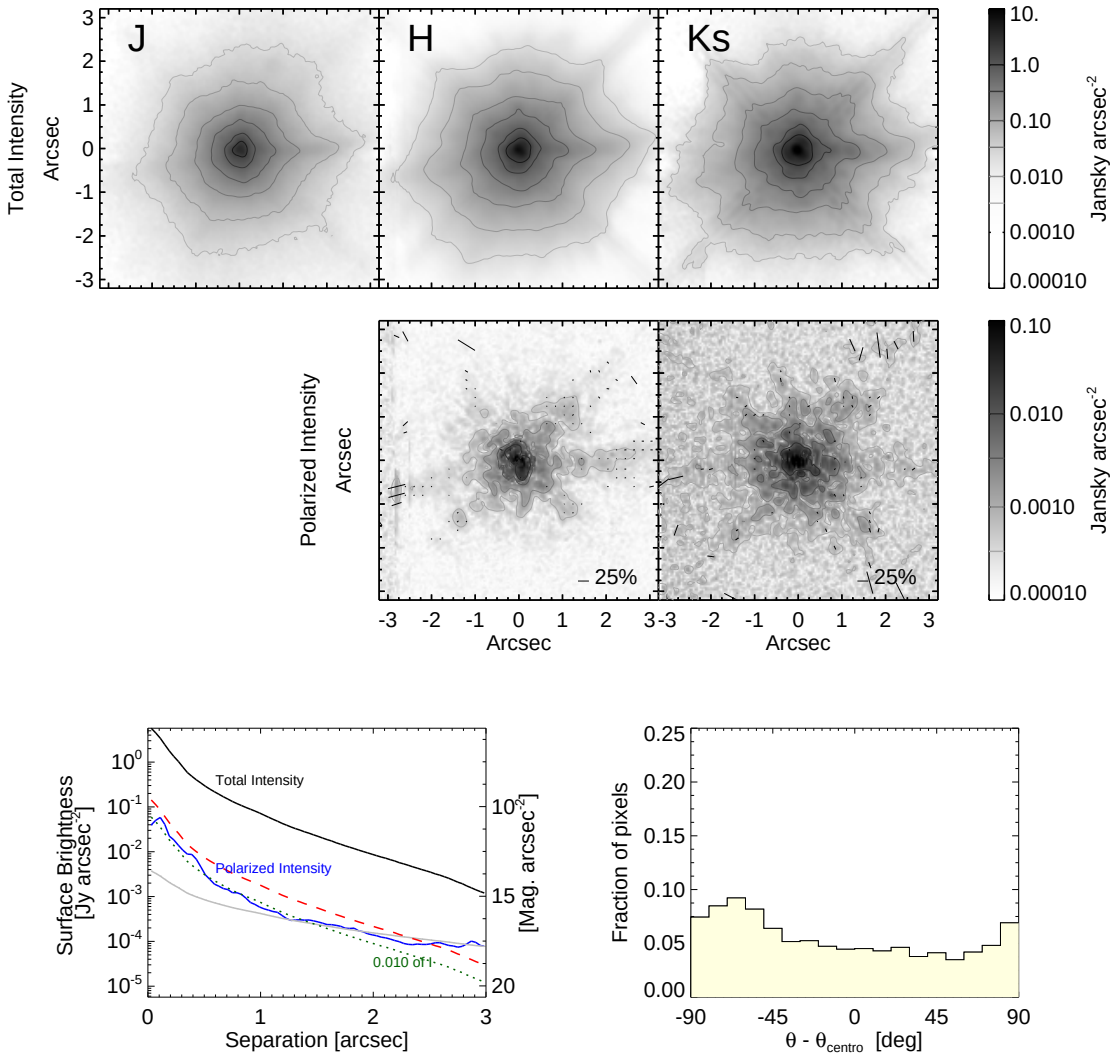

Figure 4.47: Imaging polarimetry of V380 Ori.

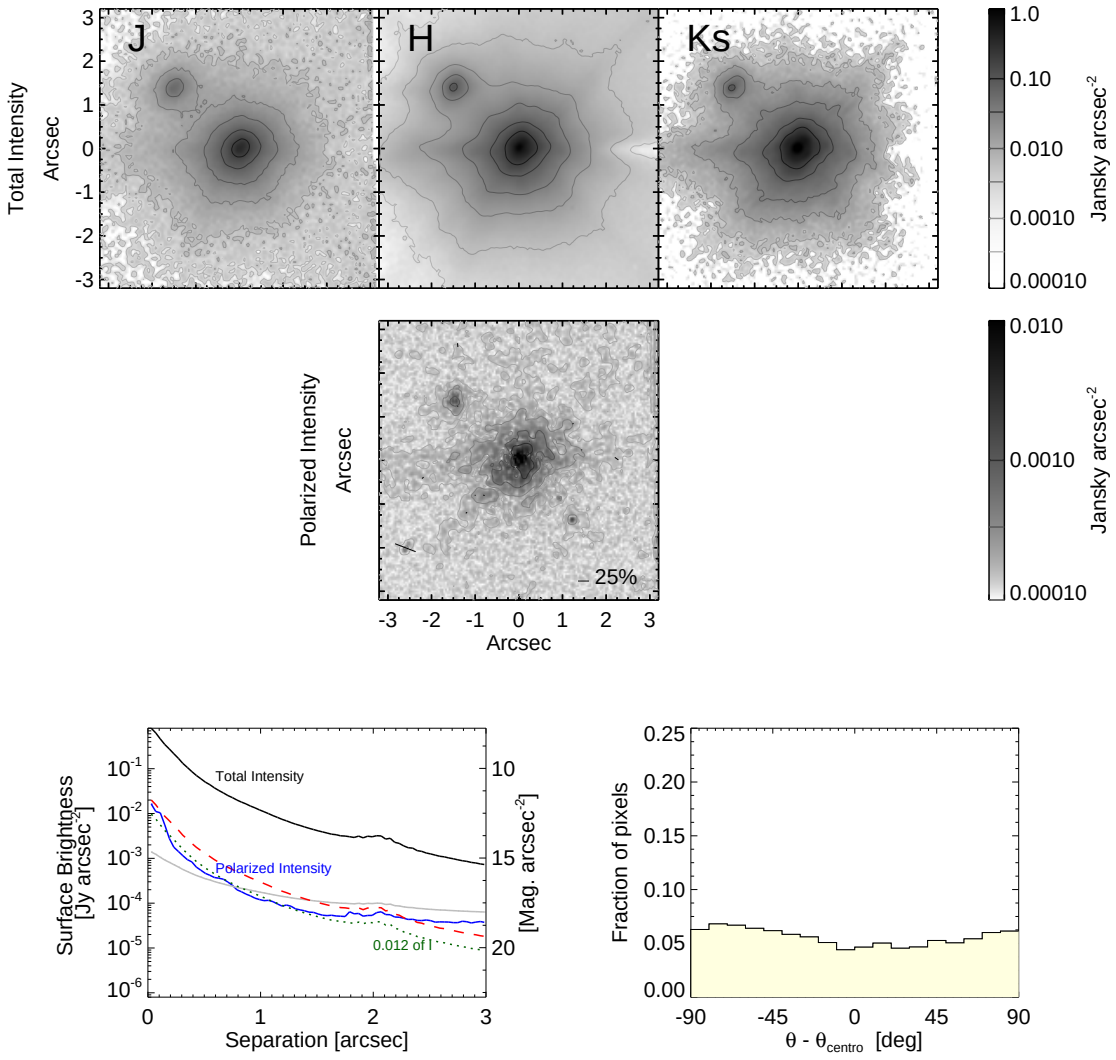

Figure 4.48: Imaging polarimetry of BF Ori.

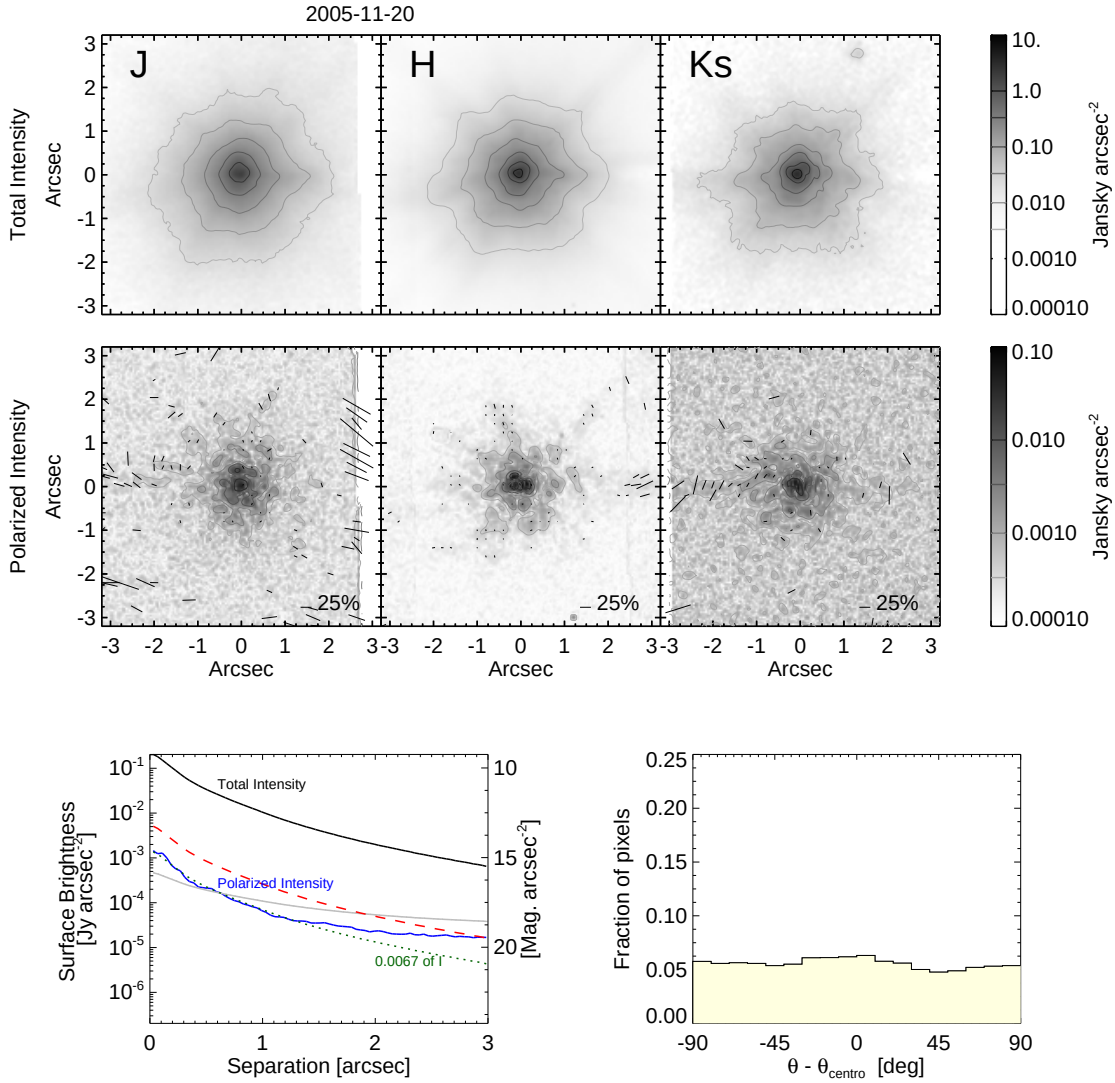

Figure 4.49: Imaging polarimetry of HD 245906. Polarized light is not detected at a significant level. In the K_s Stokes I image, the apparent source near the top of the frame is a residual afterimage from a previously-observed saturated source, not a real astrophysical object.

4.5.34 RR Tau

RR Tau is an A0 star (Hernández et al., 2004) located at a distance of 800 pc (Finkenzeller & Mundt 1984), with $V = 12.1$ (Herbst & Shevchenko 1999). An alternative distance of 160 pc has been argued for by Kenyon et al. (1994). Deep NIR images show a relatively crowded stellar environment around RR Tau, but with no local density enhancement (Testi et al., 1998).

It was observed at Lick on 2005-10-18 UTC in cloudy and humid conditions. No polarized light was detected in the near-IR (Fig. 4.50)

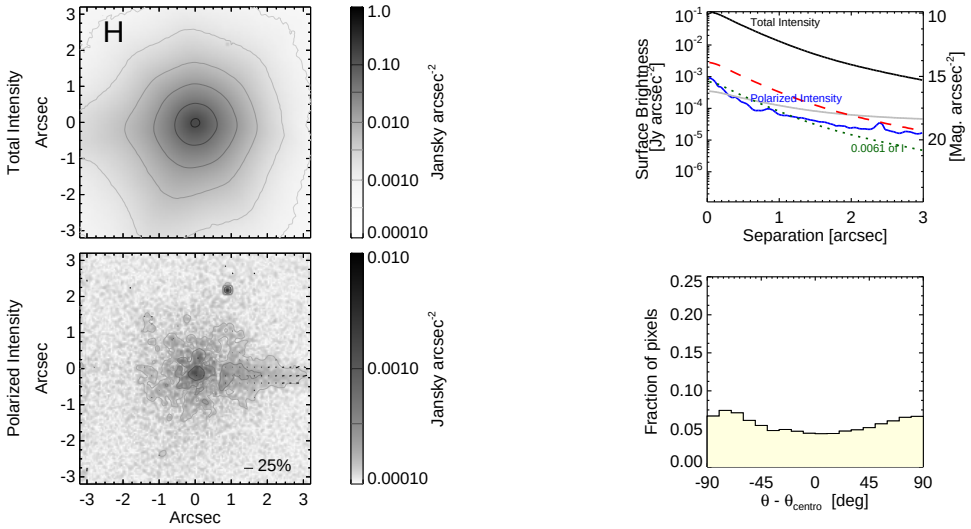

Figure 4.50: Imaging polarimetry of RR Tau.

4.5.35 MWC 120

MWC 120, also called HD 37806, is a B9Vesh star (Oudmaijer et al., 1992) with $V = 7.9$. The distance to this object is not well known, but may be around 280 pc (Dent et al., 2005). Interferometric observations by Eisner et al. (2004) are consistent with a circumstellar disk some ~ 5 mas in angular size.

It was observed at Lick on 2005-10-18 UTC in cloudy and humid conditions. No polarized light was detected in the near-IR (Fig. 4.51). The apparent region of polarization to the west of the star results from mediocre PSF subtraction in the polarimetry reduction and is not a real detection of polarized light.

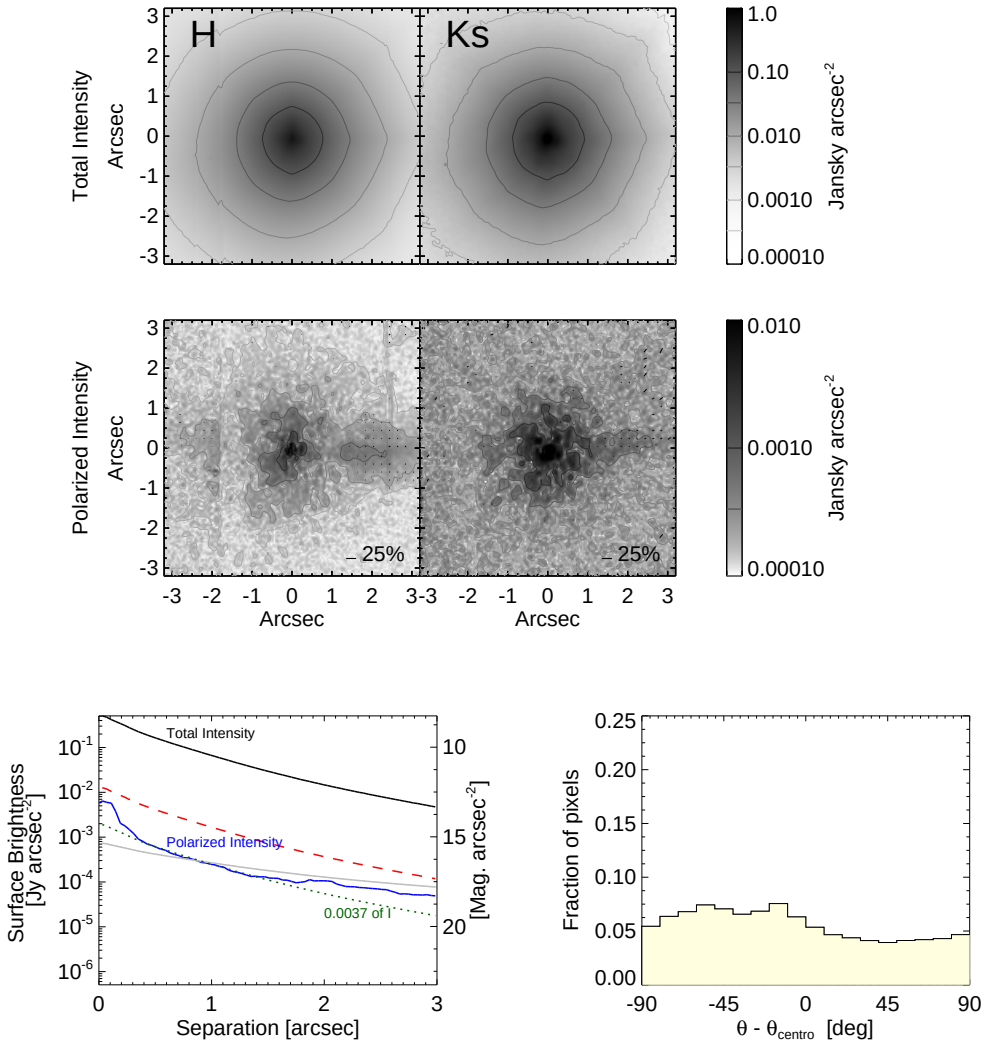

Figure 4.51: Imaging polarimetry of MWC 120.

4.5.36 MWC 778

MWC 778, also called PDS 204 and Kohoutek 2, is a little-studied candidate Herbig Be star. It is located in a HII region, IC 2144, and shows strong Hα , FeII, [FeII] and [SII] in emission, plus a very unusual SED rising almost linearly with wavelength (Allen, 1974). Garcia-Lario et al. (1997) identified it as the optical counterpart to IRAS 05471+2351 and classified it as a YSO on the basis of its NIR colors. It is a B1 star with $V = 14.0$, giving a photometric distance of 2600 pc, though it is possibly associated with the WB 711 star forming region at 1100 pc (Vieira et al., 2003).

It was observed at Lick on 2005-11-23 UTC in good conditions, and at Gemini North on 2005-12-16 UTC. Both observations reveal an impressive pinwheel-shaped nebula around MWC 778 (Figs. 4.52, 4.53). This nebula is even visible in the NIR Stokes I images, though its structure is clearer in the polarized images. Two curved arms spiral out from the star, roughly to the north and south. The arms are asymmetrical, with the northern arm visible out to $8''$, the southern only to $6''$. In all the polarization images, a dark lane cuts across the nebula near the position of the star at a PA of $\sim 25°$, and the 18 μm image, a small depression is visible in the nebula along the same position angle. Together, these images suggest the presence of a circumstellar disk, but oddly, one that appears to be nearly perpendicular to the spiral arms. The 11 μm image shows the continuation of the northern arm as it curves around to the east and south again, but no such extension of the southern arm is visible. At 18 μm, only the inner $\sim 1\farcs5$ of the spiral arms are visible.

The northern arm is split by a gap about $2''$ from the star. Very intruigingly, there is a second point source located just outside this gap, $2\farcs5$ from the star. It is tempting to conjecture that this is a bound companion to MWC 778, which is responsible for stirring up the spiral arms through its orbital motion.

Such "pinwheel-shaped nebulae" have been observed around a handful of Wolf-Rayet stars (Tuthill et al., 1999; Monnier et al., 1999), but the angular scale is off by two orders of magnitude: tenths of an arcsecond versus ten arcseconds here, for stars located at comparable distances of 1-2 kpc. A related possibility is that we see spiral density waves churned up in a circumstellar disk by a companion, as in simulations by Mark Wyatt (Wyatt, in prep.) and others. However, there are a few problems with this scenario: spiral arms outside an orbiting companion are expected to trail behind that companion, whereas here they appear to lead ahead of the putative companion. Furthermore, the scale here is still unexpectedly large: The observed mid-IR nebula is more than $11''$ across, or 12,000

AU using the 1100 pc distance estimate—far larger than any simulated disk that I know of. MWC 778 and its surprising spiral arms are definitely in need of further study.

4.5.37 HD 249879

HD 249879, also called PDS 20, is a little-studied ∼B8 star located at a distance of 1200 pc with $V = 10.6$ (Vieira et al., 2003).

It was observed at Lick on 2005-10-18 UTC in cloudy and humid conditions. No polarized light was detected in the near-IR (Fig. 4.54)

4.5.38 HD 250550

HD 250550 is a B9 star with $V = 9.5$ (Hernández et al., 2004). It shows a strong P Cygni profile in Hα (Finkenzeller and Mundt, 1984). The distance to this star is uncertain; Hillenbrand et al. (1992) gives 700 pc, while (Carpenter et al., 1995) claims 1500. Testi et al. (1998) detect a faint nebulosity some $20 - 40''$ north of HD 250550, outside of IRCAL's field of view.

It was observed at Lick on 2005-10-18 UTC in cloudy and humid conditions. A peak in the centrosymmetry histogram indicates the detection of circumstellar dust. This dust appears as several fans or filaments of polarized light, extending approximately $3\farcs5$ to the north, northeast, and southeast of the star. Low signal to noise makes it difficult to state anything with certainty about the nature of these filaments, but there are hints of symmetry across an axis drawn from southwest to northeast. Perhaps the we see here the limb-brightened walls of a cavity carved out by stellar outflows; further observations are needed.

4.5.39 LkHα 208

LkHα 208 is a UX Orionis star located at a distance of 1000 pc, with $V = 11.6$ (Natta et al., 1997; Testi et al., 1998). Estimates for its spectral type range from F0 (Natta et al., 1997) to A7 (Hernández et al., 2004). Leinert et al. (1997) found a companion to LkHα 208 at a separation of $0\farcs115$, PA 113°. That is slightly less than the diffraction limit of Lick at H band, and we do not detect this companion. A later study by Leinert et al. (2001) found no evidence for any resolved circumstellar dust.

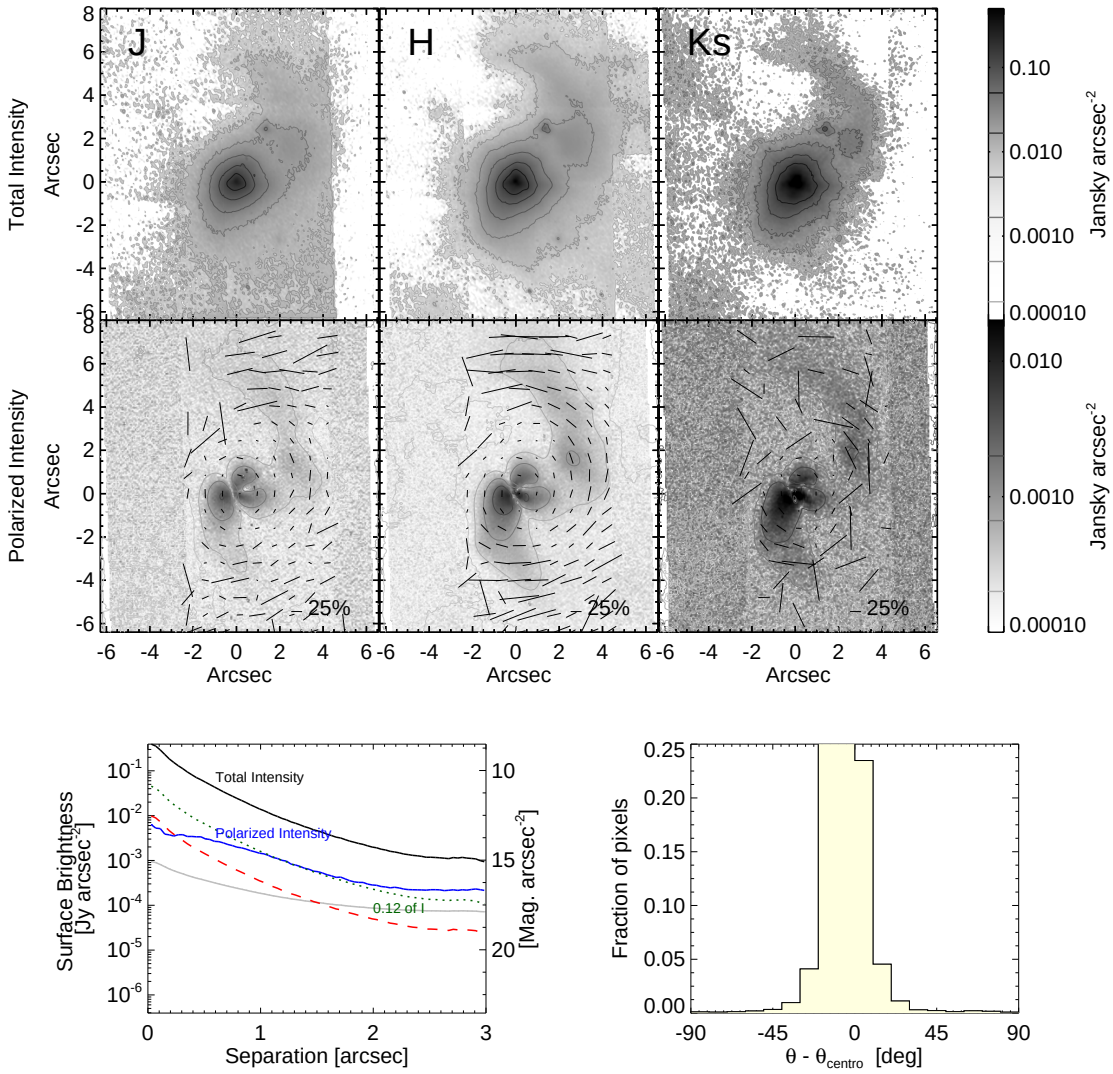

Figure 4.52: Imaging polarimetry of MWC 778.

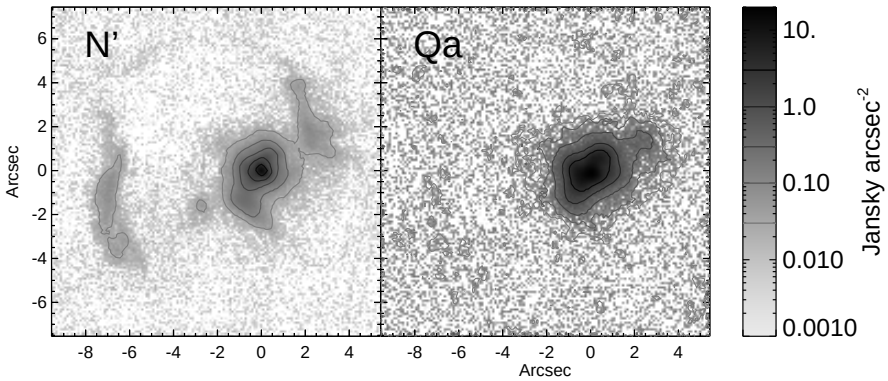

Figure 4.53: Mid-IR imaging of MWC 778.

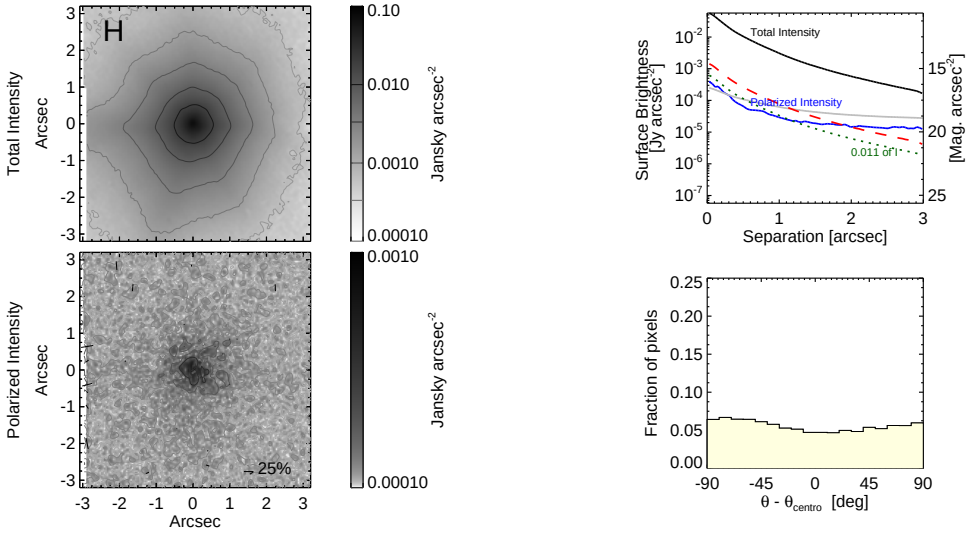

Figure 4.54: Imaging polarimetry of HD 249879.

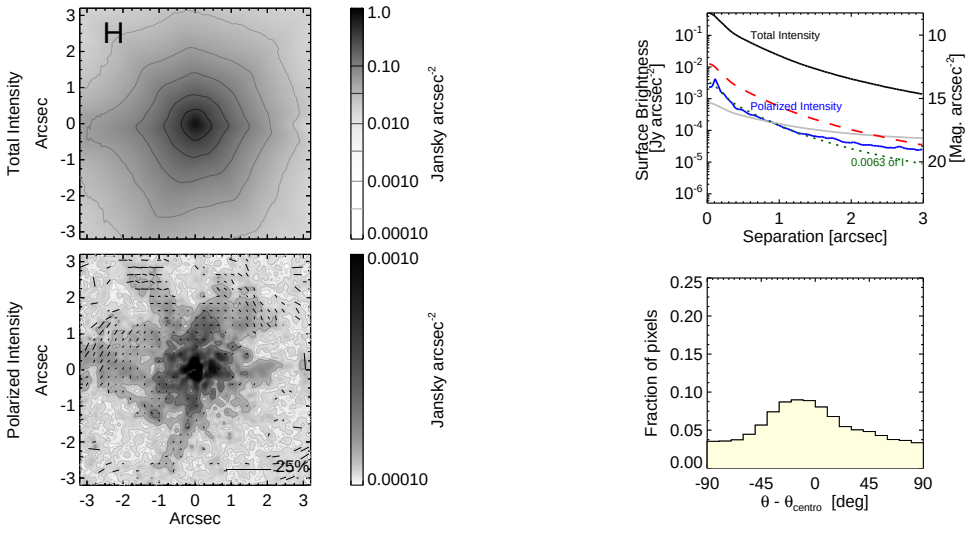

Figure 4.55: Imaging polarimetry of HD 250550.

It was observed at Lick on 2004-12-01 UTC in windy conditions, and on 2005-11-21 in good conditions. No polarized light was detected in the near-IR (Fig. 4.56)

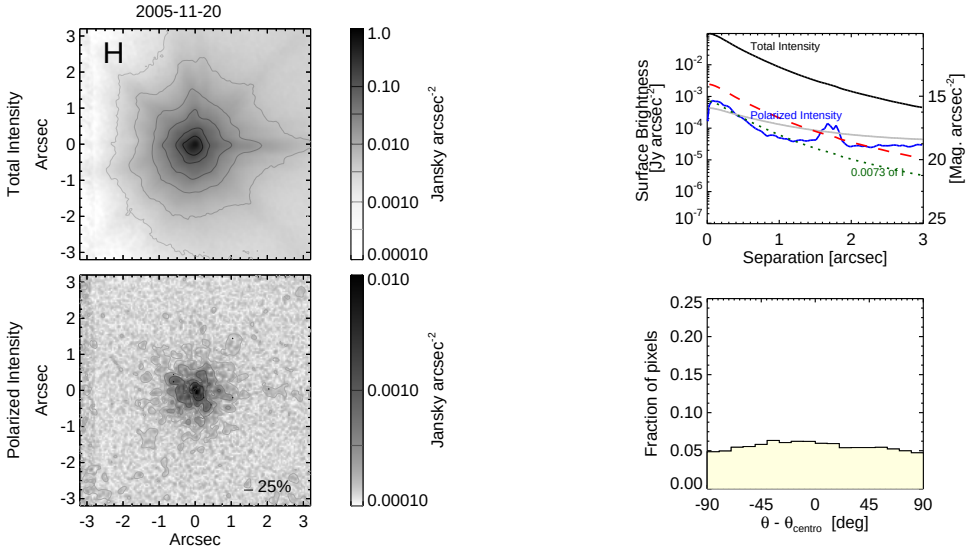

Figure 4.56: Imaging polarimetry of LkHα 208.

4.5.40 MWC 137

MWC 137 is a continuum star (Hernández et al., 2004) located at a distance of 1300 pc (Hillenbrand et al., 1992), with $V = 12.0$. Like many HAEBEs, MWC 137's physical parameters are in dispute; see Hillenbrand et al. (1992) and Berrilli et al. (1992). It was once believed to be a planetary nebula (Perek & Kohoutek, 1967) but this interpretation has been discarded based on IRAS colors and radio observations showing it to be located in an HII region (Zijlstra et al., 1990). On the other hand, van den Ancker et al. (1998) include it on their list of "stars lacking evidence for circumstellar dust". Finkenzeller and Mundt (1984) report that has one of the strongest and broadest Hα emission profiles of all stars, plus copious other emission lines.

Di Francesco et al. (1997) found MWC 137 to be very spatially extended at 50 and 100 μm, with a FWHM of $58 - 66''$, which they interpreted to be due to an extended circumstellar envelope. Mannings et al. (1994) similarly found it to be extended in the submillimeter. Testi et al. (1998) observed a "double shell like reflection nebulosity" around MWC 137, (see their Figure 6). With a radius of $\sim 40''$, this nebula has roughly the right spatial extent to be the same dust responsible for the FIR and submillimeter nebulosity.

It was observed at Lick on 2004-10-11 UTC in very poor conditions. No polarized light

was detected in the near-IR (Fig. 4.57) The shell like nebula seen by Testi et al. (1998) falls outside IRCAL's field of view. On the smaller spatial scales probed here, MWC 137 displays no evidence for scattered light from resolved circumstellar dust. At least 16 other point sources are detected within 10″ of MWC 137, confirming the cluster of young stars reported there by Testi et al.

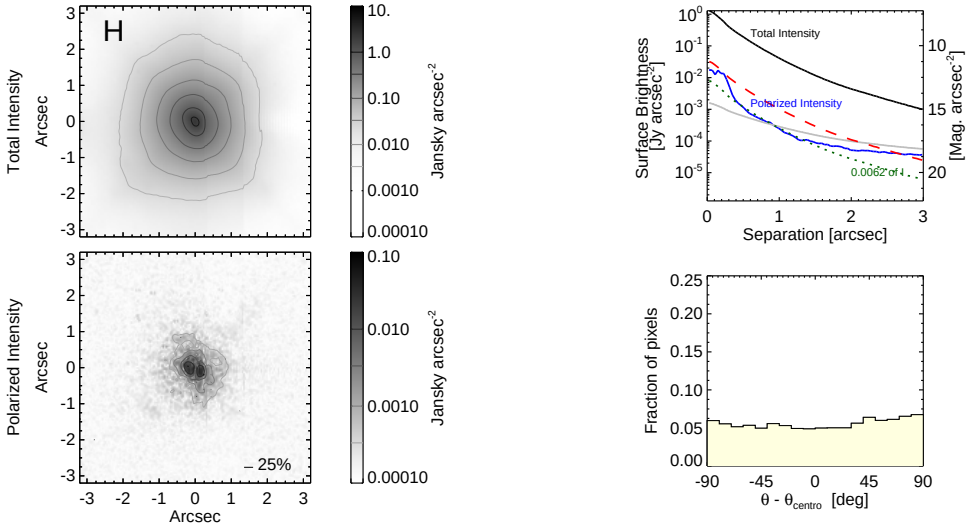

Figure 4.57: Imaging polarimetry of MWC 137.

4.5.41 NSV 2968

NSV 2968, also called PDS 23, is a B0 star with $V = 12.0$ (Kukarkin et al., 1981; Vieira et al., 2003). Gregorio-Hetem et al. (1992) and Carballo & Sahu (1994) independently identified this star as the optical counterpart to IRAS 06245-1013. It is on the edge of the L1652 dark cloud at a distance of 830 pc and has $L_* \sim 82 L_\odot$ (Carballo & Sahu, 1994).

It was observed at Lick on 2005-11-21 UTC in good conditions. No polarized light was detected in the near-IR (Fig. 4.58)

4.5.42 VY Mon

VY Mon is an Algol-like variable star in the Monoceros OB1 association $\sim$ 900 pc distant. Its spectral type is uncertain: the literature includes estimates of O9 Cohen & Kuhi (1979), B8 The et al. (1994), A5 Mora et al. (2001), and F2 Hernández et al. (2004). It has been previously reported to be slightly extended to the south in K-band imaging, and

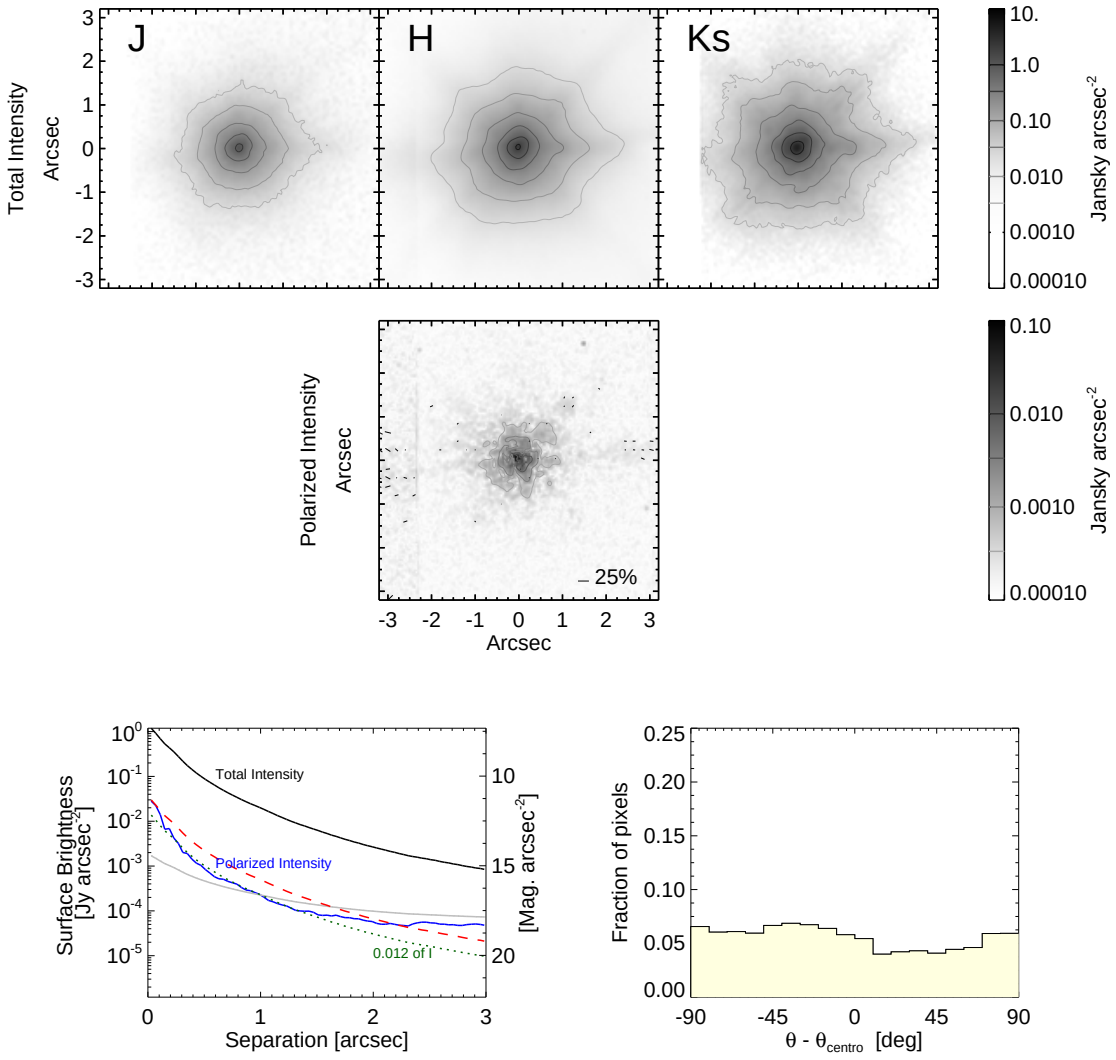

Figure 4.58: Imaging polarimetry of NSV 2968.

is coincident with the core of a $\sim 2'$ extended millimeter source Henning et al. (1998). VY Mon is the brightest mid-IR to submillimeter source in this region, appearing as a bright point source from 12-370 μm Casey & Harper (1990). Its flat SED makes it a Hillenbrand Group II object, like LkHα 198 and LkHα 233. Maffei (1967) wrote that a "remarkable difference in blue-IR behavior was detected for VY Mon. While the IR observations of this T Tau type variable show slow variations, in blue light the star remains for the most part constant and at minimum light." This is entirely consistent with a scenario in which VY Mon is seen largely in reflected light in the optical, as is its high optical extinction ($A_V \sim 7.4$, Henning et al. 1998).

It was observed at Lick on 2003-11-18 UTC in poor conditions, and on 2005-11-22 in good conditions, and at Gemini North on 2005-12-16 UTC. The star was not resolved in the mid-IR (Fig. 4.60). Polarized light scattered from circumstellar dust is clearly detected, in the form of an elliptical nebula around VY Mon. Interestingly, while the elliptical form is suggestive of an inclined circumstellar disk, the ellipse is far off center from VY Mon. It extends approximately $3''$ east from the star, but only $\sim 1\farcs75$ west; likewise it extends more to the south than to the north (consistent with the results of Henning et al.). A peak polarization of 13% is observed $2''$ east of the star, though we caution this is likely an underestimate of the intrinsic polarization due to contamination by uncorrected starlight. We re-observed VY Mon in 2005 in an attempt to obtain multicolor data, but poor seeing and clouds foiled this attempt. These data (not shown) are only minimally useful, and about all that can be said is that at J band, the polarized emission is brighter to the east of the star, just as in H. VY Mon is unresolved in our MIR observations. Our field of view does not include either of the companions imaged at 10 μm Habart et al. (2003), but we do detect a $\Delta H = 6.2 \pm 1$ companion at $\rho = 9''$, PA $= 332^\circ$ in our near-IR data.

Henning et al. (1998) presented a radiative transfer model for VY Mon based on the SED and submillimeter imaging; it would be worthwhile to revisit this model and see if it can accommodate these additional data.

4.5.43 LkHα 215

LkHα 215 is a $V = 10.5$, B6 star (Hernández et al., 2004) located at a distance of 800 pc (Hillenbrand et al., 1992). Mannings (1994) concluded based on SED modeling that LkHα 215 must possess an extended dust envelope in addition to a circumstellar disk. Consistent with this, Di Francesco et al. (1997) reported that LkHα 215 is spatially

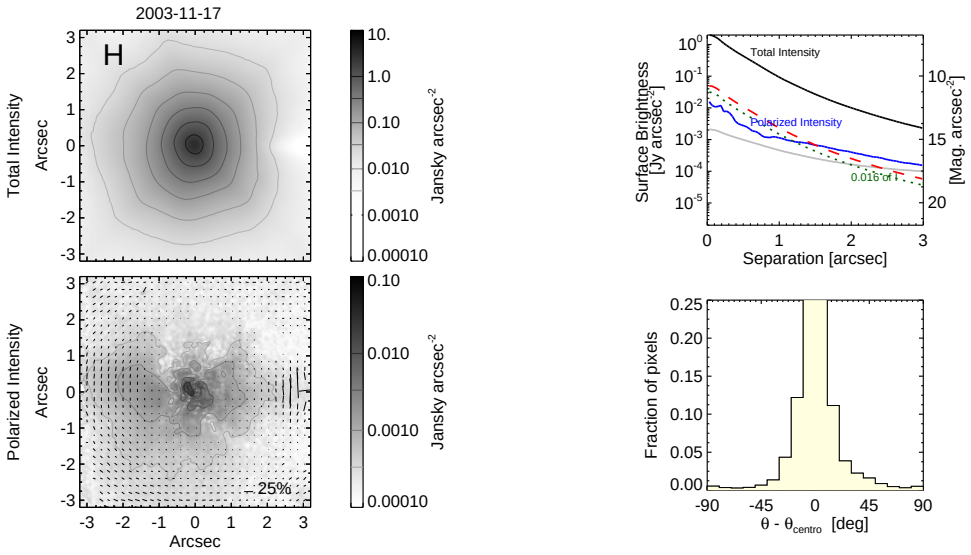

Figure 4.59: Imaging polarimetry of VY Mon.

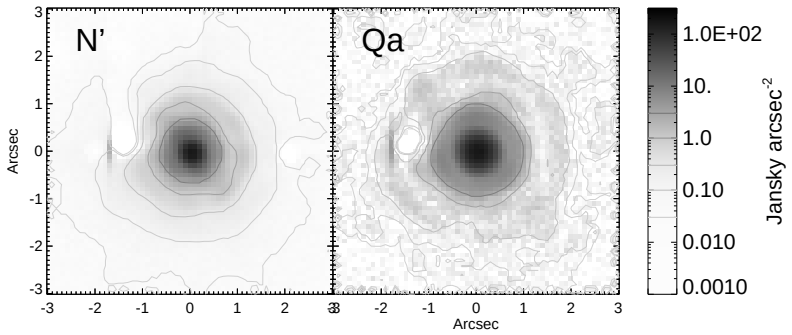

Figure 4.60: Mid-IR imaging of VY Mon.

extended at 100 μm, with a FWHM of 66″. Testi et al. (1998) found both a small cluster of stars around LkHα 215 and an arc-shaped nebulosity extending some 60″, roughly east-west. Ground-based mid-IR photometry of LkHα 215 by Herbst et al. (1982) gives fluxes an order of magnitude lower than the IRAS values, most likely because Herbst's smaller photometry aperture did not include most of the extended dust envelope. Fuente et al. (1998a) found two millimeter flux peaks offset to either side of LkHα 215.

It was observed at Lick on 2004-12-01 UTC in windy conditions. No polarized light was detected in the near-IR (Fig. 4.61) The near-IR nebulosity detected by Testi et al. falls outside our field of view. On the smaller spatial scales probed here, we find no evidence for scattered light from circumstellar dust.

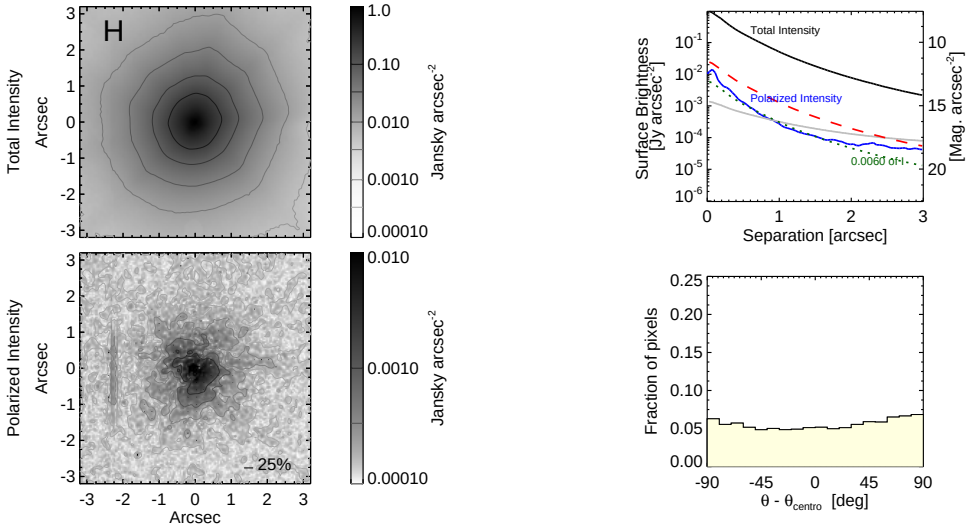

Figure 4.61: Imaging polarimetry of LkHα 215.

4.5.44 HD 259431

HD 259431, also called MWC 147, is a $V = 8.7$ B6 star (Hernandez et al., 2004). While it has traditionally been associated with NGC 2247 and Mon R1 at a distance of 800 pc (Testi et al., 1998), a HIPPARCOS distance determination puts it at closer to ~ 300 pc(Bertout et al., 1999). While Vieira & Cunha (1994) classify it as a spectroscopic binary, Corporon & Lagrange (1999) could not reproduce this result. However, it does have a $\Delta K = 5.7$ companion at $\rho = 3\farcs12, \theta = 346°$ (Millan-Gabet et al., 2001; Bouvier & Corporon, 2001). Testi et al. (1998) detected a faint infrared nebulosity around HD 259431, and Akeson et al. (2000) found the near-IR emission to originate from a radius of about 1 AU based on interferometry.

It was observed at Lick on 2002-11-21 UTC in cloudy conditions but with decent seeing. (Fig. 4.62) We easily detect the companion of HD 259431, but we also detect a diffuse and faint reflection nebula surrounding the star. There is a strong peak in the centrosymmetry plot, definitely indicating the presence of scattered light from circumstellar dust, but it is very difficult to see by eye in the data, even in heavily smoothed polarized intensity images. This was one of our deepest integrations, 2000 s, but still the detection here is fairly marginal.

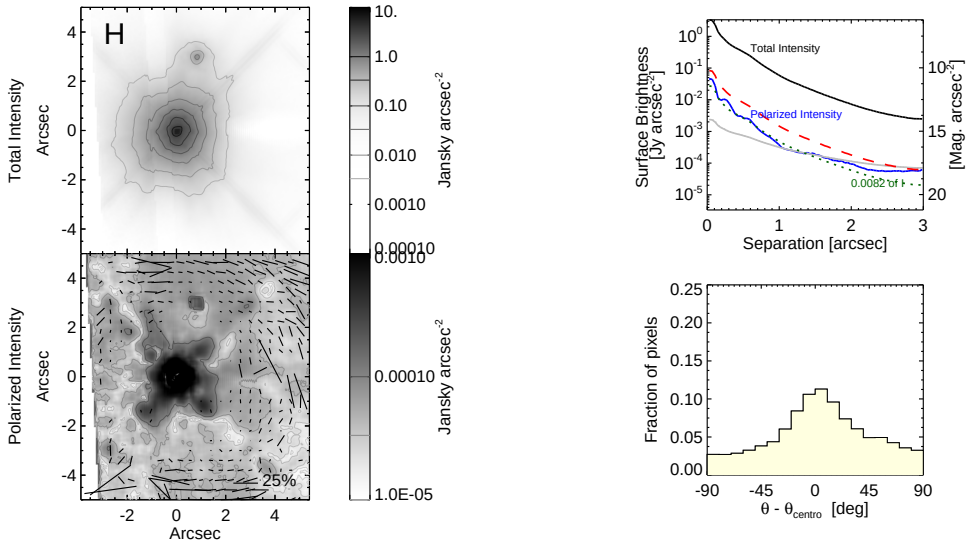

Figure 4.62: Imaging polarimetry of HD 259431.

4.5.45 R Mon

R Mon is a continuum star (Hernández et al., 2004) located at a distance of 800 pc (Hillenbrand et al., 1992), with $V = 12.1$. It has an embedded companion at $0\farcs7$, PA=331°(Bouvier & Corporon, 2001; Close et al., 1997). A detailed multiwavelength study of this object using NIR AO polarimetry plus HST optical imaging was presented by Close et al. (1997).

It was observed at Lick on 2005-10-18 UTC in cloudy and humid conditions, and at Gemini North on 2005-12-16 UTC. The IRCAL observations suffer from very poor AO performance due to bad seeing. While circumstellar dust is clearly detected at all wavelengths, in a prominent nebula extending to the northeast, our near-IR observations do not provide any insights beyond those of Close et al.

On the other hand, we present here the first high resolution images of R Mon in the mid-IR, which shows the circumstellar envelope extending towards the northwest. There is a bright bar visible in the nebula at 18 μm, about $2''$ northwest from the star. The companion reported by Close et al. is not detected. Its separation of $0\farcs7$ is twice the diffraction limit, even at 18 μm, so that is not a problem. Its location in the midst of the circumstellar nebulosity may hide it, or it may simply not have enough warm dust for detection at these wavelengths.

4.5.46 LkHα 25

LkHα 25, also called V590 Mon, is a B7 star (Hernández et al., 2004) located in the Mon OB I region at a distance of 800 pc (Finkenzeller and Mundt 1984), with $V = 12.8$ (Herbst & Shevchenko, 1999). It is part of NGC 2264, the so-called "Christmas Tree Cluster". Testi et al. (1998) found a enhancement in stellar density centered around LkHα 25. Henning et al. (1998) were unable to detect it at 1.3 mm; they note that it has only moderate flux in the first three IRAS bands ($\sim$ 5 Jy) before shooting up to $>$ 200 Jy past 60 μm, indicating widespread diffuse emission. LkHα 25 was unresolved by the NIR speckle observations of Lienert et al. (2001).

It was observed at Lick on 2003-11-18 UTC in poor conditions. Our field of view also includes a star $10''$ north approximately half as bright; it is not known whether these two stars form a bound system or not. While LkHα 25 itself does not show any evidence of polarization, this northern star does; it is $\sim$ 3% linearly polarized at a position angle of

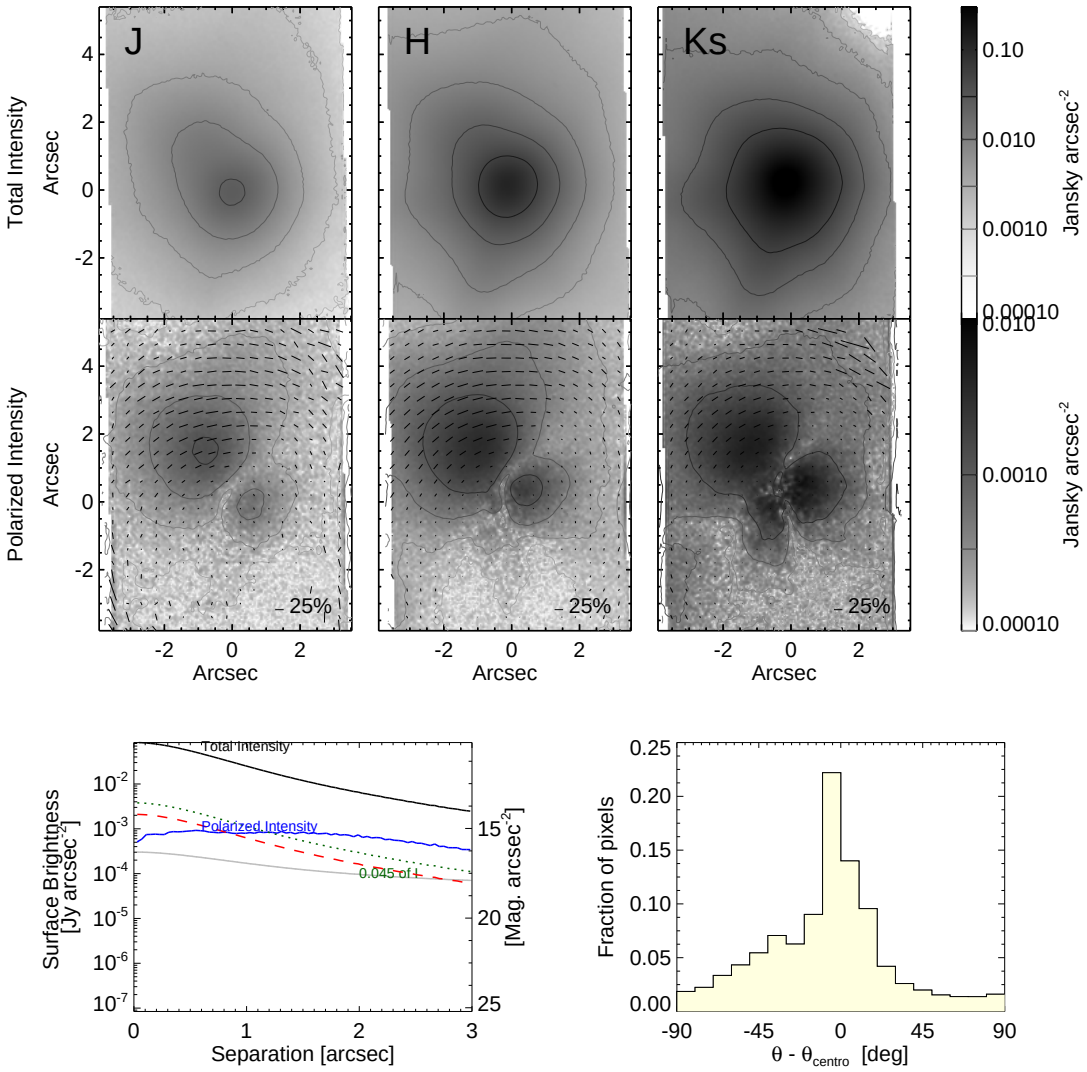

Figure 4.63: Imaging polarimetry of R Mon.

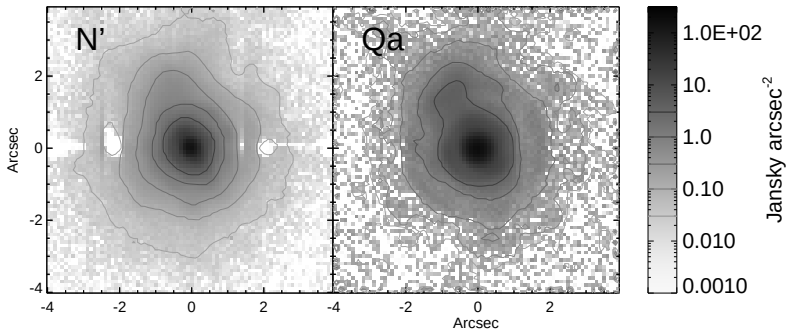

Figure 4.64: Mid-IR imaging of R Mon.

about 330°(Fig. 4.65).

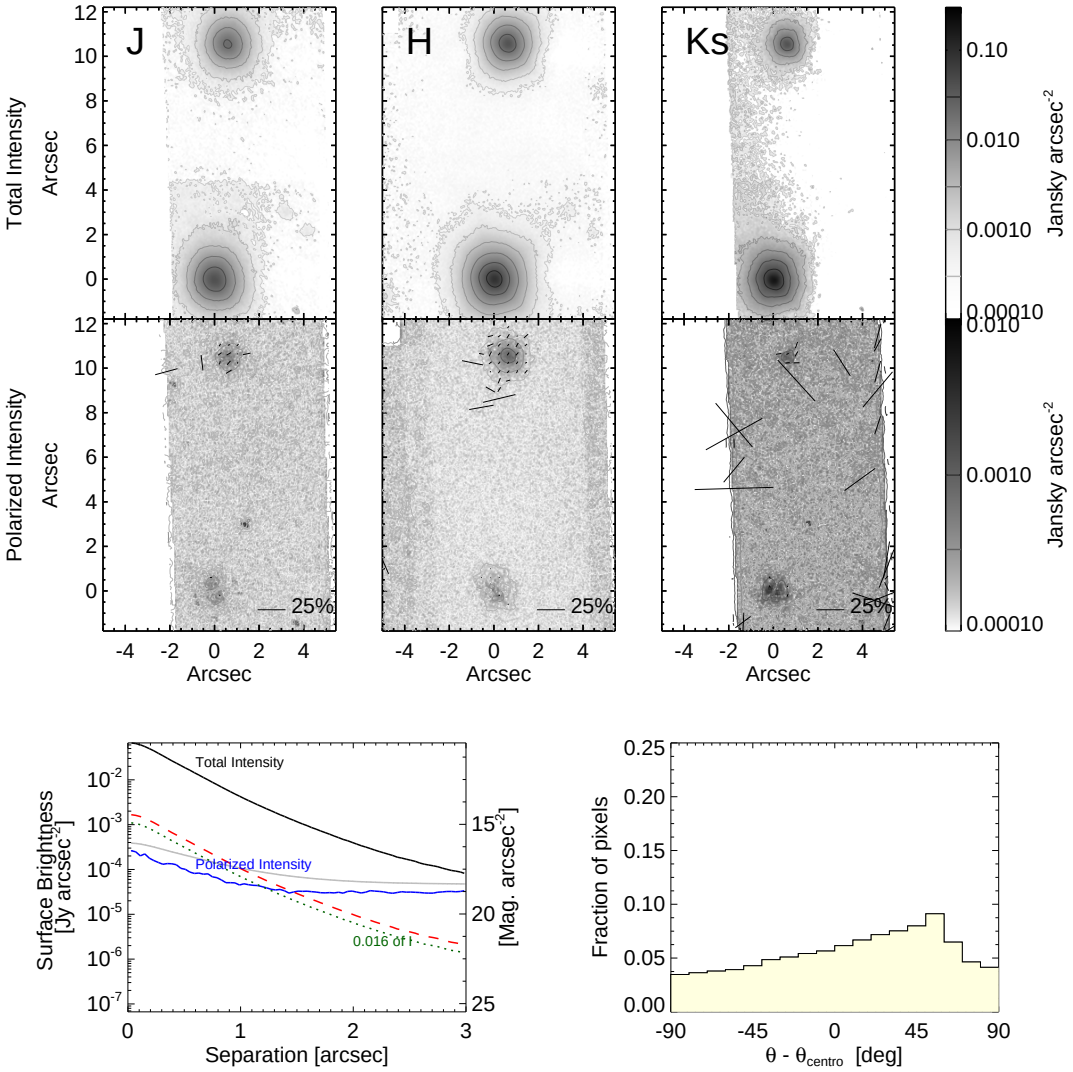

Figure 4.65: Imaging polarimetry of LkHα 25.

4.5.47 HD 52721

HD 52721, also called GU CMa and MWC 164, is a B2 star located at a distance of 910-1150 pc (Vieira et al., 2003, Herbst et al., 1982, van den Ancker et al. 1997), with $V = 6.4$ (Shevchenko et al., 1993). It was identified as a 0.″6 binary more than a century ago (Hussey, 1900). While it is located in an obscured and nebulous region, it has only a weak IR excess; its IR colors may indicate that it is a classical Be star rather than a Herbig Be star (Finkenzeller & Mundt, 1984). Consistent with this, Fuente et al. (1998a) detected

no CO emission from molecular gas in its vicinity, and van den Ancker et al. (1998) include it on their list of stars lacking evidence for dust. On the other hand, Testi et al. (1998) find an increase in stellar density around HD 52721, supporting the idea that it is a young star, and Corporon & Lagrange (1999) see strongly variable absorption features potentially indicating transiting circumstellar dust.

It was observed at Lick on 2003-11-18 UTC in poor conditions. While our AO observations easily resolve the binary, no polarized light was detected (Fig. 4.66).

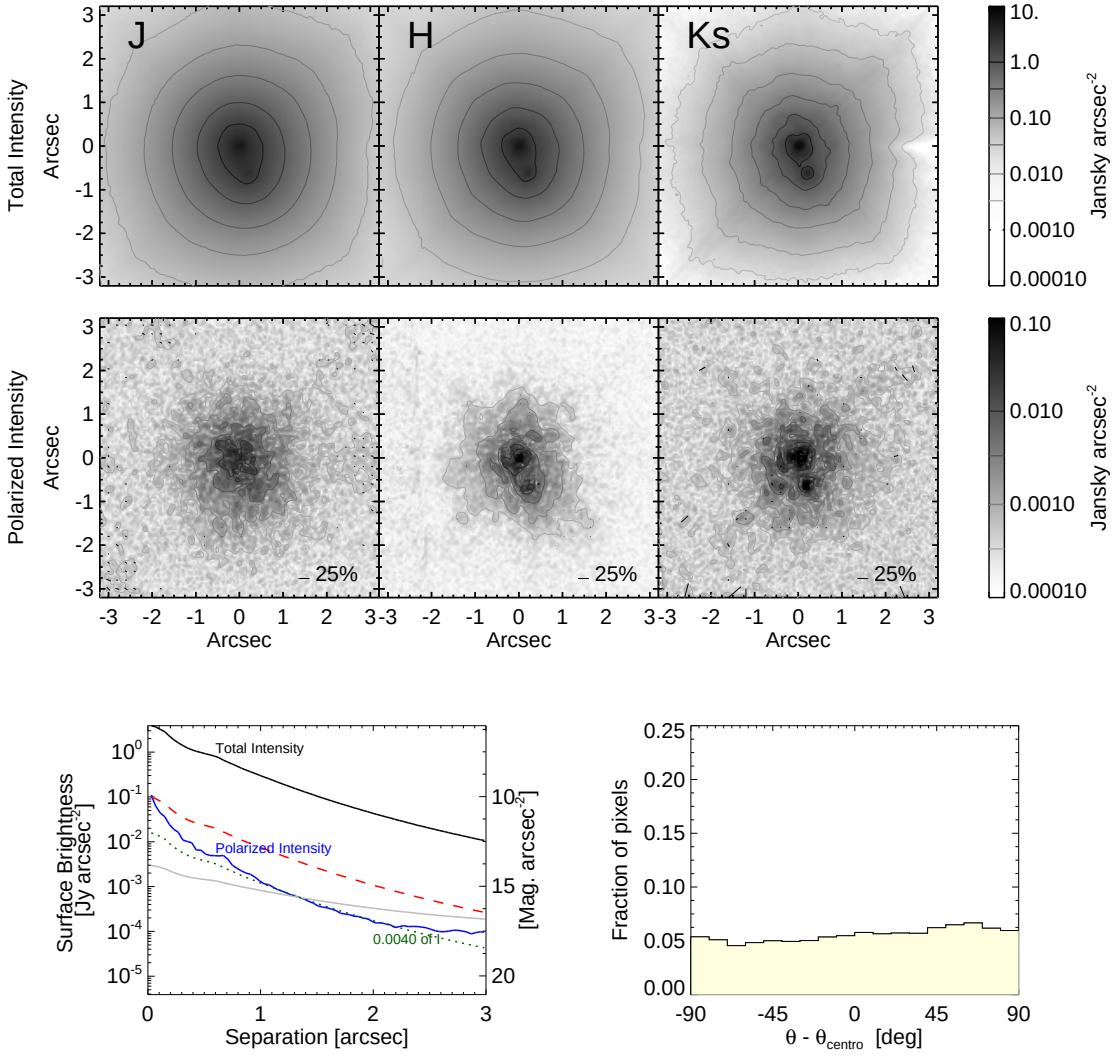

Figure 4.66: Imaging polarimetry of HD 52721.

4.5.48 Z CMa

Z CMa is a well-studied binary located at a distance of 1050 pc with $V = 9.5$ (Hillenbrand et al., 1992; Shevchenko et al., 1999). It is a $0\farcs1$ binary (Koresko et al., 1991; Haas et al., 1993) of differing spectral types, with the A component being a Herbig Be star and the B component being a FU Ori. Both components have been separately studied with the Keck Interferometer (Monnier et al., 2005; Millan-Gabet et al., 2005). Extended nebulosity was detected around Z CMa in the millimeter by Henning et al. (1998) and near-IR by Testi et al. (1998), particularly evident to the west of the star.

It was observed at Lick on 2005-11-21 UTC in good conditions. Polarized scattered light is detected around Z CMa, particularly in a ellipse or fan of nebulosity extending $\sim 4''$ southwest from the star (Fig. 4.67). This fan of scattered light is detected at low signal to noise (average SNR ~ 0.6 per spatial pixel), but does appear to be real rather than an instrumental artifact. The binary's separation of $0\farcs1$ is below the diffraction limit of the Lick 3 m, but we do marginally resolve the binary as a small elongation of the PSF.

4.5.49 PDS 241

PDS 241 is the optical counterpart to IRAS 05560+1639, a B0 star with $V = 12.1$ (Vieira et al., 2003). It has a photometric distance of 3900 pc but may alternatively be associated with the Sh 2-288 star forming region at about twice that distance. It illuminates a bright optical nebula about $2'$ across. It was observed at Lick on 2005-11-21 UTC in good conditions, and at Gemini North on 2005-12-16 UTC.

No polarized light was detected in the near-IR , but we discovered a dense cluster of stars surrounding PDS 241 (Fig. 4.68). There are no fewer than 37 additional sources within our $\sim 10 \times 14''$ FOV, most of which are very red.

Our mid-IR imaging reveals an extended butterfly-shaped nebula at 11 μm, about $5''$ across and running from northwest to southeast (Fig. 4.69). The brightest other member of the cluster is also detected as a point source, and a second small clump of diffuse emission is visible $5.8''$ northeast. The situation is less clear at 18 μm, where we are severely limited by signal to noise due to a much shorter exposure time than usual, but the diffuse emission is definitely still present.

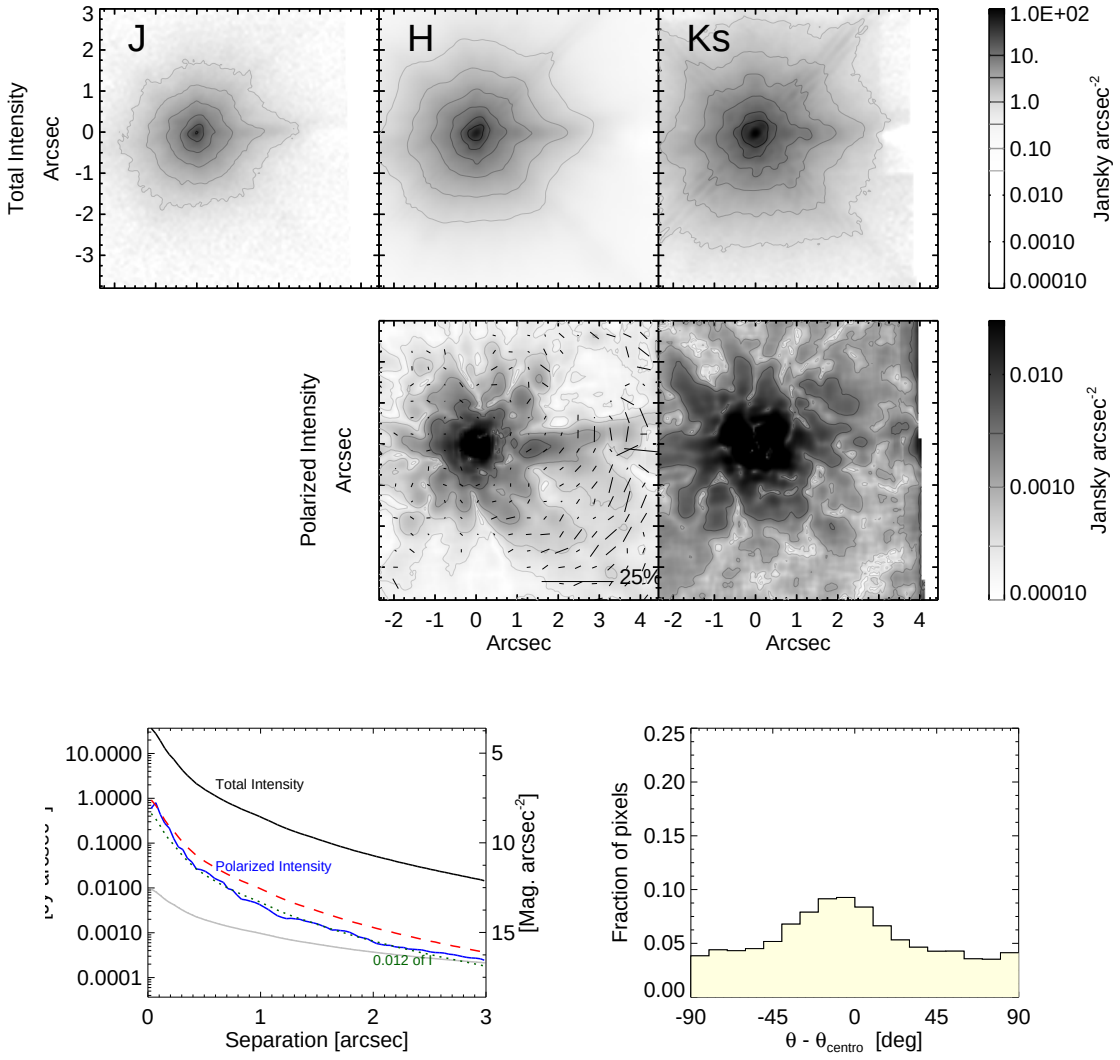

Figure 4.67: Imaging polarimetry of Z CMa.

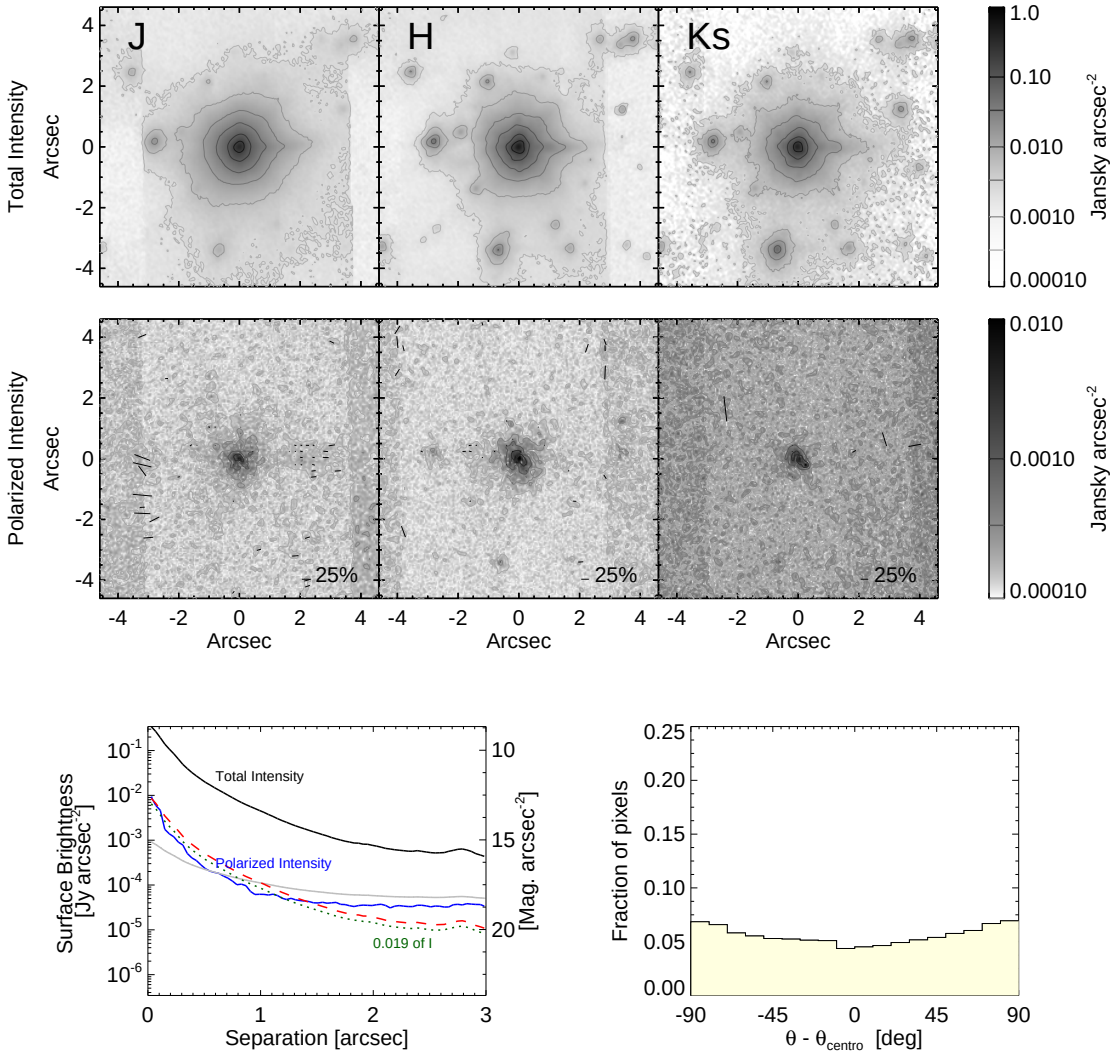

Figure 4.68: Imaging polarimetry of PDS 241.

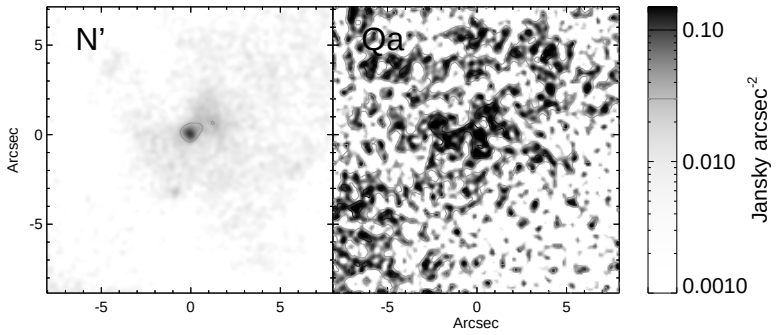

Figure 4.69: Mid-IR imaging of PDS 241.

4.5.50 DW CMa

DW CMa, also called PDS 27, is a relatively little-studied $\sim$ B2 star located at a distance of 1100 pc, with $V = 12.8$ (Vieira et al., 2003).

It was observed at Lick on 2005-11-21 UTC in good conditions, and at Gemini North on 2005-12-16 UTC. No polarized light was detected in the near-IR (Fig. 4.70), nor was the star resolved in the mid-IR (Fig. 4.71). There is an peak in the centrosymmetry histogram, but it is offset to $\sim -30°$ and appears to be due to imperfect PSF subtraction, rather than any actual polarized light.

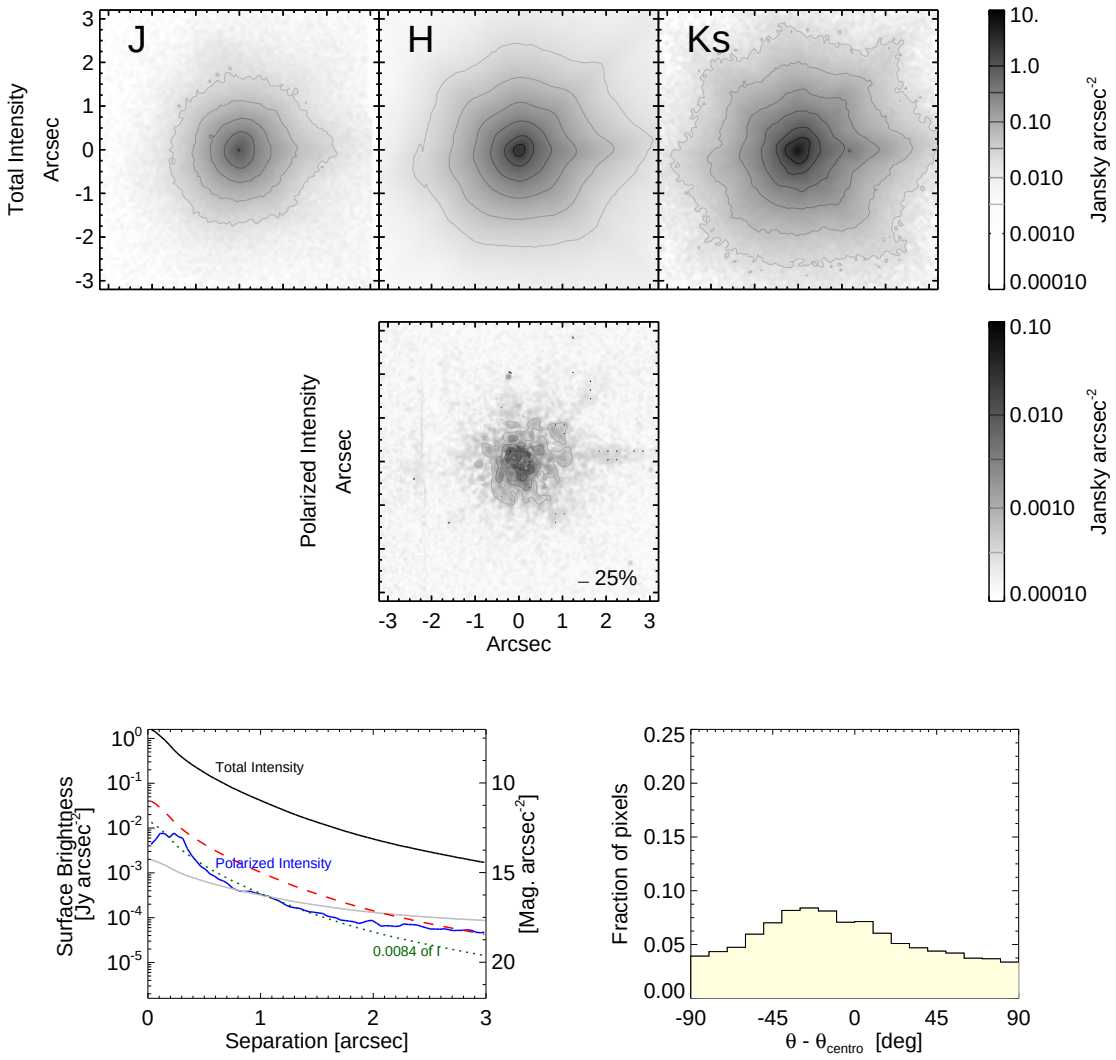

Figure 4.70: Imaging polarimetry of DW CMa.

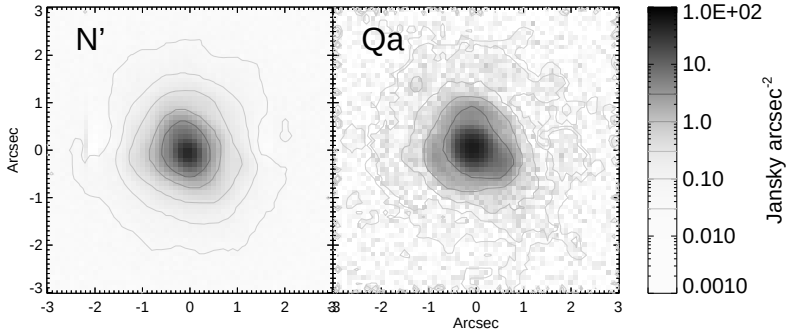

Figure 4.71: Mid-IR imaging of DW CMa.

4.5.51 PDS 144

PDS 144 is a 5″ binary system consisting of an A2 star (northern) and A5 star (southern). Our Lick AO observations on 2004-07-06 UTC revealed an edge-on circumstellar disk around PDS 144N - the first known example of a resolved, optically-thick, edge-on disk around a Herbig Ae star.

A broad range of followup observations have probed the nature of this very interesting system; see Perrin et al. (2006) or Chapter 6 for a detailed discussion of this object.

4.5.52 HD 141569

HD 141569 is one of the nearest and best-studied of Herbig Ae stars, with a spectacular disk that has been extensively imaged with the Hubble Space Telescope; see Weinberger et al. (1999); Grady et al. (2005); Clampin et al. (2003). It has two nearby companions, both of spectral type M (Pirzkal et al., 1997; Rodgers et al., 2005).

It was observed at Lick on 2003-06-17 UTC in good conditions, and on 2003-07-21 in good conditions, but we are unable to clearly detect its circumstellar disk. There is a shallow peak in the centrosymmetry plot, but nothing in the image which is clearly polarized or disk-like (Fig. 4.74). The superiority of multi-billion-dollar space telescopes over something one grad student threw together on the cheap is apparent[5].

We observed HD 141569 at Gemini North on 2006-07-05 through patchy clouds. Previous studies have found HD 141569 to be resolved in the mid-IR (Fisher et al., 2000; Marsh et al., 2002), but those studies had too small a field of view to include the two nearby M stars. We detect both of these stars for the first time in the mid-IR.

[5]I will happily buy a drink for the first member of my committee who mentions this to me.

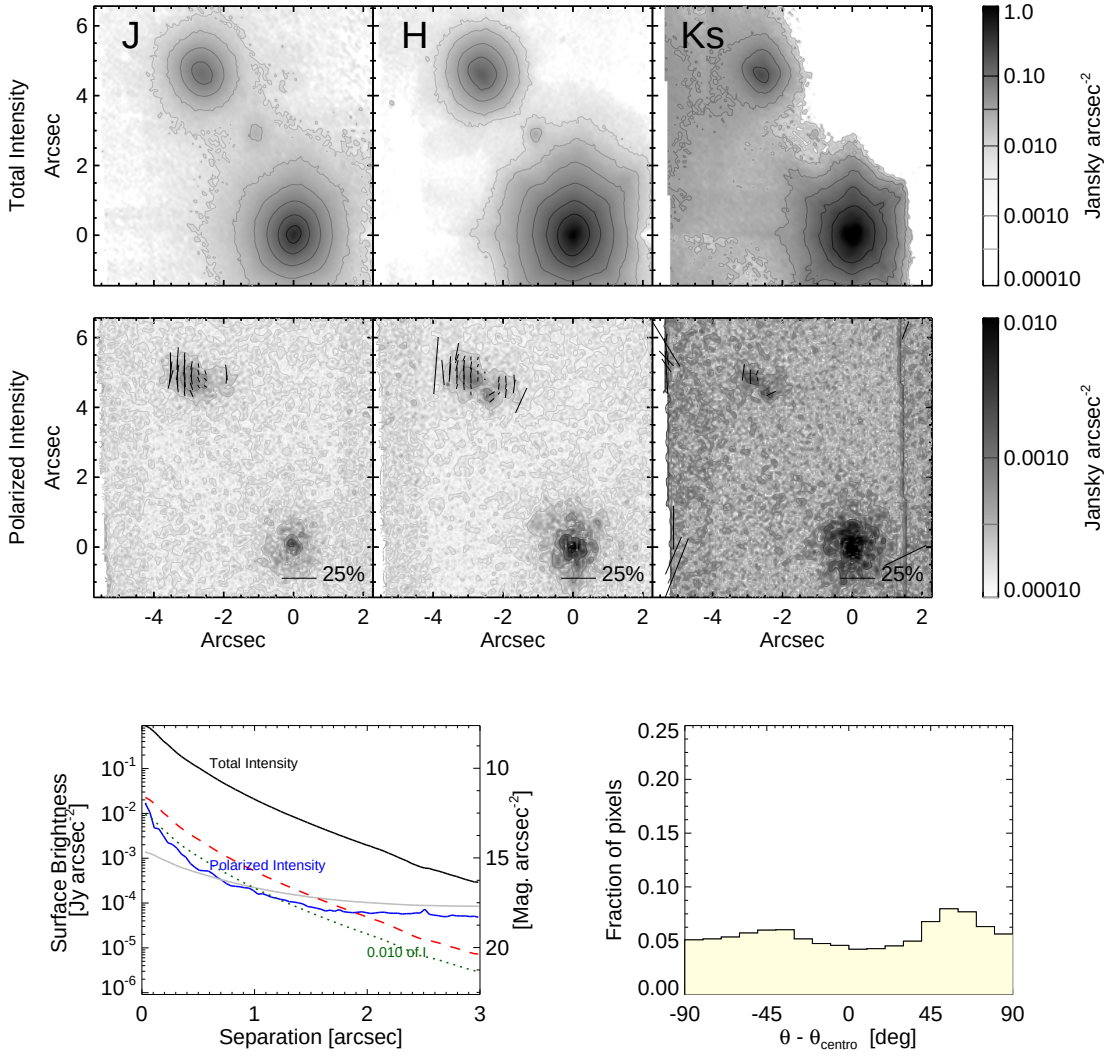

Figure 4.72: Imaging polarimetry of PDS 144.

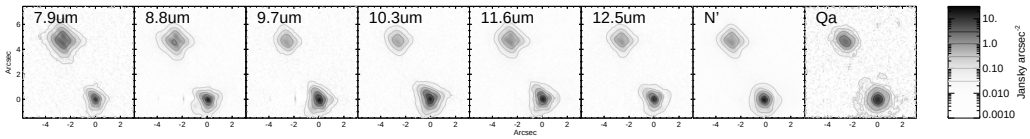

Figure 4.73: Mid-IR imaging of PDS 144.

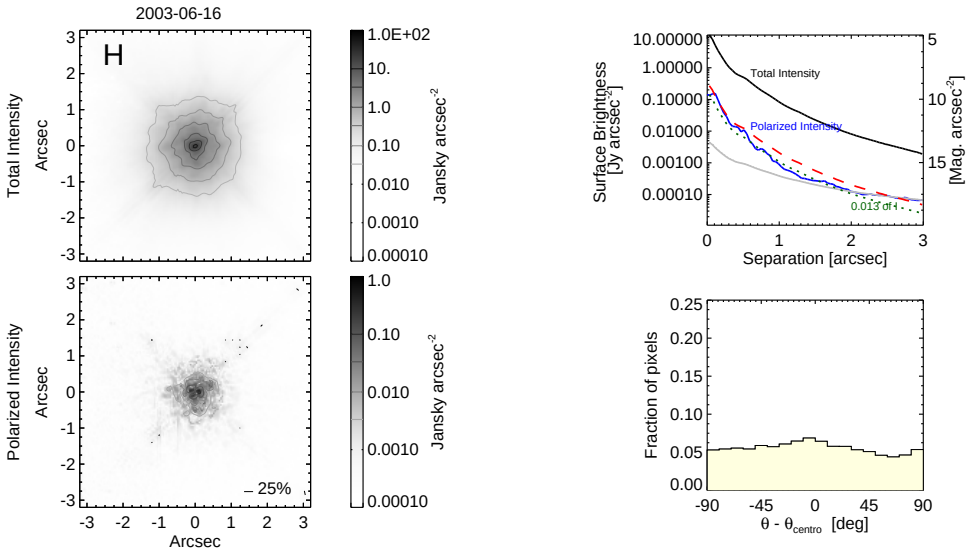

Figure 4.74: Imaging polarimetry of HD 141569.

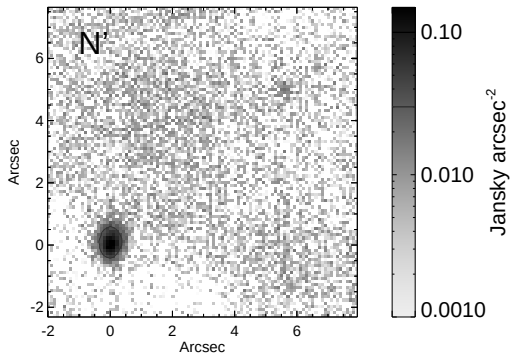

Figure 4.75: Mid-IR imaging of HD 141569. Its two companions are visible at the upper right.

4.5.53 HD 142666

HD 142666 is a $V = 8.8$ A8 star located at a HIPPARCOS distance of ~ 170 pc (Vieira et al., 2003). The SED and absorption features in the spectra indicate there is circumstellar material along the line of sight, possibly in the form of an inclined disk (Meeus et al., 1998).

It was observed at Lick on 2003-07-23 UTC in good conditions, and on 2004-07-05 in excellent conditions, and at Gemini North on 2005-06-30 UTC. No polarized light was detected in the near-IR (Fig. 4.76) The star was not resolved in the mid-IR (Fig. 4.77).

4.5.54 HD 144432

HD 144432 is a nearby A8 star located at a distance of 145 pc in the Sco OB2-2 star forming region. (Pérez et al., 2004) It was originally identified by Oudmaijer et al. (1992) who noted that it could be either a Herbig Ae star or a post-AGB star, but subsequent studies have confirmed its youth through the presence of Li absorption (Pérez et al., 2004). It has a $\Delta K = 2.5$ companion located $1\farcs4$ almost due north (Rossiter, 1955; Bouvier & Corporon, 2001), which has been identified as a K type star lacking emission lines (Pérez et al., 2004). Meeus et al. (1998) found that the combination of the SED and spectroscopic properties of HD 144432 could be fit with a flattened disk model.

It was observed at Lick on 2003-07-22 UTC in good conditions, and again on 2004-07-04 in excellent conditions, and at Gemini North on 2005-07-01. No polarized light was detected in the near-IR, though the companion is easily detected. (Fig. 4.78). In the mid-IR, we see no evidence for resolved circumstellar dust, nor can we detect the companion (Fig. 4.79).

4.5.55 HD 145718

HD 145718, also called PDS 80 and V718 Sco, is an A8 IV star with $V = 9.0$ (Vieira et al., 2003) located at a distance of 130 pc (HIPPARCOS). Despite its proximity, it has been relatively little studied. However, it is known to be an eclipsing binary (Sahade & Berón Dàvila, 1963; Friedemann et al., 1996). Dent et al. (2005) report the marginal detection of CO emission from a circumstellar disk.

It was observed at Lick on 2005-07-27 UTC in good conditions, and at Gemini North on 2005-06-30 UTC. No polarized light was detected in the near-IR (Fig. 4.80), nor was

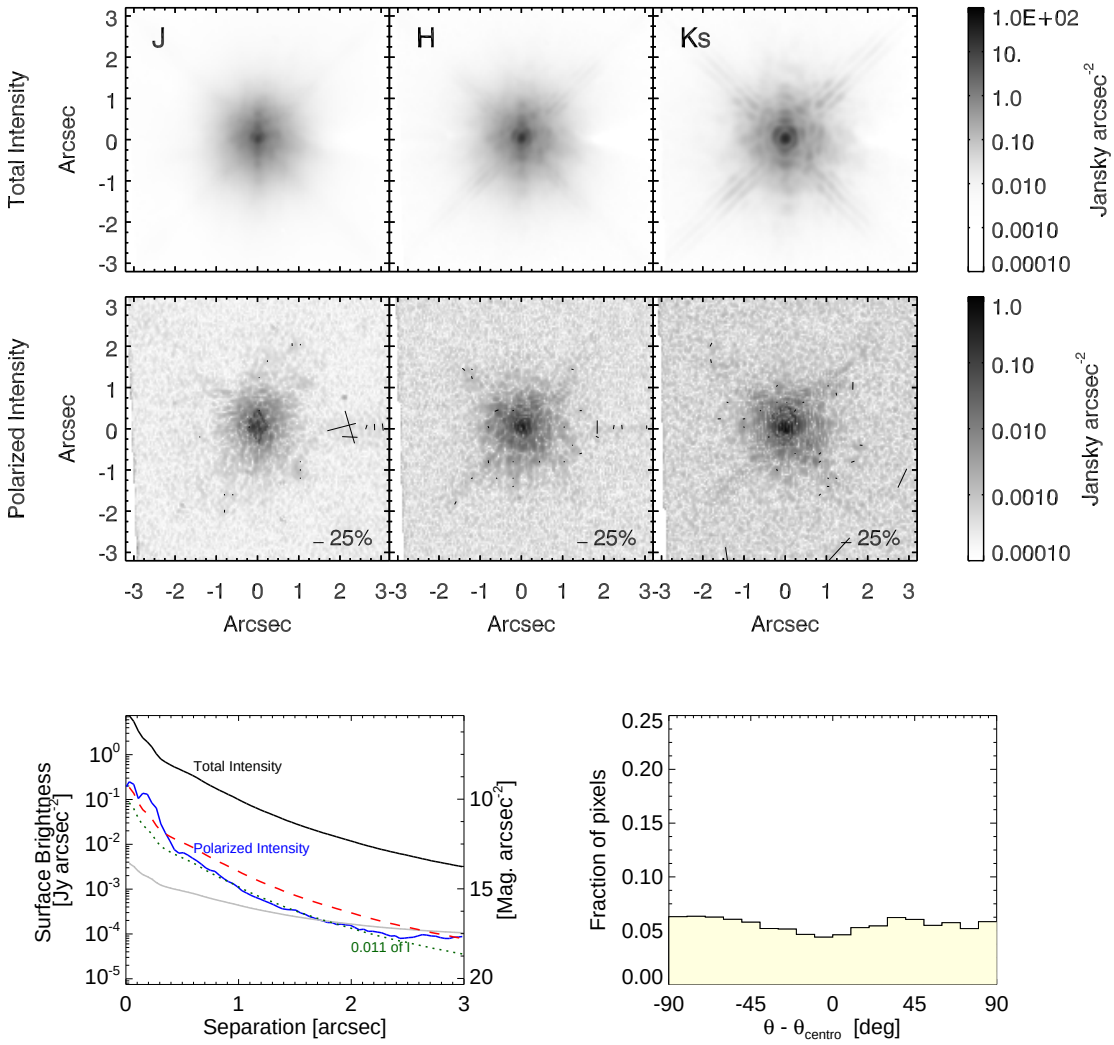

Figure 4.76: Imaging polarimetry of HD 142666.

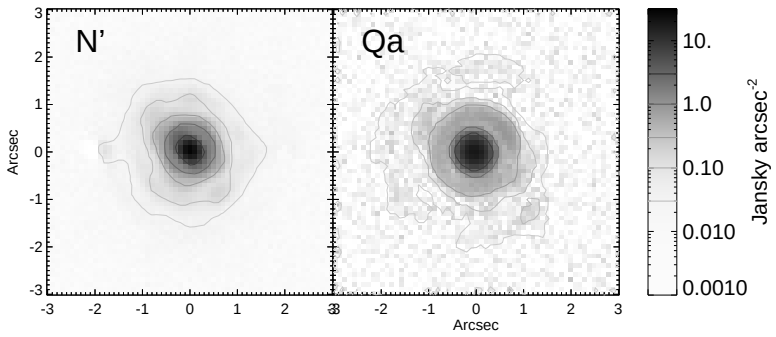

Figure 4.77: Mid-IR imaging of HD 142666.

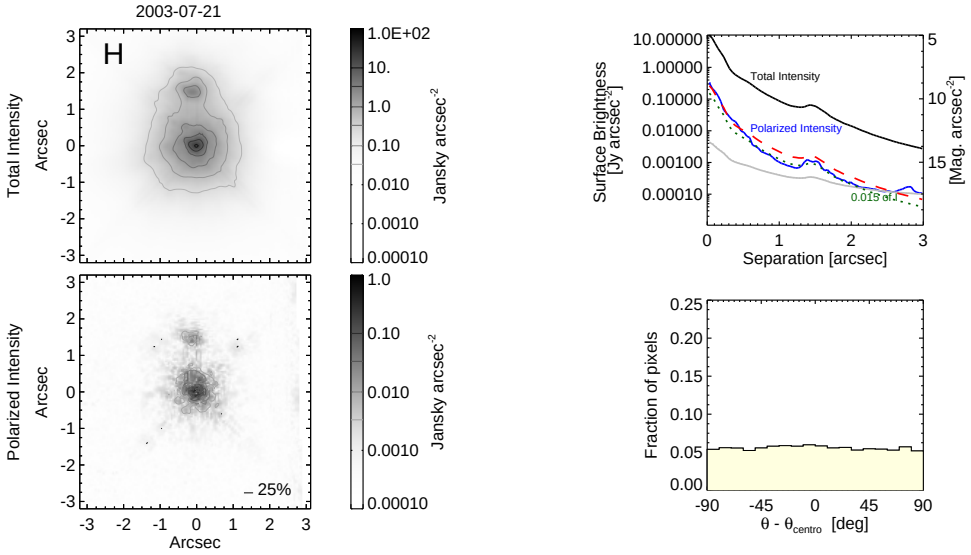

Figure 4.78: Imaging polarimetry of HD 144432.

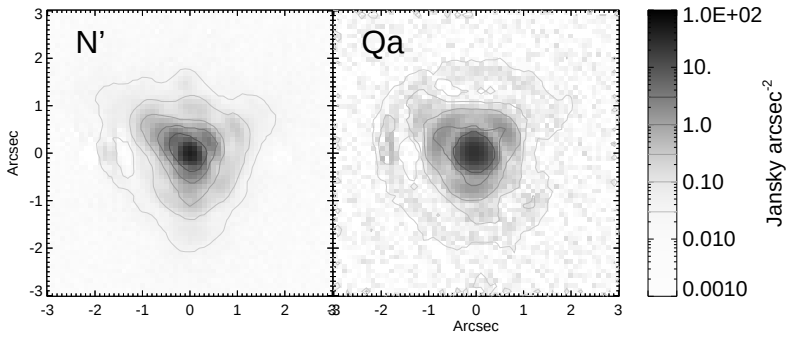

Figure 4.79: Mid-IR imaging of HD 144432.

the star resolved in the mid-IR (Fig. 4.81).

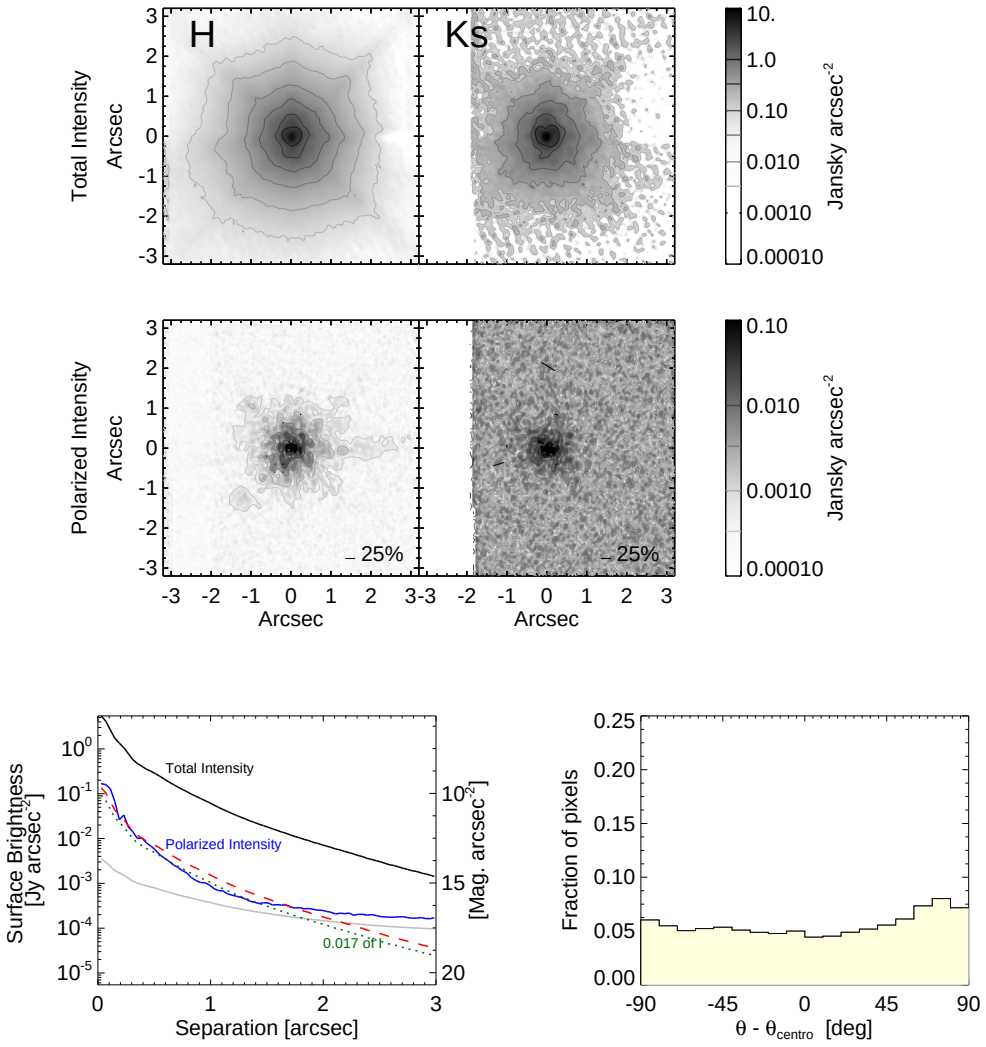

Figure 4.80: Imaging polarimetry of HD 145718.

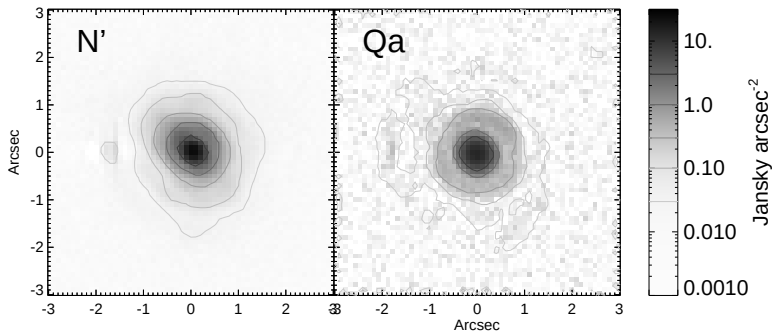

Figure 4.81: Mid-IR imaging of HD 145718.

4.5.56 PDS 415

PDS 415 is a 4.″6 binary, the brighter of which has spectral type F0V and $V = 12.0$. Vieira et al. (2003) identified it as the optical counterpart to IRAS 16156-2358, but apart from that it has been essentially unstudied. It has a photometric distance of 280 pc, but may be associated with the ρ Oph or Sco OB2 star forming region at 140 pc.

It was observed at Lick on 2005-07-28 UTC in good conditions, We detect an elliptical polarized nebula around PDS 415, with position vectors consistent with scattering from circumstellar dust (Fig. 4.82). The nebula extends 1.″5 to either side of the star, along a southeast to northwest direction, and is about 1″ thick in the perpendicular direction.

While this is not the most visually impressive of detections, it is robust: the polarization is detected at a level of $1.5 - 2\sigma$ per spatial pixel. We reobserved PDS 415 on 2006-07-10 and saw essentially the same pattern, confirming the detection.

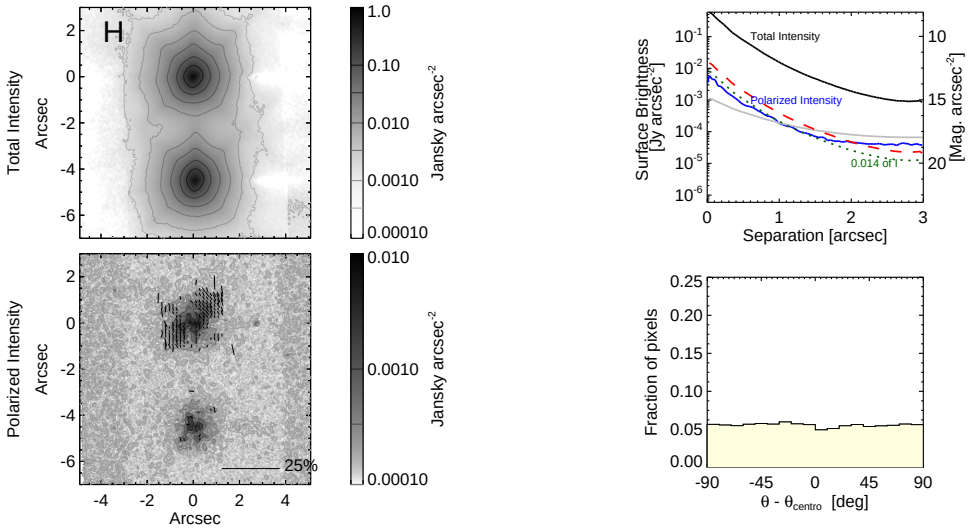

Figure 4.82: Imaging polarimetry of PDS 415.

4.5.57 HD 150193

HD 150193 is an A0 V star (Vieira et al., 2003) located at a distance of 150 pc (HIPPARCOS), with $V = 8.6$. Pirzkal et al. (1997) found a companion to HD 150193 located at a separation of 1.″1 and PA of 236°. Corporon & Lagrange (1999) observed Li absorption in the combined spectra, indicating the companion is of T Tauri type, and resolved spectroscopy by Rodgers et al. (2005) found the companion to be a G0 star with

emission lines and large NIR excess. Near-IR coronagraphic imaging by (Fukagawa et al., 2003) resolved a disk around this star extending out to 1.″5 in radius. They estimate a lower limit to the disk-to-total flux ratio of 1.3×10^{-2}.

It was observed at Lick on 2004-07-06 UTC in good conditions, but we are unable to detect the disk seen by Fukugawa et al.

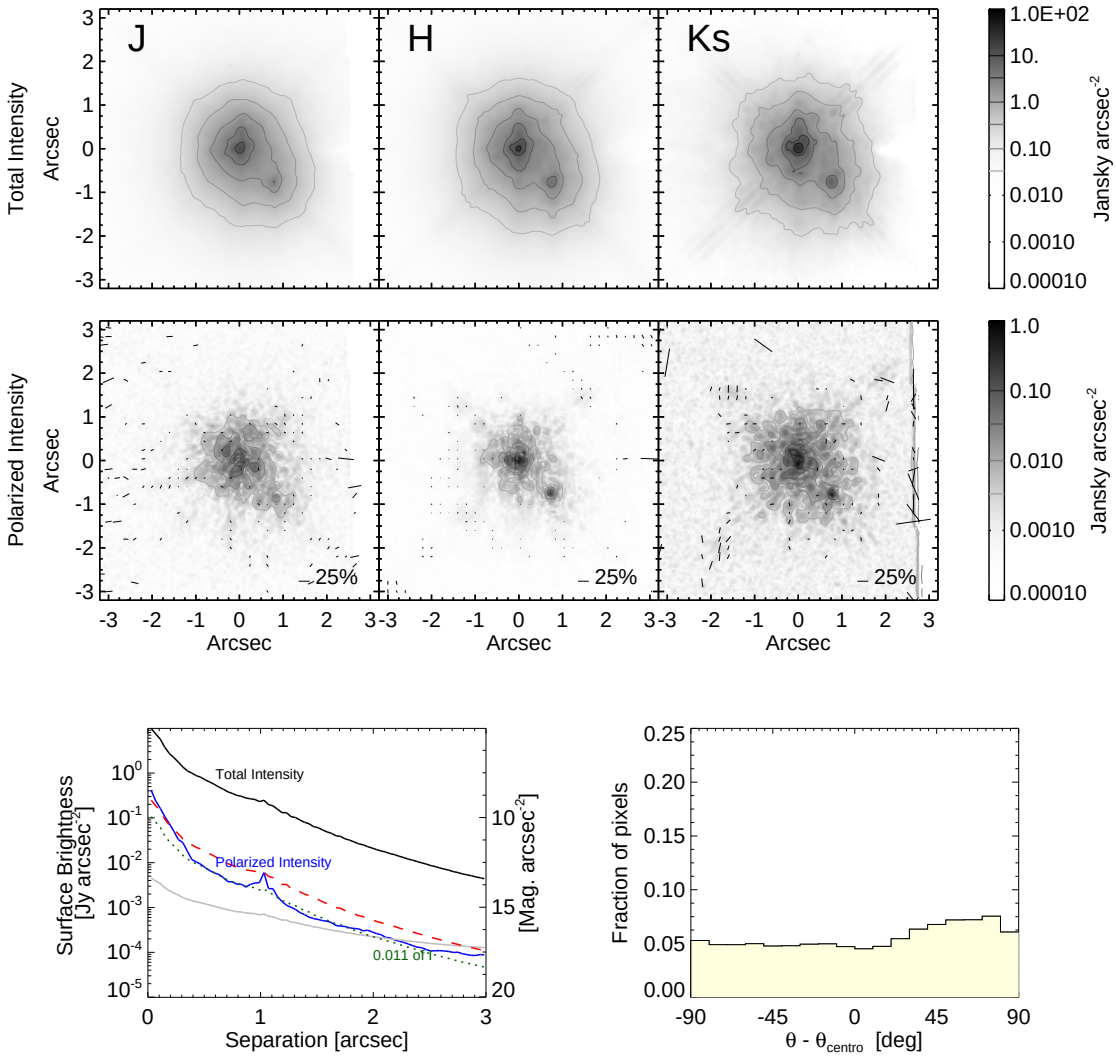

Figure 4.83: Imaging polarimetry of HD 150193.

4.5.58 KK Oph

KK Oph is a 1.″6 binary with a combined $V = 11.5$ at a distance of 160 pc (Hillenbrand et al., 1992; Lienert et al., 1997; Pirzkal et al., 1997.) KK Oph has a large number of

emission lines, which prevented (Hernández et al., 2004) from reliably spectrally classifying it; Hernández writes that it is probably between A0 and F0.

It was observed at Lick on 2004-07-05 UTC in excellent conditions, and at Gemini North on 2005-06-30 UTC. No polarized light was detected in the near-IR (Fig. 4.84) and no resolved circumstellar emission was seen in the mid-IR (Fig. 4.85). However, we easily resolve the binary at all wavelengths. The companion is about 1.15 mag. fainter than the primary in the near-IR, and 0.95 mag in the mid-IR.

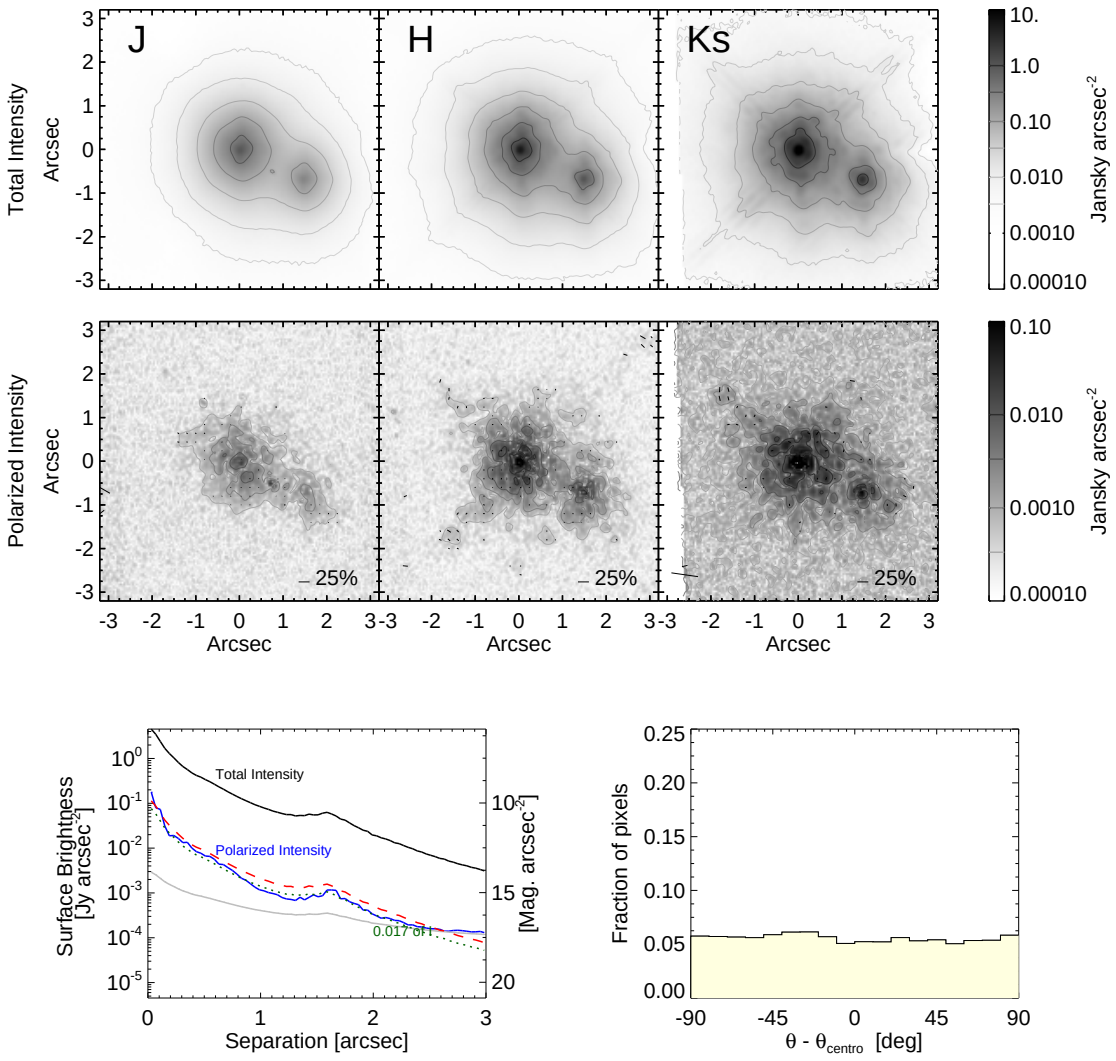

Figure 4.84: Imaging polarimetry of KK Oph.

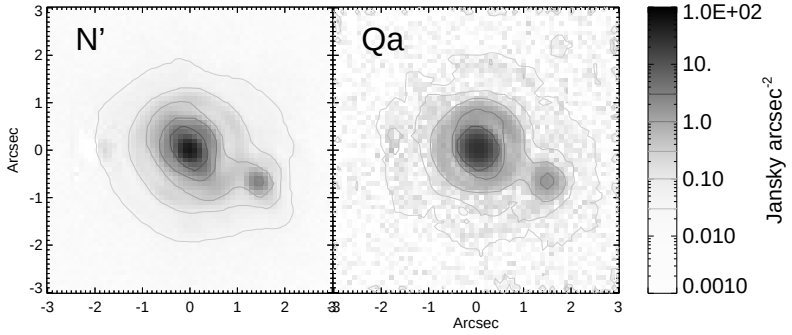

Figure 4.85: Mid-IR imaging of KK Oph.

4.5.59 PDS 453

PDS 453 is a $V = 12.9$ F2V star identified as the optical counterpart to IRAS 17178-2600 (Vieira et al., 2003). While Vieira et al. considered it to be a pre-main-sequence star, possibly associated with the dark clouds LDN 1767 and/or 1773, other authors classify it as a post-main-sequence pre-planetary nebula (Preite-Martinez, 1988; Kohoutek, 1997; Garcia-Lario et al., 1997). Further work is definitely necessary to establish the nature of this star.

It was observed at Lick on 2005-07-29 UTC in good conditions. A butterfly-shaped polarized nebula is detected around PDS 453, extending about 2″ from the northwest to southeast. The position vectors are centered on PDS 453, consistent with polarization from scattering by circumstellar dust (Fig. 4.86). We reobserved this star on 2006-07-10 and found essentially the same polarization pattern, confirming its reality. The nebula's quadrupolar morphology, with two brighter lobes offset slightly northeast from the star and two much fainter lobes on the opposite side, is strongly suggestive of a circumstellar disk seen at a high inclination. The midpoint of the bright lane is offset $\sim 0\farcs2$ from the peak total intensity at a PA of 45°. If we assume Vieira et al.'s photometric distance of 490 pc, then the disk has a radius of ~ 500 AU, but the presence of so much circumstellar dust renders a photometric distance unreliable.

In our deep H-band image, about a dozen fainter sources are visible around PDS 453, typically with $\Delta H \sim 7$. There is one relatively bright source which may be a binary companion to PDS 453, located 6″ southeast and having $\Delta H \sim 2$ It is suggestive that this star is located along the same position angle as the apparent disk, but future work is needed to tell if these two stars are indeed physically associated.

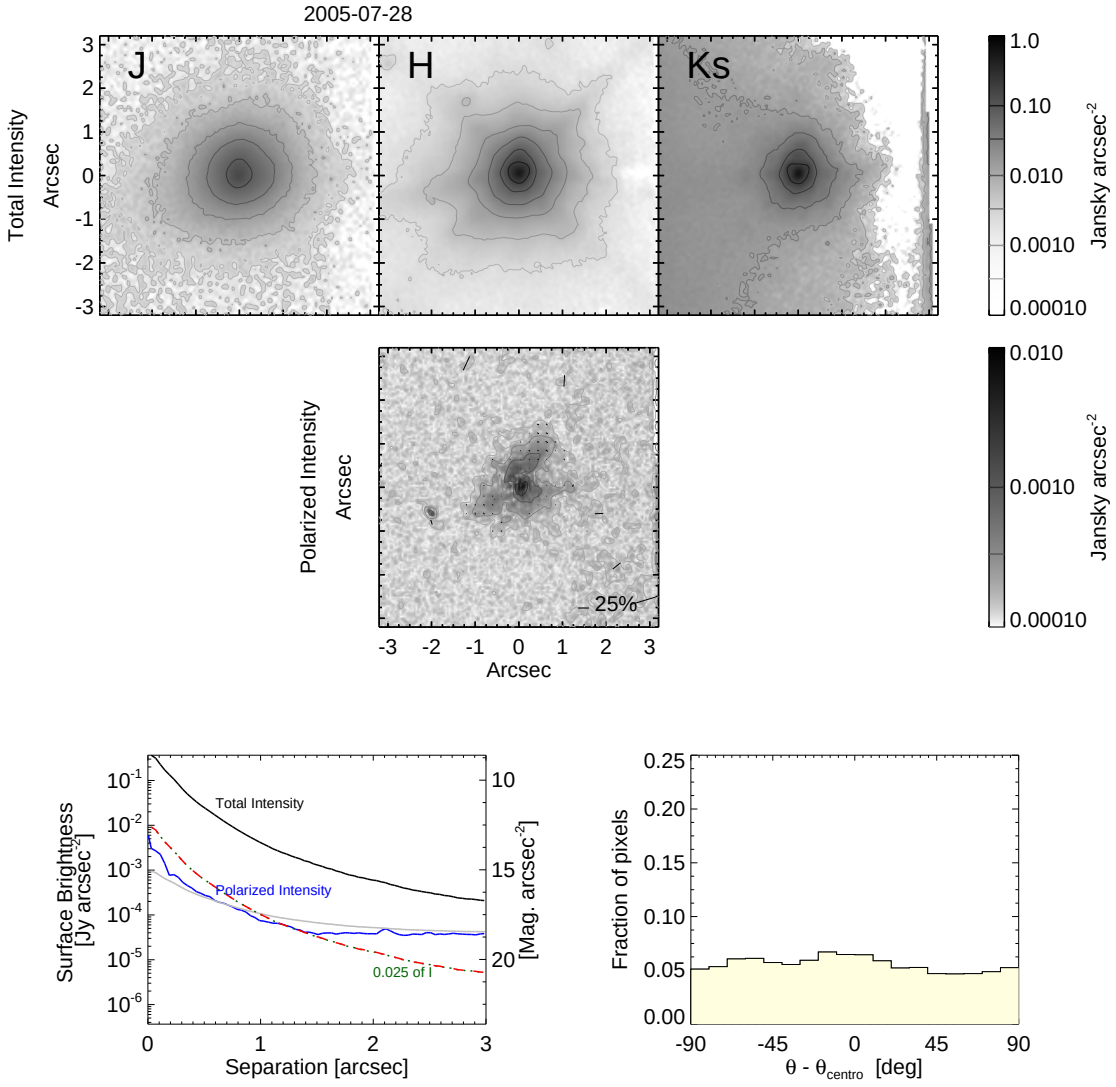

Figure 4.86: Imaging polarimetry of PDS 453.

4.5.60 PDS 469

PDS 469 is an A0 star located at a distance of 1100 pc with $V = 12.8$ (Vieira et al., 2003). Carballo & Sahu (1994) and Vieira et al. (2003) independently identified it as the optical counterpart to IRAS 17481-1415; apart from that it is essentially unstudied. It is a $7''$ apparent binary.

It was observed at Lick on 2004-09-08 UTC in excellent conditions. No polarized light was detected in the near-IR (Fig. 4.87) However, we do detect a new apparent companion, located $1\farcs67$ from PDS 469 A at a PA of 16 °. This object, which we call PDS 469 Ab, has $\Delta H = 4.35$ relative to PDS 469 A, and colors fairly similar to that star. The northern, brighter companion PDS 469 B has $\Delta H = 3.42$.

4.5.61 HD 163296

HD 163296 is an extensively studied nearby A0 star with a well-known circumstellar disk. It was first resolved in millimeter interferometry by Mannings and Sargent (1997), and soon thereafter imaged in scattered light using STIS on HST (Grady et al., 2000). A blueshifted jet is visible in Ly α extending towards the southwest (Devine et al., 2000).

It was observed at Lick on 2004-07-06 UTC in excellent conditions, and on 2005-07-29 in good conditions, and at Gemini North on 2005-07-01 UTC. No polarized light was detected in the near-IR (Fig. 4.88), nor was it resolved in the mid-IR (Fig. 4.89).

4.5.62 PDS 477

PDS 477 is a B1 star with $V = 14.4$. It has a photometric distance of 2900 pc but may be associated with the Sgr R1 star forming region at 900-1400 pc (Vieira et al., 2003). It was identified as the optical companion to IRAS 17575-1647 by the PDS survey, but apart from that is entirely unstudied.

It was observed at Lick on 2005-07-29 UTC in good conditions. and at Gemini North on 2006-07-05 through patchy clouds. Two potential companions are detected in the near-IR. The centrosymmetry histogram has a peak near 90°; this is due in part to the brighter of the two companions, which appears to be $\sim 3\%$ polarized at a PA of $\sim 270°$. This companion must therefore itself be a dusty young star. There is also some evidence for a fan of polarization to the west of PDS 477, but not at a statistically significant level (Fig. 4.90).

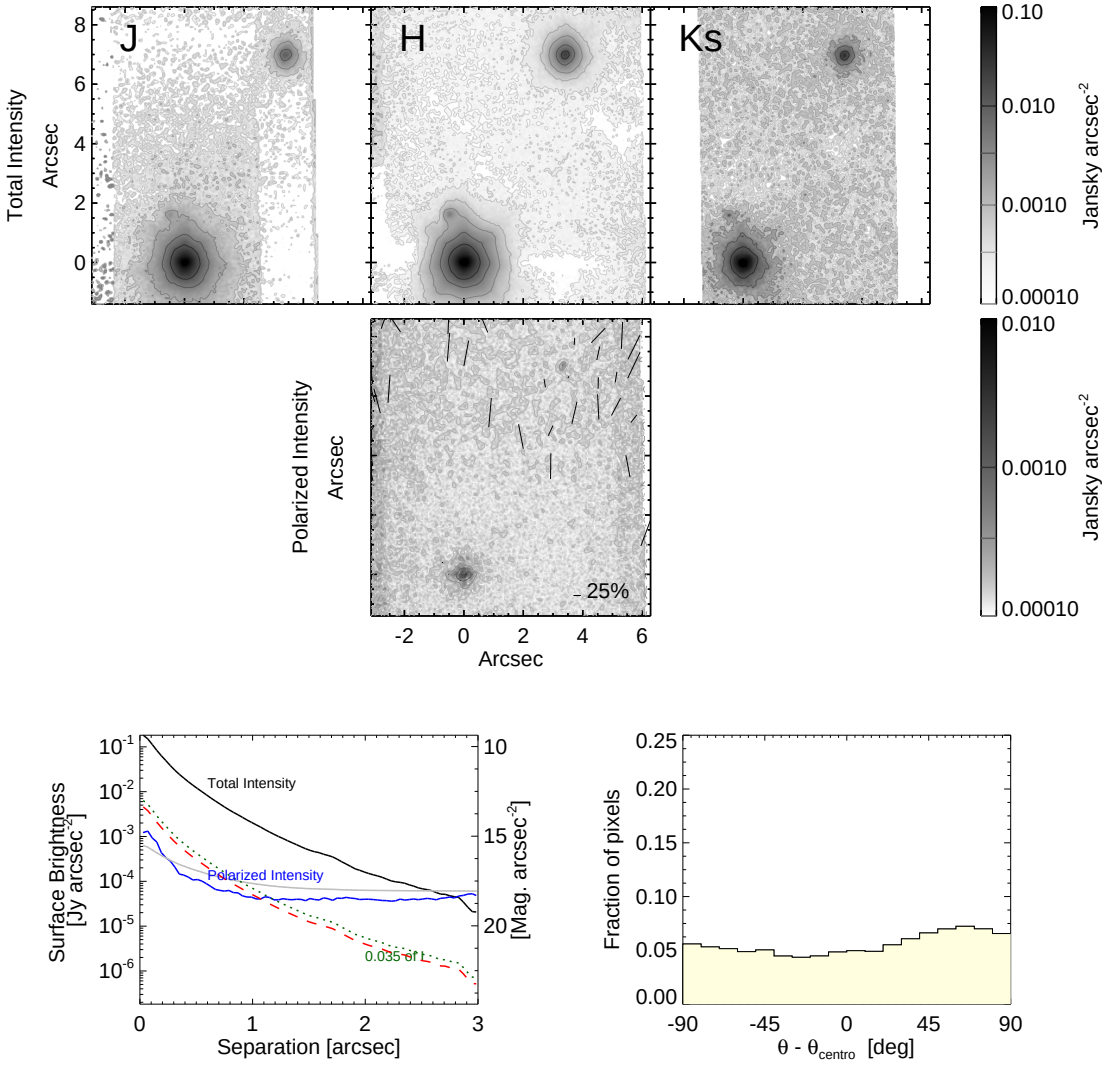

Figure 4.87: Imaging polarimetry of PDS 469.

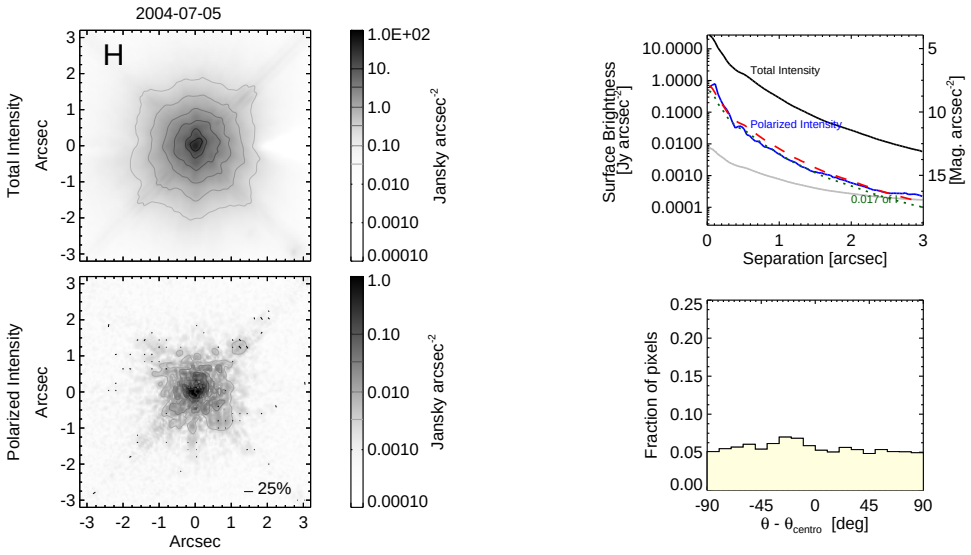

Figure 4.88: Imaging polarimetry of HD 163296.

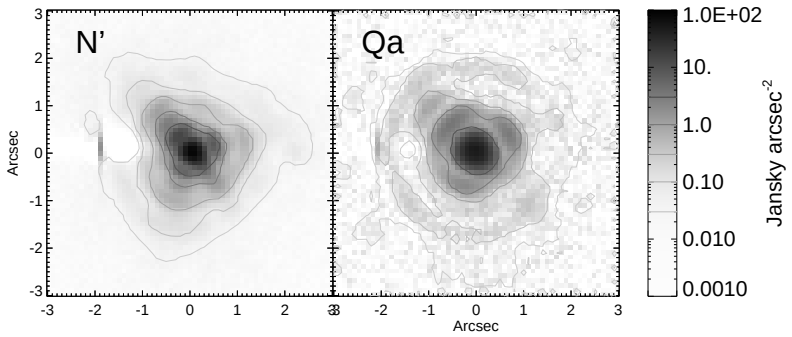

Figure 4.89: Mid-IR imaging of HD 163296.

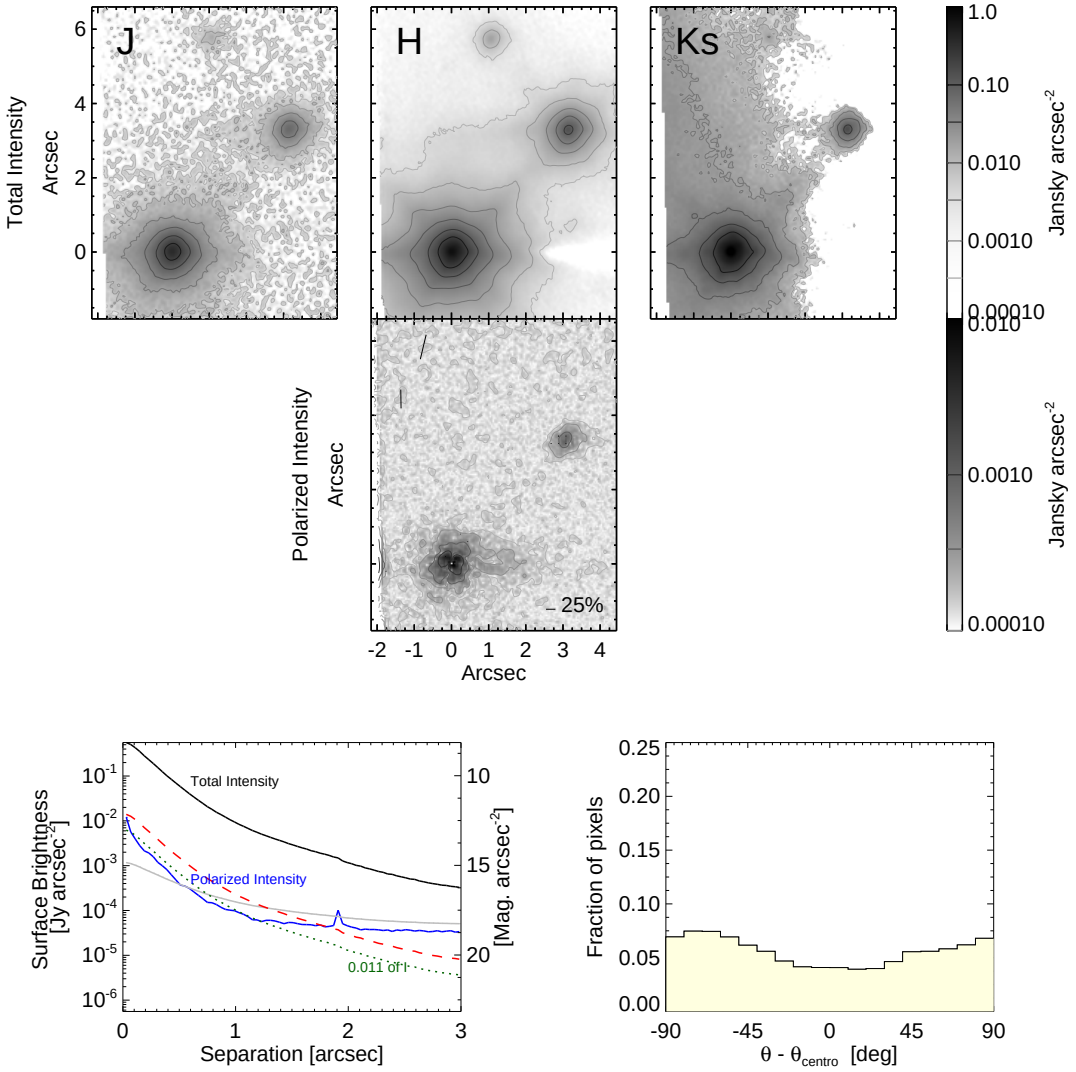

Figure 4.90: Imaging polarimetry of PDS 477.

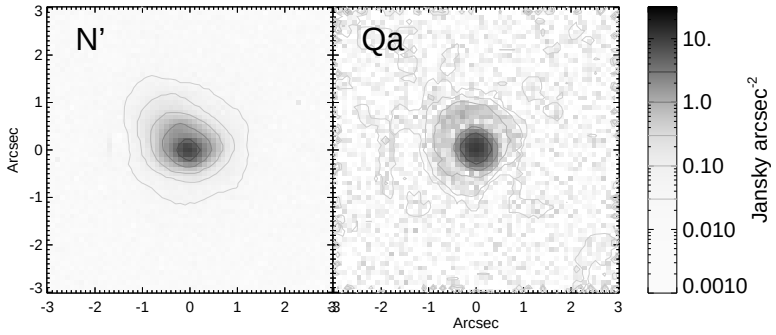

Figure 4.91: Mid-IR imaging of PDS 477.

4.5.63 LkHα 118

LkHα 118 is a B1 star (Hernández et al., 2004) located at a distance of 1950 pc (Kozok, 1985), with $V = 11.2$. Its evolutionary status is uncertain: While the star does show Hα emission (Herbig, 1957), IRAS did not detect a source at this location, and the star was rejected as a member of the HAEBE class by The et al. (1994). Hernández et al. (2004) report that while LkHα 118 appears to have a small IR excess using the usual $R_V = 3.0$ extinction law, this excess disappears if $R_V = 5.0$ is used instead. Those authors include LkHα 118 on their list of objects which need further study to clarify their evolutionary state.

It was observed at Lick on 2005-07-28 UTC in good conditions. No polarized light was detected in the near-IR (Fig. 4.92), but a dozen fainter point sources are detected in our field of view. The brightest is 3.″44 from LkHα 118 at PA=209°and has $\Delta H = 5.8$.

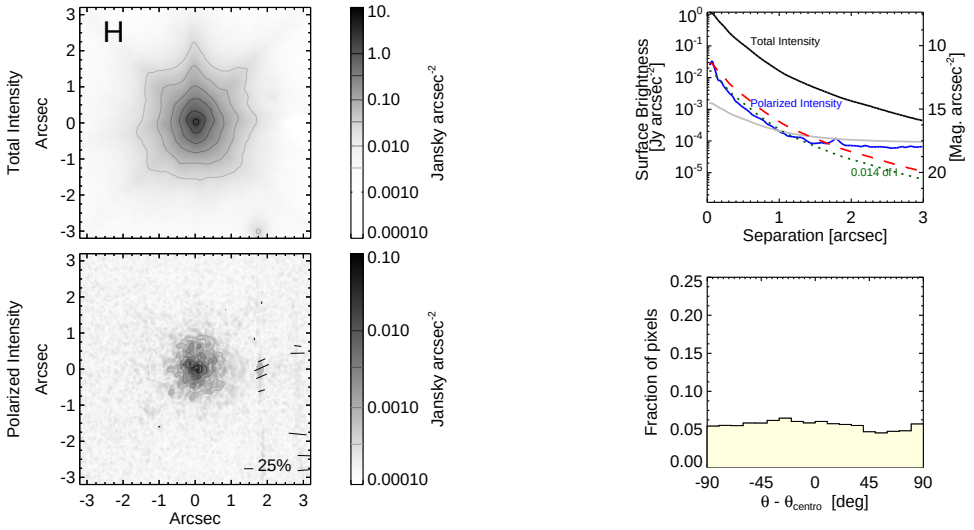

Figure 4.92: Imaging polarimetry of LkHα 118.

4.5.64 HD 169142

HD 169142 is an A5 or A9 star located at a distance of 145 pc, with $V = 8.2$ (Sylvester et al., 1996; Dunkin et al., 1997a,b; Vieira et al., 2003). A circumstellar disk was detected around this star in differential AO polarimetry observations by Kuhn et al. (2001a), and has more recently been resolved in the submillimeter (Raman et al., 2006) and mid-IR (Okamoto et al., 2005; Honda et al., 2005). Its polarized surface brightness as reported by

Kuhn et al. is about 1%, comparable to the sensitivity floor of the IRCAL polarimeter. We detect the disk at low signal to noise; it is visible as a peak in the centrosymmetry histogram but is not readily apparent even in heavily smoothed versions of the Stokes Q, U and polarized intensity P images.

It was observed at Lick on 2004-09-08 UTC in excellent conditions, and at Gemini North on 2005-06-30 UTC. In our near-IR data, we detect a 1.6σ peak in the centrosymmetry histogram; see §4.7.1. The star was resolved in the mid-IR (Fig. 4.94). See §4.7.3 for a discussion of this and other sources slightly resolved in the mid-IR.

4.5.65 MWC 297

MWC 297 is an O9 or B0 star (Hillenbrand et al., 1992; Vieira et al., 2003) located at a distance of 250 pc (Drew et al., 1997), with $V = 12.3$. It exhibits large X-ray flares with long decay timescales (Hamaguchi et al., 2000, 2005) and very strong Hα emission (Finkenzeller and Mundt, 1984). Di Francesco et al. (1994) report that MWC 297 is significantly extended at 50 and 100 μm, with an angular FWHM of $\sim 55''$. They interpreted this to be an extended circumstellar envelope rather than a disk, but caution that this interpretation may be wrong if there are other nearby sources causing confusion.

It was observed at Lick on 2004-09-08 UTC in excellent conditions, and at Gemini North on 2005-07-01 UTC. No polarized light was detected in the near-IR (Fig. 4.95) In contrast to the far-IR observations of Di Francesco et al., my near and mid-IR observations do not resolve any extended dust around MWC 297, nor do they detect any additional sources in the field (Fig. 4.96). The mid-IR photometry is in good agreement with the 12 and 20 μm IRAS fluxes, indicating that there is no additional warm infrared source present within the IRAS beam. Thus we are left with a picture in which MWC 297 is surrounded by a spatially extended cloud of cold dust ($\lesssim$ 100K) which is only visible in thermal emission at wavelengths longer than 20 μm.

4.5.66 VV Ser

Estimates for the spectral type of VV Ser range from B1 to A2 (Finkenzeller & Mundt, 1984; Chavarria-K. et al., 1988; Acke & van den Ancker, 2004). It has $V = 11.9$ and a distance of about 440 pc (Hillenbrand et al., 1992). There is a growing body of evidence that it is a self-shadowing UX Ori star: It is very photometrically variable, and has strong red absorption in the NaD line possibly due to cold accreting material (Finkenzeller &

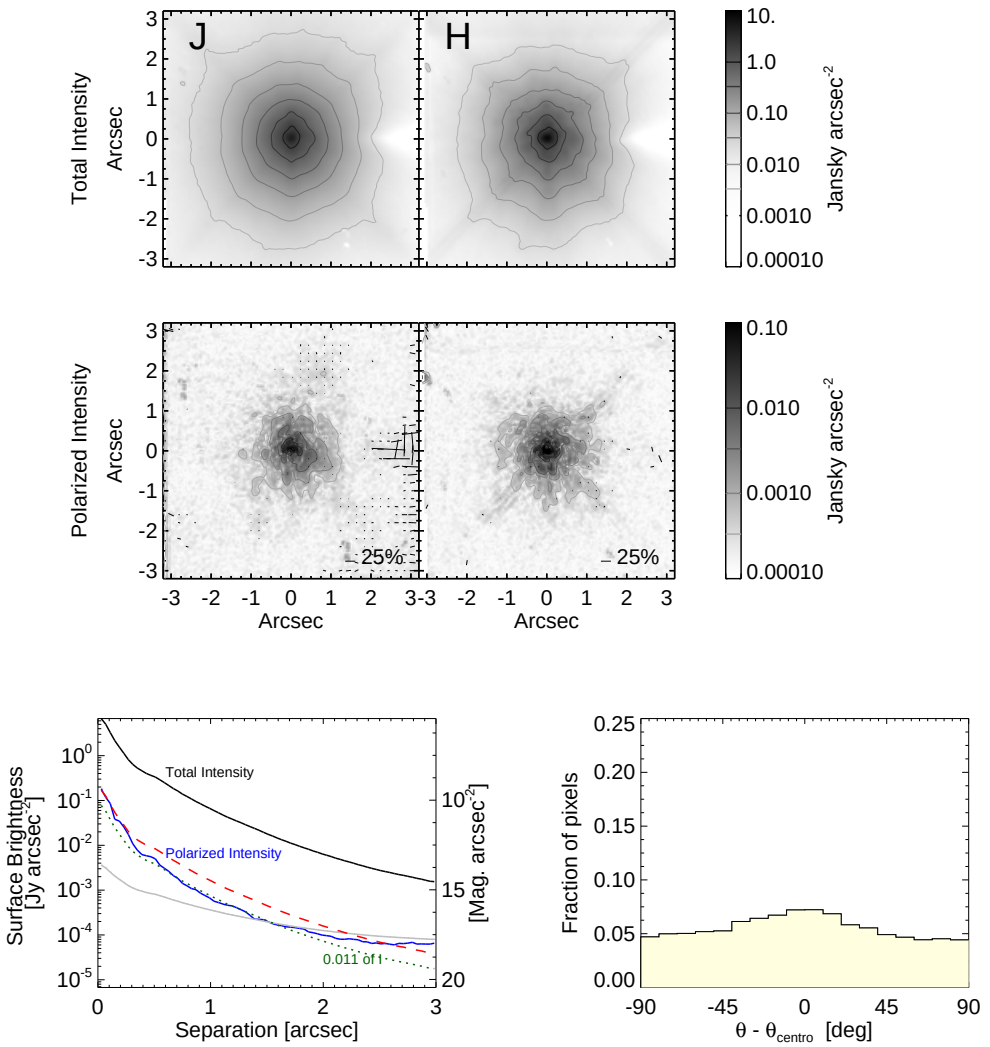

Figure 4.93: Imaging polarimetry of HD 169142.

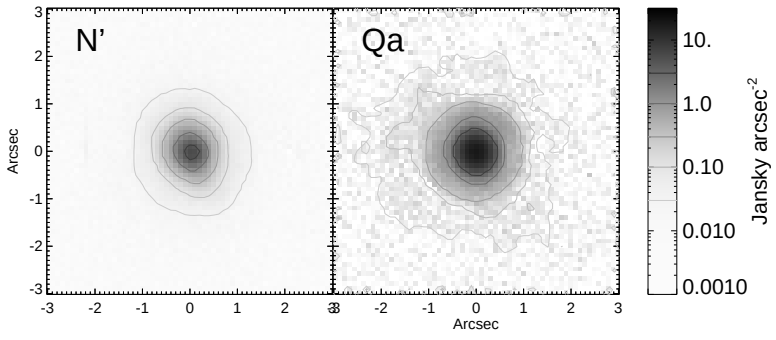

Figure 4.94: Mid-IR imaging of HD 169142.

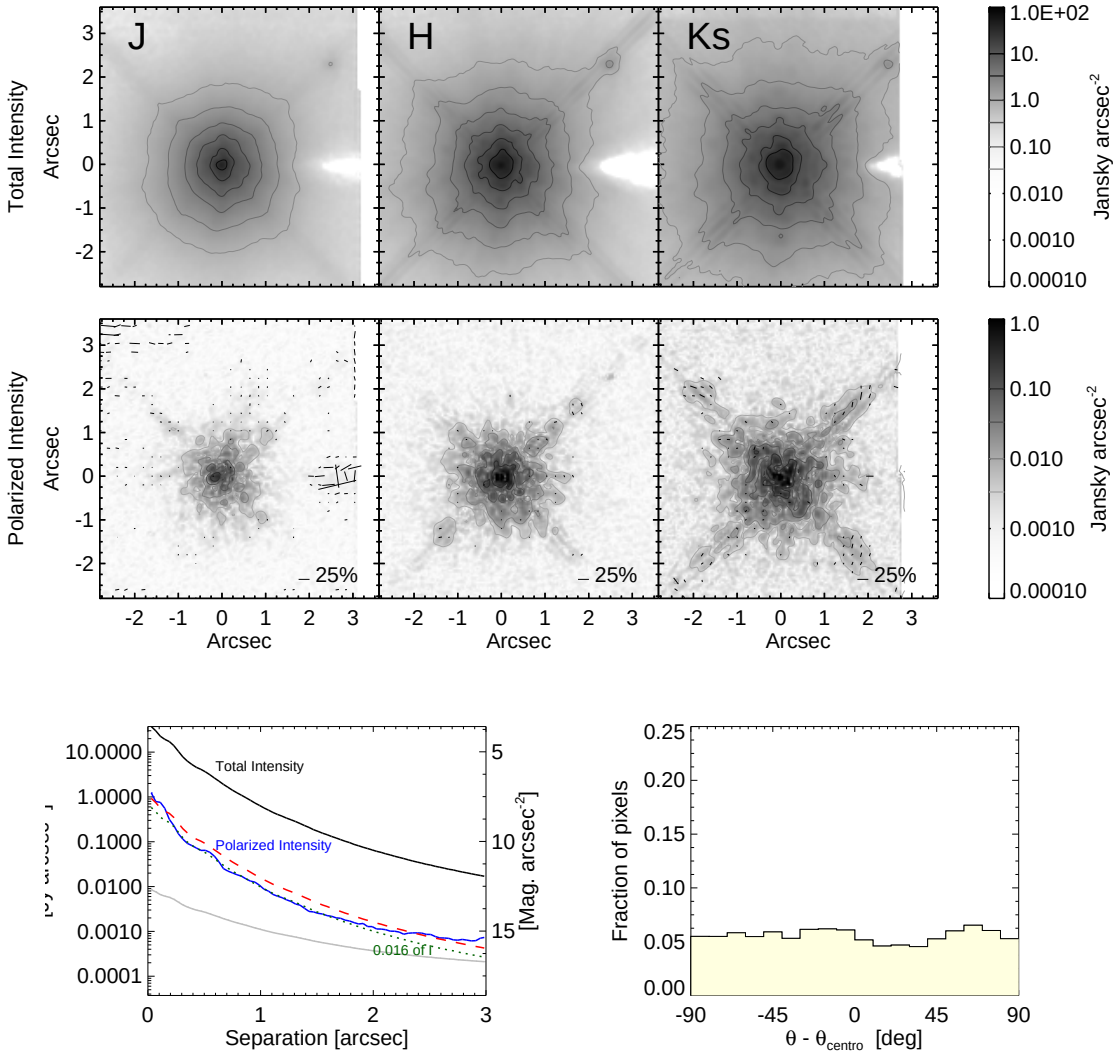

Figure 4.95: Imaging polarimetry of MWC 297.

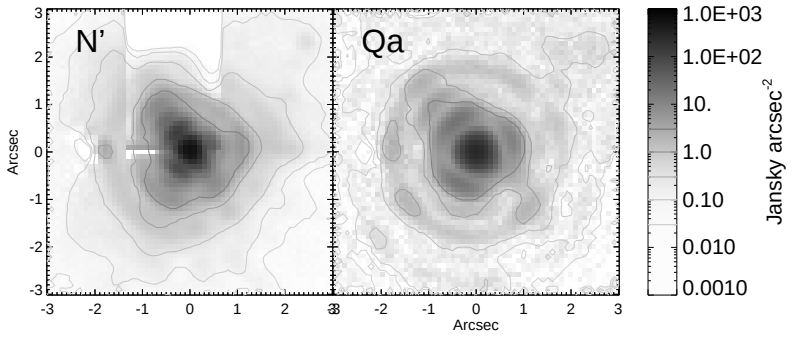

Figure 4.96: Mid-IR imaging of MWC 297.

Mundt, 1984). Leinert et al. (2001) report a 0.″6 FWHM halo around VV Ser, slight elongated east-west. Its interferometric visibilities are well-modeled by a nearly edge-on disk (Eisner et al., 2004), and Spitzer IRAC observations reveal a broad X-shaped nebula cut by a dark lane whose position angle is roughly consistent with the inferred disk (Eisner, private communication, 2006).

It was observed at Lick on 2004-07-06 UTC in excellent conditions, and at Gemini North on 2006-07-05 through patchy clouds. No polarized light was detected in the near-IR (Fig. 4.97), nor was it resolved in the mid-IR (Fig. 4.98).

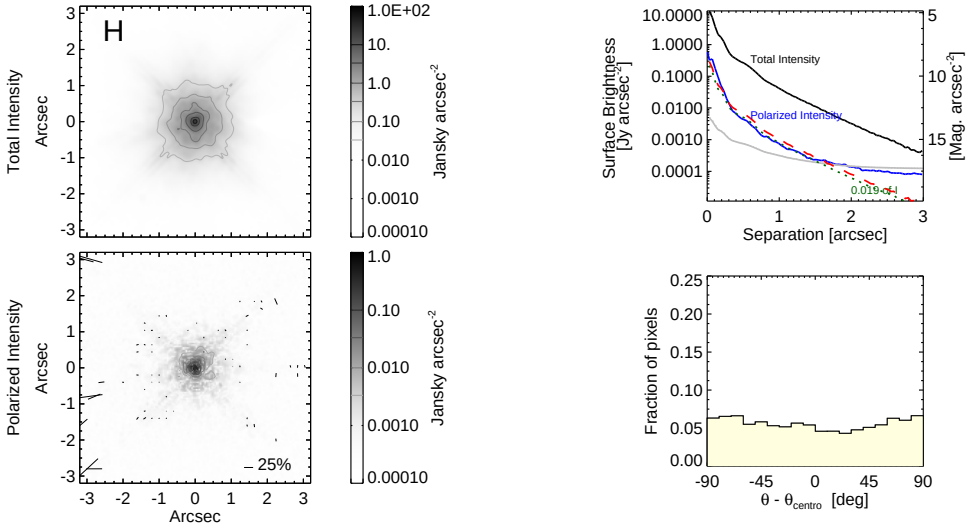

Figure 4.97: Imaging polarimetry of VV Ser.

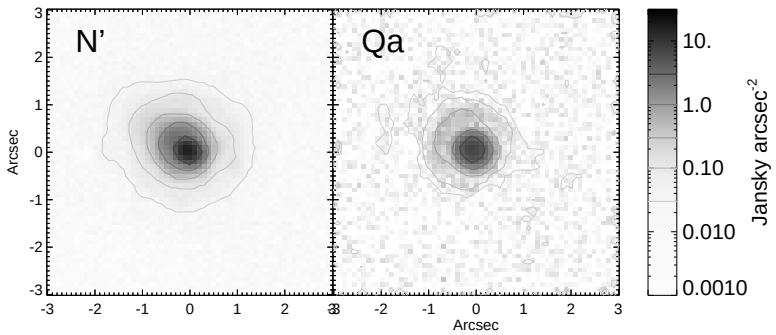

Figure 4.98: Mid-IR imaging of VV Ser.

4.5.67 MWC 300

MWC 300 is a ∼ Be star (Testi et al., 1999) located at a distance of 15500 pc (Leinert et al., 1997), with $V = 10.0$. The distance and spectral classification of this star are both quite uncertain. Corporon & Lagrange (1999) found it to be a spectroscopic binary, while speckle observations by Leinert et al. (2001) found evidence for a faint halo around this star, with FWHM 1.″1. MWC 300 shows broad Hα emission, plus P Cygni profiles in the NaD and HeI lines (Finkenzeller & Mundt, 1984). There is some doubt as to the pre-main-sequence nature of this star (Herbig and Rao, 1972; Finkenzeller and Mundt, 1984).

It was observed at Lick on 2004-07-06 UTC in excellent conditions, and at Gemini North on 2005-07-01 UTC. No polarized light was detected in the near-IR (Fig. 4.99) The star was not resolved in the mid-IR (Fig. 4.100). Despite its very large infrared excess, and the reported detection by Leinert et al., we detect no evidence for resolved circumstellar dust in the NIR.

4.5.68 PDS 520

PDS 520 is a F3 V star with $V = 14.7$, the optical counterpart to IRAS 18275+0040 (Vieira et al., 2003). It has a photometric distance of 180 pc, but its location on the outskirts of the Serpens molecular cloud suggests it may be located somewhat further away (though the distance to Serpens itself remains a matter of debate). Palla & Giovanardi (1989) observed water maser emission from this source.

It was observed at Lick on 2004-09-08 UTC in excellent conditions, and at Gemini North on 2005-07-01 UTC. No polarized light was detected in the near-IR (Fig. 4.101), nor was it resolved in the mid-IR (Fig. 4.102). A potential companion is detected 5.″2 west of PDS 520 in the NIR, but is not detected in our MIR images.

4.5.69 AS 310

AS 310 is a $V = 12.5$ B1 star (Hernández et al., 2004) located in a small cluster of stars at a distance of 2500 pc (Ageorges et al., 1997; Testi et al., 1998). Millimeter observations indicate the presence of a large amount of dust and gas in this region (30 $M_{\odot}$of gas; Henning et al. 1994), which along with the presence of H_2O masers (Palla & Prusti, 1993) suggest this is a site of ongoing star formation. AS 310 shows prominent emission lines

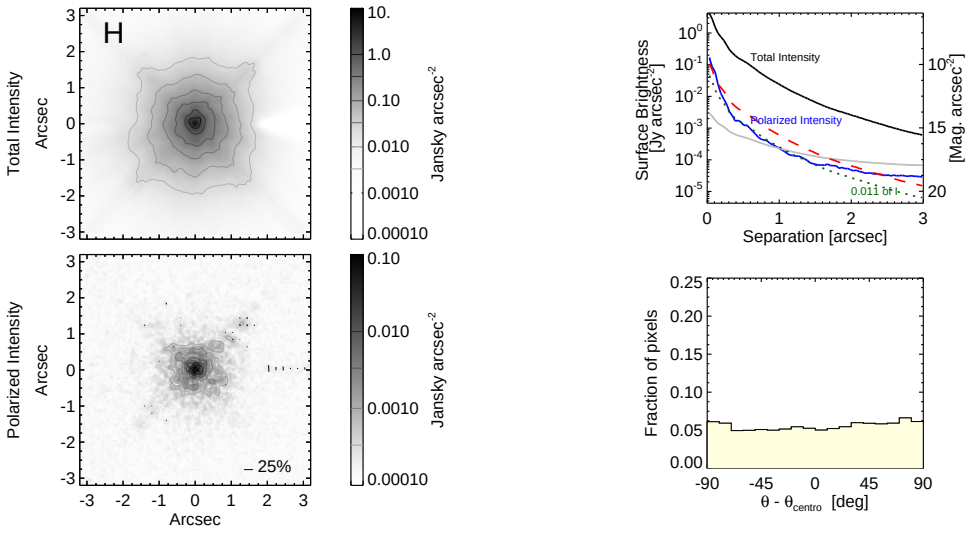

Figure 4.99: Imaging polarimetry of MWC 300.

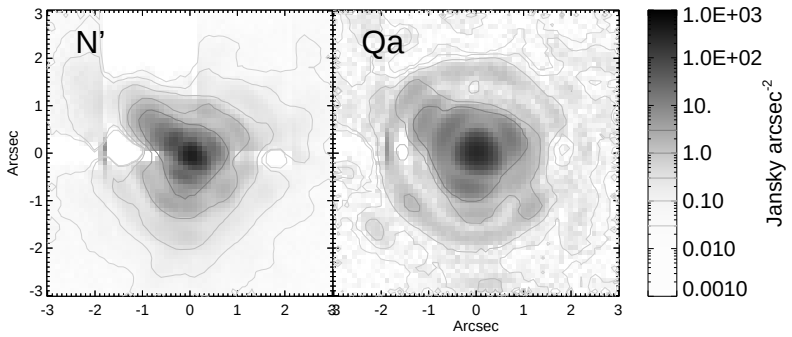

Figure 4.100: Mid-IR imaging of MWC 300.

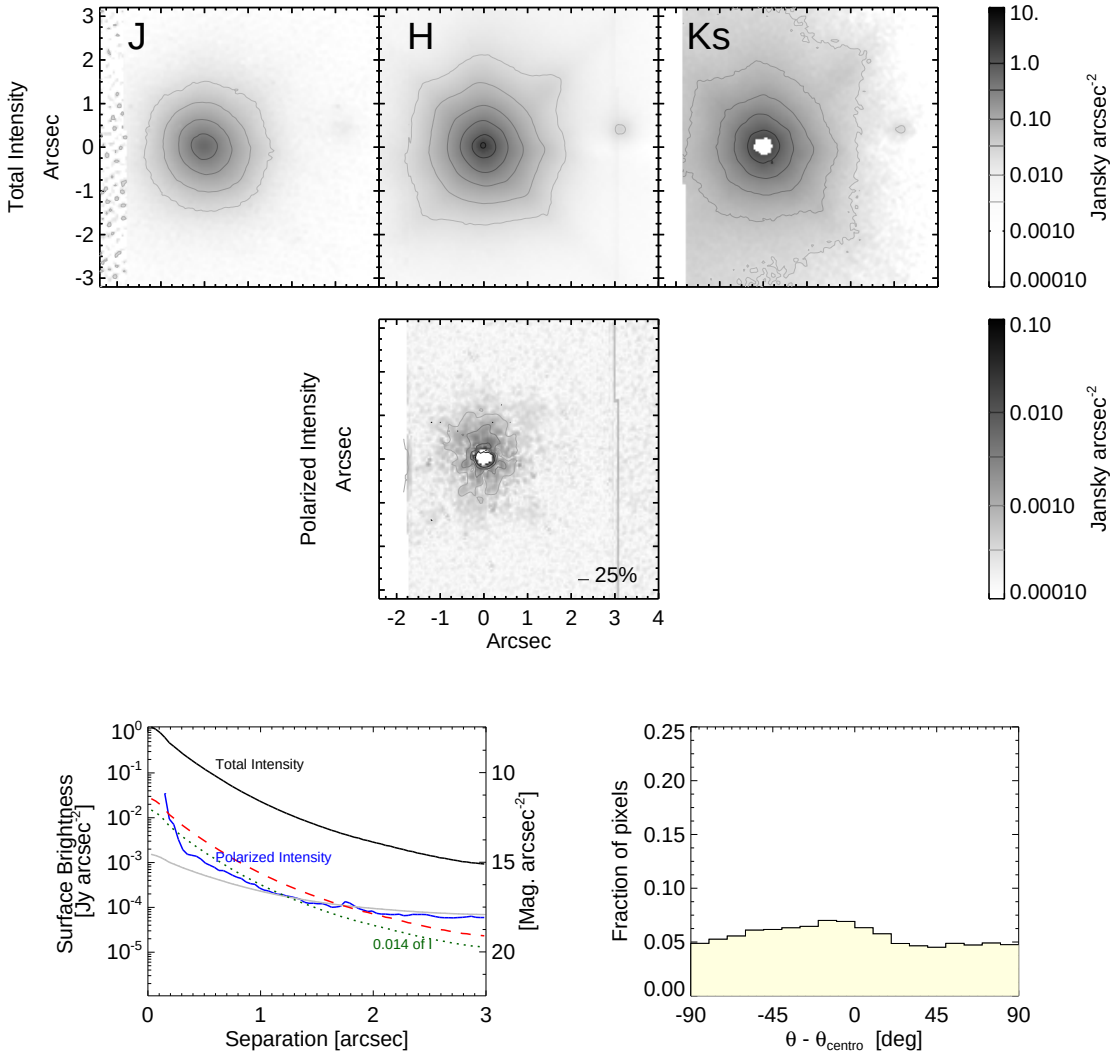

Figure 4.101: Imaging polarimetry of PDS 520. Unfortunately the K_s and H Stokes U images are saturated.

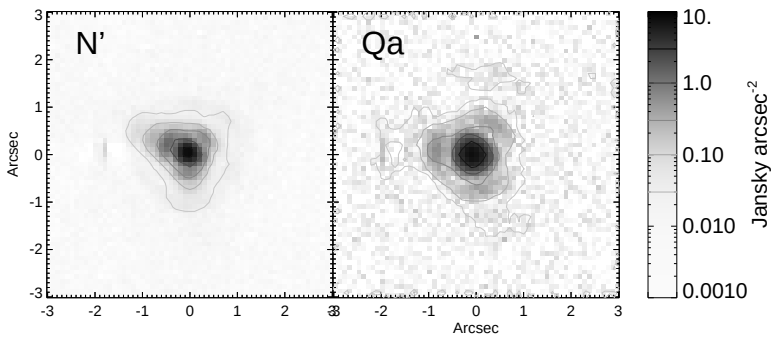

Figure 4.102: Mid-IR imaging of PDS 520.

from several species in addition to Hα , including [SII], [OI], and [FeII] (Merrill & Burwell, 1950; Herbig & Kameswara Rao, 1972; Cohen & Kuhi, 1979; Goodrich, 1993). Several close companions are located within a few arcseconds of AS 310 (Ageorges & Walsh, 1999), and there is some evidence for a bipolar jet (Goodrich, 1993).

It was observed at Lick on 2003-07-23 UTC in good conditions, and at Gemini North on 2005-06-30 UTC. In addition to the usual polarimetry observations, we obtained direct imaging observations of AS 310 in order to have a sufficient field of view to study the whole cluster. We detect a plethora of point sources, concentrated along the southern edge of a bright nebula.

Mid-IR imaging shows a tremendous amount of extended emission around AS 310. Indeed, the source is entirely nebulous at long wavelengths with no point source visible at the location of AS 310 A. (The nearby sources AS 310 C and AS 310 E are visible at 11 μm, however. AS 310 C is also seen at 18 μm, while AS 310 E is not detectable above the background nebula.) As in the near-IR, the mid-IR nebulosity extends primarily to the north and northwest from the star, but several bars and filaments extend in other directions.

In summary, AS 310 appears to be a very young cluster embedded in a tremendous amount of warm dust. As Ageorges et al. wrote, the "possible stellar cluster around AS 310 calls for further studies because embedded clusters associated with Herbig Ae/Be stars are pivotal to understanding the star formation mechanism," because they are poised on the edge between tightly clustered high-mass star formation and the relatively loose groups of young low-mass stars.

4.5.70 PDS 530

PDS 530 is a F0 star located at a distance of 1000 pc with $V = 14.0$ (Vieira et al., 2003) . Apart from the PDS survey identification as the optical counterpart to IRAS 18391+0805, it has been essentially unstudied. On the DSS plates, it can be see to lie in a reflection nebulosity on the edge of a small dark cloud.

It was observed at Lick on 2005-07-29 UTC in good conditions, and at Gemini North on 2006-07-05 through patchy clouds. Three other NIR-bright stars are visible within $8''$ to the south. Two regions of polarization are visible in our near-IR images: first is an apparent jet extending due north from PDS 530, and second is a roughly circular nebula $3\farcs8$ southeast towards PA=120°. The polarization vectors for the jet indicate that it is

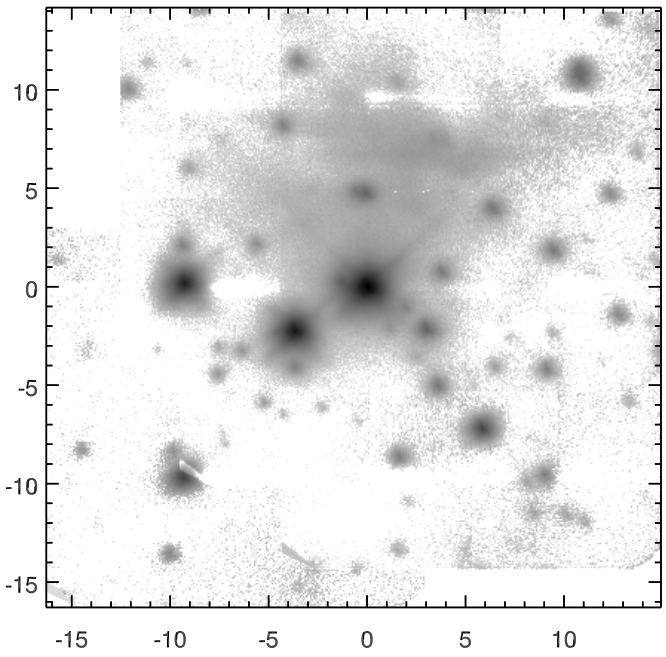

Figure 4.103: *H* band IRCAL imaging of AS 310, showing the cluster around it. We detect all of the sources found by Ageorges et al., plus many others. Their Source C, 5″ north of AS 310, appears to be a binary. An extensive nebula fans out to the north as well.

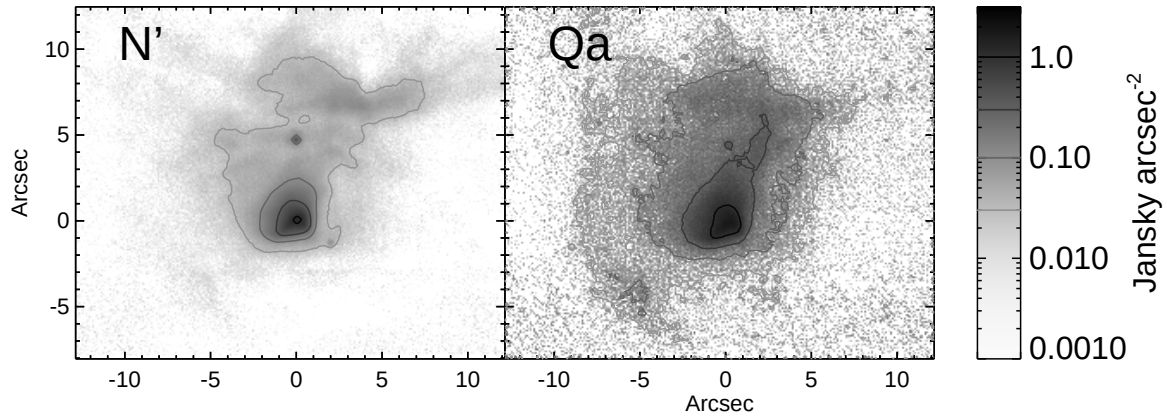

Figure 4.104: Mid-IR imaging of AS 310. It has the brightest and most extensive mid-IR nebula of any Herbig Ae/Be star observed in this study.

scattering light from PDS 530. However, the circular nebula is polarized north-south, rather than perpendicular to PDS 530. This suggests that it is scattering light from some other, more deeply embedded source, probably within the dark cloud.

Our mid-IR photometry is a factor of 2.5 below IRAS at 12 μm, indicating the presence of additional warm dust in the region (or else large variability, surprising in the mid-IR). No other sources are visible in our mid-IR image, including nothing at the location of the circular nebula.

4.5.71 PDS 543

PDS 543 is a B1 star with $V = 12.5$, giving a photometric distance of 414 pc (Vieira et al., 2003); it is the optical counterpart to IRAS 18454+0250. Likkel (1989) included it in her radio survey of objects with IRAS colors characteristic of cold circumstellar dust envelopes, and found it had H_2O maser emission suggestive of a cloud source. While it is included in the catalog of potential planetary nebulae by Condon et al. (1999), those authors follow Likkel in considering it likely a pre-main sequence object.

It was observed at Lick on 2004-11-01 UTC in very windy conditions; AO correction was poor. No polarized light was detected in the near-IR (Fig. 4.107)

4.5.72 MWC 610

MWC 610, also called PDS 545, is a B2e star with $V = 8.9$, giving a photometric distance of 560 pc (Vieira et al., 2003). It was found to be a $4\farcs3$ binary more than a century ago (Hussey, 1900) but has been relatively little-studied since.

It was observed at Lick on 2004-09-07 UTC in excellent conditions, and at Gemini North on 2005-07-01 UTC. No polarized light was detected in the near-IR (Fig. 4.108) No circumstellar dust was spatially resolved around MWC 610 in the mid-IR, but we do barely detect emission at the location of MWC 610 B (Fig. 4.109).

4.5.73 PDS 551

The PDS survey identified PDS 551 as the optical counterpart to IRAS 18528+0400. It is an $\sim$ O9 star with $V = 16.6$, giving a photometric distance of $\sim$ 3500 pc (Vieira et al., 2003). Apart from the PDS survey, it is entirely unstudied.

It was observed at Lick on 2006-07-10 UTC in good conditions. No polarized light

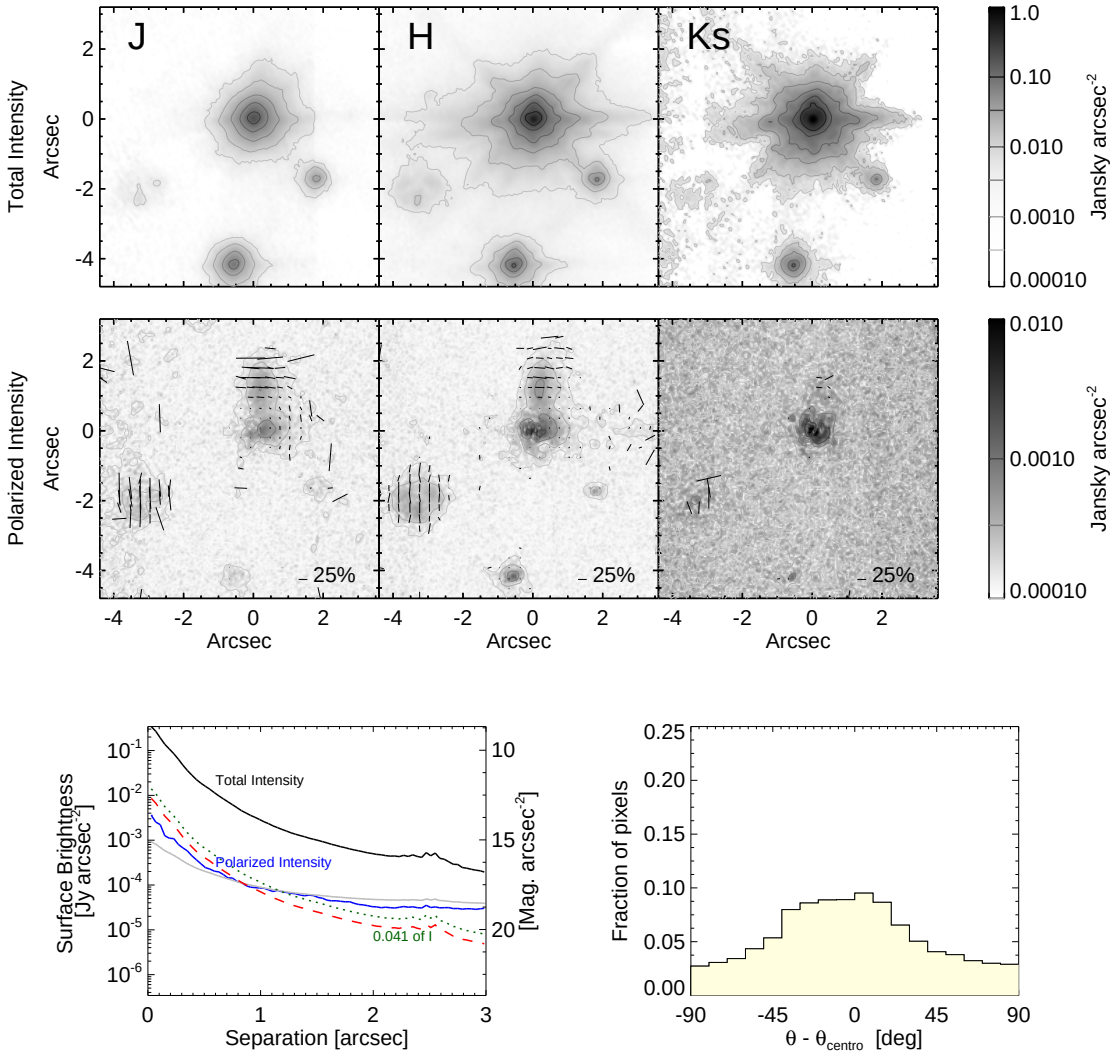

Figure 4.105: Imaging polarimetry of PDS 530.

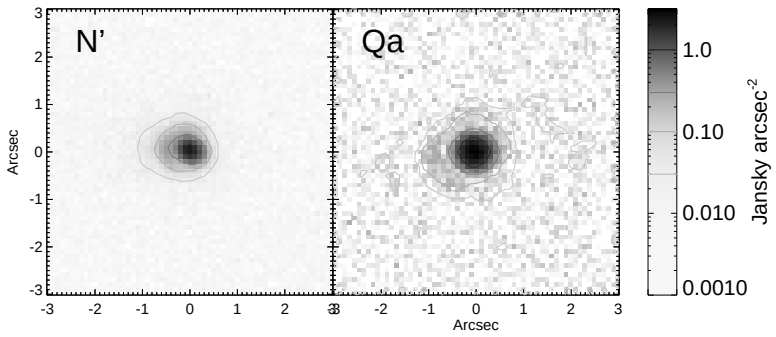

Figure 4.106: Mid-IR imaging of PDS 530.

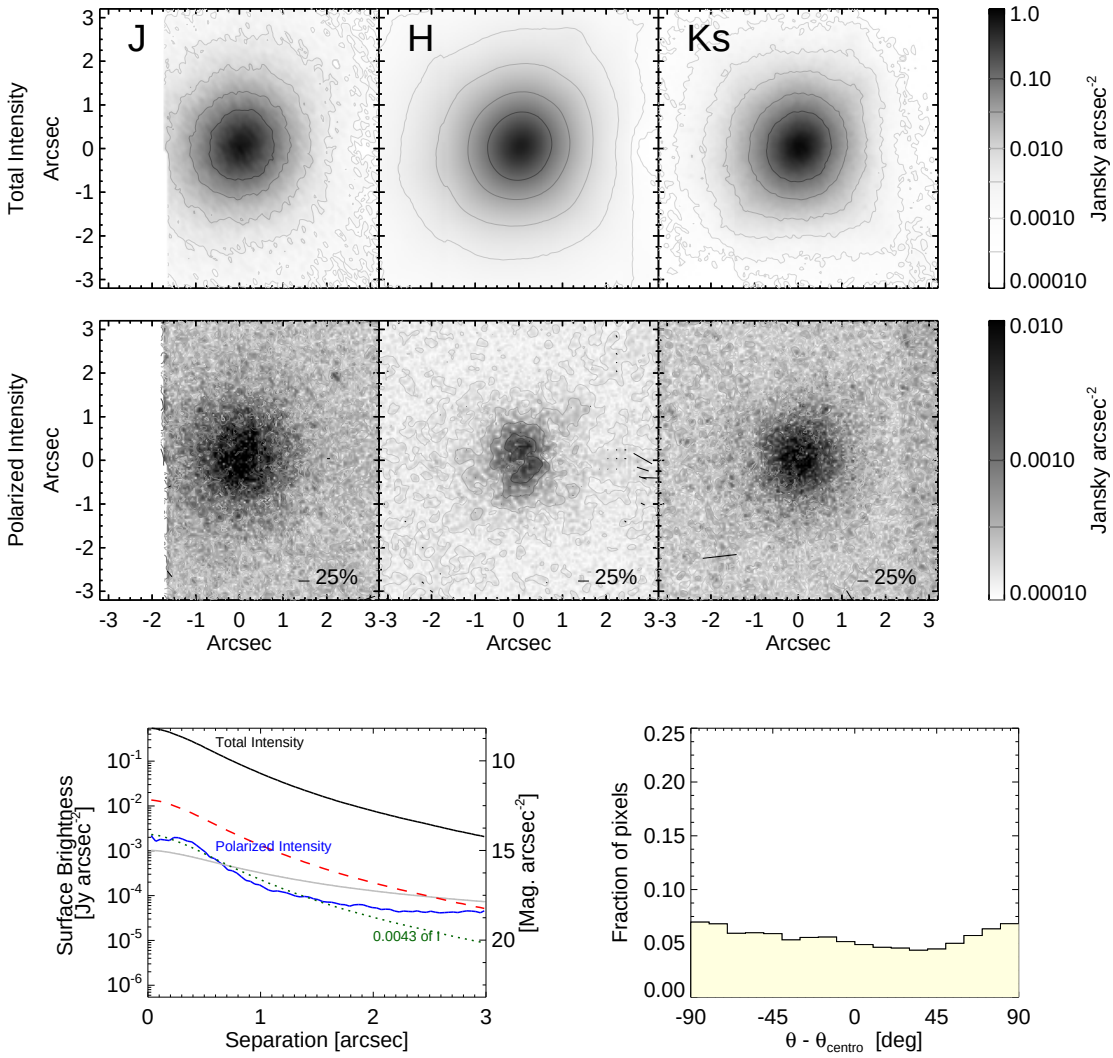

Figure 4.107: Imaging polarimetry of PDS 543.

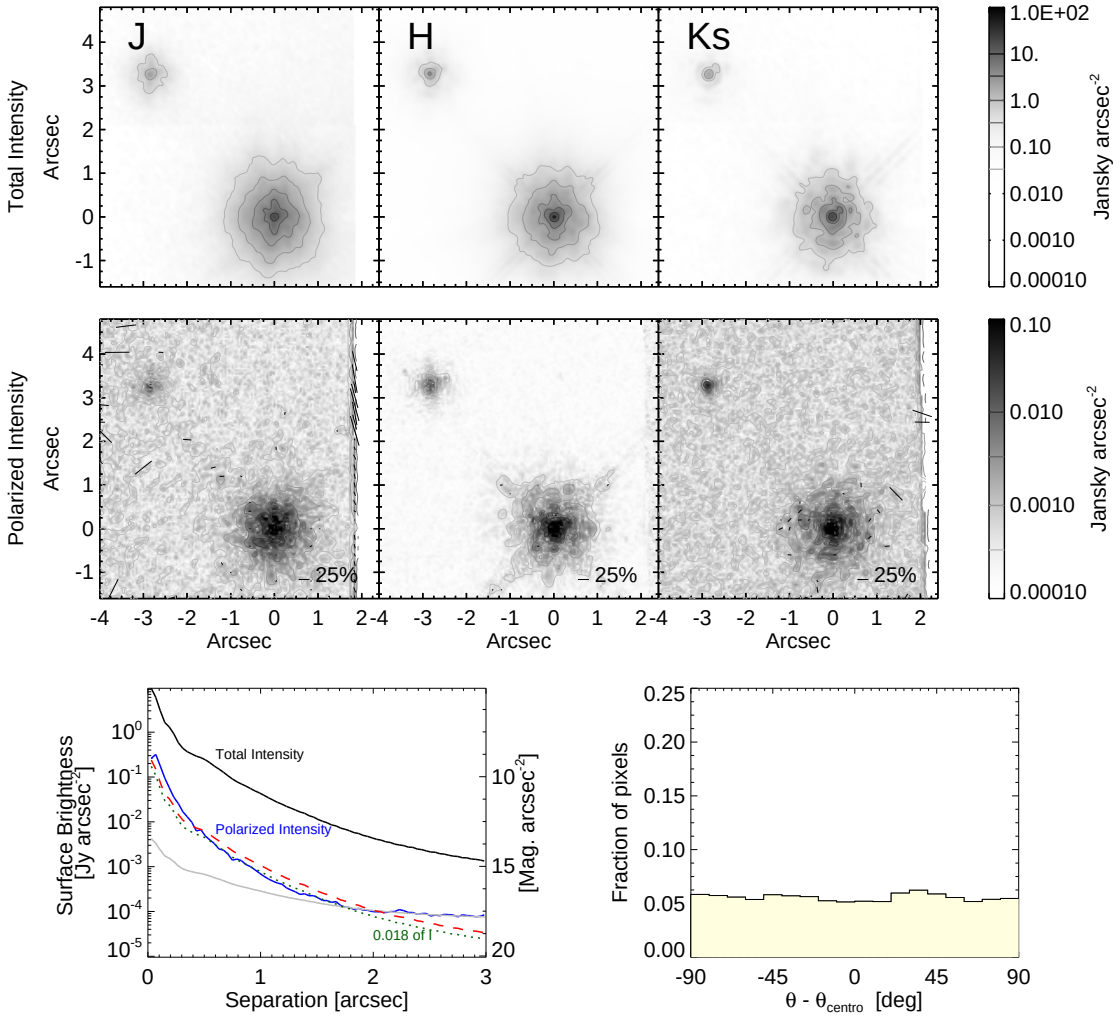

Figure 4.108: Imaging polarimetry of MWC 610.

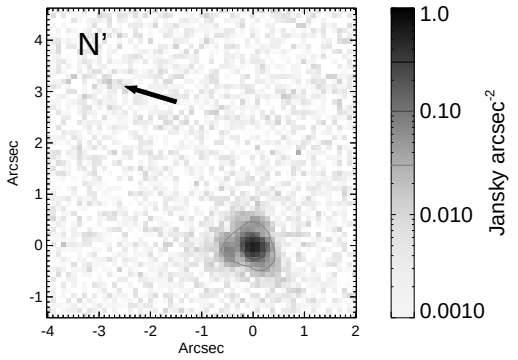

Figure 4.109: Mid-IR imaging of MWC 610. The arrow indicates the position of MWC 610 B, faintly detected.

was detected in the near-IR (Fig. 4.110). Several nearby sources are visible in our field of view, but given its location essentially on the galactic plane, they are likely to be unrelated field stars.

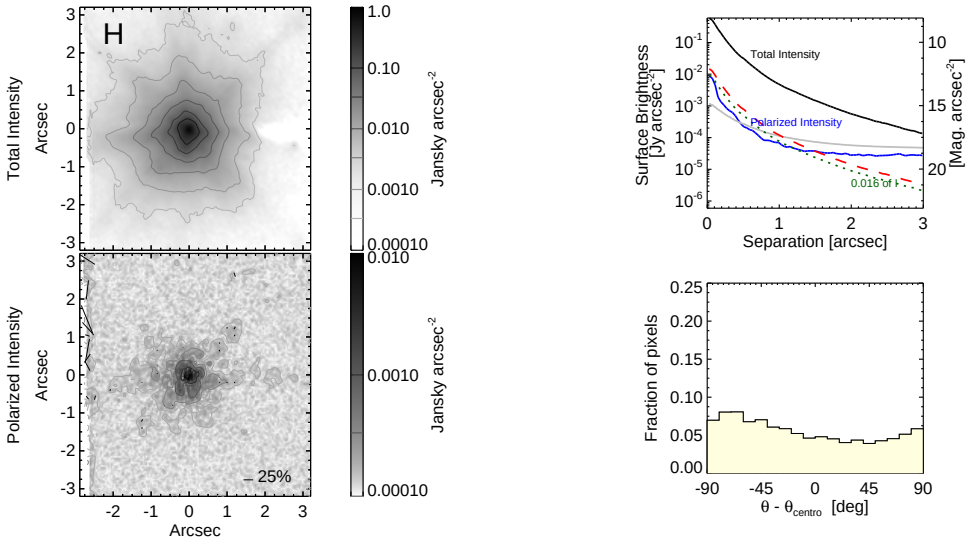

Figure 4.110: Imaging polarimetry of PDS 551.

4.5.74 HD 179218

HD 179218 is an A0 V star located at a distance of 200-240 pc, with $V = 7.2$ (van den Ancker et al., 1998; Vieira et al., 2003). Extensive mid-IR spectroscopy has revealed the presence of crystalline silicates and PAHs around this star (Malfait et al., 1998; Acke & van den Ancker, 2004).

It was observed at Lick on 2003-07-21 UTC in good conditions, and again on 2004-07-05 in excellent conditions, and at Gemini North on date 2005-07-01 UTC. No polarized light was detected in the near-IR (Fig. 4.111) nor was the star resolved the mid-IR (Fig. 4.112). Two $\Delta H \sim 5$ potential companions are visible within $3\farcs5$.

4.5.75 WW Vul

WW Vul is an A3 star (Hernández et al., 2004) located at a distance of 550 pc (Pirzkal et al., 1997), with $V = 10.7$, and is a member of the UX Orionis stars (Natta et al., 1997). It was observed at Lick on 2004-07-05 UTC in excellent conditions. No polarized light was detected in the near-IR (Fig. 4.113).

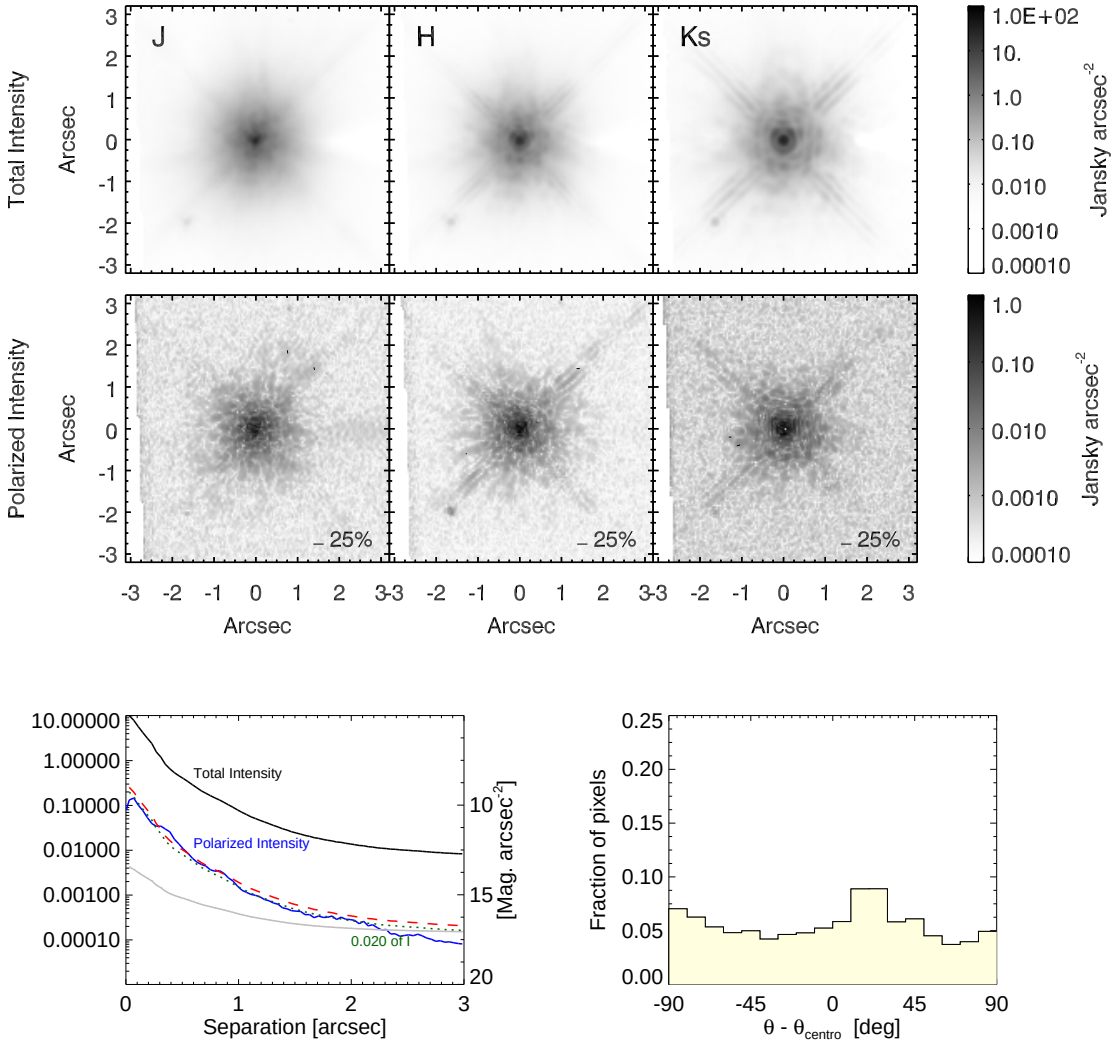

Figure 4.111: Imaging polarimetry of HD 179218.

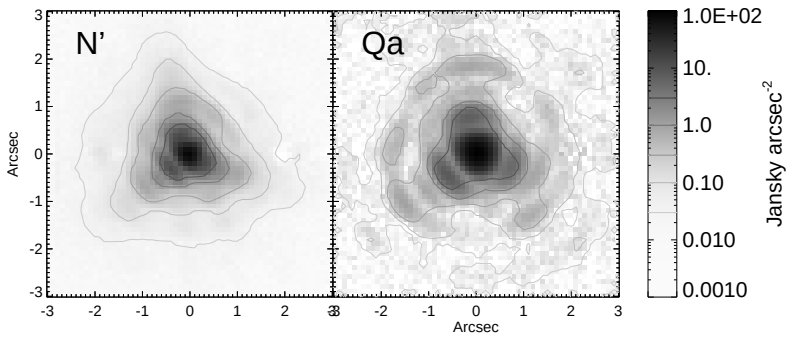

Figure 4.112: Mid-IR imaging of HD 179218.

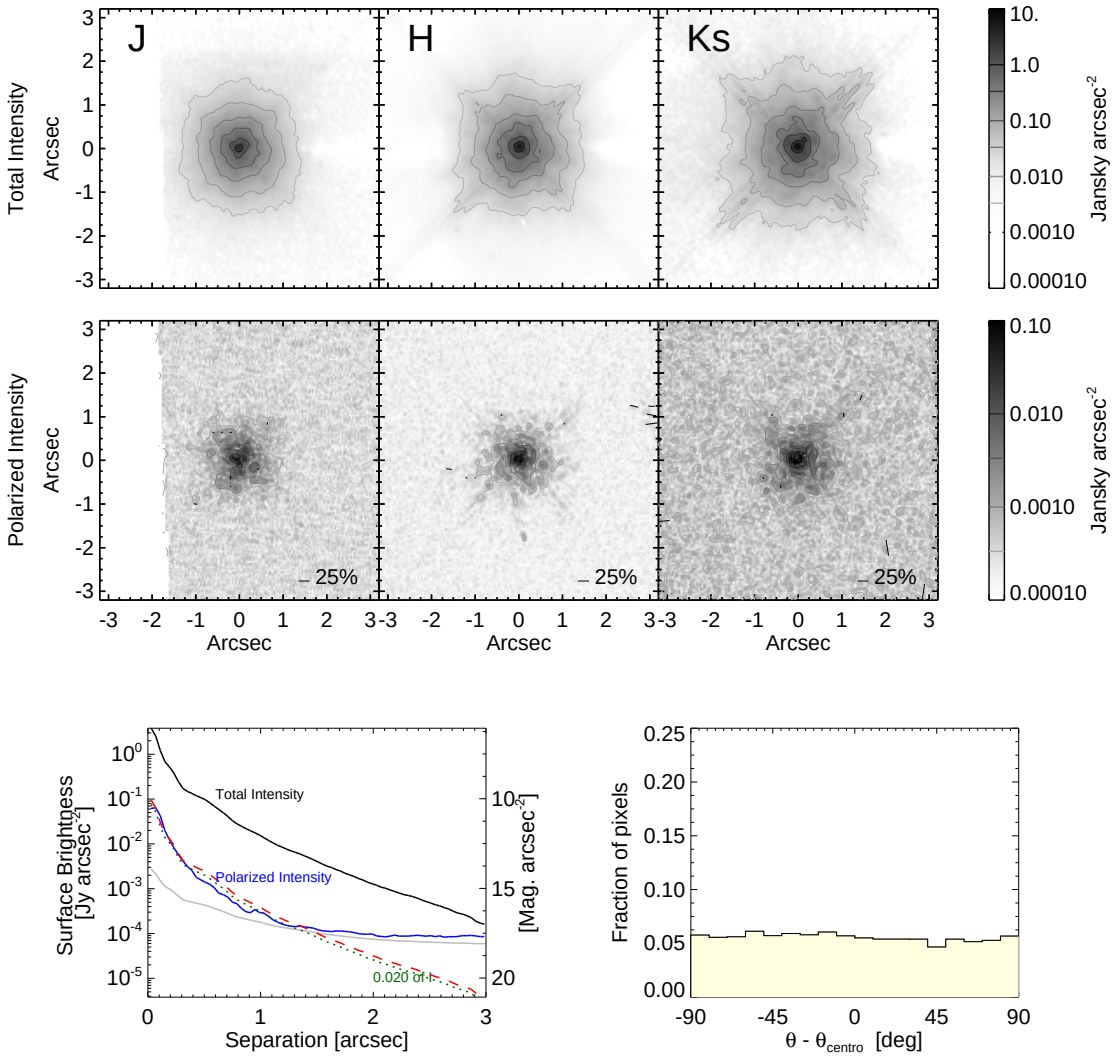

Figure 4.113: Imaging polarimetry of WW Vul.

4.5.76 PX Vul

PX Vul, also called RNO 110 and HBC 293, is a F3 star (Hernandez et al., 2004) located at a distance of 420 pc (Herbst et al., 1982), with $V = 11.7$.

It was observed at Lick on 2004-09-08 UTC in excellent conditions. No polarized light was detected in the near-IR (Fig. 4.114)

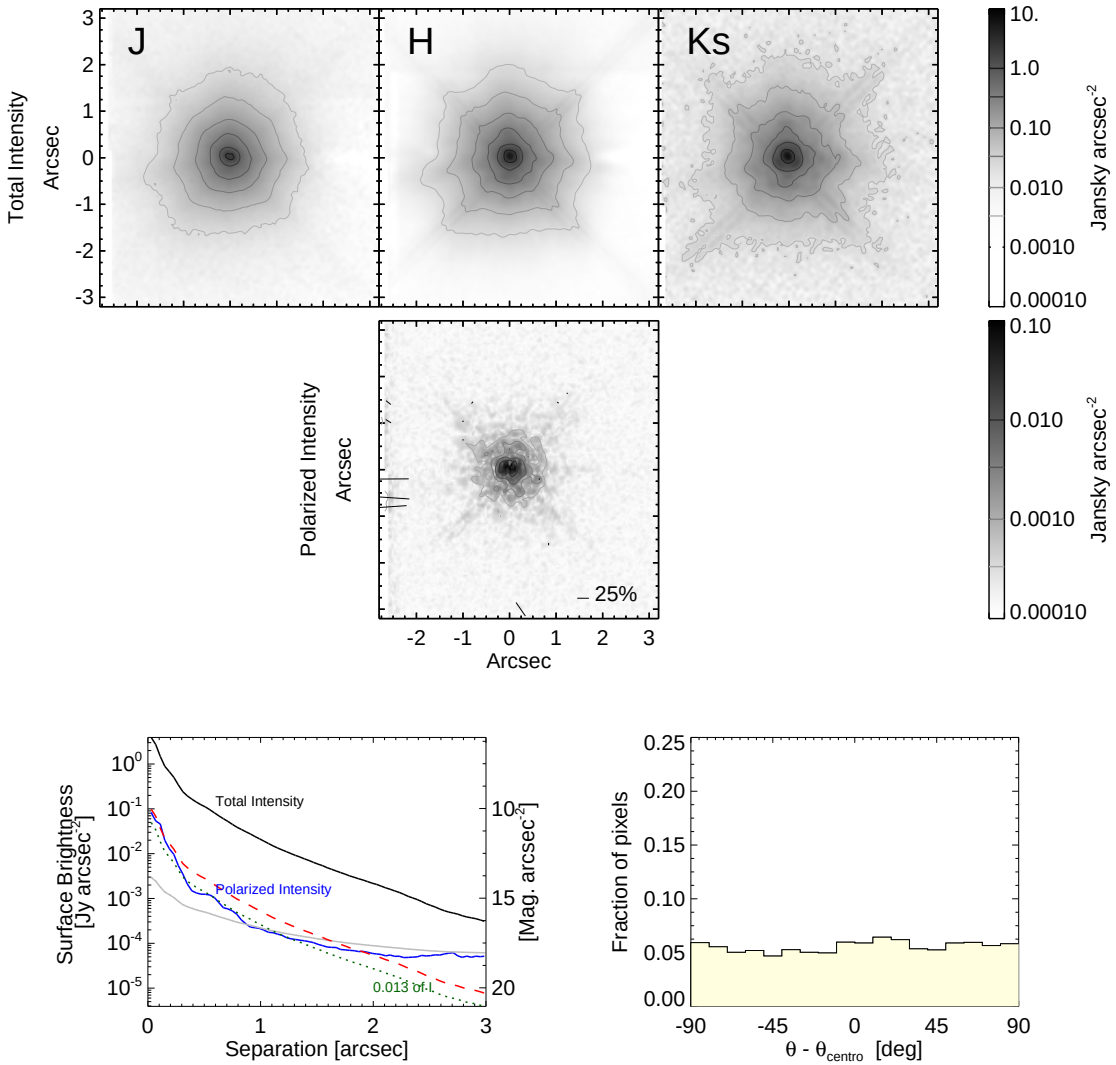

Figure 4.114: Imaging polarimetry of PX Vul.

4.5.77 Parsamian 21

Parsamian 21 is a $V = 13.9$ F8 or A5V FU Orionis star (Hillenbrand et al., 1992; The et al., 1994) located at a distance of 400 pc (Hillenbrand et al., 1992). It sits at the head of a cometary nebula extending to the north. It was unresolved in the millimeter observations of Henning et al. (1998).

It was observed at Lick on 2004-07-04 UTC in excellent conditions, and at Keck on 2004-07-26 UTC. In the near-IR it takes the form of a highly polarized three-pronged, "y" shaped nebula. Were this a *four*-lobed nebula, it would be very similar to several other sources with envelopes and bipolar cavities, but here the fourth lobe is absent. However, hints of such a lobe are faintly visible on deep Keck LGSAO images, and OSIRIS imaging spectroscopy detects [FeII] 1.644 μm emission along the central axis of this source, consistent with a polar outflow oriented north-south. (Perrin et al., in prep.)

The star was not significantly resolved in the mid-IR (Fig. 4.116). The apparent extension of the PSF to the north is probably an LWS PSF artifact.

4.5.78 HD 190073

HD 190073, also known as MWC 325, is a B9-A2 star which has recently been recognized to be a Herbig Ae star after some decades in which it was thought to be a post-main-sequence star (Allen & Swings, 1976; Cidale et al., 2000; Mora et al., 2001; Vieira et al., 2003). It is located at a distance of ≥ 290 pc (van den Ancker et al., 1998). Pogodin et al. (2005) presented high resolution UV and optical spectra of this star, revealing a forest of time-variable emission lines unique among Herbig Ae stars, which they interpreted in terms of a complex wind flowing from the star, possibly pole-on to Earth.

It was observed at Lick on 2004-09-08 UTC in excellent conditions, and at Gemini North on 2005-07-01 UTC. No polarized light was detected in the near-IR (Fig. 4.117), nor was it resolved in the mid-IR (Fig. 4.118).

4.5.79 HBHA 3203-03

HBHA 3203-03 is a B star (Leinert et al., 1997) located at a distance of 1000-4500 pc (Leinert et al., 1997), with $V = 16.0$. As "G70.7+1.2", this star was observed by Leinert et al. (2001), who report a strong infrared halo at all wavelengths from $1 - 5$ μm. The name "G70.7+1.2" more properly refers to the HII region around the star, and we prefer

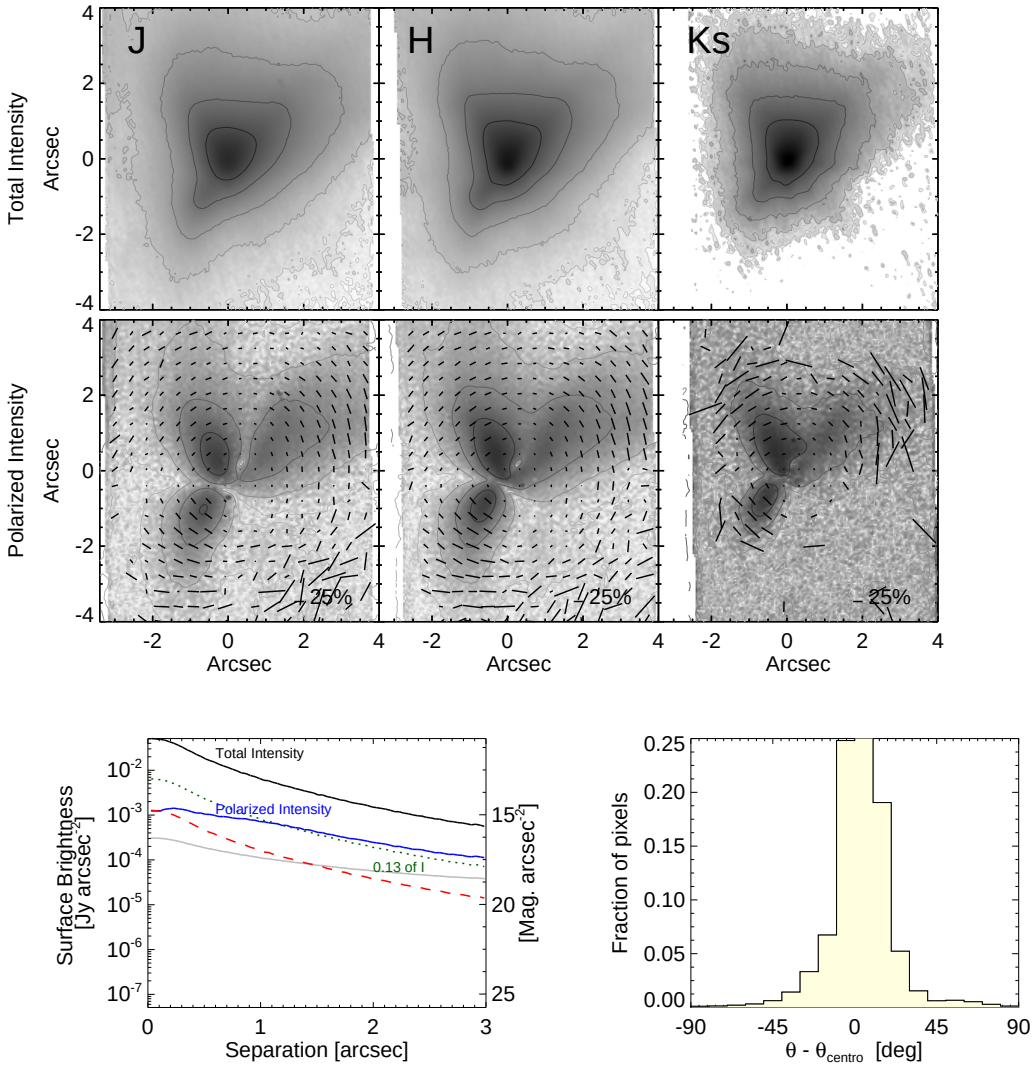

Figure 4.115: Imaging polarimetry of Parsamian 21.

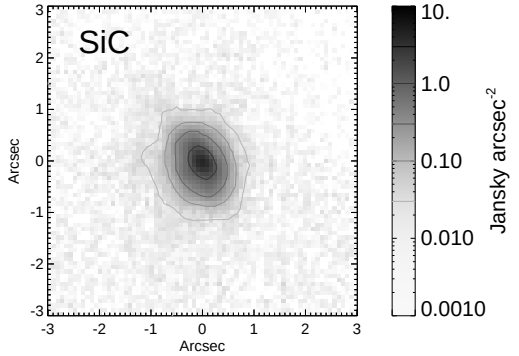

Figure 4.116: Mid-IR imaging of Parsamian 21.

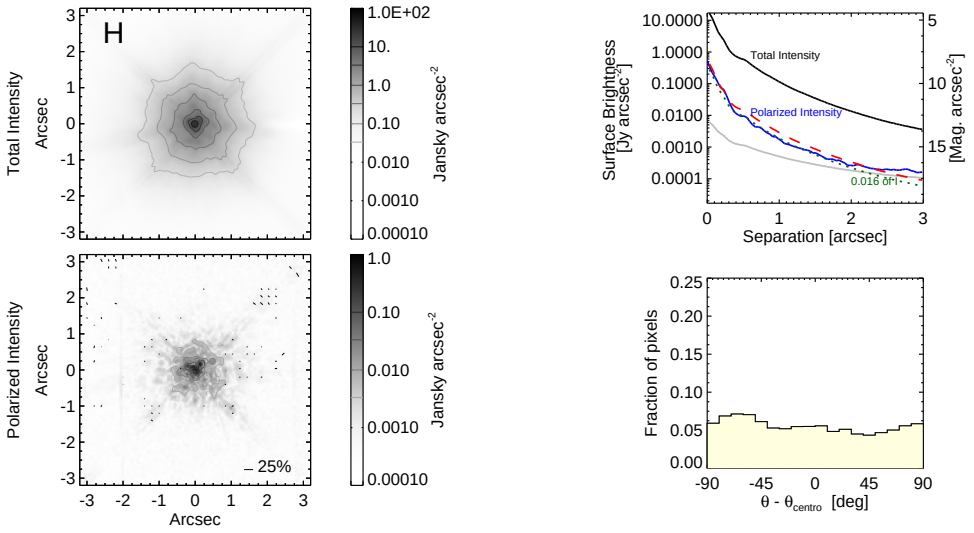

Figure 4.117: Imaging polarimetry of HD 190073.

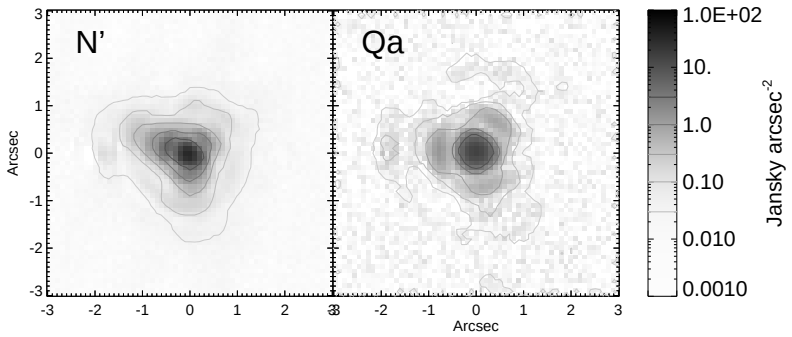

Figure 4.118: Mid-IR imaging of HD 190073.

to refer to this object by its stellar designation from the Hamburg-Bergedorf Hα survey, HBHA 3203-03.

It was observed at Lick on 2006-07-10 UTC in good conditions. No polarized light was detected in the near-IR (Fig. 4.119) Prominent nebulous arcs are detected to the west of the star at all NIR wavelengths. These arcs are clearly seen in the total intensity images as well as in polarized intensity. A small cluster of stars is also seen surrounding HBHA 3203-03. There are two main arcs, one extending from about 7.″5 east of the star to 5.″2 northeast, and the other extending from 3.″7 southeast to 9″, almost due north. A faint bar of emission is also seen 8.″5 northwest of the star in our H image, but it is mostly off the field of view of our J data and too faint to be detected in K_s.

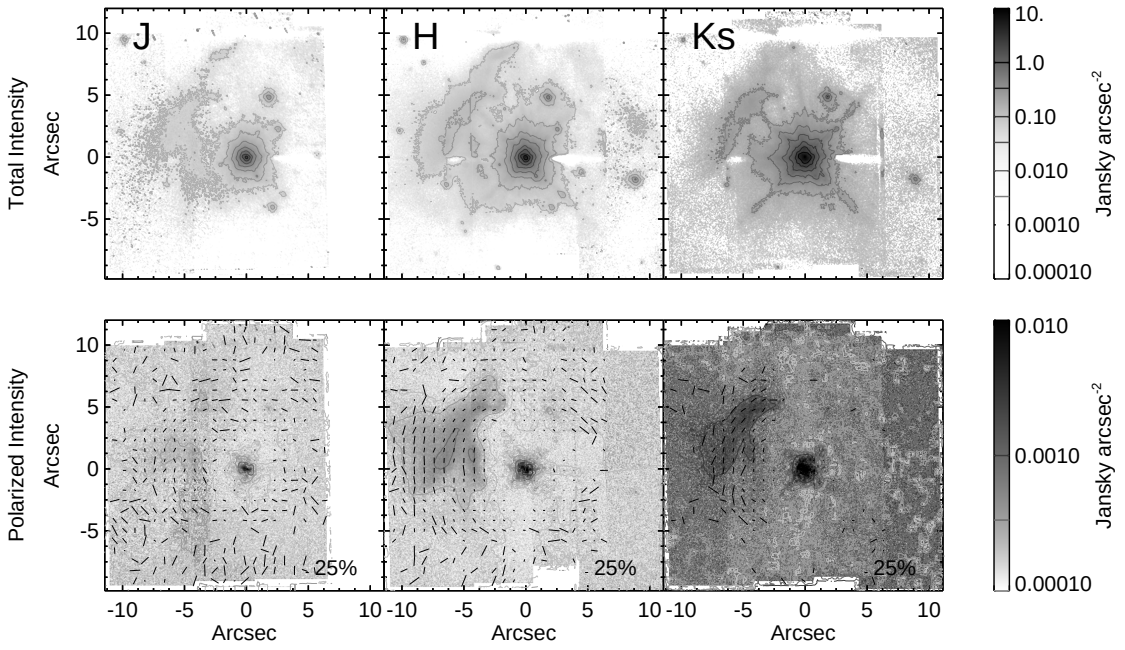

Figure 4.119: Imaging polarimetry of HBHA 3203-03.

4.5.80 BD +40 4124

BD +40 4124 is a B3 star (Hernández et al., 2004) located at a distance of 980 pc (van den Ancker et al., 1998), with $V = 10.7$. It is the optically-brightest star in a very young, small cluster also containing LkHα 224 and LkHα 225; see Hillenbrand et al. (1995) for detailed discussion of this cluster and its properties. It has a $0\farcs7$ companion at PA=239°(Bouvier & Corporon, 2001). This companion is barely detected in our IRCAL data; it is essentially indistinguishable from a bright speckle and is only identifiable as a companion based on its prior detections from the literature. Leinert et al. (2001) detect a faint $1\farcs1$ infrared halo around this star.

It was observed at Lick on 2004-07-06 UTC in excellent conditions, and on 2005-11-23 in good conditions, and at Keck on 2004-08-27 UTC. The star was not resolved in the mid-IR (Fig. 4.121). A peak in the centrosymmetry histogram indicates the presence of polarized light scattered from circumstellar dust. This polarized light takes the form of an extremely faint nebula stretching south and southwest from the star. This nebula is detected at relatively low signal to noise, no more than $3 - 4\sigma$ per $0\farcs2$ smoothed region and typically much less. However, it has much larger spatial extent than the halo reported by Leinert et al., extending at least $7''$ to the edge of our field of view. Close examination of the Stokes Q and U images provides evidence for nebulosity north of the star as well, but even fainter still.

4.5.81 LkHα 224

LkHα 224, also called V1686 Cyg, is a irregularly variable PMS star located in the the same young cluster containing BD +40 4124 and LkHα 225, at a distance of 980 pc (Hillenbrand et al., 1995). Its spectral type is extremely uncertain, with estimates including B2 (The et al., 1994), B5 (Hillenbrand et al., 1995), A5 (Mora et al., 2001), F2 (Terranegra et al., 1994) and even F9 (Hernández et al., 2004). Hernández et al. note that these discrepancies may be related to the high time-variability of its spectral features. Along with its extreme photometric variability, this places LkHα 224 into the class of UX Ors.

It was observed at Lick on several occasions; we show below the data from 2003-11-05 which best display the circumstellar dust. Like a diamond set into an engagement ring, LkHα 224 is located at one edge of a ring of dust, whose existence was first reported by

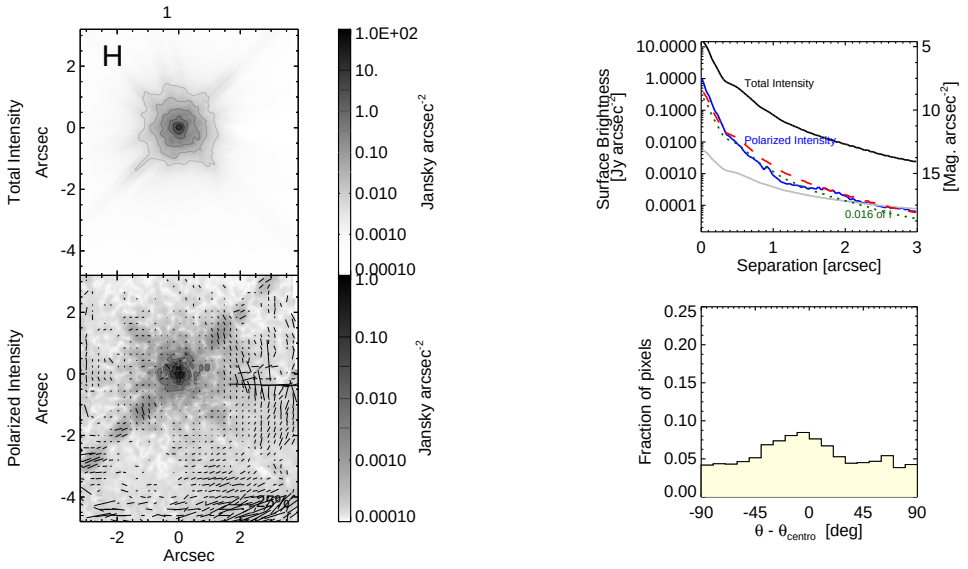

Figure 4.120: Imaging polarimetry of BD +40 4124. In order to show the faint polarization, vectors are shown for any region with SNR > 1.5 per 0.″2 (5-pixel) smoothed region, as opposed to the usual SNR > 3 masking.

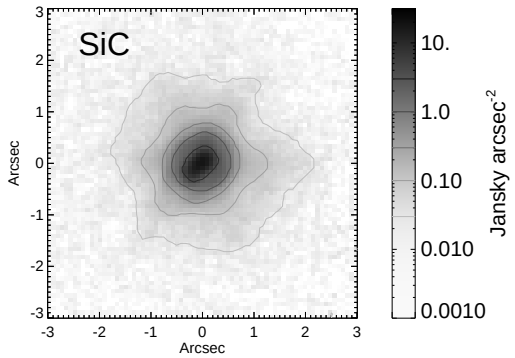

Figure 4.121: Mid-IR imaging of BD +40 4124.

Hillenbrand et al. (1995). The ring extends towards the southeast (PA $\sim 130°$), and the side more distant from LkHα 224 is broader and more extended than the portion of the ring it "sits on". It is somewhat elliptical, with a major axis of approximately $9\farcs5$ and a minor axis of $7\farcs5$.

Also visible in the IRCAL data are the nearby objects recorded as stars 5 and 6 from Hillenbrand et al. (1995). Star 5 turns out to be an $0\farcs3$, equal-magnitude binary. Our Keck mid-IR observations did not resolve LkHα 224 in the mid-IR (Fig. 4.123), nor are any of the nearby sources detected. The mid-IR photometry is fairly consistent with that of Strom et al. (1972), despite the fact that LkHα 224 is known to vary by nearly 5 mag. in the optical.

It is tempting to associate the observed dust ring with the circumstellar dust that is believed to be responsible for LkHα 224's variability. But what then is the origin of the ring? Is it actually a physical ring of dust? More plausibly, we may be seeing the edges of a cavity excavated in circumstellar dust by a stellar outflow, with the opposing bipolar cavity embedded and invisible. Indeed, millimeter observations show that LkHα 224 is located on the edge of a ridge of dust, lending support to this picture (Henning et al., 1998).

4.5.82 LkHα 225

LkHα 225, also called V1318 Cyg, is a $5''$ binary consisting of a Herbig Be primary and a T Tauri secondary, located to just the southwest of BD +40 4124 at a distance of 1000 pc (Davies et al., 2001). It has been proposed that LkHα 225 consists of a young, low-mass star, LkHα 225 N, and an intermediate-mass, very young Herbig Ae/Be star, LkHα 225 S, based on luminosity arguments (Aspin et al., 1994). The two stars have JHK colors and K-band spectra typical of YSOs, with an additional component of emission coming from a more extended envelope; the extinction to the stars is $A_V \sim 10$ mag (Davies et al., 2001).

It was observed at Lick on 2003-07-22 UTC in good conditions, and at Keck on 2004-07-25 and 2004-08-28. Both components of the binary are detected in the mid-IR, with the southern remaining the more luminous (Fig. 4.125). No extended mid-IR emission is visible.

In the near-IR, a comma-shaped reflection nebula extends from LkHα 225N towards LkHα 225S (Davies et al., 2001). This appears as the bright filament evident in our imaging polarimetry. We discover a fainter bar extending west from LkHα 225S. In these

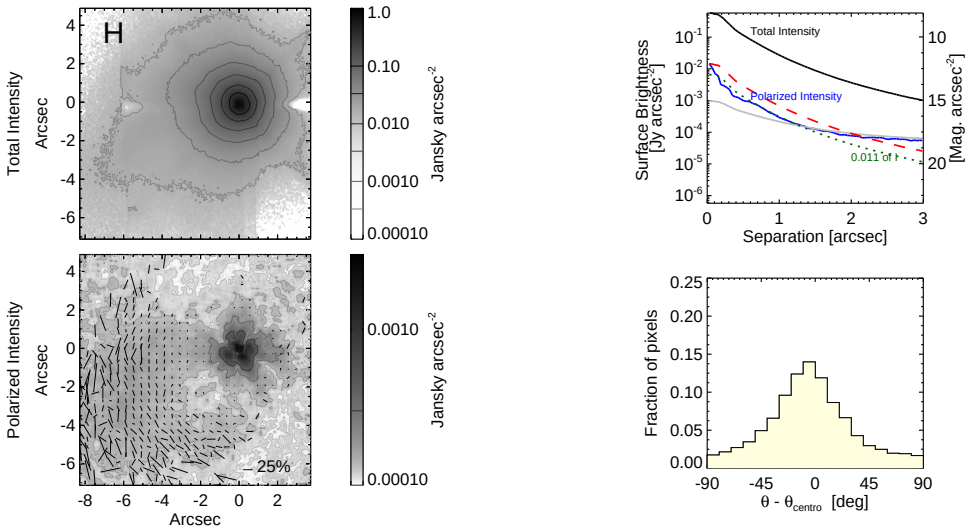

Figure 4.122: Imaging polarimetry of LkHα 224.

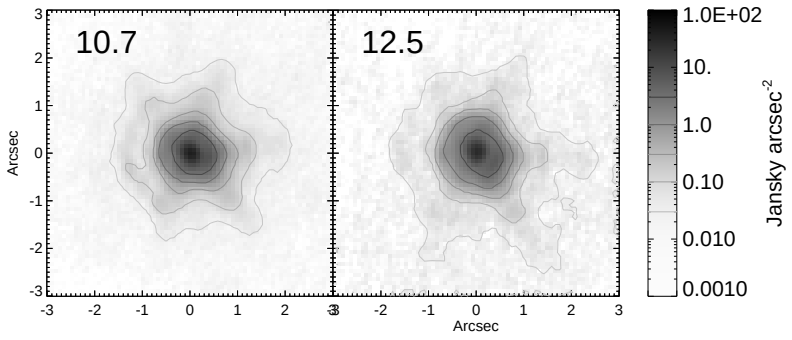

Figure 4.123: Mid-IR imaging of LkHα 224.

new observations a continuous streamer can be traced from the NW of LkHα 225N, though LkHα 225S and terminating 2″ west of LkHα 225S. A disconnected region of scattered light appears about 4″ NE of LkHα 225S; the polarization position angle indicates that this is illuminated by LkHα 225S. We measure at H band the binary position angle of LkHα 225 to be 356° and the separation 4.″9, or about 4800 AU at the distance of the cluster (980 pc, Hillenbrand et al., 1995). We also detect three nearby faint point sources, with $\Delta H = 4.9, 4.9, 5.5$; $\rho = 10.''8, 3.''3, 3.''5$ and PA= $350°, 140°, 130°$ respectively relative to 225S.

The orientation of the polarization vectors confirms that both LkHα 225N and 225S illuminate the filament: the vectors are centered on 225N at the north end of the filament, changing smoothly to the south to become centered around 225S. These objects are thus physically associated rather than just being a chance line-of-sight alignment. The polarization is highest on the inner side of the curved filament, facing towards 225N; the outer side may be less polarized due to higher optical depth resulting in multiple scattering, or because illumination from both 225S and 225N arrives from different position angles. Likewise, there is an indication that LkHα 225N has a faint bar to its north.

The filament may be a remnant from the collapse of the cloud core from which the stars formed, may be associated with the outflow from LkHα 225S, or as the morphology suggests, may be material tidally stripped from the circumstellar environments of LkHα 225 N and S in a close encounter. It has been proposed that drag caused by gravitational star-disc interactions could be an important binary formation mechanism (Larson, 1990). For the most common encounters, in which the periastron distance is much greater than the disc radius, energy and angular momentum are in general transferred from the disc to the stars (Ostriker, 1994). Thus long-range encounters do not provide a mechanism for capture. Further observations and modeling of this system will be necessary to estimate periastron passage. The putative tidal streamers in the field of LkHα 225 are resolved into clumps. Weak interactions can trigger fragmentation of the disc, via tidally and compressionally induced gravitational instabilities, leading to the formation of additional stars and substellar objects (Boffin et al., 1998).

The T Tauri system SR 24 also shows a bridge of material extending from SR 24 S to SR 24 Nab. As with LkHα 225, polarimetric observations have confirmed that this material is physically associated with the stars (Potter & Andrews, 2002). Comparative studies of these two objects may further illuminate the role of collisional encounters in

both low and intermediate mass star formation.

4.5.83 V1515 Cyg

V1515 Cyg is a FU Orionis star (Kenyon et al., 1991) located at a distance of 1000 pc (Racine, 1968), with $V = 12.3$. The Keck Interferometer has recently spatially resolved the near-IR emission from this system for the first time (Millan-Gabet et al., 2006).

It was observed at Lick on 2004-09-08 UTC in excellent conditions. No polarized light was detected in the near-IR (Fig. 4.126)

4.5.84 BD +41 3731

BD +41 3731 is a B3 star located at a distance of 1000 pc with $V = 9.9$ (Hillenbrand et al., 1992). It appears to be an extremely rapid rotator ($v \sin i \sim 400$ km s^{-1}, Finkenzeller and Mundt 1984); due to the lack of strong Hα emission and small IR excess, it is not clear whether this star is truly a Herbig Be star or instead a classical Be star. Van den Ancker et al. (1998) included it on their list of stars lacking evidence for circumstellar dust.

It was observed at Lick on 2004-10-30 UTC in poor conditions. No polarized light was detected in the near-IR (Fig. 4.127)

4.5.85 Parsamian 22

Parsamian 22 is an A5eV star (Calvet & Cohen, 1978) located at a distance of 1200 pc (Scarrott et al., 1993), with $V = 13.3$. Two companions are located just southwest of Parsamian 22 (Bouvier & Corporon, 2001).

It was observed at Lick on 2004-07-04 UTC in excellent conditions, and at Keck on 2004-07-26 UTC. Our observations resolve all three sources (though the faintest is only clearly detected in K_s band). Several clumps of polarized dust are visible around the star to the south, east, and northeast, and the two companions are also a few percent polarized.

In the mid-IR we resolve all three sources, though the the fainter is again only marginally resolved from its brighter neighbor. No extended emission is visible (Fig. 4.129).

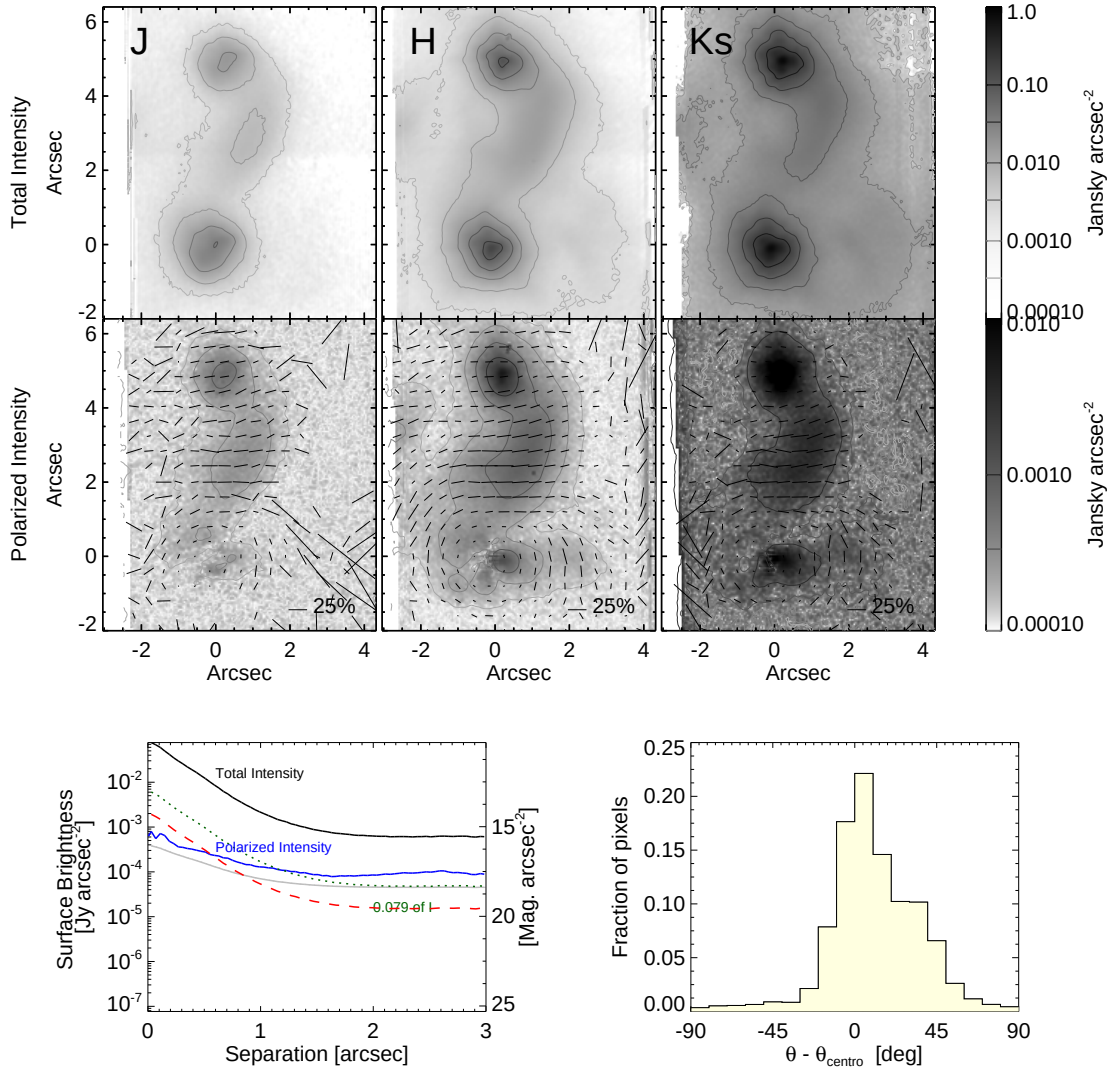

Figure 4.124: Imaging polarimetry of LkHα 225.

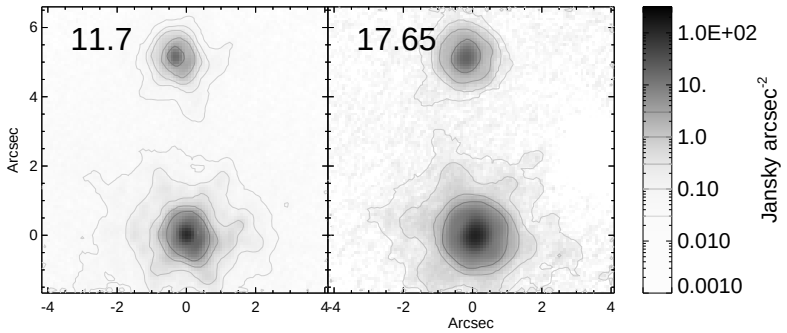

Figure 4.125: Mid-IR imaging of LkHα 225.

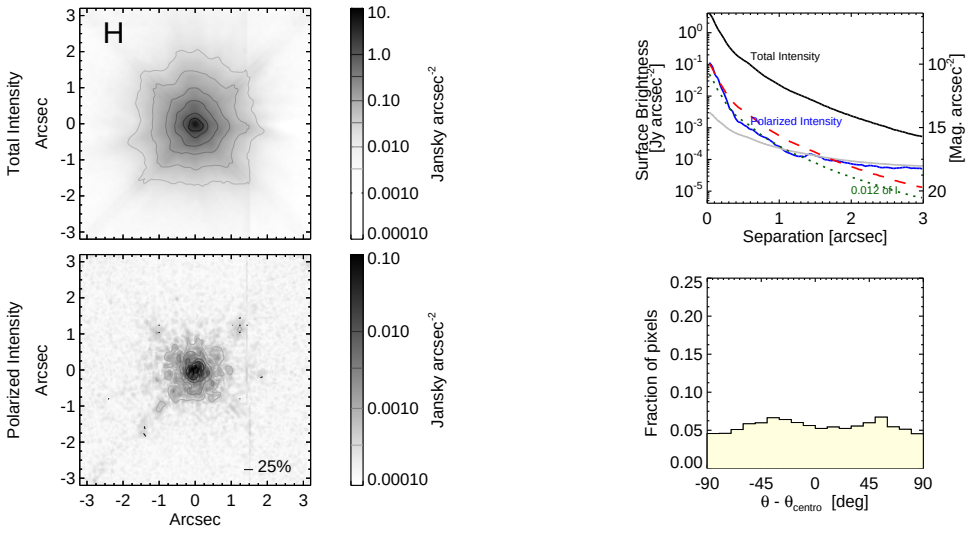

Figure 4.126: Imaging polarimetry of V1515 Cyg.

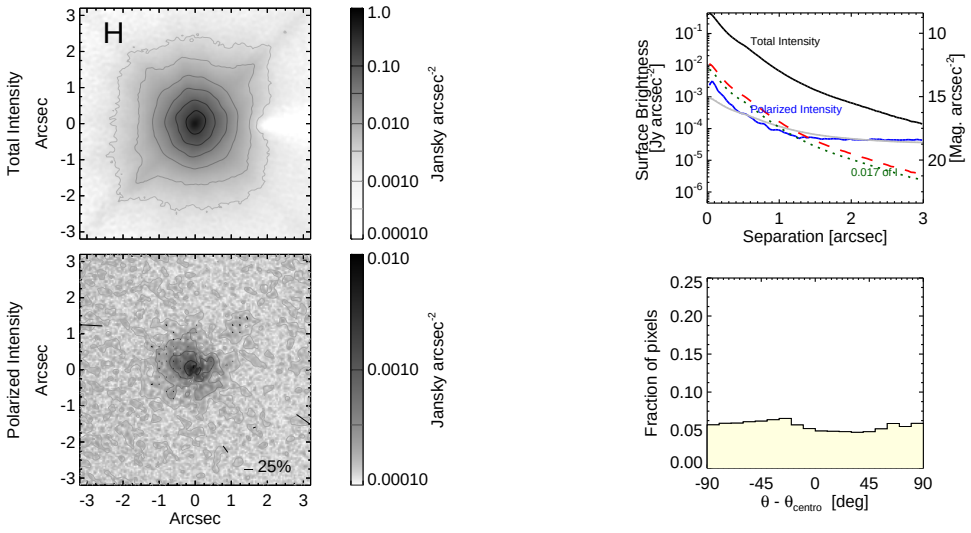

Figure 4.127: Imaging polarimetry of BD +41 3731.

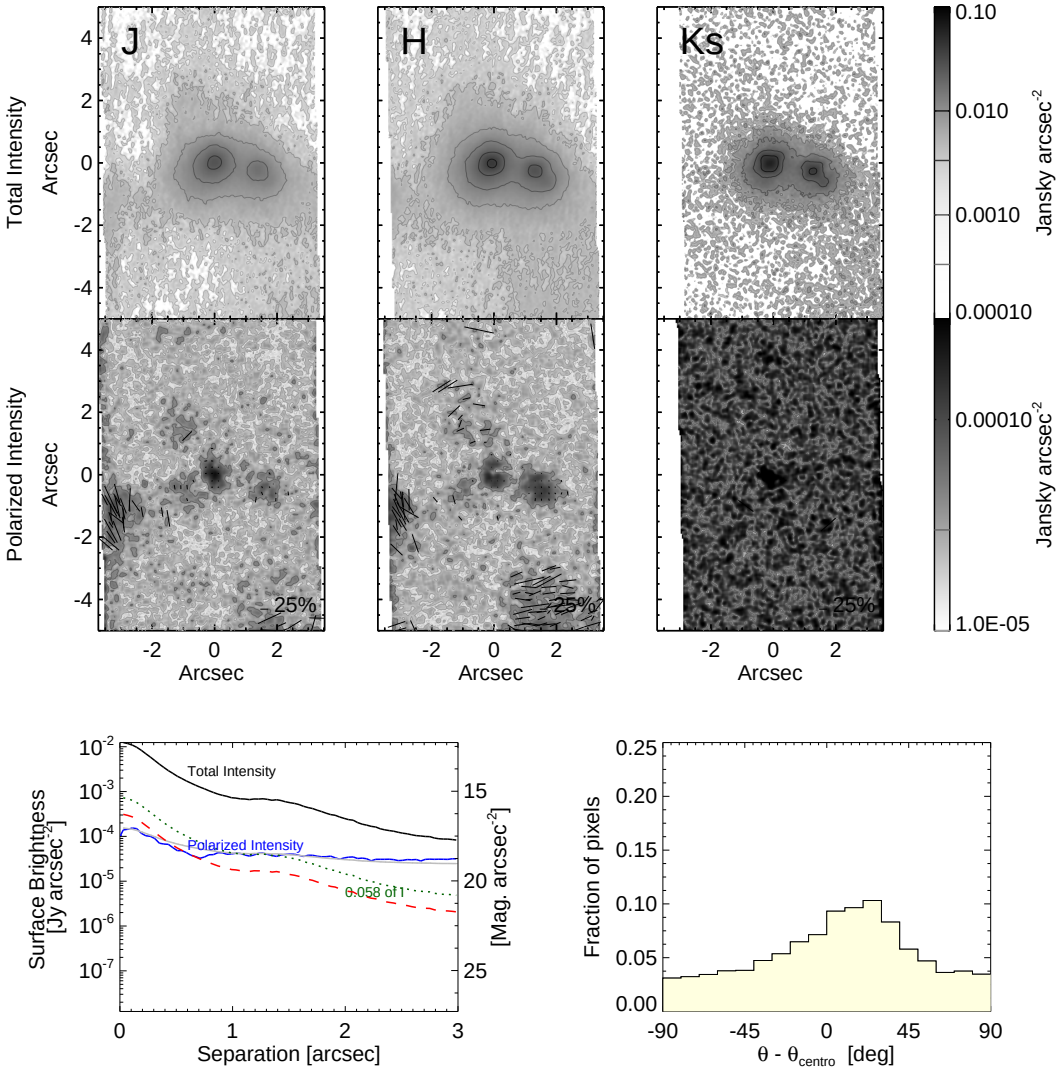

Figure 4.128: Imaging polarimetry of Parsamian 22.

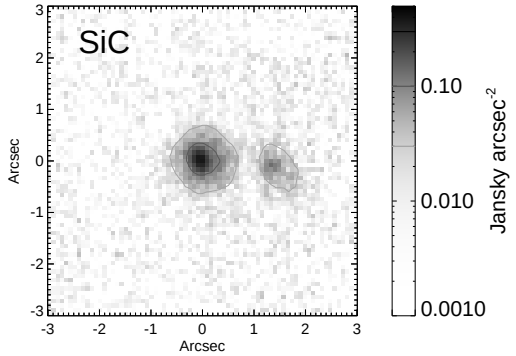

Figure 4.129: Mid-IR imaging of Parsamian 22.

4.5.86 MWC 349

MWC 349, also called V1478 Cyg, is a $V = 13.2$ apparent binary with a separation of $\sim 2.5''$. Component A has a large number of emission lines preventing a spectral classification more precise than "Be", while component B has spectral type BOIII. Radio observations reveal a square-ish nebula around the A component, split by a dark lane indicating a nearly edge-on circumstellar disk (Cohen et al., 1985; White & Becker, 1985). MWC 349 A has variously been interpreted as a pre-main-sequence Be star, an evolved B[e] supergiant, or several other possibilities; see White and Becker (1985) and Meyer et al. (2002) for an overview. It shows maser and laser emission at a wide range of wavelengths stretching from radio down to 19 μm, which may originate in a dense plasma created by photoionization of a passive circumstellar disk (Thum et al., 1998, and references therein). Keck aperture masking reveals a ~ 50 mas radius disk oriented at the predicted position angle of 100°(Danchi et al., 2001). Optical spectropolarimetry by Meyer et al. (2002) shows that the interstellar polarization towards MWC 349 is consistent with its being located in Cyg OB2, that MWC 349 A has a strong intrinsic polarization consistent with the presence of a circumstellar disk, and that the polarization level of MWC 349 suggests it may be a more distant background star rather than a physical companion. Because MWC 349 B is an apparently-evolved BOIII star, if it is not a bound companion then MWC 349 A is more plausibly pre-main-sequence.

MWC 349 was observed at Lick on 2004-09-07 UTC in excellent conditions, and at Keck on 2004-07-26 UTC. The centrosymmetry histogram has a peak near 0°, suggesting the presence of circumstellar dust, consistent with the high optical polarization of the star. However, the only formally significant polarization in these data is detected along the diffraction spikes, and the position vectors there are rather scattered (Fig. 4.130). By binning down the data to improve the SNR, greater evidence for a centrosymmetric polarization pattern appears within the inner $1\farcs5$ or so. The X-shaped nebula detected in the radio by White and Becker is unfortunately almost perfectly aligned with the IRCAL diffraction spikes, rendering any claimed detection here speculative at best. MWC 349 A appears unresolved in the mid-IR (Fig. 4.131).

In the AO images, I measure the position of MWC 349 B to be $\rho = 2\farcs78 \pm 0.01, \theta = 286°$ from MWC 349 A. This is significantly different from the $2\farcs4 \pm 0\farcs1$, PA=280°, reported by Cohen et al. (1985). A proper motion of $0\farcs4$ in 20 years translates to a space velocity of 113 km s^{-1} at the estimated distance of 1200 pc. This is far in excess of the escape velocity

the system would have if it were a true binary. *My IRCAL astrometry strongly suggests that these two stars are not physically associated.* Furthermore, the putative companion is much bluer than MWC 349 A: It has $J - K_s = 0.9$, versus $J - K_s = 3.05$ for MWC 349 A. The companion is not clearly detected at all in our 11.7 μm LWS data, though one of the PSF diffraction spikes from the very bright MWC 349 A falls near its position, limiting our detection sensitivity. I caution that the observed change in the separation of the two stars is in a different direction from that expected based on the USNO UCAC2 proper motion, and that the spectrum of the B component does have a few emission lines of H, possibly though not necessarily suggesting a young age. Still, the astrometry, combined with the very different colors of these two stars, seems to indicate that they are not physical companions.

4.5.87 AS 442

AS 442 is a B8Ve star (Mora et al., 2001) located at a distance of 600 pc (Eisner et al., 2004), with $V = 11.0$. Corporon & Lagrange (1999) found it to be a single-lined spectroscopic binary. PTI interferometric observations by Eisner et al. (2004) suggest the presence of a disk a few milliarcseconds in radius and with inclination $\sim 47°$, though Eisner notes that a binary star model gives an even better fit to the data. Keck Interferometer observations by Monnier et al. (2005) give a similar result.

It was observed at Lick on 2004-09-07 UTC in excellent conditions, and at Keck on 2004-08-27 UTC. AS 442 is unresolved in both my NIR and MIR observations (Figs. 4.5.87, 4.133. A possible companion is detected in the near-IR at $\rho = 4\farcs74 \pm 0.01, \theta = 54.28°$ with $\Delta H = 5.35$ mag.

4.5.88 LkHα 134

LkHα 134 is a B2 star located at a distance of 700 pc, with $V = 11.3$ (Corcoran & Ray, 1998b). It was observed at Lick on 2004-10-31 UTC in mediocre conditions, and at Gemini North on 2005-06-30 UTC. No polarized light was detected in the near-IR (Fig. 4.134), nor was the star resolved in the mid-IR (Fig. 4.135).

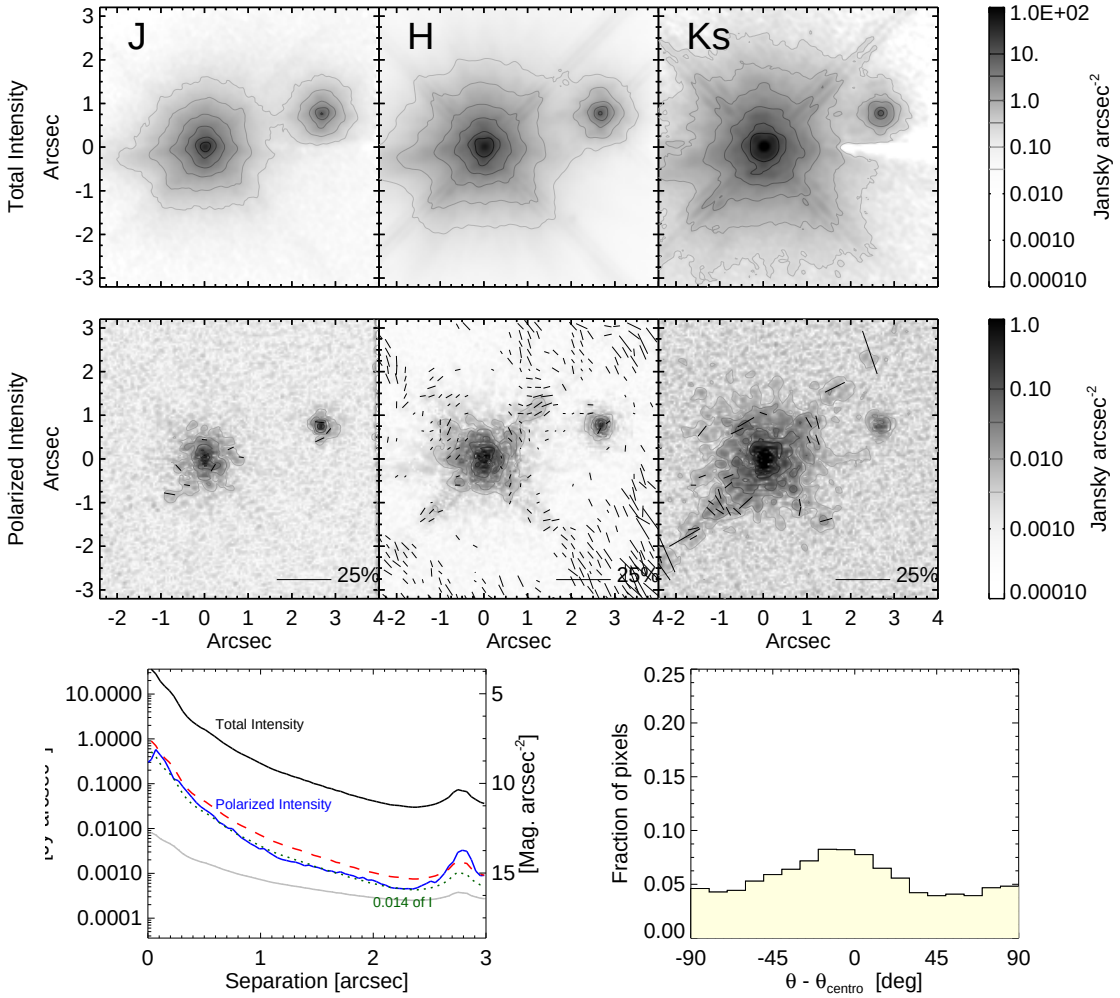

Figure 4.130: Imaging polarimetry of MWC 349.

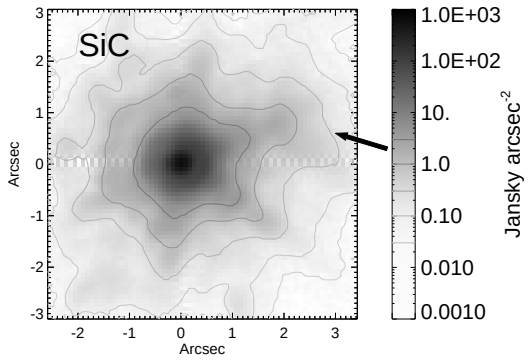

Figure 4.131: Mid-IR imaging of MWC 349. The arrow indicates the position of MWC 349 B from our AO image. There is an extension of the 0.3 Jy arcsec^{-2} contour near this position, but no convincing detection.

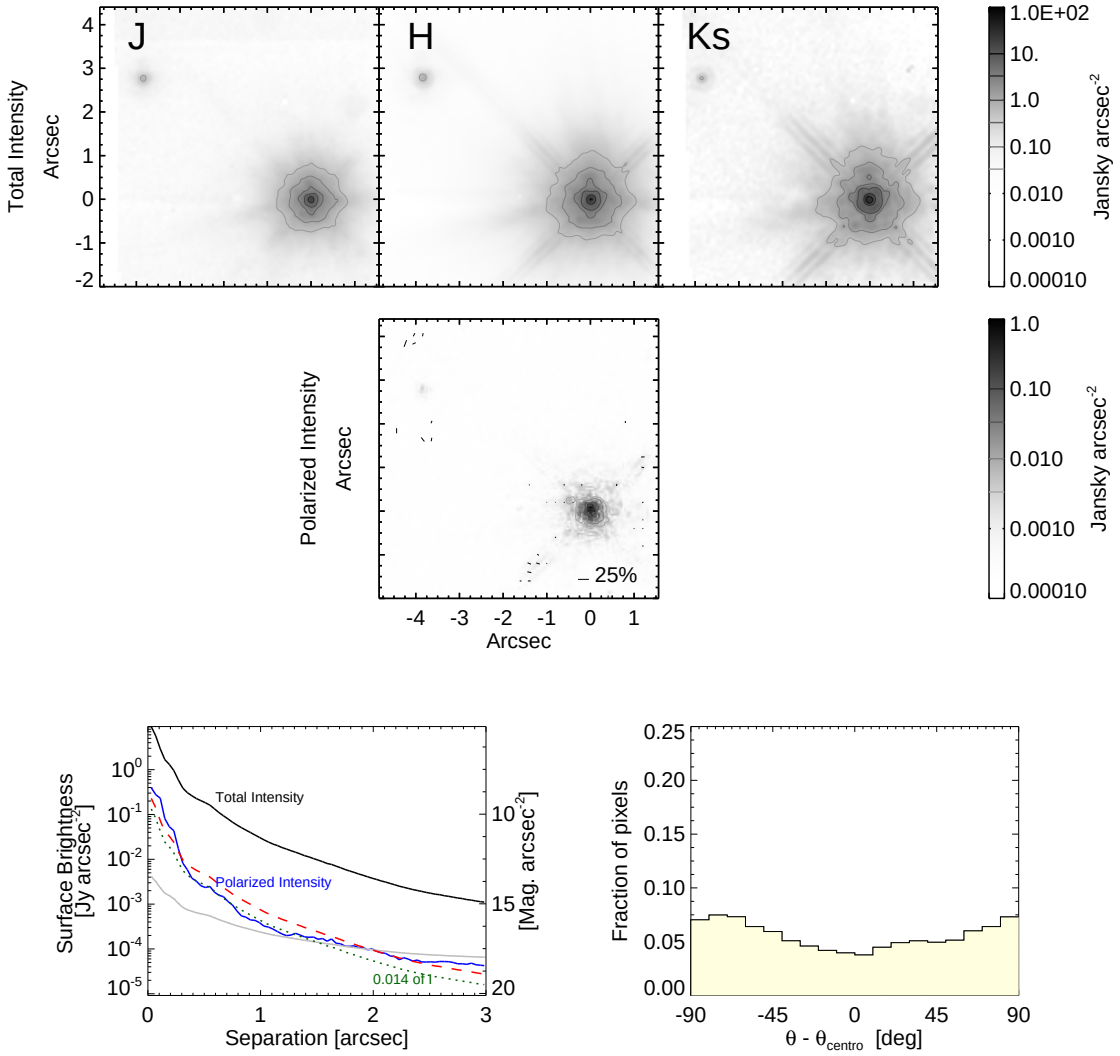

Figure 4.132: Imaging polarimetry of AS 442.

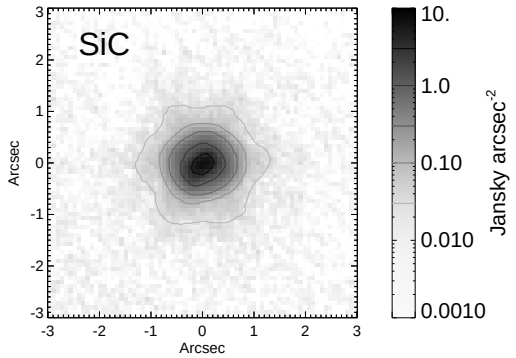

Figure 4.133: Mid-IR imaging of AS 442.

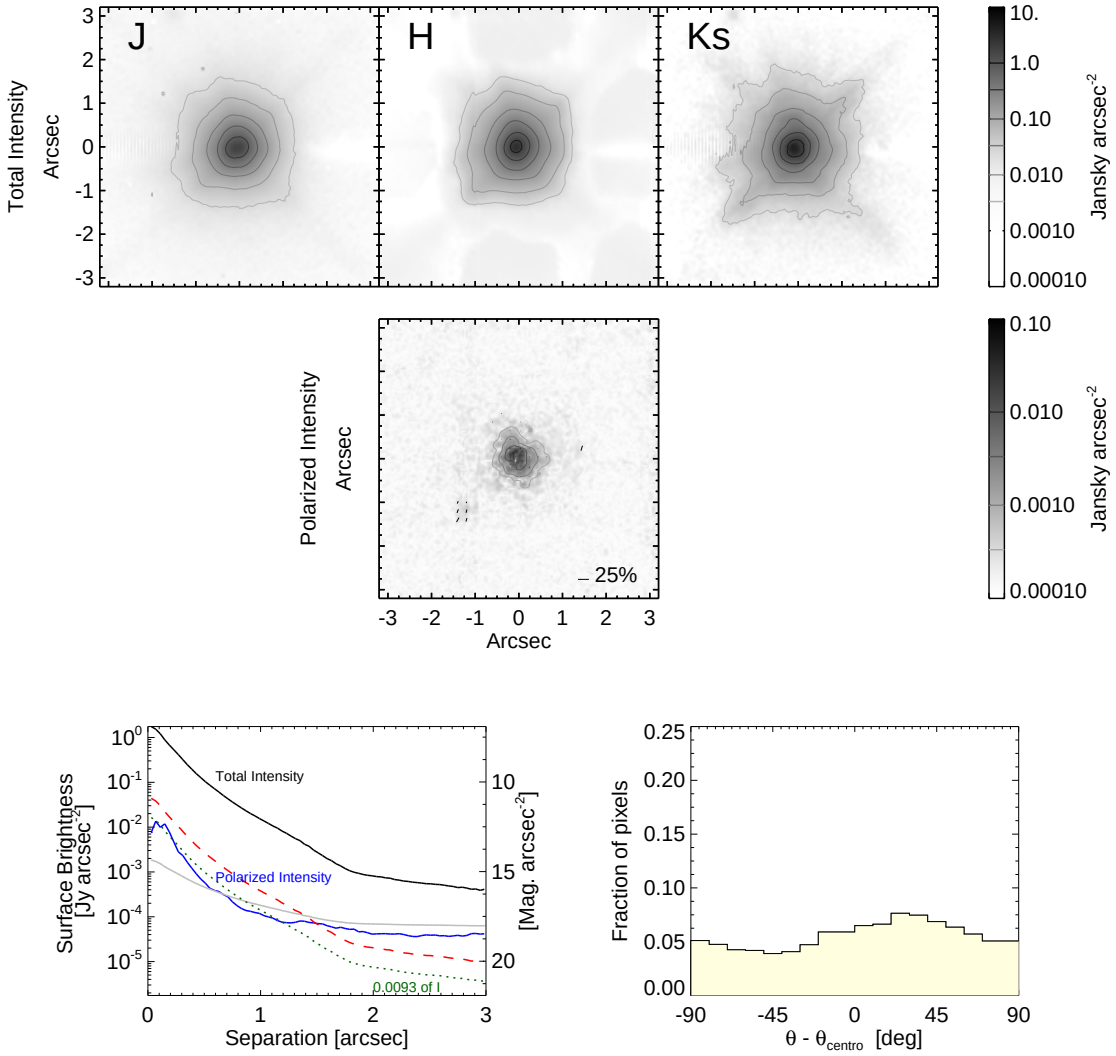

Figure 4.134: Imaging polarimetry of LkHα 134.

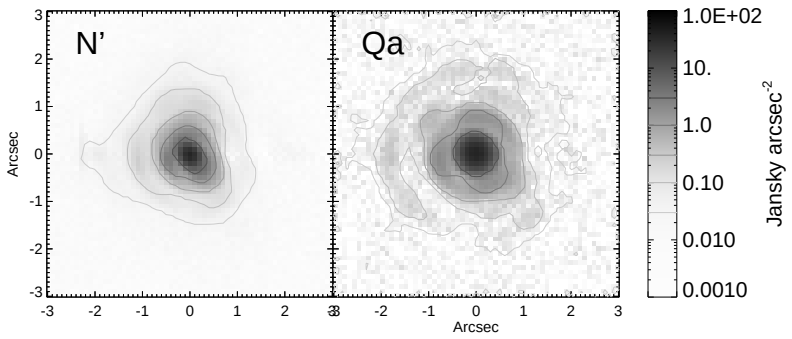

Figure 4.135: Mid-IR imaging of LkHα 134.

4.5.89 LkHα 147

LkHα 147 is a B2 star (Hernández et al., 2004) located at a distance of 800 pc (Natta et al., 2001), with $V = 14.5$. It has a 1.″62 companion at PA=341°(Bouvier & Corporon, 2001) It was observed at Lick on 2005-07-27 UTC in good conditions. No polarized light was detected in the near-IR (Fig. 4.136). The companion was easily detected at all wavelengths.

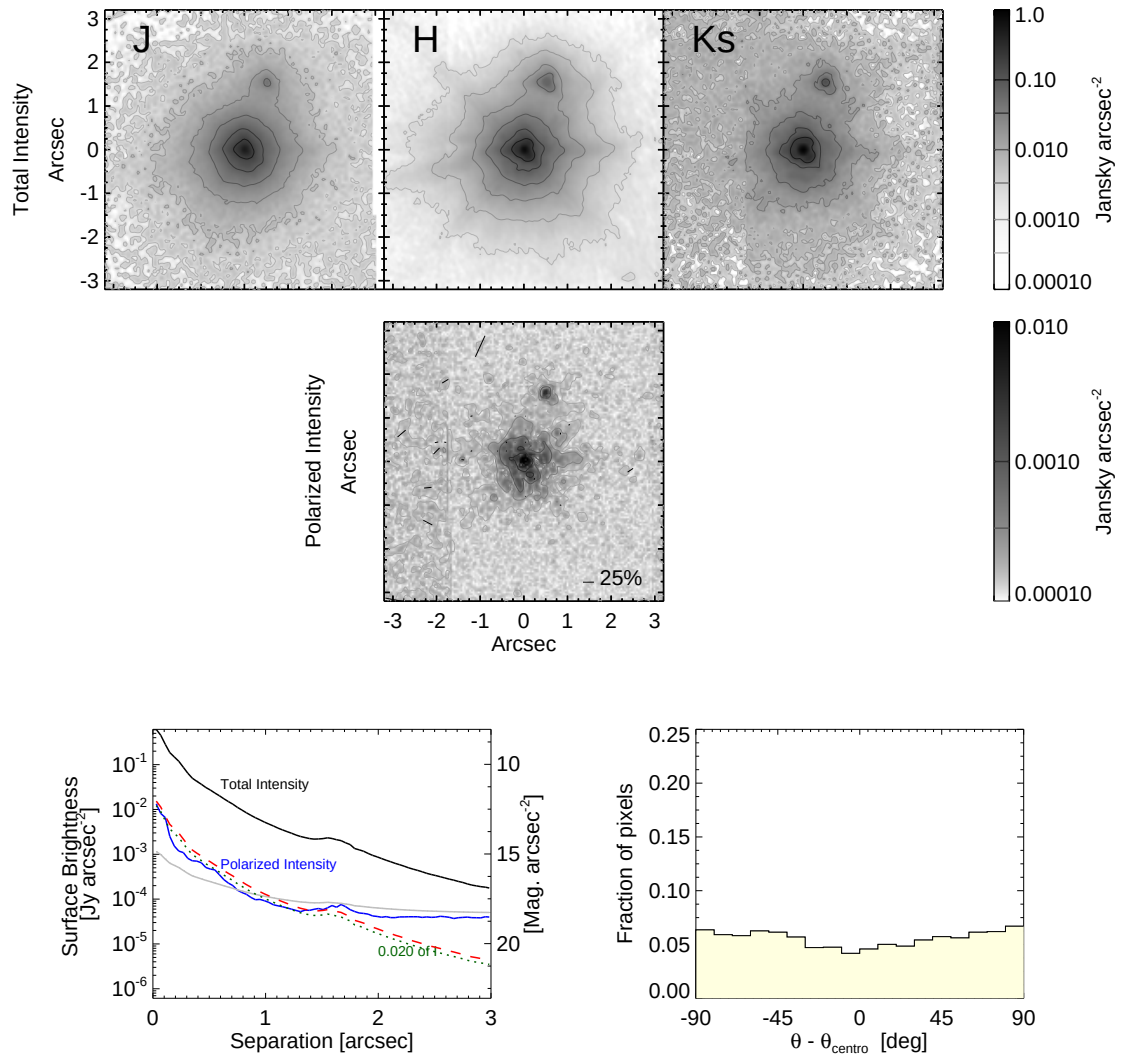

Figure 4.136: Imaging polarimetry of LkHα 147.

4.5.90 V1057 Cyg

V1057 Cyg is a FU Orionis star, with photospheric spectral type F7/G3I/IIe star (Herbig et al., 2003) located at a distance of 550 pc (Straizys et al., 1989), with $V = 11.6$.

It was observed at Lick on 2005-07-29 UTC in good conditions, and on 2005-10-18 in cloudy and humid conditions. While there is a peak in the centrosymmetry histogram suggestive of the presence of circumstellar dust, there appear to be larger than usual PSF subtraction residuals in these data. Several regions of the image have polarization position vectors substantially offset from centrosymmetry (see Fig. 4.137, particularly north and west of the star). This is not a convincing detection of resolved circumstellar dust.

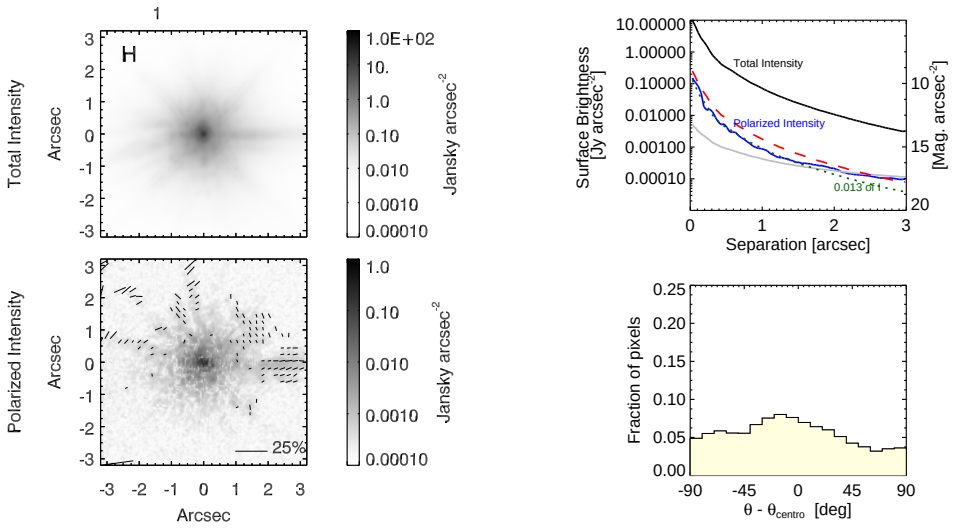

Figure 4.137: Imaging polarimetry of V1057 Cyg.

4.5.91 LkHα 120

LkHα 120, also called V1331 Cyg, is an FU Ori object, or perhaps a pre-FU Orionis object (Welin, 1976). Weintraub et al. (1991) suggested based on submillimeter data that it has a nearly edge-on circumstellar disk. Millimeter observations by Henning et al. (1998) did not resolve dust around this object, unlike for several other FU Oris. See also Ábrahám et al. (2004); Sandell & Weintraub (2001).

It was observed at Lick on 2004-07-05 UTC in excellent conditions, and at Gemini North on 2005-12-16 UTC. No polarized light was detected in the near-IR (Fig. 4.138) The star was not resolved in the mid-IR (Fig. 4.139). There is a low broad peak in the

centrosymmetry histogram for LkHα 120. While this is suggestive of scattered light from circumstellar dust, it is not a robust detection.

4.5.92 HD 200775

HD 200775 is a $V = 7.4$ B3 star (Hernández et al., 2004) that illuminates the reflection nebula NGC 7023 a distance of 429 pc (Bertout et al., 1999). Li et al. (1994) discovered a companion to HD 200775 located $2\farcs25$ south at PA 164°, and Corporon & Lagrange (1999) also found it to be an unresolved spectroscopic binary. Millimeter CO observations show that it is located in an evacuated biconical cavity carved out of a larger molecular cloud (Fuente et al., 1998b).

It was observed at Lick on 2003-11-18 UTC in poor conditions, and at Keck on 2004-07-26 and 2004-08-28, and at Gemini North on 2005-07-01 UTC. No polarized light was detected in the near-IR (Fig. 4.140), but in the mid-IR a nebulous arc curves to the northeast.

4.5.93 LkHα 324

LkHα 324 is a B6-B8 star with $V = 12.7$ (Cohen & Kuhi, 1979; Herbig & Dahm, 2006) located at a distance of 780 pc in L988 (Chavarria et al., 1983). It lies in a small cluster of stars also containing the Herbig Ae/Be star LkHα 324 SE, discussed in detail by Herbig & Dahm (2006). There has been occasional confusion in the literature between these two stars, with some photometric measurements erroneously attributed to the wrong star, which Herbig and Dahm clarify.

It was observed at Lick on 2004-07-06 UTC in excellent conditions, and at Keck on 2004-07-26 UTC. It was not resolved in the mid-IR, and in fact is only barely detected (Fig. 4.143). This confirms that while LkHα 324 is the optically brightest star in the region, other sources contribute far more to the total IR flux.

There is a small peak to the centrosymmetry histogram centered at zero, suggesting the marginal detection of polarized light. (Fig. 4.142) There are two other point sources in our IRCAL field of view: one companion located $5\farcs7$ northwest of LkHα 324 (previously cataloged as IfAHα 643), and another $10''$ south (IHα 644). The histogram peak is actually due to a small region around this southern star which appears to be slightly polarized. Given the pre-main-sequence nature of this star, it may indeed illuminate an IR reflection nebula; it is located in a nebulous region in the R band image of Herbig and Dahm.

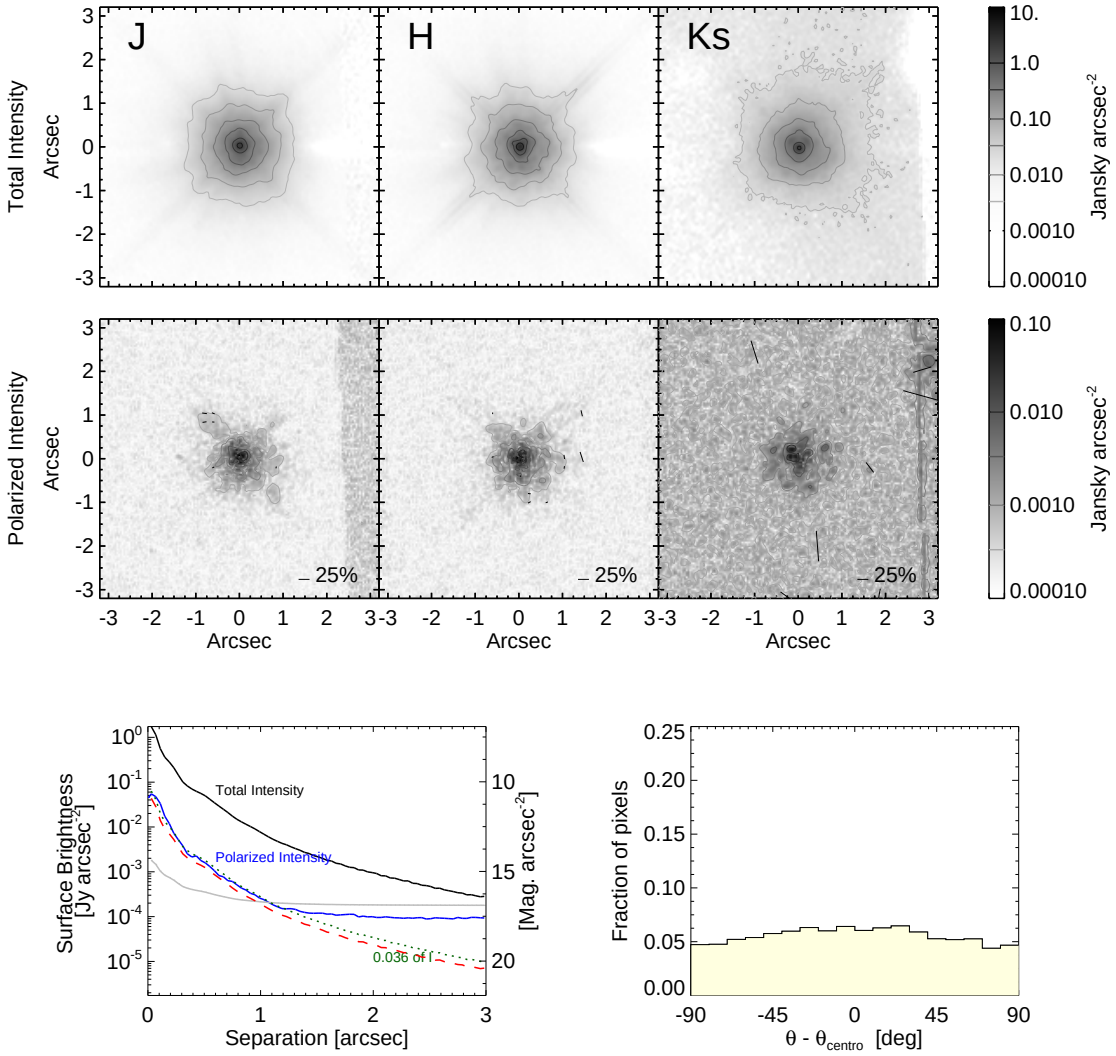

Figure 4.138: Imaging polarimetry of LkHα 120.

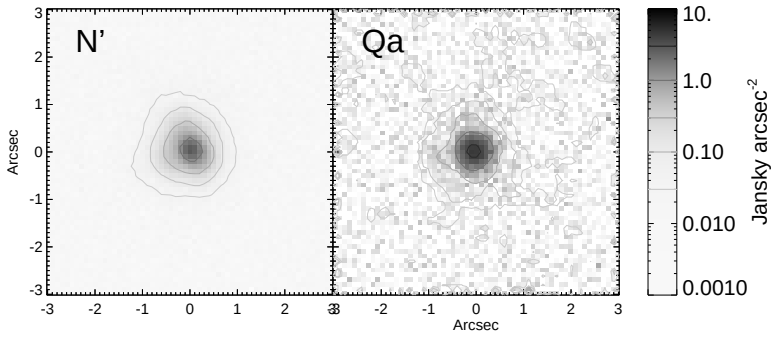

Figure 4.139: Mid-IR imaging of LkHα 120.

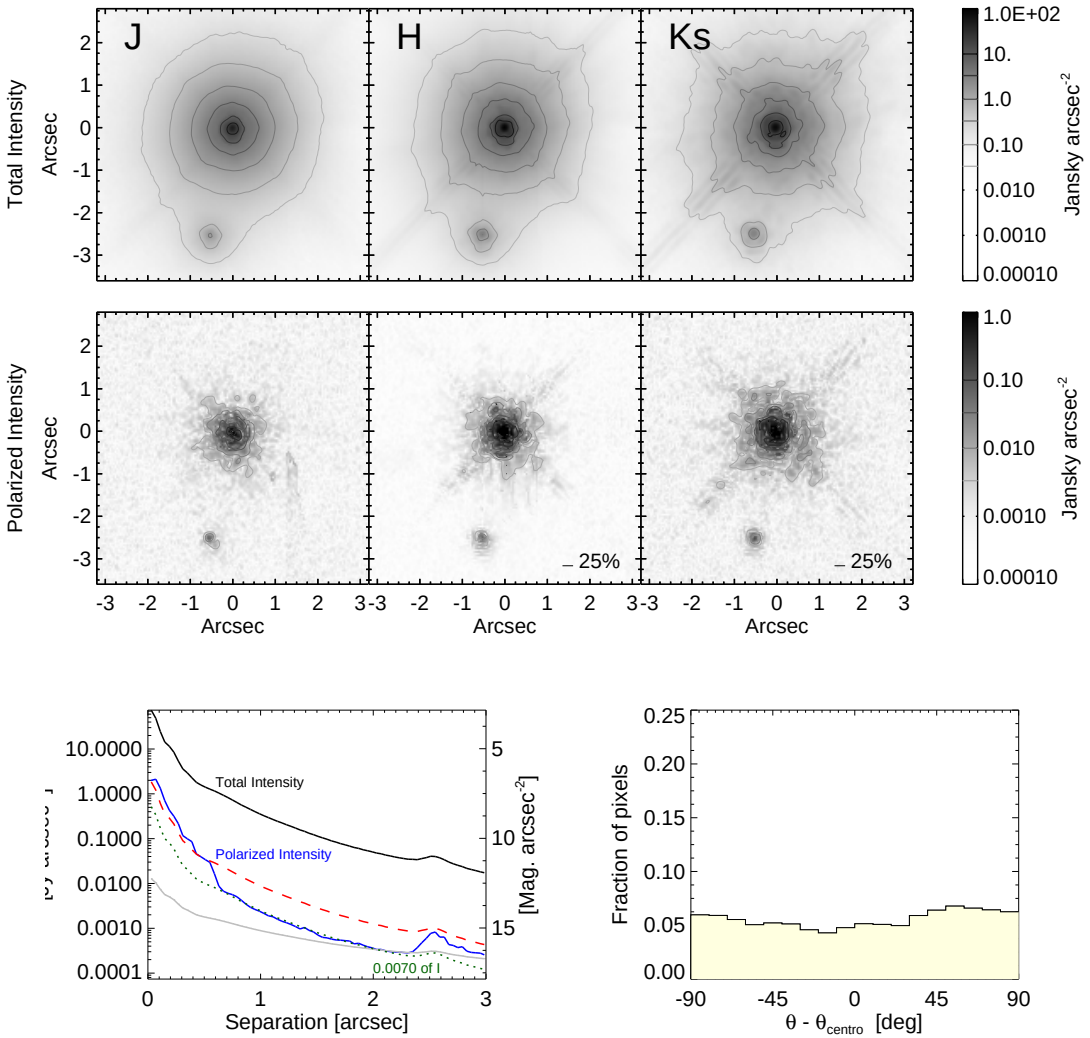

Figure 4.140: Imaging polarimetry of HD 200775.

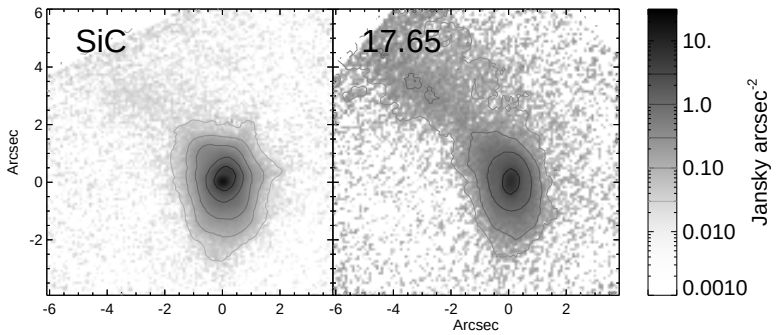

Figure 4.141: Mid-IR imaging of HD 200775.

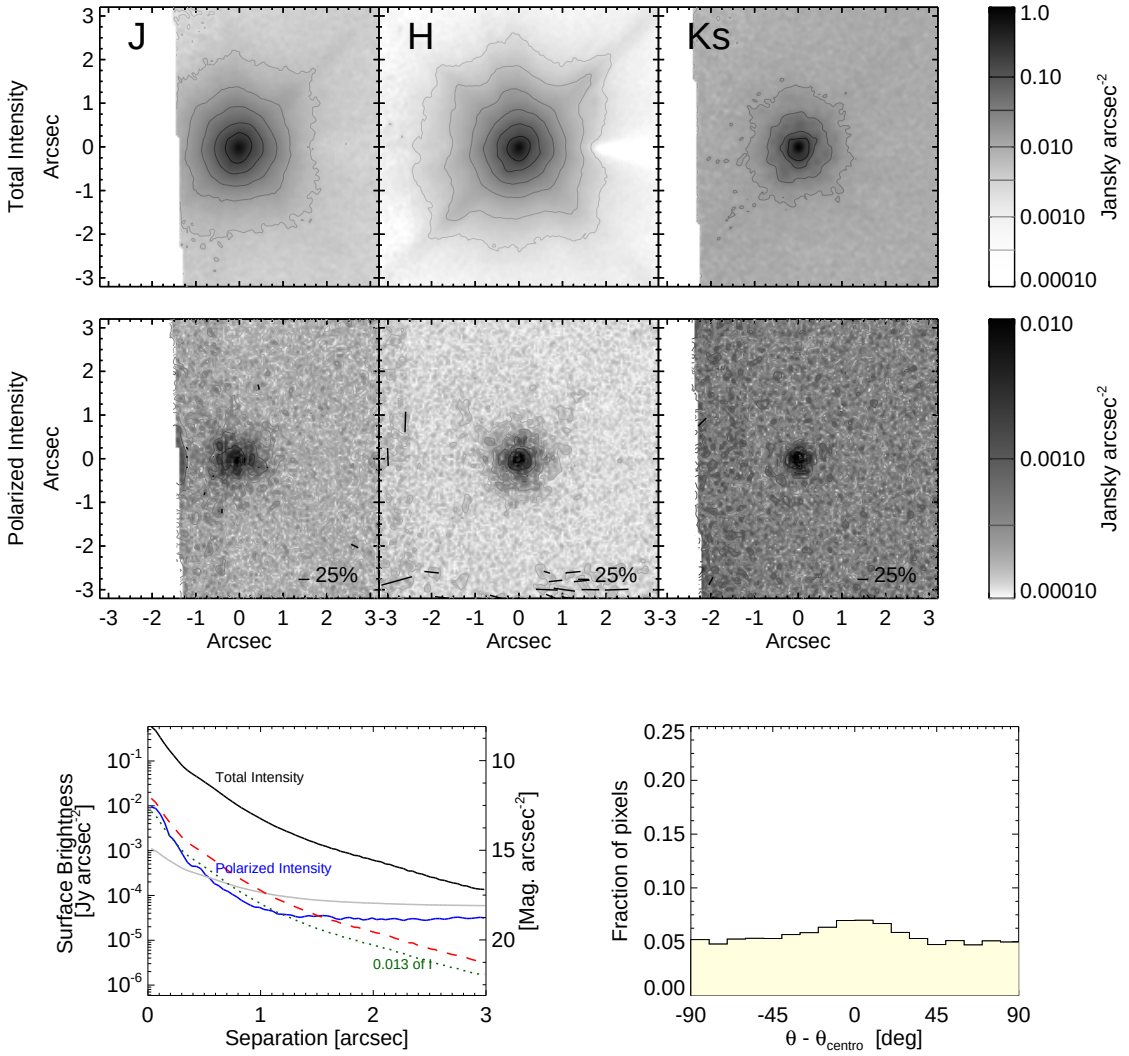

Figure 4.142: Imaging polarimetry of LkHα 324.

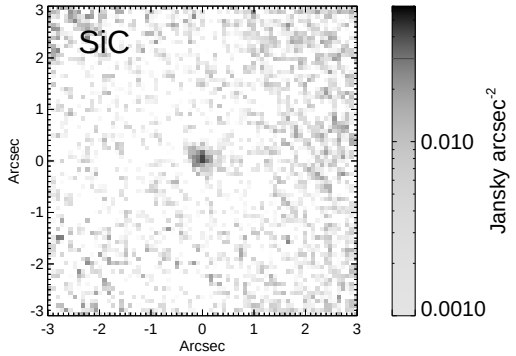

Figure 4.143: Mid-IR imaging of LkHα 324.

4.5.94 LkHα 324 SE

LkHα 324 SE is located in L988 along with the just-discussed LkHα 324 SE. It has P Cygni-type line profiles and strong [O I] and [S II] emission, and illuminates a (Herbig & Dahm, 2006, , hereafter HD06). While LkHα 324 SE has the position of a $\sim 1.5 M_{\odot}$ star in the extinction-corrected color-magnitude diagram of HD06 (their Fig. 6) it is so deeply embedded ($A_V \sim 25$, based on 2MASS colors from Fig. 7 of HD06!) that this mass estimate is extremely shaky. I include it here as a candidate Herbig Ae/Be star. Its spectrum from HD06 contains no absorption features which might help pin down its classification.

It was observed at Lick on 2005-07-28 UTC in good conditions, and at Gemini North on 2006-07-05 UTC. HD06 report that "the star image itself is elongated, as if another faint star or small bright nebulosity were present at about 1.″2 at P.A. = 270°", but we see no evidence for such a source. The fan-shaped nebulosity also described by HD06, on the other hand, shows up spectacularly in our AO images. LkHα 324 SE's surroundings have the four-lobed morphology of an envelope split by bipolar outflow cavities, similar to LkHα 233. The geometry is fully consistent with the northwest outflow described by HD06. The south and east lobes (the redshifted side) are somewhat greater in extent, about 4″ versus 2″ to the north and west.

In the mid-IR, LkHα 324 SE is indeed a highly luminous object, with its SED apparently peaking around 11 μm and decreasing somewhat to 18 μm. No mid-IR nebulosity or other point sources are visible within our 20 × 30 field of view, but move east another 30″west and the situation changes. There we detect in both the star IHα 645 from HB06 and another source 16″ due northwest. No optical or near-IR counterpart is visible for that latter, either in 2MASS or in the deeper images of HB06.

4.5.95 HD 203024

HD 203024 is 0.″23 equal-magnitude binary (Bouvier & Corporon, 2001), with spectral type A5V star and combined magnitude $V = 8.9$ (Mora et al., 2001). Its distance is very uncertain. Curiously, Corporon & Lagrange (1999) report the detection of Li absorption in the combined spectra, indicating the presence of a young low-mass star, but the two stars here appear to be identical and of earlier spectral type. Perhaps there is an unseen low-mass companion.

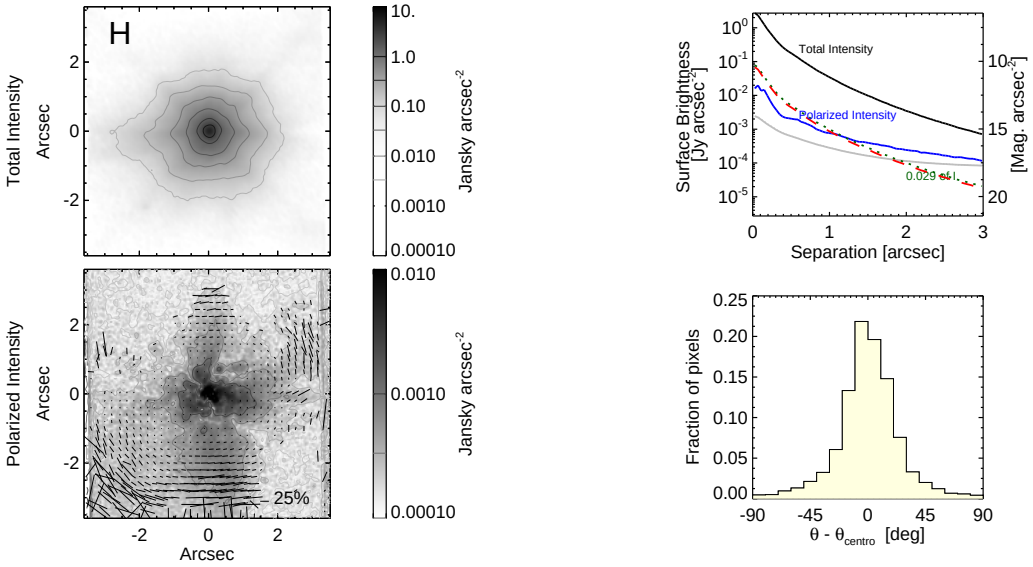

Figure 4.144: Imaging polarimetry of LkHα 324 SE.

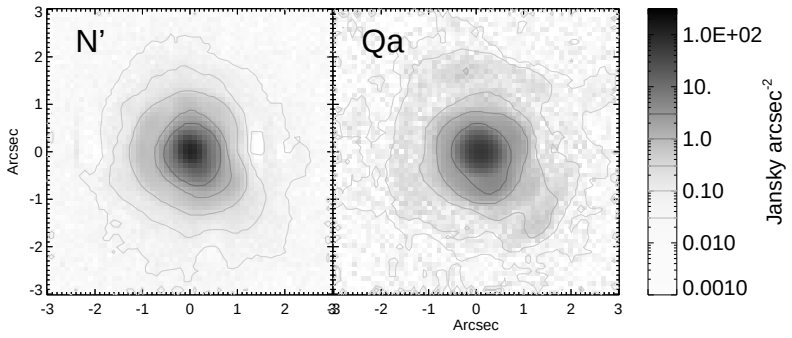

Figure 4.145: Mid-IR imaging of LkHα 324 SE.

It was observed at Lick on 2004-10-31 UTC in mediocre conditions, and at Gemini North on 2005-06-30 UTC. No polarized light was detected in the near-IR (Fig. 4.5.95) While the binary is clearly resolved in our AO data, only one point source is apparent in the mid-IR (Figs. 4.5.95 and 4.148), so most of the dust must be around only one star; it is not clear which of the two this is.

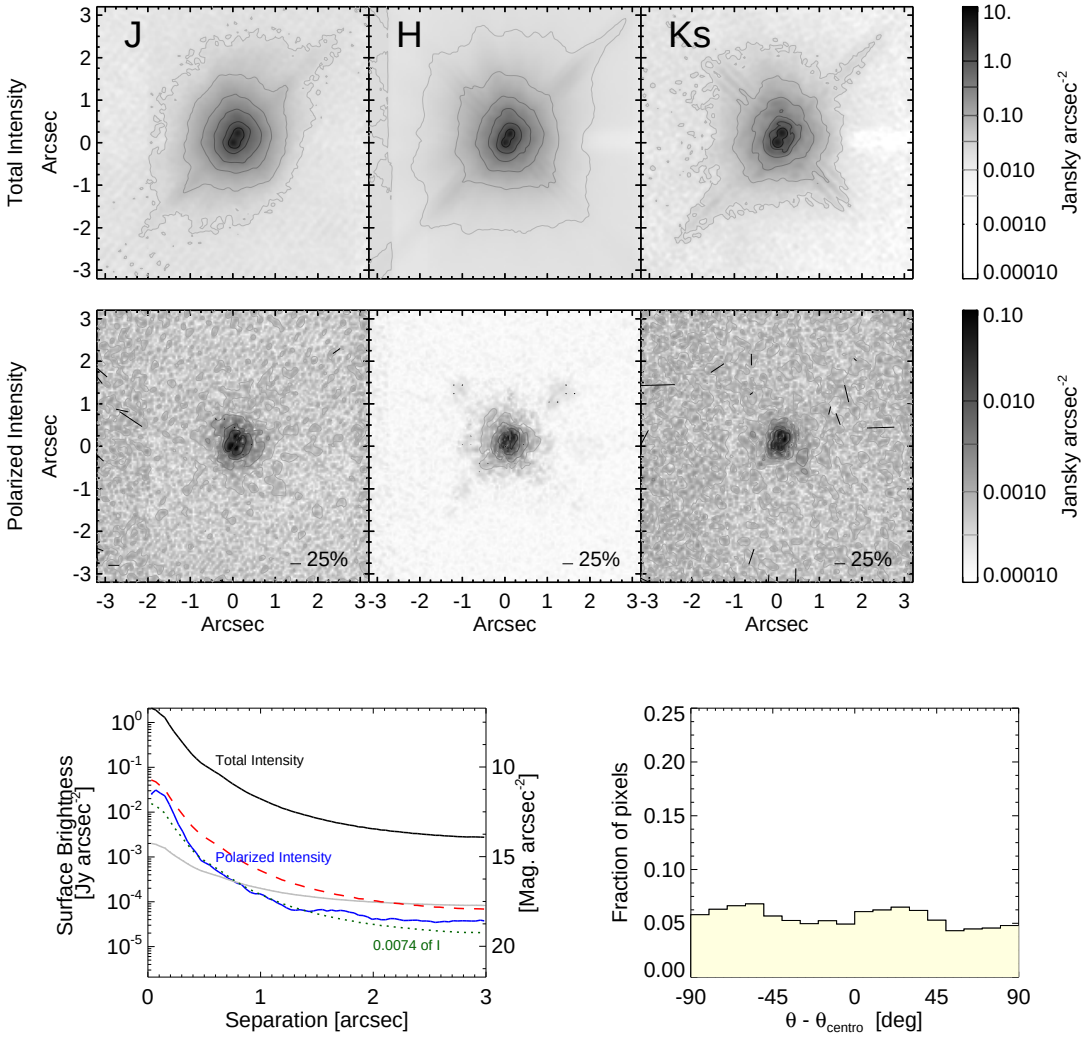

Figure 4.146: Imaging polarimetry of HD 203024.

4.5.96 LkHα 349c

LkHα 349c, also called HBC 729, is located at a distance of 750 pc in the dark globule IC 1396A, the "Elephant Trunk Nebula" (Weikard et al., 1996), one of the very first

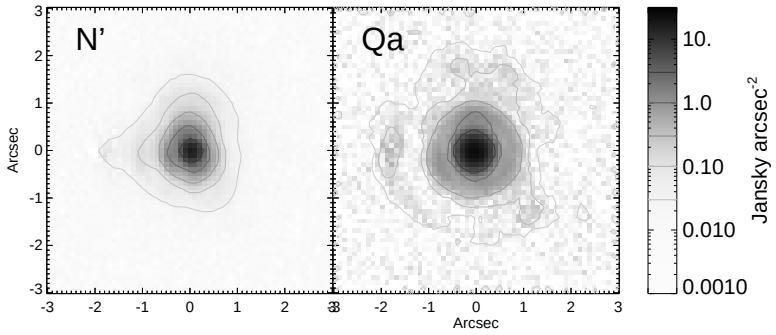

Figure 4.147: Mid-IR imaging of HD 203024.

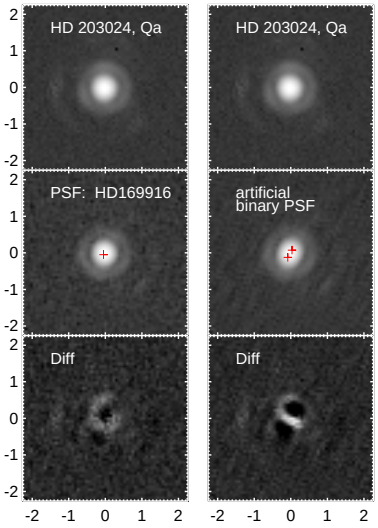

Figure 4.148: PSF subtractions for HD 203024 demonstrate that only one of the two stars possesses dust emitting at 18 μm. The top row shows our Qa band Michelle image of this system. The second row shows at left a single PSF star, and at right an artificial binary PSF created by replicating the PSF using the known separation of HD 203024, indicated by the crosses. The bottom row shows the subtracted residuals (on a different image display stretch than the upper two rows). While the single star subtraction is not perfect, the binary star subtraction is noticeably worse, with correlated subtraction residuals along the binary's separation axis. Repeating this process with other PSF stars gives similar results, and we conclude that only one of the two stars in this system possesses dust emitting at this wavelength.

targets observed with the Spitzer Space Telescope (Reach et al., 2004). This dark cloud is sculpted by radiation pressure from a nearby O6 star and 20 B stars into a elaborate comet-shaped nebula that has been described as a "flying dragon" by the Spitzer press office. These infrared observations reveal a the nebula as a "cauldron of protostars". The optically brightest star in IC 1396A is the $3M_{\odot}$ intermediate-mass T Tauri star LkHα 349, which launches an extremely strong wind that has blown out a cavity within the head of the nebula (Nakano et al., 1989; Hessman et al., 1995). Despite the apparent pre-main-sequence nature of this star, the Spitzer observations do not detect any evidence for infrared excess out to 24 μm; it appears to not possess any circumstellar dust.

Our target LkHα 349c lies 16″ northwest (Cohen & Kuhi, 1979). While some 1.5 mag fainter in the optical, it is far the brighter of the two in the infrared; Spitzer observations show strong IR excess out to 24 μm confirming the presence of a massive circumstellar disk. Based on the optical and IR photometry, Reach et al. (2004) estimate an age of 2.0 Myr.

It was observed at Lick on 2005-07-28 UTC in good conditions. No polarized light was detected in the near-IR (Fig. 4.149), however we do resolve it into a 0.″65 binary at a PA of 42°. The companion is redder than the primary, rising from $\Delta J = 2.80$ to $\Delta K_s = 2.04$.

4.5.97 V645 Cyg

V645 Cyg is a $V = 13.5$ star located in the so-called "Duck Nebula" (Goodrich, 1986). The spectral type and distance of V645 Cyg remain in doubt, with Cohen (1977) and Val'Tts et al. (2002) stating O7 at 6 kpc, while Goodrich (1986) and others give A0 at 3500 pc. A CO outflow was detected from this star by Torrelles et al. (1987) and Verdes-Montenegro et al. (1991). Goodrich (1986) observed a bright nebula surrounding V645 Cyg, which he termed the Duck Nebula for its shape. This same circumstellar dust was also detected in the far IR by Natta et al. (1993). Testi et al. (1998) detected a cluster of stars around V645 Cyg with a projected radius of 0.6 pc (assuming a stellar distance of 6 kpc). This star was unresolved by the NIR observations of Leinert et al. (2001).

It was observed at Lick on 2004-07-04 UTC in excellent conditions, and at Keck on 2004-07-26 UTC. In the near-IR, an arc of circumstellar dust some 5-6″ in radius is seen near V645 Cyg. There is also a fan of dust extending some 3″ immediately west from the star. The star was not unambiguously resolved in the mid-IR (Fig. 4.151); however, there is a possible nebulous extension visible to the immediate west of the star. While this

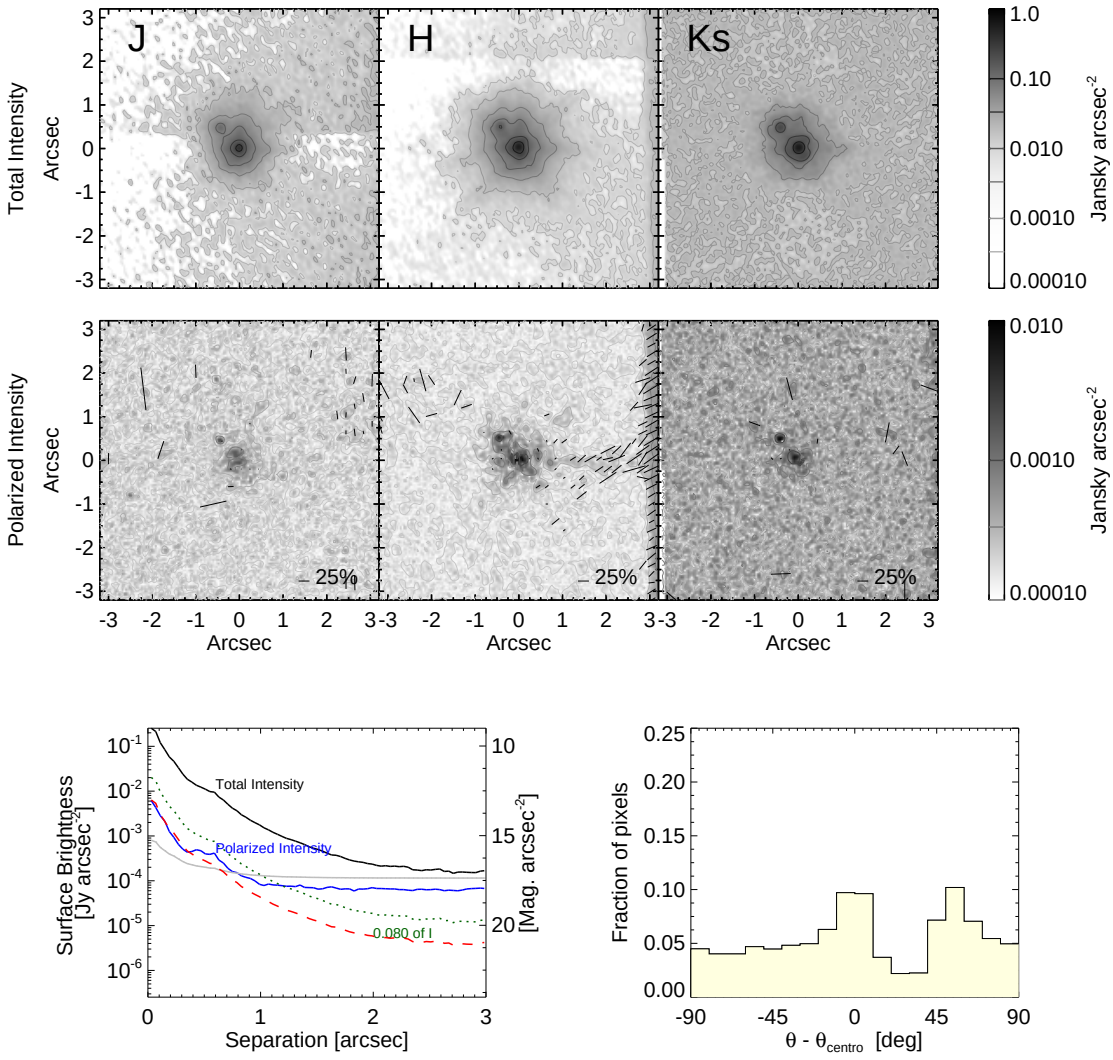

Figure 4.149: Imaging polarimetry of LkHα 349c.

extension could possibly just be PSF variability, it may in fact be thermal emission from the same dust which causes the NIR scattering at this location.

4.5.98 V361 Cep

V361 Cep is a B4 star (Hernández et al., 2004) located at a distance of 1250 pc (van den Ancker et al., 1998), with $V = 10.2$. V361 Cep is part of the same cluster of stars that includes LkHα 234. It is slightly the more massive of the two, with spectral type B4 to LkHα 234's B7. However, unlike its neighbor it appears to be associated with only a small amount of circumstellar dust. Fuente et al. (1998) found that it is located in a region devoid of molecular material, while LkHα 234 is in a region with plentiful molecular gas. Furthermore, from their millimeter continuum and CO fluxes, the star is associated with a relatively small amount of circumstellar gas and dust. Thus these two stars, despite their neighboring locations and presumably coeval ages, appear to have very different circumstellar environments.

It was observed at Lick on 2004-07-05 UTC in excellent conditions, and at Keck on 2004-07-26 UTC. No polarized light was detected in the near-IR (Fig. 4.152) The star was not resolved in the mid-IR (Fig. 4.153). V361 Cep is barely detected in our mid-IR imaging, with a 11 μm flux of only 0.098 Jy.

4.5.99 LkHα 234

LkHα 234 is a B7 star (Hernández et al., 2004) located at a distance of 1000 pc (Pirzkal et al., 1997), with $V = 12.2$. LkHα 234 is an 8.4 $M_\odot$ Herbig Ae/Be star associated with NGC 7129 (Hillenbrand et al., 1992). Weintraub et al. (1994) detected an embedded companion $3''$ northwest in K band polarimetric imaging, and conclude that this source is the most likely driver for the outflows in the region.

Di Francesco et al. (1997) found LkHα 234 to be spatially extended in the FIR, with a FWHM of $\lesssim 24''$, but state that given the presence of embedded companions, the relative contributions of each source at 100 μm remains unknown.

It was observed at Lick on 2002-08-03 and 2005-07-29 UTC in good conditions, and at Keck on 2004-07-26 and 2004-08-28. These images demonstrate the importance of multi-wavelength polarimetric observations of star forming regions: We detect four regions of polarization with substantially different colors around LkHα 234, to the north, south, west, and southwest. The southwest outflow is the reddest, visible only at H and K_s; we identify

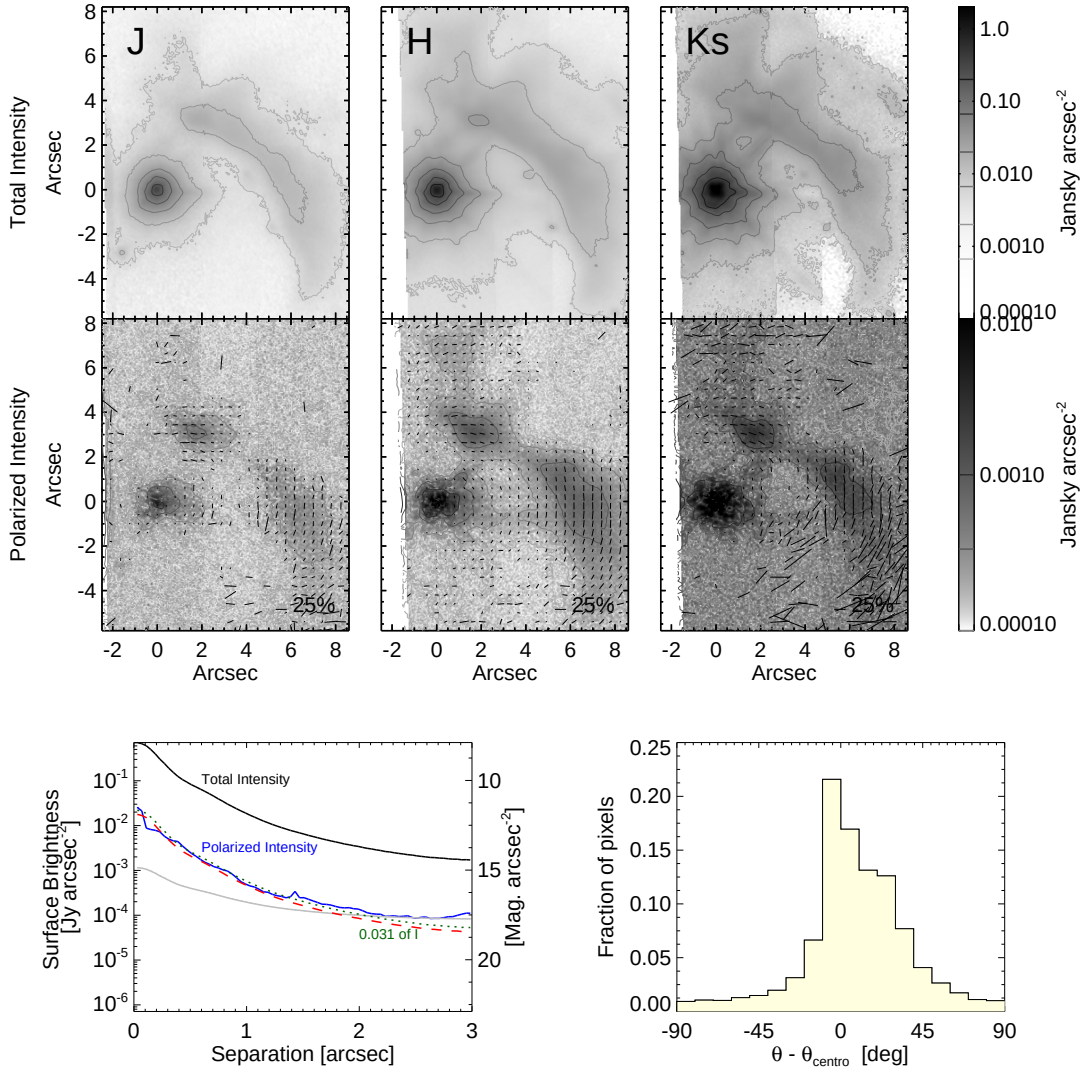

Figure 4.150: Imaging polarimetry of V645 Cyg.

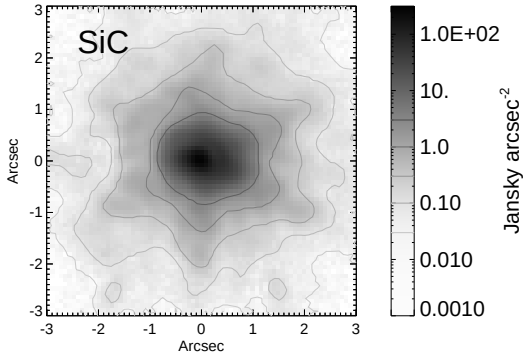

Figure 4.151: Mid-IR imaging of V645 Cyg.

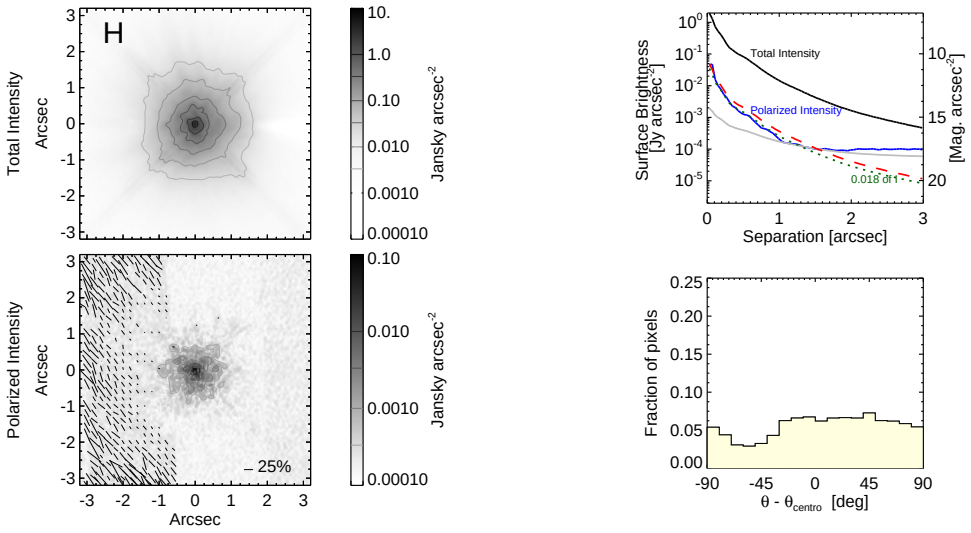

Figure 4.152: Imaging polarimetry of V361 Cep.

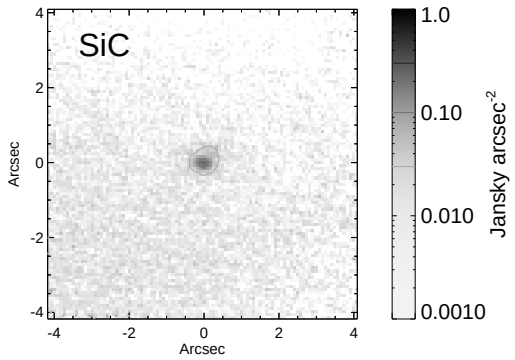

Figure 4.153: Mid-IR imaging of V361 Cep.

this as an outflow from Weintraub's embedded source. The north and south outflows are detected only at J and H. The geometry suggests these may in fact be bipolar outflows from LkHα 234 itself, although the northern region has a faint extension curving to the east which may contradict that interpretation. To the northeast of the star there is a roughly triangular region lacking polarization throughout the near-IR.

Several interesting features are visible in the mid-IR. Weintraub et al.'s embedded source to the northwest is revealed to be *two* embedded sources to the northwest, the inner of which is extended in a roughly triangular shape, and the outer of which is more point-source-like (Fig. 4.155). On the other side of LkHα 234, an upside-down-comma shaped nebula curves to the northeast. This nebula's position corresponds precisely to the region lacking polarized light in the near IR. This is consistent with its being slightly in front of, and blocking the light from, the polarized scattered light nebula.

The companion visible $2''$ east of the star in the near-IR is not visible at longer wavelengths.

4.5.100 AS 477

AS 477, also called BD +46 3471 and V1578 Cyg, is a $V = 10.1$ A0 star located at a distance of 900 pc (Hillenbrand et al. 1992, Hernandez et al., 2004). It shows P Cygni profiles at Hα and NaD (Finkenzeller and Mundt 1984). A total of four companions are now known (Pirzkal et al., 1997; Li et al., 1994; Bouvier & Corporon, 2001).

It was observed at Lick on 2003-11-05 UTC in windy and poor conditions, and on 2003-11-18 in poor conditions, and at Keck on 2004-07-26 UTC. No polarized light was detected in the near-IR (Fig. 4.156) The star was not resolved in the mid-IR (Fig. 4.157). However, all four companions are detected, easily in the NIR and somewhat more marginally in the mid-IR.

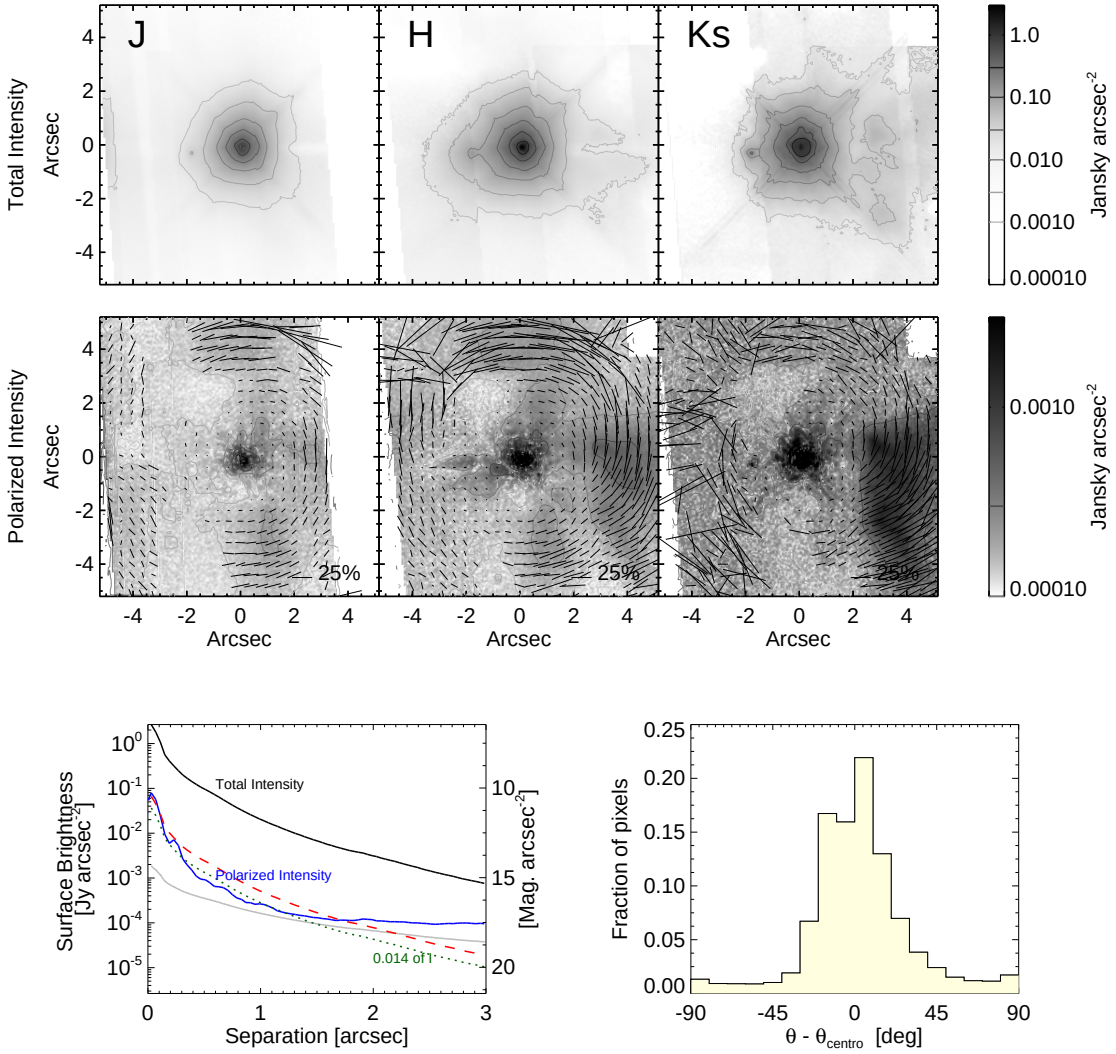

Figure 4.154: Imaging polarimetry of LkHα 234.

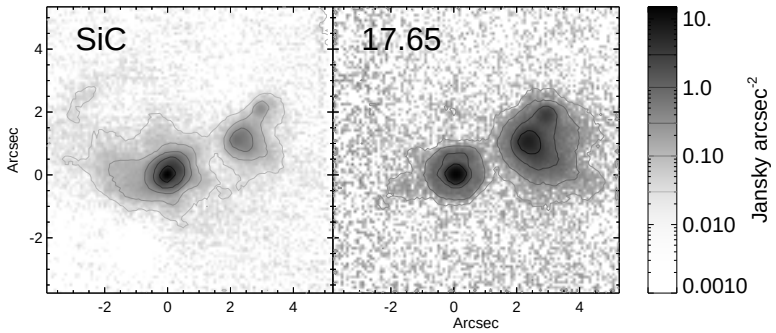

Figure 4.155: Mid-IR imaging of LkHα 234.

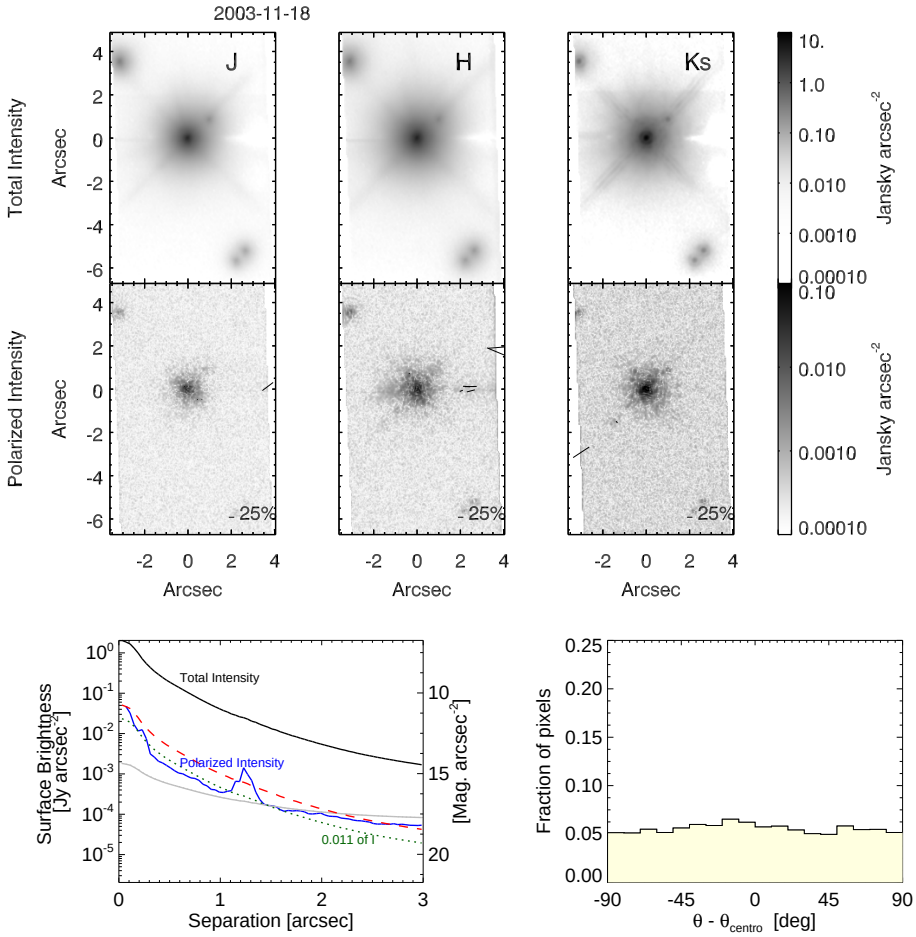

Figure 4.156: Imaging polarimetry of AS 477. The spike in the polarized intensity profile at around 1″.2 is an artifact from the nearby companion.

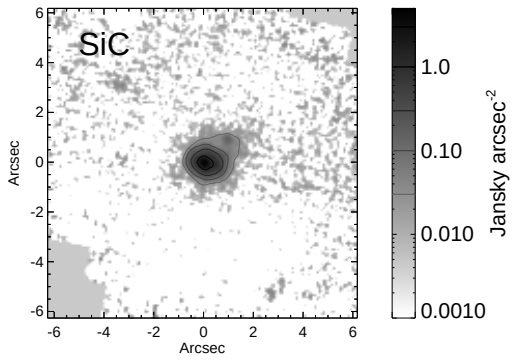

Figure 4.157: Mid-IR imaging of AS 477. All four companions are visible, though faint. Compare with Fig. 4.156 for their positions.

4.5.101 LkHα 257

LkHα 257 is a B8 star located at a distance of 900 pc (Damiani et al., 1994), with $V = 13.4$ (Herbst & Shevchenko, 1999). LkHα 257 was observed by Li et al. (1994), but no extended emission was detected, nor did Testi et al. (1998) find an increase in stellar density around LkHα 257.

It was observed at Lick on 2005-07-28 UTC in good conditions. No evidence for resolved circumstellar dust was detected in our observations (Fig. 4.158). A faint potential companion was detected some 6″ northwest of the star.

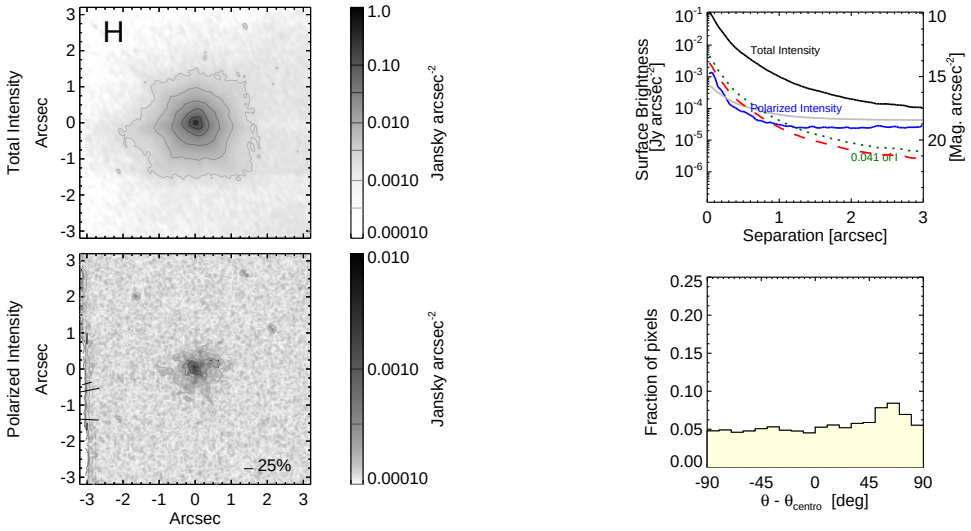

Figure 4.158: Imaging polarimetry of LkHα 257.

4.5.102 BH Cep

BH Cep is a F5 star (Hernández et al., 2004) located at a distance of 450 pc (Kun, 1998), with average $V = 11.2$. It is an irregular variable star with unpredicted Algol-like drops in brightness (Hoffmeister, 1944; Wenzel & Bruckner, 1978).

It was observed at Lick on 2004-09-07 UTC in excellent conditions, and at Keck on 2004-08-27 UTC. No polarized light was detected in the near-IR (Fig. 4.159) The star was not resolved in the mid-IR (Fig. 4.160). No polarized light is significantly detected in our data.

Baines et al. (2006) observed BH Cep using the technique of spectro-astrometry and did not detect any companions. However, two potential companions are clearly visible

nearby in our AO images. The brighter, with ΔH=5.58, is located 3.″26 west of BH Cep, while the fainter (ΔH = 5.89) is located 2.″12 east. Given the fact that the three stars appear to lie approximately in a line, while most triple systems are hierarchical in nature, it is likely that no more than one of these stars is an actual companion to BH Cep. These stars are not very red in the near IR (both have $J - K \approx 0.5$), and neither is visible in the mid-IR.

4.5.103 BO Cep

BO Cep is a F4 star (Hernández et al., 2004) located at a distance of 400 pc (Kun, 1998), with V = 11.6. Like its neighbor BH Cep, it is an irregular variable, though in recent years its variability seems reduced to $\lesssim 0.1$ mag (Wenzel & Bruckner, 1978; Herbst & Shevchenko, 1999). However, it displays the opposite correlation of color with brightness than most irregular variables do, suggesting further study is needed (Pugach, 2003).

It was observed at Lick on 2004-09-07 UTC in excellent conditions, and at Keck on 2004-08-27 UTC. No polarized light was detected around BO Cep in the near-IR (Fig. 4.161). However, its companion BO Cep B, located 8.″29 north at a PA of 26.2°, is itself resolved into a 0.″29 binary, with the southern source showing statistically significant polarization. The new source BO Cep Bb is clearly resolved in all three NIR bands and is approximately 1.2 magnitudes fainter than BO Cep Ba. In H band, BO Cep Bb is polarized at a level of 2.9%, with the position angle oriented perpendicular to the direction to BO Cep Ba. Given the point source appearance and polarization of Bb, I conjecture that it is a bound stellar companion of Ba, but which retains a larger amount of dust around it that scatters light from its more luminous neighbor.

In my LWS 11 μm data, one relatively faint source is visible with a flux of 0.041±0.005 Jy; I identify this as BO Cep A (Fig. 4.162). A second source is visible as a negative image from the chopped beam, in the correct position to be BO Cep B and with flux about half that of the brighter source. This confirms that BO Cep B is also a young and dusty system.

4.5.104 SV Cep

SV Cep is an A0 UX Orionis star (Hernández et al., 2004) located at a distance of 400-715 pc (Kun, 1998; Natta et al., 1997), with V = 11.0. Mora et al. (2004) found complex time-variable spectral absorption features indicative of accreting and outflowing gas moving dynamically in the circumstellar environment. SV Cep has a known companion

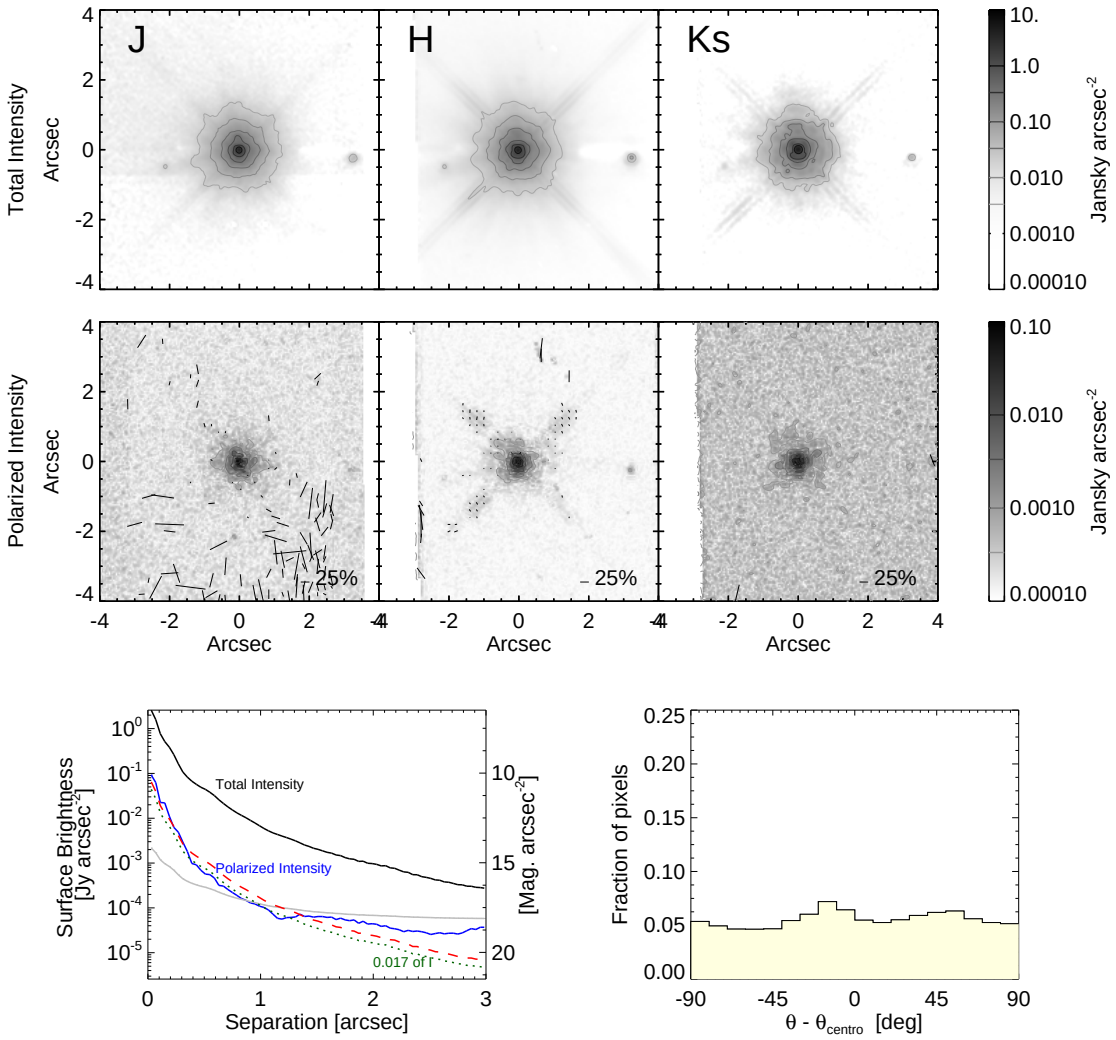

Figure 4.159: Imaging polarimetry of BH Cep.

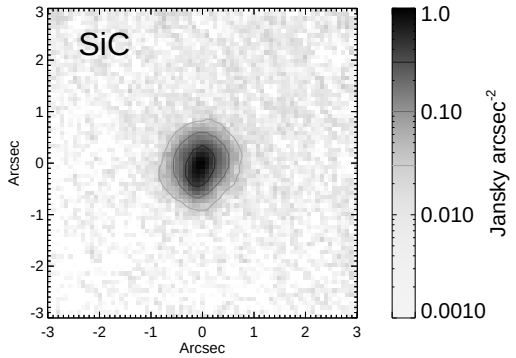

Figure 4.160: Mid-IR imaging of BH Cep.

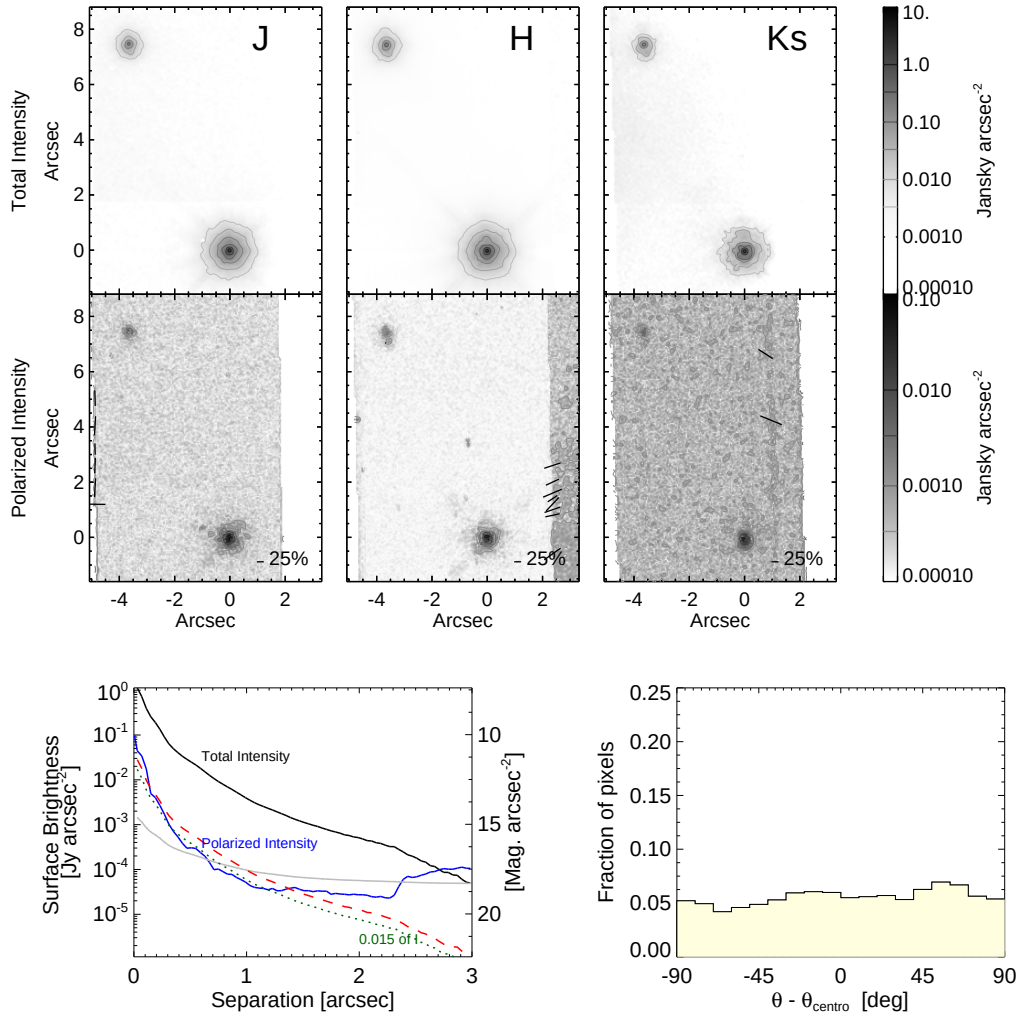

Figure 4.161: Imaging polarimetry of BO Cep.

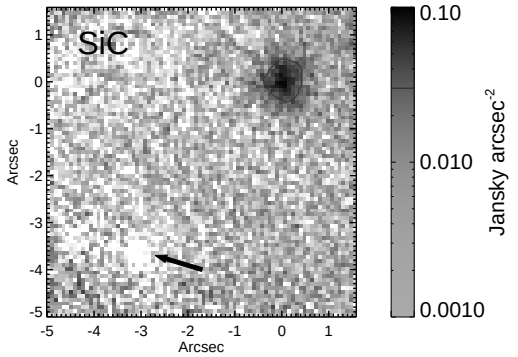

Figure 4.162: Mid-IR imaging of BO Cep. The arrow indicates the location of the negative image of BO Cep B, which was located in the chopped beam offset 10″ north from BO Cep A.

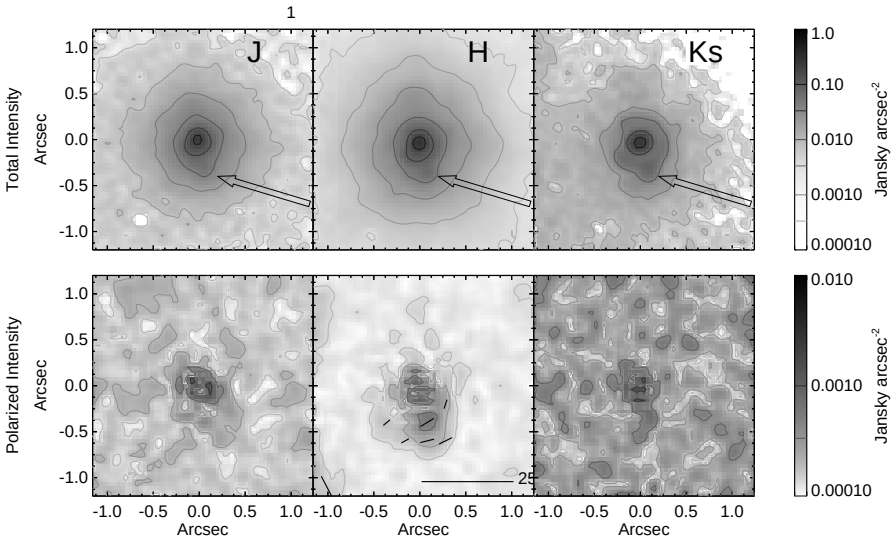

Figure 4.163: Same as Figure 4.161, but zoomed in on the northern star to show BO Cep Ba and Bb.

at $\rho = 1'', \theta = 311°$ (Bouvier & Corporon, 2001), which is well resolved in my Lick AO data.

SV Cep was observed at Lick on 2004-09-08 UTC in excellent conditions. No polarized light was detected in the near-IR (Fig. 4.164)

4.5.105 LkHα 233

LkHα 233 is an A4 star (Hernández et al., 2004) located at a distance of 880 pc (Testi et al., 1998), with $V = 13.6$. Leinert et al. (2001) found a strong infrared halo around this star, with two components oriented to the NNE and NNW.

It was observed at Lick on 2003-07-23 UTC in good conditions, and at Keck on 2004-07-25 UTC, and at Gemini North on 2005-12-16 UTC. The star was not resolved in the mid-IR (Fig. 4.166). Our imaging polarimetry of LkHα 233 reveals four distinct lobes bisected by a narrow, unpolarized lane with PA$\approx$ 150°. These results have already been reported in the literature (Perrin et al., 2004b); see Chapter 6 for more detailed discussion.

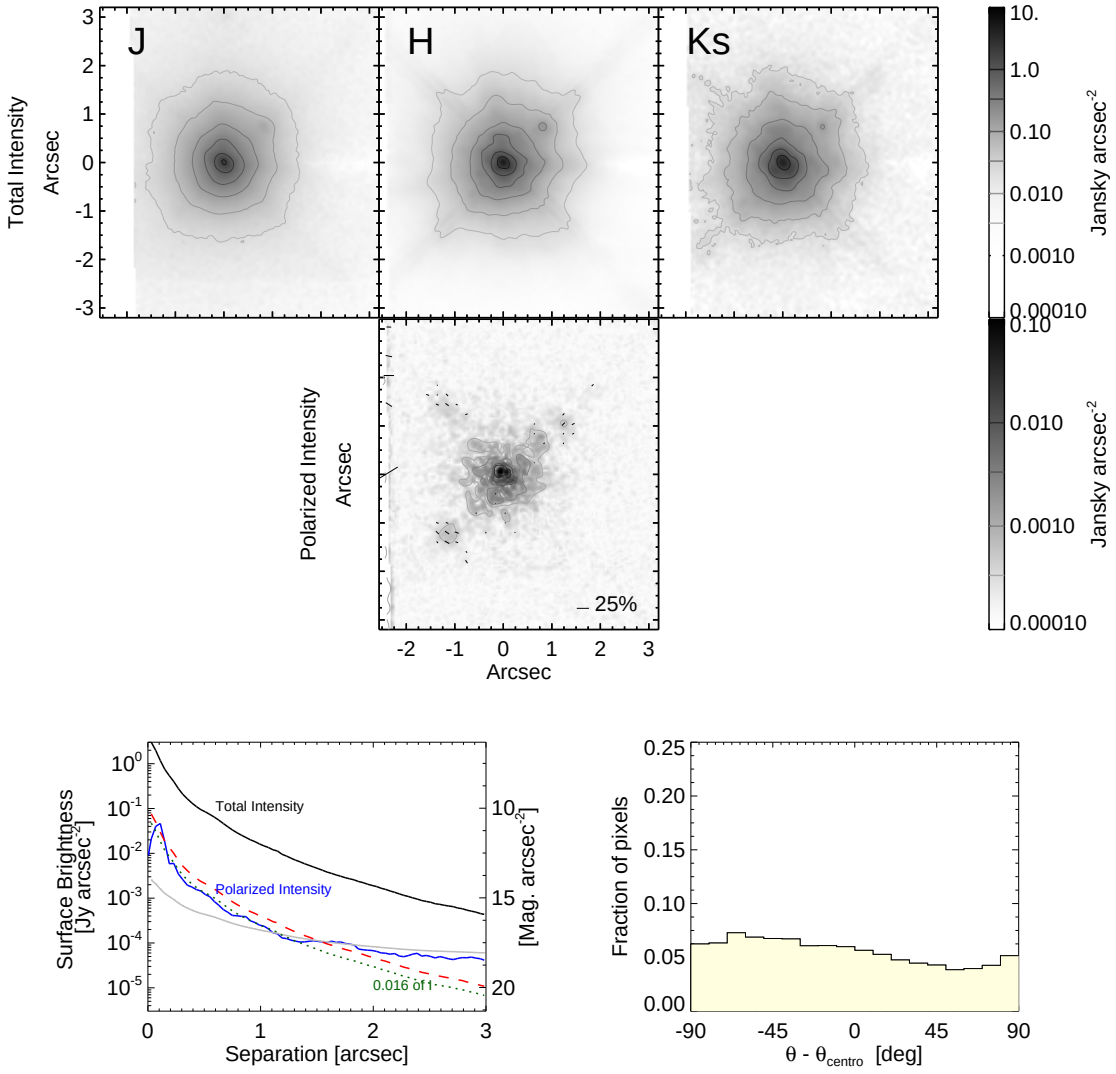

Figure 4.164: Imaging polarimetry of SV Cep.

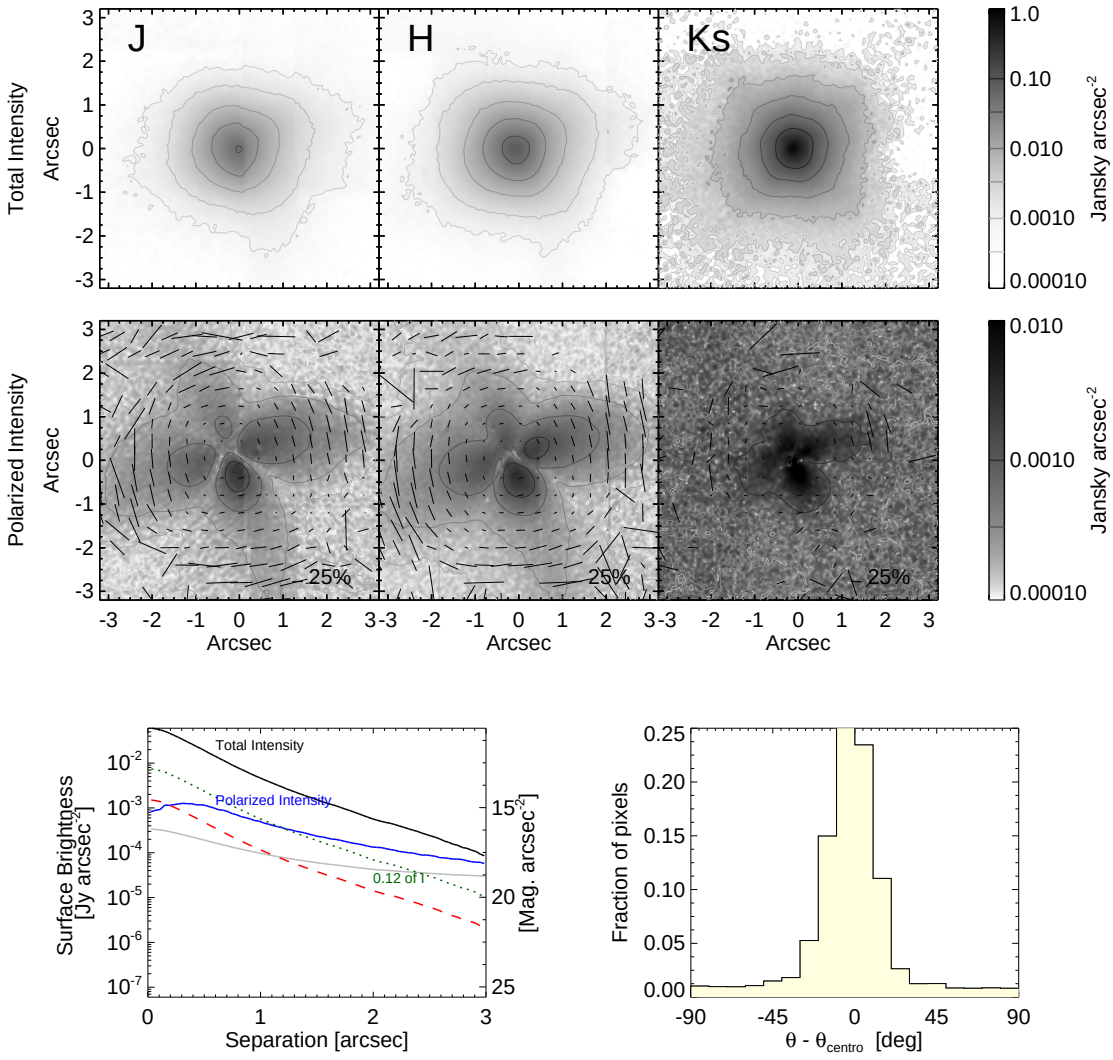

Figure 4.165: Imaging polarimetry of LkHα 233.

4.5.106 HD 216629

HD 216629, also known as IL Cep, is a 7.″8 binary Be star, the optically brighter of which has $V = 9.3$ (Espin, 1902; Merrill & Burwell, 1949) Assousa et al. (1977) recognized it as a Herbig Ae/Be star in the Cep OB3 association, with an age of about 3 Myr. Its distance is about 690 pc (Mel'Nikov et al., 1995). The southern star has spectral type B3e (Finkenzeller, 1985); no measurement of the spectral type of the northern star could be found. While van den Ancker et al. (1998) considered HD 216629 to lack evidence for circumstellar dust, our mid-IR observations clearly establish the dusty nature of this system.

HD 216629 was observed at Lick on 2004-09-07 UTC in excellent conditions, and at Keck on 2004-08-28 UTC. No polarized light was detected in the near-IR (Fig. 4.167). Our LWS data suffered from severe shifts in stellar location due to poor chop/nod performance; our usual reduction method produces multiple images of each star. We therefore chose to individually register each frame before the chop subtraction, which gives images with single PSFs for each star but with somewhat higher background noise due to more imperfect sky

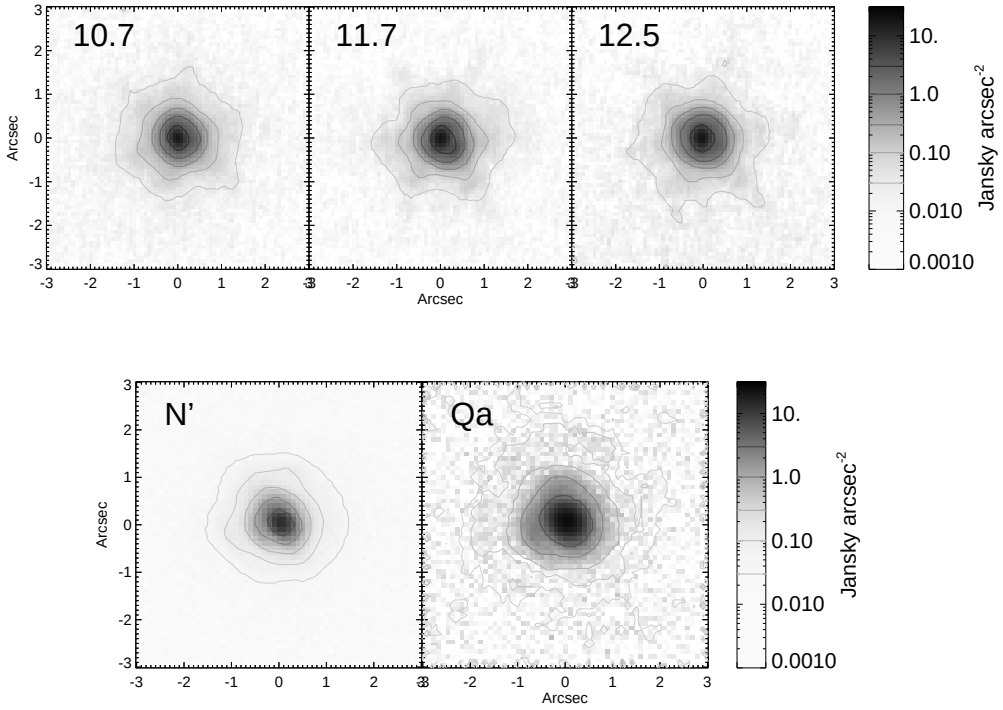

Figure 4.166: Mid-IR imaging of LkHα 233. Top is LWS, bottom is Michelle.

subtraction (Fig. 4.168).

There is a clear flux reversal between the two members of HD 216629. While the northern star is 2.5 mag. fainter than the southern at V, Pirzkal et al. (1997) discovered the two stars to be of equal brightness at K_s. Our observations confirm this and show that the trend continues to longer wavelengths, with the northern star becoming the brighter of the two in the mid-IR. In fact, the southern star is only barely detected at 18 μm; the northern star is far the dustier of the two.

4.5.107 V374 Cep

V374 Cep, also called BHJ 71, is a B0 star located at a distance of 720 pc, with $V = 10.9$ (Blaauw et al., 1959; Finkenzeller & Mundt, 1984; Berrilli et al., 1992). Assousa et al. (1977) recognized it as a Herbig Ae/Be star in the Cep OB3 association, with an age of about 3 Myr. Testi et al. (1998) marginally detected a cluster of other stars around it.

It was observed at Lick on 2004-09-08 UTC in excellent conditions. No polarized light was detected in the near-IR (Fig. 4.169). There is a peak in the centrosymmetry histogram for V374 Cep, probably indicating the marginal detection of light scattered from circumstellar dust. However, the detection is not clear enough for anything to be stated with confidence about the amount or spatial distribution of this dust.

4.5.108 MWC 1080

MWC 1080 is a $V = 11.5$ star whose strong veiling prevents a precise spectral classification; it may be anywhere between A0 and B0 (Cohen & Kuhi, 1979; Hernández et al., 2004). Its distance is also highly uncertain, with estimates ranging from 200 to 2500 pc (Canto et al., 1984; Hillenbrand et al., 1992). Di Francesco et al. (1997) found MWC 1080 to be spatially extended in the FIR, with a FWHM of 29″ at 100 μm. Pirzkal et al. (1997) reported the presence of two companions to MWC 1080, one 4.″7 east of it and the other 0.″6 west. Shevchenko et al. (1994) discovered MWC 1080 is an eclipsing binary with a 2.88 day period, while Corporon & Lagrange (1999) detect it as a spectroscopic binary. A bipolar outflow oriented north-south is seen in molecular CO (Yoshida et al., 1991), extending into a trail of HH objects (Poetzel et al., 1992). Millimeter continuum observations reveal an elongated bar of dust extending southeasts to northwest; this is a very dusty region with more than 12 $M_\odot$of circumstellar material (Henning et al., 1998). Mid-IR maps of this region by Polomski et al. (2002) show diffuse emission extending 10″

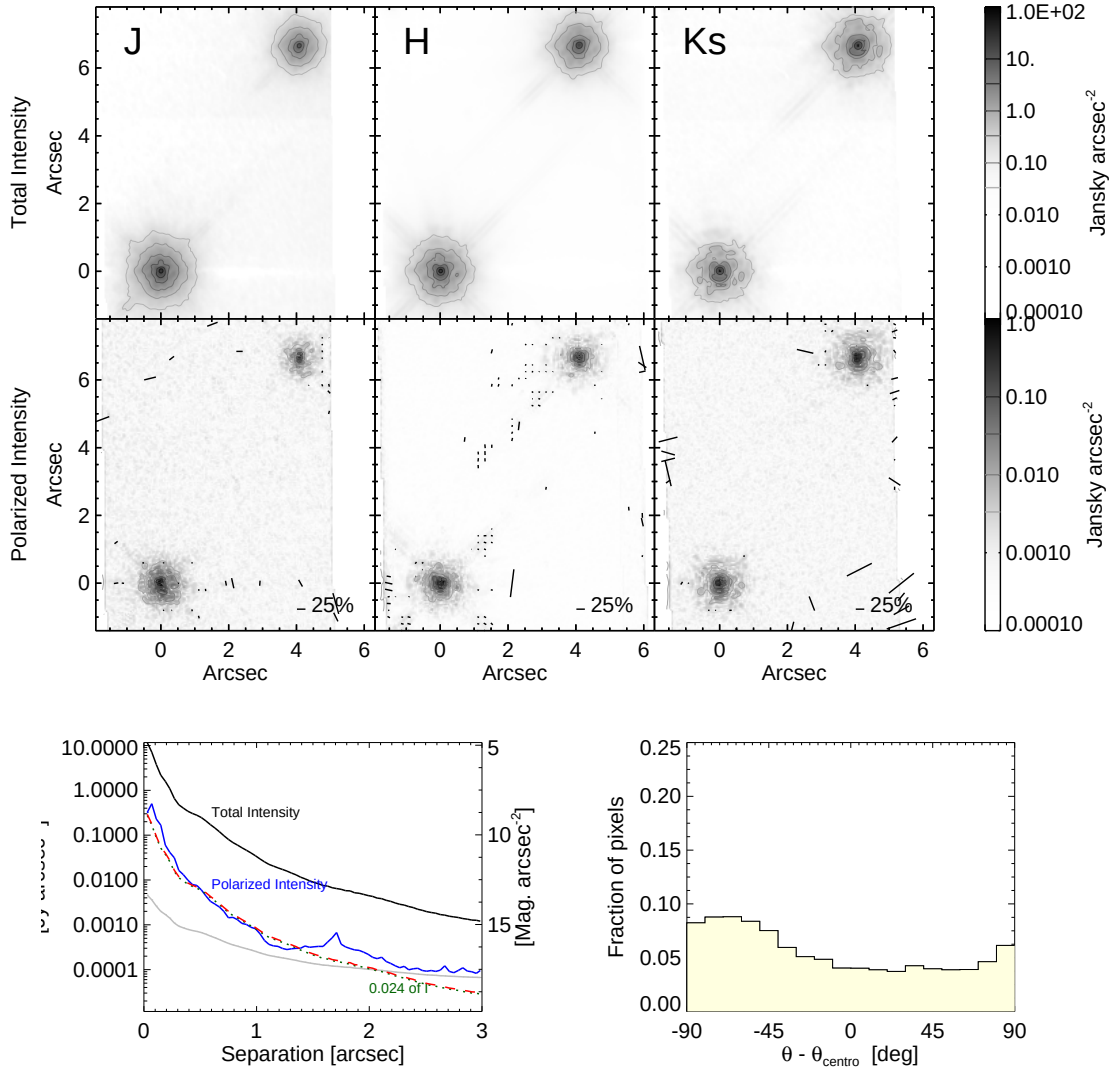

Figure 4.167: Imaging polarimetry of HD 216629.

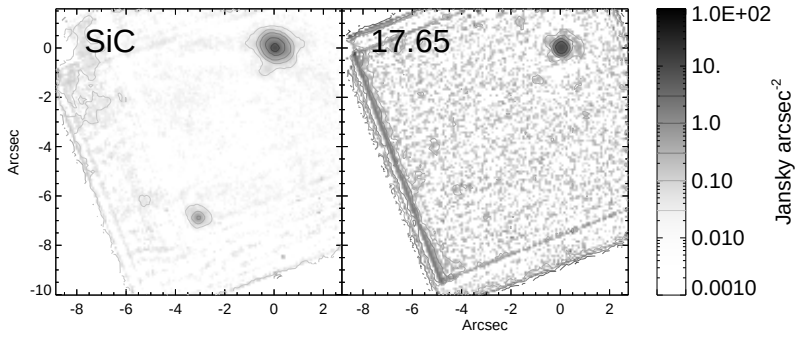

Figure 4.168: Mid-IR imaging of HD 216629.

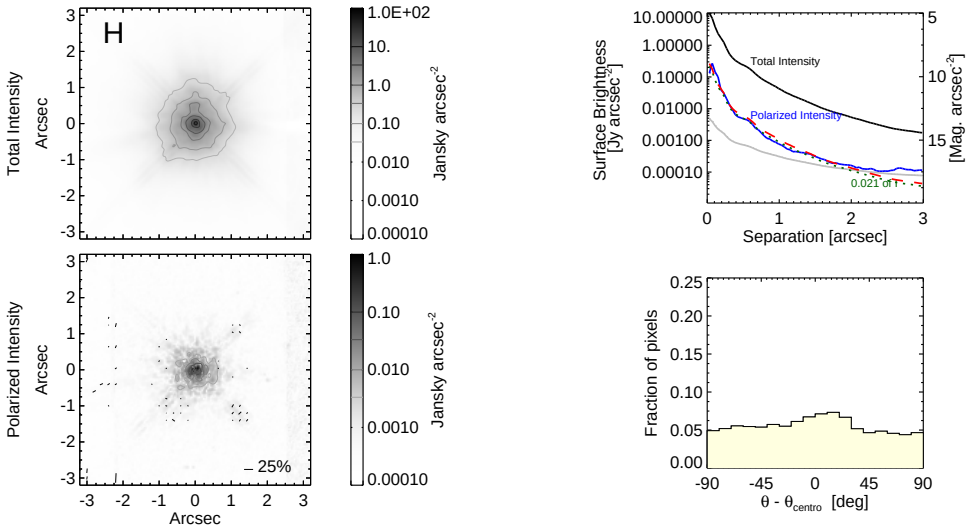

Figure 4.169: Imaging polarimetry of V374 Cep.

from the source, plus half a dozen companions.

It was observed at Lick on 2003-11-18, and at Keck on 2004-07-26 and 2004-08-28. (Fig. 4.171). (Fig. 4.170).

Our near and mid-IR observations resolve the circumstellar dust into a series of bar-shaped nebulae. MWC 1080 somewhat resembles a pinwheel, with opposing arms curving off to the northwest and southeast. It is not quite symmetrical, though: a spur splits off due south from the the southeast nebula, but no such feature is seen to the northwest. Our mid-IR maps are roughly similar to those of Polomski et al. (2002), but our larger field of view reveals an additional mid-IR point source just to the east of their Source E (possibly corresponding to their IR Source 1). The pinwheel morphology and the presence of at least two close companions (the resolved companion and the closer spectroscopic companion) area very reminiscent of the Wolf-Rayet stars observed by Tuthill et al. (1999) and Monnier et al. (1999).

4.5.109 BM And

BM And is a K5 UX Orionis star located at a distance of 440 pc, with $V = 12.1$ (Natta et al., 1997). It was observed at Lick on 2005-11-21 UTC in good conditions. No polarized light was detected in the near-IR (Fig. 4.172) AO imaging here reveals BM And to be a $0\farcs28$ binary, with a K_s flux ratio of approximately 8. No mention of the binarity of this source was found in a brief literature search; however, it does appear that both

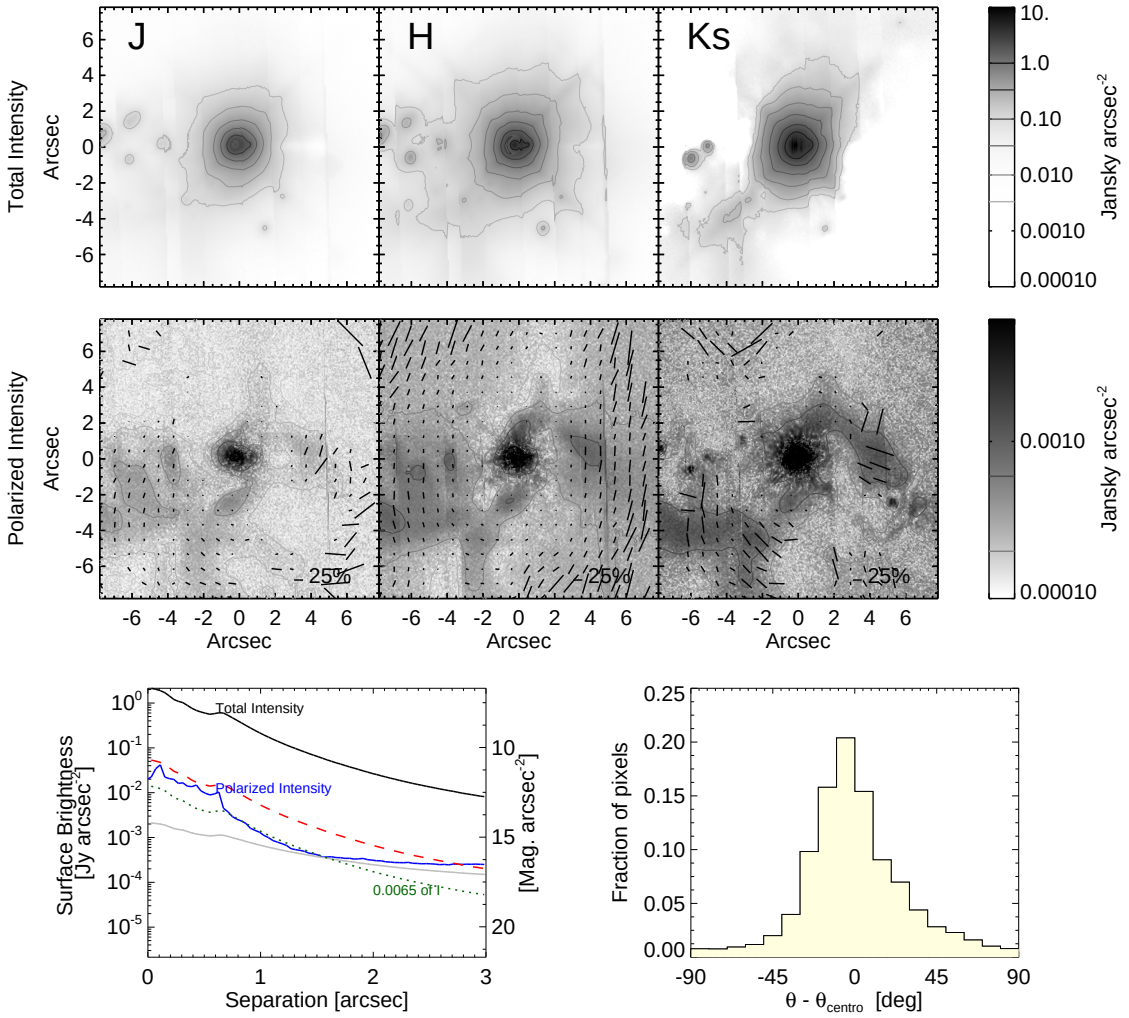

Figure 4.170: Imaging polarimetry of MWC 1080. The mis-oriented vectors at the far right of the K_s image are an artifact resulting from slight frame misalignments in this large mosaic.

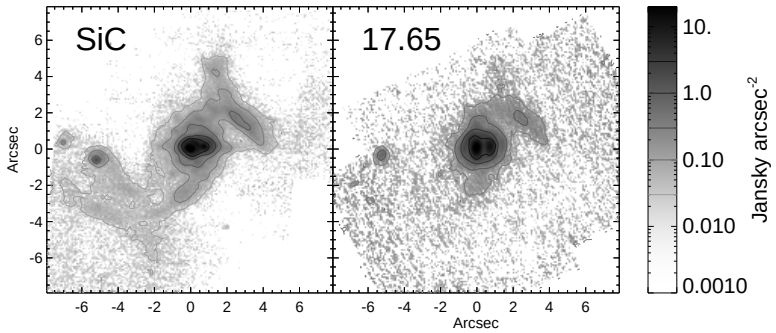

Figure 4.171: Mid-IR imaging of MWC 1080.

members are cataloged in the HST Guide Star Catalog. In addition, a third, much fainter source is observed 1.″85 northwest of the primary. The physical association of this source remains uncertain.

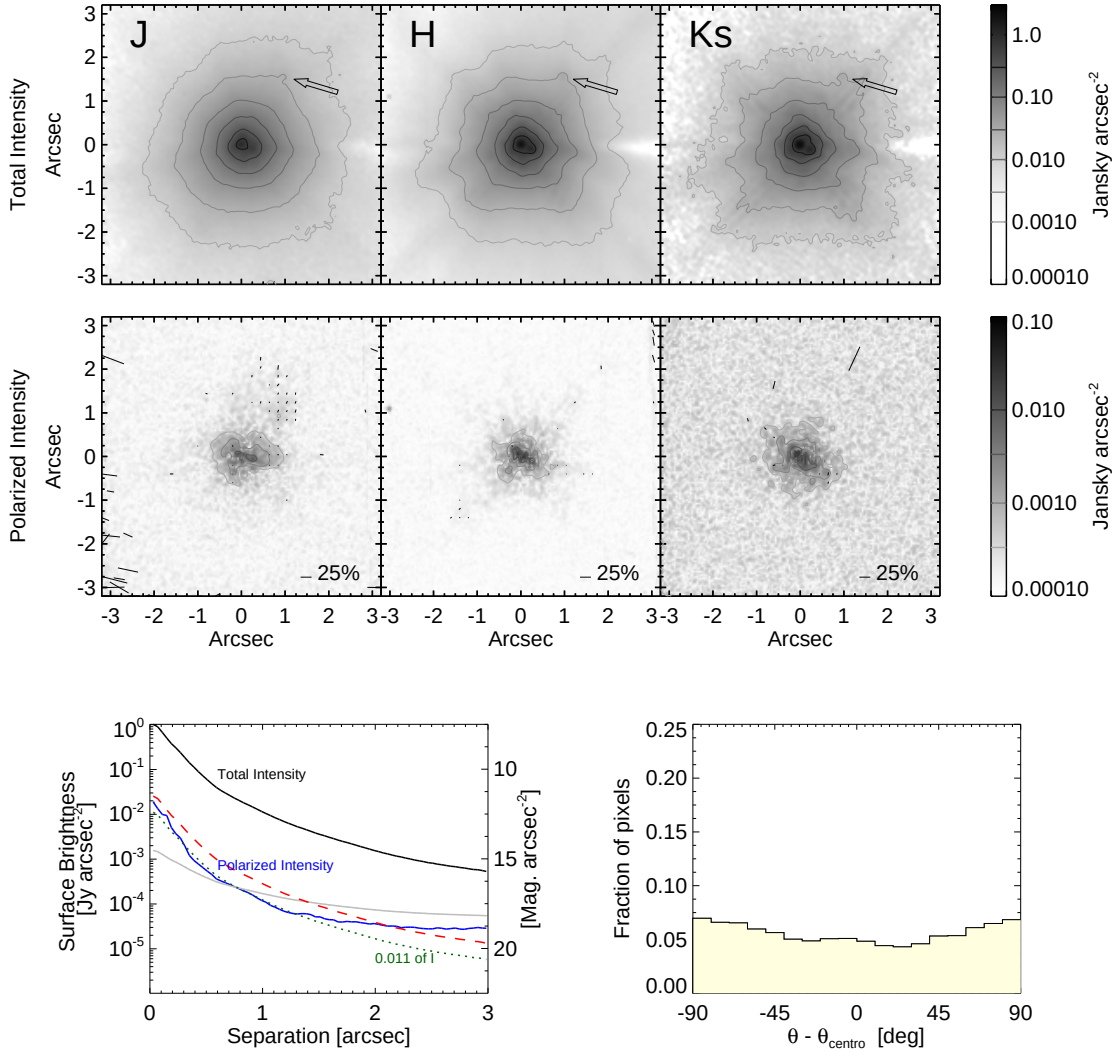

Figure 4.172: Imaging polarimetry of BM And. The arrow indicates the position of the faint third source in the region.

4.5.110 LkHα 259

LkHα 259, also known as MacC H4, is of uncertain spectral class and distance. Hernández et al. (2004) were unable to classify it due to high reddening but note that it is likely earlier than A5. This is in contrast to the A9 classification derived by Cohen & Kuhi (1979).

LkHα 259 was observed at Lick on 2004-09-07 UTC in excellent conditions, however because of the star's faintness ($V \sim 14.7$) the NGS AO system could barely be closed and the AO correction was limited. No polarized light was detected in the near-IR, nor was the star resolved in our Keck mid-IR imaging (Fig. 4.174). A companion was detected $5\farcs36$ from LkHα 259 at PA = 325°by Bouvier & Corporon (2001). This companion is visible in all our NIR data, but is not detected at 11 μm.

4.6 Other Sources Observed

Several targets were observed during the course of the survey which were at the time of observation believed to be Herbig Ae/Be stars, but which in fact appear to be evolved stars or preplanetary nebulae[6]. These are stars transitioning from the asymptotic giant branch to the planetary nebulae phase of stellar evolution, whose photospheres remain too cool to photoionize their envelopes. Hence, as massive stars surrounded by copious circumstellar dust, they appear in many ways similar to Herbig Ae/Be stars, even though they lie at the opposite end of the stellar lifecycle. Several objects classified as Herbig Ae/Be stars by the PDS survey turned out to be well-known and well-studied preplanetary nebulae.

While these data are not directly useful to our study of dust around young stars, we present the observations here nonetheless, both for completeness' sake and in the hope that they may be of interest to scholars of such objects.

4.6.1 PDS 465 (Hen 3-1475)

PDS 465 is the well-known pre-planetary nebula Hen 3-1475.

[6]Often termed "proto-planetary nebulae" but entirely unrelated to protoplanets. See Sahai et al. (2005) for a discussion of this unfortunate misnomer.

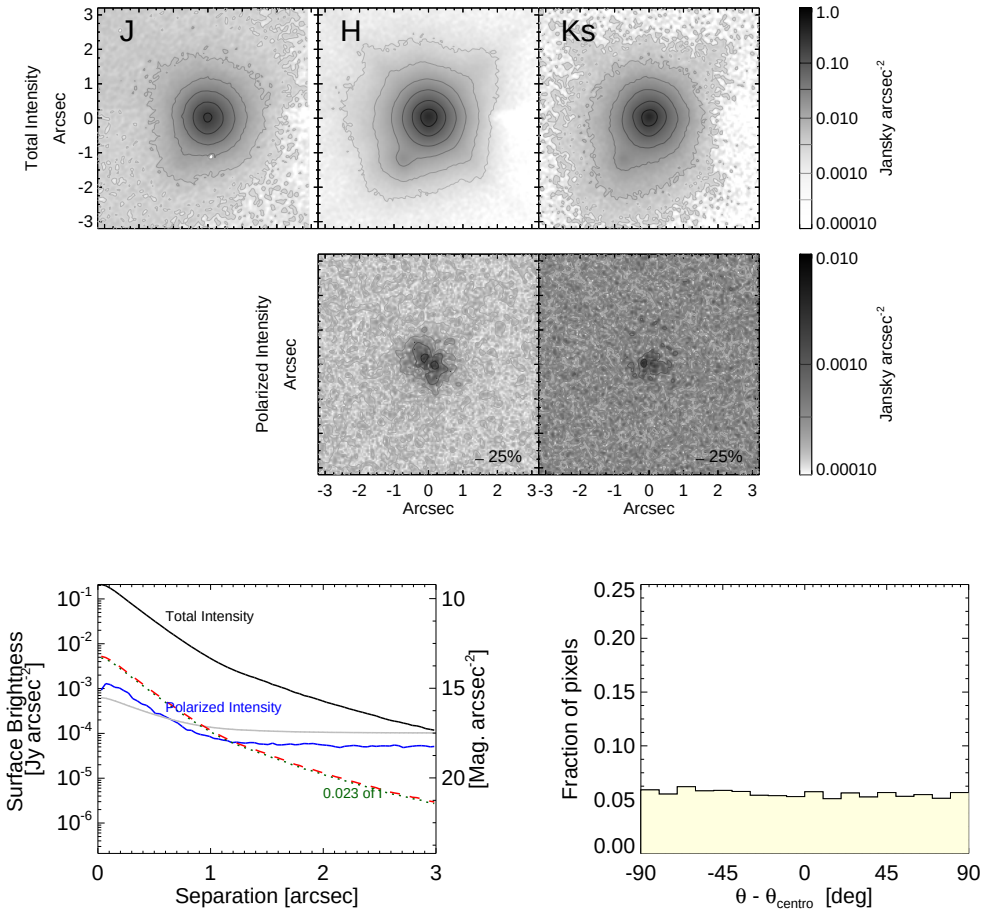

Figure 4.173: Imaging polarimetry of LkHα 259.

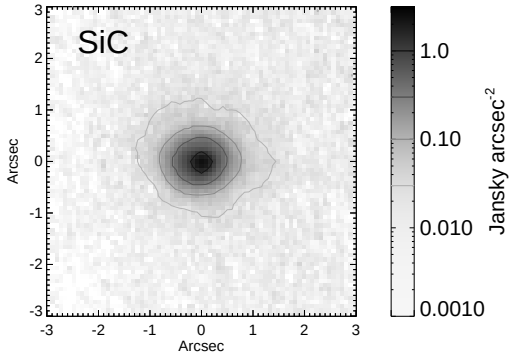

Figure 4.174: Mid-IR imaging of LkHα 259.

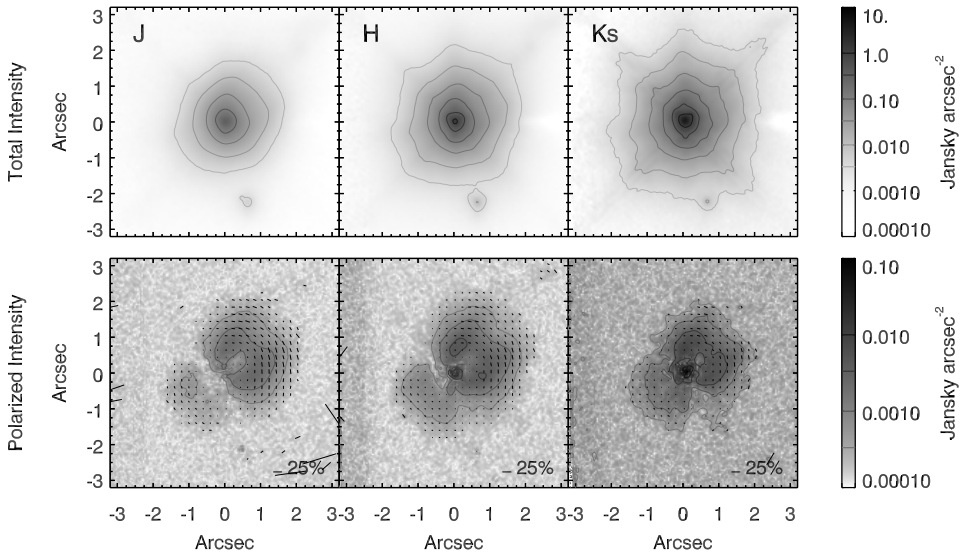

Figure 4.175: Imaging polarimetry of Hen 3-1475 (aka PDS 465).

4.6.2 MWC 922

MWC 922 (IRAS 18184-1302) was identified as an $H\alpha$ emission line star by R. Minkowski (Merrill & Burwell, 1949). While it was included in the catalog of Herbig Ae/Be stars by The et al. (1994), it has also been considered a post-main-sequence object (Henize, 1976; Voors, 1999). It was marginally resolved in the mid infrared by Meixner et al. (1999), who considered it a candidate proto-planetary nebula. Molster et al. (2002) present an optical spectrum showing many absorption lines and discuss the nature of this object, concluding that it might be a post-AGB object or a supergiant B[e] star.

The IRCAL observation reveals a stunningly perfect cross-shaped nebula, very similar to the Red Rectangle Based on the observed morphology, MWC 922 is without a doubt a post-main-sequence star on its way to becoming a planetary nebula, observed almost exactly edge-on.

4.6.3 PDS 581 (M1-92)

PDS 581 is the pre-planetary nebula M1-92, also called "Minkowski's Footprint". In my observations, it displays a beautiful pair of symmetric bipolar lobes some $5\farcs8$ in extent. A nebulous patch of polarized light $1\farcs3$ in diameter is located $7\farcs8$ west of the star. The orientation of polarization vectors indicate that this clump of material is indeed scattering

light from M1-92, but it is not located along any of the apparent axes of the system and its nature and origin are unclear based on these data.

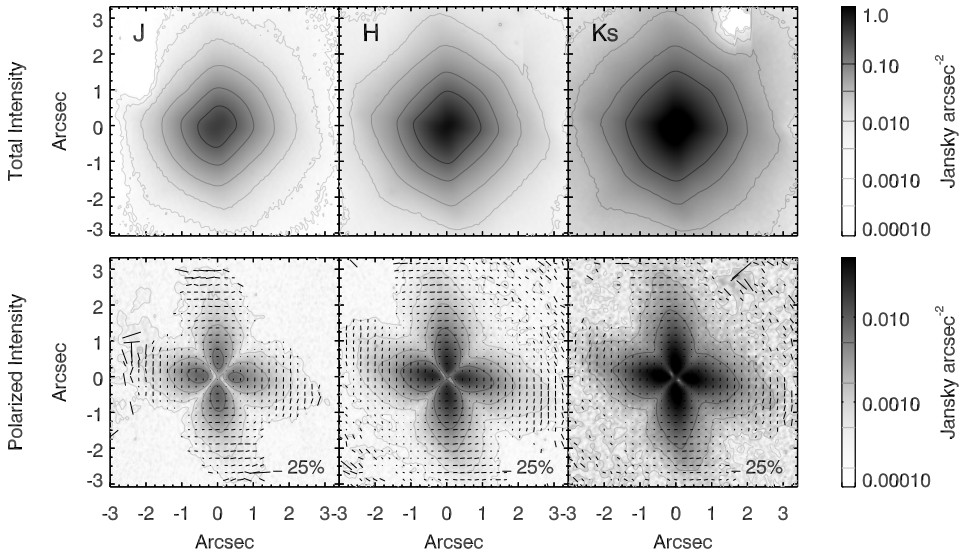

Figure 4.176: Imaging polarimetry of MWC 922. This is not a simulation - it really is that perfect!

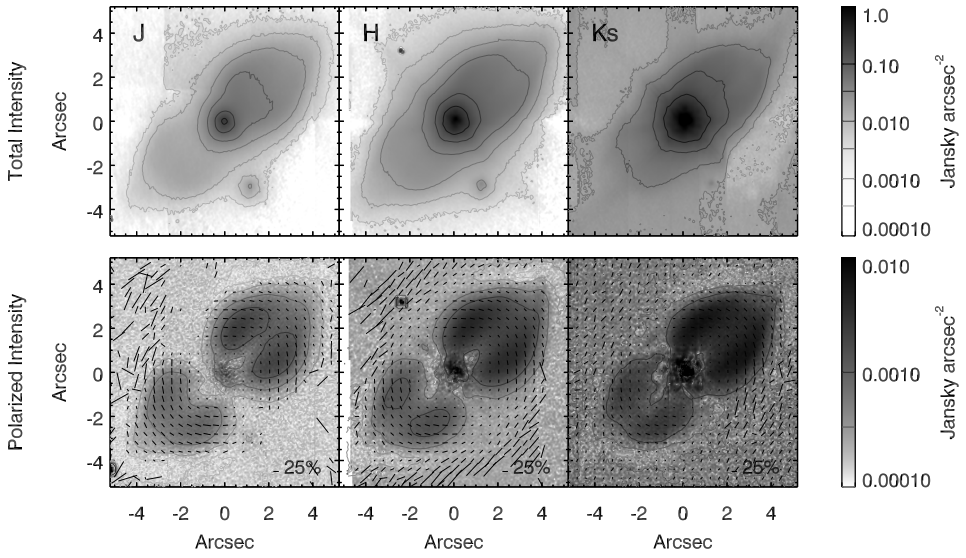

Figure 4.177: Imaging polarimetry of M1-92 (aka PDS 581).

4.7 Discussion

4.7.1 Quantifying the Detection of Polarized Light

About two dozen of our targets have immediately apparent large polarized nebulae. For targets with less obvious indication of scattered light, the centrosymmetry histogram is a powerful tool for objectively distinguishing between low- and no-polarization sources.

Figure 4.178 shows the histograms for all targets, plus Gaussians fit to each data set to locate peaks. One issue which must be addressed is which pixels to include when creating these histograms. This figure was drawn using for each source all pixels which were more than $2\sigma_{sky}$ above the sky background - i.e. most of the stellar PSF. With this approach, most sources show relatively flat histograms with occasional small deviations, and a handful of sources show very large peaks.

This can be improved by using the uncertainty masks for each image. Fig. 4.179 again shows the histograms, but now plotted only for pixels which are at least 3 σ_P polarized, as measured using the per-pixel uncertainty image, in addition to being above the sky noise. The combination of these two criteria allows a robust selection of the most trustworthy subset of data and empirically works better than either criterion alone. In the uncertainty-masked histograms, some peaks have become more apparent (e.g., HD 163296 and HD 169142) while others have become less so (DW CMa, HD 179218). The fact that the former set includes objects which are known from HST observations to have resolved disks on these spatial scales lends credence to this approach.

We can now define an objective criterion for disk detection, using the Gaussian fits to each histogram. Figure 4.180 shows the peak amplitude A and peak angle θ_{peak} for each fit[7]. It is encouraging that the sources with large peaks ($A > 0.03$, indicating a large fraction of the image area is polarized) are highly centrosymmetric, as expected. Only two highly polarized sources have their peaks offset from the centrosymmetry axis, PDS 144 and LkHα 25. Both of these are binary systems, in which the *secondary* possesses extended circumstellar dust, not the primary. The centrosymmetry plots were computed with respect to the primary, though, which is responsible for the apparent offset from centrosymmetry.

After excluding these large peaks, I computed the standard deviation σ_A of the re-

[7]Note that θ_{peak} represents the average angular offset between the observed position angles and the expected centrosymmetric position angles, rather than any one specific position angle itself.

maining of peak amplitudes, finding $\sigma_A = 0.0065$. With this, the statistical significance of any claimed detection can now be assessed. By this measure, there are 20 sources[8] detected at $> 5\sigma$, 32 sources detected at between 1 and 5σ[9], and the remaining 58 sources below $1\sigma_A$.

The 32 sources that fall into the intermediate range are worthy of closer scrutiny. Unlike the high-polarization sources, these span a wide range in θ_{peak}. Two subsets are apparent, one near the centrosymmetry axis and the other not; the separation between these two subsets is based on the lack of any sources with peak positions at around 35-45°. We draw a cut between the two groups at $\theta_{peak} = \pm 35°$, depicted by the dashed bos in Fig. 4.180; there are 20 sources inside this threshold and 12 outside. For half of the sources in the more centrosymmetric group, examination of the data quickly confirms the reality of the detection (e.g., PDS 530, Parsamian 22, PDS 415 and 453), while for others the situation is less clear (NSV 1832, for instance). HD 169142 and HD 163296 both fall into this category, and as previously mentioned these both have well-known disks. Likewise the sources V892 Tau and LkHα 101 have prior detections of $\sim 1''$ IR halos by Leinert et al. (2001). It would be difficult to make a convincing case for the presence of dust around all of these objects based solely on this polarimetric data, but we can turn that argument around: the presence of many objects with confirmed faint IR nebulosity in this set supports the idea that less-familiar members of the set, such as MQ Cas and NSV 1832, also do in fact possess extended circumstellar dust. One way to think about this classification based on θ_{peak} is as a sort of confidence interval, with objects falling in the $1-5\sigma$ group being those at a 50% confidence interval. These objects are worthy of further study.

But what about the sources with $1 - 5\sigma_A$ polarization, that have θ_{peak} offset $\gtrsim 35°$ from centrosymmetry? This appears to be a more heterogenous set. The stars HD 150193 and HD 144432 have both been found to be polarized but unresolved in recent UKIRT observations by Hales et al. (2006). Remarkably, their position angles for these two sources(57 and 75°, respectively) are very close to the offsets measured here in θ_{peak} (63 and 80°), but since θ_{peak} denotes the average deviation from centrosymmetry rather than any one specific position angle, it is unclear whether this agreement is merely a coincidence or has

[8]HBC 1, LkHα 198, V376 Cas, RNO 1BC, AFGL 4029, AB Aur, MWC 778, VY Mon, R Mon, LkHα 25, PDS 144, Parsamian 21, HBHA 3203-03, LkHα 224, LkHα 225, LkHα 324 SE, V645 Cyg, LkHα 234, LkHα 233, MWC 1080

[9]See Table 4.3.

physical meaning. The disk around HD 150193 was also resolved in Subaru coronagraphic observations (Fukagawa et al., 2003).

On the other hand, several of the sources with offset θ_{peak} appear to be the result of instrumental errors. In particular, the cluster of several sources around $-70°$ is caused by an intermittent electronic crosstalk problem in IRCAL which results in a streaky PSF artifact to the west of any star; this artifact ends up causing spurious polarization signals in that region of the detector. But this effect does not occur for *all* sources with offset θ_{peak}. Several of the other sources with offset θ_{peak} are binaries: HD 35187, XY Per, HD 216629. As has already been discussed for PDS 144 and LkHα 25, binarity can cause offsets in these histogram plots, either through a disk located around the opposite star giving a distorted centrosymmetry histogram (as in PDS 144 and LkHα 25), or through differing amounts of close circumstellar dust causing different polarization for the two sources. Recall that our reduction process scales the raw frames to minimize the subtraction residual, but this can only be optimized for one star at a time.

In any case, it appears that these sources which display offset θ_{peak} are a heterogenous bunch: some are clearly due to instrumental effects, some are in fact astrophysical in origin, and most are indeterminate. Future observations may be able to clarify what's going on for these sources, but for now we will not discuss them further.

These histograms are not a perfect discriminant. HD 141569, which has a disk beautifully revealed by ACS and NICMOS coronagraphic imaging, falls below our detection threshold at $0.6\sigma_A$. Conversely, a few of the sources above $1\sigma_A$ are statistically speaking likely to be the upper members of the underlying measurement noise distribution. This is a heterogeneous data set, taken in varying atmospheric conditions over a period of several years in which both the AO system and science camera went through several upgrades, and to suppose that we can completely characterize it by a single Gaussian distribution is surely an oversimplification. Indeed, the process by which we compute σ_A is biased, because it is the standard deviation of a sample including sources that do possess resolved circumstellar dust. For σ_A to be an accurate assessment of purely instrumental uncertainties would require its computation using a comparably sized set of stars known to lack resolved circumstellar dust, a refinement I do not attempt. Still, even the moderately unsophisticated approach shown here demonstrates the efficacy of this detection metric.

In our sample of 110 targets, we have detected 20 sources with a high degree of polarization, and a further 20 with a lower polarization and correspondingly higher uncer-

tainties. While the above-discussed factors render a handful of these detections uncertain, there is no reason to suspect that the uncertainties are biased toward either false positives or false negatives. In other words, it is equally likely that one or two of our non-detections actually possess extended dust which we failed to detect, or that one or two of our claimed marginal detections are false. Indeed, we know of at least one such false negative, for HD 141569, where Hubble coronagraphic imaging detects a disk we do not see here. So the overall statistical conclusions of our survey are not biased by the uncertainties on any individual source. Thus we can conclude that about $35\% \pm 5\%$ of Herbig Ae/Be stars possess extended circumstellar dust on scales of 0.1-1″, with surface brightnesses of approximately 15-17 mag arcsec^{-2}, that are detectable in polarized dust-scattered light.

Table 4.2: Highly Polarized Sources (detected at $> 5\sigma$).

Name	**NIR Morphology**	New detection?
HBC 1	Cometary nebula	
LkHα 198 IR	Cometary nebula	
LkHα 198	Bipolar nebula + disk	
V376 Cas	Irregular nebula	
RNO 1B	Tidal tails?	
RNO 1C	Tidal tails?	
AFGL 4029 W	Outflow cavity?	
AFGL 4029 E	Bipolar Nebula	
AB Aur	Disk	
MWC 778	Spiral nebula	Y
VY Mon	Elliptical nebula/ Disk?	Y
R Mon	Bipolar nebula	
LkHα 25	Binary with polarized secondary	Y
PDS 144 N	Edge-on Disk	Y
Parsamian 21	Bipolar/cometary nebula	
HBHA 3203-03	Arcs of dust	
LkHα 224	Ring-shaped nebula	
LkHα 225 N	Tidal tails?	
LkHα 225 S	Tidal tails?	
LkHα 324 SE	Bipolar nebula	Y
V645 Cyg	Arcs	
LkHα 234	Multi-polar nebula	
LkHα 233	Disk+envelope w/ bipolar outflows	
MWC 1080	Irregular nebula	

Table 4.3: Sources detected at $1 - 5\sigma$.

Name	**NIR Morphology**	New detection?
V892 Tau	?	
HK Ori	?	
HD 250550	Faint fan of nebulosity	
HD 259431	Faint fan of nebulosity	
Z CMa	Fan of nebulosity	
PDS 415	Disk	Y
PDS 453	Disk or Elliptical nebula	Y
PDS 530	Jet or elongated nebula	Y
Parsamian 22	Polarized companion plus faint nebula	Y
BD +40 4124	Faint fan of nebulosity	
HD 163296	Disk	
HD 169142	Disk	
MQ Cas	?	
LkHa 101	?	
NSV 1832	?	Y
HD 190073	?	
MWC 349	?	
V361 Cep	?	
V1057 Cyg	?	
BH Cep	?	Y

4.7.2 Observed Source Morphologies

Some authors have argued that, because adaptive optics only improves the PSF within a finite "AO control radius" (Perrin et al., 2003), AO has little benefit for polarimetry

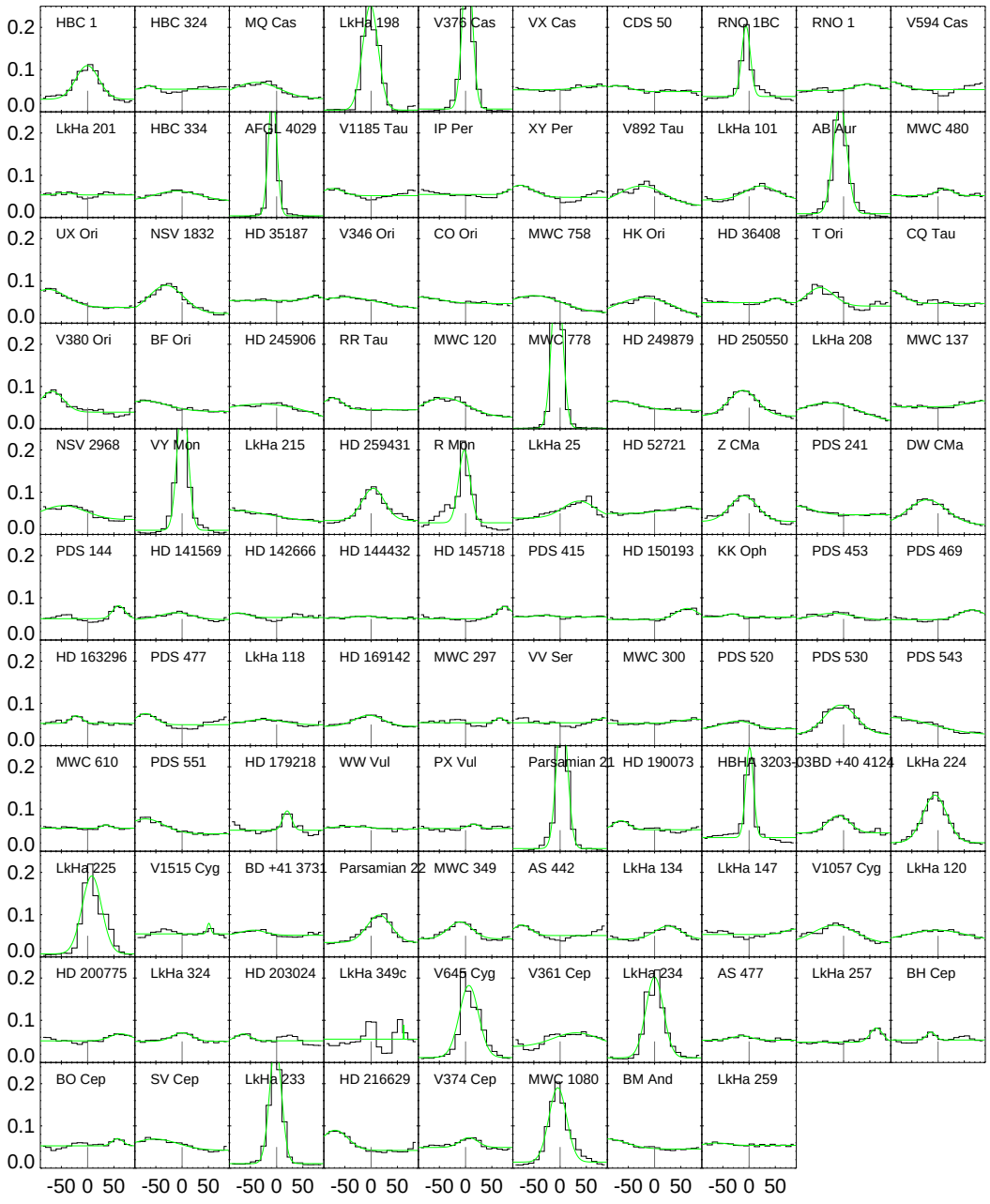

Figure 4.178: Centrosymmetry histograms for all targets. Black lines show the fraction of pixels which have Stokes $I > 2\sigma_I$ above the sky noise that have polarization in each 10°bin. Green lines show the fitted Gaussians. About one fifth of sources have an obvious peak at $\theta = 0$.

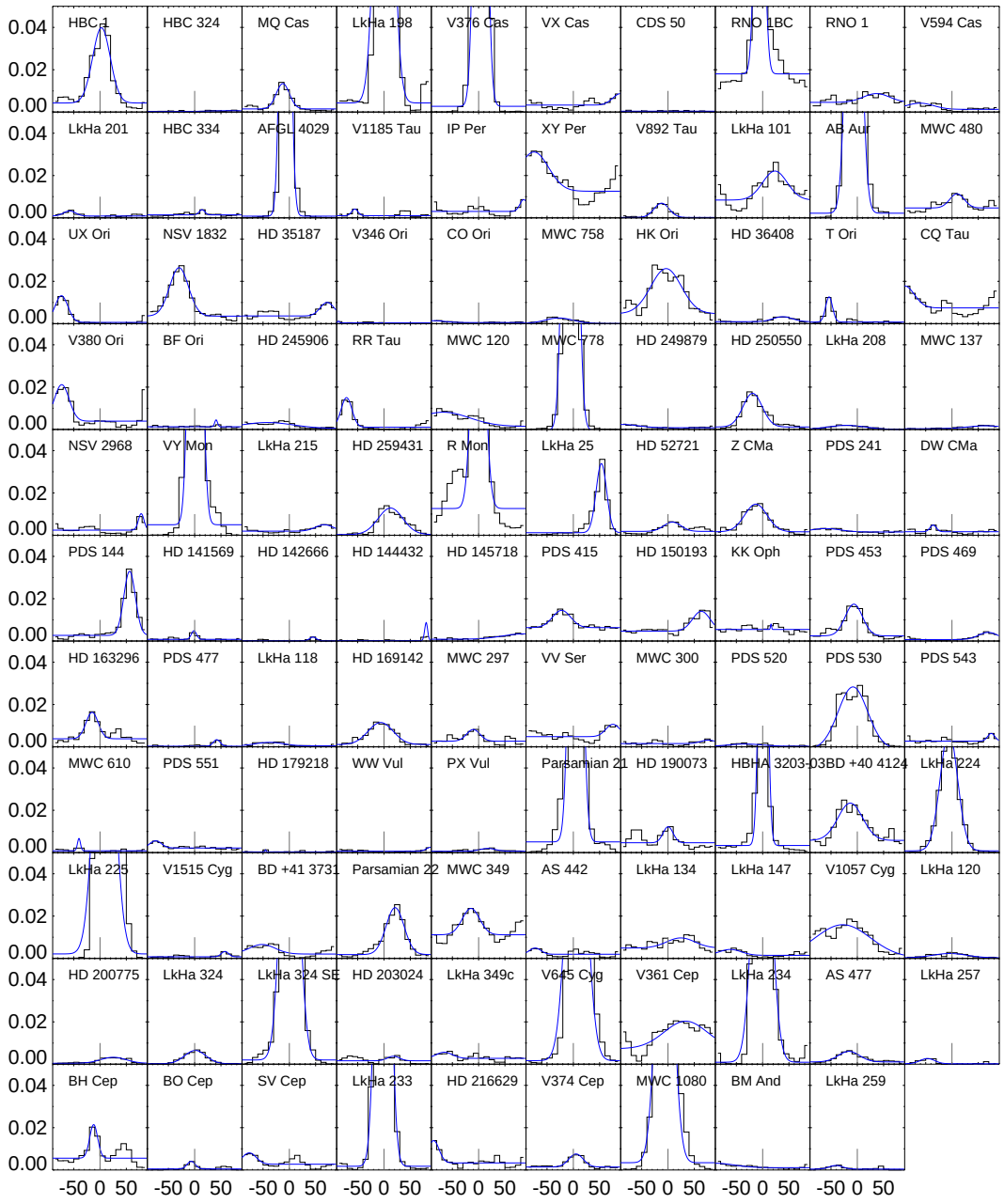

Figure 4.179: The same as Fig. 4.178, except here the histograms are drawn only from pixels which are both $I > 2\sigma_I$ above the sky noise and $P > 3\sigma$. Note the smaller y axis scale compared with the previous figure. The use of the error mask for P when computing the histograms allows peaks to be seen for many additional sources.

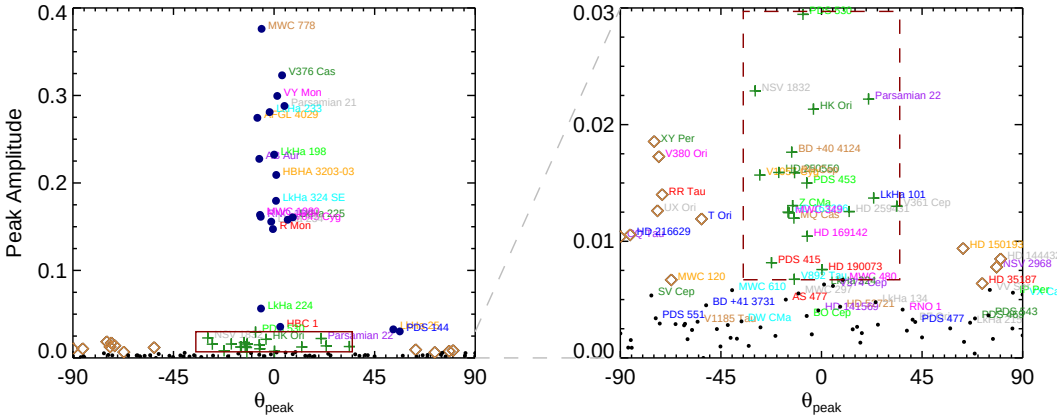

Figure 4.180:

Peaks in the centrosymmetry plot for each star. The **left** figure shows the full set of data; the spike of very highly polarized objects is clear. The **right** figure zooms in to the bottom end of the range to show peaks between 1 and 5 σ. These data naturally fall into groups separated in θ_{peak} value and position angle; see the text for discussion. The dashed box identifies the group of sources which fall above the 50% confidence level for detection of polarized light; most of these sources (but not necessarily all!) do represent actual detections of dust-scattered light. Symbols are as follows: • peaks $> 5\sigma$ (objects which are highly extended and polarized), + peaks $1-5\sigma$ inside 35°(The 50-50 confidence interval; an equal mix of objects which are definitely extended and polarized, but less so than the first group, and objects with ambiguous or uncertain evidence for polarized light), $\diamond$ peaks $1-5\sigma$ outside 35°(most likely due to instrumental errors), · peaks $< 1\sigma$ (unpolarized sources). The colors of the source name labels don't signify anything and are used solely to distinguish overlapping text.

outside of the central few tenths of an arcsecond (e.g., Kuhn, 2005), but this is not correct. On the contrary, while AO correction does not remove any stellar light from the outer portion of the PSF, it does allow *fine subarcsecond detail in the structure of the polarized nebula itself to be seen*, once the stellar PSF has been removed.

The resolved dust geometries seen around Herbig Ae/Be stars are tremensdously varied in appearance. The revealed dust structures variously include face-on and edge-on disks, extended circumstellar envelopes, bipolar outflow cavities, and tidal streamers between binary stars. Most sources are very asymmetric. These are young systems, and the residual impact of initial conditions is still quite large. Tables **??**, **??** and 4.4 briefly summarize the observed characteristics of each source, and indicate for which sources circumstellar material is resolved for the first time here. (For the other sources, previous observations demonstrated the existence of extended dust, but the observations presented

here in most cases improve on the angular resolution or widen the wavelength coverage.)

4.7.3 Quantifying the Detection of Barely-resolved Mid-IR Sources

Many of our targets display very extended mid-IR nebulae, in one case extending more than 10″ across, corresponding to a physical size of around 10,000 AU (though the distance to this source, MWC 778, is highly uncertain). But many previous studies have found certain Herbig Ae/Be stars to be slightly resolved, on scales of a few tenths of an arcsecond. Thus it is worth examining each of the apparent mid-IR "point sources" more closely. To do this, I have computed for each star the mean radial profile (Figs. 4.181-4.184). PSF quality varied between the two instruments and changed from night to night with ambient seeing, so the radial profiles are grouped by date and wavelength.

In addition to the sources with highly extended mid-IR emission, several targets did prove to be slightly extended in these data: HD 169142 in both N' and Qa bands, and both PDS 144 S and LkHα 198 in the Qa band. We also confirm the previously-known extension of HD 141569. There are also a number of sources for which the data are inconclusive, hinting of spatial extent but not at such a level that seeing-related PSF variations are definitively ruled out.

Table 4.4: Sources Resolved in the Mid-Infrared

Name	**MIR Morphology**	New detection?
LkHa 198	Slightly resolved	
RNO 1B	Tidal tail?	
RNO 1C	Tidal tail?	
AFGL 4029 W	Bipolar/filamentary nebula	
AFGL 4029 E	H2 region or bow-shock shaped nebula	
MWC 778	Spiral nebula	Y
NSV 1832	Irregular nebula	Y
R Mon	Bipolar nebula	
PDS 241	Butterfly-shaped nebula	Y
PDS 144 S	Slightly resolved	Y
PDS 144 N	Edge-on Disk	Y
HD 169142	Slightly resolved	Y
AS 310	Extensive nebula	
HD 200775	Arc-shaped nebula	Y
LkHα 234	Curved nebula and embedded companions	
LkHα 324 SE	Slightly resolved	Y
MWC 1080	Filamentary nebula	

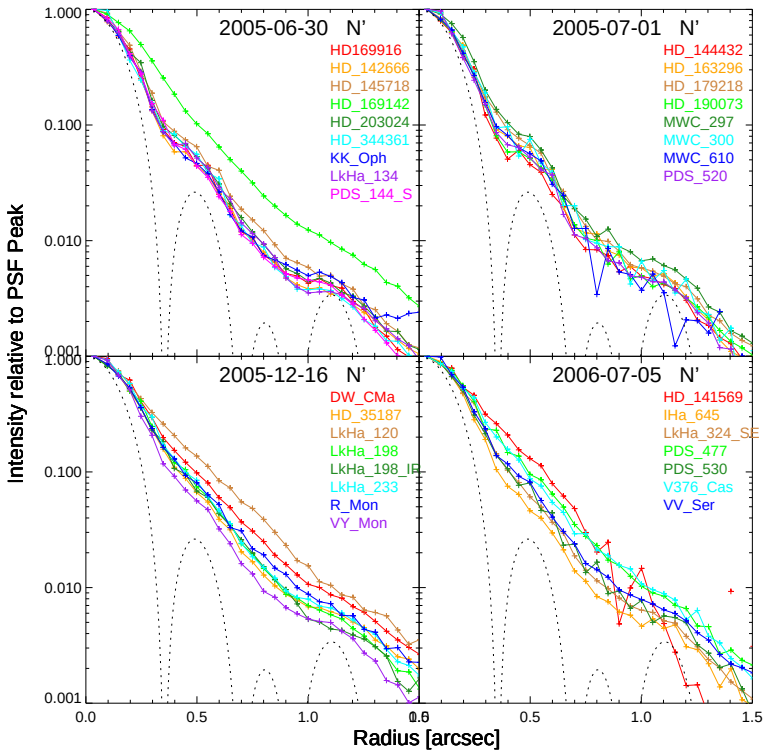

Figure 4.181: Radial profiles for targets observed with Michelle in the N' band, organized by date. The dotted line shows the diffraction-limited perfect PSF profile. HD 169142 is well-resolved on 2005-06-30. The 2005-12-16 observations suffer from somewhat degraded seeing and have poorer PSFs; the apparent extension of LkHα 120 is not conclusive. On 2006-07-05, again weather limits our sensitivity, though the most extended object here, HD 141569, has indeed been previously reported to be extended at this wavelength.

4.7.4 Correlations with Stellar Properties

To what extent do the observed properties of circumstellar dust depend on the nature of the central star? I present here a few figures addressing this, though it will be possible to address this question with much more rigor once quantitative disk and envelope models have been fit to these data.

Extended circumstellar dust is found predominantly around the reddest, faintest sources in our sample—a fact not entirely unsurprising. What *was* surprising was the strength of this effect. About $\sim 15\%$ of our target sample was so faint that observations required the use of laser guide star mode with Lick AO. *Of laser guide star AO targets, fully 70% possess extended nebulosity, versus no more than 15% for our natural guide star*

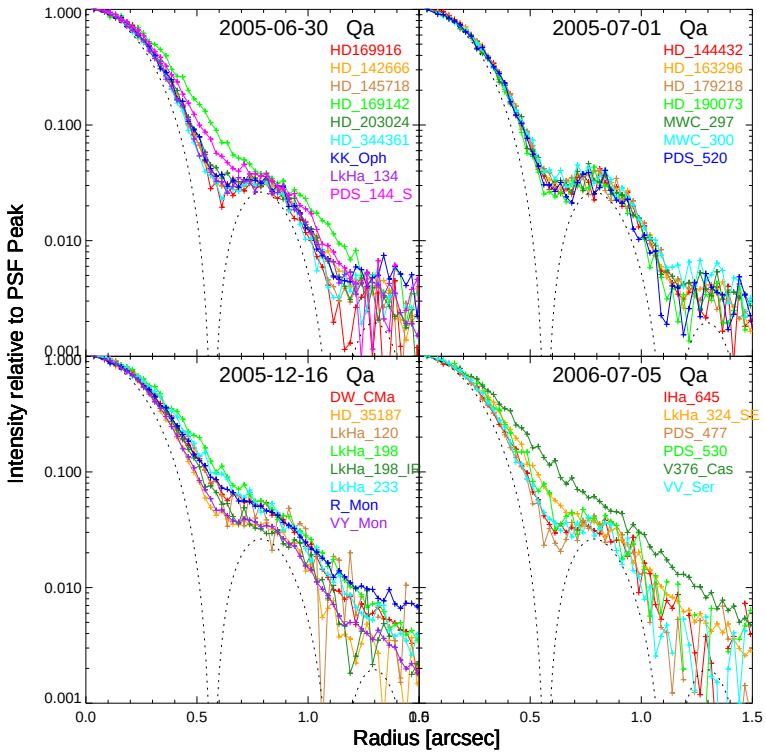

Figure 4.182: Radial profiles for targets observed with Michelle in the Qa band, organized by date. HD 169142 and PDS 144S are both resolved on 2005-06-30. On 2005-12-16, the most extended objects are LkHα 198, LkHα 233, and R Mon. For LkHα 198 we have an convenient simultaneous PSF reference from the nearby star LkHα 198 IR; the latter star's profile falls off significantly more steeply than the former, confirming that LkHα 198 is indeed extended at this wavelength. Given measurement uncertainties, I'm not as sure about DW CMa and LkHα 120. On the last night, V376 Cas appears to be very extended, but this is a bad measurement resulting from a highly astigmatic PSF. Our LWS observation of this star is nowhere near as extended. LkHα 324 SE shows some evidence for being extended here as well.

AO targets (Fig. 4.185). Without LGSAO, we would have been unable to observe the vast majority of our most interesting targets. These are presumably the youngest objects, still most deeply embedded in their natal clouds.

This correlation extends to a broad range of astronomical colors. In a 2MASS JHK_s color-color diagram, I find that the most extended sources are also preferentially the reddest, though there is considerable scatter about this relation (Figs. 4.188 and 4.189). Similarly the presence of extended emission is much more common around objects with flat or rising SEDs, Group II in the Hillenbrand et al. (1992) classification system (Fig.

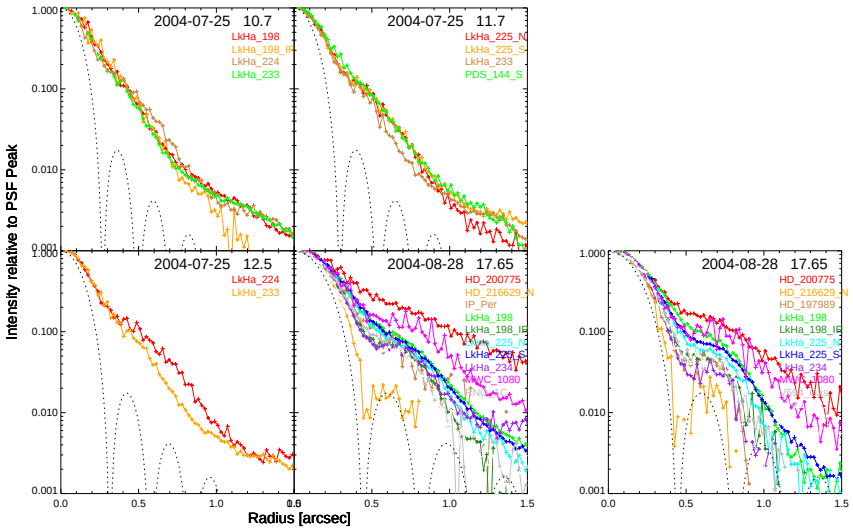

Figure 4.183: Radial profiles for targets observed with LWS in filters other than SiC, organized by date (left panel). HD 200775 and MWC 1080 are resolved at 17.65 μm; nothing is unambiguously resolved in the other filters. LkHα 224 looks like it might be extended in 12.5 μm, but given the small number of data points and the fact that it's even less extended-looking at 10.7, this is inconclusive.
At 17.65 μm, HD 216629 N has a much higher quality PSF than the other targets. I hypothesized that this might be due to the use of shift-and-add with that star and not the others, so I re-reduced the other observations using the same shift-and-add as HD 216629 (right panel). This improved some of the PSFs slightly, but still HD 216629 N is far and away the best (perhaps just a moment of great seeing?). Still, in the shift-and-added data we can more easily see that LkHα 198 is extended compared to LkHα 198 IR (cf. the Michelle Qa data, Fig. 4.182). LkHα 225 N *and* LkHα 225 S both have slightly extended profiles, but given that both are extended, and by about the same amount, it is very possible that this is just due to seeing changes.

4.187).

The presence of extended emission does not appear to be strongly correlated with spectral type (Fig. 4.186), at least not based on this preliminary analysis.

4.7.5 The Effects of Binarity

A number of studies have previously examined the influence of binarity on circumstellar disk properties (Maheswar et al., 2002; Jensen et al., 2004; Smith et al., 2005; McCabe et al., 2006). Relatively few Herbig Ae/Be stars have been observed at high spatial resolution in the mid-IR. For many of my targets, the observations presented here are the first to resolve the components of the binary, and thus provide new constraints for SED

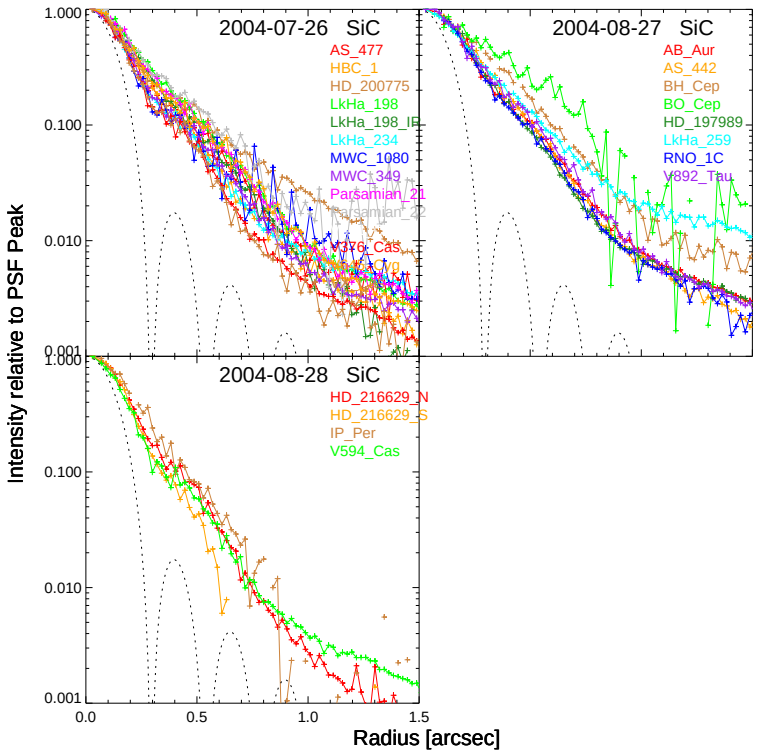

Figure 4.184: Radial profiles for targets observed with LWS in the SiC filter, organized by date. HD 200775 is the only target unambiguously resolved in these data. BO Cep and LkHα 259 both look extended, but given the signal-to-noise for both of these objects this is not unambiguous.

models. The detailed modeling of the sources presented here is an ongoing project.

However, a brief examination of the observed properties of circumstellar dust around stars in binary systems does have one clear result. Maheswar et al. (2002) argued based on aperture polarimetry that most Herbig Ae/Be binaries have disks coplanar with the binary orbital plane. But in several instances, binaries in my sample show evidence for non-coplanar disks, either through direct imaging and mid-IR spectroscopy, as in the case of PDS 144, or through differing polarization states for the two stars, as in the case of LkHα 25. Even more striking are the instances in which the amount of circumstellar dust around the two stars is discrepant. HD 216629 is a good example: the southern star, 2.5 mag brighter in the optical than its neighbor, fades to near-undetectability by 18 μm, while the optically-faint southern star rises to become almost 5 mag brighter than northern. In Hillenbrand et al.'s SED classification scheme, they are type III and type I, respectively: the northern has emission from dust consistent with a substantial circumstellar disk, while

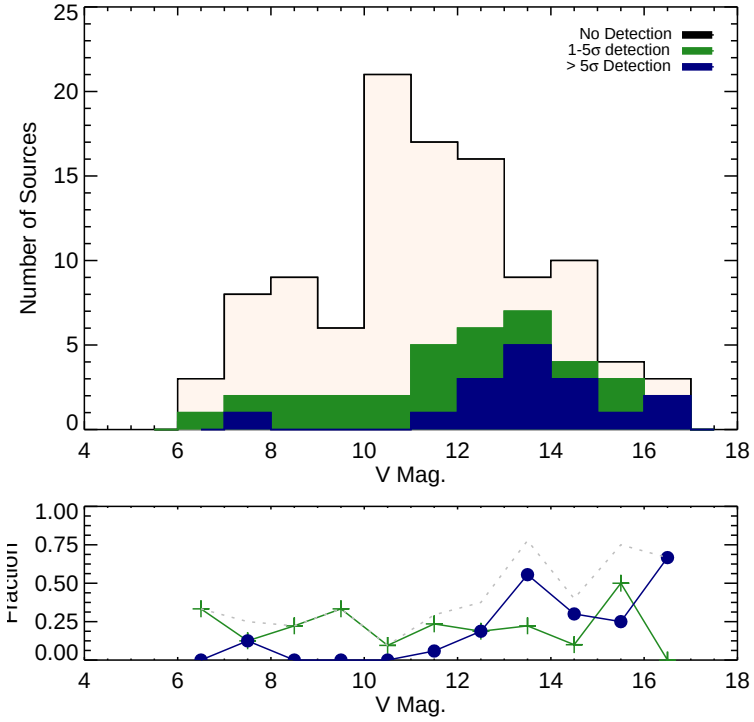

Figure 4.185: Top: A histogram of detected sources versus V magnitude. Bottom: The same data, presented as a plot of the fraction of sources detected for each magnitude bin. The grey dotted line is the sum of the green and blue lines, which are the fractional counts for moderately polarized and highly polarized YSOs , respectively. Most of the highly extended and polarized sources are found among the visually dimmest Herbig Ae/Be stars. The only notable exception is AB Aur with $V = 7$, though many of the $1 - 5\sigma_P$ detected sources are also around that brightness.

the southern star has only a minimal infrared excess from a small amount of dust.

These systems—PDS 144, HD 216629, and others—are presumably coeval. In PDS 144's case, the spectral types are similar as well, so the stars have comparable mass. Yet the dust properties of the stars in each binary vary tremendously. We are left with a picture in which dust processing must depend on parameters other than merely stellar mass and age. The stochastic growth of planetesimals into planets, and subsequent clearing of gaps in the primordial disks by those planets, probably plays a central role in determining the lifetime of disks—a conclusion also supported by Spitzer observations of disk fractional incidence in several young nearby clusters.

We also find evidence for interaction among members of binary star systems. LkHα

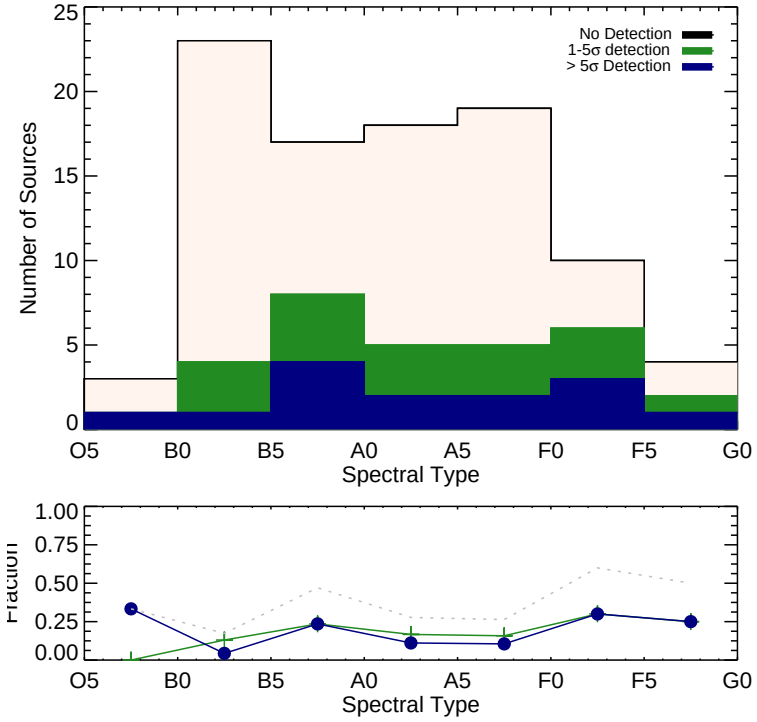

Figure 4.186: Histogram of detected sources versus stellar spectral type. No obvious trends are visible, but I haven't done any rigorous statistical tests.

225 and RNO 1B/1C both have dust lanes that arc gracefully between the two stars, suggesting the tidal disruption of disks during previous close stellar encounters.

4.8 Conclusions

1. I have surveyed 110 Herbig Ae/Be stars (or binary stars) for resolved circumstellar dust using a sensitive differential polarimeter on the Lick AO system. This represents a large fraction of all known Herbig Ae/Be stars.

2. Histograms of the degree of centrosymmetry in the polarization position vectors provide a powerful tool for identifying faint polarized signals in the data. The effectiveness of these histograms is greatly enhanced by the use of per-pixel uncertainty maps produced during the data reduction process.

3. Half of the observed sources have centrosymmetry peaks $> 1\sigma$ suggesting the pres-

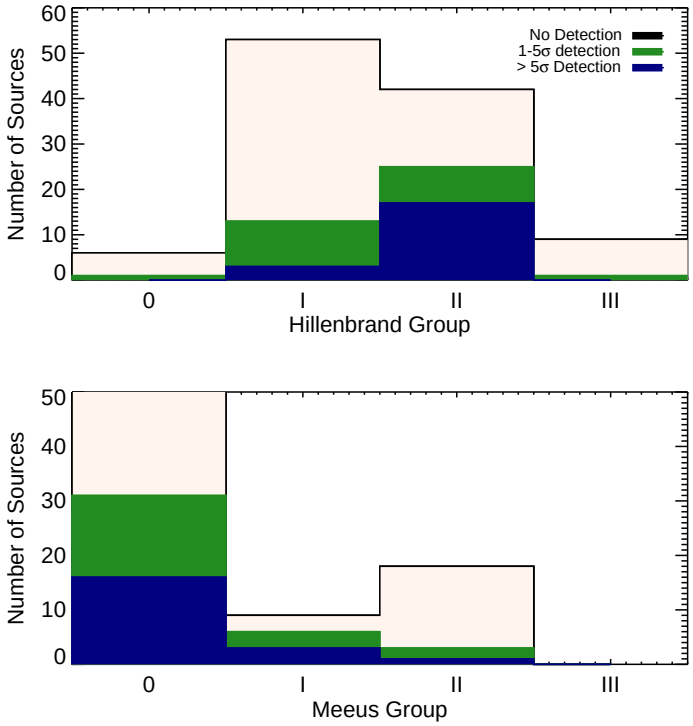

Figure 4.187: Detected sources versus the SED classification systems of Hillenbrand et al. (1992) and Meeus et al. (2001) (see Chap 1.). "Group 0" is objects presently lacking classifications in that system. There are significantly more targets with extended polarized nebulae for Hillenbrand Group II objects than for Group I.

ence of polarized dust-scattered light on scales of $\sim 1''$. Most display the expected centrosymmetric pattern, though 13 have their peaks substantially offset from the expected position angle, for reasons which are not yet entirely clear.

4. 20% of the targets have large polarized nebulae spanning several arcseconds. These are predominantly the reddest, most embedded sources, often requiring laser guide star AO for observation.

5. The observed sources display a tremendous diversity of morphologies, including disks, envelopes, tidal tails, and circumstellar arcs of dust.

This project has resulted in a the collection of a rich dataset that lends itself to further studies. Planned future projects include, for selected sources, simultaneously fitting Monte Carlo disk and envelopes models to the SED and the resolved images; multiwavelength

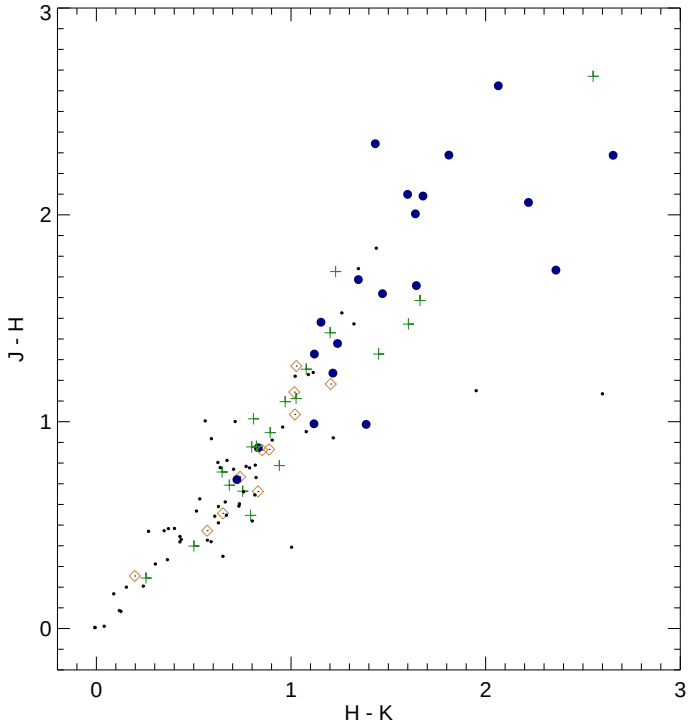

Figure 4.188: Symbols have the same meaning as in Fig. 4.180. More highly polarized source are in general redder.

comparisons with resolved HST images and Spitzer SEDs and IRS spectra; searches for Herbig-Haro outflows from bipolar-nebulae-looking sources by wide field CCD imaging in Hα and [SII] emission lines; and OSIRIS integral field spectroscopy of the inner regions of such outflows.

Acknowledgements

Henry Roe graciously supplied us with his grid of BFATS Mauna Kea atmospheric models. David Fanning provided invaluable assistance with the development of the asinh scaling image display routines in IDL, as well as wide-ranging guidance and inspiration through the wilds of IDL programming. We greatly appreciate the excellent work of the Lick and Keck observatory staffs, in particular Elinor Gates, Mark Kassis, and Randy Campbell. We also thank Bob Becker for his gracious flexibility in trading LWS observing time, and a two dollar bill. Sergio Vieira and Carlos Torres provided helpful discussions

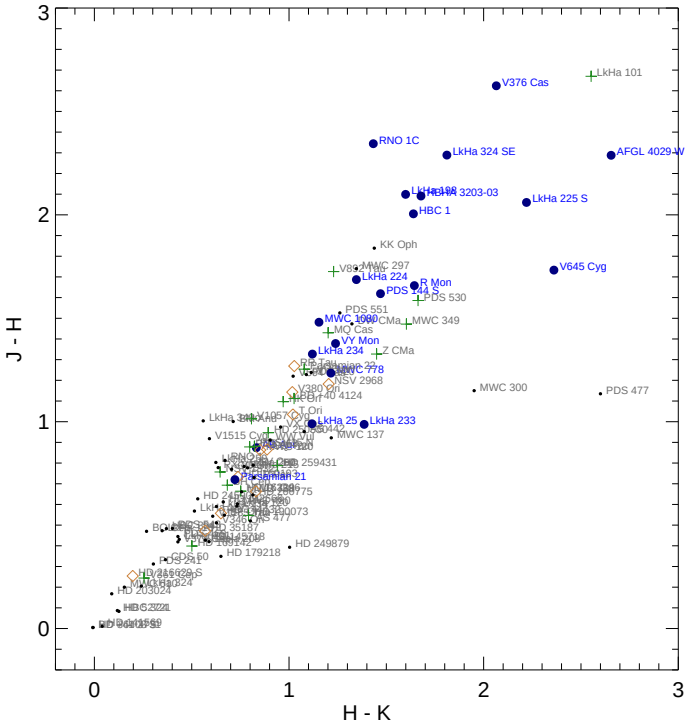

Figure 4.189: 2MASS color-color diagram for my targets, as in Fig.4.188, but with labels for the individual sources. Sources labeled in blue definitely have resolved polarized light.

regarding their PDS survey observations. We recognize that Mauna Kea has always been a site of great significance to the Hawaiian people, and we are most fortunate to have the opportunity to observe from this mountain.

Part II

Studies of Individual Stars

Chapter 5

Laser Guide Star Adaptive Optics Imaging Polarimetry of LkHα 198 and LkHα 233

Abstract

We have used laser guide star adaptive optics and a near-infrared dual-channel imaging polarimeter to observe light scattered in the circumstellar environment of Herbig Ae/Be stars on scales of 100-300 AU. We discover a strongly polarized, biconical nebula 10 arcseconds in diameter (6000 AU) around the star LkHα 198, and also observe a polarized jet-like feature associated with the deeply embedded source LkHα 198-IR. The star LkHα 233 presents a narrow, unpolarized dark lane consistent with an optically thick circumstellar disk blocking our direct view of the star. These data show that the lower-mass T Tauri and intermediate mass Herbig Ae/Be stars share a common evolutionary sequence. [1]

5.1 Introduction

Diffraction-limited optical and infrared astronomy from the ground requires adaptive optics (AO) compensation to eliminate atmospheric wavefront disturbances. Bright stars

[1] This chapter has been previously published as Perrin et al. (2004b) and is reproduced here with the permission of all coauthors.

Figure 5.1: The Lick Observatory LGS AO system in operation on 2003 July 22. The laser beam is visible in Rayleigh scattered light for several kilometers. The faint cirrus clouds illuminated by the Moon remained outside our pointing direction and did not interfere with the observations. The yellowish cast of the dome is due to the street lights of nearby San Jose.

may be used as wavefront references for this correction, but most astronomical targets lack nearby guide stars. AO observations of these targets from the ground can only be accomplished using artificial laser guide stars (LGS) (Happer et al., 1994).

Herbig Ae/Be stars are young stars with masses between 1.5 and 10 times that of the sun; they are the intermediate-mass counterparts of the more common T Tauri stars. Excess infrared and millimeter emission shows that Herbig Ae/Be stars are associated with abundant circumstellar dust (Hillenbrand et al., 1992). Visible and near-infrared (NIR) light scattered from dust is typically polarized perpendicular to the scattering plane (Bastien, 1987), making polarimetry a useful tool for probing the distribution of this material (Weintraub et al., 2000). While Herbig Ae/Be stars are intrinsically very luminous, many are so distant or extincted that they are too faint to act as their own wavefront references and thus require LGS AO.

The Herbig Ae/Be stars LkHα 198 and LkHα 233 (Table 5.1) were observed on 2003 July 22 at the 3-m Shane telescope at Lick Observatory (Fig. 5.1) using the Lawrence Livermore National Laboratory LGS AO system (Max et al., 1997) and the Berkeley NIR camera IRCAL (Lloyd et al., 2000). The atmospheric seeing was 0.8 arcseconds at 550

nm, and the AO-corrected wavefront produced images with Strehl ratios $\approx 0.05 - 0.1$ at 2.1 microns and full-width at half maximum resolution of 0.27 arcseconds.

IRCAL's imaging polarimetry mode utilizes a cryogenic $LiYF_4$ Wollaston prism to produce two simultaneous images of orthogonal polarizations. The sum of the two channels gives total intensity, and the difference gives a Stokes polarization. The dominant noise source near bright stars in AO images is an uncorrected seeing halo. Because this halo is unpolarized and thus vanishes in the difference image, dual-channel polarimetry enhances the dynamic range in circumstellar environments (Potter et al., 2000). The observing techniques and data reduction methods are based on Kuhn et al. (2001b).

5.2 LkHα 198

LkHα 198 is located at the head of an elliptical loop of optical nebulosity extending 40 arcseconds to the star's southeast (Li et al., 1994). This complex region 600 parsecs distant includes a molecular CO outflow (Canto et al., 1984) and two Herbig-Haro jets (Corcoran et al., 1995), as well as two additional Herbig Ae/Be stars in the immediate vicinity (V376 Cas and LkHα 198-IR) (Hajjar & Bastien, 2000) and a millimeter source (LkHα 198-MM) believed to be a deeply embedded protostar (Sandell & Weintraub, 1994). This proximity of sources requires high resolution observations to disentangle the relationships between the various components (Koresko et al., 1997). We discover a biconical nebula $\sim$10 arcseconds in diameter (6000 AU), oriented north-south, with polarization vectors concentric with respect to LkHα 198 (Fig. 5.2). The lobes of the reflection nebula are divided by a dark, unpolarized lane that we interpret as a density gradient towards the equatorial plane of a circumstellar disk and/or a flattened envelope. The north-south orientation indicates that LkHα 198 is unlikely to have created the giant elliptical nebula or the molecular outflow to the southeast. However, it is consistent with LkHα 198 being the source for the Herbig-Haro flow at a position angle (PA, measured east from north) of 160°, a conclusion supported by the extension of the polarized reflection nebula along this PA. However, this is 20° away from the observed symmetry axis of the nebula, requiring an inner disk axis tilted or precessing with respect to the outer envelope.

The embedded source LkHα 198-IR (Lagage et al., 1993) is detected in our H and K_s band data 5.5 arcseconds from LkHα 198 at PA=5°. A polarized, extremely blue, jet-like feature extends >2 arcseconds (1200 AU) from LkHα 198-IR at PA=105° (Fukagawa

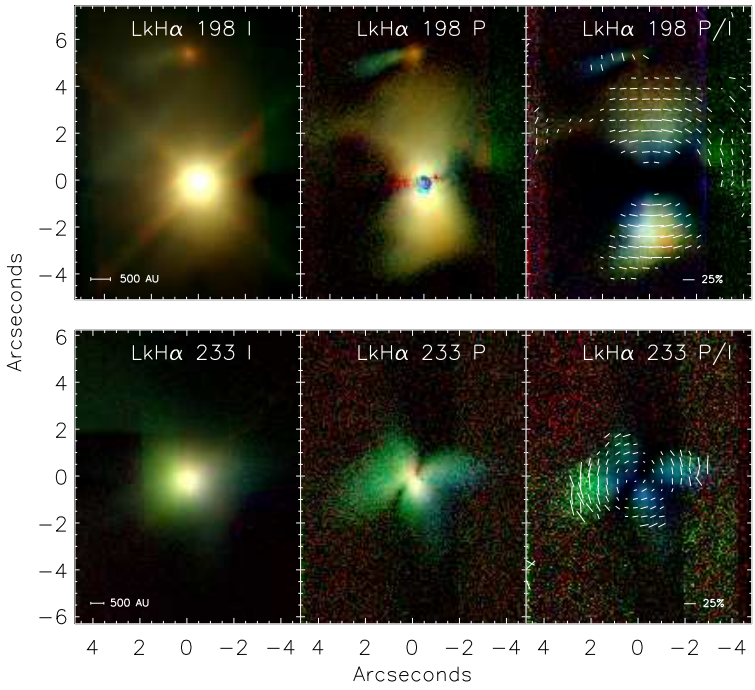

Figure 5.2: Three-color LGS AO mosaics of LkHα 198 and LkHα 233. Plotted from left to right for each object are the total intensity (Stokes I), the polarized intensity ($P = \sqrt{Q^2 + U^2}$) and the polarization fraction (P/I). I and P are displayed using log stretches, while P/I is shown on a linear stretch. Red is K_s band (2.1 microns), green H (1.6 microns), and blue J (1.2 microns). Polarization vectors for H band are overplotted on the P/I image; while the degree of polarization changes somewhat between bands, the position angles do not vary much. Integration times per band were 960 s and 1440 s for LkHα 198 and LkHα 233, respectively. The dimmest circumstellar features detected in our polarimetric observations are approximately $1 - 2 \times 10^4$ fainter than the stellar intensity peaks. The IRCAL polarimeter is sensitive to polarization fractions as low as a few percent, resulting in a signal-to-noise ratio of 5-10 per pixel for the typical polarizations of 15-40% observed around our targets.

et al., 2002). The polarization vectors of this apparent jet are perpendicular to its long axis, indicating that LkHα 198-IR is the illuminating source, not LkHα 198. The jet appears to be half of a parabolic feature opening toward the southeast, with its apex at LkHα 198-IR and its southern side partially obscured by the envelope around LkHα 198. We suggest that the northwest side of a bipolar structure around LkHα 198-IR may be hidden at NIR wavelengths by the dust indicated by millimeter observations (Henning et al., 1998). The orientations of circumstellar structures revealed by our images confirm that LkHα 198-IR is the best candidate for the origin of the Herbig-Haro outflow to PA 135°, though based on geometrical considerations we cannot entirely exclude the protostar LkHα 198-MM. By extension, the large elliptical nebula was most likely created by outflow from LkHα 198-IR, although we see it primarily in scattered light from the optically much brighter LkHα 198.

5.3 LkHα 233

LkHα 233 is an embedded A5e-A7e Herbig Ae/Be star which is associated with a blue, rectangular reflection nebula 50 arcseconds in extent, located in the Lac OB1 molecular cloud at 880 parsecs. Our imaging polarimetry reveals four distinct lobes bisected by a narrow, unpolarized lane with PA$\approx$150° (Fig. 5.2). The nebulosity around LkHα 233 is extremely blue in the NIR, with its east-west extent decreasing from 6 arcseconds (5300 AU) at J and H to 2 arcseconds (1800 AU) at K_s. The orientation of the lobes relative to the dark lane suggests that they are the limb-brightened edges of a conical cavity in a dusty envelope illuminated by a highly extincted star. The radial extent of the dark lane (1000 AU) suggests that it is associated with an equatorial torus characteristic of a flattened infalling protostellar cloud (Terebey et al., 1984), and not a rotationally-supported disk.

We find that the intensity peak of the star is shifted southwest relative to the polarization centroid, with the displacement increasing from 0.15 arcseconds at K_s to 0.35 arcseconds at J. This too indicates that the lane consists of optically thick foreground material which has a flattened spatial distribution consistent with a circumstellar disk or infalling protostellar cloud. We do not see the star directly, but instead view a scattering surface above the disk midplane.

Our results are consistent with low-resolution, wide-field optical imaging polarimetry (Aspin et al., 1985), which suggests a circumstellar torus in the northwest-southeast direction perpendicular to a bipolar reflection nebula. Our interpretation is also consistent

with the existence of an optical [S II] emission line jet (Corcoran & Ray, 1998a) blue-shifted to the southwest. The jet both bisects the nebulosity and lies perpendicular to the proposed disk. The geometry of the reflection nebula indicates that the outflow is only poorly collimated ($\Delta\theta \approx 70^{\circ}$) despite the apparently narrow jet traced by optical forbidden line emission. Because [S II] line emission arises preferentially in regions denser than the critical density for this transition, the surface brightness distributions can take on the appearance of a highly collimated jet, despite the fact that the streamlines collimate logarithmically slowly (Shu et al., 1994).

5.4 Discussion

Observations of T Tauri stars have led to a general understanding of the origin of solar-type stars (Shu et al., 1987): The fragmentation and collapse of an interstellar cloud creates a self-gravitating protostar surrounded by a Keplerian accretion disk fed by an infalling, rotationally-flattened envelope. The disk mediates the outflows common to low-mass young stellar objects, which play a key role in the dispersal of the natal gas and dust.

It has been hypothesized that the more massive Herbig Ae/Be stars and the T Tauri stars form and evolve in similar manners (Palla & Stahler, 1993), but this remains controversial. On large spatial scales, the disk-like nature of the circumstellar matter around Herbig Ae/Be stars is well established. Flattened structures around several sources have been resolved on 100 AU scales (Mannings & Sargent, 1997), or have Keplerian kinematics (Mannings et al., 1997). However, the evidence seems to be ambiguous on scales of tens of AU and below, with some authors arguing for a spherical geometry (di Francesco et al., 1994) and others favoring disks (Natta et al., 2001).

LkHα 198 and LkHα 233 are both classified as Hillenbrand Group II Herbig Ae/Be stars: they have infrared spectra that are flat or rising towards longer wavelengths. This means that they are young stars that may or may not possess circumstellar disks but do possess circumstellar envelopes which are not confined to a disk plane. We observe such envelopes around both of our sources in the form of centrosymmetrically polarized biconical nebulosities viewed approximately edge-on to the midplanes.

We compared our observations with radiative transfer models computed for a sequence of circumstellar dust distributions around T Tauri stars (Whitney et al., 2003b,a). These

models provide both total and polarized intensity images, which we convolved with a model instrumental point spread function to match our observed resolution (Fig. 6.6). Bipolar outflow cavities in these models produce a limb-brightened appearance at near-infrared wavelengths, with the brightening stronger in polarized light than in total intensity.

For both LkHα 233 and LkHα 198, the peak polarization differs between the two lobes. These asymmetries may indicate the sign of the inclination of each object. In Whitney's model envelopes, which use dust grain properties fit to an extinction curve for the Taurus molecular cloud, the closer lobe was brighter overall but had lower fractional polarization by several percent. For LkHα 198, the polarization in the northern lobe of the bipolar nebulosity is generally 10-15% lower than the southern lobe at all wavelengths (20% vs. 35% at H, for instance), suggesting that the northern lobe is oriented towards us. For LkHα 233, the southwest lobe is 14% polarized on average versus 26% for the northeast lobe. This indicates that the southern lobe is facing us, consistent with the the blueshift of the CO jet in that direction, and the southwest shift of the intensity peak relative to the polarization centroid.

LkHα 233's limb-brightened appearance provides compelling evidence for the presence of cavities swept out by bipolar outflow from the star. Cavity models with an opening angle of 30-40° seen at an inclination of 80° reproduce both the observed polarization fraction of 25-40% and the higher degree of limb brightening seen in the near lobe.

The absence of limb brightening may be evidence that LkHα 198 lacks polar cavities, or at most possesses very narrow ones. The detectability of limb brightening for a given angular resolution depends on the opening angle between the symmetry axis and edge of the cavity. At our resolution, envelope models with cavity opening angles greater than $\sim 20°$ predict detectable limb brightening, while we observe for LkHα 198 an opening angle of 45° without limb brightening. Thus our observations do not support the presence of evacuated cavities in the envelope of LkHα 198. The observed morphology can instead be explained by the illumination of a cavity-free, rotationally-flattened envelope by the central star; the bipolar appearance would then arise from light escaping along the path of least optical depth. However, these cavity-free infalling envelope models have opening angles which increase with wavelength, while we observe a constant opening angle, suggesting a geometric rather than optical depth origin for the observed morphology. This discrepancy may be resolvable by varying the dust particle properties.

Based on these observations, LkHα 233 is the more evolved of the two systems, with

well-defined cavities swept out by bipolar outflow and bisected by a very dark lane. LkHα 198 is a less evolved system, which is only in the early stages of developing bipolar cavities and possesses lower extinction in the apparent disk midplane.

The observed circumstellar environments are consistent with the rotationally-flattened infall envelopes models developed for T Tauri stars, indicating that the process of envelope collapse has similar phases, despite the large disparities in mass and luminosity between these two classes of young stars. This morphological similarity leads us to infer that the conservation and transport of angular momentum is the dominant physical process for both classes of stars. Alternate formation pathways have been suggested for OB stars that invoke new physical mechanisms, such as magnetohydrodynamic turbulence (McKee & Tan, 2003) or stellar mergers (Bonnell et al., 1998). The Herbig Ae stars studied here appear to be below the mass threshhold at which such effects become important.

5.5 Methods and Materials

The Lick Adaptive Optics system was developed at Lawrence Livermore National Laboratory, and can operate in both natural and laser guide star modes (Max et al., 1997; Gavel et al., 2002). In the laser guide star mode, the atmospheric wavefront reference is created by a laser tuned to the sodium D2 line at 589 nm, which excites mesospheric sodium at roughly 90 km altitude. The 589 nm light is generated by a tunable dye laser pumped by a set of frequency-doubled solid-state (Nd:YAG) lasers. Typically, 11-14 W of average laser power is projected into the sky with a pulse width of 150 ns and a pulse repetition rate of 13 kHz. Laser guide star systems are insensitive to tip and tilt, requiring a separate tip/tilt sensor using a natural guide star. For the observations presented here, the science targets served as their own tip/tilt references.

The sodium guide star has an apparent size of 2 arcseconds in 1 arcsecond seeing and a magnitude which depends on the atmospheric sodium density, which varies on all timescales from hourly to seasonally. The sodium level was low during July 2003, decreasing the magnitude of the guide star, and forcing the adaptive optics system to operate at its lowest frame rate of 55 Hz. As a result, the Strehl ratios achieved were modest (S 0.05-0.1) despite the good atmospheric seeing. Correspondingly the full-width at half-maximum (FWHM) of the point spread function was larger than the FWHM of a diffraction limited beam, 0.27 arcseconds versus 0.15 arcseconds respectively at 2.1 microns.

The science camera used with the Lick AO system is IRCAL (Lloyd et al., 2000), which has as its detector a 256^2 pixel HgCdTe PICNIC array manufactured by Rockwell. The observations presented in this paper used the standard astronomical J (1.24 micron), H (1.65 micron), and K_s (2.15 micron) broad-band filters. IRCAL's plate scale, 0.0754 arcsec/pixel, was chosen to Nyquist sample the diffraction-limited beam at K_s. The imaging polarimetry mode of IRCAL utilizes a cryogenic $LiYF_4$ (frequently called "YLF") Wollaston prism to produce simultaneous images of orthogonal polarizations. YLF was chosen for its excellent achromaticity throughout the near infrared. A rotating achromatic half-wave plate mounted immediately before the camera entrance window modulates the polarization, allowing measurement of both Stokes parameters Q and U.

Each target was observed for the same amount of time in J, H, and K_s, divided equally between Stokes Q and U observations. Typical exposures were 30-90 s in duration, with small dithers performed every few exposures. Total integration time was 1440 s per band for LkHα 233, and 960 s per band for LkHα 198. The data were flat-fielded and bias-subtracted in the standard manner for near infrared astronomical data. Sky background frames were obtained in polarimetric mode and subtracted from the data. However, the near infrared sky is nearly unpolarized so this step is not essential. The data from different dither positions were registered together via a Fourier transform cross-correlation code and stacked to produce mosaic Stokes I, Q, and U images. These observing techniques and data reduction methods are based on those of (Kuhn et al., 2001b).

The instrumental polarization bias was established through observations of standard stars known to be unpolarized; From the derived bias (2% at a position angle of -85°) we calculate the effective Mueller polarization matrix for the instrument and apply the inverse of this matrix to the Stokes mosaics to remove the bias.

Acknowledgements

We are indebted to the Lick Observatory staff who assisted in these observations, including Tony Misch, Kostas Chloros, and John Morey, and also to the many individuals who have contributed to making the laser guide star system a reality. We thank Barbara Whitney for providing us with electronic versions of her models. Onyx Optics fabricated our YLF Wollaston prisms. This work has been supported in part by the National Science Foundation Science and Technology Center for Adaptive Optics, managed by the University of California at Santa Cruz under cooperative agreement No. AST-9876783; and also under

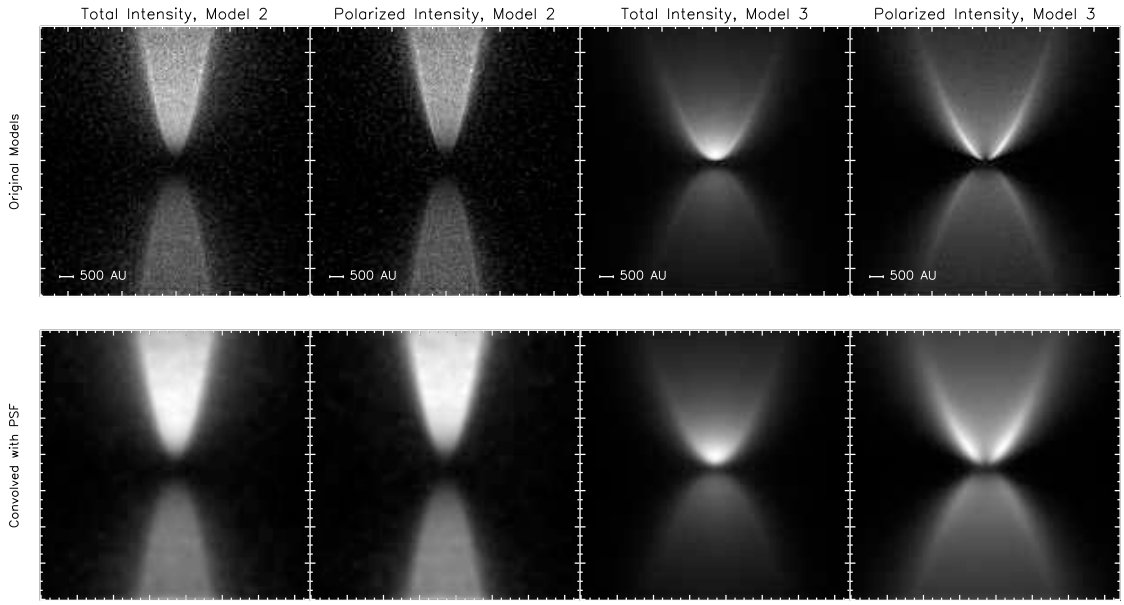

Figure 5.3: Example radiative transfer models of envelopes around class I T Tauri stars. These are models 2 and 3 from Whitney et al. (2003a) at H band (1.6 microns), which were computed for rotationally supported envelopes with bipolar outflow cavities with 10 and 20 opening angles, respectively. For each model we display both total intensity I and polarized intensity P , at top in original form from the Monte Carlo simulation output as provided to us by B. Whitney, and below convolved to match the angular resolution of our LGS observations. For model 2, with a 10 degree opening angle, there is no limb brightening. Limb brightening for model 3 (with a 20 degree opening angle) is visible in the original total intensity image but only extremely marginally in the reduced resolution version. However, model 3 is strongly limb brightened in both polarized intensity images. Models with larger opening angles display increasingly more pronounced limb brightening. The morphology of Model 3 here is similar to that we observe around LkHα 233.

Table 5.1: Target Summary

Object	V (magnitudes)	Distance (parsec)	Spectral Type	Luminosity ($L_\odot$)	Mass ($M_\odot$)	Time per band (s)
LkHα 198	14.3	600	A5e-A7e	5.6	1.2	960
LkHα 233	13.6	880	A5e	28.2	2.6	1440

V magnitude, distance, luminosity, and mass are from Hillenbrand et al. (1992).

Note. — Extinction ratios for the Polaroid/prism combination. The Polaroid used was designed for 1.0-2.0 μmonly and we believe that its polarizing efficiency drops beyond 2 μm, explaining the otherwise surprisingly large values there. Also listed is the ratio of transmission fraction for the right to left channels, calculated as the ratio of peak brightnesses. It is not known why this ratio is so much lower at H than at J or K_s.

the auspices of the U.S. Department of Energy, National Nuclear Security Administration by the University of California, Lawrence Livermore National Laboratory under contract No. W-7405-Eng-48. PK received additional support from the NASA Origins Program under grant NAG5-11769. MDP is supported by a NASA Michelson Graduate Fellowship, under contract to the Jet Propulsion Laboratory (JPL). JPL is managed for NASA by the California Institute of Technology.

Chapter 6

Discovery of an Optically Thick, Edge-on Disk around the Herbig Ae star PDS 144N

Abstract

We have discovered an optically thick, edge-on circumstellar disk around a Herbig Ae star in the binary system PDS 144, providing the first intermediate-mass analog of HK Tau and similar T Tauris. This system consists of a $V \sim 13$ mag. primary and a fainter companion, with spectra of both stars showing evidence for circumstellar disks and accretion; both stars were classified as Herbig Aes by the Pico dos Dias survey. In Lick adaptive optics polarimetry, we resolved extended polarized light scattered from dust around the northern star. Followup Keck adaptive optics and mid-infrared observations show that this star is entirely hidden by an optically thick disk at all wavelengths from 1.2 to 11.7 microns. The disk major axis subtends $\sim 0\farcs8$ on the sky, corresponding to ~ 800 AU at a distance of 1000 pc. Bright "wings" extend $0\farcs3$ above and below the disk ansae, due most likely to scattering from the edges of an outflow cavity in a circumstellar envelope. We discuss the morphology of the disk and the spectral energy distributions of

the two PDS 144 stars, present preliminary disk models, and identify a number of open questions regarding this fascinating system. [1]

6.1 Introduction

Circumstellar disks inescapably form around young stars, as angular momentum conservation prevents infalling matter from accreting directly onto the stellar surface. Transfer of angular momentum between different parcels of matter in these disks not only allows continued accretion, but has been implicated in the launching of spectacular bipolar jets and winds (Shu et al., 1994). Studying the detailed physics of such disks is thus important for understanding the nature of these outflows, which provide feedback into the star formation process and help limit the star formation rate. The standard model for T Tauri stars invokes magnetic fields to drive the outflows. While strong magnetic fields are inevitable in convective, low mass stars, the intermediate mass Herbig Ae/Be stars (Herbig, 1960; Waters & Waelkens, 1998) have much shallower convective zones and consequently have much weaker dynamos. Thus it is natural to suppose that disk environments around these stars may differ substantially from those around T Tauri stars.

Characterizing these disks also illuminates the conditions in which planet formation takes place. The tremendous diversity of recently discovered extrasolar planetary systems raises the question of whether this diversity arises from widely differing initial conditions in circumstellar disks, or if instead all solar systems begin similarly but evolve apart via planetary dynamics. Are conditions around A- and B-type stars as conducive to planet formation as are those around lower-mass stars? Present Doppler planet searches generally exclude A and B stars due to their relatively featureless spectra (though see Galland et al. (2005) for an exception to this rule), yet the presence of debris disks around the A stars Vega (Aumann et al., 1984) and β Pic (Smith & Terrile, 1984) provided the first evidence for the existence of extrasolar planetary systems. Indeed, more recent observations of perturbations to the disks of Vega and Fomalhaut indicate the presence of Jupiter-mass planets around those stars (Wilner et al., 2002; Kalas et al., 2005). The Herbig Ae/Be stars (Herbig, 1960) are the progenitors of Vega-like debris disks. By studying the circumstellar material around these stars, we aim to quantify the evolution of dust properties and spatial distribution with stellar age, and thereby gain insight into the growth

[1] This chapter has been previously published as Perrin et al. (2006) and is reproduced here with the permission of all coauthors.

of larger dust particles and ultimately planets.

Optically thick, edge-on disks are particularly amenable to spatially resolved observations in the visible or infrared. Disk imaging is frequently complicated by point spread function (PSF) subtraction artifacts, especially on small angular scales. For optically thick, edge-on disks, the lack of direct starlight greatly reduces the dynamic range needed to image the disk. At the same time, modeling the observed light distribution can constrain the disk's physical parameters, such as the degree of flaring and dust grain growth (D'Alessio et al., 2001; Watson & Stapelfeldt, 2004). Edge-on disks are particularly valuable for such studies, as the disk's vertical structure is directly apparent. By modeling multiwavelength observations of edge-on disks, one can determine the wavelength dependence of the dust scattering opacity, which provides insight into dust grain properties (Cotera et al., 2001; Watson & Stapelfeldt, 2004). Edge-on disks in binary systems may additionally shed light on aspects of the binary formation process and disk/disk interactions.

Edge-on disks are known around a number of lower-mass T Tauri stars, most notably HH 30 (Burrows et al., 1996), HK Tau B (Stapelfeldt et al., 1998), and HV Tau C (Monin & Bouvier, 2000), but until now no edge-on disk has been seen around a Herbig Ae or Be star. We present in this paper our discovery of such an edge-on circumstellar disk around the Herbig Ae star PDS 144N ($\alpha = 15^h49^m15.5^s$, $\delta = -26°00'50.2"$, J2000).

Carballo et al. (1992) identified IRAS 15462-2551 with a previously anonymous 12th magnitude star in Scorpius. The Pico dos Dias Survey, a spectroscopic followup to IRAS sources (Torres et al., 1995), subsequently named this source PDS 144, discovered it to be a $5''$ binary, and classified both members as Herbig Ae stars. Vieira et al. (2003) report a spectral type of A2IV for the northern member and A5V for the southern. We follow their notation in referring to these stars as "PDS 144N" and "PDS 144S", respectively. In addition to the Hα emission signature of accretion, they found [SII] $\lambda\lambda$ 6717, 6730 and [OII] $\lambda\lambda$ 3726, 3728 emission around both stars, indicative of a photodissociation region. These lines are good tracers of outflows around other young stars, and their presence makes it probable that such outflows are present around both PDS 144 stars. The physical association of these two stars has not yet been rigorously shown, but given their proximity and the fact that both are Herbig Ae stars which are currently accreting and thus of similar age, it is very likely that they are indeed bound and coeval.

We describe our observations in §2, and discuss the distance to PDS 144 in §3. In §4, we examine the observed disk's morphology, before presenting preliminary models for the

Table 6.1. Observation Log

Telescope	Instrument	Filter	Date	t_{int} (s)	θ ($''$)
Lick 3 m	IRCAL	J	2004 July 5	320	0.38
···	···	H	2004 July 5	480	0.33
···	···	K_s	2004 July 5	240	0.30
Keck II	NIRC2	H	2004 Aug 29,30	120	0.055
···	···	K'	2004 Aug 29	90	0.058
···	···	PAH	2004 Aug 30	144	0.07
···	···	L'	2004 Aug 30	90	0.08
Keck I	LWS	11.7 μm	2004 Aug 28	85	0.35

Note. — Observing Log for PDS 144. t_{int} is the total integration time in each filter, and θ is the achieved resolution in arcseconds, measured from a point source. See Table 2 for a detailed description of filter properties.

disk in §5. Lastly, §6 recapitulates our conclusions and identifies a number of remaining open questions about this intriguing system.

6.2 Observations

PDS 144N's disk was discovered in observations obtained with Lick Observatory's 3-m Shane telescope, and was subsequently imaged with both 10-m W. M. Keck telescopes. Together, these observations span the wavelength range 1.2 to 11.7 microns. An observation log is presented in Table 6.1, while Table 6.2 gives our measured photometry for both PDS 144 stars.

6.2.1 Lick

We first observed PDS 144 as part of our ongoing adaptive optics polarimetry survey of Herbig Ae/Be stars (Perrin et al., 2004b), being carried out with the Lick Observatory Adaptive Optics (AO) system (Gavel et al., 2002) and the IRCAL camera (Lloyd et al., 2000). IRCAL's differential polarimetry mode incorporates a Wollaston prism and rotating

half-wave plate to obtain high-contrast images in polarized light (Perrin et al., 2004a). For these observations, the AO system was locked on PDS 144S. The seeing was excellent (Fried's parameter $r_0 \sim 16$ cm at 550 nm), but the target was observed at an airmass of 2.25, and AO correction was limited to a Strehl ratio of 0.1 at K_s band. After dark subtraction and flat fielding, the polarimetric data were reduced via a double-differencing code based on the algorithm of Kuhn et al. (2001b), resulting in images of the Stokes parameters I, Q, and U for each near infrared band. These data were then flux calibrated using the standards HD 161903 (Elias et al., 1982) and [PMK98] 9170 (Persson et al., 1998).

The northern source is resolved at all wavelengths, while the southern is point-like (Figure 6.1). At H and especially K_s band, PDS 144N appears as an elliptical nebula bisected by a dark lane. In polarized light, PDS 144N is extended $\sim 1''$ from northeast to southwest, with polarization position vectors roughly perpendicular to this. Centrosymmetric polarization vectors are the signature of scattered starlight, and the presence of such vectors along one axis is precisely what is expected for an edge-on circumstellar disk. The observed polarization fractions range between 5-10%, though this is a lower limit for the true polarization since the observed values are biased downward by AO-uncorrected light.

In polarized light, PDS 144S appears only at the 1-2% level of systematic subtraction residuals expected for an unpolarized source. The position vectors are not centrosymmetric, and based on these polarization data alone there is no direct evidence for a disk around PDS 144S.

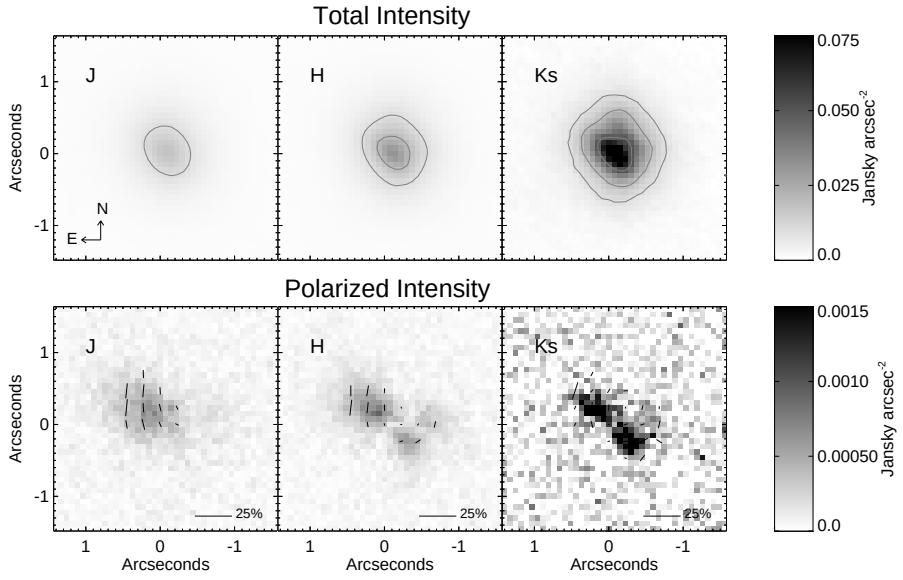

Figure 6.1: Lick AO polarimetry observations of PDS 144N. The top row shows total intensity, I, while the second row shows polarized intensity, $\sqrt{Q^2 + U^2}$, with position vectors showing the orientation and magnitude of polarization. The color scales are the same for each row, as shown at right. Contours are at 0.01, 0.02, and 0.05 Jy arcsec^{-2}. In total intensity, the morphology is clearest in K_s band, where the higher Strehl ratio PSF resolves a dark lane crossing PDS 144N. In polarized intensity, a bright bar of nebulosity is visible at a position corresponding to the southeast side of the dark lane–presumably the disk face inclined toward us. A portion of the northwest face is visible in the K_s and H bands, while in J only the far eastern end of the nebula is detected. The differences between wavelengths may be due to obscuring foreground material, or may be artifacts of the relatively low Strehl ratio (3%) of our J band observations. These patterns of position vectors are consistent with light scattered from circumstellar material around PDS 144N.

6.2.2 Keck

Shortly after the disk was discovered at Lick, we obtained additional near-infrared data with the Keck II AO system (Wizinowich et al., 2000) and NIRC2 camera (Matthews, K., in preparation). PDS 144S again served as the wavefront reference. The Keck images have much superior AO correction than the Lick data, in part because PDS 144 is observable at a more favorable airmass from Keck (Figs. 6.2 and 6.3). Because the exposure times were chosen to maximize SNR on the PDS 144N disk, PDS 144S is saturated in all wavelengths other than K'. These imaging data were reduced via the usual steps of dark and sky subtraction, flat fielding, and mosaicing, and were flux-calibrated using the same photometric standard, [PMK98] 9170. For the 3.3 μm PAH filter, no photometric standard observations were available nor was a typical zeropoint available from the NIRC2 documentation. We therefore estimated a zeropoint for the PAH filter relative to our measured zeropoints for the other filters, using the known PAH filter response, detector quantum efficiency, and the typical Mauna Kea atmospheric transmission across the filter bandpass (Roe, 2002). To evaluate the reliability of this synthetic PAH zeropoint, we similarly estimated a K' zeropoint; the estimated and measured K' zeropoints agreed within 0.05 mag.

The center of PDS 144N is located $5\farcs40 \pm 0\farcs01$ from PDS 144S, at a position angle of $28.7 \pm 0.3°$. It is difficult to define an exact center for an extended, obscured object; neither the location of peak brightness nor the photocenter are appropriate, so we used a position roughly in the middle of the dark lane but displaced slightly toward the brighter face. Based on our disk models discussed below, this is a reasonable estimate for the location of the hidden star.

In addition to the two known members of PDS 144, we detect three other point sources within our full field of view mosaics (roughly $13'' \times 11''$). Photometry and astrometry for these sources are given in Table 6.3. Most notably, there is a faint source located almost directly between the two stars of PDS 144. These are most likely field stars, either foreground or background. If so, and assuming they are not high proper motion foreground objects, they may be useful as astrometric references for PDS 144. Its proper motion of 8 mas/year (Teixeira et al., 2000) corresponds to one K_s-band Keck resolution element per four years, so proper motion tests will be possible rapidly.

During the same observing run we also obtained a mid-infrared image with the Long Wavelength Spectrometer (LWS; Jones & Puetter (1993)) on Keck I (Fig. 6.3). LWS was used with the 11.7 μm filter in chop-nod imaging mode with a $10''$ chop throw at a

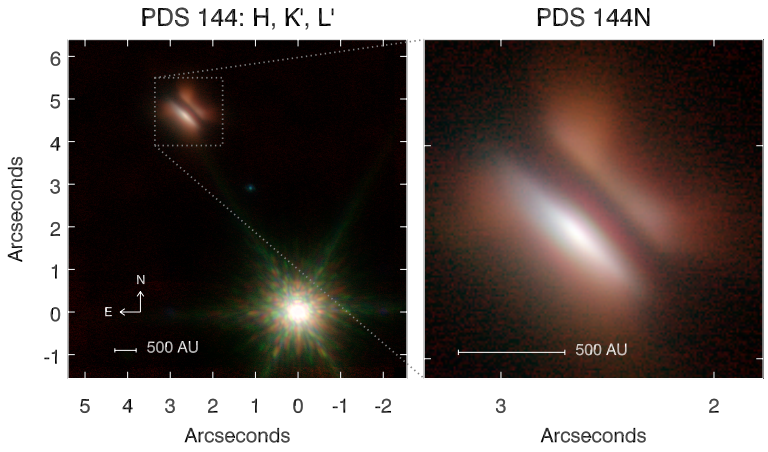

Figure 6.2: Keck AO imaging of PDS 144. The H, K' and L' bands are shown as blue, green, and red respectively. PDS 144N appears as an edge-on disk seen in silhouette against brighter nebulosity, which extends vertically on both sides of the disk plane. Both PDS 144N and the brighter PDS 144S are Herbig Ae stars, while the nature of the faint third source located almost directly between them is unknown. The scale bar in AU assumes a distance of 1000 pc; see section 6.3. The nebulosity around PDS 144N flares vertically near its edges, reminiscent of a pair of opposing wingnuts. In the northwestern, fainter face of the nebula, the wings are sufficiently prominent that the nebula is brighter toward its outer edges than in the middle: there is a local minimum in intensity on the symmetry axis. The presence of a circumstellar envelope in addition to a disk is required to explain these "wings".

position angle of 0° and a chop frequency of 2.5 Hz. Data were reduced using the standard double-difference subtraction to remove sky, telescope, and instrumental backgrounds; no flat fielding was performed. The photometric standards HD 197989 and HD 2486 (Cohen et al., 1999) were used to flux-calibrate the data. We rotated and rebinned the LWS data to register it with our NIRC2 data, using the documented plate scales of 9.94 and 84.7 mas/pixel respectively. Image quality was near diffraction limited (FWHM$\sim$ 0.″35). The LWS image shows very similar morphology to the near-IR data, particularly if the near-IR data are reduced to the same resolution as the LWS image.

6.2.3 Spitzer

Spitzer observations of PDS 144 are available from the Spitzer Archive. These observations, originally carried out as part of the "Molecular Cores to Planets" legacy program

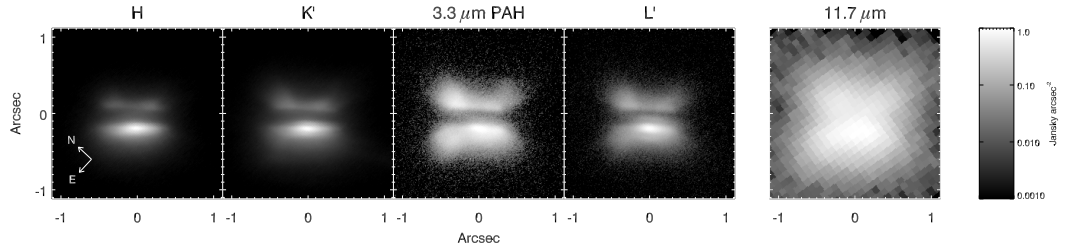

Figure 6.3: The PDS 144N disk, as observed with NIRC2 on Keck II (left four frames) and LWS on Keck I (right frame). All are displayed with the same logarithmic intensity scale, as indicated at right. Contours are at 0.01, 0.025, 0.05, 0.1, 0.25, and 0.5 Jy arcsec^{-2}. The vertical extent of the dark lane and the overall width of the nebulosity do not change significantly across the four NIR filters, but the "wings" of the nebula become more prominent in L' and especially the 3.3 μm PAH filter. The relative brightness of the 3.3 μm image indicates that PAH grains must be present around PDS 144N. In the 11.7 μm filter, the dark lane is no longer visible as a local minimum, but appears as a broad plateau to one side of the bright southeast disk face. The presence of PAHs complicates the interpretation of the 11.7 μm image: The light we detect at this wavelength may be scattered thermal emission from the hot inner disk, fluorescent emission from the 11.3 μm PAH feature, which lies within the filter bandpass, or most likely a mix of the two.

(Evans et al., 2003), span 3.6-70 μm using IRAC and MIPS. We retrieved the pipeline-processed "Post-BCD" mosaics from the archive and performed photometry with the APEX package (Makovoz & Marleau, 2005). APEX was able to successfully de-blend the sources, even with the substantial PSF overlap at longer wavelengths. Since PDS 144 was the only source in the field, no contemporaneous PSF measurement was available and so we used the reference PSFs from the Spitzer web site. The Spitzer photometry is presented in Table 6.2 and figure 6.4.

We note in passing that the summed fluxes for PDS 144 in the MIPS 24 μm band are in excellent agreement with the 20 μm measurement by IRAS, which did not resolve the two sources. However, the 60 μm IRAS flux is three times the MIPS 70 μm measurement, indicating that the IRAS measurement at that wavelength suffers from confusion due to the large beam size. No other bright sources are present in the MIPS field of view, so it is unknown whether other source(s) or extended emission from diffuse gas are responsible for this confusion.

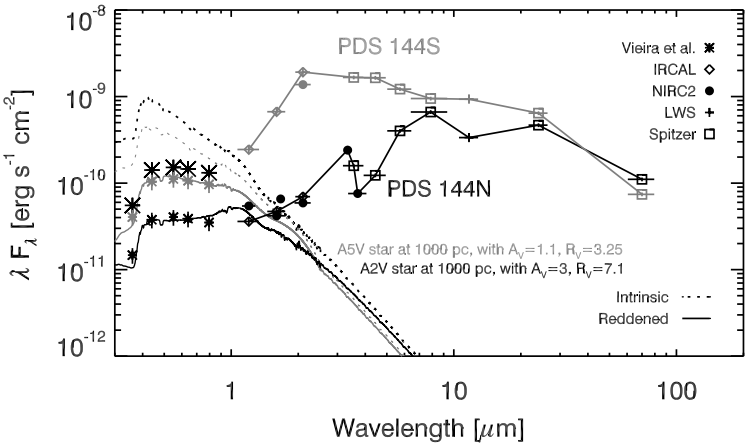

Figure 6.4: Spectral Energy Distribution for PDS 144. The key at right indicates which instrument each plotted point is from. Horizontal bars indicate the FWHMs of each filter bandpass, while vertical bars (typically smaller than the plot symbols) show the uncertainties. For the optical points from Vieira et al. (2003), the larger asterisks (top) are their reported total fluxes for both stars of PDS 144, while the two rows of smaller symbols are our estimates for the two stars' individual fluxes, as discussed in §6.3. We overplot both intrinsic and reddened stellar spectra for the two stars. The A5 spectrum for PDS 144S has been attenuated by $A_V = 1.1, R_V = 3.1$ using the extinction curve of Cardelli et al. (1989). Since PDS 144N is seen entirely in scattered light at optical wavelengths, it is a crude approximation to fit it with a reddened stellar spectrum. We show here an A2 spectrum reddened by $A_V = 3, R_V = 7.1$ to demonstrate that the observed optical magnitudes can be obtained with a moderate amount of dust, and caution that $A_V = 3$ does *not* represent the direct line-of-sight extinction to the star through the highly optically thick disk midplane.

6.2.4 Spectral Energy Distribution

The spectral energy distribution (SED) for the PDS 144 system is shown in figure 6.4. In addition to our own measurements, we plot the optical points from Vieira et al. (2003). We overplot flux-calibrated stellar spectra corresponding to the spectral types of PDS 144: A5 and A2 for PDS 144N and PDS 144S, respectively. We assume here a distance of 1 kpc, but see §3 for a detailed discussion of the distance to PDS 144, which remains very uncertain.

PDS 144S's SED rises sharply from 1 to 2 microns before leveling off, while PDS 144N's SED is nearly flat throughout the optical and near IR. They are both therefore Class II Herbig Ae stars in the classification system of Hillenbrand et al. (1992). Other

Table 6.2. Measured Fluxes

Instrument	Filter	λ (μm)	FWHM (μm)	PDS 144N (Jy)	PDS 144S (Jy)	PDS 144N (mag.)	PDS 144S (mag.)
IRCAL	J	1.238	0.267	0.014 ± 0.002	0.098 ± 0.012	12.61 ± 0.07	10.53 ± 0.06
···	H	1.650	0.297	0.025 ± 0.003	0.357 ± 0.026	11.52 ± 0.06	8.64 ± 0.05
···	K_s	2.150	0.320	0.049 ± 0.006	1.343 ± 0.102	10.31 ± 0.10	6.71 ± 0.10
NIRC2	H	1.633	0.296	0.023 ± 0.003	$> 0.228 \pm 0.031$	11.64 ± 0.02	$< 9.15 \pm 0.02$
···	K'	2.124	0.351	0.043 ± 0.004	0.997 ± 0.118	10.48 ± 0.02	7.06 ± 0.02
···	PAH	3.290	0.056	0.277 ± 0.034	$> 1.576 \pm 0.196$	7.58 ± 0.05	$< 5.70 \pm 0.05$
···	L'	3.776	0.700	0.094 ± 0.013	$> 1.132 \pm 0.161$	8.56 ± 0.04	$< 5.85 \pm 0.04$
LWS	11.7	11.698	1.104	1.352 ± 0.249	3.751 ± 0.692	3.28 ± 0.10	2.17 ± 0.10
IRAC	3.6	3.550	0.75	0.188 ± 0.010	1.97 ± 0.099	7.94 ± 0.06	5.39 ± 0.06
···	4.5	4.439	1.01	0.182 ± 0.009	2.44 ± 0.123	7.49 ± 0.06	4.67 ± 0.06
···	5.8	5.731	1.42	0.767 ± 0.039	2.33 ± 0.118	5.44 ± 0.06	4.23 ± 0.06
···	8.0	7.872	2.93	1.74 ± 0.089	2.49 ± 0.127	3.92 ± 0.06	3.53 ± 0.06
MIPS	24	23.7	4.7	3.74 ± 0.190	5.15 ± 0.260	0.70 ± 0.06	0.35 ± 0.06
···	70	71.4	19	2.58 ± 0.140	1.73 ± 0.100	-1.31 ± 0.06	-0.88 ± 0.06

Note. — Photometry for PDS 144. The IRCAL and NIRC2 measurements used a $1''$ radius aperture, while $1\farcs7$ was used for LWS. Aperture correction factors were computed using the Keck AO PSF model of Sheehy et al. (in preparation) and are typically 2-4%. Flux calibrations are as discussed in the text; the filter wavelengths listed above are isophotal wavelengths computed according to the method of Cohen et al. (1999). Columns marked with a $<$ or $>$ are limits derived from saturated observations of PDS 144S. The flux uncertainties in Jy include contributions from both the aperture photometry and the absolute flux calibration. For Spitzer data, filter properties are taken from Fazio et al. (2004) and Rieke et al. (2004). Photometry and statistical uncertainties were computed with the APEX package, plus an estimated 5% absolute flux calibration error for all Spitzer bands.

Herbig Ae stars with SEDs similar to PDS 144N include LkHα 233 and Parsamian 21. Those sources are both embedded deeply enough that the stars are completely hidden at optical and near-IR wavelengths and only scattered light is seen (Staude & Neckel, 1992; Perrin et al., 2004b), just as in PDS 144N.

At 70μm, PDS 144N is brighter than its southern neighbor. This suggests that while both stars possess substantial circumstellar dust, PDS 144N has a greater amount of cool dust at larger orbital radii than does PDS 144S.

6.3 The Distance to PDS 144

The distance to PDS 144 remains frustratingly uncertain. Previous estimates in the literature range from 140 to 2000 parsecs. The nearer distance was suggested by Teixeira et al. (2000), who assumed that PDS 144 lies in the Upper Scorpius–Ophiucus star forming region, based primarily on its position in the sky. The more distant estimate is from Vieira et al. (2003), who derived an optical photometric distance of 2000 pc for PDS 144N, and 1030 pc for PDS 144S.

The lack of resolved optical photometry for PDS 144 complicates the determination

Table 6.3. Additional sources detected

Source #	R.A. Offset ($''$)	Dec. Offset ($''$)	H Mag.
3	1.122	3.000	15.50 ± 0.10
4	7.768	3.480	16.55 ± 0.20
5	8.908	2.505	17.90 ± 0.20

Note. — R.A. and Dec. offsets are relative to PDS 144S, and have uncertainties of $\pm 0''.005$.

of a photometric distance. Resolved optical photometry will be available from HST observations scheduled for the near future. Until then, we must make do with a best estimate from the currently available data. Our near-IR measurements are unsuitable for photometric distance measurements, since they are presumably contaminated by IR excess from circumstellar dust. We note that the K' band flux of PDS 144S is consistent with the photospheric flux from an A5 star located at 140 pc. Since the true K' luminosity is presumably greater than photospheric, the actual distance must be ≥ 140 pc.

While Vieira et al. (2003) only report combined photometry for PDS 144 ($V = 12.8$ mag), they measured $\Delta V = 1.1$ mag. from the relative counts of the two sources in their spectroscopic observations (Carlos Torres, private communication). This implies $V = 13.1$ and 14.2 for PDS 144S and 144N, respectively. From these numbers, Vieira et al. derived their 1030 and 2000 pc photometric distances. Since we see PDS 144N only in scattered light, it seems certain that its 2000 pc photometric distance is an overestimate. But the photometric distance for the less-obscured PDS 144S may be accurate. Given PDS 144S's unresolved appearance, it is plausible that we see its photosphere directly; certainly it is not as obscured as PDS 144N. If we assume this is the case, then we can follow Vieira et al. (2003) and derive a photometric distance to PDS 144S.

We estimated the optical fluxes of PDS 144S from the combined $UBVRI$ magnitudes and ΔV from Vieira et al., assuming that the flux ratio between the two sources is the same for all wavelengths. (Though this assumption is crude, the following results are only weakly dependent on it.) We then performed a nonlinear least squares fit to PDS 144S using a flux-calibrated ZAMS $A5V$ stellar spectrum, reddened by dust using the extinction

law of Cardelli et al. (1989) and then multiplied by appropriate filter bandpasses. The free parameters of the fit were the distance d, the visual extinction A_V and the reddening parameter R_V; we assume there is only one dust component along the line of sight. The best fit parameters are $d = 1030 \pm 130$ pc, $A_V = 1.1 \pm 0.46$, $R_V = 3.25 \pm 0.65$ (see Fig 6.5). These formal errors underestimate the true uncertainty, given the various assumptions that went into the model. Changes in the assumed flux ratio between PDS 144S and 144N can shift the resulting best-fit distance by an additional $\sim$ 100 pc. Future work is certainly needed to pin down the distance to PDS 144 more precisely. Nonetheless, for the moment we will adopt 1000 ± 200 pc as a working estimate.

A major assumption in this distance fit is that PDS 144S has luminosity for an A5 star on the ZAMS. Many Herbig Ae/Be stars have luminosities a few times greater than ZAMS values. If PDS 144 is significantly pre-main-sequence and thus more luminous than we assume, it will be correspondingly more distant, which will only exacerbate the problem of its height above the galactic plane (see below).

Another way to estimate the distance to PDS 144 is by comparison with other Herbig Ae stars of known distance and similar spectral type. This has the advantage of not requiring us to assume a particular luminosity for PDS 144S. For instance, IP Per is a A6 star with V=10.5 at a distance of 350 pc (Hernández et al., 2004). For it to have the same apparent brightness as PDS 144S, IP Per would need to be located at 1200 pc, assuming the extinction is unchanged. Different results are possible depending on what star is picked as the analog of PDS 144S. Using a sample of ten A4-A6 HAes taken from the literature, this procedure results in distances of 550-1900 pc. It is encouraging that our 1000 pc estimate falls in the middle of this range, but these comparisons do not reduce our uncertainty in the distance to PDS 144.

These data seem to rule out any association of PDS 144 with Upper Sco at 140 pc. Even with extraordinarily grey dust ($R_V > 20$), models of PDS 144S with a distance of 140 pc and sufficient extinction to produce $V = 13.1$ predict $V - R \approx 1$, inconsistent with the observed $V - R = 0.30$. Known Herbig Ae stars at the distance of Upper Sco are either some 3-5 mag. brighter at V than PDS 144 (e.g. KK Oph, HD 163296, or TY CrA) or are embedded objects much redder than PDS 144 (e.g. Elias 1, which has $V - R = 2.1$; Herbst & Shevchenko (1999)) A larger distance also provides a natural explanation for the low proper motion of PDS 144, which at 2 ± 4 mas/year is an order of magnitude slower than the average for Upper Sco/Oph (Teixeira et al., 2000; Ducourant et al., 2005).

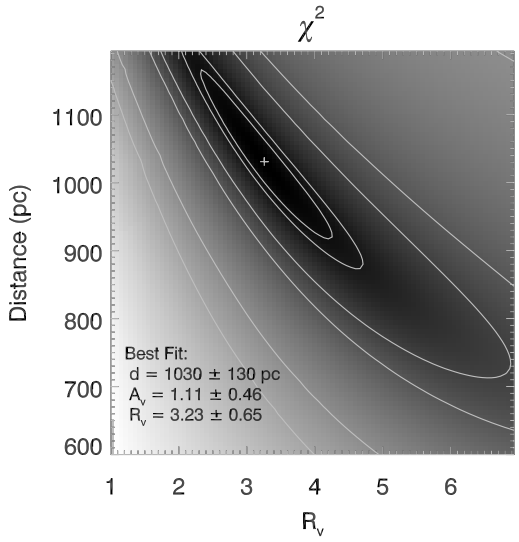

Figure 6.5: We fit synthetic $UBVRI$ photometry to PDS 144S in order to estimate its distance, as described in the text, and plot here the resulting χ^2 against distance and reddening. Vieira et al. do not provide uncertainty for their photometry; not knowing the error bars results in our χ^2 being uncertain by an arbitrary multiplicative constant. We therefore normalize our best-fit $\chi^2 = 1$ and plot here contours of 0.5, 1, 5, 10, 50, and 100 above the best-fit χ^2. Our best fit, marked by a cross, gives a distance of 1030 pc. While there is substantial covariance between the distance and the extinction law parameters, distances less than ~ 500 pc do not appear plausible.

But a 1 kpc distance is not without problems of its own. Chief among these is how did such a young system come to be so far above the Galactic plane? At a Galactic latitude of $+21°$and a distance of 1000 ± 200 pc, PDS 144 is 360 ± 70 pc above the Galactic plane. Kroupa (1998) claims that stars of all masses can be ejected at high velocities from moderate to dense clusters, so perhaps PDS 144 is a runaway from a star forming region closer to the plane. But if that is the case, it's difficult to understand how the binary would have remained bound, since the necessary velocity to reach its current position in less than a few million years (50-100 km/s) is greatly in excess of the binary orbital velocity (≈ 1 km/s). Further contradicting this scenario is that its proper motion (2 ± 4 mas/year (Ducourant et al., 2005), corresponding to a transverse velocity of 9 km/s at 1000 pc) is both slow and directed mostly *towards* the Galactic plane. We are left with the conclusion that this system must have formed far above the Galactic plane. It is unknown what star forming region may have given birth to this system; no dark clouds are found within 2 degrees of PDS 144 according to the catalog of Dobashi et al. (2005).

One possible resolution to this dilemma would be if we have entirely misinterpreted the nature of these stars, and that they are in fact evolved post-main-sequence objects rather than young stars. Proto-planetary nebulae appear similar to pre-main-sequence A stars in several aspects such as IR excess from dust, the presence of PAH emission, and optical forbidden lines such as [SII]. The PDS catalog is known to be contaminated by such interlopers (for instance, PDS 461/Hen 3-1475; García-Hernández et al., 2002). There are two reasons we reject this interpretation: First, the morphology of PDS 144N more closely resembles edge-on disk systems than it does proto-planetary nebulae such as PDS 461. Secondly, *both* stars in PDS 144 display IR excess and optical forbidden lines. Since their spectral types and presumably masses differ, we would not expect them to both evolve off the main sequence simultaneously. It is much more plausible for the pair to be young stars approaching the main sequence together rather than departing it.

PDS 144 is by no means the only Herbig Ae/Be star whose distance has proved problematic. LkHα 101, long believed to be located at 800 pc, may instead lie only 140 pc distant (Stine & O'Neal, 1998). Conversely, the distance to HD 34282 has recently been revised upwards from 160 to 350 pc (Piétu et al., 2003; Merín et al., 2004). Similar methods to those used in the just-cited papers may help clarify the distance to PDS 144. In particular, high-resolution optical spectroscopy could constrain stellar properties directly, while millimeter observations of Keplerian rotation in the disk of PDS 144N could provide a dynamical distance.

6.4 Disk morphology

6.4.1 Basic Appearance

At all wavelengths up to 11.7 μm, the exciting star within PDS 144N is hidden from direct view by the dark lane of an edge-on circumstellar disk. The dark lane is $0\farcs15$ in height and extends $\sim 0\farcs8$ in the orthogonal direction (Fig 6.2). Bright scattered-light nebulosity is visible on both sides of the disk plane, with the southeast side being brighter and therefore nearer, assuming the grains are forward scattering.

At our assumed distance, the $0\farcs8$ apparent disk diameter corresponds to a physical diameter of 800 ± 180 AU . This is comparable to disks around other Herbig Ae stars such as HD 100546 (500 AU) or HD 163296 (900 AU) (Grady et al., 2000, 2001, 2005). However, it is possible that the observed dark lane is actually a shadow cast by a smaller disk into

a surrounding envelope (Pontoppidan & Dullemond, 2005). In this case the actual disk size could be smaller than the 800 AU apparent size. Pontoppidan et al. list a number of observational criteria which can be used to discriminate disk shadows from large disks, such as the presence of a bright point source in the middle of the dark lane or a "wedge-like" shape, but none of these criteria fit PDS 144N.

PDS 144N is laterally asymmetric. In the inner region of the nebula, the peak intensity is displaced 0.″05 southwest from the vertical axis. In the outer nebula, the northeast side is more extended than the southwest. Similar asymmetries in the disk of HH 30 proved to be variable over time scales of a few years, and have been interpreted as changing illumination caused by the orbital motion of clumps at a few AU (Stapelfeldt et al., 1999). Alternatively, those asymmetries may be evidence for a hot spot on the rotating stellar surface (Cotera et al., 2001). Long term monitoring of PDS 144N is needed to see whether its lateral asymmetries also vary with time. If so, then the timescales and amplitude of the variability may clarify whether it is driven by an outflow (such as by a precessing jet), a hot spot, shadowing by orbiting dust clumps, or some other mechanism. Alternatively, the asymmetry in PDS 144N could be due to disk inhomogeneities at large radii where orbital periods are many decades, and so we may never see any changes.

6.4.2 The "wings"

One of the most striking features of the nebulosity around PDS 144N is the pronounced flaring at its outside edges: it resembles an opposing pair of wingnuts, with the outer vertical extensions being the "wings". The wings begin approximately 0.″15 on either side of the disk's vertical axis, and extend 0.″4 above and below the disk midplane, twice the extent of the scattered light near the axis. The wings are comparatively redder than the inner portions of the nebula; they are most pronounced in the PAH and L' filters, but are still visible at a lower level in H and K' (Fig. 6.3).

Hollenbach et al. (1994) proposed that massive stars can launch disk winds by photoevaporating the outer portions of circumstellar disks. Could such winds boiling off the disk be responsible for creating the wingnut morphology? The predicted wind emerges from the outer disk along outward-curving streamlines, which resemble the wings around PDS 144. The characteristic radius at which such evaporation is expected to take place is $r_{evap} = GM_*/a_s^2 \simeq 7$ AU$(M_*/M_\odot)$, where a_s is the sound speed in the disk. But at a 1 kpc distance, $r_{evap} \approx 0.''02$, an order of magnitude smaller than the observed size, and we

must find some other explanation for the wings.

Perhaps the YSO that most resembles PDS 144N is IRAS 04302+2247 (Padgett et al., 1999), sometimes called the Butterfly Star in Taurus. Like PDS 144N, it has a dark lane bisecting two bright regions of nebulosity, each of which has its center fainter than its outer edges giving an overall quadripolar morphology. Foreground extinction has been suggested as the cause of IRAS 04302+2247's quadripolar appearance, but we can rule this explanation out for PDS 144: the quadripolar appearance is still prominent at 11.7 microns despite the much greater dust-penetrating ability of photons at that wavelength. Wolf et al. (2003) modeled IRAS 04302+2247 as a disk plus an infalling circumstellar envelope with bipolar outflow cavities. The cavity walls scatter more light than the evaculated cavities themselves, providing a natural explanation for the "wings" of the "butterfly" - and perhaps also the "wings" of PDS 144N. We present disk plus envelope models of PDS 144N in section 5.

The wings become redder as one moves further from the disk midplane. Intriguingly, this is opposite the blue color seen for the envelope around HD 100546 by Ardila et al. (2005). Possible explanations for the red color include, in decreasing order of likeliness, (1) The illuminating light scattered there is redder, due to greater contribution from the hot inner disk: Grains in the envelope see a larger solid angle subtended by the inner disk than do grains nearer the disk midplane. (2) Small grains in the envelope emit thermal radiation after being transiently heated to ~ 600 K. (3) Dust grains in the envelope might instead be larger than disk grains and thus scatter red light more efficiently; this seems unlikely as it is inconsistent with our understanding of grain growth. (4) Scattered light from the envelope may experience more extinction than that from the disk. Some combination of factors 1 and 2 is most likely; these could be distinguished by future L' polarimetry observations.

6.4.3 Disk Truncation?

Like HV Tau C, PDS 144N's apparent diameter does not change significantly with wavelength. Since optical depth is a strong function of wavelength, this suggests that the circumstellar material around PDS 144N has a sharp outer edge, possibly because of tidal truncation by PDS 144S. The expected limit on disk size from tidal truncation is roughly 1/3 of the binary's separation (Artymowicz & Lubow, 1994). If we assume that PDS 144's orbit is circular with the observed separation, 5400 AU, corresponding to the major axis, then the expected tidal truncation radius is ≈ 1800 AU, several times the observed radius.

This is a lower limit on the truncation radius, since the true separation must be greater than or equal to the observed separation in the plane of the sky. Thus while PDS 144 is not inconsistent with tidal interaction models, tides do not seem to be the limiting factor on disk size here.

However, a third source, such as a brown dwarf companion, might provide an alternative source of tides. We reiterate that there is a third, much fainter source located almost directly between the two PDS 144 stars (Table 3). Future observations are required to tell if this is a comoving member of the system or not. But given the hierarchical nature of most binaries and its position equidistant from both A stars, it is most likely merely a background star.

There is another possibility: the radiative effects of PDS 144S may be more important in truncating the disk than its gravity. Far UV photons from PDS 144S could heat and evaporate the outer disk, as has been suggested to occur for disks around low-mass stars externally illuminated by nearby massive stars, (Adams et al., 2004). However, unlike typical proplyds in Orion where the external illuminating source is much brighter than the stars within the disks, in PDS 144 both sources are of comparable intrinsic luminosity. More detailed modeling is needed to disintangle the photoevaporative effects of the two stars.

We caution that the truncation of PDS 144N's disk and envelope by either tidal or photoevaporative forces is speculative. The presence of substantial IR excesses around both stars and the lack of any visible tidal streamers or other debris from a disrupted disk suggest there is an alternative argument to be made for little interaction between the two stars.

6.4.4 PAH emission

Polycyclic aromatic hydrocarbons (PAHs) produce several IR emission features frequently seen around Herbig Ae stars (Leger et al., 1989; Natta & Kruegel, 1995). These emission bands arise due to fluorescent excitation of PAHs by far-UV photons, which are produced in great quantity by hot A stars.

PDS 144N has emission several times brighter than continuum levels in the 3.3 μm PAH band (Fig. 6.3). We used for the 3.3 μm continuum a linear interpolation between the 2.1 μm K' and 3.8 μm L' filters, neither of which contain the PAH feature within their bandpasses. The PAH emission is detected over roughly the same region as is the

continuum, but their relative intensities vary. As measured in NIRC2's 0.05-μm-wide PAH filter, the PAH emission is $\sim$ 6 times brighter than continuum in the outer nebula, but in the bright core nearest the central star, the PAHs are only 2 times the continuum. In other words, the PAH emission is less centrally peaked than is the continuum.

In order for PAH emission to occur, the PAHs must be illuminated by far-UV photons. Flared disks allow starlight to directly fall on PAHs in the disk surface, favoring PAH emission, while flat disks tend to lack PAH emission because PAHs are in the shadow of the inner disk (Acke & van den Ancker, 2004; Habart et al., 2006, in press). PDS 144N is consistent with this scenario: the PAH emission we see comes primarily from particles in the envelope, high above the disk's midplane. The models of Habart et al. (2004) predict that the 3.3 μm PAH emission will be strongest within 100 AU of the star, a conclusion supported by recent observations. Here we detect that feature at several times greater distance. We find that the PAH/continuum ratio increases with distance from the star, as predicted by Habart et al. However, the models of Habart et al. were computed for face-on inclinations, so we cannot directly compare them with PDS 144N's edge-on geometry.

The Spitzer IRAC 8 μm flux for PDS 144N is significantly greater than the 11.7μm LWS flux. This suggests that PDS 144N has strong PAH emission in the 7.7 or 8.6 μm PAH bands as well, but higher spectral resolution observations are needed to confirm this.

6.4.5 The Mid Infrared

What is the origin of the photons we detect from PDS 144N at 11.7 μm? The outer disk is too cool to emit thermal photons over the observed spatial extent. Nor can the light be scattered stellar photons, since the observed flux is far in excess of the photospheric value at this wavelength. However, it may be scattered photons from the hot inner disk, as is seen around HK Tau B at this wavelength (McCabe et al., 2003). PDS 144N must have substantial thermal emission from its inner disk (unless it has a large inner radius, which we cannot exclude based on our data) providing sufficient photons to scatter and produce the observed mid-IR nebulosity. Alternatively, it could be emission from the 11.3 μm PAH band, which falls within the bandpass of LWS's 11.7 μm filter. The strength of the 11.3 μm PAH feature should correlate with the 3.3 μm feature, since both bands arise from the same aromatic C-H bonds (Bregman et al., 1994), and we know there is copious 3.3 μm PAH emission present. The energetics are favorable for PAH emission, too: A main-sequence A2V star supplies sufficient UV flux to energize PAHs enough to produce

the 11.7 μm light, even before adding any UV excess from active accretion. With these data we cannot conclusively resolve this issue. In order to further constrain the emission mechanism, we have obtained additional observations in a series of narrowband mid-IR filters with Michelle at Gemini, which will be presented in an upcoming paper (Perrin et al., in preparation).

6.4.6 PDS 144 South

Vieira et al. (2003)'s optical spectroscopy confirmed the presence of emission lines in the spectrum of PDS 144S, including [SII] $\lambda\lambda$ 6717, 6730 and [OII] $\lambda\lambda$ 3726, 3728 in addition to Hα. Therefore PDS 144S is actively accreting and must necessarily possess circumstellar material of its own. Furthermore, we find PDS 144S has almost 5 magnitudes of IR excess at K_s band, unambiguously indicating the presence of warm circumstellar dust. However, the SED alone cannot tell us the distribution of that dust; models using either disks or spherical envelopes can both adequately reproduce dusty SEDs. Resolved imaging is necessary to break the degeneracies between model parameters (Chiang et al., 2001b).

We do not resolve a disk around PDS 144S in any of these observations (though we remind the reader that our Keck data is saturated on PDS 144S in all but one waveband, preventing PSF subtraction and greatly degrading disk detection limits). Given PDS 144S's unresolved appearance, any disk around PDS 144S must be either noncoplanar with PDS 144N's disk or sufficiently less massive that it is optically thin at these wavelengths, so that the system's appearance is dominated by the direct light from the star. Jensen et al. (2004) observed 19 multiple T Tauri systems and found that 8 out of 9 binaries had polarization vectors aligned within 30°, consistent with disk alignment. However, these binaries have apparent separations 200-1000 AU, much less than PDS 144's 5400 AU. It is plausible that disk alignment mechanisms may be less effective in systems with greater separations. HK Tau provides a well-known example of non-coplanar disks in a system apparently quite similar to PDS 144 (Stapelfeldt et al., 1998; Duchêne et al., 2003).

Unlike PDS 144N, PDS 144S displays no evidence for PAH emission above continuum levels in the present observations; the difference in the shapes of the two stars' SEDs from 3.6-8 μm is quite striking. PDS 144S has sufficient far-UV flux to energize PAHs if present. Possibly the two stars' disks differ in composition, with PDS 144S lacking PAHs. Alternatively, (Acke & van den Ancker, 2004) suggests that Herbig Ae stars with flat disks have much weaker PAH emission than stars with flared disks because self-shadowing

prevents UV light from reaching the PAHs. Thus the two PDS 144 stars could have similar abundances of PAHs yet very different spectra if their circumstellar dust geometries differ.

6.5 Preliminary Disk Models

We have modeled the disk around PDS 144N using the Monte Carlo radiative transfer code made available by B. Whitney and collaborators (Whitney et al., 2003b,a). This was a first-draft modeling effort only, with model parameters tuned by eye to approximate the observed properties of PDS 144 at H band. No attempt has been made here to minimize errors in any formal statistical sense. The purpose of this exercise was to identify a reasonable starting point for future more detailed modeling, and to determine which if any features of PDS 144N are most discrepant from simple disk models. A more sophisticated fit to the complete multiwavelength data set via a multidimensional optimization code will be described in a future work. Here we shall limit ourselves to discussing the overall properties of our model, and the most notable discrepancies between model and observation.

The Whitney et al. radiative transfer code allows grain properties to vary between different regions. Briefly, grains are treated as spheres with scattering computed using the Mie theory; grains follow power-law size distributions with parameters varying from ISM-like in the envelope and outflow to larger grains in the disk and midplane. We refer readers to Whitney et al. (2003a) for a detailed discussion of assumed grain parameters; we used an identical prescription as those authors. We assumed a disk mass of 0.01 $M_{\odot}$, outer radius $r = 350$ AU, density exponent $\alpha = 2.25$, scale height $h = 0.4$ AU at $r = 50$ AU, and scale height exponent $\beta = 1.25$.

We first attempted to model PDS 144N using the simplest possible model of only a passive circumstellar disk, without any surrounding envelope. We did this computation for H band, the wavelength in which the "wings" are least pronounced. The overall shape of the disk, including the slight curvature of the dark lane, is best reproduced by disk models with inclinations of $83 \pm 1°$. Despite an extensive search of parameter space, the simple disk models were unable to reproduce the extended nebulosity around the disk. Furthermore, even though the wings are minimized at H band, the northwestern lobe still has a local minimum on the vertical axis, while the disk-only models predict a local maximum there. Thus we conclude that a circumstellar envelope is required in addition to a disk to accurately model this system.

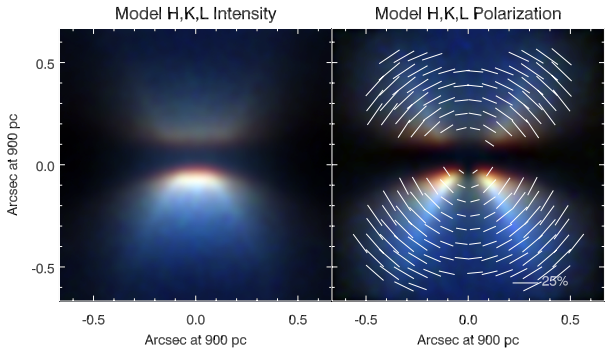

Figure 6.6: Monte Carlo model of a circumstellar disk plus envelope, at 1000 pc, convolved with a wavelength-dependent model Keck PSF computed with the Keck AO model of Sheehy et al. (in preparation). The left frame shows total intensity I while the right frame shows polarized intensity $\sqrt{Q^2+U^2}$. H, K', and L' are blue, green, and red, respectively, and the image scale is linear. Vectors in the right hand frame show the degree and orientation of K' band polarization. The disk model has mass 0.01 $M_\odot$ and radius 350 AU. Surrounding that is a rotationally supported infalling envelope (Terebey et al., 1984) with an infall rate of $2 \times 10^{-6} M_\odot$ year^{-1} and a cavity opening half angle of 15°.

Models incorporating a circumstellar envelope and outflow cavities are much more successful in reproducing the observed morphology. We added a rotationally supported infalling envelope (Terebey et al., 1984) with an infall rate of $2 \times 10^{-6} M_\odot$ year^{-1} and a cavity opening half angle of 15°. We display this model in Figure 6.6. Limb-brightening from the edges of the outflow cavity roughly reproduces the "wings" seen around PDS 144N.

However, there remain some discrepancies between this model and the data. While this is only a preliminary model, we point out some differences so that they may be addressed in future more comprehensive modeling. The observed nebula has a sharper outer edge than the model does. This is not a signal-to-noise ratio effect: the observed nebula outer radius is roughly the same at all wavelengths, even though the SNR varies substantially. Furthermore, introducing read- and sky-subtraction noise comparable to the observed levels into our model images does not truncate the apparent size of the disk. We have discussed above possible scenarios for tidal or photoevaporative truncation of the material around PDS 144N. Also, the model predicts that for an inclination of 83°, the nearer side of the disk (southwest) will have a peak surface brightness ~ 3 times the fainter side. The observed southwest side is actually 10 times brighter than the fainter side. This

difference may reflect the model's use of Mie scattering by spherical grains rather than more realistic grain scattering.

6.6 Conclusions

We have presented high resolution observations of PDS 144 from 1.2-11.7 μm obtained at Lick and Keck Observatories, plus archival Spitzer photometry from 3.6-70 μm. PDS 144N is hidden from direct view at all wavelengths from 1.2-11.7 μm by an edge-on optically thick circumstellar disk $0\farcs8$ across. Red "wings" extend vertically from the disk, most likely due to scattering from the walls of an outflow cavity in an infalling envelope of dust and gas. The wings are very bright in the 3.3 μm PAH feature, indicating the presence of small aromatic grains fluorescing due to far-UV illumination. Its nearby companion, PDS 144S, is unresolved in our data but has very strong IR excesses indicating that it, too, is surrounded by copius circumstellar dust. But a number of basic questions remain open about this fascinating system:

How far away is it? Our distance estimate of 1000 ± 200 pc is based on fitting the $UBVRI$ measurements of Vieira et al. (2003) with an extincted A5 stellar spectrum for PDS 144S. Uncertainties in the spectral type and evolutionary state of the stars, plus confusion of the two sources in the unresolved optical photometry, limit the precision possible with this method. The 1000 pc distance also results in a surprising height above the Galactic plane. We caution that this distance estimate relies on the assumption that the two stars of PDS 144 are physically associated, which is probable but unproven.

How old is it? The uncertain distance results in similarly uncertain total luminosities for the two stars, making it difficult to place them on pre-main-sequence evolutionary tracks (e.g. Palla & Stahler, 1993). The large IR excesses of both stars suggest there may be significant accretion luminosity. This further complicates placing the stars on pre-main-sequence tracks, but also implies the system is quite young.

How massive is it? The stellar masses are poorly constrained for the same reason their ages are, because their positions in the H-R diagram are imprecise. The dust mass around PDS 144N cannot be constrained with the data presented here since the disk is optically thick at these wavelengths. Resolved millimeter observations of this system would be very useful to constrain the dust masses around each star. Given the southern declination, the SMA may be the array best suited to obtaining these observations.

How have the two stars interacted? PDS 144N's envelope appears to have been truncated, perhaps due to the influence of PDS 144S, although the mechanism for this truncation remains unclear. The two stars both have circumstellar material, but have very different appearances at these wavelengths. Can this be explained entirely by geometric effects due to different viewing angles to physically similar young stars, or are the stars and their circumstellar material intrinsically different? If so, why, given that they are presumably coeval, of fairly similar mass, and formed from the same parent cloud?

Are there outflows? The presence of a bipolar cavity around PDS 144N suggests that there are, or at least once were. Polar outflows from disks around T Tauri stars may be traced by a number of low-excitation emission lines, such as in the exquisite HST images of the HH 30 disk and jet (Burrows et al., 1996). Similar outflows have been seen around a number of Herbig Ae stars (Corcoran & Ray, 1998a; Grady et al., 2000). Does PDS 144N also harbor such jets? The presence of [SII] emission in the optical suggests that it does. At near IR wavelengths where AO imaging is possible, the [FeII] 1.257,1.644 μm lines are ideal outflow tracers on account of their low ionization potential and excitations (Pesenti et al., 2003; Pyo et al., 2003).

As the first Herbig Ae star with a clearly resolved edge-on disk, PDS 144N provides an exciting opportunity for comparison of disk properties between intermediate-mass and lower-mass stars, such as the well-studied HH 30. The geometry of the PDS 144 system makes it a particularly well-suited laboratory for detailed studies of circumstellar material. Such studies need both high sensitivity and high angular resolution. Because the disk is edge-on, it blocks the direct starlight, resulting in a greatly favorable contrast ratio and thus increased sensitivity to faint emission. Furthermore, since PDS 144 is a binary, we have a bright unocculted star conveniently nearby to serve as an wavefront reference source. Just as in HK Tau, the binarity of this system enables studies which would otherwise not be possible.

Acknowledgements

We greatly appreciate the excellent work of the Lick and Keck observatory staffs, in particular Elinor Gates, Mark Kassis, and Randy Campbell. We also thank Bob Becker for his gracious flexibility in trading LWS observing time, and a two dollar bill. Sergio Vieira and Carlos Torres provided helpful discussions regarding their PDS survey observations. We recognize that Mauna Kea has always been a site of great significance to the Hawaiian

people, and we are most fortunate to have the opportunity to observe from this mountain.

This work has been supported in part by the National Science Foundation Science and Technology Center for Adaptive Optics, managed by the University of California at Santa Cruz under cooperative agreement No. AST-9876783. PK received additional support from the NASA Origins Program under grant NAG5-11769. MDP is supported by a NASA Michelson Graduate Fellowship, under contract to the Jet Propulsion Laboratory (JPL). JPL is managed for NASA by the California Institute of Technology.

Chapter 7

A Tightly Collimated Bipolar Jet from the Herbig Ae star LkHα 233

Abstract

We have used the new integral field spectrograph OSIRIS and laser guide star adaptive optics system at Keck Observatory to obtain high angular resolution ($0\farcs06$), moderate spectral resolution ($R \sim 3800$) images of the bipolar jet from the Herbig Ae star LkHα 233. This jet is narrow and tightly collimated, with an opening angle of only 9 degrees. The jet and counterjet are asymmetric, with the red-shifted jet much clumpier than its counterpart.

7.1 Introduction

Some of the most spectacular images of our universe are those featuring bipolar outflows from young stars (see, *e.g.* Bally et al 2006). But far from being merely aesthetically pleasing, these jets play a crucial role in star formation: material in molecular clouds must shed most of its angular momentum before it can accrete onto a newborn star. Jets have been identified as a key mechanism for this process, enabling accretion to continue. Recent observations have for the first time demonstrated that jets launched from several young stars rotate (Coffey et al., 2004; Woitas et al., 2005), showing that these outflows do indeed carry angular momentum away from their origin.

But the precise mechanism through which these jets are launched remains mysterious. Magnetocentrifugal acceleration may launch jets either from near the radius of magnetospherical truncation (the "X-wind theory"; see Shang et al. (2002); Shang (2006) or from a larger range of radii (the "disk wind theory"; see Pudritz (2006)). Directly observing the jet launch region requires better angular resolution than is currently possible, but observations on larger spatial scales may still indirectly place constraints on jet launch physics.

Most jets studied in depth to date have been around low mass YSOs; comparatively few are known around more massive YSOs such as Herbig Ae/Be stars. Because jet acceleration is believed to be a magnetohydrodynamic phenomenon, one might suppose that jet properties will differ between convective T Tauri stars and the Herbig Ae/Bes, which lack a surface convection zone (Waters & Waelkens, 1998). However, in those cases where jets are known around Herbig Ae/Bes, most appear generally similar to those of T Tauris, though with higher outflow velocities and indications that jet collimation decreases for higher mass objects (Mundt & Ray, 1994).

One of the few Herbig Ae/Be stars known to possess a jet is LkHα 233 (V375 Lac). This star is located at a distance of approximately 880 pc (Herbig, 1960) in condensation A of the Lac OB1 molecular cloud (Bowey et al., 2003). Hernández et al. (2004) classified it as spectral type A4, and derived $M_* = 2.9\ M_\odot$, $L_* = 80\ L_\odot$, and age = 2.61 Myr, with $A_V = 3.7$, $R_V = 5$. (However, those values must be used with caution, as they were derived without accounting for the fact that LkHα 233 is seen only in scattered light and thus likely underestimate both the extinction and the total luminosity.) It sits at the center of an X-shaped bipolar nebula visible from optical to near-infrared wavelengths (Aspin et al., 1985; Li et al., 1994). Near infrared polarimetry shows a dark lane passing in front of the star, indicating the presence of a roughly edge-on circumstellar disk (Perrin et al., 2004b).

Corcoran & Ray (1998a) discovered that LkHα 233 possesses an extended bipolar jet and counterjet visible in the optical [SII] 6716, 6731 Ålines. The blueshifted jet is at position angle 250°, along the symmetry axis of the surrounding nebula and perpendicular to the inferred circumstellar disk. The redshifted counterjet, at 70°, could not be detected within $0\farcs6$ of the star, which they interpreted as occultation by the circumstellar disk. A followup study by McGroarty et al. (2004) found that a chain of Herbig Haro objects extends almost 2 pc to either side of LkHα 233, located approximately along the jet axis but with considerable scatter.

Stellar outflows are detectable primarily in emission lines from shock-excited ions, with characteristic spatial scales of a few AU and velocities of tens to hundreds of km s^{-1}. Studying the acceleration and collimation of jets thus requires both high spatial resolution and moderate spectral resolution. In optical wavelengths, such as for the [SII] (6717, 6731 Å) and [OI] (6300, 6364 Å) emission lines, the needed angular resolution is only available from space. However, in the near-infrared, the diffraction limit is attainable from the ground with adaptive optics. In this wavelength range, the [FeII] (1.257,1.533,1.600,1.644 μm) lines are ideal (Pesenti et al., 2003; Hartigan et al., 2004).

The recent arrival at Keck of the integral field spectrograph OSIRIS provides a powerful new capability for high angular resolution infrared spectroscopy. We present here OSIRIS observations which show LkHα 233's jet and circumstellar environment with unprecedented detail.

7.2 Observations

We observed LkHα 233 on 2005 Oct 13 UTC using the integral field spectrograph OSIRIS and laser guide star adaptive optics system (Wizinowich et al., 2006) on the W. M. Keck II telescope. LkHα 233 itself served as the tip-tilt reference for the adaptive optics system. The skies were clear and seeing was average, $0\farcs6$ at K', with winds from 15-20 km hr^{-1}.

OSIRIS is a lenslet-based integral field spectrograph which provides a spectral resolution of 3800 from 1-2.5 microns (Larkin et al., 2003). We selected its 50 mas $pixel^{-1}$ spectrographic plate scale for our observations. While this scale does not Nyquist-sample the diffraction-limited PSF, it provides a larger field of view and better signal to noise per integration time than the finer plate scales. We observed LkHα 233 using the narrowband *Hn3* and *Kn3* filters, covering the wavelength ranges 1.594-1.676 and 2.121-2.229 μm, respectively. Total integration time on-source was 1800 s for Hn3 and 900 s for Kn3. Between exposures on LkHα 233, we obtained sky observations at a position 20" away.

We reduced the data using a preliminary version of the OSIRIS data reduction pipeline (Krabbe et al., 2004). The data were sky-subtracted, corrected for offsets between the 32 detector readout channels, spatially rectified to extract the individual spectra into a data cube, and corrected for cosmic rays and other blemishes. The A stars BD +9 5007 and HD 7789 served as telluric standards. We also used these stars as photometric references: we

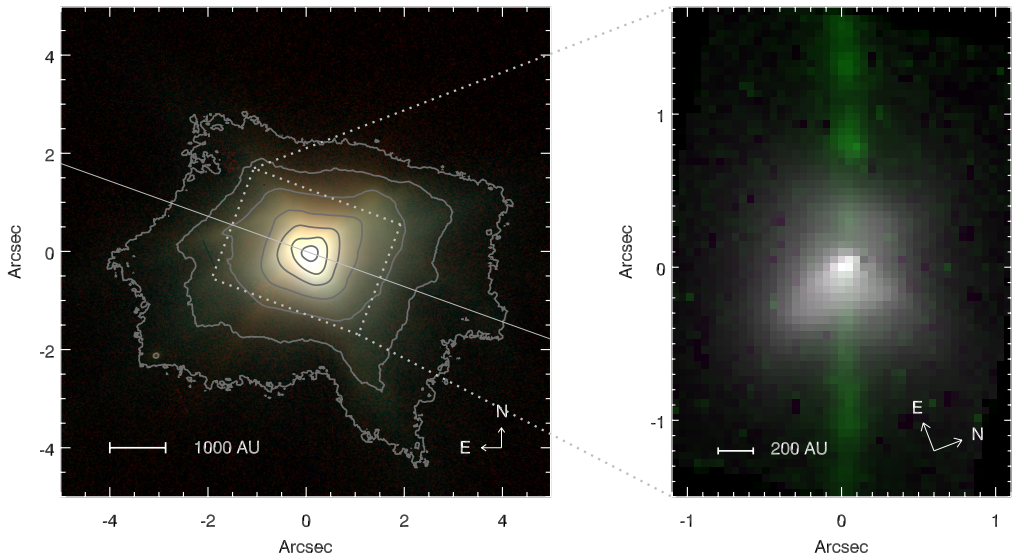

Figure 7.1: Left: This J, H, K_s composite from the OSIRIS imager shows the X-shaped envelope surrounding LkHα 233. The dashed rectangle shows the field zoomed in to on the right, while the solid line shows the outflow axis. **Right:** A portion of the OSIRIS IFU data cube, centered in wavelength on the 1.644 μm [FeII] line (in green). This image reveals a tightly collimated bipolar outflow from LkHα 233 perpendicular to an edge-on circumstellar disk. The jet is undetectable in the broadband image; only with the spectral resolution of OSIRIS can it be detected. In these data we also see a roughly edge-on circumstellar disk and a larger bipolar nebula extending perpendicular to the disk plane. The jet has excavated a cavity in this envelope, the limb-brightened edges of which form the well-known "X" centered on LkHα 233 (Aspin et al., 1985; Perrin et al., 2004b).

converted the 2MASS H and K_s magnitudes of these stars into magnitudes in the OSIRIS $Hn3$ and $Kn3$ filters via synthetic photometry, and then used those magnitudes to derive a zero point for flux-calibrating our LkHα 233 observations.

These observations were made during the instrument's commissioning period, and show a variety of instrumental artifacts, most notably ghost images at certain wavelengths caused by crosstalk between lenslets due to a grating misalignment. These ghost images do not occur in the wavelength ranges of interest to us, and so we may simply ignore them. The grating has been realigned subsequent to these observations and more recent data do not suffer from these ghosts.

OSIRIS also includes an imaging camera whose field of view is offset by 19.4" from the spectrograph field. Our sky observations were designed so that LkHα 233 would fall on

the imager field of view (FOV) while we were obtaining spectrograph skies, and vice versa. In this manner we obtained Z, J, H, and K band observations of LkHα 233, with total exposure times of 300, 360, 360, and 315 s, respectively. These observations were reduced via the usual steps of flat fielding, sky subtraction, image registration, and summation.

7.3 Results

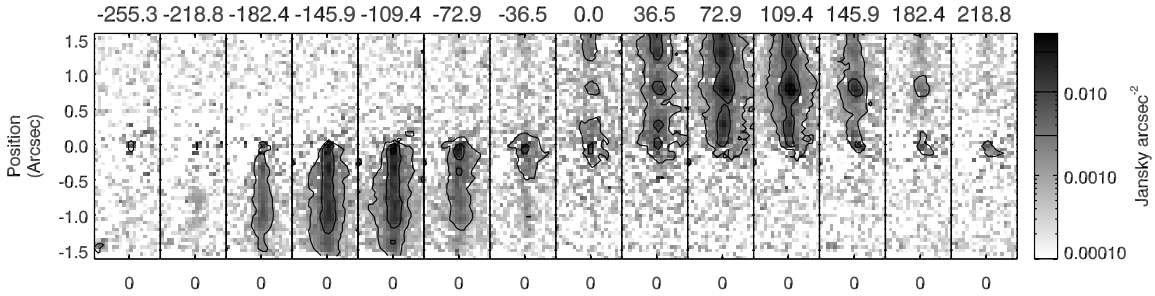

Figure 7.2: Slices through the data cube, shifted in the wavelength/velocity axis.

A tightly collimated bipolar emission-line jet extends several arcseconds on either side of LkHα 233 (Fig. 7.1), with the blueshifted jet at a position angle (PA) of 249°, and the redshifted jet at 69°. We also see a roughly edge-on circumstellar disk and the larger bipolar nebula extending roughly perpendicular to the disk plane. The jet has excavated a cavity in this envelope, the limb-brightened edges of which form the well-known "X" centered on LkHα 233. We detect the jet in the [FeII] 1.600, 1.644 μm and H Br$_\gamma$ 2.16 μm lines. Of these, the 1.644 μm line is the brightest, and we choose to concentrate our analysis on it.

The jet is narrow, tightly collimated, and knotty. The FWHM of the jet increases slowly from 100 AU near its base to $\sim$ 200 AU at the edge of our FOV, 1300 AU from the star, giving an opening angle of 9°. Three bright knots are apparent in the redshifted jet, at approximate distances of 0.3, 0.8, and 1.3″ from the star, corresponding to 260, 700, and 1150 AU. The blueshifted jet is noticeably less clumpy, but brightens considerably near its base, with peak intensity reached at 0.″1 (88 AU) from the star.

In Fig. 7.2 we show continuum-subtracted images in a range of velocity channels

centered on 1.644 μm. The red- and blueshifted jets have average velocities of $\pm$100 km s^{-1} relative to the system's mean velocity. But these data reveal many additional details. While the blueshifted jet is relatively even in velocity, the redshifted jet shows considerable variation in velocity. The middle clump, at 0.″8, has a higher velocity than the other two clumps by about 30 km s^{-1}. For both the red and blue directions, the higher velocity channels are more tightly collimated than the lower velocity channels.

We do not see much evidence for the low velocity component (LVC) found by Corcoran & Ray (1998a) at about -25 km/s. This may be due to the fact that the [FeII] 1.644 μm line traces higher densities than the [SII] 6716, 6731 Å lines. Thus in the NIR we are only sensitive to denser gas in the core of the jet.

In addition to showing the jet, these observations also clearly reveal a circumstellar disk around LkHα 233, as evidenced by the characteristic bright nebula crossed by a dark lane, the characteristic signature of a roughly edge-on circumstellar disk (Fig. 7.1, right). The presence of this disk was originally suspected based on optical polarimetry (Aspin et al., 1985). Corcoran & Ray (1998a) were unable to trace the redshifted optical [SII] emission any closer than 0.″6 to the star, and inferred the presence of a disk with this radius. We confirm here that interpretation: the circumstellar disk extends from 0.5 below to 0.6 arcsec above the locus of peak intensity. In contrast to the [SII] line, at [FeII] 1.644 μm the jet can be traced all the way in to the star on both sides (Fig. 7.2. There is at most a two-pixel-wide (0.″1) region at the base of the red jet where the emission is somewhat fainter, possibly due to obscuration. This indicates that the far lobe of the circumstellar disk is not optically thick at these wavelengths, in contrast to the optical. The observed disk morphology is consistent with that seen in visible light in HST WFPC2 observations (Stapelfeldt et al., in prep).

The continuum intensity peak remains well-resolved in these data, with a FWHM of 0.″135 versus 0.″06 for a PSF reference star. Therefore we do not observe the star directly, but rather see it in disk-scattered light. The peak intensity is located at the apex of the southwest face of the disk, which is the brighter of the two faces. This is consistent with the southwest side of the system being inclined toward us, as indicated by the blueshifted jet.

By comparison with a series of circumstellar disk models computed using the Monte Carlo radiative transfer code of Whitney et al. (2003b), we determined that LkHα 233 is inclined between 70 and 80 degrees to the line of sight. If we adopt an estimate of

$i = 75° \pm 5$, then the radial velocities we observe are only 25 ± 9 percent of the total jet velocity. A jet velocity of 400-500 km s^{-1} is consistent with outflows seen around other Herbig Ae stars (Mundt & Ray, 1994). This implies proper motions on the sky of approximately 0.″1 per year. Thus the bright knots in the jet were launched from the star within the last 5 to 15 years, and their motion should be apparent over short timescales.

We attempted to measure jet rotation following the methods of Coffey et al. (2004). We did not detect any significant difference between the velocities at positions offset ±0.″05 on either side of the jet axis.

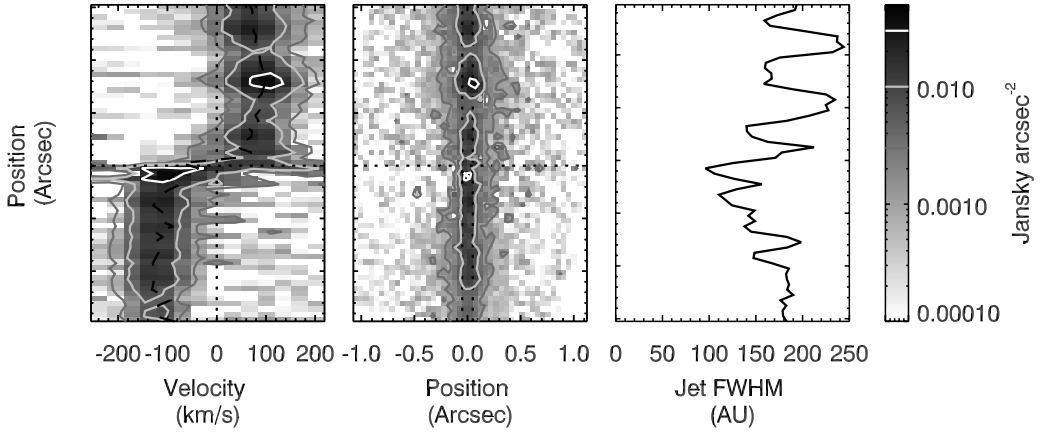

Figure 7.3: **Left:** Continuum-subtracted position velocity diagram, for a 0.″1 wide "virtual slit" centered on the jet. **Center:** Continuum-subtracted image of the jet. The upper and lower portions of this image are drawn from slightly different wavelength ranges centered on the red- and blueshifted jets, each with bandwidth 0.6 nm. **Right:** Measurements of jet FWHM versus distance from the star. This plot was constructed by fitting each row in the continuum-subtracted image with a Gaussian.

7.3.1 Mass Flux

The intensity in these lines traces the total amount of mass present in the jet, and thus allows us to estimate the mass flux. Currently the physical parameters of this jet, such as the temperature, ionization, and depletion onto grains, are not well known so this will be a rudimentary estimate at best; future observations will enable a refined calculation. We

follow the method of Podio et al. (2006):

$$\begin{aligned} \dot{M} &= \mu m_H (n_H V) v_t / l_t \\ (n_H V) &= L_{[FeII]} \left(h\nu A_i f_i \frac{FeII}{Fe} \frac{Fe}{H} \right)^{-1} \end{aligned}$$

where μ is the mean molecular weight, taken to be 1.24, m_H is the mass of hydrogen, n_H is the number density of hydrogen, V is the volume filled by the emitting gas, v_t is the transverse velocity of the jet, and l_t is the transverse length of the jet volume. Based on our estimated inclination $i = 75^\circ$ and observed $v_{radial} = 100$ km s^{-1}, I compute $v_t = 375$ km s^{-1}, and I take l_t to be the transverse length of each OSIRIS pixel, $0\farcs050 \times 880$ pc $= 44$ AU. Several assumptions are needed in order to transform the observed line luminosity $L_{[FeII]}$ into the density-volume product $n_H V$: without accurate knowledge of the temperature I have to guess at the ionization fraction and upper state fraction for iron. I assume for these that Fe is entirely ionized ($\frac{FeII}{Fe} = 1$), that the fraction of ions in the upper energy level $f_i = 0.01$, and that iron has a solar abundance but is 90% depleted onto solid grains. These assumptions are based on the conditions typically observed in the HH object jets of T Tauri stars by Podio et al.

Our IFU data actually enable us to measure the outflow mass flux rate as it varies along the jet. I collapse the 2d continuum-subtracted [FeII] image in the direction perpendicular to the jet, and for each pixel in the resulting image compute $\dot{M}$ according to the above prescription. The computed mass flux has a median value of $1.8 \times 10^{-7} M_\odot$ year^{-1}, and is fairly constant along most of the jet, varying between $1.3 - 2.3 \times 10^{-7} M_\odot$ year^{-1}. The one exception is the middle knot in the redshifted jet, where the flux rises to $4.0 \times 10^{-7} M_\odot$ year^{-1}.

I caution that these values are *approximate* at best, given the lack of knowledge of the temperature and ionization structure, and furthermore represent lower limits, because all of the outflow is not necessarily shocked and luminous, and because I have not corrected for extinction. A second method of computing the mass outflow rate is as $\dot{M} = \mu m_H n_H \pi r_J^2 v_J$; Podio et al. found masses computed with this method were often 3-5 times higher than those computed based on [FeII] fluxes. I do not know n_H, but I do know that $n_e \sim 5 \times 10^4$ cm^{-3}. Podio et al. report typical ionization fractions $x_e = 0.03 - 0.3$ for HH objects, so if I assume $x_e = 0.3$, then $n_H = 5 \times 10^5$ cm^{-3}. Using a rough estimate of $r_J = 90$ AU, I compute $\dot{M} = 1.2 \times 10^{-6} M_\odot$ year^{-1}, about 7 times higher than my first estimate. This is to be expected, since the filling fraction for [FeII] emission is less than

unity (Podio et al. 2006). These estimates are approximations at best, given our limited knowledge of the exact physical conditions in the jet, but do serve to confirm that the observed [FeII] intensity can be produced by a reasonable mass flux in the jet. The values for $\dot{M}$ computed here are about an order of magnitude larger than those computed for HH 34 and HH 111 by Podio et al, but LkHα 233 is a more massive star.

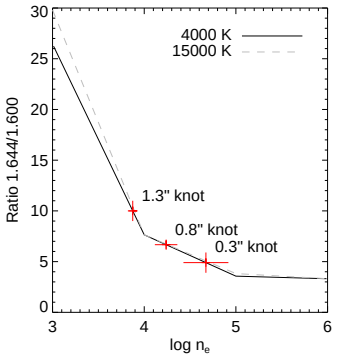

Figure 7.4: The ratio of the 1.644 μm and 1.600 μm lines provides a diagnostic for electron density n_e. The solid and dashed lines show the expected ratio as a function of n_e for two different temperatures, from Nisini et al. 2002. The measured line ratios for the three clumps in the redshifted jet of LkHα 233 are indicated; the length of the crosses shows the uncertainties. The electron density decreases along the jet as one moves away from the star; the values of $\sim 10^4 - 10^{4.5}$ are comparable to, though slightly higher than, the observed electron densities in T Tauri HH jets at somewhat greater distances from the star.

7.4 Discussion

It is striking how similar LkHα 233 appears to the T Tauri star HH 30, with its well-known edge-on disk and perpendicular outflow (Burrows et al., 1996). Like HH 30, LkHα 233's disk is asymmetric in brightness between the left and right sides. The outflow from both stars is knotty, and even the characteristic period for knot production is similar, 2.5 years for HH 30 and ≈ 4 years for LkHα 233.

The knots in LkHα 233's jet are consistent with internal working surfaces caused by variations in jet outflow velocity. In particular, the brightest knot is also that with the highest velocity, just what would be expected for more rapid material plowing into a slower

region. The fact that only the redshifted jet is knotty is curious. Similar asymmetries have been seen in outflows from T Tauri stars. Explaining these asymmetries may pose a challenge to theories of jet acceleration and collimation.

There is a growing body of evidence that outflows from high mass stars are generally less collimated than those of low mass stars. Given the tightly collimated nature of LkHα 233's outflow, the transition to poorly collimated jets must occur at a higher mass.

The near-IR lines of [FeII] allow measurement of several important physical parameters of the jet (Hartigan et al., 2004). We have shown here the measured electron density using the 1.644/1.600 μm ratio, and have also presented a very rough estimate of the mass flux rate using the 1.644 μmline. But much more can be done with a more extensive spectrum: The 1.644, 1.257, and 1.320 μm lines all originate in the same upper state, and thus their ratios directly constrain the extinction A_V. Ratios of other lines (most notably 1.644/1.600 and 1.644/1.533) provide a measure of the electron density, and comparison with *optical* [FeII] lines can measure the temperature as well (Nisini et al., 2005; Podio et al., 2006). The limited wavelength coverage of the observations presented here restricts their diagnostic capabilities; see Fig. 7.4 for the one such measurement possible with our present dataset. Future observations that include the complete optical and near-IR spectrum of [FeII] and other shock tracers will enable a complete suite of diagnostics for temperature, density, ionization, refractory element depletion, and more. Detailed modeling of LkHα 233 thus holds great promise for understanding outflow mechanisms around intermediate-mass stars.

Acknowledgements

These observations were made possible by the tremendous efforts of the OSIRIS instrument team and Keck Observatory staff, whose members are too numerous to list here in full. Special thanks in particular go to James Larkin, Shelley Wright, Mike McElwain, Randy Campbell, and Al Conrad. Conor Laver assisted with the data reduction pipeline. We recognize that Mauna Kea has always been a site of great significance to the Hawaiian people, and we are most fortunate to have the opportunity to observe from this mountain.

This work has been supported in part by the National Science Foundation Science and Technology Center for Adaptive Optics, managed by the University of California at Santa Cruz under cooperative agreement No. AST-9876783. MDP was supported by a NASA Michelson Graduate Fellowship, under contract to the Jet Propulsion Laboratory (JPL). JPL is managed for NASA by the California Institute of Technology.

Chapter 8

Conclusions

8.1 Principal Results

I have developed a dual-channel imaging polarimetry mode for IRCAL, the science camera for adaptive optics at Lick Observatory. This instrument provides a factor of nearly 100 reduction in the halo of AO-uncorrected starlight against which scattered light from circumstellar dust must be detected. This reduction factor is determined by a complicated interplay between a variety of instrumental noise sources; trends in the light suppression level with PSF FWHM suggest that numerical errors from pixel undersampling and/or registration and interpolation errors are the dominant factors.

Data reduction for differential imagers is a complex and challenging subject. Many hurdles lurk along the way toward reaching the photon-noise performance of an ideal system, waiting to snare an unexpecting polarimetrist or two. Flat fielding must be carefully attended to, as must the issue of accurately registering saturated or coronagraphically occulted deep images. The resulting Stokes parameter images may be evaluated for faint patterns of centrosymmetric polarization position vectors, the characteristic signal of light scattered from polarized circumstellar dust.

With this instrument, I have surveyed over 110 Herbig Ae/Be stars, a large majority of the total set of such stars observable at Lick Observatory. I find that 30% of these possess extended nebulae seen in polarized light, with observed geometries including both disks and envelopes in different cases. A further 20% of sources show peaks in centrosymmetric polarization vectors indicating the presence of circumstellar dust, but either too faint or too small in angular size to resolve directly.

These observations strongly support the idea that Herbig Ae stars, at least in some cases, possess circumstellar disks very similar to those seen around T Tauri stars. The binary PDS 144 is strikingly similar to T Tauri binaries such as HK Tau or HV Tau. In each of those systems, an edge-on geometry enables us to directly see a thin circumstellar disk around one star, while the other does possess dust but is not resolved at infrared wavelengths. LkHα 233 is a higher mass analog of HH 30 and other T Tauri stars which launch bipolar outflows. But there are differences as well as similarities. The strong UV radiation from PDS 144 N illuminates PAH molecules leading to fluorescent emission, a process not generally seen around the cooler T Tauris. LkHα 233 may be the exception rather than the rule, with higher-mass stars such as AFGL 4029 IRS 1 and MWC 1080 launching generally less-collimated outflows. Indeed, while several Ae stars show very clear evidence for circumstellar disks of the type seen around T Tauri stars, the case for disks around Be stars remains much more tenuous.

This survey also turned up a number of surprising and intriguing objects: MWC 778 with its giant pinwheel nebula, the potential tidal tails between the stars of LkHα 225 and RNO 1B/1C, the extensive circumstellar arcs of HBHA 3203-03 and V645 Cyg. Further studies are needed to clarify the processes at work around these stars.

8.2 Looking toward the future

In this thesis, I have repeatedly demonstrated the value of pushing the technological envelope of astronomical instrumentation. The combination of differential polarimetry and adaptive optics provides high sensitivity to circumstellar dust around young stars. This led to the first peer-reviewed science from a sodium laser guide star system (Perrin et al., 2004; Chapter 5), revealing new evidence for dusty disks embedded in the bipolar circumstellar envelopes around LkHα 198 and LkHα 233, and to the discovery of the first resolved edge-on disk around a Herbig Ae star (Perrin et al. 2006; Chapter 6). In only a few short years since the dawn of LGS AO science, the state of the art has advanced to include integral field spectroscopy with LGS AO from the world's largest telescope, providing spectacular and highly informative images of LkHα 233's tightly collimated bipolar outflow (Chapter 7).

This is a common pattern in science: Advances in technology enable advances in our understanding of the cosmos, which spurs new questions that in turn drive further

advances in technology. The rise of sensitive infrared detectors led to the discovery of infrared excesses around Vega and similar stars, prompting efforts to image the dust around these systems. Precision radial velocity Doppler surveys have now discovered hundreds of extrasolar planets, driving a tremendous interest in direct imaging of these planets. With this goal in mind, several teams are currently developing high contrast AO systems for 8-m telescopes, most notably the Gemini Planet Imager for Gemini South and ESO SPHERE project for the VLT. Both of these instruments will incorporate differential polarimeters for observations of circumstellar disks. High contrast polarimetry today has also been used to very good success in a number of Hubble Space Telescope instruments. However, JWST NIRCAM currently has no provisions for polarimetry. Thus in the future, the importance of ground-based polarimetry will only increase.

A number of mechanical and optical design tradeoffs for IRCAL polarimetry were made in the name of expediency when retrofitting polarimetry into an existing camera. Future systems ought to be able to substantially improve on the scattered light performance achieved here, through a combination of straightforward mechanism improvements, the use of lenslet arrays to pixellate the image plane before polarimetric beam splitting, and the optimal location of the polarizing beamsplitter after the system pupil is defined.

Also, optical designs that incorporate balanced reflections can minimize instrumental polarization effects, but for complex optical trains like an adaptive optics beam relay this sort of mitigation may not be feasible. For instruments mounted at a Cassegrain focus, the instrumental polarization should be very stable, so that in principle it can be removed in calibration. On the other hand, for Cassegrain instruments on large altazimuth telescopes, sky rotation will introduce an additional complication not present in IRCAL. Future high contrast imagers are expected to operate in fixed-pupil mode rather than with the traditional use of sky derotators. But this means that each observed image frame is a measurement of polarization in its own coordinate system rotated relative to the sky differently from all other frames. The optimum way to combine such data remains in need of further study.

The mid-infrared is an area of tremendous importance, particularly for its diagnostic power over mineralogy and grain growth. Spitzer is by far the most sensitive mid-IR instrument today, but has a limited life and there is a gap until JWST comes on line. But even in the era of JWST, ground-based mid-IR observations will be tremendously important because of their higher angular resolution. Gemini and the VLT, and soon the

Large Binocular Telescope, are the premiere mid-IR imagers today, but the planned Thirty Meter Telescope has tremendous potential for revolutionizing mid-IR observations. Disks barely resolved by today's imagers, such as HD 169142 and PDS 144 S, will become well resolved in the future. Mid-IR interferometry provides much higher angular resolution, but resolves out the outer disk. Imaging and interferometry here are complimentary techniques.

* * *

Astronomical high contrast imaging remains in is infancy. Barely twenty years after the first detection of circumstellar dust around Vega and Beta Pic, it is now clear that dusty disks are a near-ubiquitious element of the star formation process, and that many—but not all—stars retain debris disks over timescales of hundreds of millions of years. But the transition from primordial disks to debris disks remains mysterious, and it is during this transition that planets are believed to be born. Current and near-future instruments such as Hubble and Spitzer, GPI and SPHERE will continue unveiling the secrets of these disks. But just beyond them, in the slightly more distant future, are a suite of truly massive projects including the Thirty Meter Telescope, James Webb Space Telescope, and Atacama Large Millimeter Array. The science cases for each of these billion-dollar eyes to the sky are driven in large part by questions about star formation, circumstellar disk evolution, and the assembly of planets. If and when these giant observatories come to fruition, partway through the next decade, we will be able to peer into the depths of dusty circumstellar disks and gaze upon the origins of worlds.

Bibliography

Ábrahám, P., Kóspál, Á., Csizmadia, S., Kun, M., Moór, A., & Prusti, T. 2004, A&A, 428, 89

Acke, B. & van den Ancker, M. E. 2004, A&A, 426, 151

Adams, F. C., Hollenbach, D., Laughlin, G., & Gorti, U. 2004, ApJ, 611, 360

Adamson, A., Aspin, C., & Davis, C., eds. 2005, Astronomical Polarimetry: Current Status and Future Directions

Ageorges, N., Eckart, A., Monin, J.-L., & Menard, F. 1997, A&A, 326, 632

Ageorges, N. & Walsh, J. R. 1999, A&AS, 138, 163

Akeson, R. L., Ciardi, D. R., van Belle, G. T., Creech-Eakman, M. J., & Lada, E. A. 2000, ApJ, 543, 313

Alcalá, J. M., Wachter, S., Covino, E., Sterzik, M. F., Durisen, R. H., Freyberg, M. J., Hoard, D. W., & Cooksey, K. 2004, A&A, 416, 677

Allen, D. A. 1974, MNRAS, 168, 1

Allen, D. A. & Swings, J. P. 1976, A&A, 47, 293

Apai, D., Pascucci, I., Brandner, W., Henning, T., Lenzen, R., Potter, D. E., Lagrange, A.-M., & Rousset, G. 2004, A&A, 415, 671

Ardila, D. R., Golimowski, D. A., Krist, J., Clampin, M., Ford, H. C., & Illingworth, G. D. 2005, in Protostars and Planets V, Proceedings of the Conference held October 24-28, 2005, in Hilton Waikoloa Village, Hawai'i. LPI Contribution No. 1286., p.8511, 8511–+

Artymowicz, P. & Lubow, S. H. 1994, ApJ, 421, 651

Aspin, C., McCaughrean, M. J., & McLean, I. S. 1985, Astron. Astrophys., 144, 220

Aspin, C., Sandell, G., & Weintraub, D. A. 1994, Astron. Astrophys., 282, L25

Asselin, L., Menard, F., Bastien, P., Monin, J.-L., & Rouan, D. 1996, ApJ, 472, 349

Assousa, G. E., Herbst, W., & Turner, K. C. 1977, ApJ, 218, L13

Aumann, H. H., Beichman, C. A., Gillett, F. C., de Jong, T., Houck, J. R., Low, F. J., Neugebauer, G., Walker, R. G., & Wesselius, P. R. 1984, ApJ, 278, L23

Baines, D., Oudmaijer, R. D., Porter, J. M., & Pozzo, M. 2006, MNRAS, 367, 737

Bastien, P. 1987, Astrophys. J., 317, 231

Bauman, B. J., Gavel, D. T., Waltjen, K. E., Freeze, G. J., Hurd, R. L., Gates, E. L., Max, C. E., Olivier, S. S., & Pennington, D. M. 2002, in Proc. SPIE Vol. 4494, p. 19-29, Adaptive Optics Systems and Technology II, Robert K. Tyson; Domenico Bonaccini; Michael C. Roggemann; Eds., Vol. 4494, 19–29

Beichman, C. A. 1979, Ph.D. Thesis

Berrilli, F., Corciulo, G., Ingrosso, G., Lorenzetti, D., Nisini, B., & Strafella, F. 1992, Astrophys. J., 398, 254

Bertout, C., Robichon, N., & Arenou, F. 1999, A&A, 352, 574

Bibo, E. A. & The, P. S. 1991, A&AS, 89, 319

Blaauw, A., Hiltner, W. A., & Johnson, H. L. 1959, ApJ, 130, 69

Boffin, H. M. J., Watkins, S. J., Bhattal, A. S., Francis, N., & Whitworth, A. P. 1998, Mon. Not. R. Astron. Soc., 300, 1189

Bonnell, I. A., Bate, M. R., & Zinnecker, H. 1998, Mon. Not. R. Astron. Soc., 298, 93

Bouvier, J. & Corporon, P. 2001, in IAU Symposium, ed. H. Zinnecker & R. Mathieu, 155–+

Bowey, J. E., Adamson, A. J., & Yates, J. A. 2003, MNRAS, 340, 1173

Breckinridge, J. B. & Oppenheimer, B. R. 2004, ApJ, 600, 1091

Bregman, J., Larson, K., Rank, D., & Temi, P. 1994, ApJ, 423, 326

Burrows, C. J., Stapelfeldt, K. R., Watson, A. M., Krist, J. E., Ballester, G. E., Clarke, J. T., Crisp, D., Gallagher, J. S., Griffiths, R. E., Hester, J. J., Hoessel, J. G., Holtzman, J. A., Mould, J. R., Scowen, P. A., Trauger, J. T., & Westphal, J. A. 1996, ApJ, 473, 437

Butler, R. P., Wright, J. T., Marcy, G. W., Fischer, D. A., Vogt, S. S., Tinney, C. G., Jones, H. R. A., Carter, B. D., Johnson, J. A., McCarthy, C., & Penny, A. J. 2006, ApJ, 646, 505

Calvet, N. & Cohen, M. 1978, MNRAS, 182, 687

Canto, J., Rodriguez, L. F., Calvet, N., & Levreault, R. M. 1984, Astrophys. J., 282, 631

Carballo, R. & Sahu, M. 1994, A&A, 289, 131

Carballo, R., Wesselius, P. R., & Whittet, D. C. B. 1992, A&A, 262, 106

Cardelli, J. A., Clayton, G. C., & Mathis, J. S. 1989, ApJ, 345, 245

Carpenter, J. M., Snell, R. L., & Schloerb, F. P. 1995, ApJ, 445, 246

Casey, S. C. & Harper, D. A. 1990, ApJ, 362, 663

Chavarria, C., de Lara, E., Finkenzeller, U., Appenzeller, I., & Cardona, O. 1983, A&A, 118, 189

Chavarria-K., C., de Lara, E., Finkenzeller, U., Mendoza, E. E., & Ocegueda, J. 1988, A&A, 197, 151

Chen, C. H. & Jura, M. 2003, ApJ, 591, 267

Chiang, E. I. & Goldreich, P. 1997, ApJ, 490, 368

—. 1999, ApJ, 519, 279

Chiang, E. I., Joung, M. K., Creech-Eakman, M. J., Qi, C., Kessler, J. E., Blake, G. A., & van Dishoeck, E. F. 2001a, ApJ, 547, 1077

—. 2001b, ApJ, 547, 1077

Cidale, L., Zorec, J., & Morrell, N. 2000, in ASP Conf. Ser. 214: IAU Colloq. 175: The Be Phenomenon in Early-Type Stars, ed. M. A. Smith, H. F. Henrichs, & J. Fabregat, 87–+

Clampin, M., Krist, J. E., Ardila, D. R., Golimowski, D. A., Hartig, G. F., Ford, H. C., Illingworth, G. D., Bartko, F., Benítez, N., Blakeslee, J. P., Bouwens, R. J., Broadhurst, T. J., Brown, R. A., Burrows, C. J., Cheng, E. S., Cross, N. J. G., Feldman, P. D., Franx, M., Gronwall, C., Infante, L., Kimble, R. A., Lesser, M. P., Martel, A. R., Menanteau, F., Meurer, G. R., Miley, G. K., Postman, M., Rosati, P., Sirianni, M., Sparks, W. B., Tran, H. D., Tsvetanov, Z. I., White, R. L., & Zheng, W. 2003, AJ, 126, 385

Close, L. M., Roddier, F., Hora, J. L., Graves, J. E., Northcott, M., Roddier, C., Hoffmann, W. F., Dayal, A., Fazio, G. G., & Deutsch, L. K. 1997, ApJ, 489, 210+

Code, A. D. & Whitney, B. A. 1995, ApJ, 441, 400

Coffey, D., Bacciotti, F., Woitas, J., Ray, T. P., & Eislöffel, J. 2004, ApJ, 604, 758

Cohen, M. 1977, ApJ, 215, 533

—. 1980, AJ, 85, 29

Cohen, M., Bieging, J. H., Welch, W. J., & Dreher, J. W. 1985, ApJ, 292, 249

Cohen, M. & Kuhi, L. V. 1979, ApJS, 41, 743

Cohen, M., Walker, R. G., Carter, B., Hammersley, P., Kidger, M., & Noguchi, K. 1999, AJ, 117, 1864

Condon, J. J., Kaplan, D. L., & Terzian, Y. 1999, ApJS, 123, 219

Corcoran, D., Ray, T. P., & Bastien, P. 1995, Astron. Astrophys., 293, 550

Corcoran, M. & Ray, T. P. 1998a, Astron. Astrophys., 336, 535

—. 1998b, A&A, 331, 147

Corporon, P. & Lagrange, A.-M. 1999, A&AS, 136, 429

Cote, J. & Waters, L. B. F. M. 1987, A&A, 176, 93

Cotera, A. S., Whitney, B. A., Young, E., Wolff, M. J., Wood, K., Povich, M., Schneider, G., Rieke, M., & Thompson, R. 2001, ApJ, 556, 958

D'Alessio, P., Calvet, N., & Hartmann, L. 2001, ApJ, 553, 321

Damiani, F., Micela, G., Sciortino, S., & Harnden, Jr., F. R. 1994, ApJ, 436, 807

Danchi, W. C., Tuthill, P. G., & Monnier, J. D. 2001, ApJ, 562, 440

Davies, J. K., Evans, A., Bode, M. F., & Whittet, D. C. B. 1990, MNRAS, 247, 517

Davies, R. I., Tecza, M., Looney, L. W., Eisenhauer, F., Tacconi-Garman, L. E., Thatte, N., Ott, T., Rabien, S., Hippler, S., & Kasper, M. 2001, Astrophys. J., 552, 692

de Zeeuw, P. T., Hoogerwerf, R., de Bruijne, J. H. J., Brown, A. G. A., & Blaauw, A. 1999, AJ, 117, 354

Deharveng, L., Zavagno, A., Cruz-Gonzalez, I., Salas, L., Caplan, J., & Carrasco, L. 1997, A&A, 317, 459

Dent, W. R. F., Greaves, J. S., & Coulson, I. M. 2005, MNRAS, 359, 663

Devine, D., Grady, C. A., Kimble, R. A., Woodgate, B., Bruhweiler, F. C., Boggess, A., Linsky, J. L., & Clampin, M. 2000, ApJ, 542, L115

di Francesco, J., Evans, N. J., Harvey, P. M., Mundy, L. G., & Butner, H. M. 1994, Astrophys. J., 432, 710

di Francesco, J., Evans, N. J., Harvey, P. M., Mundy, L. G., Guilloteau, S., & Chandler, C. J. 1997, Astrophys. J., 482, 433

Dobashi, K., Uehara, H., Kandori, R., Sakurai, T., Kaiden, M., Umemoto, T., & Sato, F. 2005, PASJ, 57, 1

Drew, J. E., Busfield, G., Hoare, M. G., Murdoch, K. A., Nixon, C. A., & Oudmaijer, R. D. 1997, MNRAS, 286, 538

Duchêne, G., McCabe, C., Ghez, A. M., & Macintosh, B. A. 2004, ApJ, 606, 969

Duchêne, G., Ménard, F., Stapelfeldt, K., & Duvert, G. 2003, A&A, 400, 559

Ducourant, C., Teixeira, R., Périé, J. P., Lecampion, J. F., Guibert, J., & Sartori, M. J. 2005, A&A, 438, 769

Dullemond, C. P. & Dominik, C. 2004, A&A, 417, 159

Dullemond, C. P. & Natta, A. 2003, A&A, 408, 161

Dullemond, C. P., van den Ancker, M. E., Acke, B., & van Boekel, R. 2003, ApJ, 594, L47

Dunkin, S. K., Barlow, M. J., & Ryan, S. G. 1997a, MNRAS, 286, 604

—. 1997b, MNRAS, 290, 165

Dunkin, S. K. & Crawford, I. A. 1998, MNRAS, 298, 275

Eisner, J. A., Lane, B. F., Hillenbrand, L. A., Akeson, R. L., & Sargent, A. I. 2004, ApJ, 613, 1049

Elias, J. H. 1978, ApJ, 224, 857

Elias, J. H., Frogel, J. A., Matthews, K., & Neugebauer, G. 1982, AJ, 87, 1029

Espin, T. E. 1902, Astronomische Nachrichten, 158, 241

Evans, N. J., Allen, L. E., Blake, G. A., Boogert, A. C. A., Bourke, T., Harvey, P. M., Kessler, J. E., Koerner, D. W., Lee, C. W., Mundy, L. G., Myers, P. C., Padgett, D. L., Pontoppidan, K., Sargent, A. I., Stapelfeldt, K. R., van Dishoeck, E. F., Young, C. H., & Young, K. E. 2003, PASP, 115, 965

Fazio, G. G., Hora, J. L., Allen, L. E., Ashby, M. L. N., Barmby, P., Deutsch, L. K., Huang, J.-S., Kleiner, S., Marengo, M., Megeath, S. T., Melnick, G. J., Pahre, M. A., Patten, B. M., Polizotti, J., Smith, H. A., Taylor, R. S., Wang, Z., Willner, S. P., Hoffmann, W. F., Pipher, J. L., Forrest, W. J., McMurty, C. W., McCreight, C. R., McKelvey, M. E., McMurray, R. E., Koch, D. G., Moseley, S. H., Arendt, R. G., Mentzell, J. E., Marx, C. T., Losch, P., Mayman, P., Eichhorn, W., Krebs, D., Jhabvala, M., Gezari, D. Y., Fixsen, D. J., Flores, J., Shakoorzadeh, K., Jungo, R., Hakun, C., Workman, L., Karpati, G., Kichak, R., Whitley, R., Mann, S., Tollestrup, E. V., Eisenhardt, P., Stern, D., Gorjian, V., Bhattacharya, B., Carey, S., Nelson, B. O., Glaccum, W. J., Lacy, M., Lowrance, P. J., Laine, S., Reach, W. T., Stauffer, J. A., Surace, J. A., Wilson, G., Wright, E. L., Hoffman, A., Domingo, G., & Cohen, M. 2004, ApJS, 154, 10

Finkenzeller, U. 1985, A&A, 151, 340

Finkenzeller, U. & Mundt, R. 1984, A&AS, 55, 109

Fisher, R. S., Telesco, C. M., Piña, R. K., Knacke, R. F., & Wyatt, M. C. 2000, ApJ, 532, L141

Fitzgerald, M. P. & Graham, J. R. 2006, ApJ, 637, 541

Friedemann, C., Guertler, J., & Loewe, M. 1996, A&AS, 117, 205

Fruchter, A. S. & Hook, R. N. 2002, PASP, 114, 144

Fuente, A., Martin-Pintado, J., Bachiller, R., Neri, R., & Palla, F. 1998a, A&A, 334, 253

Fuente, A., Martin-Pintado, J., Rodriguez-Franco, A., & Moriarty-Schieven, G. D. 1998b, A&A, 339, 575

Fukagawa, M., Hayashi, M., Tamura, M., Itoh, Y., Hayashi, S. S., Oasa, Y., Takeuchi, T., Morino, J.-i., Murakawa, K., Oya, S., Yamashita, T., Suto, H., Mayama, S., Naoi, T., Ishii, M., Pyo, T.-S., Nishikawa, T., Takato, N., Usuda, T., Ando, H., Iye, M., Miyama, S. M., & Kaifu, N. 2004, ApJ, 605, L53

Fukagawa, M., Tamura, M., Itoh, Y., Hayashi, S. S., & Oasa, Y. 2003, ApJ, 590, L49

Fukagawa, M., Tamura, M., Suto, H., Itoh, Y., Murakawa, K., Oasa, Y., Hayashi, S. S., Naoi, T., Kaifu, N., & Doi, Y. 2002, Pub. Astron. Soc. Japan, 54, 969

Gahm, G. F., Ahlin, P., & Lindroos, K. P. 1983, A&AS, 51, 143

Galland, F., Lagrange, A.-M., Udry, S., Chelli, A., Pepe, F., Queloz, D., Beuzit, J.-L., & Mayor, M. 2005, A&A, 443, 337

García-Hernández, D. A., Manchado, A., García-Lario, P., Domínguez-Tagle, C., Conway, G. M., & Prada, F. 2002, A&A, 387, 955

Garcia-Lario, P., Manchado, A., Pych, W., & Pottasch, S. R. 1997, A&AS, 126, 479

Gavel, D. T., Max, C. E., Olivier, S. S., Bauman, B. J., Pennington, D. M., Macintosh, B. A., Patience, J., Brown, C. G., Danforth, P. M., Hurd, R. L., Gates, E. L., Severson, S. A., & Lloyd, J. P. 2002, in Proc. SPIE Vol. 4494, p. 336-342, Adaptive Optics Systems

and Technology II, Robert K. Tyson; Domenico Bonaccini; Michael C. Roggemann; Eds., 336–342

Gehrels, T., ed. 1974, Planets, stars and nebulae studied with photopolarimetry

Glasse, A. C., Atad-Ettedgui, E. I., & Harris, J. W. 1997, in Proc. SPIE Vol. 2871, p. 1197-1203, Optical Telescopes of Today and Tomorrow, Arne L. Ardeberg; Ed., ed. A. L. Ardeberg, 1197–1203

Goodrich, R. W. 1986, ApJ, 311, 882

—. 1993, ApJS, 86, 499

Grady, C. A., Devine, D., Woodgate, B., Kimble, R., Bruhweiler, F. C., Boggess, A., Linsky, J. L., Plait, P., Clampin, M., & Kalas, P. 2000, ApJ, 544, 895

Grady, C. A., Polomski, E. F., Henning, T., Stecklum, B., Woodgate, B. E., Telesco, C. M., Piña, R. K., Gull, T. R., Boggess, A., Bowers, C. W., Bruhweiler, F. C., Clampin, M., Danks, A. C., Green, R. F., Heap, S. R., Hutchings, J. B., Jenkins, E. B., Joseph, C., Kaiser, M. E., Kimble, R. A., Kraemer, S., Lindler, D., Linsky, J. L., Maran, S. P., Moos, H. W., Plait, P., Roesler, F., Timothy, J. G., & Weistrop, D. 2001, AJ, 122, 3396

Grady, C. A., Woodgate, B., Bruhweiler, F. C., Boggess, A., Plait, P., Lindler, D. J., Clampin, M., & Kalas, P. 1999, ApJ, 523, L151

Grady, C. A., Woodgate, B. E., Bowers, C. W., Gull, T. R., Sitko, M. L., Carpenter, W. J., Lynch, D. K., Russell, R. W., Perry, R. B., Williger, G. M., Roberge, A., Bouret, J.-C., & Sahu, M. 2005, ApJ, 630, 958

Gregorio-Hetem, J., Lepine, J. R. D., Quast, G. R., Torres, C. A. O., & de La Reza, R. 1992, AJ, 103, 549

Grinin, V. P., Kiselev, N. N., Chernova, G. P., Minikulov, N. K., & Voshchinnikov, N. V. 1991, Ap&SS, 186, 283

Haas, M., Christou, J. C., Zinnecker, H., Ridgway, S. T., & Leinert, C. 1993, A&A, 269, 282

Haas, M., Leinert, C., & Richichi, A. 1997, A&A, 326, 1076

Habart, E., Natta, A., & Krügel, E. 2004, A&A, 427, 179

Habart, E., Natta, A., & Testi, L. ad Carbillet, M. 2006, in press, A&A

Habart, E., Testi, L., Natta, A., & Vanzi, L. 2003, A&A, 400, 575

Hajjar, R. & Bastien, P. 2000, Astroph. J., 531, 494

Hales, A. S., Gledhill, T. M., Barlow, M. J., & Lowe, K. T. E. 2006, MNRAS, 365, 1348

Hamaguchi, K., Terada, H., Bamba, A., & Koyama, K. 2000, ApJ, 532, 1111

Hamaguchi, K., Yamauchi, S., & Koyama, K. 2005, ApJ, 618, 360

Happer, W., MacDonald, G. J., Max, C. E., & Dyson, F. J. 1994, Optical Society of America Journal, 11, 263

Hartigan, P., Raymond, J., & Pierson, R. 2004, ApJ, 614, L69

Hartmann, L. & Kenyon, S. J. 1996, ARA&A, 34, 207

Hartmann, L., Kenyon, S. J., & Calvet, N. 1993, ApJ, 407, 219

Heiles, C. 2000, AJ, 119, 923

Henize, K. G. 1976, ApJS, 30, 491

Henning, T., Burkert, A., Launhardt, R., Leinert, C., & Stecklum, B. 1998, Astron. Astrophys., 336, 565

Herbig, G. H. 1957, ApJ, 125, 654

—. 1960, Astrophys. J. Suppl. Ser., 4, 337

—. 1977, ApJ, 217, 693

Herbig, G. H. & Bell, K. 1988, Catalog of emission line stars of the orion population : 3 : 1988 (Lick Observatory Bulletin, Santa Cruz: Lick Observatory, —c1988)

Herbig, G. H. & Dahm, S. E. 2006, AJ, 131, 1530

Herbig, G. H. & Kameswara Rao, N. 1972, ApJ, 174, 401

Herbig, G. H., Petrov, P. P., & Duemmler, R. 2003, ApJ, 595, 384

Herbst, W., Holtzman, J. A., & Klasky, R. S. 1983, AJ, 88, 1648

Herbst, W., Holtzman, J. A., & Phelps, B. E. 1982, AJ, 87, 1710

Herbst, W. & Shevchenko, V. S. 1999, AJ, 118, 1043

Hernández, J., Calvet, N., Briceño, C., Hartmann, L., & Berlind, P. 2004, AJ, 127, 1682

Hessman, F. V., Beckwith, S. V. W., Bender, R., Eisloeffel, J., Goetz, W., & Guenther, E. 1995, A&A, 299, 464

Hillenbrand, L. A., Meyer, M. R., Strom, S. E., & Skrutskie, M. F. 1995, Astron. J., 109, 280

Hillenbrand, L. A., Strom, S. E., Vrba, F. J., & Keene, J. 1992, Astrophys. J., 397, 613

Hoffmeister, C. 1944, Astronomische Nachrichten, 274, 232

Hollenbach, D., Johnstone, D., Lizano, S., & Shu, F. 1994, ApJ, 428, 654

Honda, M., Kataza, H., Okamoto, Y. K., Yamashita, T., Fujiyoshi, T., Miyata, T., Sako, S., Okada, Y., Sakon, I., Fujiwara, H., & Onaka, T. 2005, in Protostars and Planets V, 8090–+

Hough, J. H. 2005, in Astronomical Society of the Pacific Conference Series, ed. A. Adamson, C. Aspin, & C. Davis, 3–+

Hussey, W. J. 1900, AJ, 21, 35

Jayawardhana, R. & Ivanov, V. 2006, Science

Jensen, E. L. N., Mathieu, R. D., Donar, A. X., & Dullighan, A. 2004, ApJ, 600, 789

Jones, B. & Puetter, R. C. 1993, in Proc. SPIE Vol. 1946, p. 610-621, Infrared Detectors and Instrumentation, Albert M. Fowler; Ed., 610–621

Kalas, P., Graham, J. R., & Clampin, M. 2005, Nature, 435, 1067

Kalas, P., Graham, J. R., Clampin, M. C., & Fitzgerald, M. P. 2006, ApJ, 637, L57

Kant, I. 1798, Allgemeine Naturgeschichte und Theorie des Himmels (Zeitz, Bei W. Webel, 1798. Neue aufl.)

Kataza, H. & Maihara, T. 1991, A&A, 248, L1

Kawamura, A., Onishi, T., Yonekura, Y., Dobashi, K., Mizuno, A., Ogawa, H., & Fukui, Y. 1998, ApJS, 117, 387

Keller, C. U. 2002, in Astrophysical Spectropolarimetry, 303–+

Kenyon, S. J., Dobrzycka, D., & Hartmann, L. 1994, AJ, 108, 1872

Kenyon, S. J., Hartmann, L., Gomez, M., Carr, J. S., & Tokunaga, A. 1993, AJ, 105, 1505

Kenyon, S. J., Hartmann, L. W., & Kolotilov, E. A. 1991, PASP, 103, 1069

Kim, S.-H., Martin, P. G., & Hendry, P. D. 1994, ApJ, 422, 164

Kohoutek, L. 1997, Astronomische Nachrichten, 318, 35

Koresko, C. D., Beckwith, S. V. W., Ghez, A. M., Matthews, K., & Neugebauer, G. 1991, AJ, 102, 2073

Koresko, C. D., Harvey, P. M., Christou, J. C., Fugate, R. Q., & Li, W. 1997, Astrophys. J., 485, 213

Kozok, J. R. 1985, A&AS, 62, 7

Krabbe, A., Gasaway, T., Song, I., Iserlohe, C., Weiss, J., Larkin, J. E., Barczys, M., & Lafreniere, D. 2004, in Ground-based Instrumentation for Astronomy. Edited by Alan F. M. Moorwood and Iye Masanori. Proceedings of the SPIE, Volume 5492, pp. 1403-1410 (2004)., ed. A. F. M. Moorwood & M. Iye, 1403–1410

Krist, J. E., Ardila, D. R., Golimowski, D. A., Clampin, M., Ford, H. C., Illingworth, G. D., Hartig, G. F., Bartko, F., Benítez, N., Blakeslee, J. P., Bouwens, R. J., Bradley, L. D., Broadhurst, T. J., Brown, R. A., Burrows, C. J., Cheng, E. S., Cross, N. J. G., Demarco, R., Feldman, P. D., Franx, M., Goto, T., Gronwall, C., Holden, B., Homeier, N., Infante, L., Kimble, R. A., Lesser, M. P., Martel, A. R., Mei, S., Menanteau, F., Meurer, G. R., Miley, G. K., Motta, V., Postman, M., Rosati, P., Sirianni, M., Sparks, W. B., Tran, H. D., Tsvetanov, Z. I., White, R. L., & Zheng, W. 2005, AJ, 129, 1008

Kroupa, P. 1998, MNRAS, 298, 231

Krumholz, M. R., McKee, C. F., & Klein, R. I. 2005, Nature, 438, 332

Kuhn, J. R. 2005, in Astronomical Society of the Pacific Conference Series, ed. A. Adamson, C. Aspin, & C. Davis, 22–+

Kuhn, J. R., Lin, H., & Loranz, D. 1991, PASP, 103, 1097

Kuhn, J. R., Potter, D., & Parise, B. 2001a, ApJ, 553, L189

—. 2001b, Astrophys. J. Lett., 553, L189

Kukarkin, B. V., Kholopov, P. N., Artiukhina, N. M., Fedorovich, V. P., Frolov, M. S., Goranskij, V. P., Gorynya, N. A., Karitskaya, E. A., Kireeva, N. N., Kukarkina, N. P., Kurochkin, N. E., Medvedeva, G. I., Perova, N. B., Ponomareva, G. A., Samus, N. N., & Shugarov, S. Y. 1981, in Moscow, Acad. of Sciences USSR Shternberg,1951 (1981), 0–+

Kun, M. 1998, ApJS, 115, 59

Lafrenière, D., Doyon, R., Artigau, É., Marois, C., Beaulieu, M., Nadeau, D., & Racine, R. 2006, in Ground-based and Airborne Instrumentation for Astronomy. Edited by Ian S. McLean and Masanori Iye. Proceedings of the SPIE, Volume 6269, pp. 626929 (2006).

Lagage, P. O., Olofsson, G., Cabrit, S., Cesarsky, C. J., Nordh, L., & Rodriguez Espinosa, J. M. 1993, Astrophys. J. Lett., 417, L79+

Larkin, J., Barczys, M., Krabbe, A., Adkins, S., Aliado, T., Amico, P., Brims, G., Campbell, R., Canfield, J., Gasaway, T., Honey, A., Iserlohe, C., Johnson, C., Kress, E., LaFreniere, D., Lyke, J., Magnone, K., Magnone, N., McElwain, M., Moon, J., Quirrenbach, A., Skulason, G., Song, I., Spencer, M., Weiss, J., & Wright, S. 2006, in Ground-based and Airborne Instrumentation for Astronomy. Edited by Ian S. McLean and Masanori Iye. Proceedings of the SPIE, Volume 6269, pp. 626919 (2006).

Larkin, J. E., Quirrenbach, A., Krabbe, A., Aliado, T., Barczys, M., Brims, G., Canfield, J., Gasaway, T. M., LaFreniere, D., Magnone, N., Skulason, G., Spencer, M., Sprayberry, D., & Weiss, J. 2003, in Instrument Design and Performance for Optical/Infrared Ground-based Telescopes. Edited by Iye, Masanori; Moorwood, Alan F. M. Proceedings of the SPIE, Volume 4841, pp. 1600-1610 (2003)., ed. M. Iye & A. F. M. Moorwood, 1600–1610

Larson, R. B. 1990, in ASSL Vol. 162: Physical Processes in Fragmentation and Star Formation, 389–399

Lefevre, J., Bergeat, J., & Daniel, J.-Y. 1982, A&A, 114, 341

Leger, A., D'Hendecourt, L., & Defourneau, D. 1989, A&A, 216, 148

Leinert, C., Haas, M., Ábrahám, P., & Richichi, A. 2001, A&A, 375, 927

Leinert, C., Richichi, A., & Haas, M. 1997, A&A, 318, 472

Li, W., Evans, N. J., Harvey, P. M., & Colome, C. 1994, Astrophys. J., 433, 199

Likkel, L. 1989, ApJ, 344, 350

Lloyd, J. P., Liu, M. C., Macintosh, B. A., Severson, S. A., Deich, W. T., & Graham, J. R. 2000, in Proc. SPIE Vol. 4008, p. 814-821, Optical and IR Telescope Instrumentation and Detectors, Masanori Iye; Alan F. Moorwood; Eds., Vol. 4008, 814–821

Lucas, P. W., Fukagawa, M., Tamura, M., Beckford, A. F., Itoh, Y., Murakawa, K., Suto, H., Hayashi, S. S., Oasa, Y., Naoi, T., Doi, Y., Ebizuka, N., & Kaifu, N. 2004, MNRAS, 352, 1347

Lupton, R., Blanton, M. R., Fekete, G., Hogg, D. W., O'Mullane, W., Szalay, A., & Wherry, N. 2004, PASP, 116, 133

Lupton, R. H., Gunn, J. E., & Szalay, A. S. 1999, AJ, 118, 1406

Maffei, P. 1967, ApJ, 147, 802

Maheswar, G., Manoj, P., & Bhatt, H. C. 2002, A&A, 387, 1003

Makovoz, D. & Marleau, F. R. 2005, PASP, 117, 1113

Malfait, K., Bogaert, E., & Waelkens, C. 1998, A&A, 331, 211

Mannings, V. 1994, MNRAS, 271, 587

Mannings, V., Koerner, D. W., & Sargent, A. I. 1997, Nature, 388, 555

Mannings, V. & Sargent, A. I. 1997, Astrophys. J., 490, 792

Marcy, G., Butler, R. P., Fischer, D., Vogt, S., Wright, J. T., Tinney, C. G., & Jones, H. R. A. 2005, Progress of Theoretical Physics Supplement, 158, 24

Marois, C., Doyon, R., Nadeau, D., Racine, R., Riopel, M., Vallée, P., & Lafrenière, D. 2005, PASP, 117, 745

Marois, C., Lafrenière, D., Macintosh, B., & Doyon, R. 2006, ApJ, 647, 612

Marois, C., Racine, R., Doyon, R., Lafrenière, D., & Nadeau, D. 2004, ApJ, 615, L61

Marsh, K. A., Silverstone, M. D., Becklin, E. E., Koerner, D. W., Werner, M. W., Weinberger, A. J., & Ressler, M. E. 2002, ApJ, 573, 425

Max, C., Olivier, S., Friedman, H., An, J., Avicola, K., Beeman, B., Bissinger, H., Brase, J., Erbert, G., Gavel, D., Kanz, K., Liu, M., Macintosh, B., Neeb, K., Patience, J., & Waltjen, K. 1997, Science, 277, 1649

Mayor, M. & Queloz, D. 1995, Nature, 378, 355

McCabe, C., Duchêne, G., & Ghez, A. M. 2003, ApJ, 588, L113

McCabe, C., Ghez, A. M., Prato, L., Duchêne, G., Fisher, R. S., & Telesco, C. 2006, ApJ, 636, 932

McGroarty, F., Ray, T. P., & Bally, J. 2004, A&A, 415, 189

McKee, C. F. & Tan, J. C. 2003, Astrophys. J., 585, 850

Meeus, G., Waelkens, C., & Malfait, K. 1998, A&A, 329, 131

Meeus, G., Waters, L. B. F. M., Bouwman, J., van den Ancker, M. E., Waelkens, C., & Malfait, K. 2001, A&A, 365, 476

Meixner, M., Ueta, T., Dayal, A., Hora, J. L., Fazio, G., Hrivnak, B. J., Skinner, C. J., Hoffmann, W. F., & Deutsch, L. K. 1999, ApJS, 122, 221

Mel'Nikov, S. Y., Shevchenko, V. S., Grankin, K. N., Ibragimov, M. A., & Yakubov, S. D. 1995, Astronomy Reports, 39, 42

Merín, B., Montesinos, B., Eiroa, C., Solano, E., Mora, A., D'Alessio, P., Calvet, N., Oudmaijer, R. D., de Winter, D., Davies, J. K., Harris, A. W., Cameron, A., Deeg,

H. J., Ferlet, R., Garzón, F., Grady, C. A., Horne, K., Miranda, L. F., Palacios, J., Penny, A., Quirrenbach, A., Rauer, H., Schneider, J., & Wesselius, P. R. 2004, A&A, 419, 301

Merrill, P. W. & Burwell, C. G. 1949, ApJ, 110, 387

—. 1950, ApJ, 112, 72

Meyer, J. M., Nordsieck, K. H., & Hoffman, J. L. 2002, AJ, 123, 1639

Millan-Gabet, R., Monnier, J. D., Akeson, R. L., Hartmann, L., Berger, J.-P., Tannirkulam, A., Melnikov, S., Billmeier, R., Calvet, N., D'Alessio, P., Hillenbrand, L. A., Kuchner, M., Traub, W. A., Tuthill, P. G., Beichman, C., Boden, A., Booth, A., Colavita, M., Creech-Eakman, M., Gathright, J., Hrynevych, M., Koresko, C., Le Mignant, D., Ligon, R., Mennesson, B., Neyman, C., Sargent, A., Shao, M., Swain, M., Thompson, R., Unwin, S., van Belle, G., Vasisht, G., & Wizinowich, P. 2006, ApJ, 641, 547

Millan-Gabet, R., Schloerb, F. P., & Traub, W. A. 2001, Astrophys. J., 546, 358

Miroshnichenko, A. S., Bjorkman, K. S., Chentsov, E. L., Klochkova, V. G., Gray, R. O., García-Lario, P., & Perea Calderón, J. V. 2001, A&A, 377, 854

Miroshnichenko, A. S., Gray, R. O., Vieira, S. L. A., Kuratov, K. S., & Bergner, Y. K. 1999, A&A, 347, 137

Mohanty, S., Jayawardhana, R., Huelamo, N., & Mamajek, E. 2006, American Astronomical Society Meeting Abstracts, 208, 26.04

Molster, F. J., Waters, L. B. F. M., Tielens, A. G. G. M., & Barlow, M. J. 2002, A&A, 382, 184

Monin, J.-L. & Bouvier, J. 2000, A&A, 356, L75

Monnier, J. D., Millan-Gabet, R., Billmeier, R., Akeson, R. L., Wallace, D., Berger, J.-P., Calvet, N., D'Alessio, P., Danchi, W. C., Hartmann, L., Hillenbrand, L. A., Kuchner, M., Rajagopal, J., Traub, W. A., Tuthill, P. G., Boden, A., Booth, A., Colavita, M., Gathright, J., Hrynevych, M., Le Mignant, D., Ligon, R., Neyman, C., Swain, M., Thompson, R., Vasisht, G., Wizinowich, P., Beichman, C., Beletic, J., Creech-Eakman, M., Koresko, C., Sargent, A., Shao, M., & van Belle, G. 2005, ApJ, 624, 832

Monnier, J. D., Tuthill, P. G., & Danchi, W. C. 1999, ApJ, 525, L97

Mora, A., Eiroa, C., Natta, A., Grady, C. A., de Winter, D., Davies, J. K., Ferlet, R., Harris, A. W., Miranda, L. F., Montesinos, B., Oudmaijer, R. D., Palacios, J., Quirrenbach, A., Rauer, H., Alberdi, A., Cameron, A., Deeg, H. J., Garzón, F., Horne, K., Merín, B., Penny, A., Schneider, J., Solano, E., Tsapras, Y., & Wesselius, P. R. 2004, A&A, 419, 225

Mora, A., Merín, B., Solano, E., Montesinos, B., de Winter, D., Eiroa, C., Ferlet, R., Grady, C. A., Davies, J. K., Miranda, L. F., Oudmaijer, R. D., Palacios, J., Quirrenbach, A., Harris, A. W., Rauer, H., Cameron, A., Deeg, H. J., Garzón, F., Penny, A., Schneider, J., Tsapras, Y., & Wesselius, P. R. 2001, A&A, 378, 116

Mundt, R. & Ray, T. P. 1994, in ASP Conf. Ser. 62: The Nature and Evolutionary Status of Herbig Ae/Be Stars, ed. P. S. The, M. R. Perez, & E. P. J. van den Heuvel, 237–+

Nakajima, T. & Golimowski, D. A. 1995, AJ, 109, 1181

Nakano, M., Tomita, Y., Ohtani, H., Ogura, K., & Sofue, Y. 1989, PASJ, 41, 1073

Natta, A., Grinin, V. P., Mannings, V., & Ungerechts, H. 1997, ApJ, 491, 885

Natta, A. & Kruegel, E. 1995, A&A, 302, 849

Natta, A., Palla, F., Butner, H. M., Evans, N. J., & Harvey, P. M. 1993, ApJ, 406, 674

Natta, A., Prusti, T., Neri, R., Wooden, D., Grinin, V. P., & Mannings, V. 2001, Astron. Astrophys., 371, 186

Natta, A. & Whitney, B. A. 2000, A&A, 364, 633

Nisini, B., Bacciotti, F., Giannini, T., Massi, F., Eislöffel, J., Podio, L., & Ray, T. P. 2005, A&A, 441, 159

Okamoto, Y. K., Kataza, H., Honda, M., Yamashita, T., Sakon, I., Fujiwara, H., Miyata, T., Sako, S., Onaka, T., & Fujiyoshi, T. 2005, in Protostars and Planets V, 8417–+

Oliva, E. 1997, A&AS, 123, 589

Oliva, E., Gennari, S., Vanzi, L., Caruso, A., & Ciofini, M. 1997, A&AS, 123, 179

Ostriker, E. C. 1994, Astrophys. J., 424, 292

Oudmaijer, R. D., van der Veen, W. E. C. J., Waters, L. B. F. M., Trams, N. R., Waelkens, C., & Engelsman, E. 1992, A&AS, 96, 625

Padgett, D. L., Brandner, W., Stapelfeldt, K. R., Strom, S. E., Terebey, S., & Koerner, D. 1999, AJ, 117, 1490

Palla, F. & Giovanardi, C. 1989, A&A, 223, 267

Palla, F. & Prusti, T. 1993, A&A, 272, 249

Palla, F. & Stahler, S. W. 1993, Astron. J., 418, 414

Patat, F. & Romaniello, M. 2006, PASP, 118, 146

Perek, L. & Kohoutek, L. 1967, Publ. House Czech. Acad. Sci., 1

Pérez, M. R., van den Ancker, M. E., de Winter, D., & Bopp, B. W. 2004, A&A, 416, 647

Perrin, M. D., Duchene, G., Kalas., P., & Graham, J. R. 2006, ApJ, 645, 1272

Perrin, M. D., Graham, J. R., Kalas, P., Lloyd, J. P., Max, C. E., Gavel, D. T., Pennington, D. M., & Gates, E. L. 2004a, in Advancements in Adaptive Optics. Edited by Domenico B. Calia, Brent L. Ellerbroek, and Roberto Ragazzoni. Proceedings of the SPIE, Volume 5490, pp. 309-320 (2004)., 309–320

Perrin, M. D., Graham, J. R., Kalas, P., Lloyd, J. P., Max, C. E., Gavel, D. T., Pennington, D. M., & Gates, E. L. 2004b, Science, 303, 1345

Perrin, M. D., Graham, J. R., Kalas, P., Lloyd, J. P., Max, C. E., Gavel, D. T., Pennington, D. M., & Gates, E. L. 2005, in Astronomical Society of the Pacific Conference Series, ed. A. Adamson, C. Aspin, & C. Davis, 379–+

Perrin, M. D., Sivaramakrishnan, A., Makidon, R. B., Oppenheimer, B. R., & Graham, J. R. 2003, ApJ, 596, 702

Persson, S. E., Murphy, D. C., Krzeminski, W., Roth, M., & Rieke, M. J. 1998, AJ, 116, 2475

Pesenti, N., Dougados, C., Cabrit, S., O'Brien, D., Garcia, P., & Ferreira, J. 2003, A&A, 410, 155

Piétu, V., Dutrey, A., & Kahane, C. 2003, Astron. Astrophys., 398, 565

Pirzkal, N., Spillar, E. J., & Dyck, H. M. 1997, ApJ, 481, 392

Podio, L., Bacciotti, F., Nisini, B., Eislöffel, J., Massi, F., Giannini, T., & Ray, T. P. 2006, ArXiv Astrophysics e-prints

Poetzel, R., Mundt, R., & Ray, T. P. 1992, A&A, 262, 229

Pogodin, M. A., Franco, G. A. P., & Lopes, D. F. 2005, A&A, 438, 239

Polomski, E. F., Telesco, C. M., Piña, R., & Schulz, B. 2002, AJ, 124, 2207

Polomski, E. F., Woodward, C. E., Holmes, E. K., Butner, H. M., Lynch, D. K., Russell, R. W., Sitko, M. L., Wooden, D. H., Telesco, C. M., & Piña, R. 2005, AJ, 129, 1035

Pontoppidan, K. M. & Dullemond, C. P. 2005, A&A, 435, 595

Porras, A., Christopher, M., Allen, L., Di Francesco, J., Megeath, S. T., & Myers, P. C. 2003, AJ, 126, 1916

Potter, D. & Graham, M. 2005, Bulletin of the American Astronomical Society, 37, 1441

Potter, D. E. 2003a, Ph.D. Thesis

—. 2003b, Ph.D. Thesis

Potter, D. E. & Andrews, S. M. 2002, Bulletin of the American Astronomical Society, 34, 1217

Potter, D. E., Close, L. M., Roddier, F., Roddier, C., Graves, J. E., & Northcott, M. 2000, Astrophys. J., 540, 422

Preite-Martinez, A. 1988, A&AS, 76, 317

Price, S. D. & Walker, R. G. 1976, AFGL-TR-0208 Environemental Research papers

Pudritz, R. E. 2006, in Protostars and Planets V, Proceedings of the Conference held October 24-28, 2005, in Hilton Waikoloa Village, Hawai'i. LPI Contribution No. 1286., p.8511

Pugach, A. F. 2003, Kinematika i Fizika Nebesnykh Tel, 19, 234

Pyo, T., Kobayashi, N., Hayashi, M., Terada, H., Goto, M., Takami, H., Takato, N., Gaessler, W., Usuda, T., Yamashita, T., Tokunaga, A. T., Hayano, Y., Kamata, Y., Iye, M., & Minowa, Y. 2003, ApJ, 590, 340

Racine, R. 1968, AJ, 73, 233

Racine, R. ., Walker, G. A. H., Nadeau, D., Doyon, R. ., & Marois, C. 1999, PASP, 111, 587

Raman, A., Lisanti, M., Wilner, D. J., Qi, C., & Hogerheijde, M. 2006, AJ, 131, 2290

Reach, W. T., Rho, J., Young, E., Muzerolle, J., Fajardo-Acosta, S., Hartmann, L., Sicilia-Aguilar, A., Allen, L., Carey, S., Cuillandre, J.-C., Jarrett, T. H., Lowrance, P., Marston, A., Noriega-Crespo, A., & Hurt, R. L. 2004, ApJS, 154, 385

Rieke, G. H., Young, E. T., Engelbracht, C. W., Kelly, D. M., Low, F. J., Haller, E. E., Beeman, J. W., Gordon, K. D., Stansberry, J. A., Misselt, K. A., Cadien, J., Morrison, J. E., Rivlis, G., Latter, W. B., Noriega-Crespo, A., Padgett, D. L., Stapelfeldt, K. R., Hines, D. C., Egami, E., Muzerolle, J., Alonso-Herrero, A., Blaylock, M., Dole, H., Hinz, J. L., Le Floc'h, E., Papovich, C., Pérez-González, P. G., Smith, P. S., Su, K. Y. L., Bennett, L., Frayer, D. T., Henderson, D., Lu, N., Masci, F., Pesenson, M., Rebull, L., Rho, J., Keene, J., Stolovy, S., Wachter, S., Wheaton, W., Werner, M. W., & Richards, P. L. 2004, ApJS, 154, 25

Roberts, Jr., L. C., Perrin, M. D., Marchis, F., Sivaramakrishnan, A., Makidon, R. B., Christou, J. C., Macintosh, B. A., Poyneer, L. A., van Dam, M. A., & Troy, M. 2004, in Advancements in Adaptive Optics. Edited by Domenico B. Calia, Brent L. Ellerbroek, and Roberto Ragazzoni. Proceedings of the SPIE, Volume 5490, pp. 504-515 (2004)., ed. D. Bonaccini Calia, B. L. Ellerbroek, & R. Ragazzoni, 504–515

Rodgers, B. M., van der Bliek, N. S., Brandvig, B., Thomas, S., Doppmann, G., & Bouvier, J. 2005, Bulletin of the American Astronomical Society, 37, 1288

Roe, H. G. 2002, Ph.D. Thesis

Rossiter, R. A. 1955, Publications of Michigan Observatory, 11, 1

Sahade, J. & Berón Dàvila, F. 1963, Annales d'Astrophysique, 26, 153

Sahai, R., Sánchez Contreras, C., & Morris, M. 2005, ApJ, 620, 948

Sandell, G. & Weintraub, D. A. 1994, Astron. Astrophys., 292, L1

—. 2001, ApJS, 134, 115

Scarrott, S. M., Draper, P. W., & Tadhunter, C. N. 1993, MNRAS, 260, 171

Schmid, H. M., Joos, F., & Tschan, D. 2006, A&A, 452, 657

Schneider, G., Silverstone, M., Hines, D., Augereau, J.-C., Pinte, C., Menard, F., Krist, J., Clampin, M., Grady, C., Golimowski, D., Ardila, D., Henning, T., Wolf, S., & Rodmann, J. 2006, in press., ApJ

Shang, H. 2006, in Protostars and Planets V, Proceedings of the Conference held October 24-28, 2005, in Hilton Waikoloa Village, Hawai'i. LPI Contribution No. 1286., p.8511

Shang, H., Glassgold, A. E., Shu, F. H., & Lizano, S. 2002, ApJ, 564, 853

Sheehy, C. D., McCrady, N., & Graham, J. R. 2006, ApJ, 647, 1517

Shevchenko, V. S. 1999, Astronomy Reports, 43, 246

Shevchenko, V. S., Grankin, K. N., Ibragimov, M. A., Mel'Nikov, S. Y., & Yakubov, S. D. 1993, Ap&SS, 202, 121

Shu, F., Najita, J., Ostriker, E., Wilkin, F., Ruden, S., & Lizano, S. 1994, Astrophys. J., 429, 781

Shu, F. H., Adams, F. C., & Lizano, S. 1987, Ann. Rev. Astron. Astrophys., 25, 23

Siebenmorgen, R., Prusti, T., Natta, A., & Müller, T. G. 2000, A&A, 361, 258

Sivaramakrishnan, A. & Oppenheimer, B. R. 2006, ApJ, 647, 620

Skinner, S. L., Brown, A., & Stewart, R. T. 1993, ApJS, 87, 217

Smith, B. A. & Terrile, R. J. 1984, Science, 226, 1421

Smith, K. W., Balega, Y. Y., Duschl, W. J., Hofmann, K.-H., Lachaume, R., Preibisch, T., Schertl, D., & Weigelt, G. 2005, A&A, 431, 307

Smith, K. W., Balega, Y. Y., Hofmann, K.-H., Preibisch, T., Schertl, D., & Weigelt, G. 2004, A&A, 413, 217

Soummer, R. & Aime, C. 2004, Astrophys. J. Lett., 0, Submitted

Stanke, T., Smith, M. D., Gredel, R., & Szokoly, G. 2002, A&A, 393, 251

Stapelfeldt, K. R., Krist, J. E., Menard, F., Bouvier, J., Padgett, D. L., & Burrows, C. J. 1998, ApJ, 502, L65+

Stapelfeldt, K. R., Watson, A. M., Krist, J. E., Burrows, C. J., Crisp, D., Ballester, G. E., Clarke, J. T., Evans, R. W., Gallagher, J. S., Griffiths, R. E., Hester, J. J., Hoessel, J. G., Holtzman, J. A., Mould, J. R., Scowen, P. A., & Trauger, J. T. 1999, ApJ, 516, L95

Staude, H. J. & Neckel, T. 1992, ApJ, 400, 556

Stine, P. C. & O'Neal, D. 1998, AJ, 116, 890

Straizys, V., Meistas, E., Vansevicius, V., & Goldberg, E. P. 1989, A&A, 222, 82

Strom, K. M., Strom, S. E., Breger, M., Brooke, A. L., Yost, J., Grasdalen, G., & Carrasco, L. 1972, ApJ, 173, L65+

Struve, F. G. W. 1837, Astronomische Nachrichten, 14, 249

Subramaniam, A., Sahu, D. K., Sagar, R., & Vijitha, P. 2005, A&A, 440, 511

Sylvester, R. J., Skinner, C. J., Barlow, M. J., & Mannings, V. 1996, MNRAS, 279, 915

Tamura, M., Fukagawa, M., Kimura, H., Yamamoto, T., Suto, H., & Abe, L. 2006, ApJ, 641, 1172

Teixeira, R., Ducourant, C., Sartori, M. J., Camargo, J. I. B., Périé, J. P., Lépine, J. R. D., & Benevides-Soares, P. 2000, A&A, 361, 1143

Terebey, S., Shu, F. H., & Cassen, P. 1984, Astrophys. J., 286, 529

Terranegra, L., Chavarria-K., C., Diaz, S., & Gonzalez-Patino, D. 1994, A&AS, 104, 557

Testi, L., Natta, A., Shepherd, D. S., & Wilner, D. J. 2003, A&A, 403, 323

Testi, L., Palla, F., & Natta, A. 1998, A&AS, 133, 81

—. 1999, A&A, 342, 515

Testi, L., Palla, F., Prusti, T., Natta, A., & Maltagliati, S. 1997, A&A, 320, 159

The, P. S., de Winter, D., & Perez, M. R. 1994, A&AS, 104, 315

Thum, C., Martin-Pintado, J., Quirrenbach, A., & Matthews, H. E. 1998, A&A, 333, L63

Tinbergen, J. 1996, Astronomical polarimetry (Cambridge, New York: Cambridge University Press, —c1996, ISBN 0521475317)

Torrelles, J. M., Anglada, G., Rodriguez, L. F., Canto, L. F., & Barral, J. F. 1987, A&A, 177, 171

Torres, C. A. O., Quast, G., de La Reza, R., Gregorio-Hetem, J., & Lepine, J. R. D. 1995, AJ, 109, 2146

Tuthill, P. G., Monnier, J. D., & Danchi, W. C. 1999, Nature, 398, 487

—. 2001, Nature, 409, 1012

Val'Tts, I. E., Slysh, V. I., Voronkov, M. A., & Migenes, V. 2002, in ASP Conf. Ser. 279: Exotic Stars as Challenges to Evolution, ed. C. A. Tout & W. van Hamme, 279–+

van den Ancker, M. E., de Winter, D., & Tjin A Djie, H. R. E. 1998, A&A, 330, 145

Verdes-Montenegro, L., Gomez, J. F., Torrelles, J. M., Anglada, G., Estalella, R., & Lopez, R. 1991, A&A, 244, 84

Vieira, S. L. A., Corradi, W. J. B., Alencar, S. H. P., Mendes, L. T. S., Torres, C. A. O., Quast, G. R., Guimarães, M. M., & da Silva, L. 2003, AJ, 126, 2971

Vieira, S. L. A. & Cunha, N. C. S. 1994, Informational Bulletin on Variable Stars, 4090, 1

Vink, J. S., Drew, J. E., Harries, T. J., & Oudmaijer, R. D. 2002, MNRAS, 337, 356

Voors, R. H. M. 1999, Ph.D. Thesis

Waters, L. B. F. M. & Waelkens, C. 1998, ARA&A, 36, 233

Watson, A. M. & Stapelfeldt, K. R. 2004, ApJ, 602, 860

Weikard, H., Wouterloot, J. G. A., Castets, A., Winnewisser, G., & Sugitani, K. 1996, A&A, 309, 581

Weinberger, A. J., Becklin, E. E., Schneider, G., Smith, B. A., Lowrance, P. J., Silverstone, M. D., Zuckerman, B., & Terrile, R. J. 1999, ApJ, 525, L53

Weingartner, J. C. & Draine, B. T. 2001, ApJ, 548, 296

Weintraub, D. A., Goodman, A. A., & Akeson, R. L. 2000, Protostars and Planets IV, 247

Weintraub, D. A. & Kastner, J. 1993, ApJ, 411, 767

Weintraub, D. A., Kastner, J. H., Gatley, I., & Merrill, K. M. 1996, ApJ, 468, L45+

Weintraub, D. A., Kastner, J. H., & Mahesh, A. 1994, ApJ, 420, L87

Weintraub, D. A., Sandell, G., & Duncan, W. D. 1991, ApJ, 382, 270

Welin, G. 1976, A&A, 49, 145

Wenzel, W. & Bruckner, V. 1978, Zentralinstitut fuer Astrophysik Sternwarte Sonneberg Mitteilungen ueber Veraenderliche Sterne, 8, 35

White, R. L. & Becker, R. H. 1985, ApJ, 297, 677

Whitney, B. A. 2004, in ASP Conf. Ser. 309: Astrophysics of Dust, 755–+

Whitney, B. A., Wood, K., Bjorkman, J. E., & Cohen, M. 2003a, Astrophys. J., 598, 1079

Whitney, B. A., Wood, K., Bjorkman, J. E., & Wolff, M. J. 2003b, Astrophys. J., 591, 1049

Wilner, D. J., Holman, M. J., Kuchner, M. J., & Ho, P. T. P. 2002, ApJ, 569, L115

Wizinowich, P., Acton, D. S., Shelton, C., Stomski, P., Gathright, J., Ho, K., Lupton, W., Tsubota, K., Lai, O., Max, C., Brase, J., An, J., Avicola, K., Olivier, S., Gavel, D., Macintosh, B., Ghez, A., & Larkin, J. 2000, PASP, 112, 315

Wizinowich, P. L., Le Mignant, D., Bouchez, A. H., Campbell, R. D., Chin, J. C. Y., Contos, A. R., van Dam, M. A., Hartman, S. K., Johansson, E. M., Lafon, R. E., Lewis, H., Stomski, P. J., Summers, D. M., Brown, C. G., Danforth, P. M., Max, C. E., & Pennington, D. M. 2006, PASP, 118, 297

Woitas, J., Bacciotti, F., Ray, T. P., Marconi, A., Coffey, D., & Eislöffel, J. 2005, A&A, 432, 149

Wolf, S., Henning, T., & Stecklum, B. 1999, A&A, 349, 839

Wolf, S., Padgett, D. L., & Stapelfeldt, K. R. 2003, ApJ, 588, 373

Wood, D. O. S., Myers, P. C., & Daugherty, D. A. 1994, ApJS, 95, 457

Wood, K., Koerner, D., Whitney, B., Schneider, G., Stassun, K., & Bjorkman, J. 2002, Bulletin of the American Astronomical Society, 34, 761

Yang, J., Ohashi, N., & Fukui, Y. 1995, ApJ, 455, 175

Yonekura, Y., Dobashi, K., Mizuno, A., Ogawa, H., & Fukui, Y. 1997, ApJS, 110, 21

Yoshida, S., Kogure, T., Nakano, M., Tatematsu, K., & Wiramihardja, S. D. 1991, PASJ, 43, 363

Zapata, L. A., Rodríguez, L. F., & Kurtz, S. E. 2001, Revista Mexicana de Astronomia y Astrofisica, 37, 83

Zavagno, A., Lagage, P. O., & Cabrit, S. 1999, A&A, 344, 499

Zijlstra, A., Pottasch, S., & Bignell, C. 1990, A&AS, 82, 273

Appendix A

An Updated Catalog of Herbig Ae/Be Stars

It has been more than a decade since the last systematic catalog of Herbig Ae/Be stars by (The et al., 1994). In that time, several dozen additional HAEBEs and candidate HAEBEs have been identified, many by the Pico dos Dias survey (Torres et al., 1995; Vieira et al., 2003) but also through the work of a large cast of others (Hillenbrand et al., 1992; Miroshnichenko et al., 1999; Polomski et al., 2002). Meanwhile, it has become clear that a few sources included in the The et al. catalog are not in fact HAEBEs, but instead post-main-sequence Be stars. And of course, additional observations have been obtained for most of the previously-known HAEBEs, providing a wealth of new information. .

In the course of my thesis research, I collected and collated much of the recent literature into an updated catalog of Herbig Ae/Be stars, presented here. Though the data were drawn broadly from across the literature, a few of the most salient papers (beyond the ones already mentioned) were those by Meeus et al. (2001), van den Ancker (1998), Malfait et al. (1998); Acke & van den Ancker (2004) and Hernandez et al. (2004). The catalog is implemented using the MySQL relational database and is fully accessible in IDL through a collection of interface routines.

For space reasons, I show here only a few of the most important properties for each star: the coordinates, the most recent spectral type and distance determination, and the V and K_s magnitudes. The full catalog contains many additional properties, including (but not limited to) alternate spectral classifications, estimates of age, luminosity, temperature, mass, radius and extinction, notes on unusual spectral features, and classifications in both

the Hillenbrand and Meeus groupings. The catalog also contains photometry for each source spanning from the visible to the submillimeter, which is presented in a series of SED plots immediately following the table.

Table A.1: A Catalog of Herbig Ae/Be Stars.

Name	RA (J2000.0)	Dec (J2000.0)	Sp.Type	d (pc)	V	K_s	References
HBC 1	00 07 02.570	+65 38 38.6	Unclas	850	16.76	7.26	27, 32, 47, 54
HBC 324	00 07 11.398	+65 39 13.6	A7	850	10.77	9.69	30, 43, 78
MQ Cas	00 09 37.540	+58 13 11.0	A0Vae	?	11.70	7.46	44, 61
LkHa 198 IR	00 11 25.97	+58 49 29.1	?	600	-	-	48, 82
LkHa 198	00 11 25.970	+58 49 29.1	B9	600	14.18	6.29	27, 30, 48, 63
V376 Cas	00 11 26.090	+58 50 03.5	Unclas	600	15.55	6.30	27, 32, 34, 48
V594 Cas	00 43 18.257	+61 54 40.1	Contin	650	10.58	5.90	27, 31, 33, 47
CD-53 251	01 17 43.506	-52 33 30.8	F3 V	340	10.73	9.31	61, 69, 71
HBC 334	02 16 30.100	+55 22 57.0	B3	1600	14.52	11.42	24, 30, 63
AFGL 4029 W	03 01 31.25	+60 29 13.1	?	2200	-	7.25	48
AFGL 4029 E	03 01 34.280	+60 29 14.1	?	2200	-	10.00	48
AFGL 490	03 27 38.400	+58 47 04.0	?	1000	-	5.72	58
V1185 Tau	03 39 00.600	+29 41 46.0	A0	580	10.74	8.51	61, 69, 71
XY Per E	03 49 36.341	+38 58 55.5	A5	120	9.21	-	22, 26, 30, 47
XY Per W	03 49 36.341	+38 58 55.5	?	120	-	-	22, 47
V892 Tau	04 18 40.611	+28 19 15.5	B8	160	15.24	5.79	27, 30, 47, 63
LkHa 101	04 30 14.390	+35 16 24.3	Contin	140?	15.90	3.05	31, 61
PDS 168	04 30 50.050	+23 00 06.2	F1	130	18.08	5.86	61, 69, 71
AB Aur	04 55 45.844	+30 33 04.3	A1	144	7.05	4.23	27, 30, 47, 70
MWC 480	04 58 46.267	+29 50 37.0	A3 V	150	7.80	5.53	61, 69, 71
NSV 1832	05 06 55.499	-03 21 13.0	B3	1700	12.84	8.49	61, 69, 71
V1012 Ori	05 11 36.548	-02 22 48.5	A3II+s	460	12.20	8.83	44, 61, 63
HD 34700	05 19 41.407	+05 38 42.8	G0IV+G	340	-	7.48	1, 81
HD 35187	05 24 01.174	+24 57 37.6	A2Ve+A	220	7.80	5.91	16, 61, 71
HD 287823	05 24 08.049	+02 27 46.9	A0	470	9.67	7.90	61, 69, 71
V346 Ori	05 24 42.801	+01 43 48.3	A8 V	300	10.10	8.56	61, 69, 71
HD 290409	05 27 05.475	+00 25 07.6	B9	730	9.96	8.63	61, 69, 71
CO Ori	05 27 38.337	+11 25 38.9	F8	460	10.60	6.51	49, 49, 61
HD 35929	05 27 42.792	-08 19 38.4	?	510	8.10	6.67	61, 80
HD 290500	05 29 48.034	-00 23 43.2	A2	360	11.04	9.59	61, 69, 72
HD 244314	05 30 19.001	+11 20 20.0	A1	510	9.30	8.05	61, 69, 71
MWC 758	05 30 27.530	+25 19 57.1	A8 V	140	8.30	5.80	61, 69, 71
HK Ori	05 31 28.043	+12 09 10.3	Unclas	460	11.71	7.34	10, 27, 32, 34
HD 244604	05 31 57.299	+11 17 41.0	?	336	9.40	7.12	61, 80
UY Ori	05 32 00.298	-04 55 54.3	B9	1600	12.79	9.33	61, 69, 71
HD 36408 N	05 32 14.141	+17 03 29.3	B8	342	5.46	6.02	35, 61, 69
HD 36408 S	05 32 14.557	+17 03 21.8	?	180	6.49	6.28	69, 71
HD 245185	05 35 09.606	+10 01 51.5	A1	336	9.89	8.02	27, 30, 80
T Ori	05 35 50.449	-05 28 35.0	A0	460	10.63	6.22	10, 27, 30, 63
CQ Tau	05 35 58.467	+24 44 54.1	F3	130	10.27	6.17	27, 30, 84
V380 Ori	05 36 25.432	-06 42 57.7	Contin	460	10.49	5.95	9, 27, 31, 34
V586 Ori	05 36 59.251	-06 09 16.4	?	510	9.75	7.69	27, 80
HD 290770	05 37 02.450	-01 37 21.4	B9	550	9.30	7.08	61, 69, 71
HD 37357 A	05 37 47.078	-06 42 30.2	?	?	-	-	
HD 37357 B	05 37 47.078	-06 42 30.2	?	?	-	-	
HD 290764	05 38 05.250	-01 15 21.7	F0 V	270	9.82	7.41	61, 69, 71
PDS 193	05 38 09.230	-06 49 15.9	A5	600	13.67	7.98	27, 69, 71
HD 37411	05 38 14.506	-05 25 13.3	B9	230	9.90	7.58	61, 69, 71
V599 Ori	05 38 58.638	-07 16 45.7	F0	190	15.20	7.59	61, 69, 71
HD 37490	05 39 11.146	+04 07 17.3	B3	360	4.57	4.80	33, 64, 66, 67
HD 245906	05 39 30.480	+26 19 55.1	A6	2000	10.47	7.98	24, 30, 37
V350 Ori	05 40 11.765	-09 42 11.1	A1	460	11.47	8.37	30, 63, 79
MWC 120	05 41 02.292	-02 43 00.7	B9Vesh	280	7.90	5.40	12, 52, 61
HD 38120	05 43 11.893	-04 59 49.9	B9	480	9.08	7.16	61, 69, 71
V351 Ori	05 44 18.794	+00 08 40.4	A7 V	170	8.95	6.85	27, 69, 71
MWC 778	05 50 13.500	+23 52 17.0	B1?	2600	14.00	7.73	48, 61, 69, 71
GSC 05352-00159	05 53 42.501	-10 24 01.0	B7?	380	13.40	5.96	61, 69, 71
GSC 5360-1033	05 57 49.600	-14 05 42.0	B5?	1700	13.91	10.06	61, 69, 71
HD 249879	05 58 55.600	+16 39 58.0	B8?	1200	10.64	9.06	61, 69, 71
HD 250550	06 01 59.989	+16 30 56.7	B9	700	9.54	6.64	27, 30, 62, 63
AS 116	06 02 14.899	-10 00 59.0	B5?	1100	9.60	7.46	61, 69, 71
AS 117	06 03 37.000	-14 53 03.0	A0	690	11.00	9.19	61, 69, 71

Continued on next page...

Table A.1 – Continued

Name	RA (J2000.0)	Dec (J2000.0)	Sp.Type	d (pc)	V	K_s	References
GSC 4794-0827	06 06 58.500	-05 55 08.0	A0	1000	12.44	9.81	61, 69, 71
GSC 1876-0892	06 07 16.100	+29 58 01.0	B2	600	14.01	12.50	61, 69, 71
LkHa 208	06 07 49.460	+18 39 26.3	A7	1000	11.65	9.24	27, 30, 62, 63
PDS 211	06 10 17.499	+29 25 16.0	B9	1100	13.70	9.81	61, 69, 71
LkHa 338	06 10 47.034	-06 12 47.9	B9	830	15.12	8.61	24, 25, 30
LkHa 339	06 10 57.801	-06 14 37.0	A1	830	13.66	9.73	25, 27, 30
GSC 4795-0492	06 13 36.200	-06 25 01.0	A7 V	500	11.82	9.13	61, 69, 71
MWC 137	06 18 45.505	+15 16 52.4	Contin	1300	12.00	6.62	7, 27, 31, 33
CPM 25	06 23 56.160	+14 30 27.6	B2	2700	14.67	8.99	61, 69, 71
NSV 2968	06 26 53.800	-10 15 34.0	B0	1700	12.00	7.63	61, 69, 71
VY Mon	06 31 06.938	+10 26 05.0	Unclas	800	13.47	5.46	27, 32, 48, 63
HD 46150	06 31 54.000	+04 56 00.0	06e	1500	4.80	6.44	15, 60, 61
LkHa 215	06 32 41.796	+10 09 33.6	B6	800	10.54	7.03	27, 29, 30, 34
HD 259431	06 33 05.189	+10 19 20.0	B6	800	8.73	5.73	10, 27, 30, 63
R Mon	06 39 09.946	+08 44 10.8	Contin	800	12.15	6.38	27, 31, 33, 48
LkHa 25	06 40 44.637	+09 48 02.2	B7	800	12.77	9.33	27, 30, 56, 63
GSC 5950-0021	06 40 51.187	+09 44 46.2	B9	1800	13.26	10.18	61, 69, 71
GSC 5379-0359	06 49 58.801	-07 38 52.0	B9	1200	13.40	9.42	61, 69, 71
HD 50083	06 51 45.753	+05 05 03.9	B3	360	6.92	6.29	61, 69, 71
IRAS 06523-2458	06 51 45.753	+05 05 03.9	A3	790	12.50	9.56	61, 69, 71
GSC 4805-1872	06 55 39.300	-03 09 45.0	A0	1600	13.13	13.64	61, 69, 69
GSC 4805-1306	06 58 44.220	-03 41 08.6	O9?	4200	15.04	13.74	61, 69, 71
HD 52721	07 01 49.510	-11 18 03.3	B2	910	6.62	6.04	9, 38, 69, 70
LkHa 218	07 02 42.534	-11 26 11.8	A0	1050	11.87	8.58	27, 30, 59
LkHa 220	07 04 06.703	-11 26 08.5	B8	1050	11.81	9.12	27, 30, 59
HD 53367	07 04 25.532	-10 27 15.7	B4	250	7.00	6.12	9, 27, 69, 70
PDS 241	07 08 38.800	-04 19 08.0	B0	3900	12.06	9.94	48, 61, 69, 71
NX Pup	07 19 28.260	-44 35 11.3	F+sh	500	10.61	6.08	55, 69, 70
DW CMa	07 19 35.940	-17 39 18.7	B2?	1100	12.80	6.44	48, 61, 69, 71
GSC 6546-3156	07 24 16.901	-26 16 01.0	A0	2300	14.20	13.37	61, 69, 71
GSC 6542-2339	07 24 37.000	-24 34 48.0	O9?	4100	15.01	9.58	61, 69, 71
SPH 6	07 25 04.900	-25 45 48.0	B6	2500	13.13	9.29	61, 69, 71
HD 58647	07 25 56.100	-14 10 43.6	?	?	-	5.44	
SS73 6	07 31 48.900	-19 27 33.0	B1?	4500	12.50	10.22	61, 69, 71
SS 127	07 32 27.200	-21 55 27.0	B6	1800	12.15	12.89	61, 69, 71
GSC 5988-2257	07 41 41.201	-20 00 14.0	B3	3000	15.45	10.22	61, 69, 71
GSC 8143-1225	07 59 11.497	-50 22 45.8	F3 V	309	11.81	8.99	61, 69, 71
HD 68695	08 11 44.572	-44 05 08.7	A0 V	600	9.89	8.08	61, 69, 71
CD-38 4380	08 23 12.299	-39 07 03.0	F3 V	210	9.96	8.02	61, 69, 71
HD 72106 S	08 29 34.898	-38 36 21.1	A0	670	8.58	7.91	61, 69, 71
ESO 313-10	08 42 17.399	-40 44 09.0	?	700	15.80	8.82	41, 61
GSC 8581-2002	08 44 23.635	-59 56 57.8	A5 V	492	10.91	9.96	61, 69, 71
GSC 7679-0293	08 48 46.399	-40 48 22.0	A0	1400	12.34	10.28	61, 69, 71
PDS 34	08 49 58.700	-45 53 06.0	B2	2900	13.99	9.22	61, 69, 71
HD 76534	08 55 08.708	-43 27 59.9	B3	870	7.96	7.80	33, 33, 65
SAO 220669	08 55 45.959	-44 25 14.1	B4	340	8.89	7.32	61, 69, 71
RCW 34	08 56 25.001	-43 05 40.0	B3	870	11.81	6.60	28, 33, 33, 77
Hen 3-248	09 06 00.011	-47 18 58.2	B0 V	560	12.12	6.60	61, 69, 71
GSC 8584-2884	09 26 11.799	-52 42 18.0	B7	1800	14.51	14.01	61, 69, 71
GSC 8593-2802	09 26 11.799	-52 42 18.0	A7?	770	12.03	6.56	69, 69, 71
HD 85567	09 50 28.535	-60 58 03.0	B9	1000	8.57	5.77	61, 69, 70
HD 87403	10 02 51.464	-59 16 54.7	A1	435	9.24	8.97	61, 69, 71
Hen 3-373	10 10 00.330	-57 02 07.4	B2?	720	12.50	6.97	61, 69, 71
HD 305298	10 33 05.299	-60 19 43.0	O8	6500	9.40	10.12	61, 69, 71
PDS 322 N	10 52 08.701	-56 12 07.0	B3	3800	12.01	10.91	69, 69, 71
HD 94509	10 53 27.261	-58 25 24.5	?	?	9.20	8.93	61
PDS 324	10 57 25.001	-62 53 10.0	B1?	5500	14.45	13.11	69, 69, 71
HD 95881	11 01 57.620	-71 30 48.3	A0	118	8.20	5.73	61, 69, 81
HD 96042	11 03 40.558	-59 25 59.1	B1	1200	8.51	8.03	61, 69, 71
HD 97048	11 08 03.318	-77 39 17.5	A0	180	8.46	5.94	9, 38, 49, 84
HD 98922	11 22 31.674	-53 22 11.4	B9	1040	6.80	4.28	61, 69, 70
HD 100453	11 33 05.577	-54 19 28.5	A9 V	110	7.79	5.60	61, 69, 71
HD 100546	11 33 25.441	-70 11 41.2	B9 V	190	6.70	5.42	61, 69, 71
He 3-692	11 33 25.441	-70 11 41.2	A0	410	9.20	7.47	61, 69, 71
VdBH 52	11 40 32.802	-64 32 05.0	B5?	4100	13.11	11.84	61, 69, 71
HD 104237	11 53 13.162	-62 05 21.2	A0+Sh	115	6.60	4.59	61, 69, 71
PDS 139	11 53 13.162	-62 05 21.2	B0	2200	13.31	9.33	69, 69, 71
GSC 8645-1401	12 17 47.600	-59 44 00.0	F2	290	13.13	8.52	61, 69, 71
Hen 2-80	12 22 23.280	-63 17 16.7	B5?	1200	13.08	7.48	61, 69, 71
DK Cha	12 53 17.219	-77 07 10.6	A?	178	19.00	5.19	61, 69, 76
IRAS 12496-7650	12 53 17.219	-77 07 10.6	Ae	180	-	5.19	36, 76
V1028 Cen	13 01 17.805	-48 53 18.8	B5	?	10.57	7.80	61, 69
GSC 8993-0397	13 03 24.001	-62 13 29.0	B3	2700	12.85	13.42	69, 69, 71

Continued on next page...

Table A.1 – Continued

Name	RA (J2000.0)	Dec (J2000.0)	Sp.Type	d (pc)	V	K_s	References
HD 114981	13 14 40.686	-38 39 05.6	B5	457	7.12	7.44	61, 69, 71
WRAY 15-1090	13 20 03.582	-62 23 54.1	B2	2600	12.50	9.65	61, 69, 71
IRAS 13395-6153	13 43 02.098	-62 08 52.0	?	4000	-	6.37	23
PDS 371 N	13 47 31.699	-36 39 52.0	O9?	6000	-	-	69, 71
Hen 3-938	13 52 42.902	-63 32 48.0	O9?	1700	13.30	6.15	61, 69, 71
Her 4636 N	13 57 44.12	-39 58 44.2	B3	1200	-	7.15	69, 71
HD 130437	14 50 50.255	-60 17 10.3	?	?	10.00	7.28	61
SS73 44	15 03 25.302	-63 23 05.0	B	?	12.75	7.82	61, 69
HD 132947	15 04 56.052	-63 07 52.6	?	?	8.90	8.62	61
PDS 389	15 14 48.501	-62 16 54.0	A3 V	240	14.18	8.53	69, 69, 71
HD 135344	15 15 48.439	-37 09 16.0	F4Ve	140	-	5.84	17, 81
PDS 394	15 35 17.000	-61 59 05.0	F0	670	13.54	10.60	69, 69, 71
HD 139614	15 40 46.381	-42 29 53.5	A8 V	160	8.25	6.75	61, 69, 71
PDS 144 N	15 49 15.425	-26 00 52.5	A2 IV	2000	-	7.50	48, 69, 71
PDS 144 S	15 49 15.425	-26 00 52.5	A5 V	1030	-	7.50	48, 69, 71
HD 141569	15 49 57.748	-03 55 16.4	A0 V	170	7.00	6.82	48, 61, 69, 71
HD 141926	15 54 21.826	-55 19 44.8	B2 III	888	8.62	6.51	51, 61, 69
HD 142527	15 56 41.891	-42 19 23.3	F7IIIe	145	-	4.98	81, 84
GSC 7855-0815	16 05 03.929	-39 45 03.2	A5 V	1200	13.93	9.89	61, 69, 71
HD 144432	16 06 57.957	-27 43 09.8	A8	119	8.16	5.89	48, 61, 69, 71
HD 145718	16 13 11.591	-22 29 06.6	A8 IV	139	8.98	6.69	48, 61, 69, 71
PDS 415 N	16 18 37.23	-24 05 18.2	F0 V	280	12.04	7.49	61, 69, 71
PDS 415 S	16 18 37.23	-24 05 22.7	?	280	-	7.90	
WL 16	16 27 02.501	-24 37 30.0	?	280	14.30	8.06	61
Hen 3-1191	16 27 15.092	-48 39 26.9	?	?	13.50	6.30	61
HD 149914	16 38 28.652	-18 13 13.7	?	?	-	5.69	
HD 150193	16 40 17.922	-23 53 45.2	A0 V	150	8.64	5.48	9, 27, 69, 70
V921 Sco	16 59 06.775	-42 42 08.4	B7	160	11.43	4.52	2, 28, 33, 33
KK Oph	17 10 08.064	-27 15 18.2	Unclas	160	11.45	5.80	27, 32, 34, 48
PDS 453	17 20 56.147	-26 03 30.8	F2 V	490	12.92	9.17	61, 69, 71
IRAS 17216-3801	17 25 06.52	-38 04 00.4	?	?	-	4.99	
HD 319896	17 31 05.852	-35 08 29.3	B4	950	13.42	8.66	61, 69, 71
HD 323771	17 34 04.622	-39 23 41.8	B5 Vp	1300	11.40	7.60	61, 69, 71
PDS 469	17 50 57.803	-14 16 11.0	A0	1100	12.77	10.35	61, 69, 71
HD 163296	17 56 21.292	-21 57 21.9	A0	160	6.88	4.78	27, 48, 69, 71
PDS 477	18 00 29.297	-16 47 23.0	B1	2900	14.40	9.09	48, 61, 69, 71
HD 169142	18 24 29.780	-29 46 49.4	A9	130	8.15	6.41	48, 61, 69, 71
MWC 297	18 27 39.602	-03 49 52.0	B0	230	12.28	3.04	27, 48, 69, 71
PDS 520	18 30 06.899	+00 42 34.0	F3 V	180	14.69	7.52	48, 69, 69, 71
AS 310	18 33 21.204	-04 58 02.0	B1	2500	12.45	11.71	27, 30, 48, 63
PDS 530	18 41 34.797	+08 08 22.0	F0	1000	14.00	9.14	48, 61, 69, 71
PDS 543	18 48 00.403	+02 54 13.0	B1	414	12.50	7.50	61, 71, 73
MWC 610	18 50 47.175	+08 42 10.1	B2	560	8.89	7.08	48, 61, 69, 71
PDS 551	18 55 21.497	+04 04 29.0	O9?	3500	16.60	8.67	61, 69, 71
TY CrA	19 01 40.833	-36 52 33.9	B9	130	9.37	6.67	9, 27, 69, 71
T CrA	19 01 58.777	-36 57 49.9	F5	130	12.86	6.60	27, 33, 33, 74
HD 179218	19 11 11.257	+15 47 15.6	A0 V	197	7.20	5.99	48, 61, 69, 71
PX Vul	19 26 40.254	+23 53 50.8	F3	420	11.49	7.91	19, 29, 30
MWC 623	19 56 31.802	+31 06 16.0	?	?	-	-	
HD 190073	20 03 02.512	+05 44 16.7	A0 IVp	5000	7.80	5.86	48, 61, 69, 70
HBHA 3203-03	20 04 22.397	+33 38 59.0	B	1000	16.00	6.56	40, 40, 61
BD +40 4124	20 20 28.250	+41 21 51.6	B3	980	10.69	5.77	27, 30, 47, 84
LkHa 225 S	20 20 30.461	+41 21 26.8	?	1000	-	10.02	11, 47
BD +41 3731	20 24 15.718	+42 18 01.4	B3	1000	9.89	9.63	27, 33, 33, 42
Parsamian 22	20 24 29.487	+42 14 03.7	A5eV	1200	13.30	11.73	5, 47, 57, 61
MWC 349	20 32 45.439	+40 39 36.8	?	1200	13.20	3.15	47, 61
PV Cep	20 45 53.965	+67 57 38.9	Contin	440	17.80	7.29	31, 61, 75
AS 442	20 47 37.463	+43 47 25.0	B8Ve	600	11.01	6.62	18, 27, 46, 47
LkHa 134	20 48 04.783	+43 47 25.8	B2	700	11.35	8.24	8, 8, 27, 48
LkHa 147	20 51 02.717	+43 49 32.0	B2	800	14.45	9.48	27, 30, 50
V1493 Cyg	20 52 04.651	+44 37 30.4	Unclas	?	15.34	8.12	27, 32
HD 200775	21 01 36.921	+68 09 47.8	B3	429	7.37	4.65	4, 27, 30, 47
LkHa 324	21 03 54.141	+50 15 10.4	B8	780	12.61	9.57	6, 19, 30, 47
V361 Cyg	21 10 48.003	+45 30 30.0	?	1000	-	14.19	20
HD 203024	21 16 03.025	+68 54 52.1	A5V	1250	8.90	8.12	45, 48, 61
V645 Cyg	21 39 58.242	+50 14 21.2	O7e	3500	13.47	6.85	21, 27, 47, 68
V361 Cep	21 42 50.186	+66 06 35.2	B4	1250	10.18	8.47	27, 30, 47, 84
LkHa 234	21 43 06.680	+66 06 54.6	B7	1000	12.21	7.08	27, 30, 47, 53
LkHa 257	21 54 18.779	+47 12 09.7	B8	900	13.35	9.73	27, 63, 64
BH Cep	22 01 42.869	+69 44 36.5	F5	450	11.16	8.31	27, 30, 39, 47
BO Cep	22 16 54.053	+70 03 45.1	F4	400	11.60	9.58	27, 30, 39, 47
SV Cep	22 21 33.186	+73 40 27.1	A0	400	10.98	7.74	27, 30, 39
LkHa 233	22 34 40.979	+40 40 04.3	A4	880	13.56	8.92	27, 30, 48, 63

Continued on next page...

Table A.1 – Continued

Name	RA (J2000.0)	Dec (J2000.0)	Sp.Type	d (pc)	V	K_s	References
HD 216629 N	22 53 15.608	+62 08 45.0	?	725	-	7.09	14, 47
HD 216629 S	22 53 15.608	+62 08 45.0	B2	725	9.28	7.10	27, 47, 64
V374 Cep	23 05 07.456	+62 15 36.5	B0	720	10.90	7.09	3, 20, 61
MWC 1080	23 17 25.576	+60 50 43.3	Contin	1000	11.52	4.83	27, 31, 33, 47
LkHa 259	23 58 41.543	+66 26 12.9	Unclas	?	15.02	9.27	27, 32, 47

References: (1) Arellano Ferro & Giridhar 2003 (2) Berrelli et al. 1992 (3) Berrilli et al. 1992 (4) Bertout, Robichon, & Arenou 1999 (5) Calvet and Cohen 1978 (6) Chavarria et al. 1983 (7) Cohen & Barlow 1975 (8) Corcoran and Ray 1998 (9) Davies et al 1990 (10) Davies et al 1990,Grasdalen 1972-90, published in Hillenbrand 1992 (11) Davies et al. 2001 (12) Dent et al. 2005 (14) Distance to HD 216629 S (15) Dorland and Montmerle 1987 (16) Dunkin & Crawford 1998 (17) Dunkin et al. 1997 (18) Eisner et al. 2004 (19) Fernandez 1995 (20) Finkenzeller & Mundt 1984 (21) Goodrich 1986 (22) HIPPARCOS (23) Harju et al. 1998 (24) Herbig & Bell 1988 (25) Herbst & Racine 1976 (26) Herbst & Shevchenko (27) Herbst & Shevchenko 1999 (28) Herbst 1975 (29) Herbst et al. 1982 (30) Hernandez 2004 Table 2 (31) Hernandez 2004 Table 5 (32) Hernandez 2004 Table 7 (33) Hillenbrand 1992 Table 3 (34) Hillenbrand et al. 1992 (35) Hubrig et al. 2001 (36) Hughes et al. 1991 (37) Kawamura et al. 1998 (38) Kilkenny et al 1985 (39) Kun 1998 (40) Lienert et al. 1997 (41) Liseau et al. 1992 (42) Lorenzetti et al 1983, Strom et al 1972b (43) MacConnell 1968 (44) Miroshnichenko et al. 1999 (45) Mora et al. 2001 (46) Mora et al. 2001. (47) My LWS data (48) My Michelle data (49) Natta et al. 1997 (from literature) (50) Natta et al. 2001 (51) Neckel et al. 1980 (52) Oudmaijer et al. 1992 (53) Pirzkal et al. 1997 (54) Porras et al. 2003 (55) Reipurth 1983,Tjin a Djie, Remijn & The 1994 (56) Rydgren & Vrba 1987 (57) Scarrott et al. 1993 (58) Schreyer et al. 2002 (59) Shevchenko et al. 1999 (60) Simbad (61) Simbad, probably (62) Skrutskie 1991, published in Hillenbrand 1992,Grasdalen 1972-90, published in Hi (63) Testi et al. 1998 (64) Testi et al. 1999 (65) The et al 1985 (66) The et al 1986 (67) The et al 1986,Gehrz, Hackwell & Jones 1974 (68) Val'tts et al. 2002 (69) Vieira et al. 2003 (70) Vieira et al. 2003 HIPPARCOS distance (71) Vieira et al. 2003 Photometric distance (72) Vieira et al. 2003; distance to Ori B (73) Vieira et al. 2004 (74) Vrba, Strom & Strom 1976,Knacke et al. 1973 (75) Whitcomb et al. 1981 (76) Whittet et al. 1997 (77) Williams, Beattie & Stewart 1977 (78) Yonekura et al. 1997 (79) de Winter et al. 2001 (80) de Zeeuw et al. (1999) (81) de Zeeuw et al. 1999 (82) dist to LkHa 198 (84) van den Ancker et al. 1998

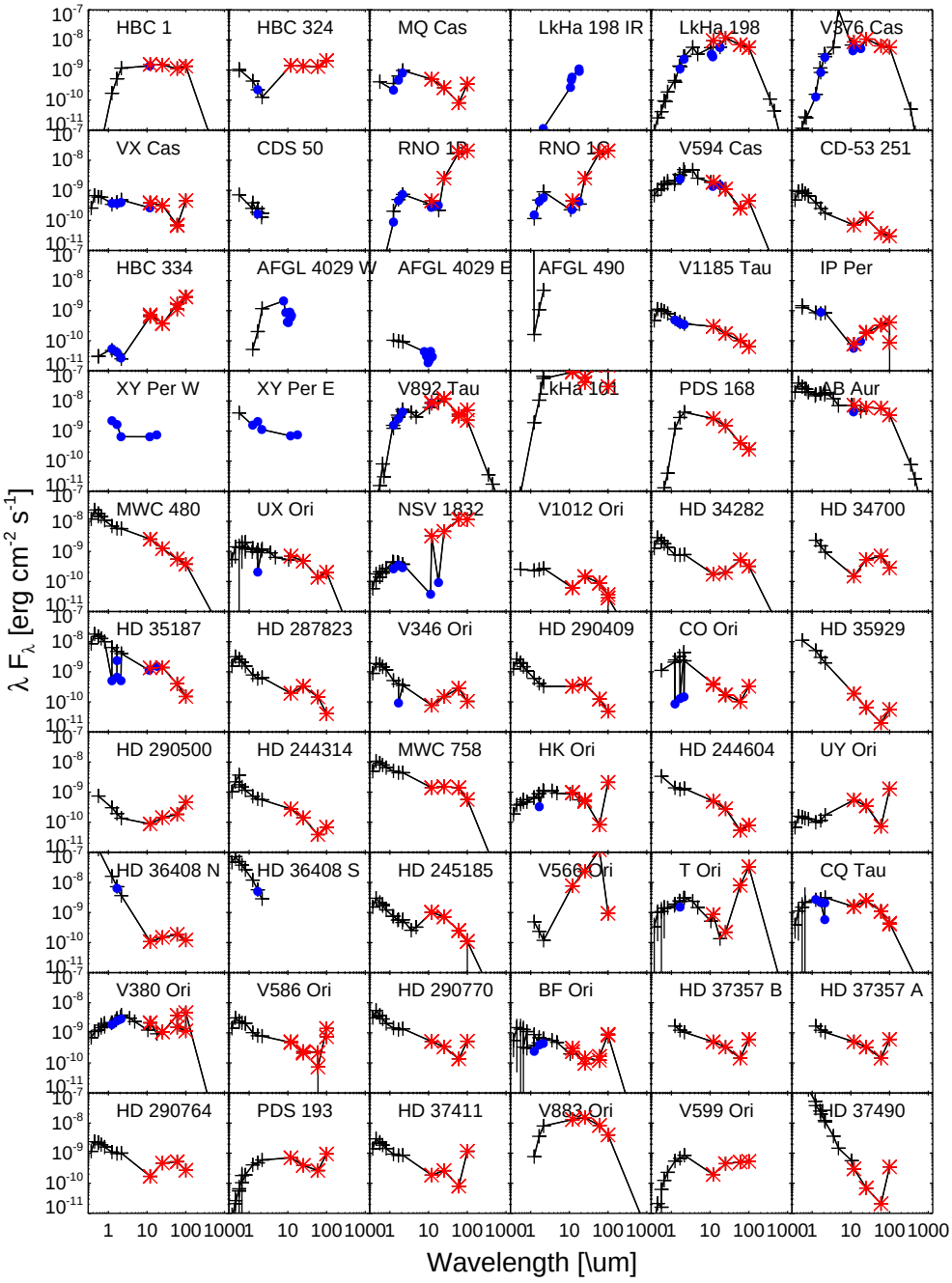

Figure A.1: SEDs for Herbig Ae/Be stars. Points marked with asterisks are drawn from the literature, while points marked with circles are photometry from this work. Red asterisks are for IRAS fluxes, either from the IRAS PSC or from Weaver (1992).

(Continued on following pages)

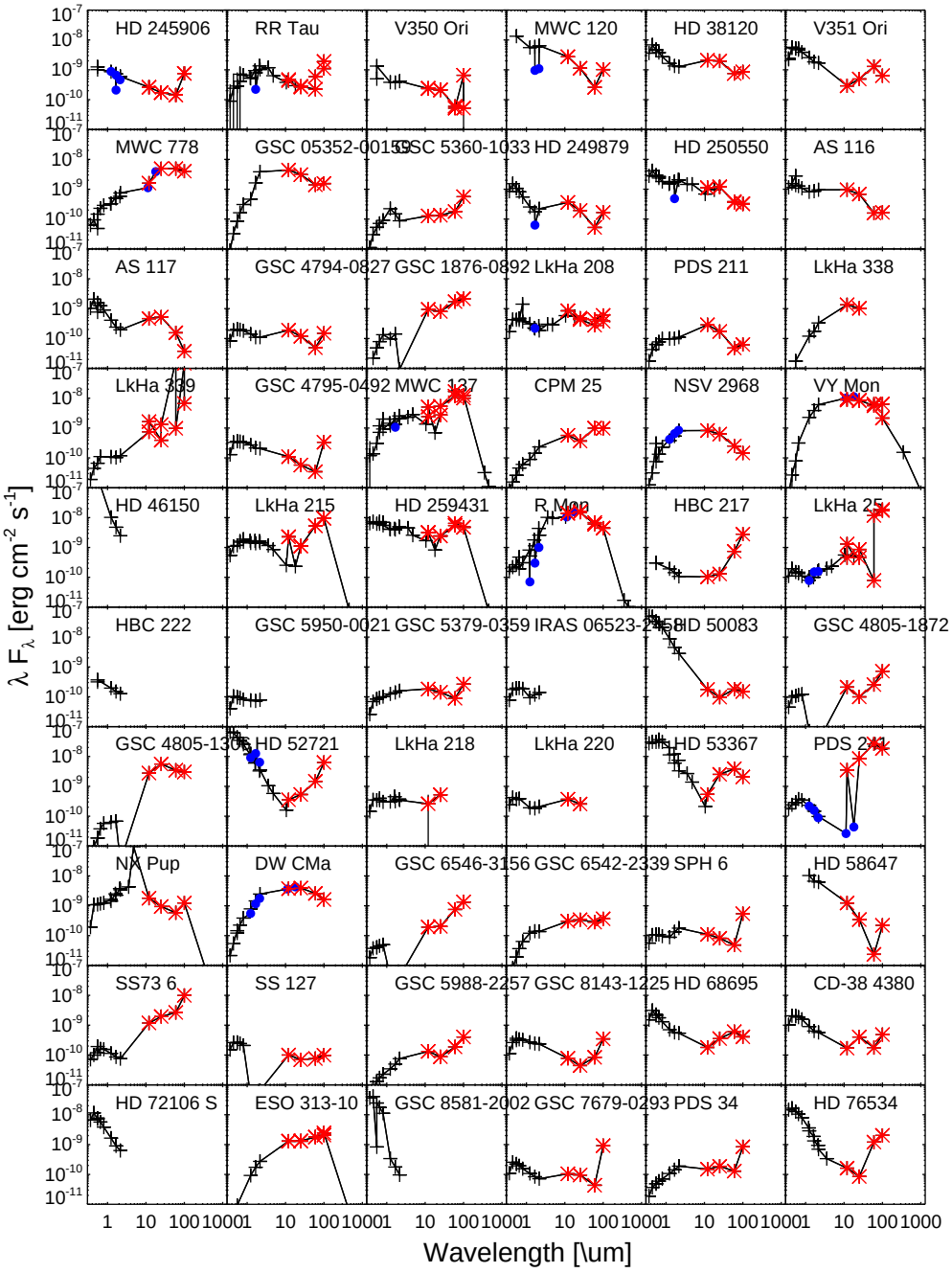

Figure A.2: SEDs for Herbig Ae/Be stars. (Continued on following pages)

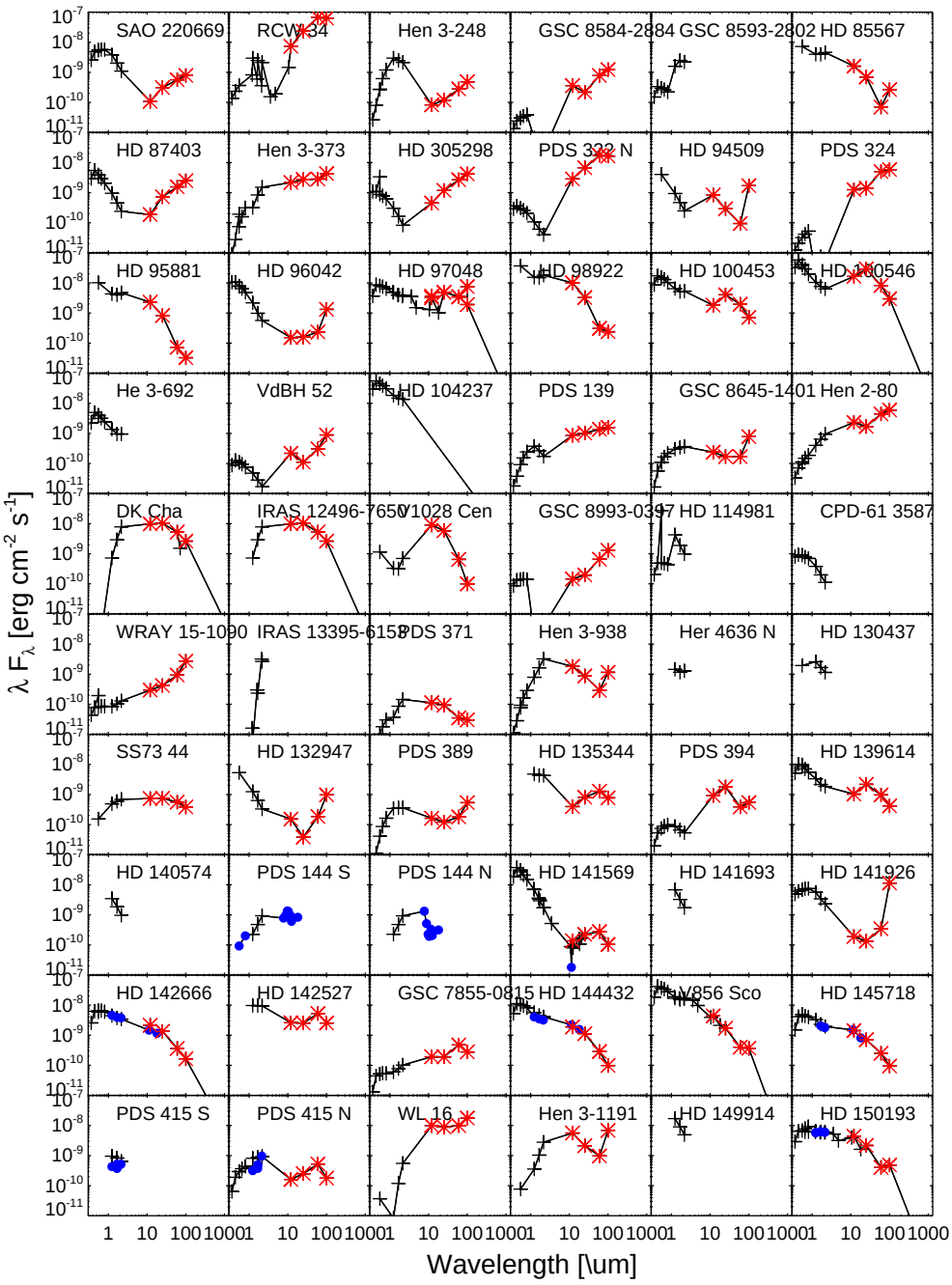

Figure A.3: SEDs for Herbig Ae/Be stars. (Continued on following pages)

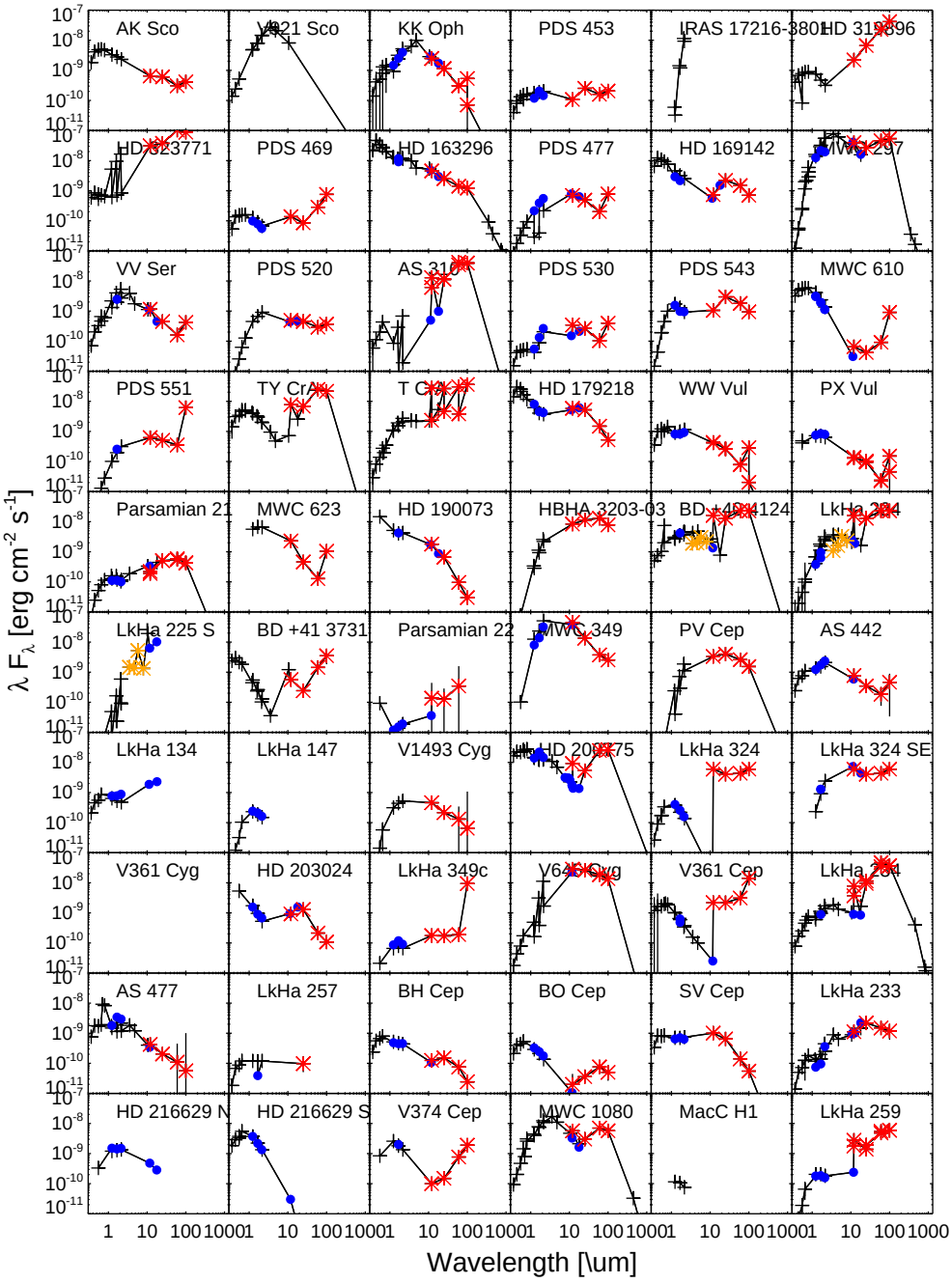

Figure A.4: SEDs for Herbig Ae/Be stars.

Appendix B

Observations Log

I present here a log of the observations for each source.

Table B.1: Observing Log

Name	Date	Instrument	Filter	Exp. Time
HBC 1	2004-07-26	LWS	SiC	238
	2004-09-07	IRCAL	H	480
	...	...	K_s	2
HBC 324	...	...	H	980
MQ Cas	2005-11-21	...	K_s	80
	...	...	J	320
	...	...	H	2000
LkHa 198	2003-07-23	...	H	960
	...	...	K_s	960
	...	...	J	960
	2004-07-25	LWS	10.7	475
	2004-07-26	...	SiC	285
	2004-08-28	...	17.65	380
	2004-10-31	IRCAL	K_s	720
	...	...	H	280
	2005-07-27	...	H	80
	...	...	K_s	152
	2005-12-16	MICHELLE	N'	235
	...	...	Qa	163
V376 Cas	2004-07-26	LWS	SiC	285
	2004-10-31	IRCAL	K_s	160
	...	...	H	160
	...	...	J	600
	2005-07-27	...	H	570
	...	...	J	240
	...	...	K_s	400
VX Cas	2004-07-26	LWS	SiC	285
	2004-09-07	IRCAL	H	1200
	...	...	K_s	320
	...	...	J	120
CDS 50	2005-11-23	...	H	1040
RNO 1B	2004-08-27	LWS	SiC	570
	2004-08-28	...	17.65	285
RNO 1	2004-09-08	IRCAL	H	80
	...	...	K_s	11
V594 Cas	2004-08-28	LWS	17.65	190
	...	...	SiC	190
	2004-09-07	IRCAL	H	800

Continued on next page...

Observing log – continued.

Name	Date	Instrument	Filter	Exp. Time
LkHa 201	2005-07-28	...	H	720
HBC 334	2005-11-22	...	J	120
	...	...	H	720
	...	...	K_s	180
LkHa 264	2005-11-21	...	K_s	320
	...	...	H	1120
	...	...	J	180
AFGL 4029 W	2005-12-16	MICHELLE	10.3μm	88
	...	...	11.6μm	104
	...	...	12.5μm	94
	...	...	7.9μm	94
	...	...	8.8μm	104
	...	...	9.7μm	88
	...	...	N'	376
	...	...	Qa	326
V1185 Tau	2004-09-08	IRCAL	K_s	20
	...	...	J	20
	...	...	H	800
IP Per	2004-08-28	LWS	17.65	285
	...	...	SiC	95
	2004-09-07	IRCAL	H	840
V892 Tau	2004-08-27	LWS	SiC	285
	2005-11-22	IRCAL	H	840
	...	...	K_s	94
	...	...	J	45
LkHa 101	2003-11-02	...	H	480
	...	...	K_s	240
	...	...	J	200
GG Tau	2005-11-21	...	J	110
	...	...	K_s	1160
AB Aur	2002-11-21	...	H	1640
	2004-08-27	LWS	SiC	285
MWC 480	2002-11-25	IRCAL	H	312
UX Ori	2005-10-18	...	H	560
NSV 1832	2005-11-21	...	K_s	240
	...	...	J	150
	...	...	H	1680
	2005-12-16	MICHELLE	N'	282
	...	...	Qa	218
V346 Ori	2005-10-18	IRCAL	H	480
CO Ori	2004-11-01	...	K_s	180
	2005-10-18	...	H	80
	...	...	J	80
	...	...	K_s	80
MWC 758	2004-12-01	...	H	320
HK Ori	...	...	H	710
T Ori	2004-10-11	...	H	420
CQ Tau	2005-10-17	...	K_s	80
	2005-11-21	...	K_s	80
	...	...	H	848
	...	...	J	40
V380 Ori	...	...	H	1264
	...	...	K_s	216
	...	...	J	35
BF Ori	...	...	H	880
	...	...	K_s	60
	...	...	J	40
HD 245906	2005-10-18	...	H	720
	2005-11-21	...	J	40
	...	...	K_s	80
	...	...	H	620
RR Tau	2005-10-18	...	H	640
MWC 120	...	...	K_s	160
	...	...	H	840
MWC 778	2005-11-23	...	H	640
	...	...	K_s	390
	...	...	J	720
	2005-12-16	MICHELLE	N'	235
	...	...	Qa	218

Continued on next page...

Observing log – continued.

Name	Date	Instrument	Filter	Exp. Time
HD 249879	2005-10-18	IRCAL	H	480
HD 250550	...	...	H	560
LkHa 208	2004-12-01	...	H	1280
	2005-11-21	...	H	800
PDS 211	2005-11-23	...	H	1200
	...	...	K_s	120
	...	...	J	120
MWC 137	2004-10-11	...	H	1040
NSV 2968	2005-11-21	...	H	800
	...	...	K_s	50
	...	...	J	40
VY Mon	2003-11-18	...	H	970
	2005-11-22	...	H	1830
	...	...	J	480
	2005-12-16	MICHELLE	N'	141
	...	...	Qa	109
LkHa 215	2004-12-01	IRCAL	H	1040
HD 259431	2002-11-21	...	H	1985
R Mon	2005-10-18	...	H	240
	...	...	J	240
	...	...	K_s	240
	2005-12-16	MICHELLE	N'	235
	...	...	Qa	163
LkHa 25	2003-11-18	IRCAL	H	1200
	...	...	K_s	240
	...	...	J	240
HD 52721	...	...	K_s	80
	...	...	J	80
	...	...	H	920
Z CMa	2005-11-21	...	K_s	48
	...	...	J	6
	...	...	H	632
PDS 241	...	...	H	960
	...	...	J	960
	...	...	K_s	1200
	2005-12-16	MICHELLE	N'	94
	...	...	Qa	27
DW CMa	2005-11-21	IRCAL	K_s	32
	...	...	J	20
	...	...	H	952
	2005-12-16	MICHELLE	N'	141
	...	...	Qa	109
CU Cnc	2003-11-05	IRCAL	K_s	40
	2003-11-18	...	K_s	130
	2005-11-22	...	K_s	150
	...	...	J	100
	...	...	H	100
HD 141569	2003-06-17	...	H	1560
	2003-07-21	...	H	496
HD 142666	2003-07-23	...	H	488
	2004-07-05	...	K_s	320
	...	...	H	80
	...	...	J	800
	2005-06-30	MICHELLE	N'	376
	...	...	Qa	218
HD 144432	2003-07-22	IRCAL	H	522
	2004-07-04	...	J	920
	...	...	K_s	40
	...	...	H	400
	2005-07-01	MICHELLE	N'	235
	...	...	Qa	218
HD 145718	2005-06-30	...	N'	376
	...	...	Qa	218
	2005-07-27	IRCAL	K_s	40
	...	...	H	600
HD 150193	2004-07-06	...	H	640
	...	...	K_s	40
	...	...	J	40

Continued on next page...

Observing log – continued.

Name	Date	Instrument	Filter	Exp. Time
KK Oph	2004-07-05	...	J	400
	...	...	H	392
	...	...	K_s	120
	2005-06-30	MICHELLE	N'	376
	...	...	Qa	218
PDS 453	2005-07-29	IRCAL	H	1200
	...	...	J	120
	...	...	K_s	120
	2006-07-10	...	H	1200
PDS 465	2004-09-07	...	H	880
	...	...	K_s	640
	...	...	J	560
PDS 469	2004-09-08	...	K_s	120
	...	...	J	63
	...	...	H	800
HD 163296	2004-07-06	...	H	360
	2005-07-01	MICHELLE	N'	235
	...	...	Qa	218
	2005-07-29	IRCAL	H	1040
PDS 477	...	...	H	990
	...	...	K_s	90
	...	...	J	90
LkHa 118	2005-07-28	...	H	440
MWC 922	2004-07-05	...	H	800
	...	...	J	780
	...	...	K_s	400
HD 169142	2004-09-08	...	H	640
	...	...	J	640
	2005-06-30	MICHELLE	N'	376
	...	...	Qa	218
MWC 297	2004-09-08	IRCAL	H	400
	...	...	K_s	120
	...	...	J	160
	2005-07-01	MICHELLE	N'	82
	...	...	Qa	54
VV Ser	2004-07-06	IRCAL	H	320
MWC 300	...	...	H	960
	2005-07-01	MICHELLE	N'	94
	...	...	Qa	54
PDS 520	2004-09-08	IRCAL	J	61
	...	...	K_s	120
	...	...	H	485
	2005-07-01	MICHELLE	N'	235
	...	...	Qa	218
AS 310	2003-07-23	IRCAL	J	240
	2005-06-30	MICHELLE	N'	141
	...	...	Qa	218
PDS 530	2005-07-29	IRCAL	J	1200
	...	...	H	1440
	...	...	K_s	960
PDS 543	2004-11-01	...	K_s	640
	...	...	J	160
	...	...	H	1600
MWC 610	2004-09-07	...	J	40
	...	...	K_s	40
	...	...	H	680
	2005-07-01	MICHELLE	N'	235
PDS 551	2006-07-10	IRCAL	H	960
HD 179218	2003-07-21	...	H	510
	2004-07-05	...	H	440
	...	...	J	440
	...	...	K_s	200
	2005-07-01	MICHELLE	N'	235
	...	...	Qa	218
WW Vul	2004-07-05	IRCAL	H	960
	...	...	J	80
	...	...	K_s	500
PX Vul	2004-09-08	...	H	864

Continued on next page...

Observing log – continued.

Name	Date	Instrument	Filter	Exp. Time
	...	...	K_s	79
	...	...	J	75
RNO 110	2005-07-29	...	H	960
	2005-10-17	...	K_s	160
	...	...	J	480
	...	...	H	1540
Parsamian 21	2004-07-04	...	J	1440
	...	...	H	1440
	...	...	K_s	1440
	2004-07-26	LWS	SiC	285
HD 190073	2004-09-08	IRCAL	H	800
	2005-07-01	MICHELLE	N'	235
	...	...	Qa	218
HBHA 3203-03	2006-07-10	IRCAL	H	880
	...	...	K_s	1100
	...	...	J	1020
BD +40 4124	2004-07-06	...	H	1520
	2004-08-27	LWS	SiC	285
	2005-11-23	IRCAL	H	2304
	...	...	K_s	48
	...	...	J	48
LkHa 224	2003-11-05	...	H	960
	2004-07-05	...	H	800
	...	...	J	480
	2004-07-25	LWS	10.7	760
	...	...	12.5	190
	2005-11-23	IRCAL	K_s	80
	...	...	J	40
V1515 Cyg	2004-09-08	...	H	760
BD +41 3731	2004-10-30	...	H	1600
Parsamian 22	2004-07-04	...	K_s	960
	...	...	H	960
	...	...	J	960
	2004-07-26	LWS	SiC	285
MWC 349	...	...	SiC	190
	2004-09-07	IRCAL	H	555
	...	...	K_s	49
	...	...	J	50
AS 442	2004-08-27	LWS	SiC	285
	2004-09-07	IRCAL	H	840
	...	...	K_s	21
	...	...	J	21
LkHa 134	2004-10-31	...	K_s	150
	...	...	J	155
	...	...	H	920
	2005-06-30	MICHELLE	N'	376
	...	...	Qa	218
LkHa 147	2005-07-27	IRCAL	K_s	80
	...	...	J	100
	...	...	H	720
V1057 Cyg	2005-07-29	...	H	800
	2005-10-18	...	J	40
	...	...	K_s	80
LKHa 120	2004-07-05	...	H	200
	...	...	J	280
	...	...	K_s	100
LkHa 120	2005-12-16	MICHELLE	N'	235
	...	...	Qa	163
HD 200775	2003-11-18	IRCAL	J	176
	...	...	K_s	176
	...	...	H	984
	2004-07-26	LWS	SiC	238
	2004-08-28	...	17.65	285
	2005-07-01	MICHELLE	10.3μm	221
	...	...	11.6μm	259
	...	...	12.5μm	235
	...	...	7.9μm	235
	...	...	8.8μm	259
	...	...	9.7μm	221

Continued on next page...

Observing log – continued.

Name	Date	Instrument	Filter	Exp. Time
LkHa 324	2004-07-06	IRCAL	K_s	160
	...	...	J	160
	...	...	H	880
	2004-07-26	LWS	SiC	380
HD 203024	2004-10-31	IRCAL	K_s	80
	...	...	J	80
	...	...	H	1600
	2005-06-30	MICHELLE	N'	376
	...	...	Qa	218
LkHa 349c	2005-07-28	IRCAL	H	240
	...	...	J	240
	...	...	K_s	240
V645 Cyg	2004-07-04	...	J	480
	...	...	H	480
	...	...	K_s	520
	2004-07-26	LWS	SiC	285
V361 Cep	2004-07-05	IRCAL	H	800
	2004-07-26	LWS	SiC	285
BD +65 1638	2004-10-31	IRCAL	H	800
LkHa 234	2002-08-03	...	J	1980
	...	...	K_s	1960
	...	...	H	1960
	2004-07-26	LWS	SiC	285
	2004-08-28	...	17.65	285
	2005-07-29	IRCAL	H	1440
AS 477	2003-11-05	...	H	440
	2003-11-18	...	H	90
	...	...	J	160
	...	...	K_s	128
	2004-07-26	LWS	SiC	380
LkHa 257	2005-07-28	IRCAL	H	960
BH Cep	2004-08-27	LWS	SiC	285
	2004-09-07	IRCAL	H	920
	...	...	J	80
	...	...	K_s	110
BO Cep	2004-08-27	LWS	SiC	285
	2004-09-07	IRCAL	H	840
	...	...	J	80
	...	...	K_s	80
SV Cep	2004-09-08	...	J	60
	...	...	K_s	65
	...	...	H	800
LkHa 233	2003-07-23	...	H	1680
	...	...	K_s	1350
	...	...	J	1440
	2004-07-25	LWS	10.7	475
	...	...	11.7	360
	...	...	12.5	475
	2005-12-16	MICHELLE	N'	235
	...	...	Qa	218
V374 Cep	2004-09-08	IRCAL	H	880
MWC 1080	2003-11-18	...	H	1240
	...	...	J	1240
	...	...	K_s	1270
	2004-07-26	LWS	SiC	285
	2004-08-28	...	17.65	380
BM And	2005-11-21	IRCAL	J	320
	...	...	K_s	400
	...	...	H	1440
LkHa 259	2004-08-27	LWS	SiC	285
	2004-09-07	IRCAL	H	280
	...	...	K_s	320
	...	...	J	70

Appendix C

Point Source Photometry

While the primary focus of this work was on extended circumstellar dust, it also provided a wealth of data on the unresolved point sources in each of our fields. I present here absolute photometry of the Herbig Ae/Be stars observed, and relative photometry and astrometry for nearby point sources.

For details of the data reduction, see Chapters 3 and 4. Photometric errors for the IRCAL data are conservatively 5-10%.

In Table C.3, blank spaces for a given source and filter indicate that source was not observed using that filter, while dashes indicate that the source was observed using that filter, but was not detected. For space reasons, I have condensed the LWS and Michelle results into one table. The $\Delta 11$ μm column gives either the LWS SiC or Michelle N' magnitude difference, while $\Delta 18$ μm gives either LWS 17.65 μm or Michelle Qa. See the observation log for the specifics as to which camera was used for each field.

Table C.1: IRCAL Photometry of HAEBEs

Name	Date	J	H	K_s
HBC 324	2004-09-07		9.79	
MQ Cas	2005-11-21	10.6	8.99	7.64
LkHa 198	2005-07-27		8.06	6.51
V376 Cas	2005-07-27	11.2	8.36	6.36
VX Cas	2004-09-07	10.0	9.26	8.41
CDS 50	2005-11-23		10.1	
RNO 1C	2004-09-08	11.	9.07	8.02
V594 Cas	2004-09-07		7.24	
HBC 334	2005-11-22	12.1	11.6	11.3
V1185 Tau	2004-09-08	9.73	9.21	8.55
IP Per	2004-09-07		8.29	
XY Per E	2002-11-25	8.46	7.37	7.27
V892 Tau	2005-11-22	8.47	7.13	5.82

Continued on next page...

Table C.1 – Continued.

Name	Date	J	H	K_s
UX Ori	2005-10-18		9.87	
NSV 1832	2005-11-21	10.4	9.29	8.75
HD 35187 N	2004-10-11		7.23	
HD 35187 N	2005-10-18	9.70	8.61	8.14
V346 Ori	2005-10-18		10.8	
CO Ori	2005-10-18	11.6	10.4	9.49
HK Ori	2004-12-01		9.37	
HD 36408 S	2004-12-01		6.40	
T Ori	2004-10-11		7.71	
CQ Tau	2005-10-17			7.99
CQ Tau	2005-11-21	7.87	7.33	6.62
V380 Ori	2005-11-21	8.27	7.16	6.24
BF Ori	2005-11-21	10.5	9.15	8.28
HD 245906	2005-10-18		9.85	
HD 245906	2005-11-21	9.09	8.60	8.23
RR Tau	2005-10-18		9.79	
MWC 120	2005-10-18		8.21	7.31
HD 249879	2005-10-18		11.2	
HD 250550	2005-10-18		8.94	
LkHa 208	2005-11-21		9.80	
MWC 137	2004-10-11		8.09	
NSV 2968	2005-11-21	9.90	8.62	7.59
R Mon	2005-10-18	11.8	9.46	7.4
LkHa 25	2003-11-18	11.7	10.2	9.41
HD 52721	2003-11-18	6.55	5.41	5.39
PDS 241	2005-11-21	10.6	10.2	10.0
DW CMa	2005-11-21	9.60	8.00	6.78
HD 142666	2004-07-05	7.29	6.67	5.96
HD 144432	2004-07-04	7.43	6.8	6.14
HD 145718	2005-07-27		7.37	6.77
PDS 415 N	2005-07-28		8.96	
PDS 415 N	2006-07-09	10.2	9.22	7.44
PDS 415 N	2006-07-10		8.91	
HD 150193	2004-07-06	7.05	6.17	5.46
KK Oph	2004-07-05	8.52	7.15	5.90
PDS 453	2005-07-29	11.3	9.97	9.50
PDS 453	2006-07-10		9.87	
PDS 469	2004-09-08	11.5	10.9	10.5
HD 163296	2004-07-06		5.48	
HD 163296	2005-07-29		5.75	
PDS 477	2005-07-29	10.6	9.18	8.05
HD 169142	2004-09-08	7.79	7.32	
MWC 297	2004-09-08	6.21	4.83	4.18
VV Ser	2004-07-06		7.18	
PDS 530	2005-07-29	12.1	10.4	8.85
PDS 543	2004-11-01	8.47	8.18	7.46
MWC 610	2004-09-07	7.71	7.43	7.27
PDS 551	2006-07-10		9.63	
HD 179218	2004-07-05	6.69	6.52	5.84
WW Vul	2004-07-05	9.17	8.38	7.48
PX Vul	2004-09-08	9.26	8.33	7.65
Parsamian 21	2004-07-04	11.3	10.5	9.89
HD 190073	2004-09-08		6.59	
BD +40 4124	2004-07-06		6.60	
LkHa 224	2003-11-05		8.66	
LkHa 224	2004-07-05	10.	8.20	
Parsamian 22	2004-07-04	13.8	12.7	11.7
MWC 349	2004-09-07	6.69	5.31	3.64
AS 442	2004-09-07	8.73	7.56	6.48
LkHa 134	2004-10-31	9.24	8.43	7.54
LkHa 147	2005-07-27	10.5	9.85	9.38
HD 200775	2003-11-18	6.09	4.80	4.49
LkHa 324	2004-07-06	9.94	9.64	9.41
HD 203024	2004-10-31	8.47	8.27	7.83
LkHa 349c	2005-07-28	11.6	10.5	10.
V361 Cep	2004-07-05		8.66	
V361 Cep	2004-10-31		8.94	
LkHa 234	2005-07-29		8.29	

Continued on next page...

Table C.1 – Continued.

Name	Date	J	H	K_s
AS 477	2003-11-18	8.31	6.82	6.23
LkHa 257	2005-07-28		11.7	
BH Cep	2004-09-07	9.74	9.03	8.26
BO Cep	2004-09-07	10.2	9.69	9.29
SV Cep	2004-09-08	9.42	8.53	7.90
LkHa 233	2003-07-23	11.8	10.7	8.51
HD 216629 S	2004-09-07	7.52	7.31	7.08
V374 Cep	2004-09-08		7.40	
LkHa 259	2004-09-07	10.8	9.98	9.41

Table C.2: Mid-Infrared Photometry

Name	Date	Filter	Flux (Jy)	Uncertainty (Jy)
HBC 1	2004-07-26	SiC	5.322	0.22
LkHa 198 IR	2004-07-25	10.7	0.9345	0.042
	2004-07-26	SiC	2.247	0.095
	2004-08-28	17.65	6.404	0.64
	2005-12-16	N'	1.735	0.035
	2005-12-16	Qa	5.412	0.11
LkHa 198	2004-07-25	10.7	11.77	0.53
	2004-07-26	SiC	10.65	0.45
	2004-08-28	17.65	33.70	3.4
	2005-12-16	N'	11.87	0.24
	2005-12-16	Qa	33.70	0.70
V376 Cas	2004-07-26	SiC	24.87	1.1
	2006-07-05	N'	16.29	1.6
	2006-07-05	Qa	30.76	3.1
VX Cas	2004-07-26	SiC	1.024	0.043
RNO 1B	2004-08-27	SiC	1.061	0.021
	2004-08-28	17.65	1.869	0.19
RNO 1C	2004-08-27	SiC	0.8931	0.018
	2004-08-28	17.65	2.469	0.25
V594 Cas	2004-08-28	17.65	8.816	0.88
	2004-08-28	SiC	5.282	0.11
AFGL 4029 W	2005-12-16	10.3 μm	1.381	0.028
	2005-12-16	11.6 μm	2.283	0.046
	2005-12-16	12.5 μm	2.835	0.057
	2005-12-16	7.9 μm	5.420	0.11
	2005-12-16	8.8 μm	2.539	0.051
	2005-12-16	9.7 μm	1.353	0.027
	2005-12-16	N'	3.356	0.067
AFGL 4029 E	2005-12-16	10.3 μm	0.07504	0.0015
	2005-12-16	11.6 μm	0.1090	0.0022
	2005-12-16	12.5 μm	0.1227	0.0025
	2005-12-16	7.9 μm	0.1127	0.0023
	2005-12-16	8.8 μm	0.09006	0.0018
	2005-12-16	9.7 μm	0.05994	0.0012
	2005-12-16	N'	0.1666	0.0033
IP Per	2004-08-28	17.65	0.5619	0.056
	2004-08-28	SiC	0.2201	0.0044
XY Per E	2004-08-27	SiC	2.690	0.054
	2004-08-28	17.65	4.411	0.44
XY Per W	2004-08-27	SiC	2.518	0.050
	2004-08-28	17.65	4.392	0.44
V892 Tau	2004-08-27	SiC	33.10	0.66
AB Aur	2004-08-27	SiC	16.91	0.34
NSV 1832	2005-12-16	N'	0.4082	0.0082
	2005-12-16	Qa	4.621	0.096
HD 35187 N	2005-12-16	N'	4.234	0.085
	2005-12-16	Qa	9.097	0.19
MWC 778	2005-12-16	N'	4.210	0.084
	2005-12-16	Qa	23.33	0.48
VY Mon	2005-12-16	N'	37.73	0.75
	2005-12-16	Qa	67.63	1.4

Continued on next page..

Table C.2 – Continued.

Name	Date	Filter	Flux (Jy)	Uncertainty (Jy)
R Mon	2005-12-16	N'	39.63	0.79
	2005-12-16	Qa	92.61	1.9
PDS 241	2005-12-16	N'	0.09850	0.0020
	2005-12-16	Qa	0.2612	0.0054
DW CMa	2005-12-16	N'	13.66	0.27
	2005-12-16	Qa	25.69	0.53
PDS 144 N	2004-08-28	11.7	1.274	0.046
	2005-06-30	N'	0.9881	0.028
	2005-06-30	Qa	1.892	0.19
	2005-07-01	10.3 μm	0.6643	0.013
	2005-07-01	11.6 μm	1.245	0.12
	2005-07-01	12.5 μm	0.8501	0.017
	2005-07-01	7.9 μm	3.403	0.068
	2005-07-01	8.8 μm	1.508	0.030
	2005-07-01	9.7 μm	0.7266	0.015
PDS 144 S	2004-08-28	11.7	3.552	0.13
	2005-06-30	N'	3.674	0.10
	2005-06-30	Qa	4.992	0.50
	2005-07-01	10.3 μm	4.460	0.089
	2005-07-01	11.6 μm	3.362	0.32
	2005-07-01	12.5 μm	2.519	0.050
	2005-07-01	7.9 μm	2.006	0.040
	2005-07-01	8.8 μm	2.879	0.058
	2005-07-01	9.7 μm	4.349	0.087
HD 141569 C	2006-07-05	N'	0.002694	0.00027
HD 141569 B	2006-07-05	N'	0.005469	0.00055
HD 141569	2006-07-05	N'	0.06782	0.0068
HD 142666	2005-06-30	N'	5.521	0.16
	2005-06-30	Qa	6.965	0.70
HD 144432	2005-07-01	N'	8.335	0.72
	2005-07-01	Qa	9.328	0.93
HD 145718	2005-06-30	N'	5.631	0.16
	2005-06-30	Qa	4.901	0.49
KK Oph	2005-06-30	N'	10.90	0.31
	2005-06-30	Qa	10.39	1.0
KK Oph B	2005-06-30	N'	4.544	0.13
	2005-06-30	Qa	4.173	0.42
HD 163296	2005-07-01	N'	18.01	1.6
	2005-07-01	Qa	17.80	1.8
PDS 477	2006-07-05	N'	2.936	0.29
	2006-07-05	Qa	3.800	0.38
HD 169142	2005-06-30	N'	2.112	0.059
	2005-06-30	Qa	9.141	0.91
MWC 297	2005-07-01	N'	154.1	13.
	2005-07-01	Qa	96.66	9.7
VV Ser	2006-07-05	N'	4.241	0.42
	2006-07-05	Qa	2.715	0.27
MWC 300	2005-07-01	N'	79.79	6.9
	2005-07-01	Qa	96.61	9.7
PDS 520	2005-07-01	N'	1.654	0.14
	2005-07-01	Qa	2.799	0.28
AS 310	2005-06-30	N'	1.874	0.053
	2005-06-30	Qa	5.888	0.59
PDS 530	2006-07-05	N'	0.5697	0.057
	2006-07-05	Qa	1.279	0.13
MWC 610	2005-07-01	N'	0.1159	0.010
HD 179218	2005-07-01	N'	19.53	1.7
	2005-07-01	Qa	36.75	3.7
Parsamian 21	2004-07-26	SiC	1.299	0.055
HD 190073	2005-07-01	N'	6.524	0.56
	2005-07-01	Qa	5.213	0.52
BD +40 4124	2004-08-27	SiC	5.257	0.11
LkHa 224	2004-07-25	10.7	8.905	0.40
	2004-07-25	12.5	7.925	0.22
LkHa 225 N	2004-07-25	11.7	3.758	0.14
	2004-08-28	17.65	8.843	0.88
LkHa 225 S	2004-07-25	11.7	24.41	0.92
	2004-08-28	17.65	60.30	6.0
Parsamian 22	2004-07-26	SiC	0.1412	0.0060

Continued on next page..

Table C.2 – Continued.

Name	Date	Filter	Flux (Jy)	Uncertainty (Jy)
MWC 349	2004-07-26	SiC	149.4	6.3
AS 442	2004-08-27	SiC	2.295	0.046
LkHa 134	2005-06-30	N'	7.008	0.20
	2005-06-30	Qa	13.74	1.4
LkHa 120	2005-12-16	N'	1.111	0.022
	2005-12-16	Qa	2.251	0.047
HD 200775	2004-07-26	SiC	6.999	0.30
	2004-08-28	17.65	8.045	0.80
	2005-07-01	10.3 μm	8.980	0.18
	2005-07-01	11.6 μm	6.614	0.63
	2005-07-01	12.5 μm	5.725	0.11
	2005-07-01	7.9 μm	8.096	0.16
	2005-07-01	8.8 μm	8.926	0.18
	2005-07-01	9.7 μm	9.758	0.20
LkHa 324	2004-07-26	SiC	0.006925	0.00029
HD 203024	2005-06-30	N'	3.539	0.100
	2005-06-30	Qa	9.410	0.94
V645 Cyg	2004-07-26	SiC	88.65	3.7
V361 Cep	2004-07-26	SiC	0.09811	0.0041
LkHa 234	2004-07-26	SiC	3.517	0.15
	2004-08-28	17.65	4.997	0.50
AS 477	2004-07-26	SiC	1.347	0.057
BH Cep	2004-08-27	SiC	0.4178	0.0084
BO Cep	2004-08-27	SiC	0.04153	0.00083
LkHa 233	2004-07-25	10.7	3.422	0.15
	2004-07-25	11.7	4.055	0.15
	2004-07-25	12.5	4.265	0.12
	2005-12-16	N'	3.731	0.075
	2005-12-16	Qa	13.32	0.28
HD 216629 N	2004-08-28	17.65	1.689	0.17
	2004-08-28	SiC	1.876	0.038
HD 216629 S	2004-08-28	17.65	0.02517	0.0025
	2004-08-28	SiC	0.1177	0.0024
MWC 1080	2004-07-26	SiC	12.78	0.54
	2004-08-28	17.65	9.655	0.97
LkHa 259	2004-08-27	SiC	0.9344	0.019

Table C.3: Photometry and Astrometry of Companions

Primary	Secondary	ρ	θ	ΔJ	ΔH	ΔK_s	Δ[11]	Δ[18]
HBC 324	HBC 324 Ba	8.03	353.3		5.29			
	HBC 324 Bb	7.33	351.7		8.91			
	HBC 324 C	12.68	12.9		6.33			
LkHa 198	LkHa 198 IR	5.74	6.1		6.27	5.76	2.09	1.99
VX Cas	VX Cas B	5.34	164.6	3.57	4.15	5.51	-	
	VX Cas C	5.04	343.9	7.13	7.87	8.88	-	
CDS 50	CDS 50 B	2.80	92.6		5.76			
RNO 1B	RNO 1C	6.19	220.8	-0.59	0.07	0.28	0.19	-0.30
LkHa 201	LkHa 201 B	2.34	326.2		7.46			
HBC 334	HBC 334 B	3.90	306.4	3.00	2.39	1.92		
XY Per E	XY Per W	1.29	256.1	-0.37	0.25	0.60	0.07	0.00
V892 Tau	V892 Tau NE	4.07	23.7	3.85	3.59	3.79	7.95	
NSV 1832	NSV 1832 B	0.77	28.7	3.97	2.60	1.84	-	-
	NSV 1832 C	6.91	195.0	3.75	3.19	3.01	-	-
HD 35187 N	HD 35187 S	1.37	193.1	0.55	0.58	0.99	4.17	-
CO Ori	CO Ori B	1.90	274.9	4.03	3.85	4.25		
HK Ori	HK Ori B	0.34	36.5		1.66			
	HK Ori C	3.89	353.1		5.47			
HD 36408 N	HD 36408 S	9.71	141.1		0.25			
CQ Tau	CQ Tau B	2.10	56.4	7.51	7.02	8.19		
BF Ori	BF Ori B	2.05	47.5	2.82	3.36	4.09		
MWC 137	MWC 137 B	6.12	357.8		6.19			
	MWC 137 C	3.31	91.7		6.50			
	MWC 137 D	4.16	248.9		6.69			

Continued on next page...

Table C.3 – Continued.

Primary	Secondary	ρ	θ	ΔJ	ΔH	ΔK_s	Δ[11]	Δ[18]
	MWC 137 E	4.67	198.9		6.72			
	MWC 137 F	4.65	272.1		7.60			
LkHa 25	LkHa 25 B	10.59	356.8	0.86	1.08	1.91		
HD 52721	HD 52721 B	0.65	196.6	1.53	1.54	1.51		
PDS 241	PDS 241 C1	3.43	168.7	5.00	3.71	2.82	-	-
	PDS 241 C10	4.07	260.4	8.44	7.86	5.56	-	-
	PDS 241 C11	1.97	133.5	4.95	5.06	5.06	-	-
	PDS 241 C12	1.98	74.7	5.04	4.92	5.11	-	-
	PDS 241 C13	3.63	290.0	5.75	5.41	4.39	-	-
	PDS 241 C14	2.39	25.4	5.71	4.67	4.89	-	-
	PDS 241 C15	4.33	55.0	5.21	4.90	4.86	-	-
	PDS 241 C16	4.44	323.3	6.39	5.11	5.27	-	-
	PDS 241 C17	4.76	315.6	5.11	4.84	4.96	-	-
	PDS 241 C18	5.18	313.5	5.24	4.36	4.42	-	-
	PDS 241 C19	5.70	306.7	6.98	5.96	6.09	-	-
	PDS 241 C2	2.80	86.0	3.96	3.36	3.48	-	-
	PDS 241 C20	6.16	308.6	6.39	5.37	5.44	-	-
	PDS 241 C21	8.62	342.9	6.15	5.33	5.10	-	-
	PDS 241 C22	8.57	339.7	6.62	6.15	6.31	-	-
	PDS 241 C23	6.65	12.8	7.50	6.28	7.05	-	-
	PDS 241 C24	7.57	25.3	7.81	6.56	6.28	-	-
	PDS 241 C25	6.69	139.7	7.79	6.93	7.00	-	-
	PDS 241 C26	7.01	137.4	9.48	6.54	7.08	-	-
	PDS 241 C27	4.79	79.4	5.79	6.46	5.89	-	-
	PDS 241 C28	5.77	56.8	5.94	5.98	6.01	-	-
	PDS 241 C29	6.81	25.3	11.38	6.91	9.25	-	-
	PDS 241 C3	10.22	198.1	7.63	5.96	5.73	-	-
	PDS 241 C30	8.96	180.8	7.69	6.79	6.54	-	-
	PDS 241 C31	3.78	135.1	8.57	7.86	7.12	-	-
	PDS 241 C32	4.35	134.3	8.69	9.21	7.29	-	-
	PDS 241 C33	3.25	240.2	6.22	6.25	6.22	-	-
	PDS 241 C34	2.45	341.6	5.97	6.61	6.78	-	-
	PDS 241 C35	3.13	3.5	7.10	7.11	7.47	-	-
	PDS 241 C36	2.94	172.4	5.88	5.45	4.93	-	-
	PDS 241 C4	5.70	153.0	7.72	6.73	6.36	-	-
	PDS 241 C5	5.57	126.0	6.76	5.27	5.23	-	-
	PDS 241 C6	3.72	207.0	6.64	5.35	4.80	-	-
	PDS 241 C7	2.83	205.3	5.89	5.36	5.32	-	-
	PDS 241 C8	4.76	227.8	6.85	7.17	5.99	-	-
	PDS 241 C9	5.54	230.1	8.09	7.58	5.98	-	-
HD 144432	HD 144432 B	1.47	4.3	2.11	1.74	2.23	-	-
PDS 415 N	PDS 415 S	4.51	180.6		0.13			
HD 150193	HD 150193 B	1.09	224.8	1.33	0.98	1.12		
KK Oph	KK Oph B	1.61	245.2	1.15	1.17	1.37	0.95	0.99
PDS 453	PDS 453 B	6.01	141.4	2.25	2.06	-		
	PDS 453 C	7.01	3.8	5.47	5.75	-		
PDS 465	PDS 465 B	2.35	195.2	5.35	6.07	7.89		
PDS 469	PDS 469 Ab	1.68	16.4	4.27	4.35	4.63		
	PDS 469 B	7.76	334.0	3.02	2.43	2.30		
HD 163296	HD 163296 B	4.02	224.5		7.01		-	-
	HD 163296 C	6.10	171.7		8.51		-	-
	HD 163296 D	4.38	219.3		10.05		-	-
PDS 477	PDS 477 B	4.55	316.4	2.42	2.66	3.27	-	-
	PDS 477 C	5.82	349.7	4.87	5.82	5.21	-	-
LkHa 118	LkHa 118 B	3.49	209.8		5.85			
	LkHa 118 C	7.54	142.6		5.87			
	LkHa 118 D	8.18	359.0		6.64			
	LkHa 118 E	9.38	151.9		7.42			
	LkHa 118 F	5.64	58.7		7.58			
	LkHa 118 G	7.03	27.3		7.71			
	LkHa 118 H	8.36	18.6		8.02			
	LkHa 118 I	3.15	276.0		8.28			
	LkHa 118 J	6.35	340.0		8.33			
	LkHa 118 K	2.25	287.9		9.09			
MWC 297	MWC 297 B	3.39	313.2	6.68	6.45	6.61	-	-
VV Ser	VV Ser B	2.53	145.4		7.74		-	-
MWC 300	MWC 300 B	5.64	150.2		7.02		-	-
PDS 530	PDS 530 B	8.22	196.2	0.86	1.45	2.72	-	-

Continued on next page...

Table C.3 – Continued.

Primary	Secondary	ρ	θ	ΔJ	ΔH	ΔK_s	Δ[11]	Δ[18]
	PDS 530 C	4.23	172.3	1.57	2.44	3.91	-	-
	PDS 530 D	4.06	124.7	4.15	4.28	6.78	-	-
	PDS 530 SE	2.51	226.3	3.12	3.90	5.10	-	-
MWC 610	MWC 610 B	4.34	41.0	3.45	3.34	3.40	-	
PDS 551	PDS 551 B	7.98	197.8		5.27			
HD 179218	HD 179218 B	2.55	139.9	6.21	5.39	5.31	-	-
	HD 179218 C	3.66	338.7	6.47	6.60	6.56	-	-
WW Vul	WW Vul B	11.13	339.8	3.82	3.88	4.42		
Parsamian 21	Parsamian 21 B	9.54	4.3	5.17	4.77	4.85	-	
LkHa 224	Hil95 S5a	9.07	333.6	-	5.01			
	Hil95 S5b	9.17	332.9	-	5.23			
	Hil95 S6	4.76	293.8	-	6.56			
V1515 Cyg	V1515 Cyg B	5.07	5.4		6.64			
Parsamian 22	Parsamian 22 B	1.46	261.9	1.35	0.50	0.25	1.14	
	Parsamian 22 C	1.86	251.8	3.12	2.45	2.04	-	
MWC 349	MWC 349 B	2.77	286.0	2.11	2.94	4.27	-	
AS 442	AS 442 B	4.75	54.0	4.69	5.36	6.19	-	
LkHa 147	LkHa 147 B	1.63	341.7	3.80	3.09	3.13		
HD 200775	HD 200775 B	2.57	168.3	3.91	3.47	3.95	-	-
	HD 200775 C	5.87	33.7	6.43	5.96	6.30	-	-
LkHa 324	LkHa 324 B	5.68	325.2	4.27	3.87	3.00	-	
HD 203024	HD 203024 B	0.23	149.0	-0.39	0.18	0.19	-	-
LkHa 349c	LkHa 349c B	0.64	42.6	2.80	2.43	2.04		
BD +65 1638	BD +65 1638 B	1.29	99.0		2.76			
	BD +65 1638 C	6.41	347.5		4.65			
	BD +65 1638 D	2.43	278.5		4.82			
LkHa 234	LkHa 234 B	1.89	97.9		4.29		-	-
	LkHa 234 C	8.45	12.3		5.29		-	-
AS 477	AS 477 B	1.31	311.4	4.09	4.27	4.30	3.59	
	AS 477 C	4.71	41.4	2.86	2.98	3.20	4.92	
	AS 477 Da	5.85	206.7	4.27	4.05	4.26	5.60	
	AS 477 Db	6.09	201.6	4.71	4.56	4.76	5.13	
LkHa 257	LkHa 257 B	6.19	344.4		4.76			
BH Cep	BH Cep B	3.26	266.3	5.42	5.61	6.48	-	
	BH Cep C	2.14	103.6	5.83	6.56	6.72	-	
BO Cep	BO Cep B	8.32	26.0	2.38	2.13	2.15	-	
HD 216629 S	HD 216629 C	12.31	347.7	6.64	6.04	7.20	-	-
	HD 216629 D	8.04	10.3	8.25	6.69	6.07	-	-
	HD 216629 N	7.81	328.5	0.98	0.46	-0.11	-3.01	-4.57
BM And	BM And B	0.28	246.8	2.05	1.93	2.35		
	BM And C	1.79	328.4	6.84	7.24	7.72		
LkHa 259	LkHa 259 B	1.36	148.6	5.83	4.12	3.56	-	